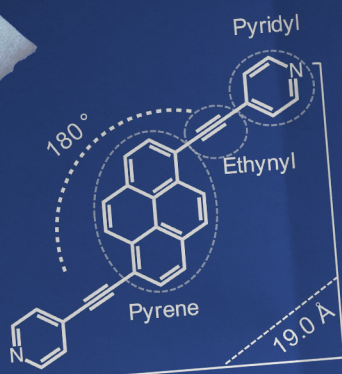


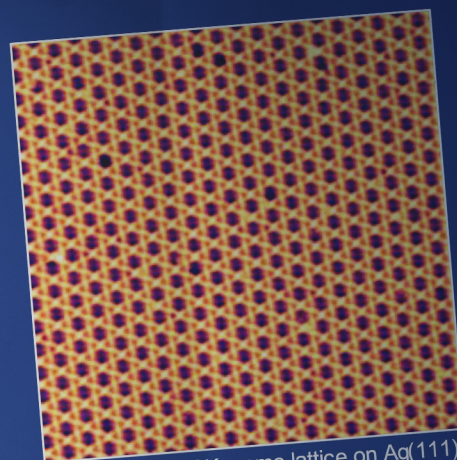
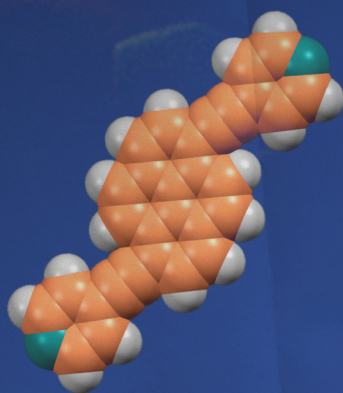
Tailoring Organic Matter

From Molecular Design to Functional Supramolecular Species

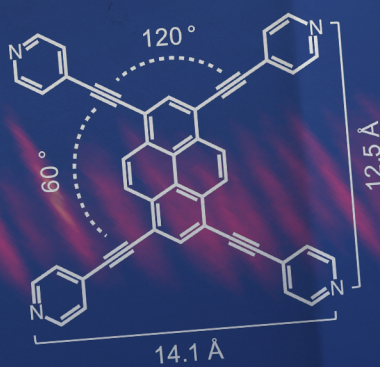
Luka Đorđević



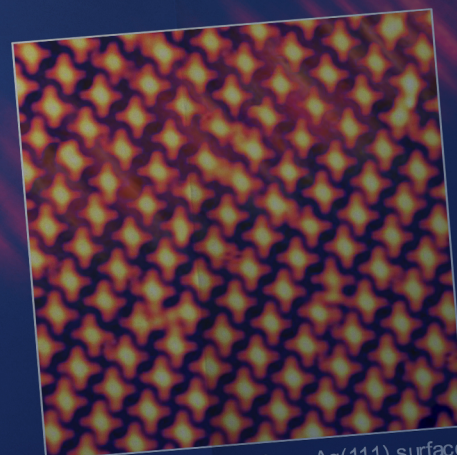
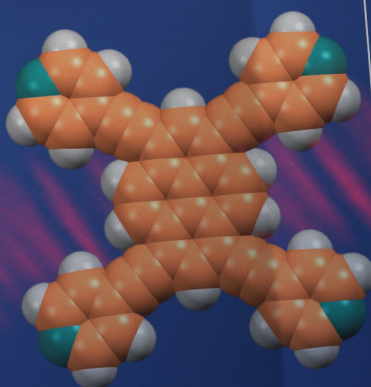
1,6-Bis(4-pyridylethynyl)pyrene
BLD408



STM image of Kagome lattice on Ag(111) surface – overview image (0.1 nA, -0.2 V)



1,3,6,8-Tetrakis(4-pyridylethynyl)pyrene
BLD318



STM image of network on Ag(111) surface – overview image (0.1 nA, -0.2 V)



UNIVERSITÀ DEGLI STUDI DI TRIESTE

**XXVII CICLO DEL DOTTORATO DI RICERCA IN SCIENZE E
TECNOLOGIE CHIMICHE E FARMACEUTICHE**

**TAILORING ORGANIC MATTER:
FROM MOLECULAR DESIGN TO FUNCTIONAL
SUPRAMOLECULAR SPECIES**

Settore scientifico-disciplinare: CHIM/06

Ph.D. Candidate:

LUKA ĐORĐEVIĆ

Ph.D. Program Director:

Prof. MAURO STENER

Advisors:

Prof. MAURIZIO PRATO

Prof. DAVIDE BONIFAZI

“Ever tried. Ever failed. No matter. Try again. Fail again. Fail better.”

Samuel Beckett - *Worstward Ho*, 1983

Acknowledgments

After eight years, one diploma and one (almost) Ph.D. later, my studies in Chemistry at the University of Trieste are approaching the end. This would have not been the same (or possible) without Prof. *Maurizio Prato*, first lecturer and then mentor. My decision to pursue this career most probably dates back to the organic chemistry laboratory course, where I remember Prof. Prato having fun in helping us with the crystallization of aspirin, while reminiscing about his time working in a lab! I will be always thankful for the opportunity he offered me to work in his research group, first at my diploma and then Ph.D. I am equally grateful to Prof. Dr. *Davide Bonifazi*, for his guidance, support and intense discussions about chemistry during these three years. During the course of my thesis I also became aware and most appreciate the responsibilities, as well as the freedom that my two mentors provided me. It was truly a privilege feeling being more of a colleague than a student for my two mentors.

Many thanks go to Dr. *Tomas Marangoni* for many teachings and scientific discussions, and what later on became a friendship. Part of this thesis would have not been possible without his collaboration.

I am grateful to all the collaborators I have encountered during these years and those that I'll continue to work with. In an order based purely on the chapters in this thesis: Dr. *Federica de Leo* for the help with molecular modeling, Dr. *Eleonora Pavoni*, Dr. *Filippo Monti*, Dr. *John Mohanraj* and Dr. *Nicola Armaroli* for the photophysical measurements of the pseudorotaxanes and chiral supramolecular polymers; Dr. *Irene Papagiannouli*, Dr. *Panagiotis Aloukos* and Prof. *Stelios Couris* for the non-linear optics measurements; Dr. *Tanja Miletić* for preparing some molecules of the chiral supramolecular polymers; Dr. *Jenifer Rubio-Magnieto* and Dr. *Mathieu Surin* for the help with the CD measurements; Dr. *Heinz Amenitsch* for the SAXS measurements; Dr. *Nicola Demitri* for the solving the crystal structures; Dr. *Mingjie Liu* and Dr. *Yasuhiro Ishida* for the magnetic alignment experiments; *Francesca Arcudi* for her work and for involving me in the project with carbon nanodots; Dr. *Volker Strauss* and Prof. *Dirk Guldi* for performing photophysical measurements on the porphyrin-carbon nanodots hybrids; *Borja Cirera* and Dr. *David Écija* for the STM experiments on the organometallic pyrenes; *Tobias Kaposi*, Prof. *Willi Auwärter* and Prof. *Johannes Barth* for the STM experiments on the pyridyl-pyrenes; *James Lawrence* and Prof. *Giovanni Costantini* for their work on the PXX system; Dr. *Domenico Milano* for the old and new collaborations and the time spend in the lab. Thanks to all of you for contributing to this thesis!

Many thanks go to the people I have met and worked with in Cambridge, it has been a great year with Dr. *Michel Weïwer*, *Alain Valery*, *Caroline Huet*, Dr. *Joshua Sacher*, Dr. *Florence Wagner* and Dr. *Ed.*

Holson. I will be always indebted for this wonderful opportunity and truly unique place. Thanks also to Dr. *Amedeo Vetere*, without him this period would have not been possible.

Although there were not involved directly in this thesis, special thanks goes to my family and my friends for being always there. Finally, I cannot thank enough *Franci*, the brightest and most gracious person I have ever met, for the time we have spent and will spend together.

Table of Contents

Abbreviations.....	I
Abstract.....	VI
Riassunto	X
1. Introduction.....	1
1.1. Supramolecular Chemistry.....	1
1.2. Some Historical Remarks in Supramolecular Chemistry	2
1.3. Nature of Supramolecular Interactions: a Brief Overview	3
1.3.1. Electrostatic Interactions	4
1.3.2. Hydrogen Bonds.....	4
1.3.3. Halogen Bonds.....	5
1.3.4. π -Interactions	6
1.3.5. Van der Waals Forces.....	7
1.4. Natural and Synthetic Tetrapyrrolic Macrocycles	7
1.4.1. Light Harvesting Antennas.....	7
1.4.2. Porphyrins.....	10
1.5. Overview of the Dissertation	16
2. Donor-Acceptor Supramolecular Assemblies for Non-Linear Optics	20
2.1. Basic Concepts about Donor-Acceptor Systems.....	20
2.1.1. [60]Fullerene	27
2.1.2. Supramolecular Porphyrin-Fullerene Assemblies	30
2.1.3. (Pseudo)rotaxanes	34
2.1.4. Non-Linear Optical Responses.....	36
2.1.5. Aim of the Project.....	37
2.2. Self-Assembly of [60]Fullerene-Porphyrin [n]Pseudorotaxanes	38
2.2.1. Syntheses	38
2.2.2. [n]Pseudorotaxane Self-Assembly.....	43
2.2.3. Molecular Modeling.....	52
2.3. Time Resolved and Steady State Photophysics Investigations of [n]Pseudorotaxanes	55
2.4. Third-Order Non-Linear Optical (NLO) Responses.....	60
2.5. Conclusions	64

3. Solvent Effects in Organic Soft Matter Nanostructuration	67
3.1. Introduction	67
3.1.1. Solvent Forces in Solution	69
3.1.2. Solvent Effects on Surfaces	87
3.1.3. Aim of the Project	101
3.2. Solvent-Dependent Molding of Porphyrin-Based Nanostructures.....	102
3.2.1. Synthesis and Characterization	102
3.2.2. Self-Assembly in Solution	107
3.2.3. Self-Assembly on Surface	111
3.3. Solvent Molding of Organic Morphologies Made of Supramolecular Chiral Polymers.....	114
3.3.1. Syntheses	114
3.3.2. NMR Investigations	116
3.3.3. Molding of the Morphologies	121
3.4. Conclusions	139
4. Carbon-Based Templates for Photo-Active Materials.....	142
4.1. Introduction	142
4.1.1. Deoxyribonucleic Acid	143
4.1.2. Zeolites.....	148
4.1.3. Carbon Nanotubes	149
4.1.4. Carbon NanoDots	154
4.1.5. Aim of the Project.....	155
4.2. Magnetically Aligned Carbon Nanotubes as Templates	158
4.2.1. Synthesis and Characterization	158
4.2.2. Porphyrin Array Formation.....	161
4.2.3. Solubilization of MWCNTs	167
4.2.4. Molecular Modeling.....	170
4.2.5. Magnetic Alignment.....	172
4.3. Towards Porphyrin-Carbon Nanodots Nanohybrids.....	175
4.3.1. Synthesis and Characterization	175
4.3.2. CNDs-Porphyrin Nanohybrids	181
4.4. Conclusion.....	185
5. Patterning Metal Surfaces	188
5.1. Introduction	188
5.1.1. Overview on Scanning Tunneling Microscopy.....	188

Table of Contents

5.1.2.	Self-Assembly on Solid Surfaces.....	192
5.1.3.	Chemical Reactions on Surfaces	206
5.1.4.	Aim of the Project.....	211
5.2.	Syntheses of Pyrene Derivatives.....	212
5.3.	Self-Assembly of Pyrenes on Ag(111)	218
5.4.	Organometallic Architectures from Pyrene Derivatives	227
5.5.	Conclusions	229
5.6.	Perspectives	231
5.6.1.	Self-Assembly of <i>Peri</i> -Xanthenoxanthene.....	231
5.6.2.	Pyridine and Bipyridine Guided Self-Assembly.....	233
5.6.3.	On-Surface Reactions with Porphyrin Precursors.....	237
6.	Experimental Section	244
6.1.	Instruments and Methods	244
6.2.	Specific Instrumentation and Techniques	246
6.2.1.	Diffusion NMR Measurements	246
6.2.2.	Chapter 2.....	247
6.2.3.	Chapter 3.....	252
6.2.4.	Chapter 4.....	252
6.2.5.	Chapter 5.....	254
6.3.	Synthetic Procedures.....	255
6.4.	Appendix	341
6.4.1.	Crystal Structures	341
6.4.2.	Selected Characterizations	347
	Bibliography.....	365
	Curriculum Vitae	410
	Publications.....	411

Abbreviations

°C	Centigrade degree
1-D	Mono-dimensional
2-D	Bi-dimensional
3-D	Tri-dimensional
Å	Angstrom
a.u.	arbitrary units
Ac	Acetyl
AcCN	Acetonitrile
AcOH	Acetic acid
AFM	Atomic Force Microscopy
aq.	aqueous
Ar	Aryl
Arg	Arginine
BINOL	1,1'-Bi-2-naphthol
BiPy	2,2'-Bipyridine
BOC	<i>tert</i> -Butyloxycarbonyl
BPE	1,2-Bis(4-pyridyl)ethane
BTA	1,3,5-Benzene trisamide
Bu	butyl
C-C	Carbon-carbon
CD	Circular Dichroism
<i>cf.</i>	<i>conferre</i> (latin) - compare
CHX	Cyclohexane
CND	Carbon Nanodot
CNT	Carbon Nanotube
conc.	concentrated
CT	Charge-Transfer
<i>d</i>	Deuterated
d	doublet (NMR)
<i>D</i> or <i>D_f</i>	Diffusion coefficient
D-A	Donor-Acceptor
DAP	2,6-Diamidopyridine
DAT	Diaminotriazine
DB24C8	Dibenzo-24-crown-8
DBA	Dibenzylammonium
DCM	Dichloromethane

Abbreviations

DDQ	2,3-Dichloro-5,6-dicyano-1,4-benzoquinone
DFT	Density Functional Theory
DMF	Dimethylformamide
DMSO	Dimethylsulfoxide
DNA	Deoxyribonucleic Acid
DOSY	Diffusion-Ordered Spectroscopy
E	Energy
<i>e.g.</i>	<i>exempli gratia</i> (latin) – for example
EDA	Ethylenediamine
ESI	Electrospray Ionization
Et	Ethyl
$E_T(30)$	Solvent polarity parameter
Et ₂ O	Diethyl ether
EtOAc	Ethyl Acetate
eV	electronvolt ($1\text{eV} = 1.602 \times 10^{-19}\text{ J}$)
exc	Excitation
FWHM	Full Width at Half Maximum
g	gram
GNR	Graphene Nanoribbon
h	hour
H-bonds	Hydrogen bonds
HBC	Hexa- <i>peri</i> -benzocoronene
HMBC	Heteronuclear Multiple Bond Correlation
HOMO	Highest Occupied Molecular Orbital
HOPG	Highly Oriented Pyrolytic Graphite
HR	High Resolution
HSQC	Heteronuclear Single Quantum Coherence
<i>i.e.</i>	<i>Id est</i> (latin) – that is to say
IR	Infrared
J	Coupling constant (NMR)
K	Kelvin degree
k	kilo (10^3)
K_a	Association constant
L	Liter
LDA	Lithium Diisopropylamine
LFER	Linear Free-Energy Relationship
LH	Light Harvesting

Abbreviations

LUMO	Lowest Unoccupied Molecular Orbital
m	multiplet (NMR), milli (10^{-3})
M	Molar, Metal
m.p.	melting point
MALDI	Matrix Assisted Laser Desorption-Ionization
MC	Merocyanine
MCH	Methylcyclohexane
MD	Molecular Dynamics
Me	Methyl
MeOH	Methanol
Mes	Mesityl
mg	milligram
MHz	Megahertz
min.	minutes
ML	Monolayer
MM	Molecular Modeling
mol	mole
<i>m</i> PE	<i>meta</i> -oligophenylene
MS	Mass Spectrometry
MWCNT	Multi-Walled Carbon Nanotube
NBS	<i>N</i> -bromosuccinimide
^{<i>n</i>} BuLi	<i>n</i> -Butyllithium
NCND	Nitrogen-doped Carbon Nanodot
NDI	Naphthalene Diimide
NLO	Non-Linear Optics
nm	nanometer
NMR	Nuclear Magnetic Resonance
ns	nanosecond
<i>o</i> -DCB	<i>ortho</i> -Dichlobenzene
OLED	Organic-Light Emitting Diode
OPE	Oligo(<i>p</i> -Phenylene Ethynylene)
OPV	Oligo(<i>p</i> -Phenylene Vinilyene)
ORTEP	Oak Ridge Thermal Ellipsoid Program
PAH	Polycyclic Aromatic Hydrocarbon
PBI	Perylene Bisimide
Ph	Phenyl
pin	pinacolato
PM6	Parameterization Method 6

Abbreviations

ppm	parts per million
ps	picosecond
PXX	<i>peri-XanthenoXanthene</i>
Pyr	Pyridine
q	quartet (NMR)
Quant.	Quantitative
r.t.	room temperature
r_h	Hydrodynamic radius
SiO ₂	Silica gel
ssDNA	single-stranded DNA
STM	Scanning Tunnelling Microscopy
SWCNT	Single-Walled Carbon Nanotube
T	Temperature
t	triplet (NMR)
^t Bu	<i>tert</i> -Butyl
TCB	1,2,4-Trichlorobenzene
TEM	Transmission Electron Microscopy
TFA	Trifluoroacetic Acid
TGA	Thermogravimetric Analysis
THF	Tetrahydrofuran
TLC	Thin Layer Chromatography
TM-AFM	Tapping mode AFM
TMEDA	Tetramethylethylenediamine
TMS	Trimethylsilyl
TMSA	Trimethylsilyl Acetylene
Tol	Toluene
TPP	Tetraphenylporphyrin
TTF	Tetrathiafulvalene
UHV	Ultra High Vacuum
U _{py}	Ureidopyrimidones
Ur	Uracyl
v/v	volume/volume
vs.	<i>versus</i> (latin) - against
VT	Variable temperature
XPS	X-ray Photoelectron Spectroscopy
δ	Chemical shift (NMR)
ϵ	Extinction coefficient
λ	Wavelength

Abbreviations

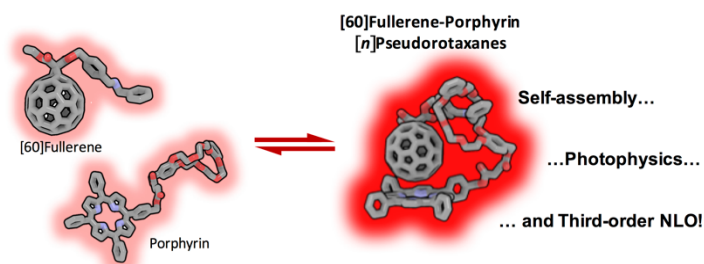
μ	Dipole moment
μ	micro (10^{-6})
μW	Microwave
τ	Lifetime
Φ (QY)	Quantum Yield

Abstract

Chemistry beyond the molecule, *supramolecular chemistry*, has advanced tremendously in the last half-century. Through the chemistry of the covalent bond, *molecular chemistry*, showed us that basically any molecule could be approached synthetically through a number of procedures. However, approaching complex molecules, macromolecules and materials through molecular chemistry is often impractical. In this regards, supramolecular chemistry, presents a leap in the evolution towards complex systems that suddenly become easily accessible. In order to do so, appropriate information has to be stored at the molecular level in the form of non-covalent functional groups, that will be retrieved, transferred and processed at the supramolecular level. In this respect, implementing functional molecules (*i.e.* molecules that integrate active components capable of operating with photons, electrons, ions and so on) with non-covalent information, holds great promise for applications and new technologies in molecular and supramolecular electronics and photonics.

In this first part of *Chapter 1*, the reader is given a short account on supramolecular chemistry as well as non-covalent interactions (for instance, hydrogen bonding or metal coordination among others) that are the most useful in storing supramolecular information. In the second part, a description of the light harvesting complex, a biological blueprint for a large number of studies devoted to create artificial, highly ordered arrays of chromophores, is presented. In this respect, synthetic equivalents of harvesting chromophores, porphyrins, are introduced. The section is concluded by a description of the most important chemical reactions used to prepare and functionalize porphyrins.

The first part of the present dissertation is described in *Chapter 2*, where the synthesis of supramolecular electron donor-acceptor pairs based on porphyrins and C_{60} , a carbon sphere that reversibly accommodates up to six electrons, are reported. This supramolecular donor-acceptor system was self-assembled through non-covalent interactions and this



process was monitored by means of different techniques, including NMR, UV-Vis-NIR, absorption and emission spectroscopies. Furthermore, the Non-Linear Optical (NLO) responses of this supramolecular systems are presented. Notably, thanks to the reversibility of supramolecular interactions, it was shown that the NLO response could be modulated in a ‘turn-on’ and ‘turn-off’ fashion.

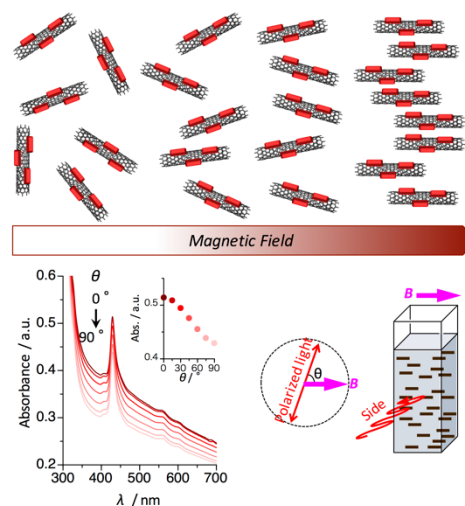
As a part of our efforts to precisely order chromophores for materials applications, *Chapter 3* describes the synthesis and the solvent-dependent nanostructuring of two supramolecular systems. In the first part, a porphyrin derivative was prepared in order to exploit stacking between these flat molecules, coordination interactions with metals and hydrogen-bonding between hydroxyl groups. The self-assembly of this chromophore was followed by solid-state, solution and surface studies. This studies showed that simple and synthetically accessible building blocks are able to, in part, mimic the organization of complex light harvesting systems. In the second part of this chapter, a heterocomplementary system based on triple hydrogen-bonding between uracil and diamidopyridine was employed to study the transfer of chirality from a molecular to a supramolecular level. In order to do so, an optically active component (1,1'-bi-2-naphthol) was implemented in order to follow the formation of chiral supramolecular polymers by



Circular Dichroism and Atomic Force Microscopy. The system was thoroughly studied and it was found that the transfer of chirality over several length scale is highly dependent on the solvent. Depending on the solvophobic properties of the liquid media, spherical, rod-like, fibrous, and helical morphologies were obtained, with the latter being the only nanostructures expressing chirality at the microscopic level. This behavior was interpreted as a consequence of an interplay among the degree of association of the H-bonded recognition, the vapor pressure of the solvent, and the solvophobic/solvophilic character of the supramolecular adducts in the different solutions under static and dynamic conditions, namely solvent evaporation conditions at room temperature.

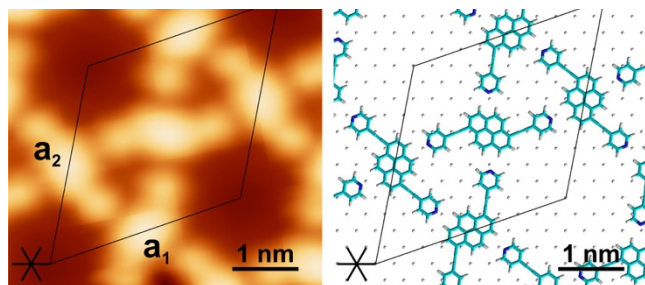
In *Chapter 4* we introduce the concept of aided organization of chromophores by using templates. In this regard, Carbon Nanostructures have attracted much attention because of their electronic and mechanical properties, to name a few. In the first part, we reported the preparation and characterization of a hybrid material, with the porphyrin chromophores organized on Carbon

Nanotubes. Then, the magnetic susceptibility, *i.e.* the ability of carbon nanotubes to align parallel to magnetic field, was used in order to probe if it's possible to affect the organization of chromophores through an external stimulus. The arrangement was also 'blocked' with *in situ* gelation in order to preserve the alignment of the hybrid system even after the magnetic field was turned off. The alignment of the gel was checked by polarized optical microscopy and polarized UV-Vis absorption that showed



notable optical anisotropy, suggesting that the templating effect of the carbon nanotubes was successful. In the second part of this Chapter, we report our efforts toward the formation of novel nano-carbon hybrid photoactive materials. In this regards the preparation of the first porphyrin-carbon nanodots (CNDs) hybrid is presented. However, since CNDs are the latest member of the carbon nanomaterials class, we developed first a novel, reliable and scalable synthesis by microwave irradiation. The prepared material was thoroughly characterized, most notably by mono- and bi-dimensional NMR techniques that were useful tools for the structural characterization of this material. Then, a porphyrin chromophore was linked in order to study its electronic properties. First results suggest the formation of a charge transfer complex between the porphyrin and the CNDs, with more detailed studies currently underway.

Chapter 5 presents the 'bottom-up' fabrication of patterned metal surfaces based on assemblies composed of pyrene chromophores. Different supramolecular approaches were employed by functionalizing the pyrene core with relevant groups. In the first part of the chapter, pyridyl groups were used in order to guide the assembly of pyrene derivatives through intermolecular N...H bonds,



into different supramolecular architectures, giving rise to rhombic arrays, porous Kagome networks and chain-like assemblies. In the second part, an organometallic approach was used. Namely, dicarboxy-pyrene was found to

coordinate lanthanides (such as dysprosium) in an eight-fold coordination motif that gave a porous network. In another study, by employing a dibromopyrene derivative, the reactive C-Br bond was used to guide the patterning of the metal surface. Specifically, by thermal treatment of the surface, the molecules underwent first partial and then almost full debromination reaction that resulted, by

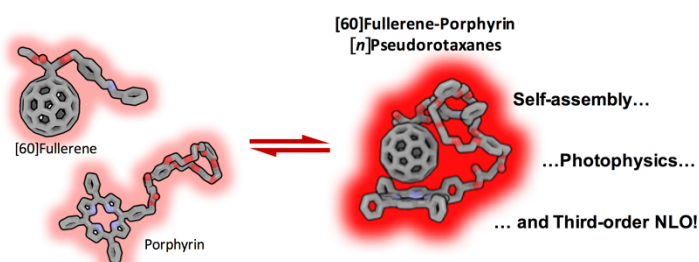
incorporation of Ag surface adatoms, in organometallic chains. The last section of *Chapter 5* presents an overview of our current work towards functional surfaces that include the formation of charge transfer complexes, pyridyl and bipyridyl driven coordination networks and on-surface reactions.

Riassunto

La chimica oltre la molecola, *chimica supramolecolare*, ha subito un considerevole sviluppo negli ultimi cinquanta anni. La chimica del legame covalente, *chimica molecolare*, ha dimostrato che ha dimostrato che dall'impiego di una varietà di procedure e approcci, è possibile ottenere oraticamente qualsiasi molecola. Tuttavia, l'approccio a molecole complesse, macromolecole e materiali mediante l'impiego della chimica molecolare risulta spesso di difficile attuazione. A tal riguardo, la chimica supramolecolare rappresenta un importante progresso verso sistemi complessi, rendendoli facilmente accessibili. Opportune informazioni vengono memorizzate a livello molecolare sotto forma di gruppi funzionali non covalenti, per poi essere riprese, trasferite e sviluppate a livello supramolecolare. Sulla scorta di tali premesse, l'associazione di molecole funzionali (*i.e.* molecole che integrano componenti attivi in grado di operare tramite fotoni, elettroni, ioni, etc.) con informazioni non-covalenti, viene considerata una strategia molto promettente a fini applicativi e per lo sviluppo di nuove tecnologie in elettronica e fotonica sia molecolare che supramolecolare.

Nella prima parte del *Capitolo 1* viene presentata una breve panoramica sia sulla chimica supramolecolare che sulle interazioni non-covalenti (incluse, tra le altre, il legame a idrogeno o la coordinazione con metalli) maggiormente impiegate per la memorizzazione delle informazioni supramolecolari. Nella seconda parte viene descritto il complesso antenna, un modello biologico per un ampio numero di studi incentrati sullo sviluppo di una serie di cromofori artificiali e altamente organizzati. A tale proposito, vengono introdotte le porfirine come equivalenti sintetici dei cromofori antenna. La sezione si conclude con la descrizione delle principali reazioni chimiche impiegate per la preparazione e la funzionalizzazione di porfirine.

La prima parte dell'elaborato, sviluppata nel *Capitolo 2*, è incentrata sulla sintesi di una coppia supramolecolare elettrone donatore-accettore basata sull'impiego di



porfirina e C_{60} , una sfera carboniosa in grado di ospitare fino a 6 elettroni. Questo sistema supramolecolare donatore-accettore si auto-assembla mediante interazioni non covalenti. Per lo studio di tale processo sono state impiegate varie tecniche, come spettroscopie NMR, UV-Vis-NIR di assorbimento ed emissione. In riferimento al predetto sistema vengono, inoltre, discusse le risposte di ottica non lineare (NLO, Non-Linear Optics) mostrando, in particolare, che tali risposte NLO

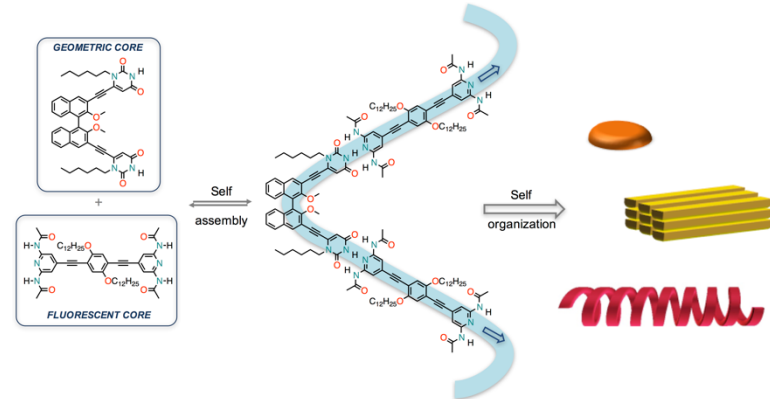
possono essere modulate come attivate/disattivate in virtù della reversibilità delle interazioni supramolecolari.

Il Capitolo 3 mostra gli sforzi volti ad una accurata disposizione di cromofori per il loro impiego nella realizzazione di materiali, mediante la sintesi di due sistemi supramolecolari e la loro nanostrutturazione dipendente dal solvente. Nella prima parte viene descritta la preparazione di un

derivato porfirinico, in grado di impilarsi tra queste molecole piatte e andare incontro a interazioni di coordinazione con metalli o a legami a idrogeno mediante i gruppi idrossilici. L'auto-assemblaggio di tale cromoforo è stato seguito mediante studi allo stato solido, in soluzione e su superficie. Questi studi



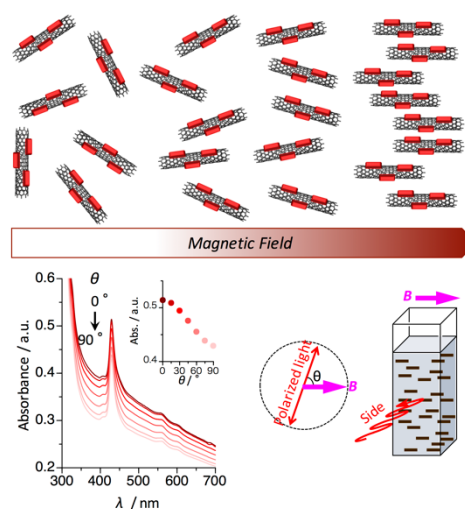
hanno mostrato che “building blocks” semplici e sinteticamente accessibili possono, in parte, imitare l'organizzazione di complessi sistemi antenna. Nel corso della seconda parte di tale capitolo, viene presentato un sistema eterocomplementare basato su tripli legami a idrogeno e ne viene discusso lo studio del trasferimento di chiralità da un livello molecolare a uno supramolecolare. A tale scopo, è stato implementato un composto otticamente attivo (1,1'-bi-2-naftolo) per seguire la formazione di polimeri supramolecolari mediante il Dicroismo Circolare e la Microscopia a Forza Atomica. Dai risultati emersi dall'ampio studio di questo sistema, è stato osservato che il trasferimento di chiralità è affetto da una notevole dipendenza dal solvente. In



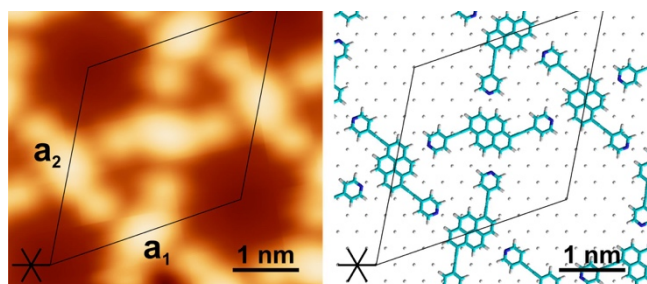
relazione alle proprietà solvofobiche della soluzione, si ottengono morfologie sferiche, astiformi, fibrose o elicoidali, con quest'ultime che rappresentano le sole nanostrutture che mostrano chiralità a livello microscopico. Questo comportamento è stato interpretato come una conseguenza delle

possibili interazioni tra il grado di associazione del riconoscimento dei legami ad idrogeno, la pressione di vapore del solvente, il carattere solvofobico/solvofilico degli addotti supramolecolari in diverse soluzioni sotto condizioni

Nel *Capitolo 4* viene introdotto il concetto di organizzazione guidata di cromofori mediante l'impiego di templati. In tale ambito, le Nanostrutture di Carbonio hanno richiamato una grande attenzione in virtù delle loro proprietà elettroniche e meccaniche, per citarne solo alcune. Nella prima parte, viene riportata la preparazione e la caratterizzazione di un materiale ibrido costituito da porfirine organizzate su nanotubi di carbonio. Inoltre la suscettività magnetica dei nanotubi, *i.e.* la loro abilità di allinearsi parallelamente al campo magnetico, è stata sfruttata per mostrare come si possa intervenire sull'organizzazione del cromoforo mediante l'impiego di un stimolo esterno. La disposizione è stata poi "congelata" con la gelificazione *in situ* al fine di preservare l'allineamento del sistema ibrido anche dopo lo spegnimento del campo magnetico. L'allineamento del gel è stato verificato mediante microscopia ottica polarizzata e assorbimento UV-Vis polarizzato, che ha mostrato una notevole anisotropia ottica, suggerendo che la funzione di templato viene brillantemente espletata dai nanotubi di carbonio. La seconda parte di questo capitolo mette in luce l'impegno dedicato alla formazione di un nuovo materiale ibrido fotoattivo nano-carbonioso. A tal fine viene discussa la preparazione del primo ibrido costituito da una porfirina e da Carbon Nanodots, membri di recente addizione alla classe di nanomateriali di carbonio. È stato inizialmente necessario lo sviluppo di una loro sintesi innovativa, affidabile e scalabile, mediante l'impiego di irradiazione di microonde. Il materiale preparato è stato ampiamente caratterizzato e tecniche NMR mono e bidimensionali hanno contribuito significativamente alla sua caratterizzazione strutturale. In seguito, la porfirina è stata legata al fine di studiarne le proprietà elettroniche. I risultati preliminari suggeriscono la formazione di un complesso a trasferimento di carica tra la porfirina e i CNDs, e ulteriori studi sono attualmente in svolgimento.



Nel *Capitolo 5* viene presentata la fabbricazione "dal basso verso l'alto" di superfici metalliche con motivi basati su assemblaggi con un nucleo pirenico. Diversi approcci supramolecolari sono stati



impiegati per la funzionalizzazione del core pirenico con gruppi di interesse. Nella prima parte del capitolo, gruppi piridinici sono stati usati per guidare l'assemblaggio di derivati del pirene, mediante legami N...H

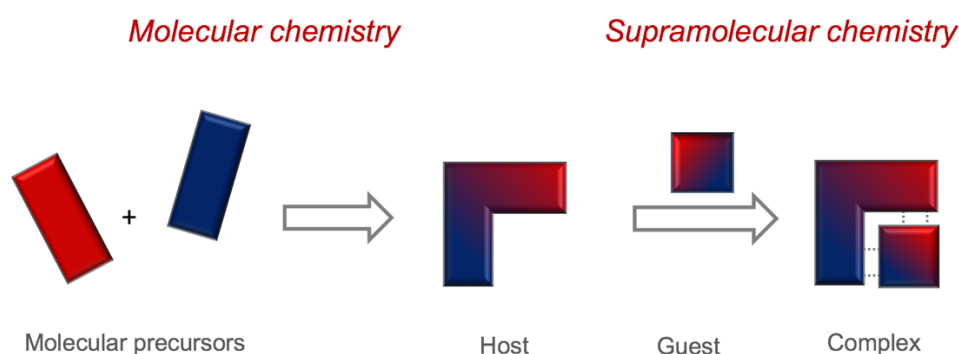
intermolecolari, verso diverse architetture supramolecolari, dando luogo a disposizioni rombiche, network porosi di Kagome e assemblaggi a catena. Nella seconda parte, è stato impiegato un approccio organometallico. In particolare, è stato osservato che il dicarbossi-pirene coordina dei lantanidi mediante un motivo di coordinazione ottaedrico dando luogo a un network poroso. In un altro studio, mediante l'impiego di un dibromopirene, il legame reattivo C-Br è stato utilizzato al fine di guidare l'organizzazione sulla superficie metallica. In particolare, attraverso il trattamento termico della superficie, le molecole subiscono prima una parziale e poi una quasi totale reazione di debrominazione che dà luogo a catene organometalliche, mediante l'incorporazione di atomi di Ag dalla superficie. Nell'ultima sezione del capitolo, viene presentata una panoramica del lavoro che è attualmente in svolgimento volto alla realizzazione di superfici funzionali che includono la formazione di complessi a trasferimento di carica, network di coordinazione guidata da piridili e bipyridili e reazioni su superfici.

1. Introduction

1.1. Supramolecular Chemistry

Chemistry has the task of bridging physics (that unravels the laws of the universe) and biology (that scrutinizes the rules of life). Indeed, it plays a central role in our lives with its interdisciplinarity and ubiquity. Chemistry, the *science of matter and of its transformations*, aids us in understanding the properties of the matter, and how to act, modify, control and invent new expressions of them. Nonetheless, chemistry is also *art of the matter*, since it is able to express its creative power in shapes and functions of molecules and materials.

Molecular chemistry, based on covalent bonds between atoms, has given us a myriad of procedures that led to molecules and materials. Going beyond the molecule, in the *supramolecular* domain (**Scheme 1.1**), by mastering non-covalent intermolecular forces, it has become possible to develop complex chemical systems.¹⁻⁵ Thus supramolecular chemistry can be considered as a step in the evolution of chemistry to an information science. By appropriate manipulation of non-covalent interactions, the *information* stored at the molecular level can operate through retrieval, transfer and processing at the supramolecular level.



Scheme 1.1. Illustration of molecular versus supramolecular approach.

The work presented in this thesis aims at the design of *programs* or molecular recognition patterns (hydrogen bonding, donor-acceptor, metal-ion coordination, *etc.*), that *operate* by spontaneous self-assembly of the components into well-defined and sophisticated supramolecular architectures. Appropriate encoding of single subunits and proper processing give access to a variety of systems.

Specifically, by integrating active components, functional supramolecular devices are easily accessible. Integration of components that operate with photons or electrons yields photoactive or electroactive devices capable of electron or energy exchange/transfer processes that pave the way to supramolecular photonics and electronics. Additionally, being intrinsically dynamic, supramolecular chemistry provides potential properties such as self-healing, error correction and sensitivity to external stimulus. Self-organization has offered a striking new chemical approach to the bottom-up nanofabrication and top-down miniaturization approaches in nanoscience and technology, avoiding laborious implementation of physical procedures.

1.2. Some Historical Remarks in Supramolecular Chemistry

Although many of the supramolecular concepts and roots can be dated back to the beginning of the 19th century, the birth of supramolecular chemistry as discipline dates back to the late 1960s and early 1970s. Much development has been done in the mid-to-late 1960s working on macrocyclic hosts for metal cations (**Figure 1.2.1**).

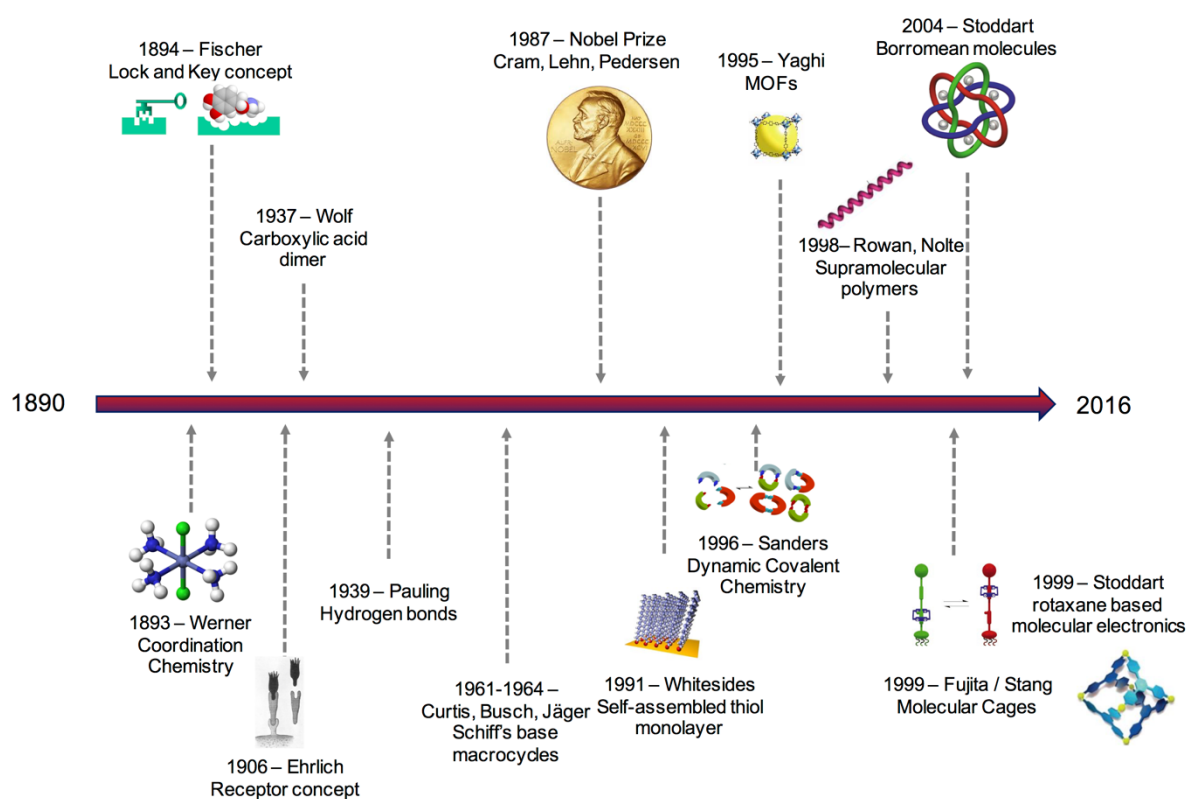


Figure 1.2.1. Illustrative timeline of the development of supramolecular chemistry.

Particularly, the work on crown ethers by Pedersen,⁶ cryptands by Lehn⁷ and spherands by Cram⁸ earned them the Nobel Prize in 1987 in Chemistry for “the development and use of molecules with structure-specific interactions of high selectivity” (Figure 1.2.2).

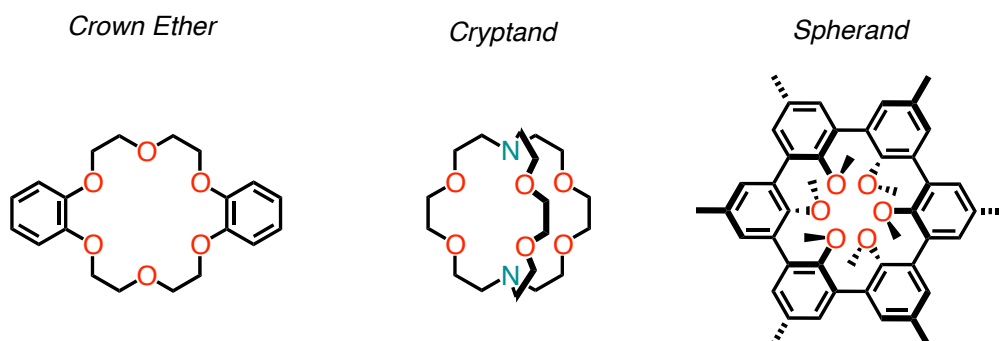


Figure 1.2.2. Chemical structures of representative crown ether, cryptand and operand that lead to the Nobel Prize in Chemistry 1987 to Pedersen, Lehn and Cram.

1.3. Nature of Supramolecular Interactions: a Brief Overview

The term ‘non-covalent interaction’ includes a range of attractive and repulsive forces. The most common non-covalent interactions, along with appropriate energies, are found in Figure 1.3.1 and will be briefly described in the next sections.

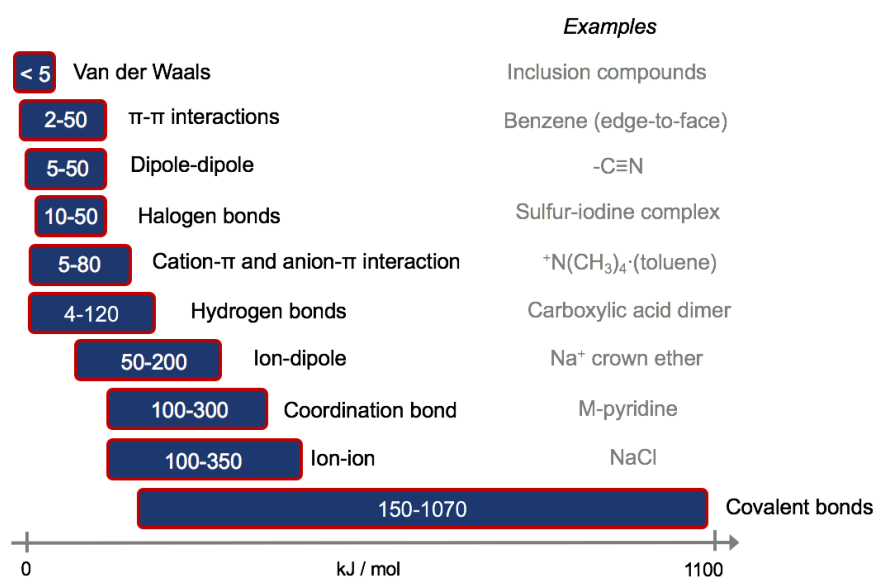


Figure 1.3.1. Comparison chart of common non-covalent bonds strengths.

1.3.1. Electrostatic Interactions

Electrostatic interactions are non-directional forces and include ion-ion, ion-dipole and dipole-dipole interactions (**Figure 1.3.2**). The strongest interactions, ion-ion, are comparable in strength to covalent bonding ($100 - 350 \text{ kJ mol}^{-1}$, e.g. sodium chloride), followed by ion-dipole ($50 - 200 \text{ kJ mol}^{-1}$, e.g. Na^+ in water) and dipole-dipole one ($5 - 50 \text{ kJ mol}^{-1}$, e.g. carbonyl compounds).

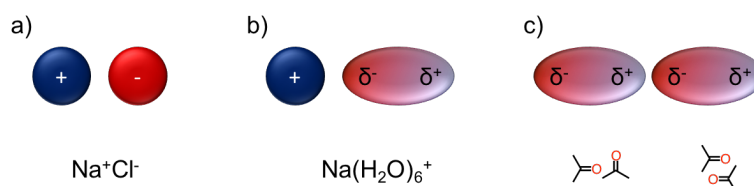


Figure 1.3.2. Ion-ion, ion-dipole and dipole-dipole electrostatic interactions along some examples.

Ion-ion interactions arise from Coulomb interaction of formal positively and negatively charged molecular species. Ion-dipole and dipole-dipole interactions result from electrostatic attraction between an ion and a molecule that is neutral but has a dipole or two molecules with dipoles, respectively.

Coordinative bonds are mostly electrostatic in cases of nonpolarisable metal cations and hard bases and therefore can be considered ion-dipole interactions. Dative bonds are also employed in supramolecular chemistry, however when there is a significant covalent component, the distinction between molecular and supramolecular species can be rather faint.

1.3.2. Hydrogen Bonds

Hydrogen bond has been described as “an attractive interaction between a hydrogen atom from a molecule or a molecular fragment $X - H$ in which X is more electronegative than H , and an atom or a group of atoms in the same or a different molecule, in which there is evidence of bond formation”.⁹ Hydrogen bonding is essential in biochemistry (e.g., in protein folding and the formation of double-stranded DNA) and was also greatly exploited in man-made supramolecules (**Figure 1.3.3**). One reason is the directionality of the hydrogen bond, that gave chemists the ability to control complex geometry and design complementarity host for a desired guest. Additionally, many host-guest systems have been studied in non-competitive solvents where the hydrogen bond becomes rather strong.

Hydrogen bonds can be classified by their binding energies in: strong hydrogen bonds (60 – 120 kJ mol⁻¹ with heteroatom – heteroatom distances of 2.2 – 2.5 Å), moderate hydrogen bonds (15 – 60 kJ mol⁻¹, 2.5 – 3.2 Å), and weak hydrogen bonds (binding energies below 15 kJ mol⁻¹, long donor – acceptor distances of up to 4 Å). Strong hydrogen bonds tend to form straight line geometries between a H-bond donor and an acceptor with a covalent contribution to the bond, while moderate and weak bonds are mainly electrostatic in nature. Accordingly, the hydrogen bonding angles range from 175-180° in strong H-bonds with great spatial control, to flexible bonds in moderate (130-180°) and weak (130-180°) hydrogen bonding.

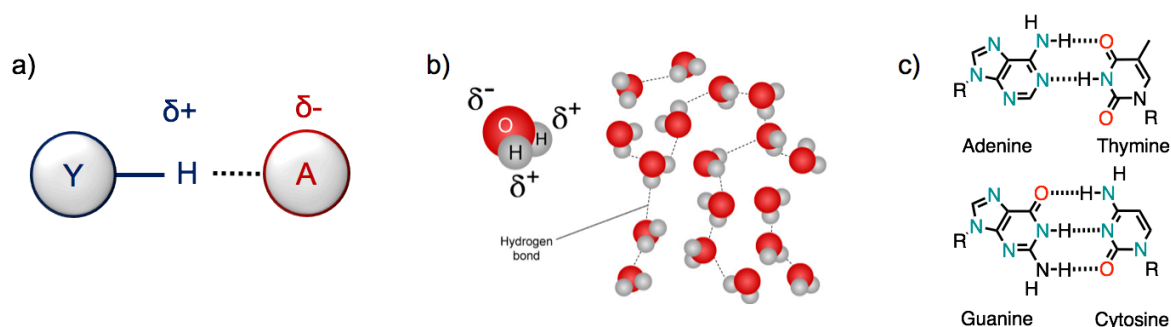


Figure 1.3.3. a) Schematic representation of a hydrogen bond; b) hydrogen bond network in water and c) DNA base pairing two-fold or three-fold hydrogen bonding.

1.3.3. Halogen Bonds

A halogen bond (XB) interaction is exemplified by an Y-X ··· D interaction between a halogen-bond donor (X) and an acceptor (A), with the intramolecular distance being less than the sum of their van der Waals (vdW) radii (**Figure 1.3.4**).¹⁰

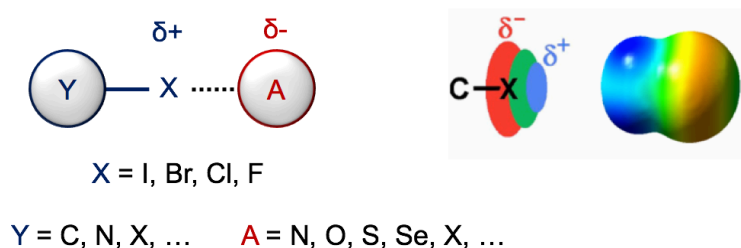


Figure 1.3.4. Schematic representation of a halogen bond along with a molecular electrostatic potential map showing the ‘sigma hole’.

The XB is comparable in strength with the hydrogen bond (usually 10 – 50 kJ mol⁻¹) and due to the anisotropic electron density of organic halides the interaction is typically collinear (175 °), although deviations occur due to secondary interactions or crystal packing effects. The bond strength usually increases with the nature of the halogen (I > Br > Cl > F) and with increasing electron-withdrawing nature of the atom/group bound to the halogen (Y) atom.¹¹

1.3.4. π -Interactions

Non-covalent interactions include also π -systems that can bind, in supramolecular fashion cations, anions or other π -systems (**Figure 1.3.5**). The cation- π interaction is an electrostatic interaction with a polarization component. Aromatic rings, such as benzene, possess a permanent quadrupole moment that gives a relative negative charge above and below the aromatic system. A cation will therefore be attracted to the negative region through an electrostatic interaction (e.g. Na⁺ to simple aromatics or tertiary ammonium ion and toluene as a sandwich complex). The anion- π interaction, on the other hand, seems counterintuitive since it would be expected to be repelled by aromatic systems. However, aromatics deficient in electron density (e.g. hexafluorobenzene), have reverse quadrupolar moment, and thus are able to exhibit favorable interactions with anion and energies comparable to those of hydrogen bonds.

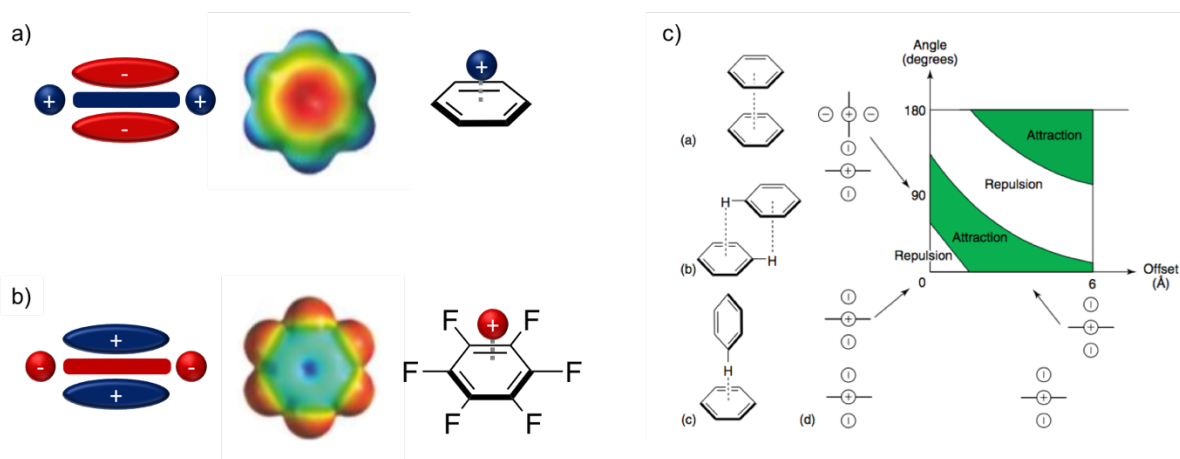


Figure 1.3.5. ab) Quadrupoles and electrostatic potential surfaces for cation- π interaction and anion- π interaction; c) π - π interactions that include face-to-face, parallel displaced and edge-to-face.

π -systems are able to interact with other π -systems, in the so-called π -stacking. Systems such as benzene tend non to interact in perfect face-to-face manner due to the two partially negative clouds

repelling each other. In order to avoid this repulsion, benzene can position itself in a edge-to-face orientation with an attractive interaction between the negative π -cloud and the σ -scaffold. Larger aromatic molecules can form face-to-face orientation, reducing repulsive forces by shifting sideways.

1.3.5. Van der Waals Forces

Van der Waals forces are the weakest and least directional among the supramolecular interactions. These forces arise from the polarization of an electron cloud when an adjacent nucleus is near, resulting in a weak electrostatic attraction. Van der Waals interactions can be divided into dispersion (London) and exchange-repulsion terms. The first one is the attractive component that results from interacting multipoles in adjacent molecules. This attraction decreases very rapidly with distance (r^6 dependence) and every bond in the molecule can be additive to the overall interaction energy.

1.4. Natural and Synthetic Tetrapyrrolic Macrocycles

Supramolecular interactions were widely exploited to mimic the organization of the light-harvesting complex (LHC),¹² the most important chromophoric array found in nature. This natural system has been used as blueprint for a large number of studies devoted to the controlled organization of functional dyes with the ultimate goal of efficiently capturing light and transfer the excitation energy to designated acceptor units.

1.4.1. Light Harvesting Antennas

The light harvesting antennas are pigment proteins that transfer the absorbed light energy to the photosynthetic reaction center. An antenna consists of small molecule(s) that absorb light (chromophores) and the protein(s) to which the chromophores are bound. Although there is a variety of pigment-protein antennas, they all share the same basic requirements: strongly absorb visible or near-infrared light, the generated excited states are sufficiently long lived, they are relatively stable, packed together in order to allow excitations to migrate to reaction centers and should be able to deactivate potentially destructive side pathways.

Chlorophylls (Chls) or bacteriochlorophylls (BChls) meet the aforementioned requirements. Chl *a* solution presents strong absorption in both the blue (430 nm) and the red (660 nm) regions of the spectrum, Chl *b* has maxima peaks around 460 and 650 nm while BChl *a* bands are around 380 and 780 nm. The peak molar absorption coefficients go from around $10^4 \text{ M}^{-1} \text{ cm}^{-1}$ (650 nm, Chl *b*) to

almost $10^5 \text{ M}^{-1} \text{ cm}^{-1}$ (780 nm band of BChl *a*). Although these molecules are strong absorbers, having the excited states at relatively low energy, Chls and BChls act as acceptors when molecules that absorb energy at shorter wavelength (e.g. carotenoids) transfer energy. In addition, carotenoids fill the green and yellow gaps that are weakly absorbed by Chls and BChs. The structures of these chromophores are typically asymmetric, which allow them to absorb well in the orange-red region, owing to the different shapes of π -system arising from reduced pyrroles or additional keto or vinyl groups (Figure 1.4.1). Usually the metal found is magnesium, that allows to extend considerably the lifetime of the excited state (as compared to iron found in heme-porphyrins) by 10 ns or longer before it relaxes to the ground state.

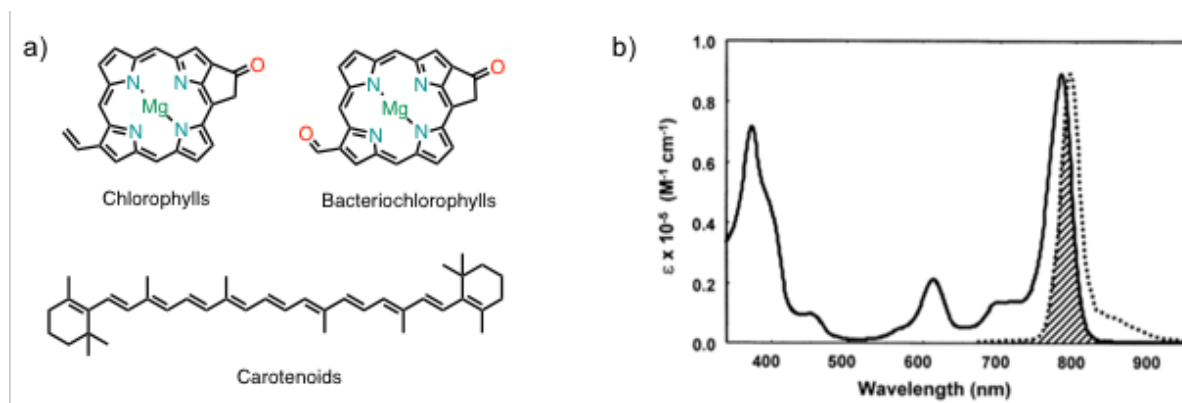


Figure 1.4.1. a) Chemical structure of photosynthetic pigments; chlorophylls, bacteriochlorophylls and carotenoids; b) example of absorption (solid line) and emission (dashed line) of bacteriochlorophyll *a* (in pyridine), with the cross-hatching indicating the overlap of the two spectra.^{13,14}

The energy transfer between molecules depends on the distance found in the photosynthetic antenna system. For a non-radiative transfer mechanism, an excited donor can release energy to an acceptor if it is not too far away. The rate of this resonance energy transfer depends on the intermolecular distance and the orientation of both the donor and the acceptor. At a fixed distance between molecules, the rate will depend on the molar absorption coefficient of the energy acceptor and also on the overlap between the absorption (donor) and the fluorescence emission (acceptor) spectra. Thus, bacterio(chlorophylls) are suited for rapid energy transfer, due to strong absorption at long wavelengths, and conserving energy, given the overlap of the absorption and emission spectra (Figure 1.4.1b).

The chromophores are bound to specific proteins, found in or associated with the photosynthetic membrane. Reaction centers are hydrophobic that makes them always embedded in the lipid bilayer. Thus, the spatial separation of charge and the evolution of biochemical processes across the membrane is possible. Although there is a variety of Prokaryotic light-harvesting antennas, the most understood is the one of purple bacteria.

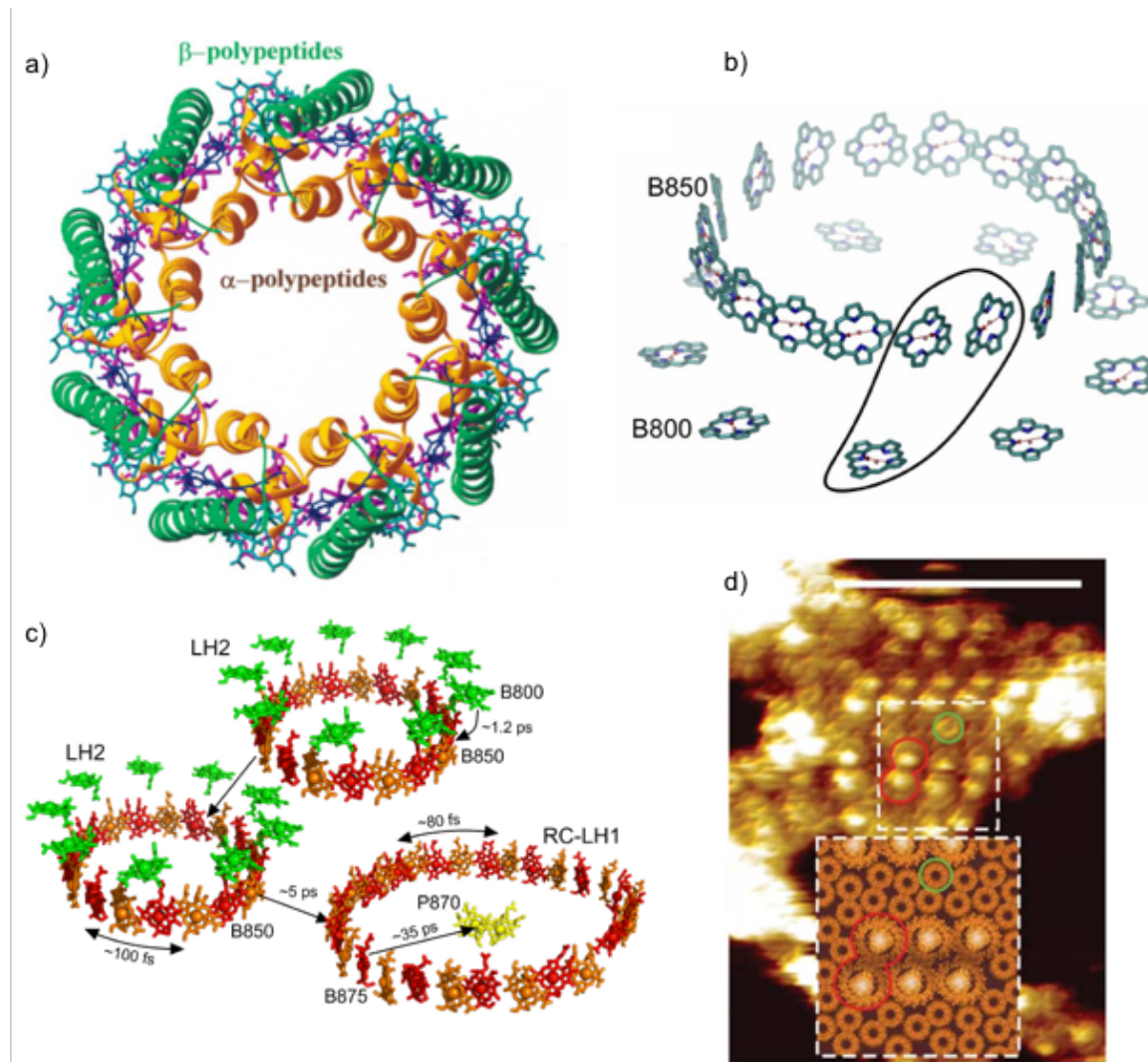


Figure 1.4.2 Light harvesting proteins structure, organization and energy transfer. a) Crystal structure of LH2 proteins from *Rhodospseudomonas acidophila* showing the nonameric complex viewed from the cytoplasmic side of the membrane, with 850-nm absorbing BChl molecules in magenta and the 800-nm absorbing BChls in cyan.^{14,15} b) Simplified side view of the nonamer with a single $\alpha\beta$ -heterodimer subunit indicated.^{15,16} c) Energy transfer events (ps) from carotenoids to neighboring BChls and energy migration (double-headed arrow, in fs) within 850-nm and 875-nm pigment rings.^{17,18} d) Atomic Force Microscopy of complex arrays surrounded by LH2 complexes (the inset is a representation of the region denoted by the dashed box in the center).¹⁹

The core antenna, called light-harvesting complex LH1, transfers excitation energy to the reaction centers. Many bacterial species also express a peripheral antenna complex, LH2. LH1 complex usually absorbs in the 870-880 nm region, while LH2 exhibits transitions at 800 and 850 nm and thus BChls are usually referred to as B followed by their absorption transition (Q_y), *i.e.* B800, B850 or B870 (**Figure 1.4.2**). LH1 and LH2 are composed of oligomers comprised of a pair of hydrophobic apoproteins, α and β , consisting mainly of a transmembrane helix. In LH1 each polypeptide binds a BChls and each pair has an associated carotenoid molecule, spanning into a ring of 16 α and β with 24-32 BChls that are oriented in a regular array with their planes perpendicular to the membrane. The peripheral antennas, in contrast, have the α and β dimers that bind a third BChls, oriented parallel to the membrane. The complex consists of a ring of 8-9 dimers with a total of 24-27 BChls, the absorption maxima at higher energy compared to LH1, facilitating the funnel type of excitation transfer. Finally, the excitation energy from the carotenoids and BChls is passed to the reaction center (RC), composed of three polypeptides and 10 co-factors: four BChls, two bacteriopheophytins (BChls without the Mg), two ubiquinones, a carotenoids and a non-heme iron. Once that the transfer of the excited state reaches the BChls in the reaction center, the photochemical charge separation is triggered, generating a proton gradient that will be used to power reactions such as synthesis of ATP, water splitting and reduction of NADP to NADPH. In the end, the products of the light reaction, ATP and NADPH will be used in the Calvin cycle of plants where carbohydrates are made from carbon dioxide.

1.4.2. Porphyrins

Porphyrins are tetrapyrrolic macrocycles, a class of uniquely functional biomolecules involved in a variety of events that comprise electron transfer, oxygen transfer and light harvesting.²⁰⁻²⁵ This class of biomolecules include chlorins, bacteriochlorins, porphynogens and protoporphyrins. They are generally present as metal complexes, owing to the coordination ability of the four nitrogens, *e.g.* iron(III) in a *heme*, involved in oxidation or transport of oxygen, or magnesium(II) in chlorophylls, crucial in natural photosynthesis (**Figure 1.4.3**).

The metal-free cores of chlorophylls and their bacterial equivalents, chlorins and bacteriochlorins are depicted in **Figure 1.4.4**. The commonality is the 16-member ring, even though the electron delocalization is not extended over all the carbon atoms because of saturated either one or two double bonds. Especially due to the presence of these saturated double bonds, the synthesis is often low-

yielding and tiresome, thus hampering their applications. Nonetheless, great efforts have been achieved and semisynthetic and synthetic derivatives have been studied.²⁶⁻³⁴

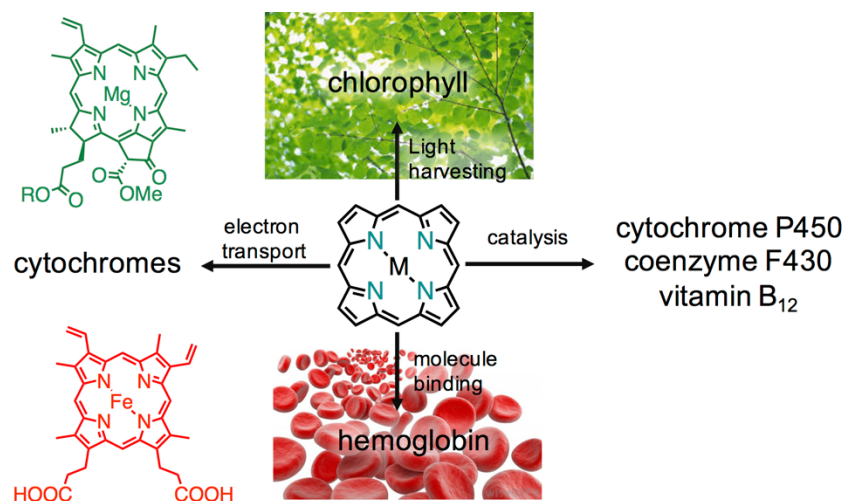


Figure 1.4.3. Tetrapyrrolic macrocycles in biological processes. Image adapted from reference.³⁵

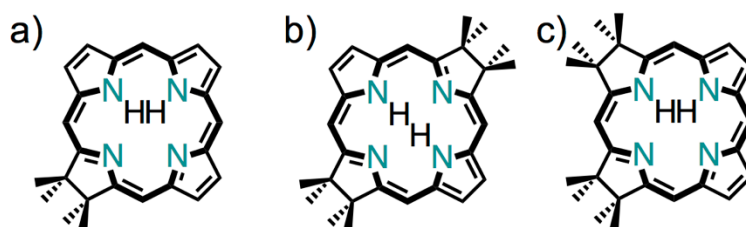


Figure 1.4.4. Cores of porphyrin-related structures found in photosynthetic processes: a) chlorins (precursor of chlorophylls); bc) bacteriochlorins (precursor of bacteriochlorophylls *a* and *b*, respectively).

Porphyrins, their fully conjugated tetrapyrrole macrocyclic analogues, possess similar electron transfer properties, excitation energies and quantum yields as chlorophylls. Therefore, they frequently replace chlorins as a fully synthetic alternative. Porphyrins usually appear purple in color, so there is no surprise that their name came from the Greek '*porphura*', meaning purple. They are macrocycles consisting of 18 π -electrons spread over four pyrroles and four methyne bridges. The IUPAC nomenclature (atoms numbered 1-24) and the trivial one can be found in **Figure 1.4.5**. Substitutions in the meso positions are most common, but can occur also in the so-called β -positions. The optical

properties arise from their π -electron rich core, its substituents and the presence of a central metal atom.

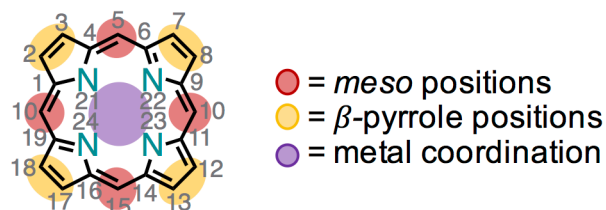


Figure 1.4.5. Porphyrin structure along with IUPAC numbering (grey) and trivial nomenclature (colored circles).

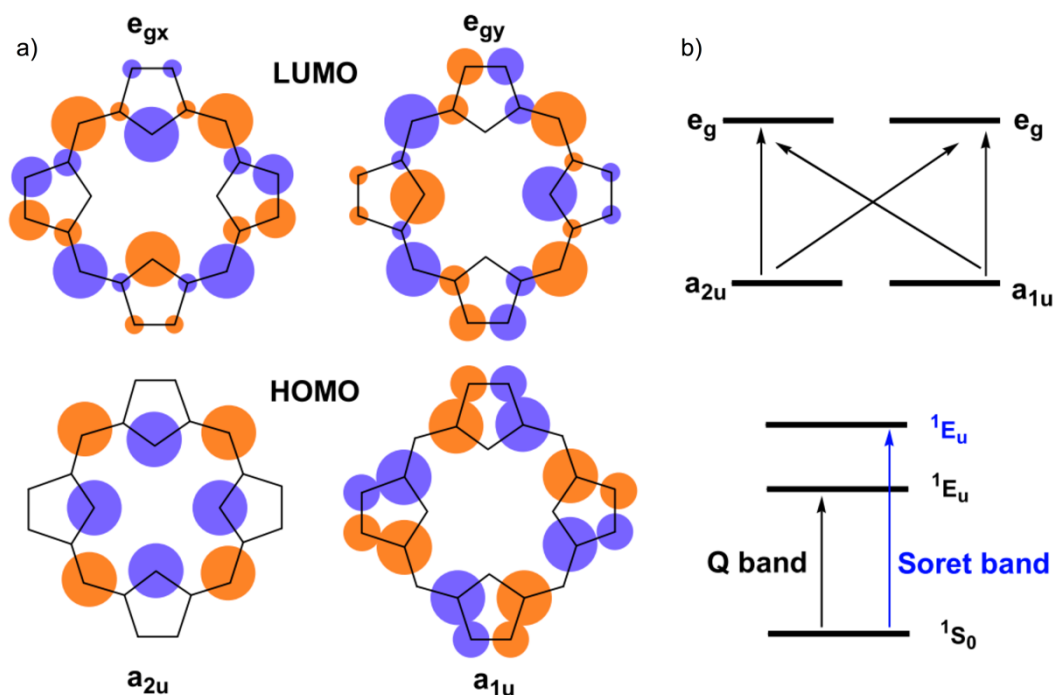
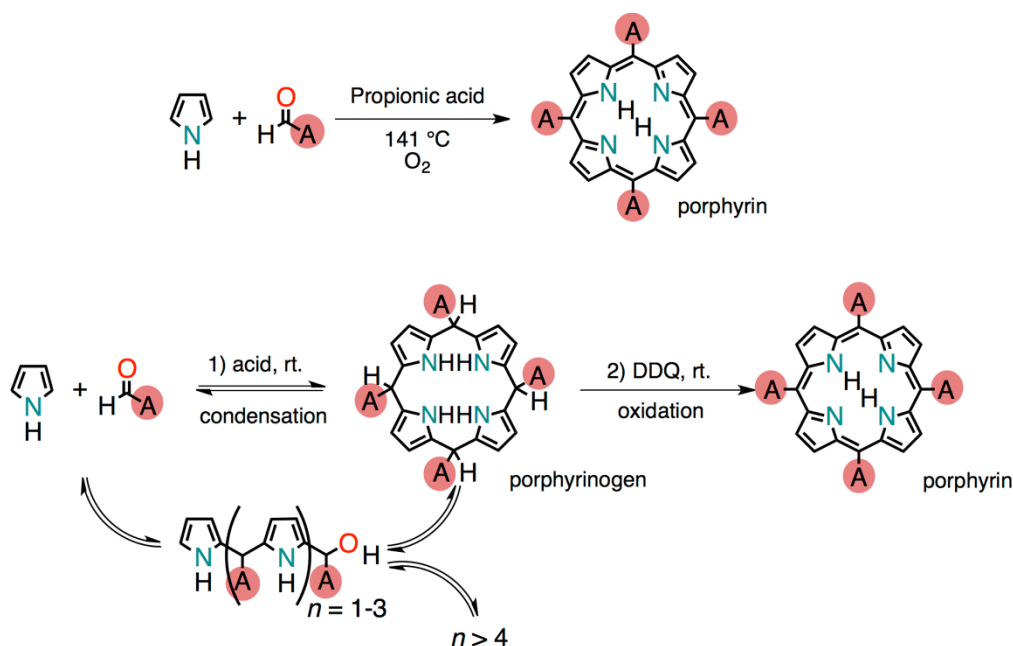


Figure 1.4.6. a) Semi-quantitative MO-based “four-orbital model” of Gouterman and b) simplified representation of one electron transitions from HOMO to LUMO. The four-orbital model considers the two HOMOs (labelled a_{1u} and a_{2u}) and LUMOs (labelled e_g) of the porphyrin derived from Hückel theory and mixes the four possible excitations between them using configuration interaction theory to account for electronic interaction.^{36–38}

Typically, an UV-Vis absorption spectrum shows the following three characteristic bands: *i*) *Q* band of the $S_0 \rightarrow S_1$ transition (occurring between 500 and 600 nm); *ii*) *B* band or *Soret* band of the $S_0 \rightarrow S_2$

transition (around 380 and 420 nm) and *iii*) N, L, M bands that are blue-shifted compared to the Soret band and correspond to high energy electronic transitions. The *Q* and *B* bands are therefore both π - π^* transitions that are explained by considering four frontier orbitals: two π orbitals (a_{1u} and a_{2u}) and a degenerate pair of π^* orbitals (e_{gx} and e_{gy}) (**Figure 1.4.6**). Nonetheless, the two π - π^* transitions result in two bands with different wavelengths and intensities. The fluorescence detected is only for $S_1 \rightarrow S_0$ transition due to the rapid internal energy conversion of the $S_2 \rightarrow S_2$ transition and, although it is associated with the π and π^* states, the lifetime is dependent on the chemical substitution on the periphery.

The chemistry of *meso*-substituted porphyrins started with the work of Rothmund.^{39,40} Firstly, the synthesis of *meso*-tetramethylporphyrin by reaction of acetaldehyde and pyrrole in methanol was investigated. Later on, the preparative synthesis of *meso*-tetraphenylporphyrin (H_2 TPP) was reported, with the Rothmund method consisting of high concentration and high temperature reaction in a sealed vessel and in absence of oxidant. In the mid-1960s, another method for preparing *meso*-substituted porphyrins was reported by Adler, Longo and coworkers (**Scheme 1.4.1** top).⁴¹



Scheme 1.4.1. Adler-Longo method (top) and Lindsey method (bottom) for the synthesis of porphyrins.

The key point was refluxing equimolar pyrrole and benzaldehyde in acidic solvent in glassware open to atmosphere. Even if the yields were found to be higher in acetic acid (35-40%), the reaction is usually performed in refluxing propionic acid because of faster reaction times, easier porphyrin

crystallization and less propensity to form the acid salt. Further mechanistic studies revealed a linear Hammett plot, with the rate of reaction increasing with electron-withdrawing nature of the *p*-substituent on the aryl aldehyde. The harsh conditions however limited the scope of these methods. A milder alternative was proposed by Lindsey (**Scheme 1.4.1** bottom) in the mid 1980s as a one-flask, two-step route: *i*) acid-catalyzed (BF_3 or TFA) condensation of pyrrole and aryl aldehyde under equilibrium and *ii*) irreversible $6e^-/6\text{H}^+$ oxidative dehydrogenation with a soluble oxidant (e.g. DDQ, 2,3-dichloro-5,6-dicyano-1,4-benzoquinone).

Although these methods can reach about 40-50 % yield of the tetra-substituted porphyrin, usually it is more useful to have different types of substituents on the porphyrin core. In principle, there are 7 types of meso-substituted porphyrins (**Figure 1.4.7**) and typically three approaches are possible: *i*) mixed condensation, *ii*) total synthesis and *iii*) functionalization of the core.

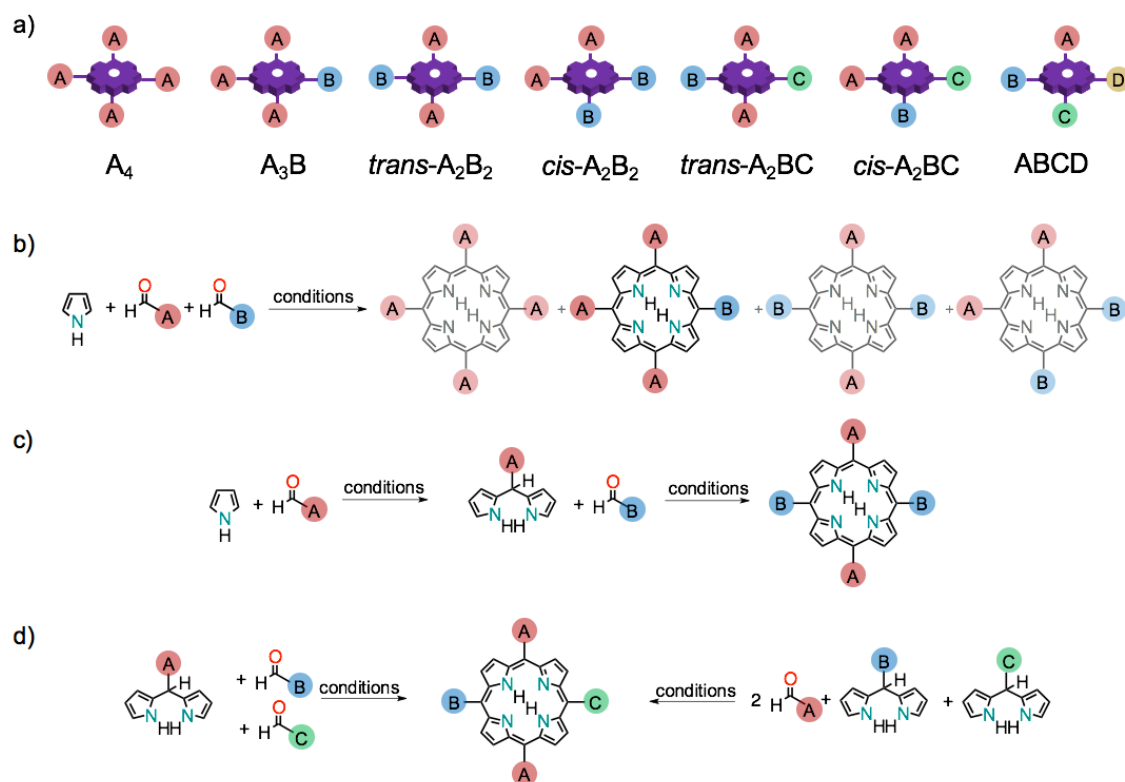
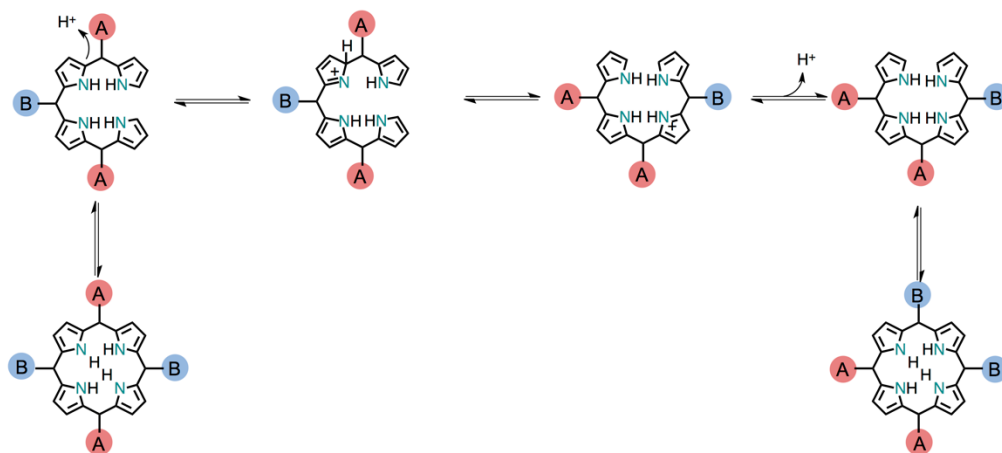


Figure 1.4.7. a) Types of meso-substituted porphyrins; b) mixed condensation leading up to A_3B type porphyrins; c) dipyrrromethane approach for A_2B_2 -type porphyrins and d) dipyrrromethane approach for A_2BC -type porphyrins.

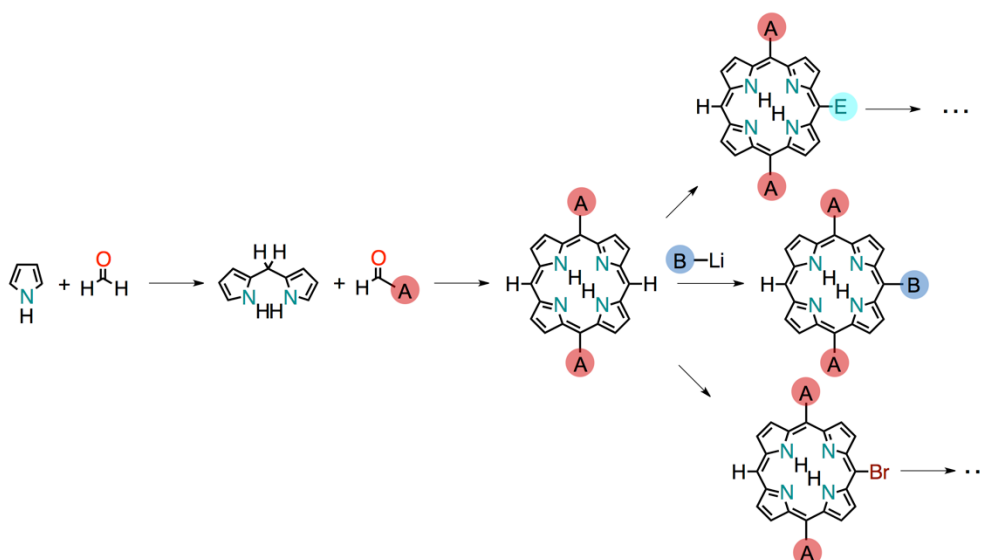
Mixed condensations (**Figure 1.4.7b**) usually refer to acid-catalyzed reaction between pyrrole and two different aldehydes and it can be applied in order to obtain A_3B type porphyrin with a pyrrole:

aldehyde A: aldehyde B in a 4:3:1 ratio. This yields a statistical mixture of porphyrin regioisomers that have to be purified by column chromatography, with the difference of polarity strongly influenced by the substituents on the starting aldehydes.

In order to reduce the number of regioisomers in the acid catalyzed condensation porphyrin synthesis, the '2+2' or MacDonald approach through dipyrromethane step can be employed (**Figure 1.4.7cd**). Unfortunately, dipyrromethanes are not stable under acidic condition and therefore fragmentation followed by recombination leads to a mixture of porphyrins (**Scheme 1.4.2**). However, scrambling can be avoided by using sterically hindered dipyrromethanes or using *meso*-free dipyrromethane.



Scheme 1.4.2. Concise scrambling mechanism of unhindered dipyrromethane that lead to a mixture of porphyrins.



Scheme 1.4.3. Reaction pathways towards more complex transformation of the porphyrin core. The A2B2 *meso*-free porphyrin can be easily functionalized for further reactions.

Additionally, the *meso*-free route allows A_2B_2 unsubstituted porphyrin that can be used as a pre-formed system on which carry out reactions (**Scheme 1.4.3**) such as halogenation (bromination, iodination), nitration or formylation among others. In alternative, the *meso*-free system can undergo nucleophilic attack with Grignard or organolithium reagents, followed by oxidation. Subsequently, the halogenated porphyrins can be subjected to cross-coupling reactions, such as Pd-catalyzed Sonogashira-Hagihara or Suzuki-Miyaura reactions.

1.5. Overview of the Dissertation

In this doctoral work, the research activities were directed towards designing and preparing building blocks through molecular chemistry that carry specific recognition patterns as information and are able to operate through their recognition. By thoughtful control of the conditions, the building blocks were able to evolve into complex materials. Accordingly, the work has been divided into four main chapters, as presented here below.

Chapter II presents the self-assembly of a donor-acceptor system through ammonium-crown ether recognition into pseudorotaxanes. The donor module is a porphyrin derivative, an 18 π -electron macrocycle that is arguably one of the most exploited chromophores to date. On the other hand, the acceptor module is a [60]fullerene, a sphere made of sp^2 carbon, frequently used as electron-acceptor in solar cells. The interaction between the donor and the acceptor moiety was studied in terms of their self-assembly, their photophysical and non-linear optical properties. Even though, the photophysical properties were in line with previous supramolecular reports for similar systems, the non-linear optics showed significant enhancement when compared to their references or their covalent counterparts, making this a novel and reversible non-linear optics system. Different techniques showed the presence of two conformations equilibrium between them in the self-assembled pseudorotaxane, a 'tight' and a 'loose' where acceptor and donor are close or distant between them, respectively. Finally, experiments performed in different solvents hinted that the porphyrin-fullerene interaction is possibly due to the solvophobic nature of the fullerene sphere in common organic solvents.

Chapter III showcases the progress we performed in controlling the shape of soft matter. In this respect, two different systems were prepared. In the first case, a porphyrin that encodes specific recognition patterns, has been studied in the solid state, in solution and on-surface in order to

elucidate its operating programs. It was found that the porphyrin is able to form slipped stacked arrangements both in solution and on surface and finally was able to form extended two-dimensional structures through lateral hydrogen-bonding. In the second part, an intrinsically chiral molecule (BINOL) was self-assembled together with a fluorescent oligo(*p*-phenylene) module through complementary three-fold hydrogen bonding. This system was used in order to probe the transfer of chirality from the molecular to the nanostructured soft material. Notably, solvent was found to play a pivotal role not just for the self-assembly in solution, but also on the surface.

Chapter IV focuses on arranging porphyrin molecules by using a templated approach. More specifically, two different templates were employed. In the first part, a carbon nanotube has been found to enable formation of porphyrin arrays through π - π stacking between the nanotube sidewalls and the pyrene 'anchor' that carries the porphyrin. The formation of the hybrid porphyrin-carbon nanotubes materials was characterized with a variety of techniques. However, the most noteworthy result is the use of the carbon nano-template magnetic susceptibility in order to align the hybrid in a preferred direction. The alignment was 'blocked' by using an organogel and the alignment was confirmed by polarized microscopy and absorption profiles at different polarized light angles. In the second part, the synthesis and characterization of a novel carbon material, carbon nanodots, and its use as template for the formation of novel nano-hybrid systems was investigated. Since the studies of this material are still in their infancy, for the first time the formation of both covalent and non-covalent ensembles is currently underway. However, promising results indicate the potential of this donor-acceptor hybrid material.

Chapter V is dedicated to the engineering of π -conjugated materials along with their STM investigations. In this first section, the formation of specific patterns on metal surfaces was found to depend on the functionalization of a polycyclic aromatic hydrocarbon, pyrene. Through molecular design it was possible to form porous surfaces, by means of weak hydrogen bonds mediated by pyridine, which were found able to accommodate small guest molecules, such as iodine. In the second part, the pyrene core was used in order to probe the formation of organometallic patterns on the metal substrates. More specifically, a novel lanthanide coordination network was formed by carboxy-pyrene derivative and dysprosium. On the other hand, the formation of an organometallic network was possible with the deposition of a dibromo-pyrene derivative, with subsequent on-surface dehalogenation reactions and formation of organometallic chains by incorporation of metals from the surface. Finally, a brief overview on the current bottom-up efforts is given. These include novel charge-transfer complexes on the surface, which also show the dependency on the substrate. Although the

acceptor molecule, tetracyanoquinone is known to form donor-acceptor complexes on the surface, the donor moiety we used an O-doped equivalent of anthanthrene, *peri*-xanthenoxanthene, a promising organic semiconductor, already used in OLED technology. Other approaches include pyridine and bipyridine mediated patterning as well as on-surface reactions.



Figure 1.5.1. Schematic representation of the work presented in this thesis: from design of supramolecular interactions in luminescent modules into functional supramolecular species

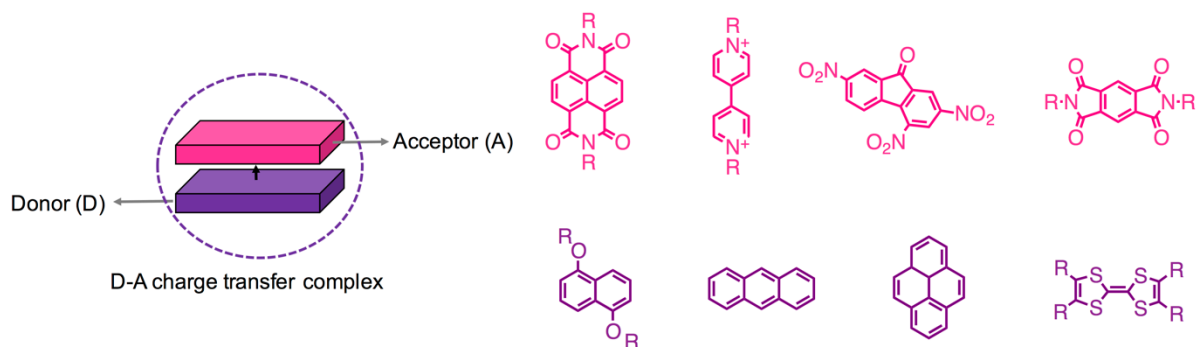
2. Donor-Acceptor Supramolecular Assemblies for Non-Linear Optics

In this chapter the preparation of porphyrin-fullerene [*n*]pseudorotaxane is discussed. The chapter is divided into four main sections. Firstly, a general overview of donor-acceptor systems is presented. Then, the self-assembly of novel supramolecular porphyrin-fullerene systems is showed, followed by their photophysical characterization. Finally, the impact of the self-assembly on the non-linear optics is presented.

The work presented in this chapter has been accomplished thanks to collaboration with *Dr. Tomas Marangoni* that helped in initiating the project, *Dr. Federica De Leo* (University of Namur, Namur, Belgium) carried out the geometry optimization, *Dr. Eleonora Pavoni* and *Dr. Filippo Monti* from the group of *Dr. Nicola Armaroli* (Istituto per la Sintesi Organica e la Fotoreattività, Consiglio Nazionale delle Ricerche, Bologna, Italy) carried out the photophysics experiments, and *Dr. Irene Papagiannouli* and *Dr. Panagiotis Aloukos* from the group of *Prof. Stelios Couris* (University of Patras, Patras, Greece) performed the NLO experiments. Part of the work discussed in this chapter has been published as “[60]Fullerene–porphyrin [*n*]pseudorotaxanes: self-assembly, photophysics and third-order NLO response” *Phys. Chem. Chem. Phys.*, **2016**, Advance Article, doi: 10.1039/C5CP06055A.

2.1. Basic Concepts about Donor-Acceptor Systems

Charge-transfer (CT) interactions generally arise from donor-acceptor (D-A) systems and drive their alternative stacking (**Scheme 2.1.1**).⁴² It is comparable to hydrogen-bonding in terms of inherent complementarity, *i.e.* alternating placement of the D and A units. However, although similar to hydrogen-bonding, CT driven self-organized systems are not as common, probably due to very low – moderate association constants found for intermolecular D-A complexes. In this respect, the CT complexes are usually reinforced by additional non-covalent interaction, such as solvophobic forces,⁴³ hydrogen bonding,^{44,45} metal-ion complexation,^{46,47} and so on.



Scheme 2.1.1. Schematic representation of a donor-acceptor (D-A) charge transfer (CT) complex, along with some π -donor and acceptor structures reported in this section.

One of the most studied D-A pair is bisalkoxynaphthalene (D) and naphthalene bisimide (A). As shown in **Figure 2.1.1a**, both compounds show significant polarization of the π -systems with the bisalkoxynaphthalene being relatively electron rich (electron-donating alkoxy) and naphthalene bisimide being relatively electron poor (electron-withdrawing carbonyl substituents).

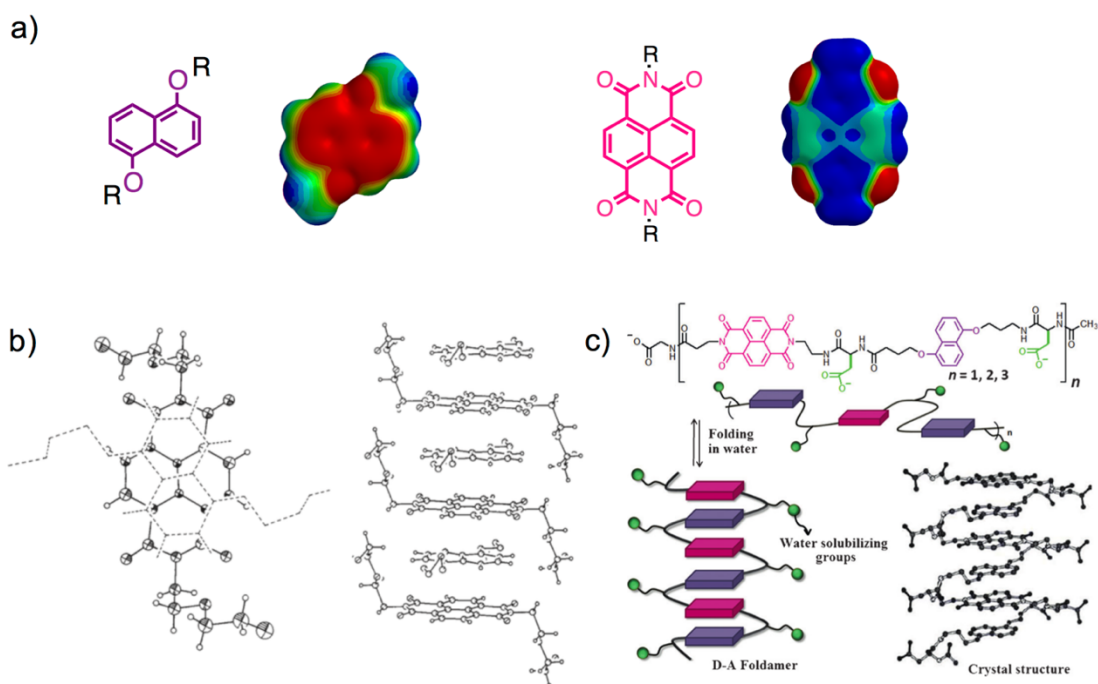


Figure 2.1.1. a) Chemical structures and electrostatic surface potentials calculated for bisalkoxynaphthalene (left) and naphthalene bisimide (right) using Gaussian 09, DFT at B3LYP 6-311G level of theory in vacuum, from 60 to +60 kJ/mol; b) solid state structure of the co-crystal showing the π -stacking of the two molecules; c) folding of D-A oligomer in aqueous medium along with its crystal structure.

The intramolecular and intermolecular interactions between these two complementary electrostatic surfaces were observed.^{43,48,49} Foldamers, synthetic oligomers capable of adopting defined conformations, made of this D-A pair and spaced by flexible amino acid linkers, showed the existence of a folded structure due to interchain stacking (**Figure 2.1.1B**).⁴⁹ This was confirmed by their crystal structure, as well as UV-Vis studies that showed reduction in band intensities and appearance of a red-shifted CT band. Similar folding was achieved by CT interaction between chains that contain either bisalkoxynaphthalenes or naphthalene bisimides.⁵⁰ The intermolecular binding of bisalkoxynaphthalene and naphthalene bisimides was studied by ¹H-NMR spectroscopy in a range of solvents from CDCl₃ to D₂O.⁴³ Association constants were calculated and ranged from 2 M⁻¹ in CDCl₃ to 2 × 10³ M⁻¹ in D₂O. Moreover, linear free energy relationship was observed between the complexation free energy and the empirical solvent polarity parameter, $E_T(30)$, with the association being driven mostly by hydrophobic interaction in polar solvents.

However, bisalkoxynaphthalene and naphthalene bisimide pair does not show complete overlap of the two surfaces and the pursue for stronger D-A pairs continued. As suggested by figure **Figure 2.1.2**, pyrene and naphthalene bisimide could form a strong D-A pair because of the highly congruent pyrene HOMO and naphthalene bisimide LUMO, resulting in an effective HOMO-LUMO overlap in alternate stacking interactions.



Figure 2.1.2. a) Pyrene HOMO (left) and naphthalene bisimide LUMO (right) along with their parallel cofacial alignment suggesting an efficient overlap as a π -stacking pair; b) co-crystal of a pyrene and naphthalene bisimide derivative.^{51,52} Molecular orbitals obtained using Gaussian 09, DFT at B3LYP 6-311G level of theory in vacuum, isovalue is set at 0.02.

This HOMO-LUMO overlap of the two molecules was found indeed to be important for forming a strong D-A pairs.^{51,52} Homopolymers and copolymers prepared by ring-opening metathesis

polymerization (ROMP), incorporating D or/and A molecules onto the poly(norbornene) backbone and the formation of CT band were reported. Among different D-A pairs, dilution UV-Vis experiments showed the highest K_a ($9.6 \times 10^4 \text{ M}^{-1}$ in CH_2Cl_2) for the pyrene-naphthalene bisimide pair. This interaction was confirmed by X-ray studies with a bis-pyrene tweezer and naphthalene bisimide derivative (**Figure 2.1.2**).

Another class of extensively studied acceptors are the cyclobis(paraquat-*p*-phenylene) (CBPQT⁴⁺) derivatives and 'extended' bipyridinium bridges.⁵³⁻⁵⁷ At first, the CT complex with a series of tetrathiafulvalene (TTF) derivatives, acting as donors, was investigated (**Figure 2.1.3a**). A remarkable dependency of the first redox potential ($E^{1/2}$) of the TTF derivatives in the association constants was found: a decrease in $E^{1/2}$ value (from + 0.51 to + 0.34 V) provided an increase by almost two orders of magnitude for K ($1 \times 10^2 \text{ M}^{-1}$ to $1 \times 10^4 \text{ M}^{-1}$ in CH_3CN). Therefore, stronger donors led to higher association constants.

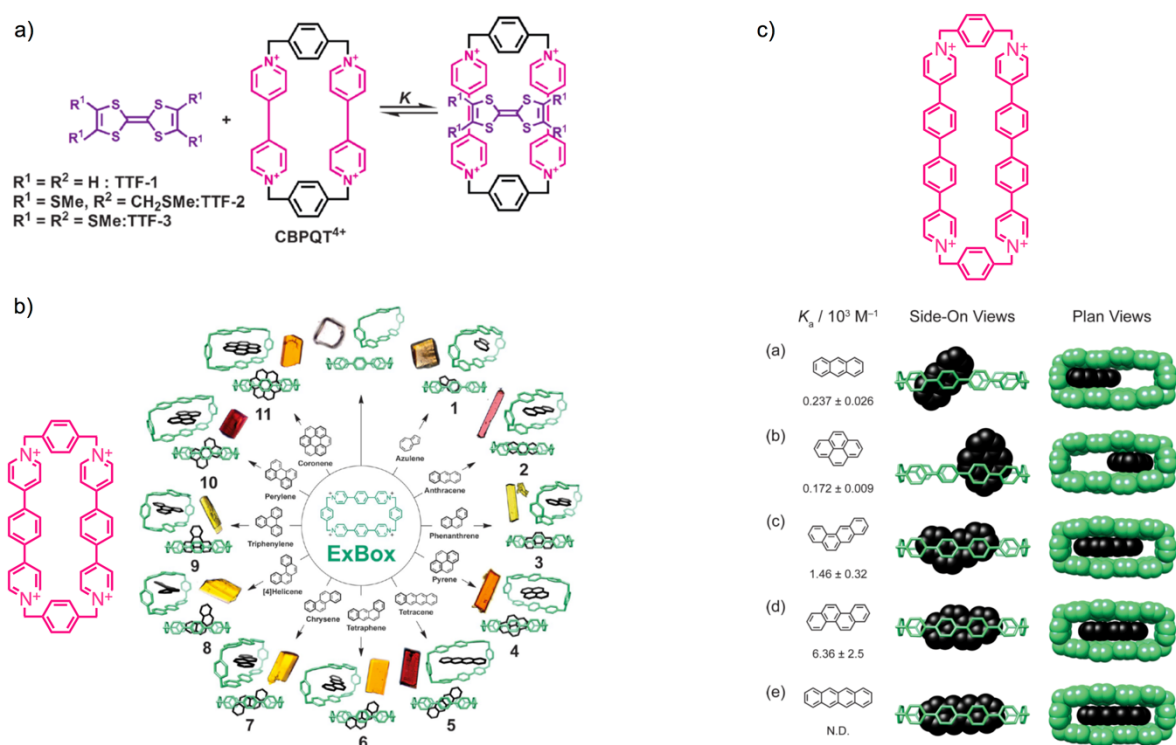


Figure 2.1.3. a) CT complex between CBPQT⁴⁺ and some TTF derivatives; b) inclusion complexes and crystal data for ExBox⁴⁺ ⊂ guest with the colors arising from charge-transfer interactions between the host and the guests (except for azulene 1); c) Ex²Box⁴⁺ along with the chemical structures of the guests, and the association constants calculated from NMR spectroscopy in CD_3CN along with the solid-state superstructures.

An ‘extended’ semi-rigid cyclophane with 1,4-phenylene-bridged bipyridinium units showed to act as a high affinity scavenger for an array of polycyclic aromatic hydrocarbons (PAHs), from anthracene to coronene (**Figure 2.1.3b**), with association constants ranging from 9×10^2 to $7 \times 10^5 \text{ M}^{-1}$, respectively.⁵⁵ Further extension to a biphenylene-bridged bipyridinium cyclophane (**Figure 2.1.3c**), showed to form binary and ternary complexes with guest molecules ranging from long π -electron rich PAHs to polyether macrocycle such as 1,5-dinaphtho[38]-crown-10.⁵⁶ Specifically, this box can realize donor-acceptor interaction with π -electro-rich guest at the pyridinium ‘ends’, while the ‘middle’ can interact with π -electron poor guests.

Another type of cyclophane, made of two perylene bisimide units, was found to bind polycyclic aromatic hydrocarbons, with binding constants up to $5 \times 10^4 \text{ M}^{-1}$ for perylene (**Figure 2.1.4**).⁵⁸ This cyclophane did not only bind PAHs, but also serve as a fluorescence ‘turn-on’ and ‘turn-off’ probe. More specifically, charge-transfer complexes were formed with electron-rich guests, resulting in quenched fluorescence. On the other hand, the complexation of electron-poor guest molecules was followed by significantly increased fluorescence.

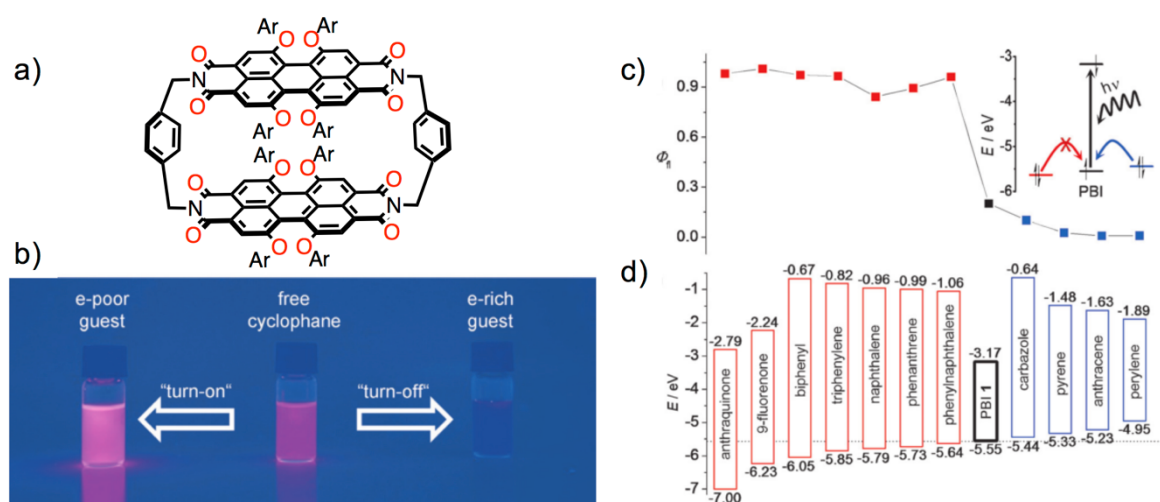


Figure 2.1.4. a) Chemical structure of *p*-xylylene bridged PBI cyclophane; b) photograph of ‘turn-on’ (PBI cyclophane \subset phenylanthracene) and ‘turn-off’ (PBI cyclophane \subset carbazole); c) plot of fluorescence quantum yield with the corresponding guest; electron-poor guests are in red and electron-rich guest are blue, with the free cyclophane black; the inset is a schematic representation of the oxidative fluorescence quenching mechanism.⁵⁸

Charge-transfer was used not only to form inclusion complexes and D-A stacks, but also to prepare supramolecular oligomers and polymers. For example, a charge-transfer interaction between electron-

deficient trinitrofluorenone (TNF) and a bisporphyrin heteroditopic monomer showed to form supramolecular polymers (**Figure 2.1.5**).⁵⁹ The monomer was found to self-assemble into polymers, with diffusion NMR spectroscopy showing a diffusion coefficient strongly dependent on the monomer concentration. Upon increasing concentration from 2 to 66 mmol L⁻¹ the diffusion coefficient significantly dropped from $3 \times 10^{-10} \text{ m}^2 \text{ s}^{-1}$ to $0.3 \times 10^{-10} \text{ m}^2 \text{ s}^{-1}$, that corresponds to aggregates of approximately 660 units (**Figure 2.1.5b**). Viscosity experiments showed, at dilute concentration regime, oligomers too short to be entangled and, above critical polymerization concentration, formation of sizable supramolecular polymers.

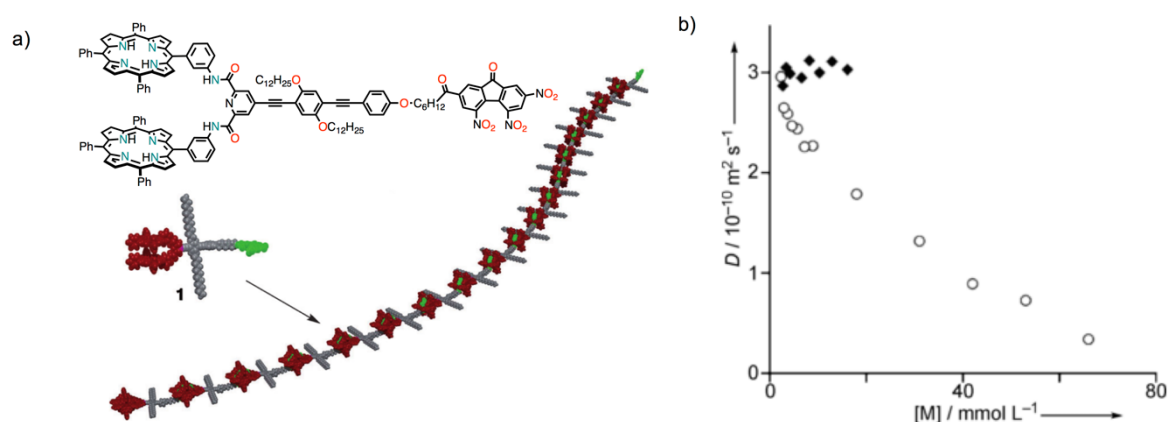


Figure 2.1.5. a) Chemical structure of the porphyrin-TNF heteroditopic dimer and b) concentration-dependent DOSY.

Recently, tetra-TTF calix[4]pyrrole derivatives were used in order to obtain self-assembled supramolecular oligomers either with C₆₁ butyric acid (PBCA) or bis-trinitrodicyanomethylenefluorene (**Figure 2.1.6**).^{60–62} A TTF-C[4]P monomer was able to assemble in the presence of ditopic trinitrodicyanomethylene carboxylate into short oligomers stabilized by hydrogen bonding and D-A CT interactions with a binding constant of $1 \times 10^5 \text{ M}^{-1}$ that fitted to a 1:1 binding isotherm (**Figure 2.1.6b**). Additionally, this supramolecular oligomer was found to de-aggregate in presence of 2,4,6-trinitrotoluene or chloride or bromide anions, making it a promising dual-analyte-responsive material. The TTF-C[4]P monomer, in the presence of another heteroditopic monomer, a phenyl C₆₁ butyric acid (PBCA) into a supramolecular ensemble that is responsive both the chemical and electrochemical stimuli (**Figure 2.1.6b**). The first step in the formation of the supramolecular polymer is the deprotonation of the phenyl C₆₁ butyric acid by an

organic base (**Figure 2.1.6bB**) that induces a change in conformation of TTF-C[4]P to an active cone (**Figure 2.1.6bA**). This change in conformation allows now the binding of the C₆₀ cage, resulting in the formation of supramolecular orthogonal self-assembly. Moreover, the resulting material could be disaggregated by addition of an organic acid (protonation of the butyric acid derivative) or electrolysis (oxidation of TTF to TTF²⁺, hence losing its ability to bind the electron-poor fullerene moiety).

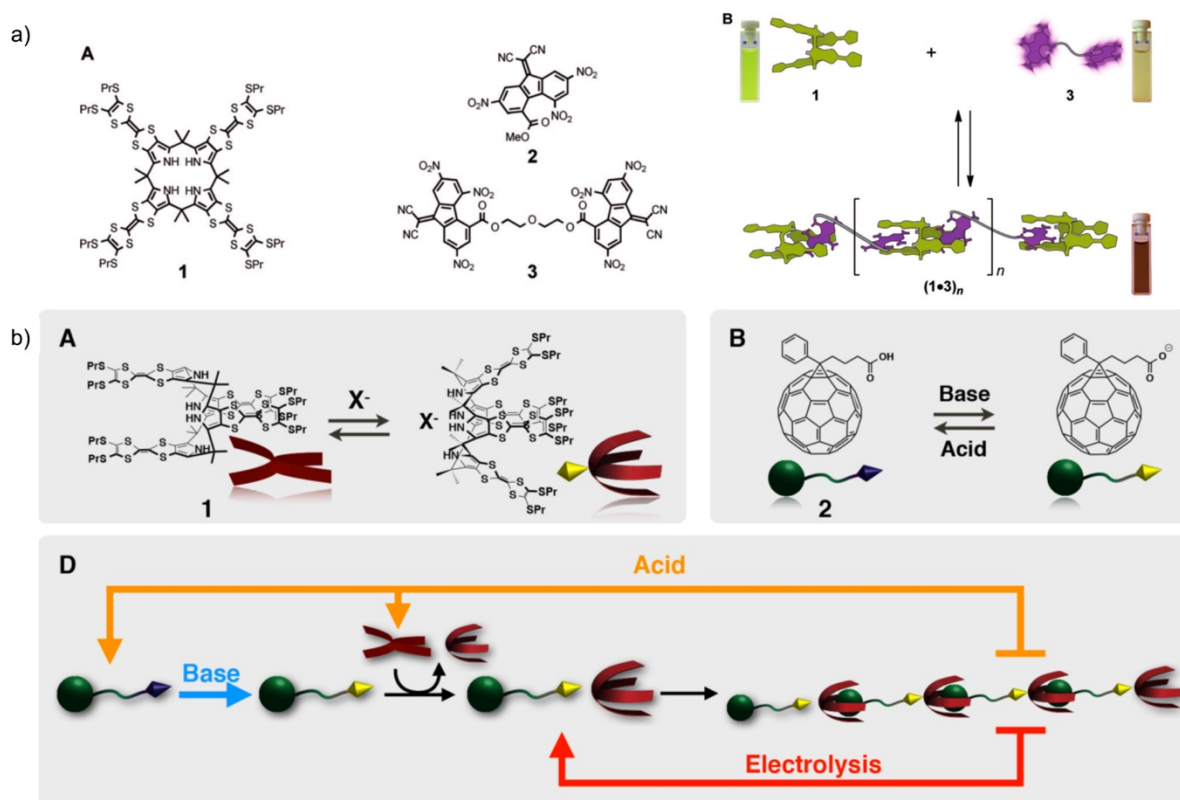


Figure 2.1.6. a) and b) chemical structures of two hetero-complementary subunits based on TTF-functionalized calix[4]pyrrole and trinitrodicyanomethylene-fluorene (TNDCE) along with graphical representation of the supramolecular assembly.

Much attention has been paid to the assembly of porphyrin-fullerene acceptor-donor pair in the context of artificial photosynthesis,⁶³ molecular wires⁶⁴ and solar cells.⁶⁵ Porphyrins have been discussed in *Chapter 1* as synthetic analogues in mimicking light harvesting chromophores. Consequently, [60]fullerene is introduced in the next section.

2.1.1. [60]Fullerene

Although the geometrical form of the truncated icosahedron inspired artist throughout centuries, e.g. the drawing shown in **Figure 2.1.7.** by Leonardo da Vinci, its existence as a molecule has been reported in 1985⁶⁶ and has earned the Nobel Prize to Kroto, Smalley and Curl in 1996. The most famous member of the fullerene family is a 60 atom cluster called “Buckminsterfullerene”, “Buckyball” or simply “Fullerene”, with the name inspired by a geodesic dome construction by architect Buckminster Fuller. The C_{60} isomer, [60]fullerene, is shaped like a soccer-ball (**Figure 2.1.7.**). C_{60} is also the most stable, abundant representative of the fullerene family and today can be produced at ton-scale by arc discharge of graphite electrodes.⁶⁷

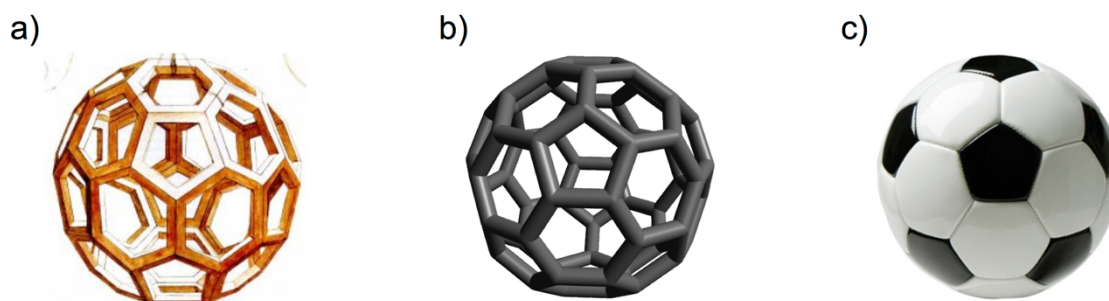


Figure 2.1.7. a) Hollow polyhedron drawing by Leonardo da Vinci;⁶⁸ b) computer mode ‘stick’ representation of a C_{60} -molecule along with c) a soccer ball showing the same geometrical features.

This soccer-ball structure has two features: (i) all twelve pentagons are isolated by hexagons; (ii) two types of bonds - those joining two hexagons (6,6 junctions, 1.38 Å) are shorter than those at the junction of a pentagon and a hexagon (5,6 junctions, 1.45 Å).

The pentagons within the fullerenes are necessary to introduce the curvature, since a network consisting of only benzenes is planar, with the C_{60} isomer being the smallest fullerene to follow the “isolated pentagon rule” (IPR).⁶⁹ The IPR predicts that all the 5-member rings are isolated by 6-member rings, a case that results in higher stability than having two adjacent 5-member rings. This is due to (i) electronic effects (resonance destabilization by pentalene-type 8π -electron systems) and (ii) steric effects (enforced bond angles resulting in an increase of strain energy). The formation of IPR structures is associated with an enhancement of the ‘sphericity’ of the molecules. A spherical shape distributes the strain as evenly as possible and minimizes the anisotropic contribution to the

strain energy.⁷⁰ The double bonds are located at the junctions of the hexagons [6,6] and only single bonds are in the pentagonal rings.⁶⁷ In [60]fullerene each hexagon exhibits cyclohexatriene character and each pentagon has radialene character (**Figure 2.1.8a**).

Both in the C_{60} and in the graphene carbons atoms are sp^2 hybridized. In fullerene's case, for a closed cage, the three bonds of each atom cannot be planar. Carbon atoms that are sp^2 hybridized (simple alkene like ethylene, C_2H_4) have trigonal planar shape (bond angles = 120°) with the p-orbital forming a 90° angle with the sp^2 plane. Carbon atoms with sp^3 hybridization (methane, CH_4) have a tetrahedral shape (bond angles = 109.5°). In fullerenes, the sp^2 hybridized carbon atom is pyramidalized and the angle between its p-orbital and the σ -bonds is 101.6° (**Figure 2.1.8b**).

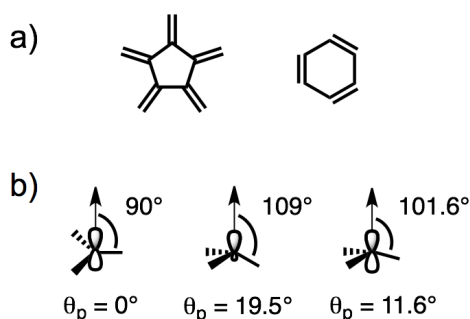


Figure 2.1.8. a) Radialene and cyclohexatriene; b) pyramidalization angle for a planar sp^2 hybridized carbon atom (C_2H_4), a tetrahedral sp^3 carbon atom (CH_4) and a non-planar sp^2 hybridized carbon atom in C_{60} .

The pyramidalization angle (θ_p) for non-planar sp^2 hybridized carbon atoms can be defined as the angle between its p-orbital and the σ -bonds minus 90° . This means that an sp^3 hybridized carbon atom (tetrahedral) has a θ_p of 19.5° , while a planar sp^2 carbon (e.g. in benzene) has a θ_p of 0° . All the carbon atoms in the [60]fullerene have θ_p of 11.6° . The curvature of the fullerene surface results in a decrease of the π -conjugation and the pyramidalization angle θ_p is a good way to measure this weakening, which, in turn, results in the chemical reactivity of fullerenes: larger the pyramidalization angle, higher is the reactivity towards addition reactions.⁷¹

The C_{60} UV-Vis spectrum in CHX (**Figure 2.1.9**) shows absorption bands in the 230–400 nm range (257 nm, 328 nm, a 377 nm shoulder, 406 nm) and two sets of broad bands whose principal maxima are *c.a.* 530 and 600 nm. The UV-Vis spectrum of monoadduct presents bands at 255 nm, 306 nm,

321 nm, a shoulder at 401 nm, a sharp feature at 430 nm (which has no corresponding feature in C_{60}) and four weak absorption bands in the 700 nm region (638, 669, 691 and 703 nm).^{72,73}

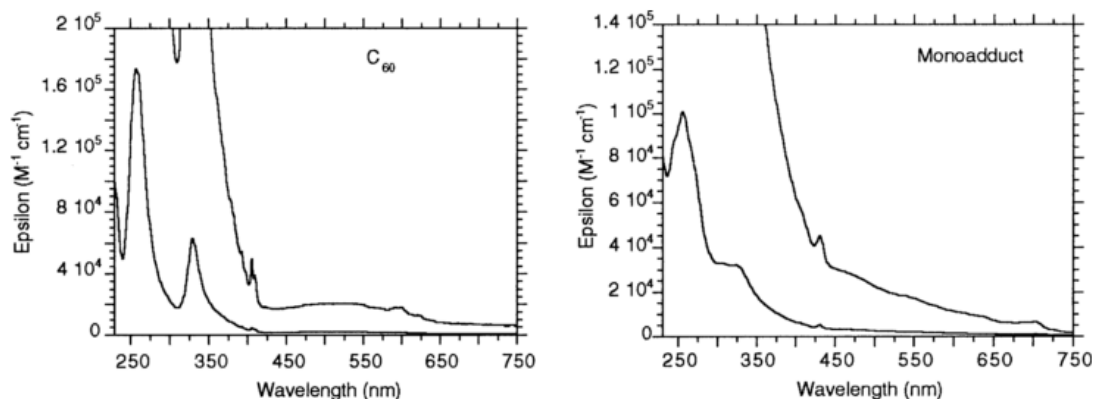


Figure 2.1.9. Absorption spectra of C_{60} and of N-mTEG[60]fulleropyrrolidine mono-adduct in cyclohexane: upper curves are 10 x in absorbance scale.⁷³

C_{60} is essentially insoluble in polar solvents (such as acetone, methanol, etc.) (Table 2.1.1). It is barely soluble in alkanes, with the solubility increasing with the number of atoms of the alkyl chains. In carbon disulfide and in aromatic solvents substantial solubility is detected. A significant increase of the solubility takes place going from benzenes to naphthalenes. Although there are trends for the solubility behavior of C_{60} , there is no direct dependence of the solubility on a certain solvent parameter like the refractive index.^{67,74} Encapsulation of C_{60} in cyclodextrins or calixarenes or water suspension preparations are useful methodologies for overcoming this insolubility, but the most versatile technique is modifying the solubility by covalent attachment of solubilizing appendages.^{67,75}

As mentioned above, the alkene double bonds do not behave as aromatic hydrocarbon and thus the chemical reactivity is similar to that of strained and electron-poor alkenes. Chemical transformations usually involve reactions on the 6-6 bond and the main driving force in addition reaction is the relief of the strain from sp^2 to sp^3 hybridization. Addition reactions to C_{60} are usually exothermic and exergonic and therefore it is difficult to stop the reaction at the monoadduct stage, unless using an excess of pristine C_{60} . Although C_{60} chemistry is vast and has been explored, the work described in this chapter has been performed by using a modified Bingel reaction in which a malonate derivate, in presence of non-nucleophilic base and I_2 , is able to form an α -halomalonate *in situ*, leading to the methanofullerene product.⁷⁶

Table 2.1.1. Frequently used solvents in laboratory to solubilize C₆₀ and the corresponding solubilities.⁷⁴

Solvent	[C ₆₀] mg/ml
CHCl ₃	0.16
CH ₂ Cl ₂	0.26
CCl ₄	0.32
CH ₂ Cl ₄	0.89
Ph-H	1.7
Ph-CH ₃	2.8
Ph-Cl	7.0
1,2-CH ₄ Cl ₂	27
CH ₃ C(O)CH ₃	0.001
CH ₃ OH	0.000
CH ₃ CN	0.000

2.1.2. Supramolecular Porphyrin-Fullerene Assemblies

Porphyrins and fullerenes seem to be attracted to each other and this has been exploited in order to prepare both discrete host-guest complexes and ordered arrays, even though this association between a curved and a flat surface seemed to challenge the traditional π - π interactions principles.⁷⁷ A distance of 2.75 Å was observed in the molecular packing of a fullerene-porphyrin covalent dyad, which was notably shorter than the usual π - π interactions that range between 3.0-3.5 Å.⁷⁸

Frequently, the more electron-rich 6-6 fullerene double bond is found centered over the electropositive center of the porphyrin or metalloporphyrin (**Figure 2.1.10**).⁷⁷ Moreover, the electron-rich nitrogen atoms of porphyrin are positioned over positive electrostatic potential region near the centers of the fullerene rings. Therefore, the main belief is that the π - π interaction is augmented by dispersion forces. However, this interaction still remains controversial since it seems that the fullerene is acting as donor and the porphyrin as acceptor, even though fullerenes are best known for their electron-acceptor properties. Nonetheless, even if fullerenes are electron acceptors in charge-transfer

complexes, it has been suggested that the locally electron-rich double bond may donate to the electropositive center of a porphyrin.⁷⁷

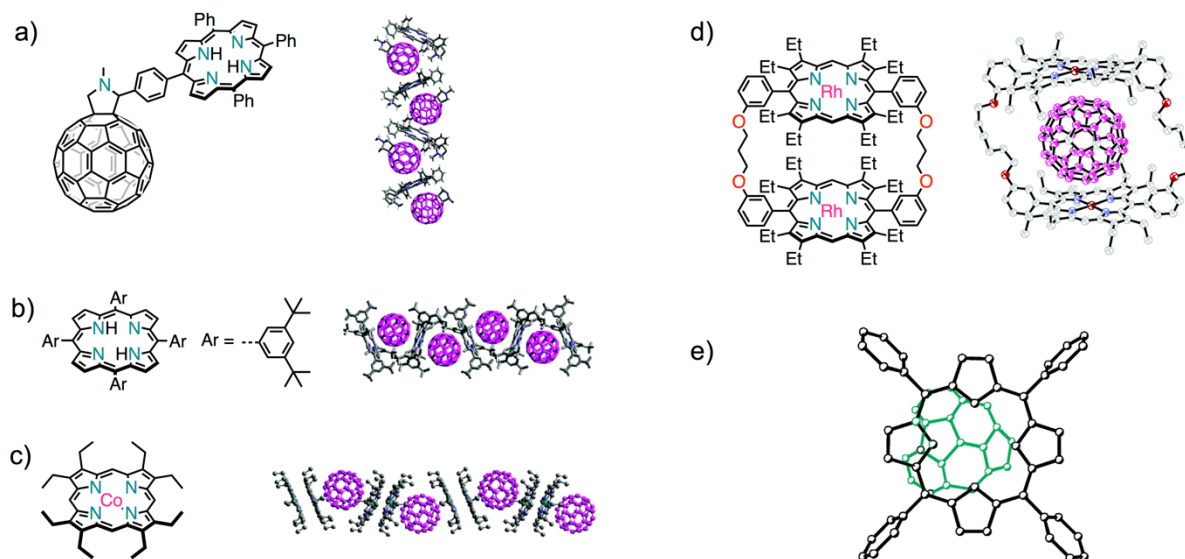


Figure 2.1.10. Representative porphyrin and C_{60} crystal structures: a) packing of a covalent dyad; b) zig-zag stacking of H_2TPP (3,5-di-*t*-butyl substituents) and C_{60} ; c) zig-zag stacking of cobalt octaethylporphyrin; d) cyclic rhodium bisporphyrin host bound to C_{60} ; e) highlighting the 6-6 ring bond of C_{60} over the porphyrin plane. Solid state images adapted from reference.⁷⁷

When moving from solid state to solution, it is more difficult to observe the fullerene-porphyrin interaction unless some sort of cavity enables the complexation of fullerene (**Figure 2.1.11a**). To this end, differently linked porphyrin ‘jaws’^{79,80} and cyclic metalloporphyrin dimers,^{81,82} trimers,⁸³ tetramers,⁸⁴ and metallo-supramolecular cages,^{35,39–41,43,51–56,58–62,77–87} were prepared and showed to host C_{60} molecules with association constants reaching up to $10^8 M^{-1}$ (in *o*-DCB) for cyclic iridium porphyrin dimers. Notably, for some host-guest interactions of cyclic porphyrin dimer-fullerene, particular attention has been placed on the solvent used in the experiments.⁸⁰ The solvent does place an important role in the energetics of the binding event, which can be divided into three parts: desolvation of the individual components, the intrinsic affinities and the re-solvation of the complex. If we consider the limited solubility of the fullerene cage in common organic solvents, it becomes clear that the solvent influences the energetic of the binding event. To this end, calix[4]arene bisporphyrin-fullerene complexes were investigated in different solvents.⁸⁰ The binding constants were found to increase from Ph-CH₃ ($2.5 \times 10^4 M^{-1}$), Ph-CN ($5 \times 10^4 M^{-1}$), CH₂Cl₂ ($9 \times 10^4 M^{-1}$) to CHX (4×10^6

M^{-1}). With the relative solubility of C_{60} decreasing in the order of $PhCH_3 > PhCN > CH_2Cl_2 > CHX$, the desolvation of the fullerene seemed to be the main factor in the host-guest formation. Additionally, the association constants were found to be the same order of magnitude ($1 \times 10^6 M^{-1}$) for the host-guest complex when a mixture of $PhCH_3/CH_3CN$ (1:1 v/v) was used to match the solubility of fullerene in CHX (0.031 mg/mL and 0.036 mg/mL, respectively).

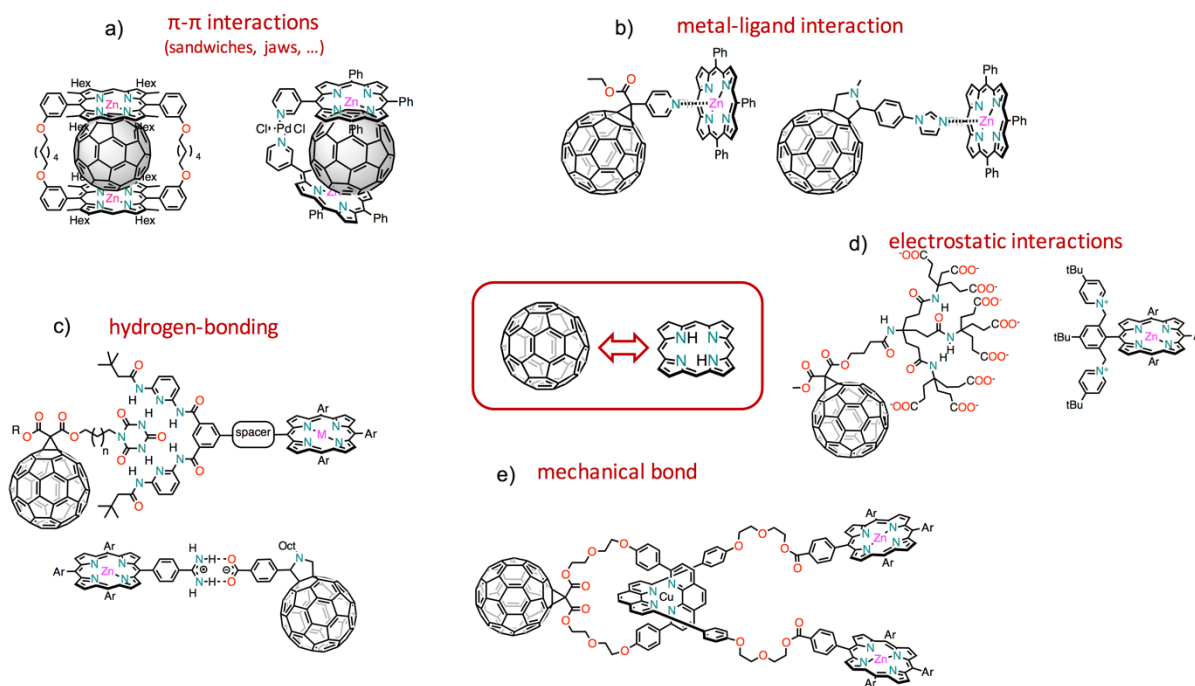


Figure 2.1.11. Examples of porphyrin-fullerene supramolecular assemblies: a) π - π interactions, b) metal-ligand interactions, c) hydrogen bonding, d) electrostatic interactions and e) mechanical bonds.

Apart from using pre-organized dimers and cages to bind fullerene by π -interactions, other supramolecular interactions were exploited in creating supramolecular porphyrin-fullerene assemblies, and include metal-ligand interactions, hydrogen bonds, electrostatic interactions and mechanical bonds (**Figure 2.1.11**). In order to employ interactions other than the π -stacking, complementary recognition motifs have to be placed both on the porphyrin and the fullerene.

First examples of such an approach was used with functionalized fullerenes carrying pyridine or imidazole moieties and metalloporphyrins, for example carrying a Zn metal (**Figure 2.1.11b**). These two are able to form a complex through a Lewis acid-base reaction between the N-containing ligand

and the metal, in order to form supramolecular dyads,⁸⁸ for example based on pyridine...Zn,⁸⁹⁻⁹¹ as well as imidazole...Zn interactions.⁹²

Hydrogen-bond complementary units were also employed for the formation of supramolecular dyads (Figure 2.1.11c). For example, a two-point amidinium-carboxylate interaction was found to favor a linear system with an efficient and long-lived ($\sim 1 \mu\text{s}$) radical-ion pair state when compared to covalent analogues.⁹³ Pairing through a Hamilton-type⁹⁴ receptor fullerene derivative and cyanuric acid bearing porphyrin through this six-point binding motif are other examples of H-bonded dyads.⁹⁵

Multiple electrostatic interactions were used in order to form a 1:1 complexes between a oligocarboxylate dendritic fullerene and octapyridinium porphyrin salt (Figure 2.1.11d) in a phosphate buffer with a high association constant (10^8 M^{-1}). Additionally, mechanically interlocked systems, such as rotaxanes and catenanes, with porphyrins and fullerenes were also prepared (Figure 2.1.11e).⁹⁶⁻⁹⁸

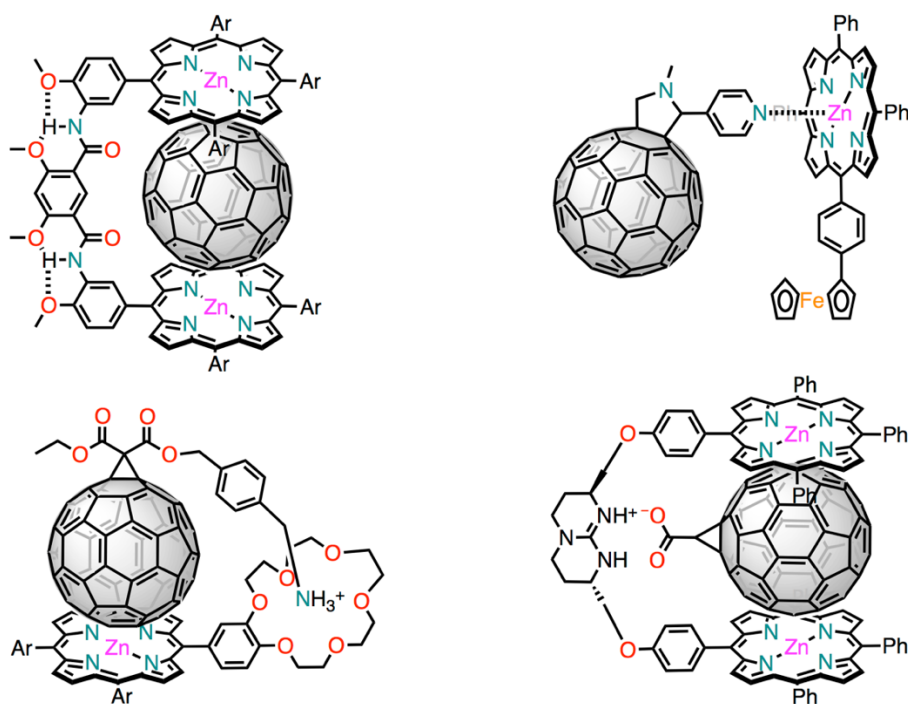


Figure 2.1.12. Multiple-type interactions lead to more stable complexes either by increase pre-organization through hydrogen bonds or additional interactions to the π - π stacking.

Another approach in order to increase the stability and versatility of the complexes is going from single type of non-covalent interactions, such as those presented above, to multiple-type interactions. Some

examples are presented in **Figure 2.1.12** and include additional hydrogen bonds that have an effect on pre-organization of the host system,⁹⁹ additional π - π stacking to metal-ligand coordination,¹⁰⁰ additional π - π stacking to crown ether-ammonium recognition^{101,102} and additional π - π stacking to two-point hydrogen bonding.¹⁰³

2.1.3. (Pseudo)rotaxanes

“Rotaxane”, from the Latin words for ‘wheel’ and ‘axle’, is a compound made of a linear species and a cyclic species, the two being bound together in a threaded structure by non-covalent forces.¹⁰⁴ The prefix “pseudo”, from Greek that stands for ‘false’, implies a supramolecular complex instead of a compound, having no bulky stoppers at the end of the linear species that allow ‘dethreading’ of the cycling species (**Figure 2.1.13**).

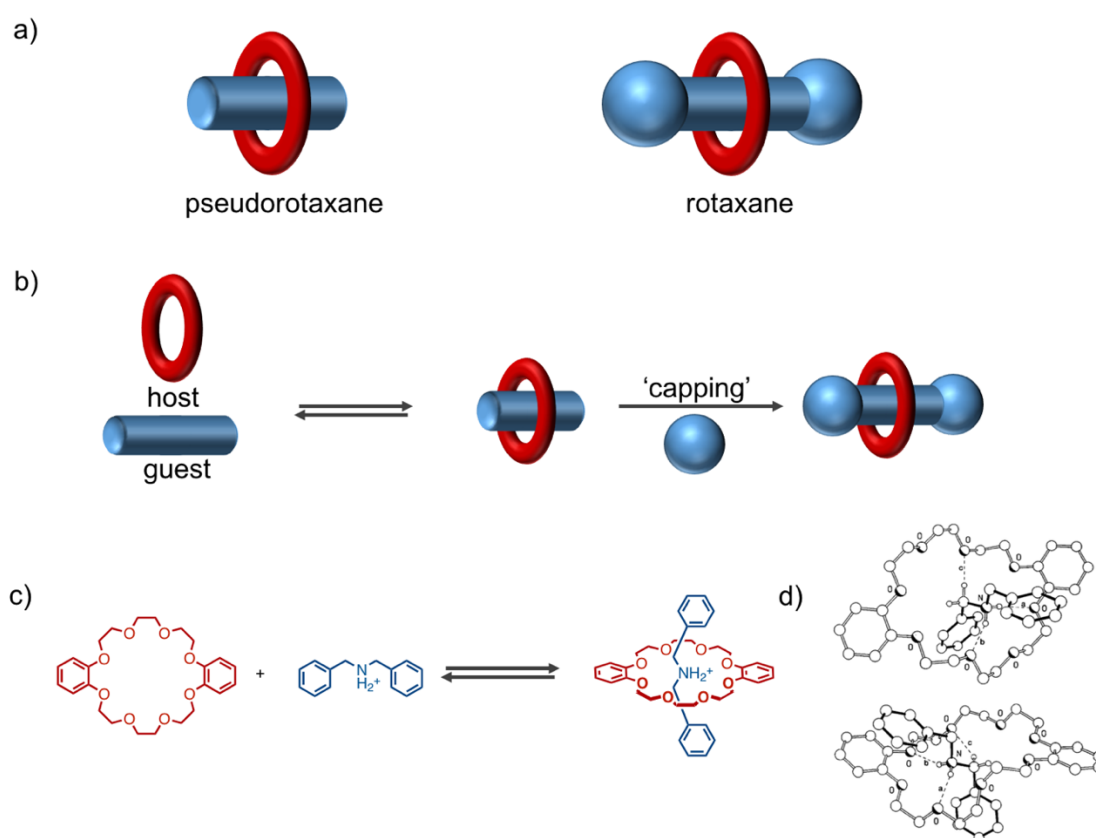


Figure 2.1.13. a) Schematic diagram of a [2]pseudorotaxane and a [2]rotaxane; b) one of (many) possible ways of synthesizing rotaxane can be achieved via ‘capping’; c) chemical structures of the very popular crown ether macrocycle and dibenzylammonium along with the related complex; d) two solid state superstructures of the 1:1 complexed formed.¹⁰⁵

Pseudorotaxanes are usually employed because of their reversibility, that has been used in the formation of molecular switches and machines.^{106–111} The reversibility can be achieved in several ways: thermally, with the deprotonation of the ammonium or addition of alkali metals, and others.^{106–111} Among crown ethers, dibenzo[24]crown-8 (DB24C8) is able to form pseudorotaxanes with secondary ammonium cations (such as dibenzyl ammonium, DBA) (Figure 2.1.13c), mainly by hydrogen bonding between $N^+–H…O$ of NH_2^+ and $C–H…O$ of NCH_2^+ and polyethers oxygen atoms of the host.^{105,112,113} The association constants of the [2]pseudorotaxane [DB24C8-DBA] were measured and found to range from $\sim 0\text{ M}^{-1}$ (DMSO- d_6) to $27\,000\text{ M}^{-1}$ ($CDCl_3$).¹⁰⁵

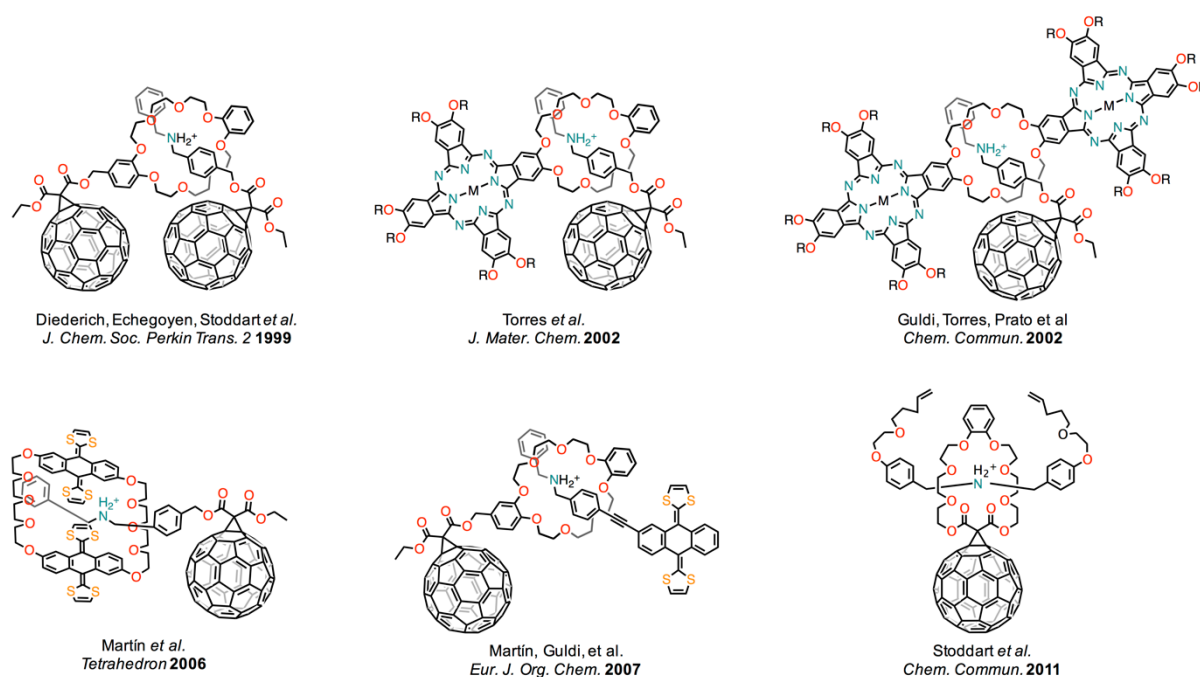


Figure 2.1.14. Examples of fullerene-containing pseudorotaxanes.

Several examples of fullerene-containing pseudorotaxanes are shown in Figure 2.1.14. The first fullerene-containing pseudorotaxane was reported as a supramolecular C_{60} dimer, in addition to C_{60} -DB24C8 complex with DBA and C_{60} -DBA complex with DB24C8.¹¹⁴ It was found that, when complexing the C_{60} -DBA derivative with DB24C8, the luminescence properties of the catechol could be used to monitor the pH-dependent, reversible formation of the pseudorotaxane-like complex. Pseudorotaxane dyads comprised of fullerene and phthalocyanine (ZnPc) or fullerene and π -extended tetrathiafulvalenes (exTTF) were reported.^{115–118} [2]Pseudorotaxane C_{60} -phthalocyanine dyads were found to bind with an association constant of around 10^4 M^{-1} (CH_2Cl_2 , fluorescence) and an efficient

ZnPc⁺-C60⁻ was observed. ExTTF were combined in [2] and [3] pseudorotaxanes with fullerenes (10³-10⁴ M⁻¹, CDCl₃/CH₃CN) and although UV-Vis investigations did not show interaction between the electroactive species, fluorescence experiments showed the presence of an electronic interaction in the excited state.

2.1.4. Non-Linear Optical Responses

Organic materials in the field of non-linear optics (NLO) have emerged as potential candidates for optical data storage technologies.¹¹⁹⁻¹²³ In general terms, an externally applied field generates a charge displacement that is responsible for the NLO. At low field strength, the induced polarization will be proportional to the applied field, being responsible for the linear response. However, at high field strengths the polarization will no longer be linear. The polarization of a molecule or macroscopic materials in an electrical field, derived for comparative purposes, will be represented by the following power series

$$P = \alpha E + \beta EE + \gamma EEE + \dots$$

with α the linear polarizability, β the quadratic or second-order hyperpolarizability and γ the third-order or cubic hyperpolarizability. For small fields E , the second- and the third-order terms can be neglected and therefore the induced polarization will be proportional to the electrical field, resulting in the linear optical behavior. However, when applying a high electric field, such as the one from a laser pulse, the quadratic and cubic terms became important, resulting in quadratic or cubic dependence of the induced polarization of the applied field.

On a macroscopic scale, the polarization can be expressed as the following series:

$$P = P_0 + \chi^{(1)}E + \chi^{(2)}EE + \chi^{(3)}EEE + \dots$$

with χ the macroscopic susceptibilities, $\chi^{(1)}$ the linear susceptibility, $\chi^{(2)}$ the quadratic (second-order) susceptibility, $\chi^{(3)}$ the cubic (third-order) susceptibility and so on. On a macroscopic level, in order to exhibit a second-order NLO response, the material has to be noncentrosymmetric, and for a large response donor and/or acceptor groups on the molecules are required. For a $\chi^{(3)}$ response, the requirements are different, with the most important one being an extended delocalized π -system.

Among the different families of π -conjugated scaffolds showing fast non-linear optical (NLO) output,^{119-121,123,124} fullerenes¹²⁵⁻¹²⁸ and porphyrins¹²⁹⁻¹³¹ – along with their hybrid conjugates – are excellent candidates due to their large excited-state absorption cross sections. Furthermore, both

fullerene and porphyrin derivatives can be easily functionalized with other electron-donating and -withdrawing groups, offering the ability to finely tune the NLO response of the final donor-acceptor system.²¹⁻²³ Although a vast number of elegant studies on the photophysical properties of fullerene-porphyrin systems has been reported,^{64,127,128,132-139} physical studies about third-order optical nonlinearity to elucidate NLO characteristics have been made only to a limited extent.

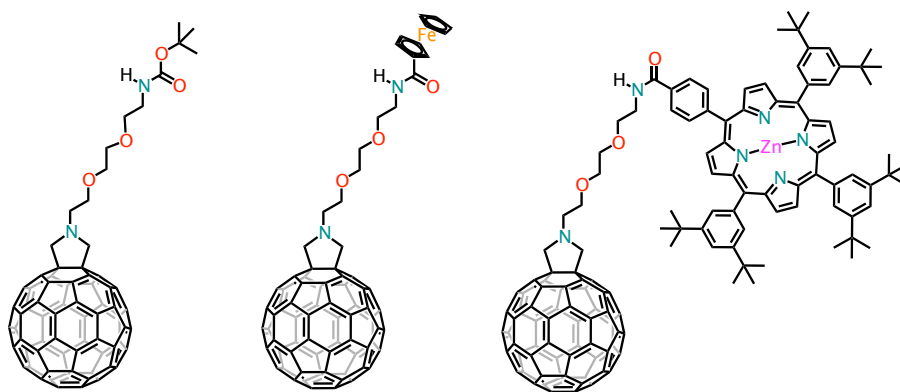


Figure 2.1.15. [60]Fullerene derivative and its covalently linked dyads that showed NLO response.^{140,141}

In that respect, we have reported the preparation and investigation of the NLO properties of a library of donor-acceptor systems featuring a [60]fullerene core covalently linked, through a flexible triethylene glycol chain, to a porphyrin or a ferrocenyl donor moiety (**Figure 2.1.15**).^{140,141} All dyads were found to display an increased third-order NLO response when compared to individual reference methano[60]fullerene or porphyrin derivatives. In particular, the porphyrin-[60]fullerene dyad showed a 20-fold enhancement of its hyperpolarizability as compared to pristine C₆₀.^{140,141} Similar results have been also reported with other covalent fullerene-containing dyads,¹⁴²⁻¹⁴⁶ however, to the best of our knowledge, the effect of non-covalent linkages on the third-order NLO responses is yet unknown for such fullerene-based systems.

2.1.5. Aim of the Project

The main aim of the project is to construct a fullerene-porphyrin [*n*]pseudorotaxanes that show enhanced NLO responses. In order to do so we use a crown ether/ammonium recognition motifs that should enable us to modulate the NLO response in a ‘turn-on’ ‘turn-off’ manner, by operating simply on acid/base equilibria. All of the NLO studies performed so far employed porphyrin-fullerene covalent conjugates, even if recently considerable attention has been placed on non-covalent

interactions, owing to their versatility.^{137,147,148} Additionally, the crown/ether recognition is a slow equilibrium (for NMR timescale) and, by implementing this recognition motif we should be able to investigate the equilibria between the ‘tight’ and the ‘loose’ conformations that correspond to the stacking or spaced units, respectively.

2.2. Self-Assembly of [60]Fullerene-Porphyrin [*n*]Pseudorotaxanes

The porphyrin and fullerene components used to prepare the corresponding [2] and [3]pseudorotaxanes are shown in **Figure 2.2.1**.

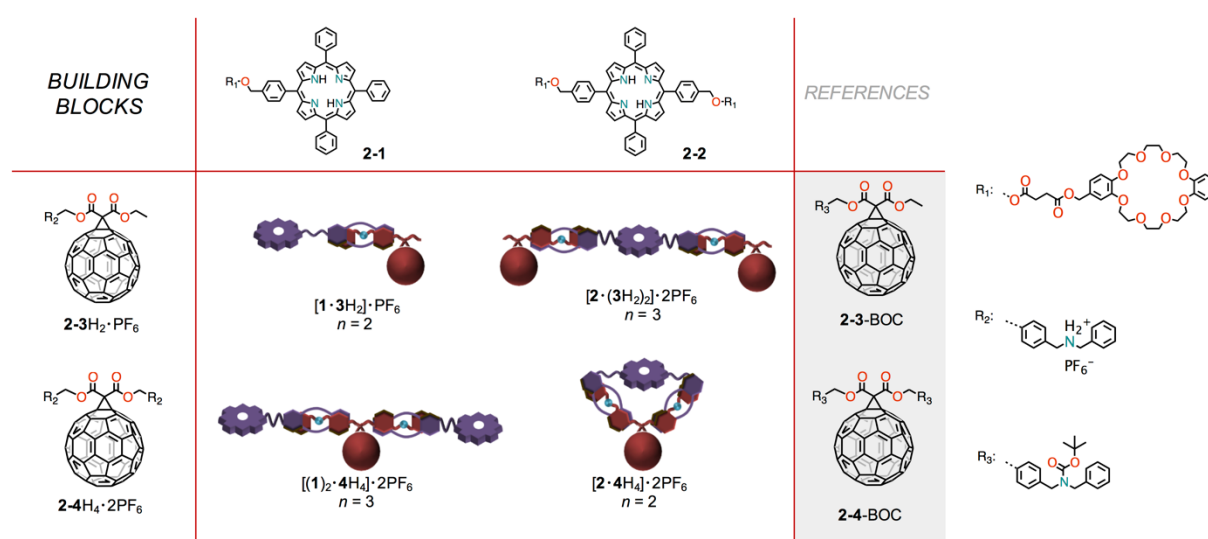
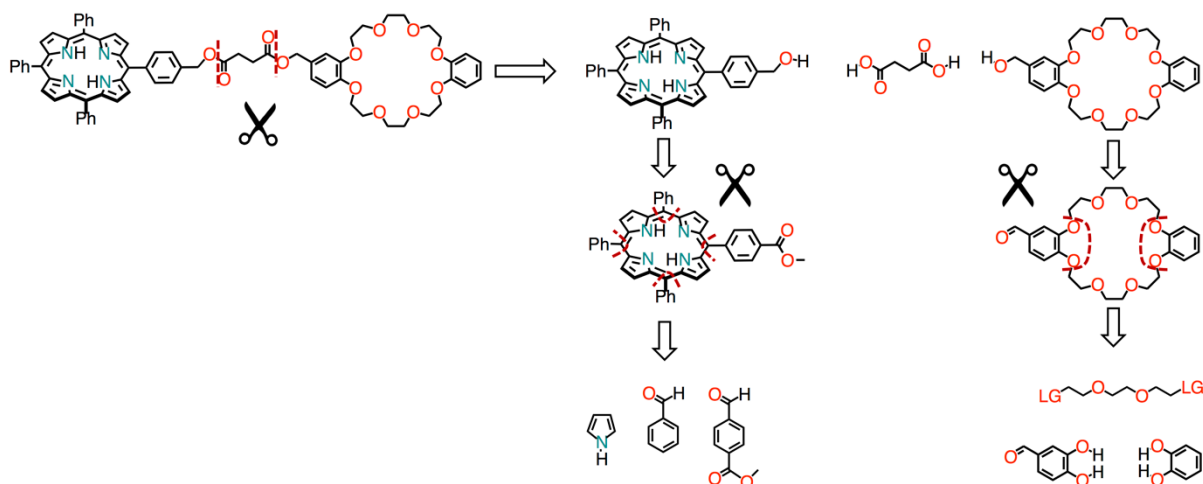


Figure 2.2.1. Library of the porphyrin- (2-1 and 2-2) and fullerene-based (2-3H₂·PF₆ and 2-4H₄·2PF₆) components for preparing [2]pseudorotaxanes [1·3H₂]·PF₆ and [2·4H₄]·2PF₆ and [3]pseudorotaxanes [(1)₂·4H₄]·2PF₆ and [2·(3H₂)₂]·2PF₆. The [*n*]pseudorotaxanes are sketched as cartoons; reference compounds 3-BOC and 4-BOC are highlighted in grey.

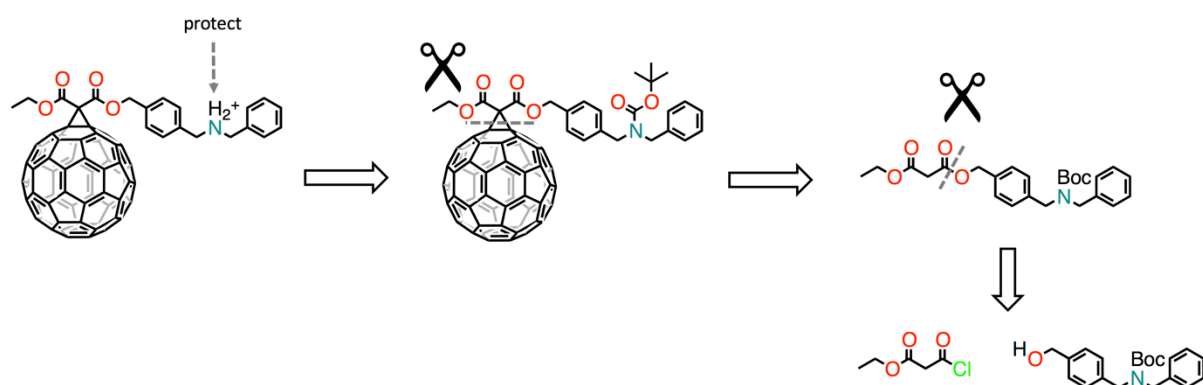
2.2.1. Syntheses

The retrosynthetic approach to the host porphyrin 2-1 is depicted in the retrosynthetic analysis **Scheme 2.2.1**. A flexible linker was regarded as necessary in order to allow the conformational equilibria between the ‘tight’ and ‘loose’ states. The key reaction is the final condensation between porphyrin benzylic alcohol and DB24C8 succinic acid derivative, due to easier scale-up of the crown ether intermediate. The crown ether could be prepared by using metal templated (dilute) macrocyclization procedure, subsequent reduction to hydroxymethyl and final nucleophilic opening of

succinic anhydride. The porphyrin, on the other hand, can be prepared by a mixed condensation under Lindsey's conditions that yields not only the A_3B , but also A_2B_2 porphyrin (*Chapter 1*). The crown ether, being asymmetric (*i.e.* the two pyrocatechol moieties are different), a lengthier route had to be taken and is described in detail in the synthetic section.



Scheme 2.2.1. Retrosynthetic analysis of porphyrin crown ether host.

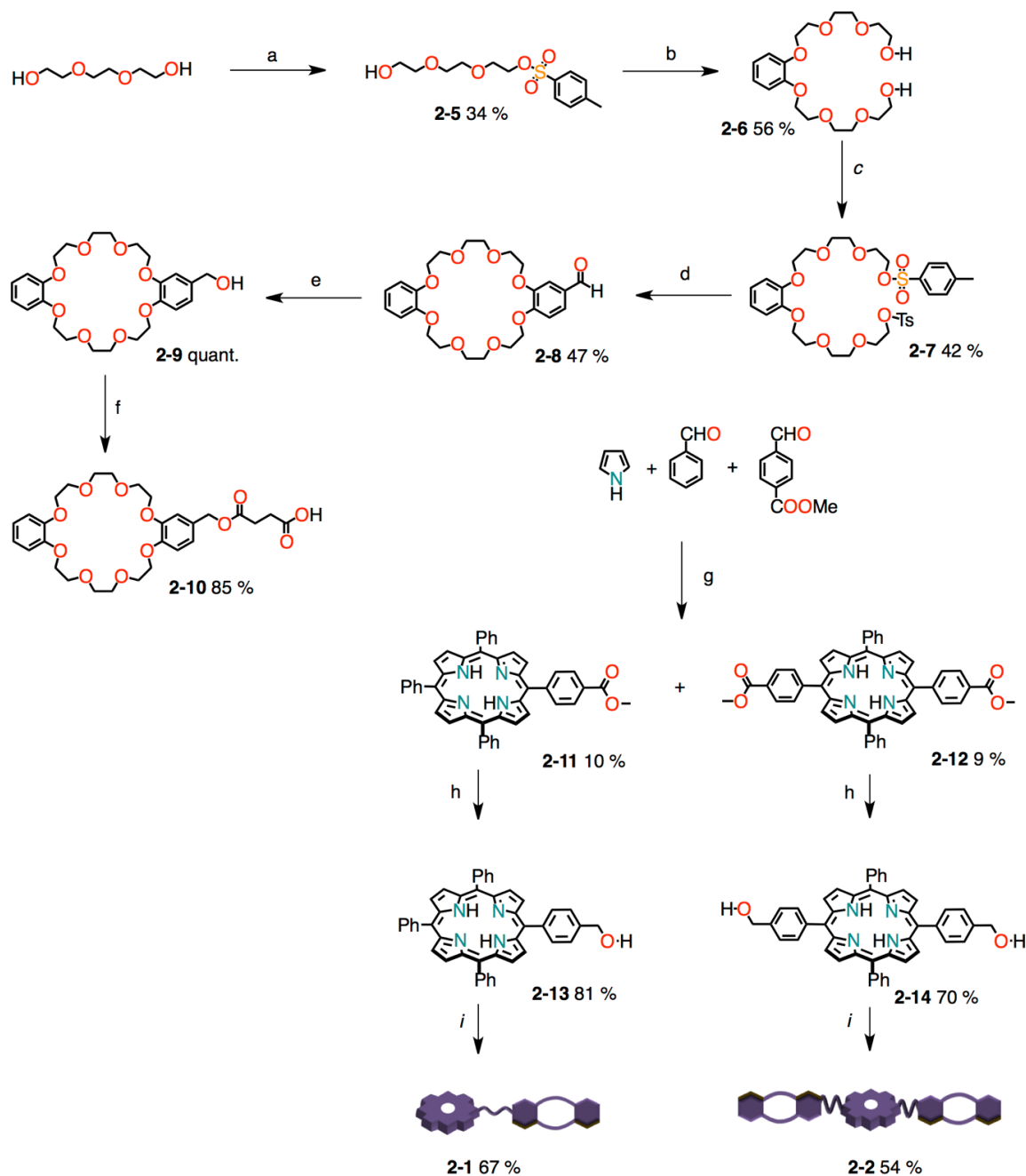


Scheme 2.2.2. Retrosynthetic analysis for fullerene dibenzylammonium cation.

For the fullerene guest bearing ammonium ion, the key step is a modified Bingel reaction with the malonate derivative and pristine C_{60} (**Scheme 2.2.2**). The malonate derivative can be obtained from commercially available ethyl malonyl chloride and the (easily accessible) BOC-protected dibenzylammonium alcohol.

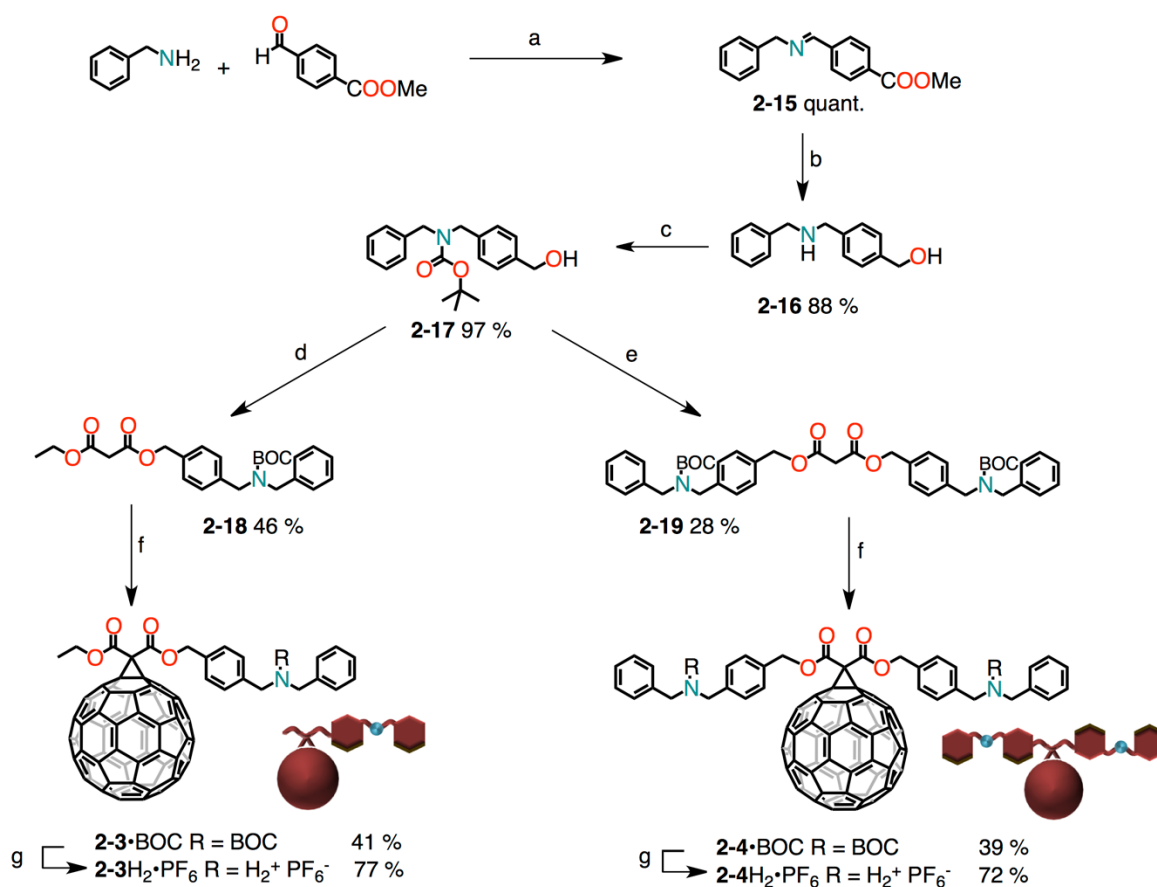
The complete synthesis of porphyrin hosts is depicted in **Scheme 2.2.3**. The DBC248 macrocycle was prepared starting from commercially available triethylenglycol. Only one alcohol group was

transformed in a leaving group, tosylate **2-5**, that was reacted with pyrocatechol in order to obtain bis-alcohol intermediate **2-6**.



Scheme 2.2.3. Synthetic scheme for preparation of crown ethers **2-1** and **2-2**. Reagents and conditions: a) tosyl chloride, NaOH, H₂O/THF, r.t.; b) pyrocatechol, K₂CO₃, CH₃CN, reflux; c) tosyl chloride, NaOH, H₂O/THF, r.t.; d) 3,4-dihydroxybenzaldehyde, K₂CO₃, LiBr cat., CH₃CN, reflux; e) NaBH₄, CH₂Cl₂/MeOH, 0 °C to r.t.; f) succinic anhydride, 4-DMAP, PhCH₃, reflux; g) BF₃·Et₂O, then DDQ, Et₃N, CH₂Cl₂, r.t.; h) LiAlH₄, THF, 0 °C to rt; i) **2-10**, EDC·HCl, 4-DMAP, CH₂Cl₂, r.t.

The bis-alcohol was once again transformed in tosylate leaving groups **2-7** that were displaced by a nucleophilic substitution reaction with 3,4-dihydroxybenzaldehyde, in order to obtain the asymmetric DB24C8 intermediate **2-8**. The aldehyde was reduced with NaBH₄ to benzylic alcohol **2-9**, that was reacted with succinic anhydride in a nucleophilic opening reaction to obtain intermediate **2-10**. Porphyrin A₃B and A₂B₂ methyl esters were prepared under Lindsey's conditions that yielded tetraphenylporphyrin and the mixture of esters. The mixture of porphyrins was then divided in multiple fractions that were purified on multiple gravity-fed silica gel column chromatographies. The isolated porphyrin **2-11** and **2-12** esters now could be reduced to benzylic alcohols **2-13** and **2-14** and reacted with the succinic acid DB24C8 **2-10** derivative, with a carbodiimide condensation reaction.



Scheme 2.2.4. Synthetic scheme for preparation of dibenzyl ammonium fullerenes **2-3** and **2-4**. Reagents and conditions: a) molecular sieves, MeOH, reflux; b) LiAlH₄, THF, 0 °C to r.t.; c) BOC₂O, 4-DMAP, r.t.; d) ethyl malonyl chloride, pyridine, CH₂Cl₂, 0 °C; e) malonyl chloride, pyridine, CH₂Cl₂, 0 °C; f) C₆₀, I₂, DBU, toluene, r.t.; g) TFA, PhCH₃; then 6 M aq. NaOH; then 4 M aq. HCl, then sat. aq. NH₄PF₆, acetone.

The fullerene guests were prepared according to **Scheme 2.2.4**. The dibenzylamino core was prepared by a condensation reaction (in presence of molecular sieves) between benzylamine and methyl 4-

formylbenzoate into an imine **2-15** that, in presence of lithium aluminum hydride, reduced both the imine to amine and ester to benzyl alcohol **2-16**. At this point the amino was BOC-protected to **2-17** before reacting with ethyl malonyl chloride (for asymmetric malonate) and malonyl chloride (for symmetric malonate) to obtain the corresponding malonate precursors **2-18** and **2-19**, that would yield ultimately the mono- and di-topic guest molecules. The malonate derivatives were used to functionalize fullerene C_{60} in a modified Bingel cyclopropanation and a final trifluoroacetic mediated BOC deprotection, followed by counterion exchange yielded the final fullerene guests.

All the new products were fully characterized. As examples, below are reported some $^1\text{H-NMR}$ spectra with full assignment of protons (**Figure 2.2.2** and **Figure 2.2.3**).

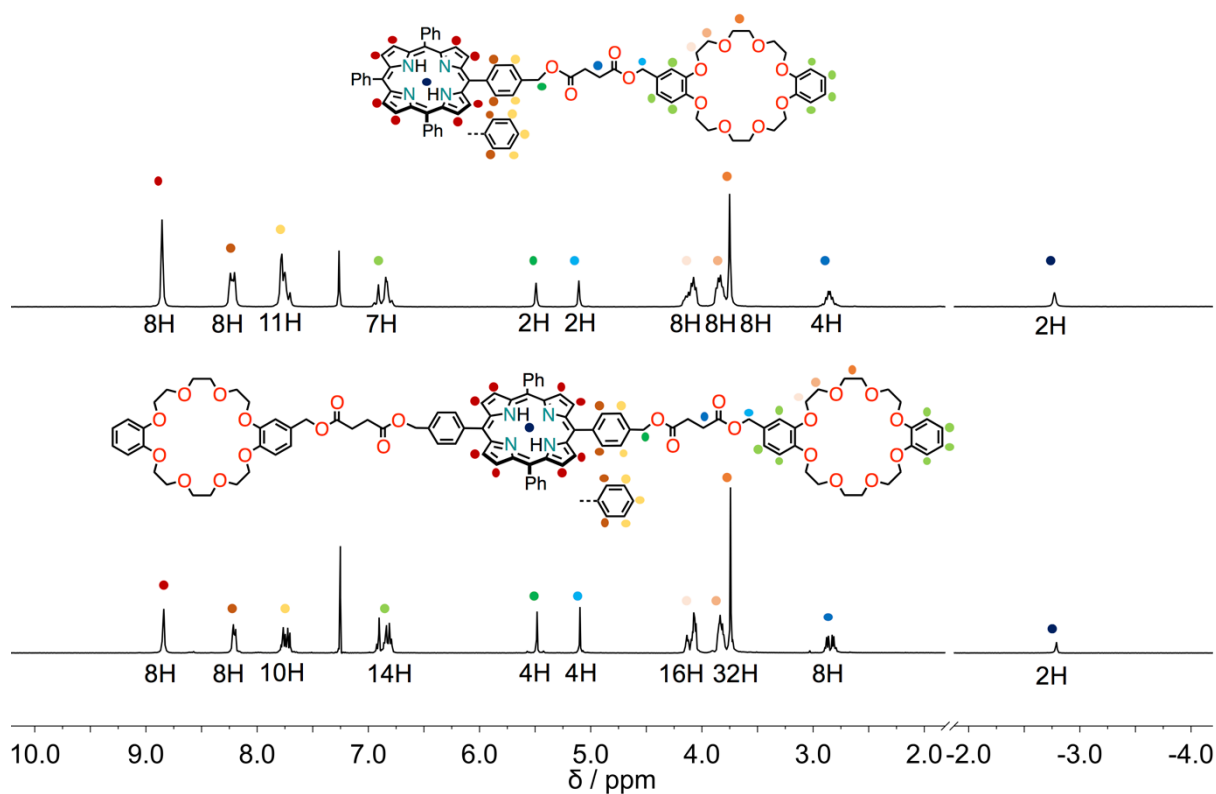


Figure 2.2.2. $^1\text{H-NMR}$ (500 MHz, CDCl_3 , 298 K) of porphyrin hosts **2-1** (top) and **2-2** (bottom).

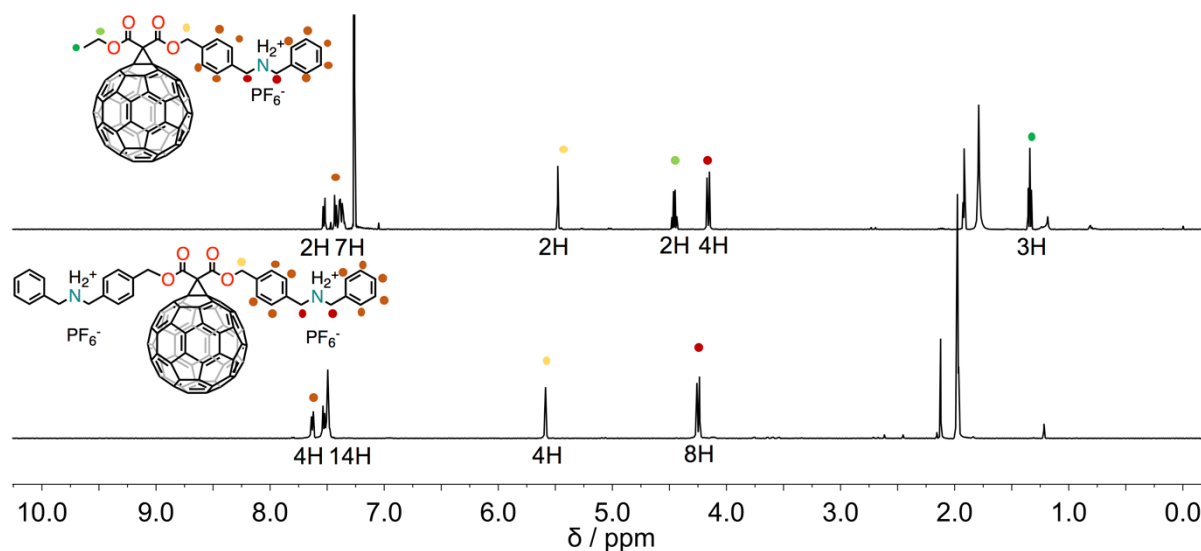


Figure 2.2.3. $^1\text{H-NMR}$ (500 MHz, 298 K) of porphyrin guests **2-1** (top, $\text{CDCl}_3/\text{CD}_3\text{CN}$ 9:1 v/v) and **2-2** (bottom, CD_3CN).

2.2.2. [*n*]Pseudorotaxane Self-Assembly

First of all, a 1:1 mixture of BOC-protected fullerene derivative **2-3-BOC** and host **2-1** was prepared and $^1\text{H-NMR}$ spectra was recorded in order to verify that no interaction is taking place. (**Figure 2.2.4**), with the spectrum of the 1:1 mixture corresponding to the sum of the spectra of individual compounds.

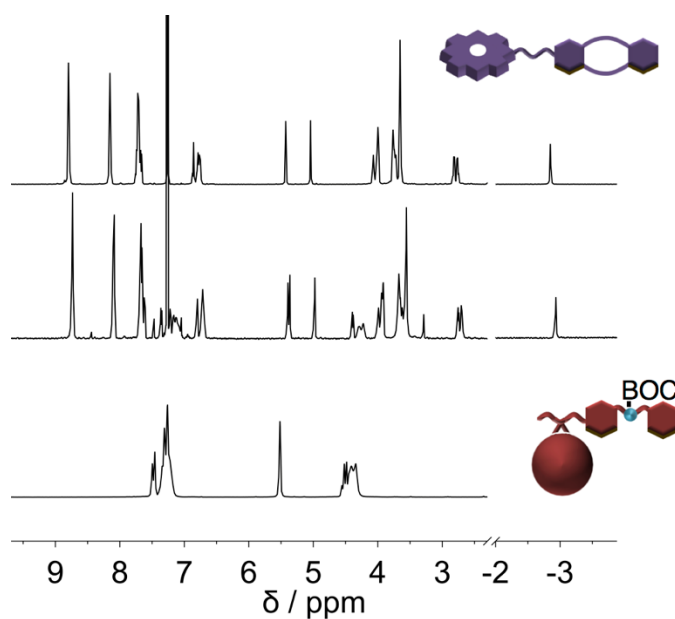


Figure 2.2.4. $^1\text{H-NMR}$ (500 MHz, CDCl_3) of **2-1** (top), **2-3-BOC** (bottom) and their 1:1 mixture (middle) did not show complex formation.

Since the fullerene guests showed very low solubility in CDCl_3 , mixtures of CDCl_3 and CD_3CN had to be used when working with ammonium hexafluorophosphate salts. At first, a 1:1 mixture of porphyrin host **2-1** and fullerene guest **2-3H₂·PF₆** was prepared in $\text{CDCl}_3/\text{CD}_3\text{CN}$ (9:1 v/v) and ^1H -NMR was recorded and compared to the spectra of the free components. The spectrum showed the appearance of a new pattern of proton resonances compared to those of the free molecular synthons, confirming the formation of the threaded complex (**Figure 2.2.5**). The system was found to be in a slow equilibrium regime, implying that the resonances of free and complex species should be present at the same time.

In particular, the presence of the diagnostic multiple resonances around 4.5 ppm, typical of the $-\text{CH}_2\text{N}-$ protons, were indicative of the threaded DBA moiety. Moreover, the singlet belonging to the benzylic position of the porphyrin is now a multiplet (resembling a double doublet), suggesting the protons have become diastereotopic. Other significant changes include appearance of a new set of upfield resonances of β and inner NH porphyrin protons. This suggest that not only the threading of the DBA through the DB24C8 is taking place, but also the presence of a second equilibrium, from a 'loose' to a 'tight' or 'face-to-face' conformer, as has been reported for other porphyrin-fullerene constructs.^{101,140,149}

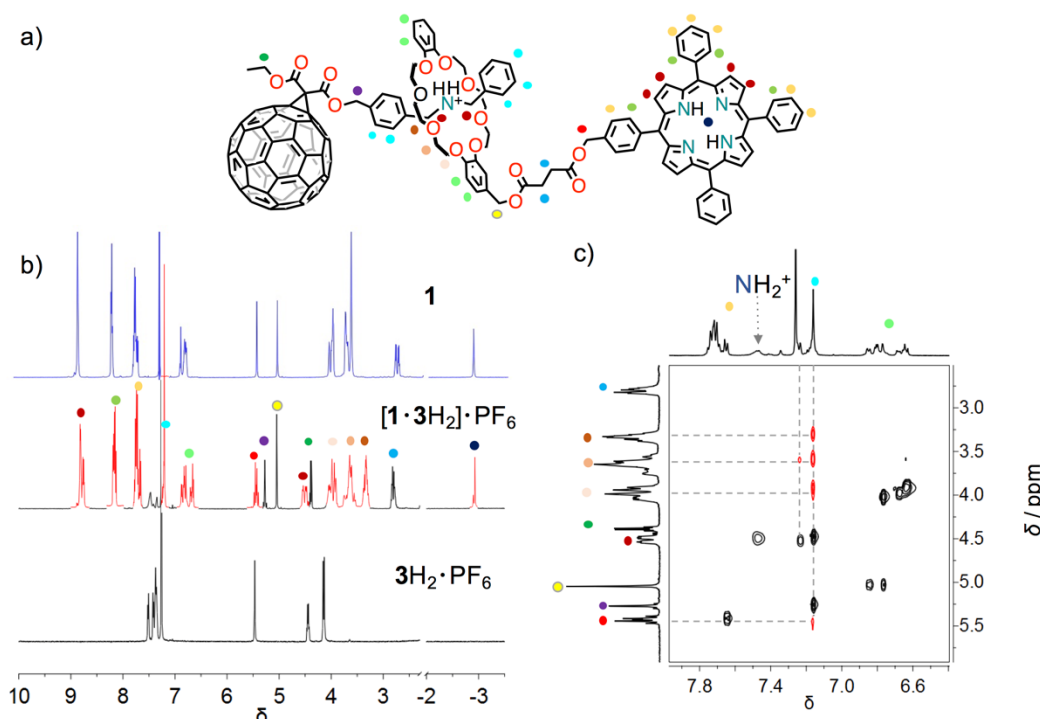


Figure 2.2.5. a) [2]Pseudorotaxane complex; b) ^1H -NMR (500 MHz, $\text{CDCl}_3/\text{CD}_3\text{CN}$, 9:1 v/v) of host (top), guest (bottom) and 1:1 complex (middle); c) ROESY spectra of 1:1 complex (the relevant resonance are highlighted in red).

In order to appreciate the effect of the secondary interaction on the overall binding, a series of additional and reference experiments were carried out. The **Figure 2.2.6** compares all free components with corresponding [2]pseudorotaxane complexes. In the cases of [2]pseudorotaxanes [1-DBA]·PF₆ and [DB24C8-COOEt·3H₂]·PF₆ although the diagnostic signals of complexation are present, the porphyrin aromatic signals (as well as inner NH) are unchanged when compared to free host **2-1**. This observation gives a clear evidence that, in the porphyrin-fullerene pseudorotaxane, a second interaction takes place, namely the fullerene cage over the porphyrin central core. Moreover, if we consider solid state structures and covalent porphyrins-fullerene structures present in literature,^{77,150} the nesting of an electron-rich double bond over the porphyrin would give an upfield shift in NMR spectroscopy. This was indeed the case here. Remarkably, we were able to observe a slow equilibrium not only for the pseudorotaxane threading event (as was expected) but also for the secondary interaction.

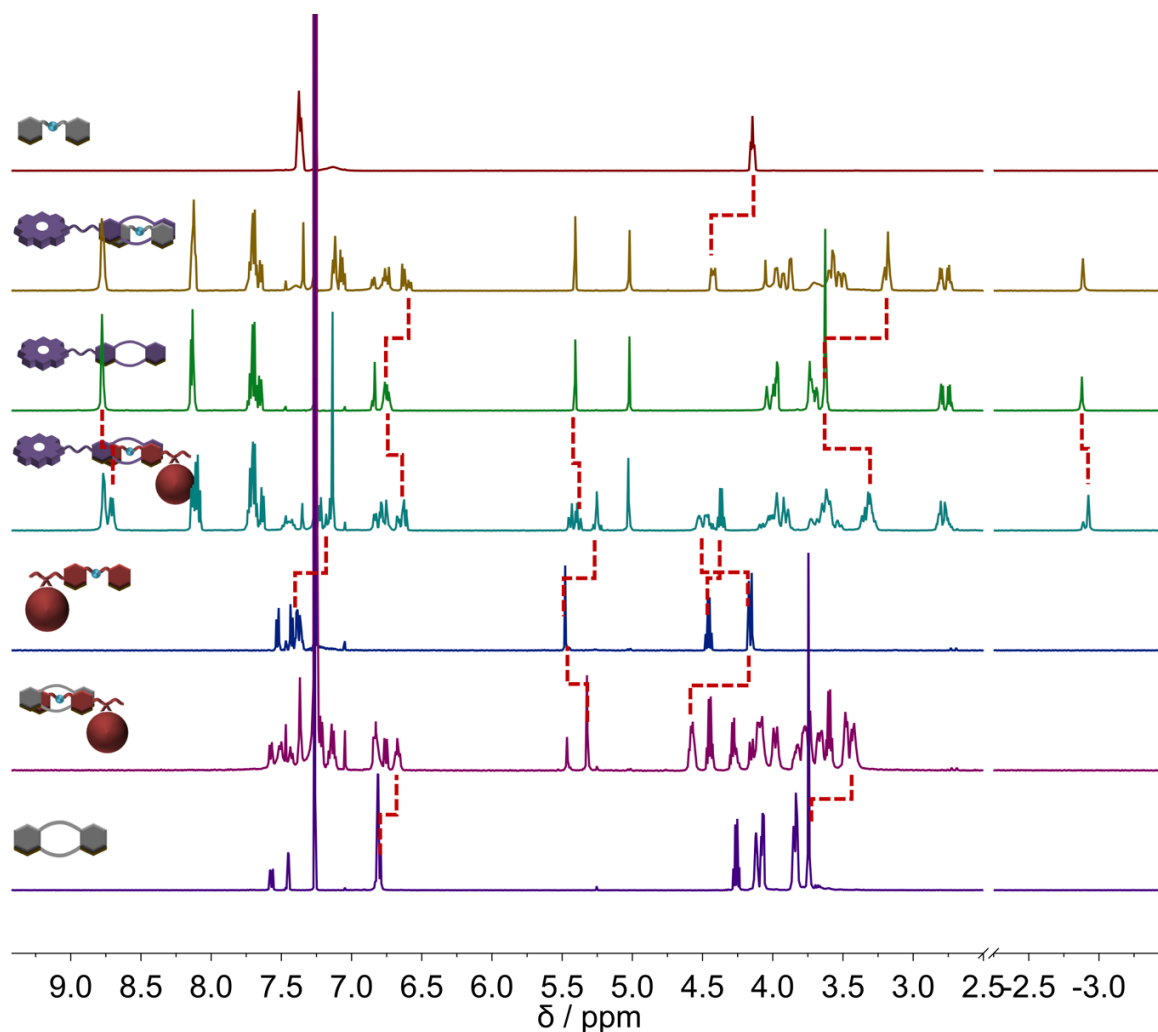


Figure 2.2.6. Stacked ¹H-NMR spectra (500 MHz, CDCl₃/CD₃CN, 9:1 v/v) of, from top to bottom, DBA·PF₆, [1-DBA]·PF₆, host **2-1**, [1-3H₂]·PF₆, **2-3H₂**·PF₆, [DB24C8-COOEt·3H₂]·PF₆, and DB24C8-COOEt.

Titration experiments showed progressive increase in concentration of the complex, until complete (Figure 2.2.7a) disappearance of the free host signals. This is even more evident by observing the inner NH resonances, moving from 'loose' to 'tight' conformation (Figure 2.2.7a).

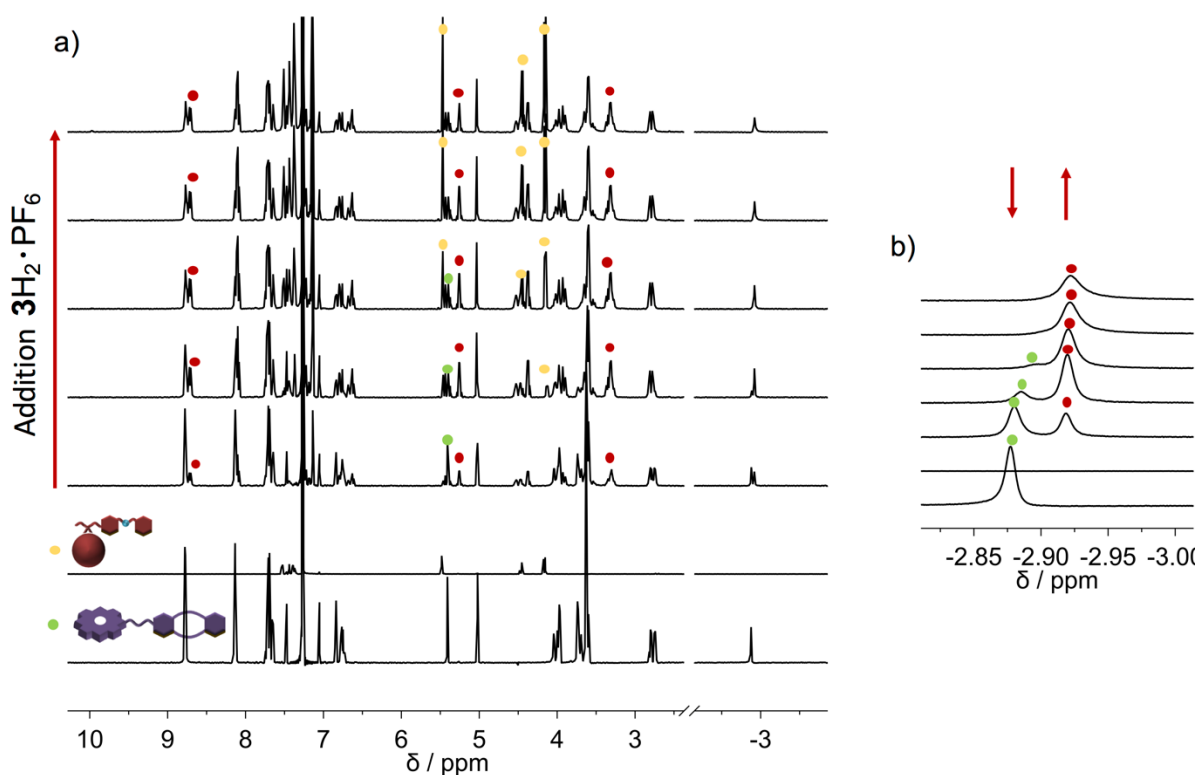


Figure 2.2.7. $^1\text{H-NMR}$ titration experiment (500 MHz, $\text{CDCl}_3/\text{CD}_3\text{CN}$, 9:1 v/v) with addition of guest $3\text{H}_2\cdot\text{PF}_6$ to host **2-1**; b) shows enlargement of the NH porphyrin region.

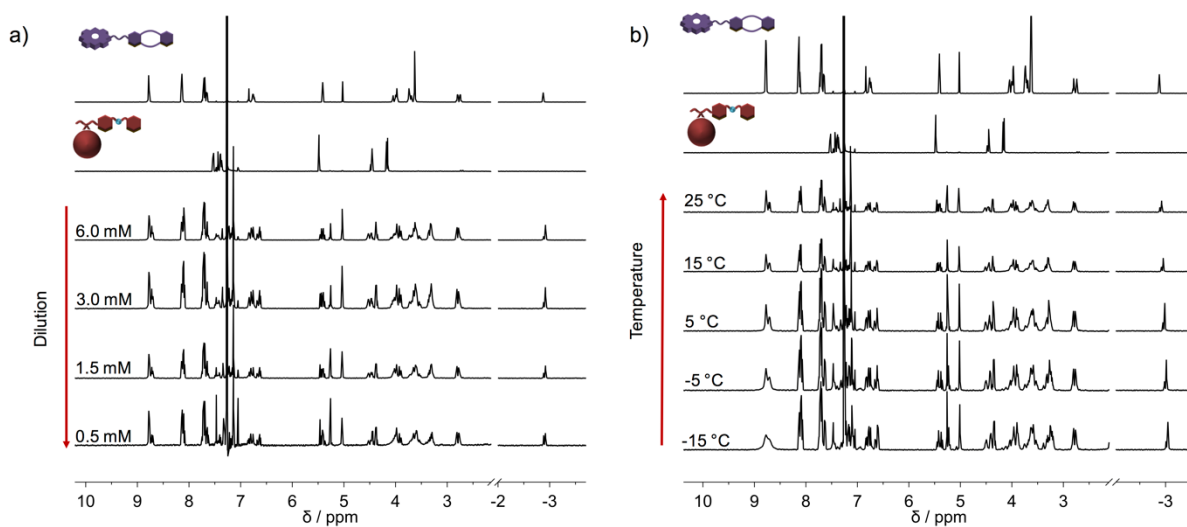


Figure 2.2.8. a) $^1\text{H-NMR}$ dilution- and b) temperature-dependent experiments (500 MHz, $\text{CDCl}_3/\text{CD}_3\text{CN}$, 9:1 v/v) for [2]pseudorotaxane $[1\cdot 3\text{H}_2]\cdot\text{PF}_6$.

This trend was confirmed by both dilution- and temperature-dependent experiments (Figure 2.2.8). By diluting a $[1\cdot3H_2]\cdot PF_6$ $CDCl_3/CD_3CN$ (9:1 v/v) solution (from 6.0 mM to 0.5 mM), a progressive disappearance of the complex resonances was observed (complex is however still present at the lowest concentration). Similarly, temperature-dependent experiments (performed at 1.5 mM) when cooling from 298 to 258 K showed, as expected, a higher concentration of complex compared to the free components.

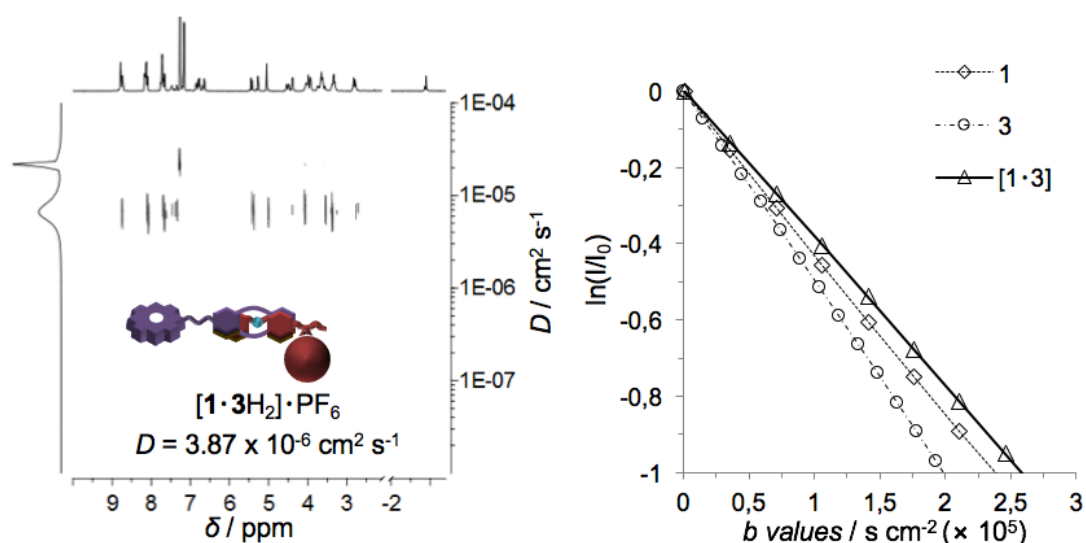


Figure 2.2.9. DOSY experiment (500 MHz, $CDCl_3/CD_3CN$, 9:1 v/v) of $[1\cdot3H_2]\cdot PF_6$ (6.0 mM).

Additional NMR experiments were used to elucidate the diffusion behavior of the species (Figure 2.2.9). DOSY-NMR of a relatively concentrated 1:1 mixture $[1\cdot3H_2]\cdot PF_6$ was performed and (apparently) only one species was observed. By calculating the hydrodynamic radius (through the Stokes-Einstein equation) and using the diffusion coefficient of the species, it was estimated a R_H of 1.1 nm. This value is very close to that measured for free host and guest species, but since the resonances that originate from the complex are present (and show the same diffusion coefficient as other signals) this suggests the presence of mostly complexed and ‘tight’ species.

Apparently, we were able to observe the two conformations and this was exploited in further experiments that were performed in order to study the influence of the secondary donor-acceptor interaction in the formation of the complex. To this end, a series of NMR experiments were performed in various solvents, ranging both in polarity and in fullerene solubility (being also commercially

available as deuterated solvents). As can be observed from **Figure 2.2.10**, the solvent does play a dramatic effect on the formation of the complex, especially if we observe the inner porphyrin *NH* resonances (around -3 ppm). In 1,1,2,2-tetrachloroethane- d_4 and *o*-dichlorobenzene- d_4 there is apparently only one signal, or due to overlapping of the free and the host signals or the ‘tight’ \rightleftharpoons ‘loose’ equilibrium is in a fast regime. Remarkably, when changing solvents from $\text{CDCl}_3/\text{CD}_3\text{CN}$ to $\text{Tol-}d_8/\text{CD}_3\text{CN}$, although the formation of the threaded pseudorotaxane is favored due to the more apolar solvent (solvent polarity ϵ decreases from 4.81 to 2.44 from CHCl_3 to Ph-CH_3 , respectively),⁷⁴ there is apparently more ‘loose’ conformer present. This is, most probably, due to an almost 20-fold higher solubility of the fullerene cage in toluene with respect to chloroform and would suggest that the porphyrin-fullerene stacking is mainly driven by desolvation of the fullerene cage.

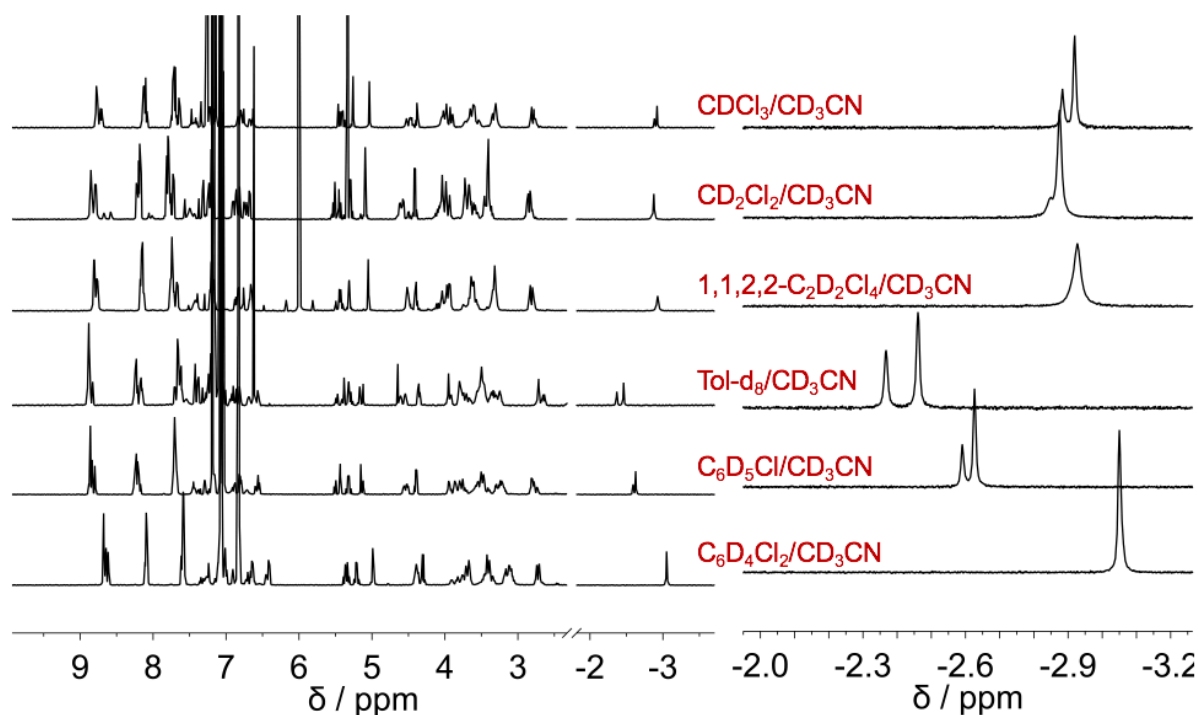


Figure 2.2.10. $^1\text{H-NMR}$ (500 MHz, 298 K) of [2]pseudorotaxane $[\mathbf{1}\cdot\mathbf{3H}_2]\cdot\text{PF}_6$ (1.5 mM) in different solvents (all in a 9:1 v/v ratio with CD_3CN).

Finally, in order to evaluate the interaction between the two aromatic system, a reference titration experiment between host *meso*-tetraphenylporphyrin (isolated from the reaction mixture of the mixed condensation under Lindsey conditions) and BOC-protected fullerene **2-3** was carried out in

the same solvent conditions ($\text{CDCl}_3/\text{CD}_3\text{CN}$, 9:1 v/v). Although the change in chemical shift is small, it allowed us to estimate a binding constant of around 70 M^{-1} by non-linear curve fitting. This is almost four-fold higher for the porphyrin-fullerene interaction reported in CDCl_3 ($K_a \sim 20 \text{ M}^{-1}$),¹⁰² and suggests that by adding a solvent in which C_{60} has no solubility⁷⁴ the association constant increases, pointing again to a solvophobic effect.

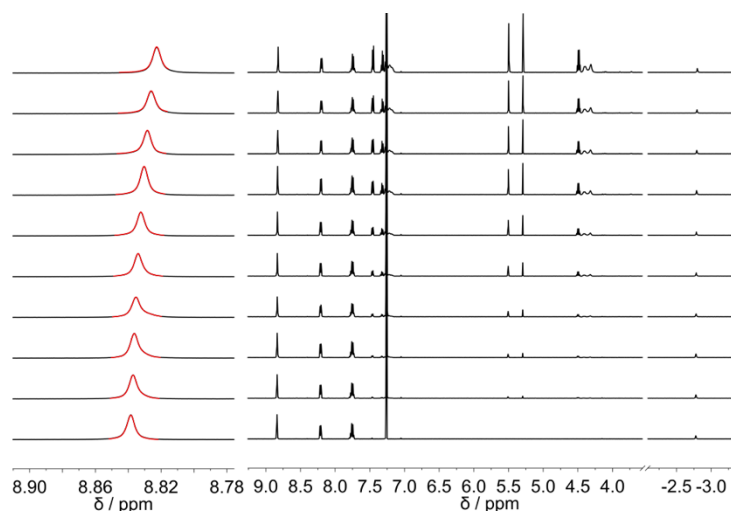


Figure 2.2.11. Reference ^1H -NMR titration experiment (500 MHz, 298 K, $\text{CDCl}_3/\text{CD}_3\text{CN}$, 9:1 v/v) of **TPP** with BOC-protected **2-3**.

The above performed experiments therefore point to equilibria of pseudorotaxane association and π - π stacking (**Figure 2.2.12**).

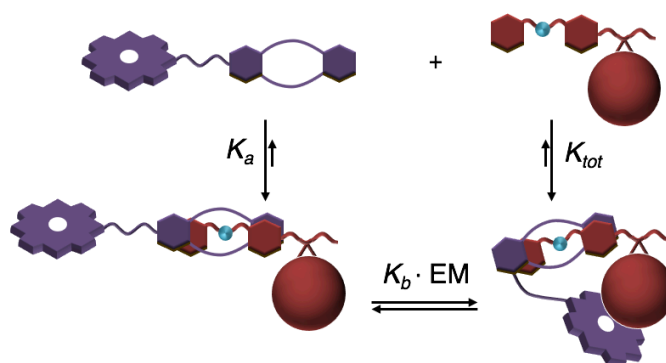


Figure 2.2.12. Proposed equilibria for the formation of [2]pseudorotaxane $[1.3\text{H}_2] \cdot \text{PF}_6$.

In such a system it should be possible to evaluate the individual contributions and ultimately quantify the effective molarity of such complexation. These experiments (by UV-Vis and fluorescence titrations) are currently underway.

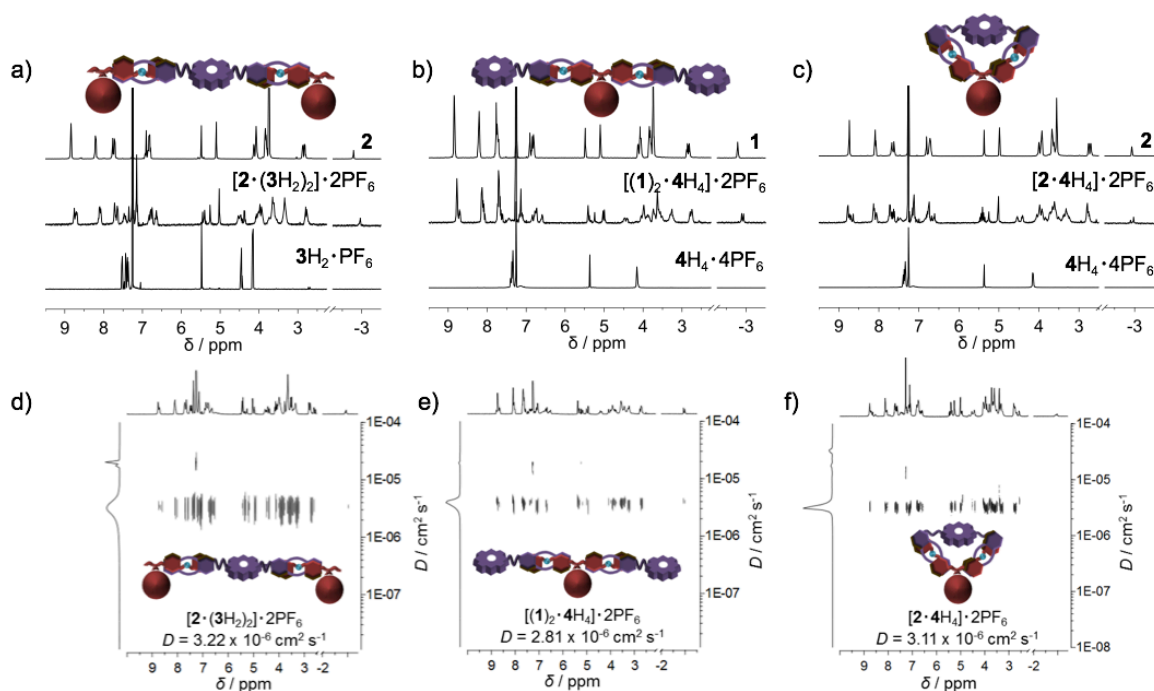


Figure 2.2.13. a) $^1\text{H-NMR}$ of $[2\cdot(3\text{H}_2)_2]\cdot 2\text{PF}_6$; b) $^1\text{H-NMR}$ of $[(1)_2\cdot 4\text{H}_4]\cdot 2\text{PF}_6$; c) $^1\text{H-NMR}$ of $[2\cdot 4\text{H}_4]\cdot 2\text{PF}_6$; d-f) 2D-DOSY contour mode plots for the [2]pseudorotaxane and [3]pseudorotaxane-like complexes (500 MHz, 298 K, $c = 6.0 \times 10^{-3}$ M) with the corresponding diffusion values.

Next, the formation of [3]pseudorotaxanes $[(1)_2\cdot 4\text{H}_4]\cdot 2\text{PF}_6$ and $[2\cdot(3\text{H}_2)_2]\cdot 2\text{PF}_6$ and [2]pseudorotaxane $[2\cdot 4\text{H}_4]\cdot 2\text{PF}_6$ was investigated. The $^1\text{H-NMR}$ spectra ($\text{CDCl}_3/\text{CD}_3\text{CN}$ 9:1 v/v, $c = 3.0 \times 10^{-3}$ M, at 298 K) showed similar results to those observed for the $[1\cdot 3\text{H}_2]\cdot \text{PF}_6$ complex (**Figure 2.2.13**). In all cases, upon addition of [60]fullerene ammonium salts $4\text{H}_4\cdot 2\text{PF}_6$ or $3\text{H}_2\cdot \text{PF}_6$, the tetrapyrrolic-centered resonances for porphyrins **1** and **2** undergo dramatic spectral changes, yielding multiplets which suggest the formation of the [2]- and [3]pseudorotaxane complexes, respectively. Notably, DOSY confirmed the formation of a [2]pseudorotaxane over a supramolecular polymer assembly for $[2\cdot 4\text{H}_4]\cdot 2\text{PF}_6$. The diffusion study showed that the complex-centered proton resonances have, within the experimental error, similar diffusion coefficients to porphyrin **2-2** alone, a value consistent with a folded conformation ($3.11 \times 10^{-6} \text{ cm}^2 \text{ s}^{-1}$).

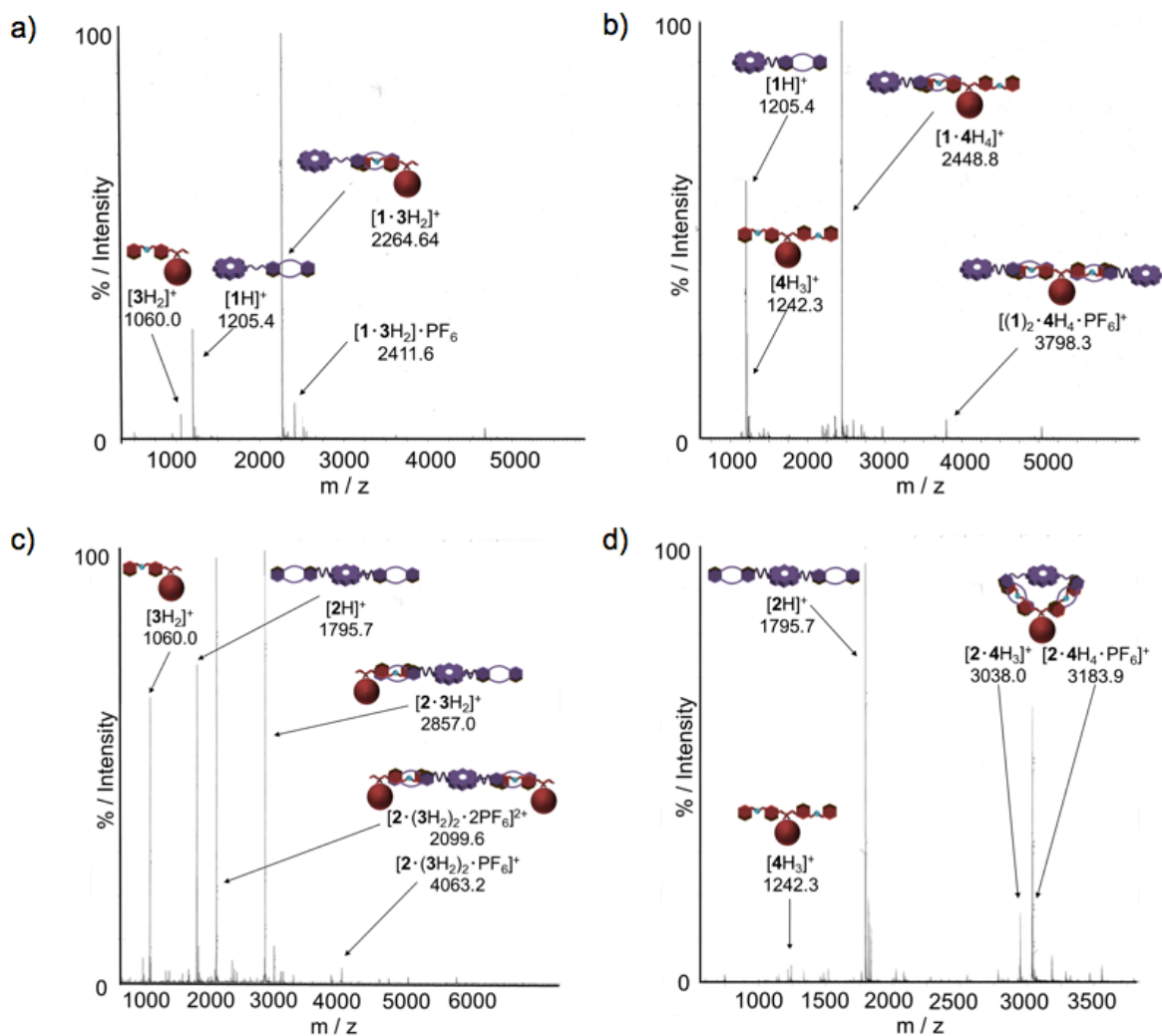


Figure 2.2.14. High-resolution (HR) MALDI-TOF mass spectra of a) $[1 \cdot 3H_2] \cdot PF_6$, b) $[2 \cdot (3H_2)_2] \cdot 2PF_6$, c) $[(1)_2 \cdot 4H_4] \cdot 2PF_6$ and d) $[2 \cdot 4H_4] \cdot 2PF_6$.

Unambiguous proofs for the formation of the different complexes were also obtained by HR-MALDI-TOF mass spectrometric analysis of the threaded complexes. In particular, the main peaks corresponding to the supramolecular ions of the pseudorotaxane complexes were observed for all the non-covalent ensembles (**Figure 2.2.14**). Peaks corresponding to the molecular ions of the constituting fullerene ammonium salts and the porphyrin crown ether conjugates were also present in the spectra (with and without PF_6^-). Notably, for the sample containing a 1:1 mixture of crown ether **2-2** and $[60]$ fullerene bisammonium salt $4H_4 \cdot 2PF_6$, the MALDI-TOF spectrum displayed only the dimeric species, thus supporting the hypothesis for which a cyclic structure for the $[3]$ pseudorotaxane $[2 \cdot 4H_4] \cdot 2PF_6$ is likely formed through an intramolecular threading process.¹⁵¹

2.2.3. Molecular Modeling

The characterization of the supramolecular species in solution, which evidenced strong fullerene-porphyrin interaction, was further complemented by the molecular models built for the $[n]$ pseudorotaxane complexes (**Figure 2.2.15**).

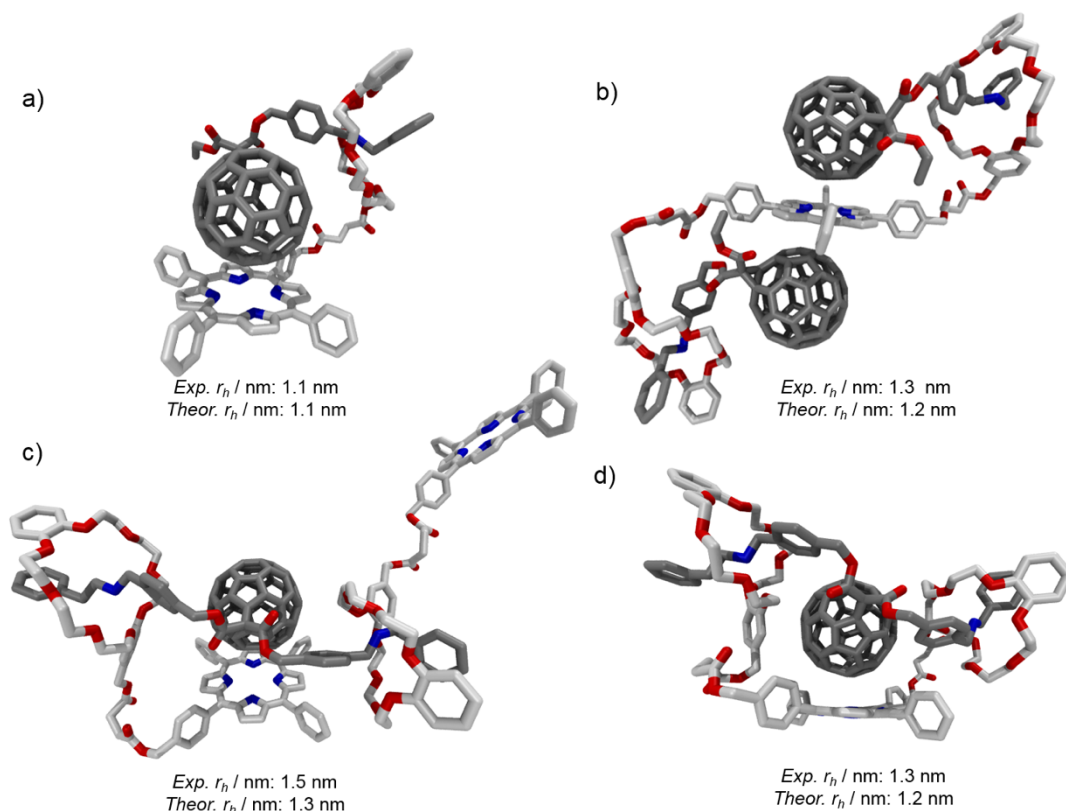
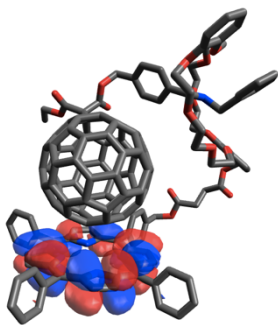
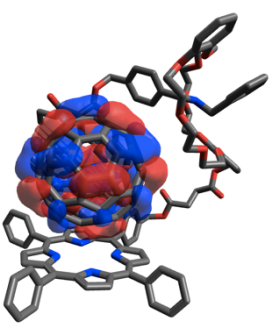
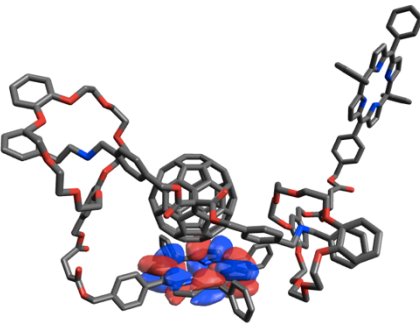
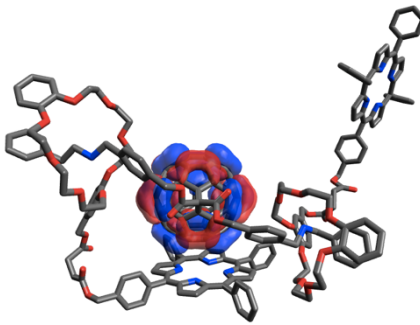
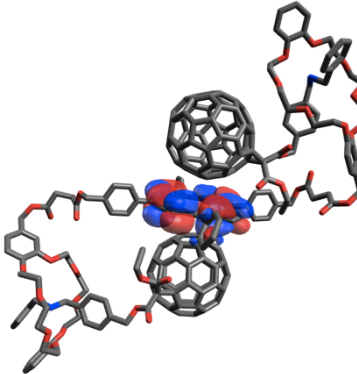
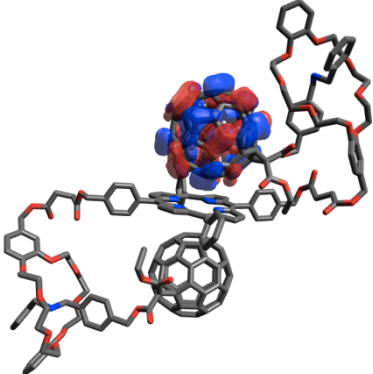
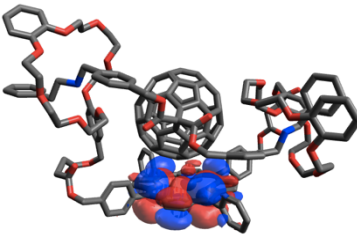
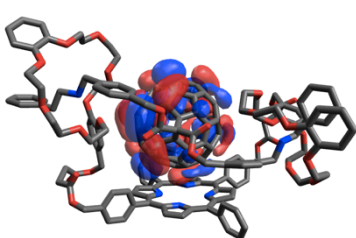


Figure 2.2.15. Optimized geometries obtained for the pseudorotaxanes a) $[1.3H_2] \cdot PF_6$, b) $[2.(3H_2)_2] \cdot 2PF_6$, c) $[(1)_2.4H_4] \cdot 2PF_6$ and d) $[2.4H_4] \cdot 2PF_6$ in the vacuum at the PM6 level of theory.

By performing geometry optimization on each derivative alone and in complex (PM6 semi-empirical level of theory, vacuum)¹⁵² it was possible to compute their molecular volumes, together with the hydrodynamic radius of an ideal sphere that included the molecules. Subsequently, the calculated (r_{calc}) hydrodynamic radius was compared with the experimental one (r_{exp}) as calculated from the DOSY-NMR experiments (values reported in **Figure 2.2.15**, under the molecular models). The geometry optimizations, in all cases, showed the presence of ‘face-to-face’ conformations. The porphyrin and the fullerene are in close contact with a distance of about 3.2 Å, as a result of the π - π intramolecular interaction (**Figure 2.2.15a**). The optimized geometry of the $[2.(3H_2)_2] \cdot 2PF_6$ complex showed a “sandwiched” complex, in which the two fullerene moieties are both ‘stacking’ in a ‘face-to-

face” fashion at a distance of 3.4 Å from the two opposite π -faces of the porphyrin macrocycle (**Figure 2.2.15b**). On the contrary, in the case of $[(\mathbf{1})_2\cdot\mathbf{4H}_4]\cdot 2\text{PF}_6$, whose ratio among the chromophores is inverted, the situation is substantially different, with only one of the porphyrin units being in close contact with the fullerene sphere (**Figure 2.2.15c**). Moreover, the hydrodynamic radius as calculated from the optimized geometry of $[\mathbf{2}\cdot\mathbf{4H}_4]\cdot 2\text{PF}_6$ (1.2 nm) proved to be in good agreement with the experimental hydrodynamic value of 1.3 nm (calculated from the diffusion coefficient in DOSY-NMR experiment through the Stokes-Einstein equation) (**Figure 2.2.15d**). This finding further corroborates the formation of the complex. Finally, the HOMO and LUMO were plotted for the molecular models and are reported in **Table 2.2.1**. The calculations were performed in order to get clues about the possible donor-acceptor assembly and charge-transfer interactions. As expected, the HOMO is present on the porphyrin moiety, while the LUMO is laying on the fullerene cage. Therefore, charge-transfer is possible and we could proceed with the photophysical investigations of the $[n]$ pseudorotaxanes.

Table 2.2.1. HOMO and LUMO molecular orbitals for $[n]$ pseudorotaxanes.

$[n]$ pseudorotaxane	HOMO	LUMO
$[1\cdot 3H_2]\cdot PF_6$	 The HOMO orbital of the [1·3H2] pseudorotaxane is shown as a 3D model. It features a central C60 fullerene cage with a large, diffuse orbital lobe extending from the top, colored in red and blue. The surrounding macrocyclic host is shown in a stick representation.	 The LUMO orbital of the [1·3H2] pseudorotaxane is shown as a 3D model. It features a central C60 fullerene cage with a large, diffuse orbital lobe extending from the bottom, colored in red and blue. The surrounding macrocyclic host is shown in a stick representation.
$[(1)_2\cdot 4H_4]\cdot 2PF_6$	 The HOMO orbital of the [(1)2·4H4] pseudorotaxane is shown as a 3D model. It features a central C60 fullerene cage with a large, diffuse orbital lobe extending from the top, colored in red and blue. The surrounding macrocyclic host is shown in a stick representation.	 The LUMO orbital of the [(1)2·4H4] pseudorotaxane is shown as a 3D model. It features a central C60 fullerene cage with a large, diffuse orbital lobe extending from the bottom, colored in red and blue. The surrounding macrocyclic host is shown in a stick representation.
$[2\cdot (3H_2)_2]\cdot 2PF_6$	 The HOMO orbital of the [2·(3H2)2] pseudorotaxane is shown as a 3D model. It features two C60 fullerene cages, one above the other, with a large, diffuse orbital lobe extending from the top, colored in red and blue. The surrounding macrocyclic host is shown in a stick representation.	 The LUMO orbital of the [2·(3H2)2] pseudorotaxane is shown as a 3D model. It features two C60 fullerene cages, one above the other, with a large, diffuse orbital lobe extending from the bottom, colored in red and blue. The surrounding macrocyclic host is shown in a stick representation.
$[2\cdot 4H_4]\cdot 2PF_6$	 The HOMO orbital of the [2·4H4] pseudorotaxane is shown as a 3D model. It features two C60 fullerene cages, one above the other, with a large, diffuse orbital lobe extending from the top, colored in red and blue. The surrounding macrocyclic host is shown in a stick representation.	 The LUMO orbital of the [2·4H4] pseudorotaxane is shown as a 3D model. It features two C60 fullerene cages, one above the other, with a large, diffuse orbital lobe extending from the bottom, colored in red and blue. The surrounding macrocyclic host is shown in a stick representation.

2.3. Time Resolved and Steady State Photophysics Investigations of [n]Pseudorotaxanes

The absorption and emission spectra, along with luminescence data and excited-state lifetimes of the individual compounds **2-1**, **2-2**, **2-3H₂·PF₆** and **2-4H₄·2PF₆** in CH₃CN at 298 K have been measured and are reported in **Figure 2.3.1** and **Table 2.3.1**.

Table 2.3.1. Luminescence data and excited state lifetimes in acetonitrile at 298 K. (a) Highest energy feature of the luminescence bands, at $\lambda_{\text{exc}} = 414$ for **2-1** and **2-2** nm and $\lambda_{\text{ex}} = 330$ nm for **2-3H₂·PF₆** and **2-4H₄·2PF₆**; (b) calculated using [Ru(bpy)₃]²⁺ as standard; (c) from time correlated single photon counting (TCSPC) apparatus using $\lambda_{\text{exc}} = 331$ nm.

	$\lambda_{\text{max}}^{(a)} / \text{nm}$	$\Phi^{(b)} / \%$	$\tau^{(c)} / \text{ns}$
2-1	650	7.1	9.3
2-2	650	7.4	9.5
2-3H₂·PF₆	700	0.08	1.3
2-4H₄·2PF₆	704	0.09	1.5

The UV-Vis absorption spectra of **2-1** and **2-2** show the narrow and intense Soret band centred at 414 nm and the weaker Q-bands from about 500 nm up to 675 nm. As expected for porphyrin derivatives,⁸⁹ **2-1** and **2-2** are relatively good fluorophores with emission quantum yields around 7%. Methanofullerenes **2-3H₂·PF₆** and **2-4H₄·2PF₆** absorb throughout the UV-Vis spectral region and exhibit weak fluorescence with emission quantum yields below 0.1%. Overall, no remarkable differences are found between reference compounds **2-1** and **2-2** and between **2-3H₂·PF₆** and **2-4H₄·2PF₆** both in absorption and luminescence properties.

The self-assembly of porphyrin crown ethers **2-1** and **2-2** with the [60]fullerene ammonium compounds **2-3H₂·PF₆** and **2-4H₄·2PF₆** leading to pseudorotaxane-like complexes were investigated with UV-Vis-NIR absorption and luminescence spectroscopy in a Et₂O/CH₃CN solution (98:2 v/v). The choice of the solvent is crucial in order to obtain strong porphyrin-fullerene interactions,

particularly when working at low concentrations (10^{-5} – 10^{-6} M), as necessary for photophysical investigations. In particular, a series of titration experiments were made to explore all the combinations between the individual moieties. The porphyrin crown ether **1** was mixed with both [60]fullerene ammonium salts **2-3H₂**·PF₆ and **2-4H₄**·2PF₆ to form a [2]pseudorotaxane-like [1·3H₂]·PF₆ and a [3]pseudorotaxane [(1)₂·4H₄]·2PF₆ complexes. Similarly, [60]fullerene ammonium salts were added to compound **2** to form [3]pseudorotaxane [2·(3H₂)₂]·2PF₆ and [2]pseudorotaxane [2·4H₄]·2PF₆.

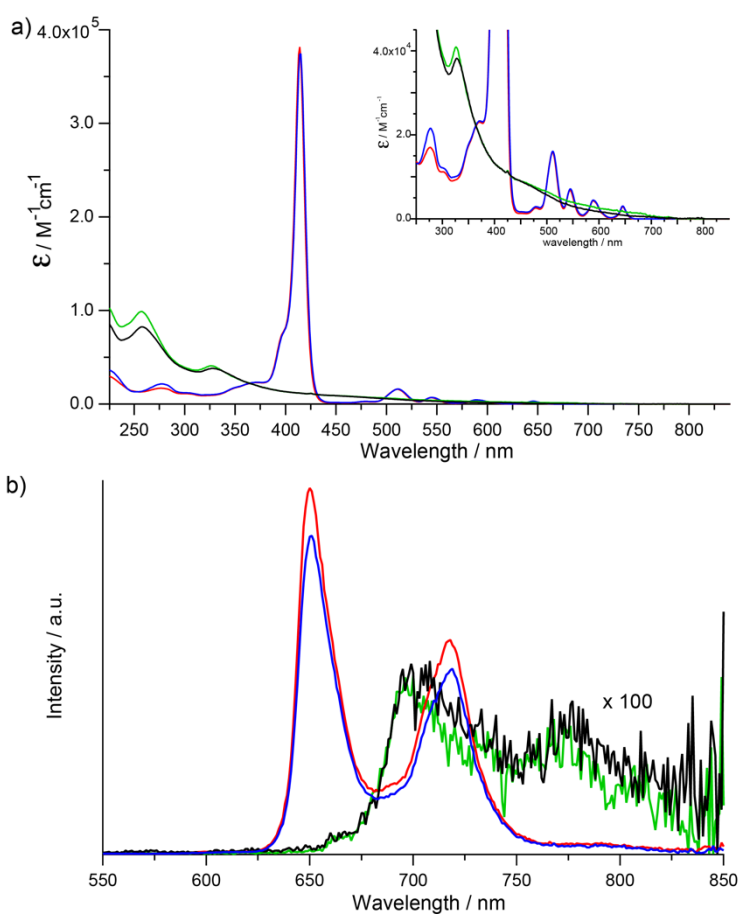


Figure 2.3.1. a) Absorption and b) luminescence spectra in CH₃CN at 298 K of **2-1** (red), **2-2** (blue), **2-3H₂**·PF₆ (green) and **2-4H₄**·2PF₆ (black). $\lambda_{\text{exc}} = 414$ nm for **2-1** and **2-2** and $\lambda_{\text{exc}} = 330$ nm for **2-3H₂**·PF₆ and **2-4H₄**·2PF₆.

The absorption spectra of porphyrin crown ethers **2-1** and **2-2** (Et₂O/CH₃CN, 98:2 v/v, 5.5×10^{-6} M) were monitored upon addition of increasing amounts of [60]fullerene ammonium compounds (**Figure 2.3.2**). The number of fullerene equivalents added to the porphyrin solutions depends on the

nature of the individual moieties. The formation of pseudorotaxanes $[1 \cdot 3H_2] \cdot PF_6$ and $[(1)_2 \cdot 4H_4] \cdot 2PF_6$ is virtually complete after the addition of about four equivalents of $3H_2 \cdot PF_6$ and $4H_4 \cdot 2PF_6$, respectively, to a solution of **2-1**. Similarly, for the porphyrin **2-2**, the titration experiments are completed upon addition of three equivalents of fullerenes $2 \cdot 3H_2 \cdot PF_6$ or $2 \cdot 4H_4 \cdot 2PF_6$. The absorption profiles of all pseudorotaxanes exhibit a decreased Soret band and the appearance of a weaker, broader and bathochromically-shifted band. Notably, a neat isosbestic point is found at 420 nm, as the concentration of fullerene increases. In agreement with previous findings, these observations suggest the occurrence of strong porphyrin-fullerene interactions, most likely related to face-to-face arrangements.¹⁴⁰

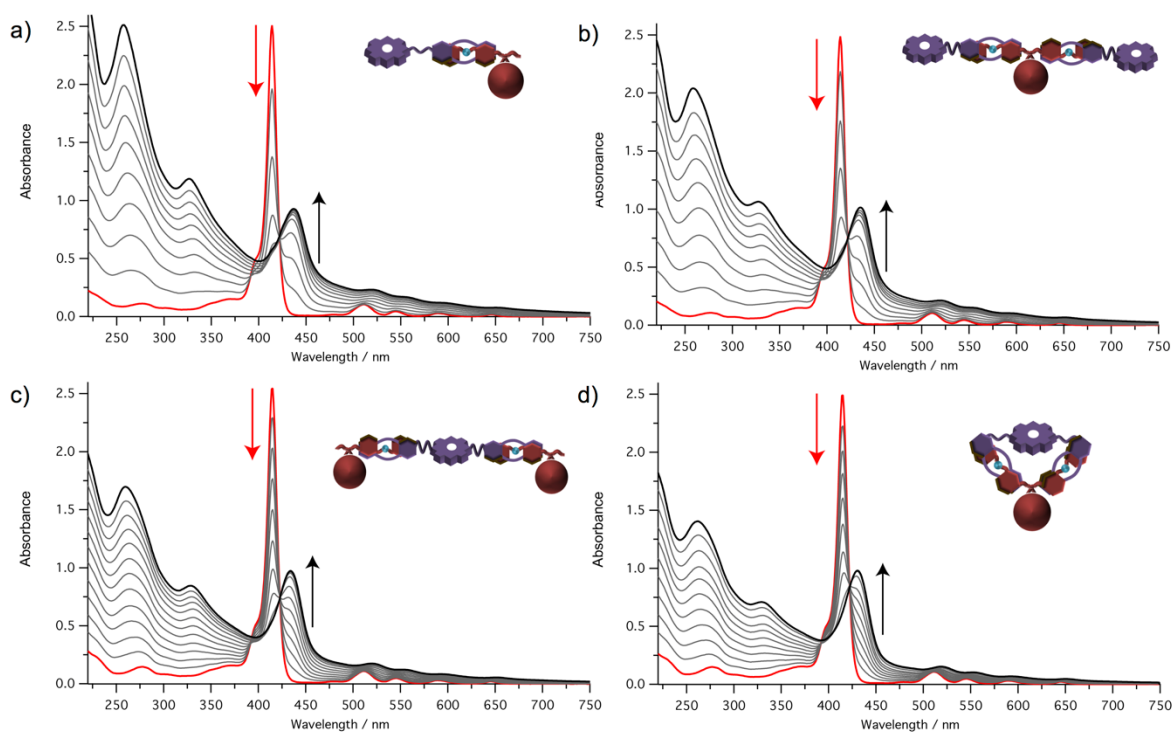


Figure 2.3.2. Absorption spectra of **2-1** and **2-2** in Et₂O/CH₃CN (98:2 v/v, 298 K, $c = 5.5 \times 10^{-6}$ M) upon addition of increasing amounts of fullerene derivatives; **1** (top, red line) + up to 4 eq. of fullerenes a) **2-3H₂·PF₆** and b) **2-4H₄·2PF₆**; **2** (bottom, red line) + up to 3 eq. of fullerenes c) **2-3H₂·PF₆** and d) **2-4H₄·2PF₆**.

The self-assembly of porphyrin crown ethers **2-1** or **2-2** and [60]fullerene ammonium molecules **2-3H₂·PF₆** and **2-4H₄·2PF₆** has been also traced by luminescence spectroscopy in Et₂O/CH₃CN (98:2 v/v, $c = 5.5 \times 10^{-6}$ M). Emission spectra were recorded by adding increasing aliquots of fullerene derivatives and exciting at the isosbestic point (420 nm), operating at the same concentrations

employed in the absorption studies; both UV-Vis (**Figure 2.3.3**) and IR (**Figure 2.3.4**) detectors were used. A progressive quenching of the porphyrin-centred fluorescence, together with the formation of a broad band around 950 nm, is found. The latter band can be attributed to a porphyrin \rightarrow fullerene charge-transfer state (CT) between the units in a ‘tight’ non-covalent ensemble, in line with earlier studies on tightly-folded fullerene-porphyrin conjugates.^{80,89,150,153–155} The lifetime associated to this state is found to be about 3.5 ns (**Table 2.3.2**).

Table 2.3.2. Luminescence data and excited state lifetimes of the CT band in Et₂O/CH₃CN (98:2 v/v) at 298 K.

[<i>n</i>]pseudorotaxane	λ_{\max} / nm	τ / ns
[1 · 3H ₂]·PF ₆	924	3.5
[(1) ₂ · 4H ₄]·2PF ₆	922	3.3
[2 ·(3H ₂) ₂]·2PF ₆	921	3.5
[2 · 4H ₄]·2PF ₆	922	3.4

The photophysical characterization of all the pseudorotaxanes was also performed in the same conditions used to study the third-order optical nonlinearity (*vide infra*). Namely, in a mixture of CH₂Cl₂/CH₃CN (9:1 v/v, $c = 2.5 \times 10^{-4}$ M) and using different ratios between the components (**Figure 2.3.5**). However, under these conditions, the CT emission bands in the NIR region were not observed. This is attributed to the greater polarity of this solvent mixture (CH₂Cl₂/CH₃CN, 9:1 v/v) compared to that used in the first set of experiments (Et₂O/CH₃CN, 98:2 v/v). In fact, it has been already demonstrated that, by increasing polarity, the CT emission band moves progressively to lower energy, decreasing its intensity until disappearance.⁷⁷ In particular, faint emission is detected in THF and no emission in benzonitrile, with CH₂Cl₂ (present case) showing intermediate dielectric constant.¹⁵³ However, clue of non-covalent porphyrin-fullerene interactions can be inferred by the dramatic quenching of the porphyrin fluorescence (**Figure 2.3.5**).

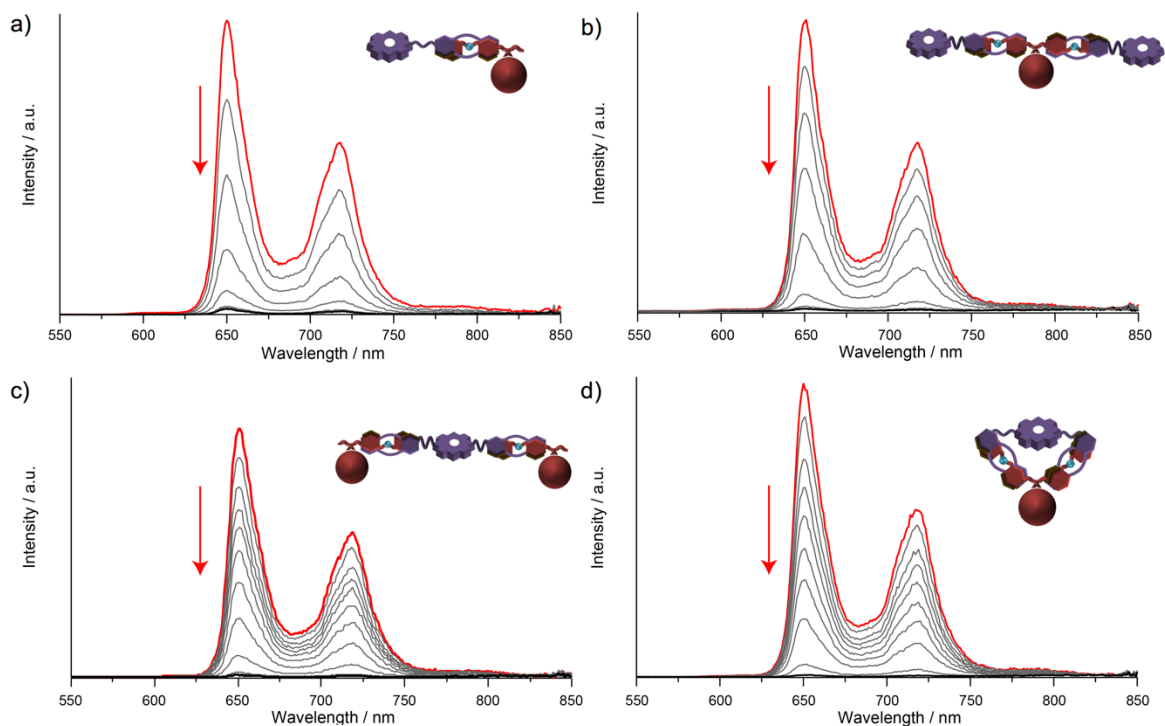


Figure 2.3.3. Luminescence spectra recorded at $\lambda_{\text{exc}} = 420$ nm in Et₂O/CH₃CN (98:2 v/v). Top: **2-1** (5.5 μ M, red line) + 4 equiv. of fullerene a) **2-3H₂-PF₆** and b) **2-4H₄-2PF₆**. Bottom: **2-2** (5.5 μ M, red line) + 3 eq. of fullerene c) **2-3H₂-PF₆** and d) **2-4H₄-2PF₆**.

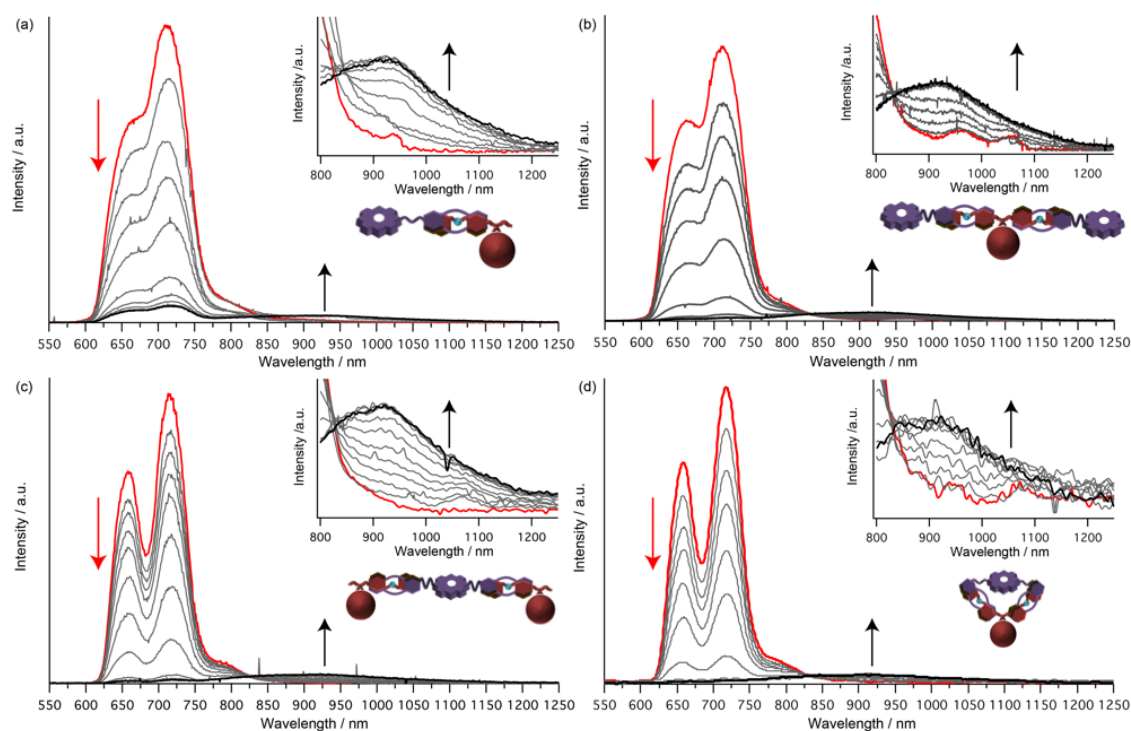


Figure 2.3.4. Luminescence spectra recorded with $\lambda_{\text{ex}} = 420$ nm and using an IR-sensitive detector in Et₂O/CH₃CN (98:2 v/v, 298 K, $c = 5.5 \times 10^{-6}$ M) ($\lambda_{\text{exc}} = 420$ nm): **2-1** (top, red line) + up to 4 eq. of fullerene a) **2-3H₂-PF₆** and b) **2-4H₄-2PF₆**; **2** (bottom, red line) + up to 3 eq. of fullerene c) **2-3H₂-PF₆** and d) **2-4H₄-2PF₆**. The insets show the charge transfer emission bands in the infrared region.

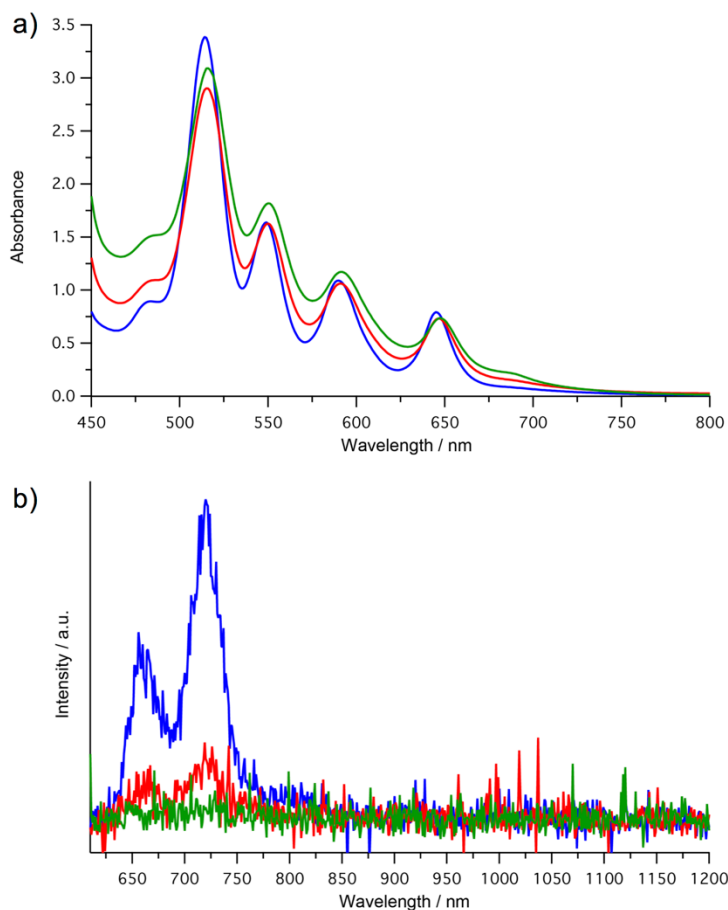


Figure 2.3.5. a) Absorption and b) emission spectra in $\text{CH}_2\text{Cl}_2/\text{CH}_3\text{CN}$ (9:1 v/v) of **2-1** ($c = 2.5 \times 10^{-3}$) upon addition of 0.5 (blue), 1 (red), 2 (green) equivalents of **2-3H₂-PF₆**. λ_{exc} 600 nm, IR detector.

2.4. Third-Order Non-Linear Optical (NLO) Responses

The third-order NLO properties of all the pseudorotaxanes and the molecular references (*i.e.*, C_{60} , fullerenes **2-3-BOC**, **2-4-BOC**, **2-3H₂-PF₆** and **2-4H₄-2PF₆**, porphyrins **2-1** and **2-2**, 1:1 mixtures of **1/3-BOC**, **2/3-BOC**, **1/4-BOC** and **2/4-BOC**) have been investigated in $\text{CH}_2\text{Cl}_2/\text{CH}_3\text{CN}$ (9:1 v/v , $c = 2.5 \times 10^{-4}$ M) solutions by means of the Z-scan technique^{156,157} under 35 ps, 532 nm laser excitation. By performing measurements on different concentrations under various incident laser excitation energies, the nonlinear absorption coefficient, β , and the nonlinear refractive index parameter, γ' , have been determined. Some characteristic “open” and “divided” Z-scans of pseudorotaxanes solutions are present in **Figure 2.4.1**. Then, the third-order susceptibility $\chi^{(3)}$ and the second hyperpolarizability γ have been deduced (the details are given in the Experimental Section, NLO part). Among these NLO parameters, the value of the second hyperpolarizability γ , being concentration independent, can be

regarded as a molecular property, allowing the direct comparison of the NLO response of different molecules. The determined values of the second hyperpolarizability γ of the studied molecules are listed in **Table 2.4.1** (which also contains the data obtained after the Et_3N addition).

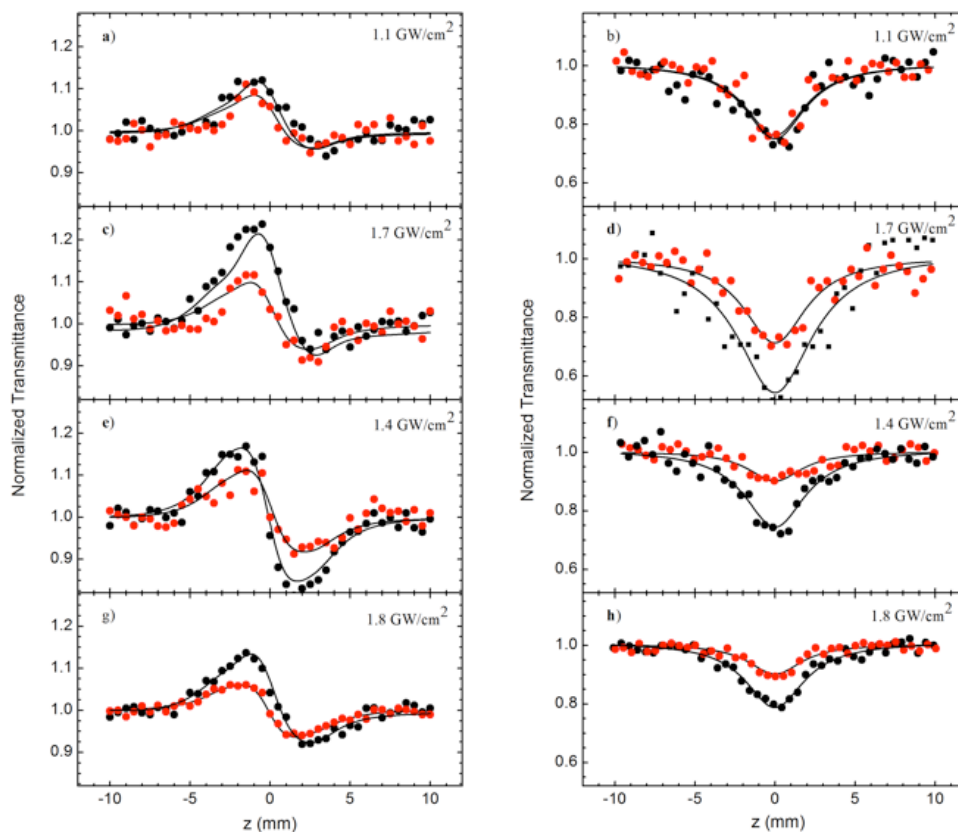


Figure 2.4.1. a,c,e,g) “Divided” and b,d,f,h) “open-aperture” Z-scans of solutions of the pseudorotaxanes assemblies $[\mathbf{1}\cdot\mathbf{3H}_2]\cdot\text{PF}_6$, $[(\mathbf{1})_2\cdot\mathbf{4H}_4]\cdot\mathbf{2PF}_6$, $[\mathbf{2}\cdot(\mathbf{3H}_2)_2]\cdot\mathbf{2PF}_6$ and $[\mathbf{2}\cdot\mathbf{4H}_4]\cdot\mathbf{2PF}_6$ (from top to bottom) in $\text{CH}_2\text{Cl}_2/\text{CH}_3\text{CN}$ (9:1 v/v) without (black lines, $c = 7.0, 7.0, 8.3$ and 9.8×10^{-4} M, respectively) and with Et_3N (red lines, $c = 6.0, 6.5, 7.2$ and 9.0×10^{-4} M, respectively). The solid lines correspond to the best numerical fits of the experimental data points and were used for the determination of the NLO parameters.

As shown, the values of the hyperpolarizability of the pseudorotaxanes were found to be larger than the sum of the hyperpolarizabilities of the reference porphyrin and the respective [60]fullerene derivative, suggesting a underlying operational mechanism leading to some synergistic action. Specifically, the enhancement of the NLO response of the pseudorotaxanes compared to the sum of the individual NLO responses of the constituents’ molecular entities becomes comprehensible considering the presence of an efficiently formed CT state. In fact, such CT states are characteristic

features of the [60]fullerene-porphyrin assemblies, whose contribution is known to be favored by the present excitation conditions (*i.e.*, under 532 nm laser excitation).⁸³⁻⁸⁶

Table 2.4.1. Second hyperpolarizability, γ , values of the pseudorotaxanes assemblies in $\text{CH}_2\text{Cl}_2/\text{CH}_3\text{CN}$ (9:1 v/v, $c = 2.5 \times 10^{-4}$ M) solutions, before and after the addition of base (Et_3N). The NLO responses of the individual molecules are also included.

Entry	Sample	$\epsilon@532\text{nm}$ ($\text{L mol}^{-1} \text{cm}^{-1}$)	$\text{Re}\gamma$ ($\times 10^{-31}$ esu)	$\text{Im}\gamma$ ($\times 10^{-31}$ esu)	γ ($\times 10^{-31}$ esu)
1	2-1	3426	$-(5.1 \pm 0.2)$	3.0 ± 0.2	5.9 ± 0.3
2	2-2	3693	$-(4.0 \pm 0.3)$	3.9 ± 0.2	5.6 ± 0.4
3	2-3H ₂ ·PF ₆	1171	-	0.32 ± 0.05	0.32 ± 0.05
4	2-4H ₄ ·2PF ₆	1403	-	0.28 ± 0.02	0.28 ± 0.02
5	[1·3H ₂]·PF ₆	4740	$-(3.3 \pm 0.3)$	4.4 ± 0.8	5.4 ± 1.0
6	[1·3H ₂]·PF ₆ + base	4567	$-(3.5 \pm 0.3)$	2.8 ± 0.9	4.5 ± 0.7
7	[(1) ₂ ·4H ₄]·2PF ₆	6332	$-(4.5 \pm 0.1)$	4.9 ± 0.2	6.7 ± 0.2
8	[(1) ₂ ·4H ₄]·2PF ₆ + base	4130	$-(3.2 \pm 0.1)$	3.8 ± 0.4	5.0 ± 0.4
9	[2·(3H ₂) ₂]·2PF ₆	5971	$-(8.4 \pm 0.9)$	7.7 ± 0.8	11.4 ± 1.2
10	[2·(3H ₂) ₂]·2PF ₆ + base	4830	$-(5.9 \pm 0.1)$	2.0 ± 0.3	6.2 ± 0.2
11	[2·4H ₄]·2PF ₆	4582	$-(6.2 \pm 0.6)$	4.4 ± 0.7	7.5 ± 0.9
12	[2·4H ₄]·2PF ₆ + base	3764	$-(2.9 \pm 0.1)$	2.7 ± 0.6	3.9 ± 0.5

Similar enhancement of the NLO response of other fullerene-based systems has been observed and reported in the literature previously.^{140,141,158,159} Another interesting observation, resulting from the present study, is the strong dependence of the magnitude of the hyperpolarizability on the number of electron-accepting fullerene appends, as pseudorotaxanes $[1\cdot 3H_2]\cdot PF_6$ and $[(1)_2\cdot 4H_4]\cdot 2PF_6$ were found to exhibit a modest increase of γ , whereas stronger enhancements were observed for pseudorotaxane $[2\cdot (3H_2)_2]\cdot 2PF_6$, with two $[60]$ fullerene. Notably, larger γ values were also found for cyclic pseudorotaxane $[2\cdot 4H_4]\cdot 2PF_6$. Presumably the presence of different conformations is reflected on the CT mechanism, namely when going from the “tight” conformation to the “loose” one, the electron transfer process could change, with substantial changes of the hyperpolarizability values of the molecular assembly. Therefore, molecular systems in which the fullerene and the porphyrin are mostly in a folded conformation, as in the case of the pseudorotaxane assemblies $[2\cdot 4H_4]\cdot 2PF_6$ and $[2\cdot (3H_2)_2]\cdot 2PF_6$, display more efficient charge transfer than for the assemblies $[1\cdot 3H_2]\cdot PF_6$ and $[(1)_2\cdot 4H_4]\cdot 2PF_6$, and thus higher NLO responses.

Additionally, 1.8 equivalents of a base (Et_3N) were added and the sum of the second hyperpolarizability γ values of the non-threaded components was observed to recover, thus further supporting our hypothesis according to which the ground-state fullerene-porphyrin interchromophoric interaction is the key requirement for enhancing the hyperpolarizability. As expected, this behavior is more pronounced for the tightly-bonded pseudorotaxane assemblies $[(1)_2\cdot 4H_4]\cdot 2PF_6$, $[2\cdot (3H_2)_2]\cdot 2PF_6$ and $[2\cdot 4H_4]\cdot 2PF_6$, while it is weaker for complex $[1\cdot 3H_2]\cdot PF_6$.

To conclude, there are numerous studies in the literature reporting on the photo-induced electron-transfer capability of porphyrin or ferrocene-fullerene dyads and triads or similar fullerene derivatives.^{64,127,128,132,134–138,140,141,146,158–163} Apart from the photophysical studies, the investigation of the NLO response of such systems provides another evidence for the formation of new charge-transfer states through the detection of any modification of the NLO properties between the electron-donor systems, pristine $[60]$ fullerene^{164,165} and the remaining individual compounds. Similarly to the present study, many others have supported the idea that electron transfer dominates the general NLO behavior and others highlighted the significance of the number of donors/acceptors in the hybrid compounds. Among those, in some previous works by our group, the influence of the functionalization of fullerenes to the final NLO response of the C_{60} derivatives has been clearly demonstrated.^{140,144,146} For instance, when studying the NLO properties of two fullerene derivatives in various configurations under 35 ps, 532 nm using Z-scan technique, one of which included ferrocene as molecular shuttle, it turned out that the presence of the electron donor in the latter (e.g. ferrocene) resulted in an

enhancement of its NLO response by almost a factor of two.¹⁴⁴ In another work, some [60]fullerene–ferrocene and [60]fullerene-porphyrin dyads were examined under 35 ps, 532 nm using the Optical Kerr effect technique and were all found to have enhanced NLO properties in comparison with C₆₀.^{164,165} Furthermore, among the various derivatives studied, the [60]fullerene-pyrrolidine and [60]fullerene-ferrocene derivatives exhibited a moderate enhancement of the NLO response while the [60]fullerene-porphyrin derivative exhibited the largest enhancement suggesting the more effective electron donation from the porphyrin rather than from the ferrocene to the fullerene.¹⁴⁰ In addition, some C₆₀-triphenylamine (TPhA) hybrids when irradiated with 35 ps, 532 nm revealed the strong dependence of their NLO response upon the number of acceptors (*i.e.*, C₆₀ molecules) with the TPhA-(C₆₀)₂ hybrid exhibiting up to seven times higher NLO response in comparison with TPhA-C₆₀ and the bisadduct TPhA-C₆₀ ones.¹⁴⁶ The pseudorotaxanes reported in the present chapter exhibit remarkably enhanced NLO response in comparison with other similar compounds. However, it should be mentioned that in general, there are two types of charge-transfer interactions between an electron donor (*e.g.* a porphyrin unit) and an electron acceptor (*e.g.* a fullerene unit). The first is covalent or “through-bond” interactions where the electron charge transfer is realized through an intermediate chain linking the donor with the acceptor. The second is non-covalent or “through-space” interactions where the electron charge transfer is succeeded by the contiguity of the donor and acceptor units in space.^{166,167} Most of the aforementioned hybrids belong in the first category (*i.e.*, covalent linkages), in contrast to the fullerene-porphyrin pseudorotaxanes (*i.e.* non-covalent linkages). This work therefore demonstrated the superiority of the charge transfer through space systems, highlighting their capability of reversing the charge transfer effect (as has been shown by the addition of Et₃N) and subsequently their potential on-off NLO performance.

2.5. Conclusions

In view of devising new NLO materials, this chapter reports the synthesis, self-assembly, photophysics and third-order NLO responses of novel porphyrin-fullerene [*n*]pseudorotaxanes. Porphyrins and fullerenes carrying complementary crown-ether ammonium recognition motifs, were prepared and characterized. In the first section, the self-assembly and the formation of the [2]pseudorotaxanes complexes was characterized by ¹H-NMR, NOESY and DOSY spectroscopies. Notably, the system was investigated also in various solvent, ranging in polarity and C₆₀ solubility, in order to probe the formation of the porphyrin-fullerene stacking interaction. Indeed, the presence of a secondary

equilibrium was noticed and was found to be dependent on the solvent, leading to formation of more stable complexes in solvent where fullerene is less soluble. Afterwards, both the [2] and [3] pseudorotaxanes were characterized by NMR spectroscopies (^1H and DOSY), MALDI and molecular modeling, with the latter one showing favorable molecular orbitals complementarity that prompted further studies.

In the following section, the [n]pseudorotaxanes were investigated by time resolved and steady state spectroscopy. UV-Vis-NIR, absorption and emission spectroscopies confirmed the formation of the [n]pseudorotaxanes and the to a porphyrin \rightarrow fullerene charge-transfer state (CT) between the units, consistent with in “tight” non-covalent ensembles.

In the final section, the NLO responses of the [n]pseudorotaxanes were studied. Remarkably, they showed that individual porphyrin and fullerene derivatives exhibit significantly lower second hyperpolarizability values when compared to their pseudorotaxanes functionalized counterparts. This proves that this class of supramolecular materials possesses relevant NLO response, which strongly depends on the structural arrangement of the chromophores in solution.

3. Solvent Effects in Organic Soft Matter Nanostructuring

This chapter is divided in three sections: the first section introduces the previous work done in understanding the role of the solvent on self-assembly and nanostructuring, the second section presents the work done on bio-inspired self-assembly of a porphyrin derivative and the final section discusses a thorough study in transferring molecular chirality from solution to the surface. Section 3.2 was done in collaboration with *Dr. Nicola Demitri* (Elettra, Sincrotrone Trieste) that solved the crystal structures. Section 3.3 has been done in a collaborative work with *Dr. Tomas Marangoni* that started this research line, *Dr. Tanja Miletić* that prepared some of the molecules, *Dr. Jenifer Rubio-Magnieto* from the group of *Dr. Mathieu Surin* (University of Mons, Mons, Belgium) carried out the CD measurements, *Dr. John Mohanraj* from the group of *Dr. Nicola Armaroli* (CNR-ISOF, Bologna, Italy) performed the quantum yield/lifetimes and *Dr. Heinz Amenitsch* (Graz University, Graz, Austria) performed the SAXS measurement.

The work presented in this chapter has been published as “Solvent Molding of Organic Morphologies Made of Supramolecular Chiral Polymers” *J. Am. Chem. Soc.* **2015**, 137, 8150–8160 and “Solvent-dependent moulding of porphyrin-based nanostructures: solid state, solution and on surface self-assembly” *Supramol. Chem.*, **2016**, doi: 10.1080/10610278.2016.1158407.

3.1. Introduction

The construction of complex functional nano-materials has fascinated and inspired the scientific community during the past half-century. In order to master the engineering from the bottom, chemists have continuously drawn knowledge and inspiration from biological nanoscale devices. With the precision and specificity of biological systems that continues to be aspired. Biological nanoscale devices function in aqueous media, making water a unique medium for self-assembly.¹⁶⁸ Moreover, water can also participate in biochemical processes, e.g. its reduction generates oxygens, protons and electrons.¹⁶⁸ Water, the solvent of nature, has been called ‘molecule of life’ among other terms and has been a critical component for achieving complexity, adaptability, and robustness.¹⁶⁹ Additionally, assemblies of non-natural modules in water has been under intense investigation.^{169–171} Self-assembly

and self-organization in water and their understanding is fundamental for matching and emulating the achievements of biological systems.¹⁷² However, design of and binding of synthetic molecules in water has been challenging and therefore most of the studies have been performed in organic solvents.¹⁷⁰ Moreover, most of applications in current technologies require the material to be soluble in an organic solvent. Therefore, gaining understanding in nano-structuration processes that occur in organic media is imperative. Surprisingly, only a limited studies over the years have systematically studied the role played by the solvent in forming the supramolecular architecture.

The development of chemistry is tightly related with the development of our knowledge of solutions.¹⁷³ Predictably, water was the first known solvent, as far back as Greek alchemist to consider 'divine water' all chemically active liquids, referring 'water' to everything dissolved or liquid. The search for a universal solvent "Menstruum universale" or "Alkahest" (as called by Paracelsus), specially from 15th to the 18th century, was not fortunate but it was successful since it led to new compounds, new reactions and, especially, new solvents. The earliest chemical rule *similia similibus solvuntur* (like dissolves like) dates back to this time. However, the dissimilarity between physical dissolution (e.g. sugar in water) and chemical change of a substrate by dissolution (e.g. metal in an acid) was not yet postulated. Even if was believed that the nature of a substance was lost upon dissolution, scholar Van Helmont was the first one to propose that the substance was not lost, but present in the solution and could be recovered. Some centuries later, polymath Lomonosov wrote about the process of dissolution: "all solvents penetrate into the pores of the body to be dissolved and gradually remove its particles. However, concerning the question of what forces cause this process of removal, there does not exist any somehow reasonable explanation, unless one arbitrarily attributes to the solvents sharp wedges, hooks or, who knows, any other kind of tools".

At the end of 19th century, three scientists were responsible for the development of modern solution theory. Raoult studied the physical properties of a solution by changing the nonionic solute/solvent ratio on freezing and boiling points of liquids. These observations led to Raoult's law, which states that vapor pressure of solvent above a solution is proportional to the mole fraction of solvent in the solution. Arrhenius and van't Hoff work led to the first Nobel Prizes in chemistry (in 1903 and 1901, respectively) for their work on electrolytic dissociation and osmotic pressure. Arrhenius developed his theory of complete and incomplete dissociation of ionic solutes into anions and cations in solution, by comparing electroconductivity and osmotic pressure of dilute electrolyte solutions measurements. Replacing pressure by osmotic pressure in laws holding for gases to solution, van't Hoff developed another crucial physiochemical solution study.

During the same time, it was also observed, by Berthelot and Péan de Saint-Gilles, by studying esterification of acetic acid with ethanol, that rates of chemical reactions are affected by the choice of the solvent. Shortly after, Menschutkin, working with trialkylamines and haloalkanes, noted that “solvents, in spite of appearing at first to be indifferent, are by no means inert; they can greatly influence the course of chemical reactions”.

Chemical equilibria were also found to be influenced by the choice of solvent. It was first discovered by Claisen, Wislicenus and Knorr in the *keto-enol tauterism* of 1,3-dicarbonyl compounds. These studies led to the Stobbe classification of solvents into two groups, according to their effect on the isomerization equilibria, that somewhat reflects the modern division into protic and aprotic solvents.

A more detailed history of development and properties of solvents in organic chemistry has been covered.^{173–177} In the context of constructing nanoscale objects that possess well-defined shapes, dimensions and patterns by self-assembly, mastering such objects is essential for the understanding and development of novel materials.^{178–181} Since these systems, being substantially different from the corresponding bulk material, have their properties closely related to the actual dimensions, shapes, and compositions hold great promise in fields such as electronics, information storage, light energy conversion, and catalysis.^{182–184} These supramolecular materials can be influenced by a variety of stimuli, such as temperature, light, pH, guest molecules, minor chemical transformation or solvent.^{104,185–190} However, only recently attention has been placed in understanding the role of the solvent on nanostructuration.^{191–193} Therefore, the following sections will give an overview of the solvent-driven forces that act upon the supramolecular structure in solution and on surface.

3.1.1. Solvent Forces in Solution

3.1.1.1. Solvophobic Forces

In order to unravel the entropic and energetic contributions of supramolecular interactions, simple systems, inspired by biological macromolecules, have been designed to isolate and study particular interactions.¹⁹⁴ Particularly, the so-called *foldamers* represent an important class in studying the folding by aromatic interactions. Specifically designed *meta*-connected phenylene ethynylene (*mPE*) oligomers with polar side chain, when long enough, tend to fold in polar solvents (**Figure 3.1.1a**).¹⁹⁵ For example, in CH_3CN , they maximize aromatic-aromatic interactions and minimize interactions of the hydrocarbon backbone with the solvent.¹⁹⁵ This folding transition was monitored by UV-Vis spectroscopy, that allowed to fit the system to a two-state model of random coil and fully helical

conformations, with the transition being cooperative (**Figure 3.1.1a**). A more polar solvent, such as CHCl_3 , acted as a ‘denaturant’ causing the folded state to unfold, analogously to what can happen with proteins. This folding-unfolding equilibrium was used, for example, to reversibly disperse and release carbon nanotubes (SWCNTs) by simply changing solvents.¹⁹⁶ Going from a CHCl_3 solution, where the *m*PE was able to disperse CNTs in solution, to CH_3CN the conformation went from unfolded to folded, causing the release of nanotubes.

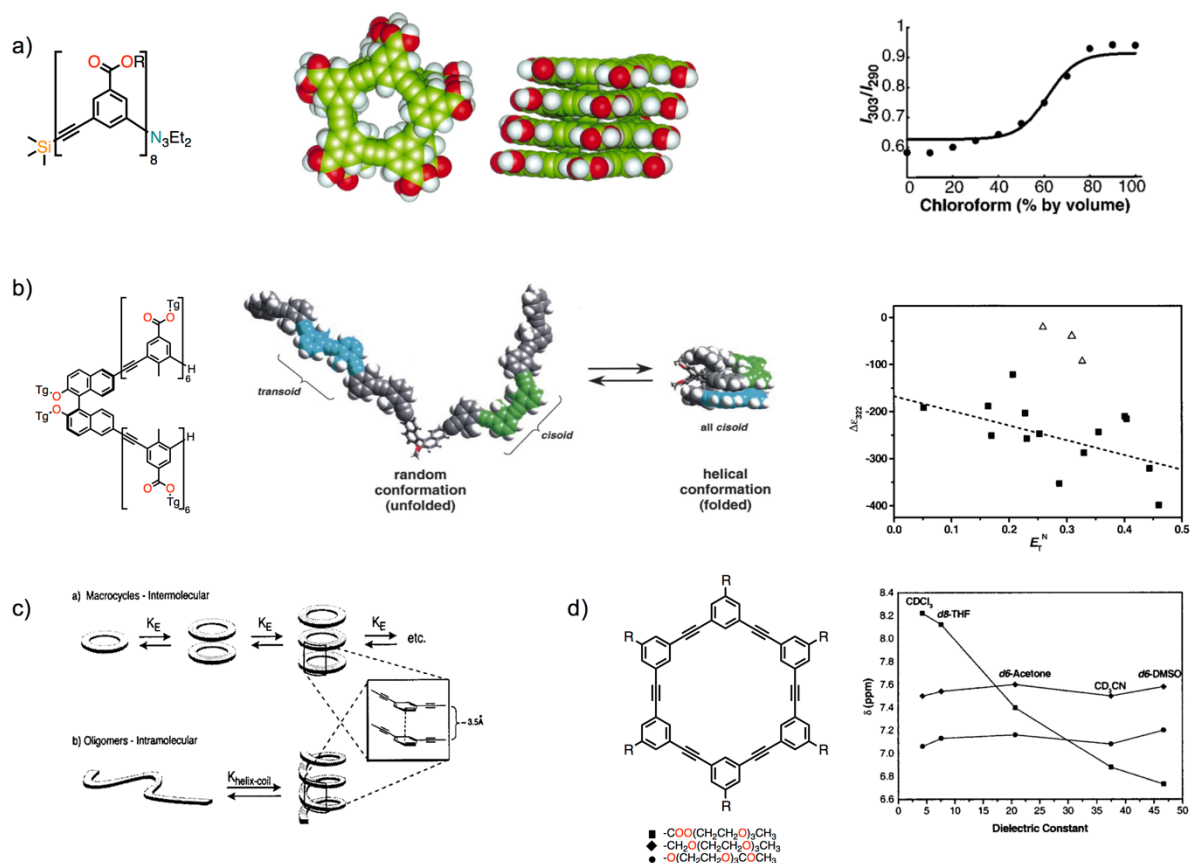


Figure 3.1.1. Solvophobic driven π -stacking of phenylene ethynylene oligomers and macrocycles; a) phenylene ethynylene octamer in a helical conformation top and side view with a cooperative fit for the transition; b) a bis-hexameric phenylene ethynylene tethered through a (*R*)-BINOL, unfolded state contains both *transoid* and *cisoid* conformations, which became all-*cisoid* in the folded state; c) scheme showing the intramolecular association of macrocycles and helical conformation of phenylene ethynylenes; d) macrocycles with different groups and their NMR chemical shift in solvents of different polarity.

The folding of the *m*PE oligomer causes the formation of a tubular cavity, that was used as a high affinity site for small hydrocarbon guests (in $\text{CH}_3\text{CN}/\text{H}_2\text{O}$ mixtures).¹⁹⁷ The binding of several monoterpenes showed the formation of a reversible 1:1 complex, reaching binding strengths of $7 \times$

10^4 M^{-1} for α -pinene (in $\text{CH}_3\text{CN}/\text{H}_2\text{O}$ 3:2 v/v). The formation of the complexes was found to be solvophobically driven, as evidenced by measuring the association constants in mixed solvents with various mole percent of H_2O in CH_3CN , with K_a linearly correlating with the mole percent of H_2O . In a further study, it was showed that the cavity of this synthetic receptor could be tuned by adjusting the length of the oligomer. For example, rodlike guests (such as 2,5-dimethyl-1,4-diphenylpiperazine) were found to bind with a higher affinity longer oligomers (up to 24 units).¹⁹⁸ In order to bind metals instead of hydrocarbon molecules, the inner of the cavity was modified with nitrile moieties.¹⁹⁹ It was found that metal coordination with silver can occur. Moreover, in a solvent such as THF (were the oligomer is present as random coil) it was found that the folding can be induced by adding Ag^+ to the solution.

It was possible not only to modify the cavity, but also the helices and the twist of the folded conformation. Since two helices (M and P) are formed in the folding of an achiral *m*PE oligomer, by incorporating an optically active BINOL derivative in the center of the oligomer (**Figure 3.1.1b**), a bias in the twist sense of the helical structure was induced in a 'poor' solvent (CH_3CN).²⁰⁰ The binaphthol tethered two-state model was subsequently examined in 30 solvents in order to estimate the conformational equilibrium and correlate it to the solvent polarity parameter (E_T^N).²⁰¹ It was found that, with exclusion of chlorohydrocarbon solvents, the conformational equilibria could be fitted linearly (reasonably well) to E_T^N . The chlorohydrocarbon solvents presumably are able to form solvent-backbone contacts (through CH- π interactions) and thus were responsible for the unfolded state. In other solvents, an increase in polarity translate in a more stabilized folded conformation, where chain collapse intramolecularly to minimize solvent-backbone contacts, while maintaining favorable triethylene glycol-solvent solvation. Conversely, introducing a kinked binaphthol unit decreases the stability when compared to oligomers without the binaphthol core. A bias in the helical twist sense, without disrupting the conformational stability, was therefore obtained or by introducing a helicene²⁰² unit instead of binaphthol or by using chiral side chains.^{203,204} In addition, the diastereomeric bias was found to lag behind the appearance of helical conformations, *i.e.* the helical formation is a necessary but not sufficient condition for obtaining a diastereomeric bias. In follow up studies, it was found that by adding H_2O to CH_3CN mixture of oligomers carrying chiral side chains, helical conformations were stabilized for shorter oligomers, while for longer ones intermolecular aggregation into columns was observed.²⁰⁵ In particular, 'sergeants and soldiers' experiments showed that a chiral oligomer is able to transfer the twist sense bias through intermolecular interactions when

aqueous CH_3CN were used. The transfer of chirality was found to be only slightly cooperative, possibly due to the small directing power of generic solvophobic effect.

The formation of folded *m*PE oligomers was achieved not only by placing them in a polar solvent, but also by reacting small fragments of such oligomers with groups that are able to undergo fast and reversible reactions, such as imine metathesis, and solvophobically drive their synthesis.²⁰⁶ For this reason, short oligomers (with 6 units) were prepared with imine capped final units, that were found to undergo metathesis in CH_3CN to form foldamers of approximately 2 turns (with $K_{\text{eq}} = 62$), in sharp contrast with a CHCl_3 solution, where a meagre association constant was found (~ 2). The solvophobic effect therefore was found to shift the ligation equilibrium in favor of the most stable solution structure.

In order to probe the difference between intermolecular or intramolecular aromatic stacking, a series of phenylene ethynylene macrocycles and oligomers, carrying different side chains (ester, benzyl ether and phenyl ether) were prepared to study their tendency to undergo solvent induced π -stacked organization (**Figure 3.1.1c**).²⁰⁷ Among the different side chains, macrocycles and oligomers with esters carrying a tri(ethylene glycol), were prone to adopt π -stacked structure in a range of solvents, both in macrocycles and oligomers. In particular, the macrocyclic *m*PE was found to range from 50 M^{-1} in CDCl_3 to $1.5 \times 10^4 \text{ M}^{-1}$ in acetone- d_6 , with the self-association generally increasing with polarity (**Figure 3.1.1c**). Therefore, the propensity of the macrocycles to associate in a given solvent is dependent on the side-chain groups, with certain linking groups (e.g. benzyl ether or phenyl ether) disfavoring stacking, even under strongly solvophobic conditions.

3.1.1.2. π Stacking

In the last example above, the *m*PE macrocycles were found to π -stack. Although in that case, it was side-chain dependent and solvophobically driven (in polar solvents), π - π interactions play an important role in aggregation of various functional dyes. Aggregation constants for a multitude of functional aromatic in solution were studied and reported starting from the simplest one, benzene, to aromatics and heteroaromatic π -conjugated systems (**Figure 3.1.2**).²⁰⁸ The complexity of π - π interaction has been pondered for quite some time^{209–212} and, additional to solvent effects,^{43,213–226} a variety of factors impact aggregation of various functional dyes: (i) the electronic nature of the π -conjugated system, *i.e.* the electrostatic complementarity of electron-rich and -deficient regions of stacked molecules; (ii) the size and geometry of the aromatic core, *i.e.* stronger π - π is expected in

larger π -systems; and (iii) substituents on the aromatic core, e.g. introduction of alkyl or poly(ethylene)glycol side chains, as well as chiral chains.

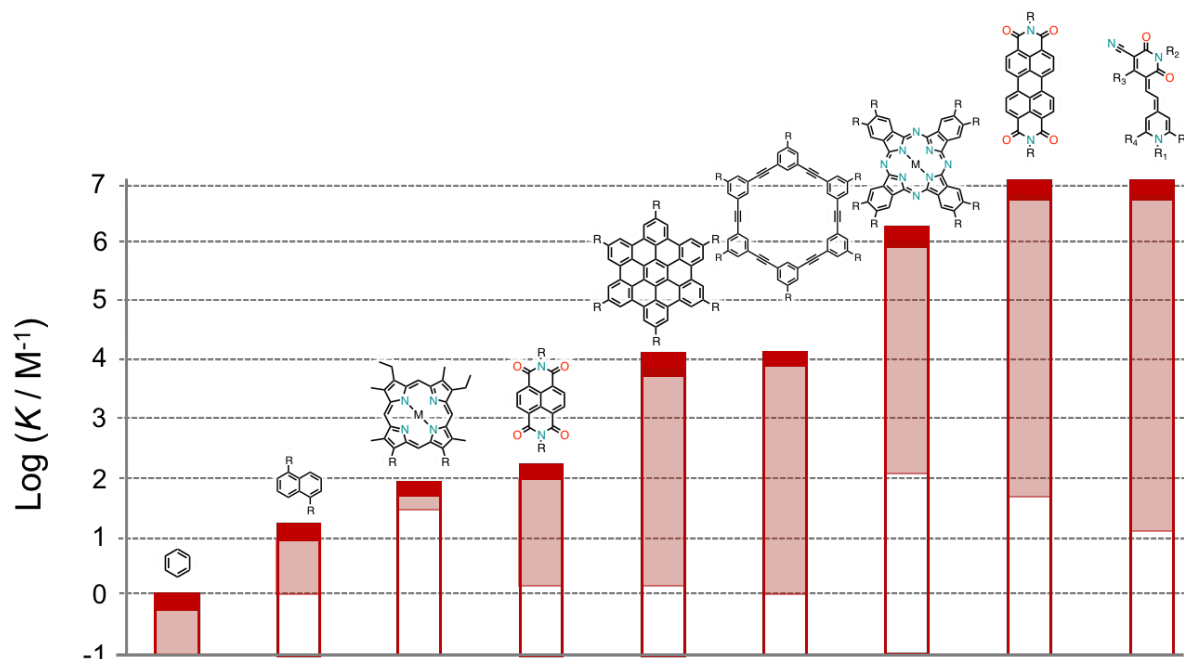


Figure 3.1.2. A comparison chart for self-association constants of different π -conjugated systems with the highest value (red bar) and the range (pink area) reported. Image adapted from reference.²⁰⁸

Unfortunately, detailed examination on Gibbs free energy of π - π stacking and respective different contributions has been rarely pursued. Therefore, it is noteworthy to highlight exceptions that are found in the studies reported here below. The encapsulation of a pyrene guest in a macrobicyclic cyclophane host was studied in water and different organic solvents in a pivotal study by Diederich and Smithrud.²¹⁵ The complexation strength, due to solvation effects, was rationalized in terms of linear free energy relationship (LFER) between Gibbs free binding energy and empirical solvent parameter $E_T(30)$. The linear correlation showed that polar solvents gave most stable complexes of these apolar host-guest molecules, with H_2O giving the largest free binding energy ($K_a = 6 \times 10^6 M^{-1}$, $-\Delta G^\circ = 39 kJ mol^{-1}$). The solvent effect on aromatic interaction was evaluated also on the donor-donor, acceptor-acceptor and donor-acceptor systems made of electron-rich 1,5-dialkoxy-naphthalene and electron-deficient naphthalene bisimide.⁴³ Also in this case, a linear free energy relationship for 1:1 donor-acceptor complex and $E_T(30)$ was found in a range of solvent from apolar ($CHCl_3$) to the most polar (H_2O), where once again the strongest binding event was observed ($2 \times 10^3 M^{-1}$). The association was found to be driven mostly by hydrophobic effect as well as the geometry of the donor-

acceptor complex, dictated by their electrostatic complementarity. Various investigations have sought to understand the underlying physicochemical principles that govern stacking interactions.^{224,227–230} A major problem has been the separation of dispersive forces and hydrophobic effects, which are both maximized in the low polarizable water. One approach in order to do so, was performed by studying complexation in H₂O of numerous substrates with water-soluble porphyrin complexes (Figure 3.1.3a).^{229,230}

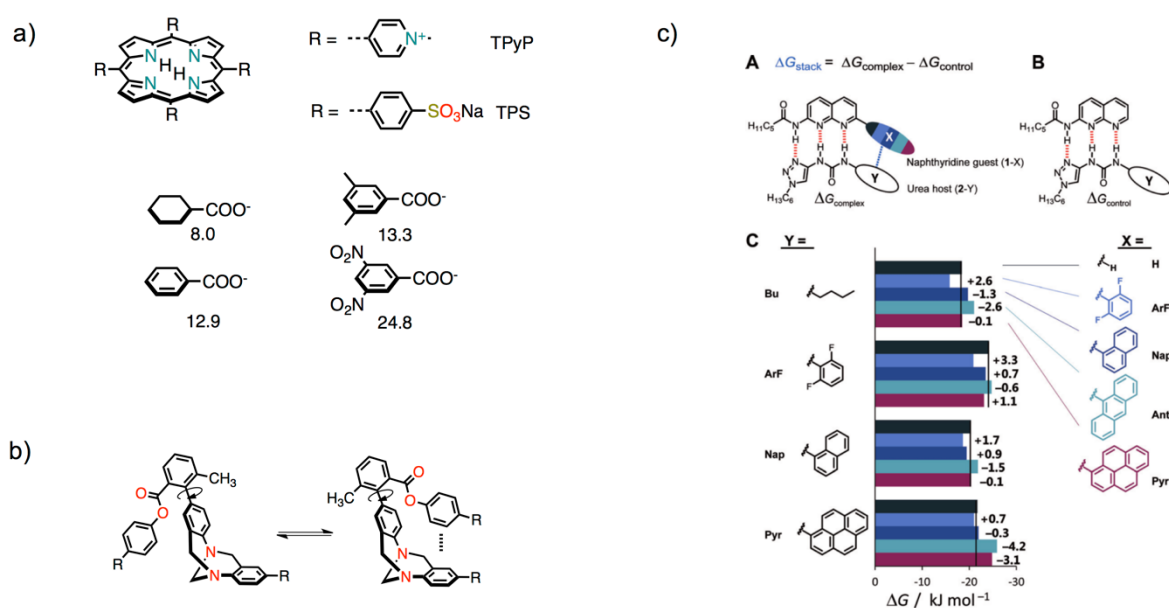


Figure 3.1.3. a) Complexation with cation or anionic porphyrin (TPyP or TPS) in water showed negligible hydrophobic contribution and a large dispersive binding contribution (ΔG values in kJ/mol for complexes formation with TPyP in H₂O); b) Wilcox 'molecular Tornio balance' used for quantifying molecular interactions; c) supramolecular complex used for measuring aromatic stacking interactions in organic solvents.

By systematically varying the substrates, a small hydrophobic effect was observed, e.g. cyclohexanoic acid showed $\Delta G = 5$ kJ mol⁻¹ while benzoic acid resulted in a $\Delta G = 14$ kJ mol⁻¹, even though the sizes of the hydrophobic surfaces of both six-member rings are approximately the same. Moreover, addition of methyl substituents on benzoic acid showed negligibly small contributions. Additionally, increased interaction with increasing polarizability was observed, such as in the case of halogen substituents, compatible with the dispersive mechanism. Similarly, an analogous and affinity enhancing effect was found for nitro, amino and methoxy groups substituted benzoic acids, with this effect being compatible with a dispersive mechanism. Other effects such as electrostatic and donor-acceptor

interactions were ruled out due to same ΔG values obtained using either the anionic or the cationic host (TPS or TPyP, respectively). By extending the complexation to polycyclic heteroarenes, it was found that their interaction with porphyrins essentially depend on the size of the arene, in line with their polarizabilities, and are quite independent on the location and presence of nitrogen atoms within the rings.²³¹ Another approach in quantifying non-covalent interactions was the use of ‘molecular balances’ as an intramolecular tool for a high geometric control that would be difficult to achieve in supramolecular systems.²²⁸ Wilcox and co-workers reported a ‘molecular torsion balance’ (**Figure 3.1.3b**) in which the conformational equilibrium is sensitive to intramolecular interactions and effects of the solvent and therefore was used as a direct-measure.²³² Specifically, in case of unsubstituted aryls (**Figure 3.1.3b**, X = Y = H) only edge-to-face interaction can occur between the two phenyl rings, and it was studied in a range of solvents.²³³ From CS₂, CCl₄, CHX to various mixture of H₂O in THF, the nonpolar interaction was found to be weak and in the range of ~ 0 to $+1$ kJ mol⁻¹, being most favored in polar solvents, pointing to a role of cohesive solvent effects (*i.e.* solvophobic effect). This approach was then took further by applying various substituents, such as alkyl and perfluoroalkyl chains.^{233,234} Even if the use of the intramolecular torsion was the most exploited approach supramolecular complex, based on naphthyridine and urea partners (**Figure 3.1.3c**), was also found to be helpful.²²⁵ The size dependency of aromatic stacking in organic solution, ranging 7.5 kJ mol⁻¹ from a phenyl-phenyl to an anthracene-pyrene stack, thus the interaction becoming more favorable as the sizes in the aromatic group increased. Moreover, theoretical energy decomposition analysis (using symmetry-adapted perturbation theory, SAPT) showed high correlation ($R^2 = 0.98$) between experimental data and only the dispersion component of the interaction. Therefore, despite the strong attenuation of dispersion forces (due to competition with polarizable CDCl₃/CD₃CN 95:5 v/v mixture), the results suggested that the aromatic stacking in an organic solvent is governed by dispersion forces.

Molecular balances and supramolecular complexes have therefore shed some light on the stacking interaction. However, due to the dependency of the results on the system used, general experimental and theoretical models are still lagging behind. Moreover, they are still far from being applied in a supramolecular chemistry context and systematic investigation on the functional molecule of interest is the most common approach. In this contexts, one of the most comprehensive studies for π - π aggregation in various solvents has been performed on perylene bisimides (PBIs), a lightfast chemically robust and optically intriguing class.^{208,235,236} First, in order to study the effects of core substitutions on the aggregation, a series of differently substituted PBIs was studied in the same solvent (CCl₄). The concentration-depended UV-Vis experiments were fitted to the isodesmic model

and the self-association was found to range from about $2 \times 10^5 \text{ M}^{-1}$ for electron-rich 3,4,5-tridodecyloxyphenyl substituents, followed by phenyl and alkyl substituents, to no aggregation for PBIs equipped with bulky 2,6-diisopropylphenyls. An 'intrinsic' binding constant of 10^2 - 10^3 M^{-1} in CCl_4 was observed for aromatic and aliphatic substituted PBIs (that did not bear steric contributions), with the 3,4,5-tridodecyloxyphenyl unit showing a substantial increase, attributed to the CT interaction with the electron-poor PBI core. Then, the aggregation was studied in 17 different solvents with various polarity, polarizability, hydrogen-bond donor and acceptors properties. Interestingly, the LFER study showed a biphasic behavior (**Figure 3.1.4a**): decreased aggregation with increasing polarity in aliphatic and dipolar aprotic solvents up to intermediate polarity (Ph-CH_3 , THF), and increased aggregation with increasing solvent polarity for dipolar and protic solvents was observed. Solvents such as CH_2Cl_2 and CHCl_3 , that are highly polarizable and of intermediate polarity, showed the smallest propensity to aggregate, owing to their capability to replace solute-solute with similar strength solute-solvent interactions. In apolar solvents (data points on the left side of **Figure 3.1.4a**) a steady increase in aggregation was observed and was rationalized in terms of electrostatic interaction between quadrupolar PBI dyes (**Figure 3.1.4c**). The electrostatic interactions obviously could not explain the increase in aggregation for polar solvents, where solvophobic interaction seemed to govern the aggregation.

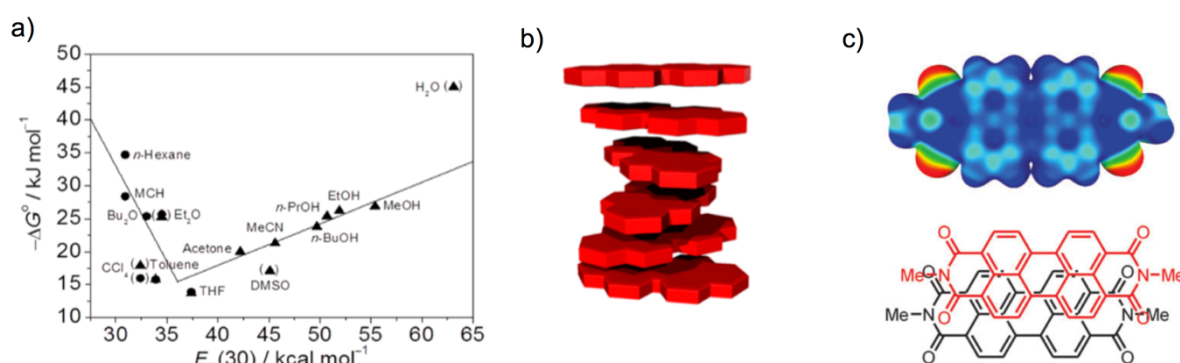


Figure 3.1.4. a) Intermolecular stacking of PBIs plot of standard Gibbs free energy for isodesmic aggregation vs. solvent polarity parameter $E_T(30)$; b) schematic representation of columnar stacks and c) electrostatic potential map for N,N'-dimehyl PBI (top) and in the solid state (down).²³⁵

In order to study further the π -stacking of PBIs, they were incorporated into foldamers. Folda-dimers, -trimers and -oligomers with long aliphatic chains were prepared,²³⁷⁻²³⁹ combined with the oligo-

phenyl ethynylene chains in order to study their properties in a clearly defined geometries (**Figure 3.1.5**). These systems are driven by π - π stacking interactions of PBIs into folded structures by carefully exploring a range of solvents (**Figure 3.1.5c**). In apolar aliphatic solvents with low polarizability (such as MCH and Bu₂O), a helical structure driven by π - π stacking was observed. In contrast, halogenated and aromatic solvents with high polarizability (CHCl₃, Ph-CH₃) induced the unfolded conformation, where the PBIs are solvated. Interestingly, it was observed that photoinduced electron transfer could occur from the electron-donor phenylene-ethynylene backbone to the electron-deficient PBI one in the extended conformation. However, once that the oligomers were in the folded state, this pathway was replaced by fast relaxation of excited PBI stacks into fluorescent excimer states.

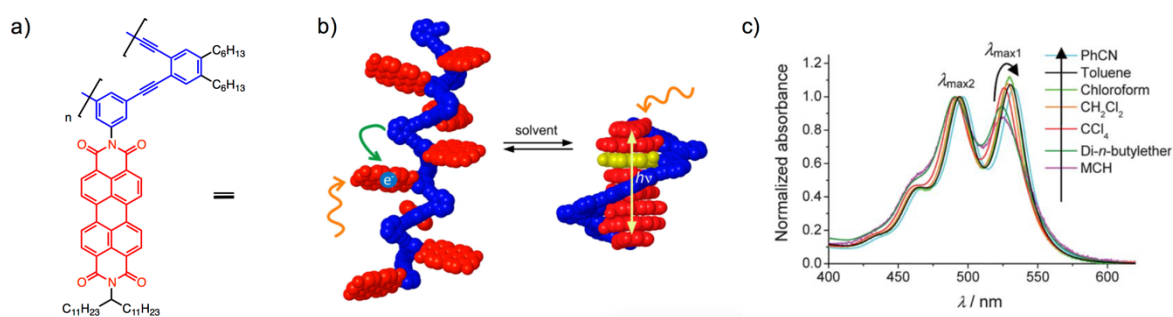


Figure 3.1.5. a) Folding of a PBI oligomer into helical H-type aggregates with its chemical structure; b) schematic representation of solvent-triggered unfolded and folded state; exhibits competitive PET (green arrow) and exciton migration followed by excimer formation (yellow arrow); c) UV-Vis absorption spectra of oligomer in various solvents.

3.1.1.3. Dipole-Dipole Interactions

The solvent dependency of the aggregation was carefully evaluated for dipolar merocyanine (MC) dyes (**Figure 3.1.6**).^{220,240} These dyes showed a large zwitterionic character and therefore possess a large dipole moment. Typically, concentration-dependent UV-Vis experiments showed hypsochromically shifted bands with isosbestic points (**Figure 3.1.6b**), pointing to dimerization of the dyes by electrostatic interaction between the electron-deficient and electron-rich parts. For a series of merocyanines, a good correlation between the Gibbs dimerization energy and the square dipole moment of the dye (μ^2) has been observed, confirming that the stacking is governed by electrostatic forces. Dimerization of MC was then explored in various solvents, ranging from apolar CCl₄ to more polar CDCl₃ and THF, with the dimerization constant stretching from 2×10^{-7} to 65, respectively

(Figure 3.1.6c). An excellent correlation of 0.99 between the Gibbs dimerization energy and the Kirkwood-Onsager function (that considers only the electrostatic contribution from the solvent, *i.e.* the solvent dipolarity) further confirmed that the dimerization is guided by electrostatic dipole-dipole interactions.^{218,220}

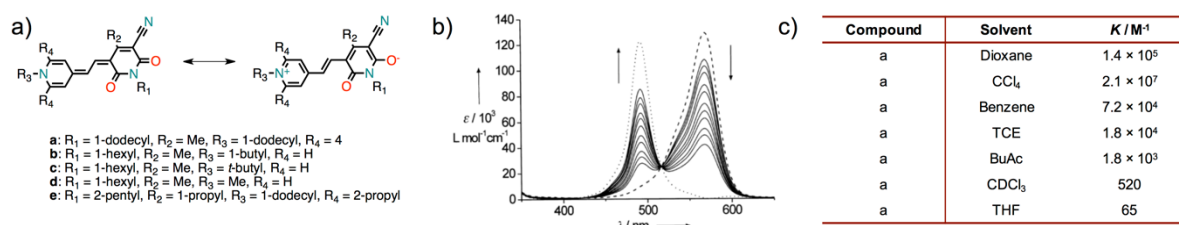


Figure 3.1.6. a) Chemical structure of typical merocyanine dyes; b) typical concentration-dependent UV-Vis spectra in dioxane; c) Table with dimerization constant in various solvents.

The dipole-dipole interactions in MC were subsequently exploited to form hierarchical supramolecular polymers with a bis-MC derivative (Figure 3.1.7).²⁴¹ Reference mono-MC self-assembled into dimeric aggregates in non-polar solvents, while bis-MC showed a more complex solvent-dependent behavior. Monomers were observed in a CH_2Cl_2 solution, while in TCE (trichloroethylene) the dimerization of bis-MC results in extended fibrillary polymer chains (Figure 3.1.7b,B). Further aggregation was achieved in apolar solvents (such as CCl_4 or MCH), with the single fibrils folding into a helical conformation (Figure 3.1.7b,C). Finally, six polymeric chains could intertwine to yield a densely packed rod (Figure 3.1.7b,D). Subunits in these aggregates presented an H-type packing in antiparallel orientation. Notably, the same UV-Vis absorption monomer, dimer and H aggregate profiles could be obtained by using THF/MCH mixtures and varying the ratio between them. Another bis-MC, tethered through a Hamilton receptor, showed a biphasic solvent-induced self-assembly in THF-MCH mixture of various ratios (Figure 3.1.7d). The first transition (0 – 70 % MCH in THF) featured a decrease of monomers and an increase of extended type H-aggregates, in a isodesmic fashion. The antiparallel aggregation resulted in a flexible polymer with aliphatic chains pointing to the solution. The second transition (> 70 % MCH in THF), in a cooperative event, gave further aggregation, characterized by spherical morphology.

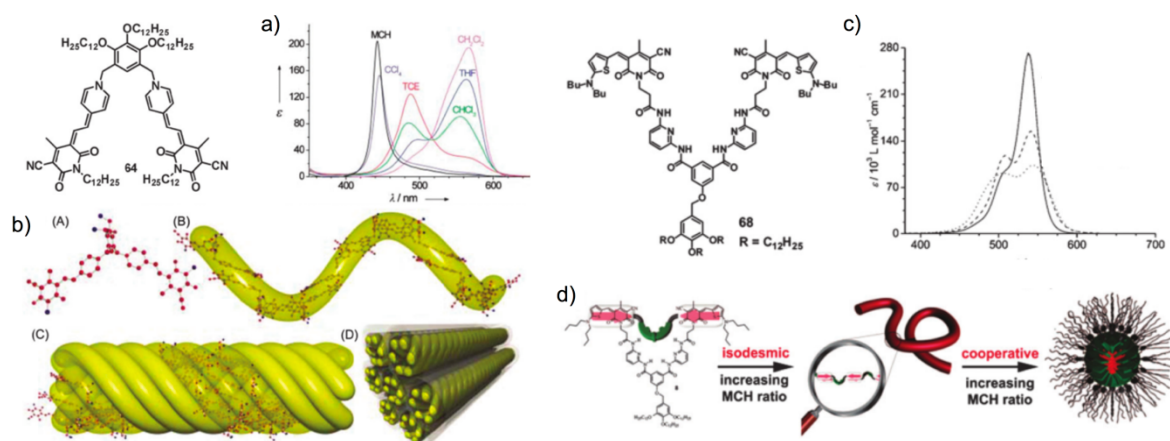


Figure 3.1.7. a) Solvent-dependent UV-Vis spectra; b) model for the hierarchical superstructure (A) optimized molecular structure, (B) helical supramolecular polymer formed by dimerization of bis-MC and (C) H-aggregation in rod type by six helical polymeric strands; d) UV-Vis absorption spectra of monomers (THF/MCH 100:0, solid line), dimerization (THF/MCH 40:60, dashed line) and final aggregate (THF/MCH 10:90, dotted line); e) schematic representation of solvent-dependent self-assembly.

3.1.1.4. Hydrogen Bonding

Solvophobic and π - π interactions however usually lack directionality and therefore, most supramolecular systems have been prepared by exploiting hydrogen-bonds due to their directionality and complementarity.^{242,243} An H-bond acceptor interacts with a H-bond donor and *vice versa*. Therefore, when a single molecule presents a sequence of acceptor and donor sites, it carries an information that dictates with which partner it will interact. The interaction is affected not only by the number and the sequence, but also by the solvent.^{244–253} In order to rationalize the solvent effects on hydrogen bonding, an approach to quantify the free energy of binding as the sum of the pairwise intermolecular interactions with two parameters (α and β) was proposed.¹⁹¹ Since repulsion, induction and dispersion were rationalized to contribute only negligibly to the intermolecular interactions, only electrostatics were used to evaluate effects on hydrogen bonding. Usually, the minimum in the electrostatic potential (of the van der Waals surface) is located on a lone pair or an area of π -electron density, with the maximum usually found near a hydrogen atom. By taking into account that in solution, there is competition between solute-solute, solvent-solvent and solute-solvent interactions (**Figure 3.1.8a**), a universal hydrogen bond scale in order to predict the free energy of interactions (in any solvent) was proposed:

$$\Delta\Delta G_{H-bond} = -(\alpha\beta + \alpha_s\beta_s) + -(\alpha\beta_s + \alpha_s\beta) = -(\alpha - \alpha_s)(\beta - \beta_s)$$

with α and β being hydrogen bond-donor and -acceptor constants for solutes, while α_s and β_s are the corresponding constants for the solvent. These constants, α and β , can be obtained from experimental values previously reported²⁵⁴ or estimated from computational molecular electrostatic potential surfaces.

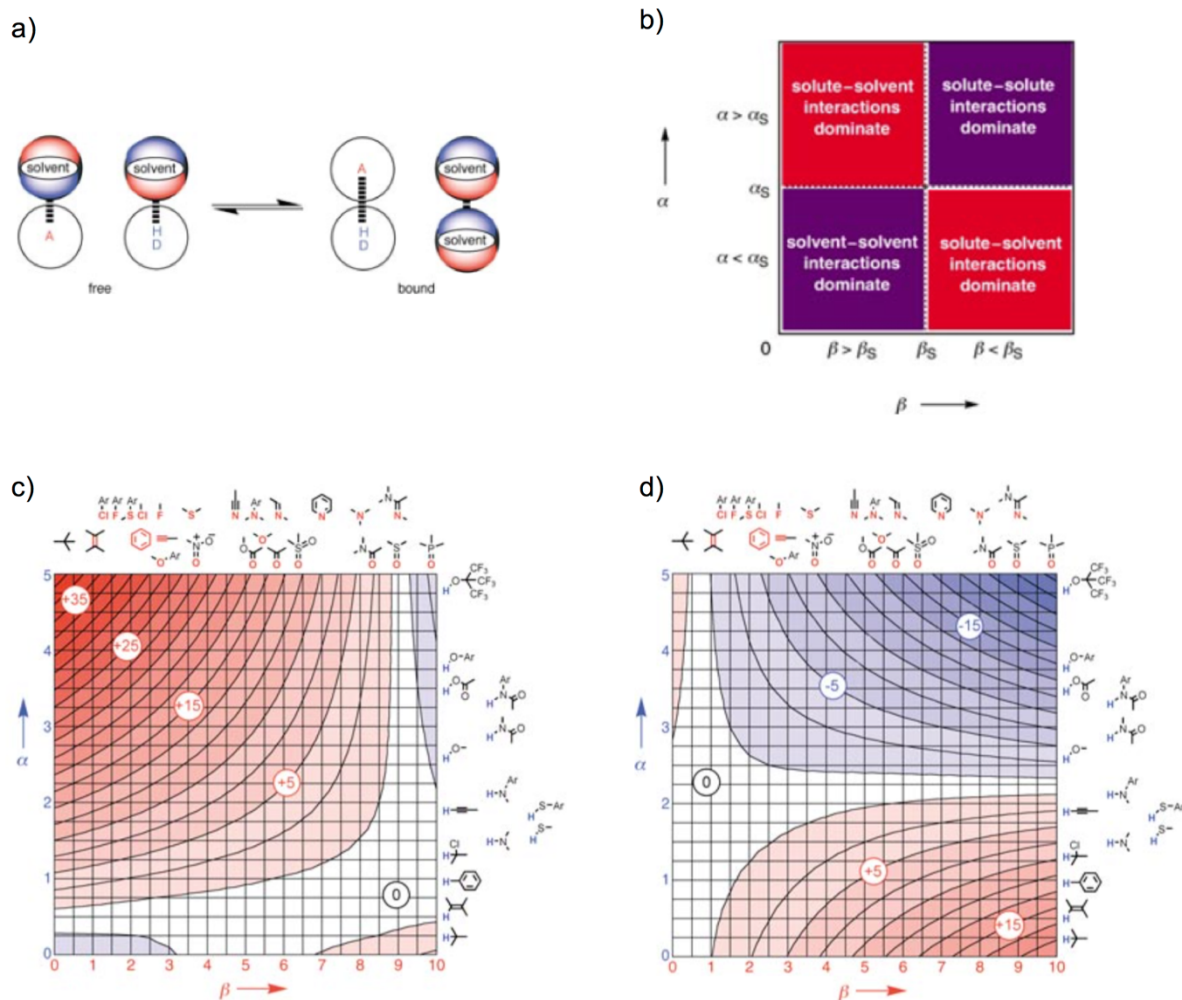


Figure 3.1.8. a) Competition between intermolecular interactions in solution between solute-solvent, solute-solute and solvent-solvent; b) generalized energy profile for hydrogen bonding in solution – $\Delta\Delta G$ is positive in red quadrants and the functional groups interaction is unfavorable, $\Delta\Delta G$ is negative in purple quadrant and the interaction is favorable; c) functional group interaction profile in DMSO ($\alpha_s = 0.8$ and $\beta_s = 8.9$) and in d) chloroform ($\alpha_s = 2.2$ and $\beta_s = 0.8$).¹⁹¹

The general features for hydrogen bond interactions for neutral functional groups in solution were therefore estimated and a favorable or unfavorable interaction could be predicted (**Figure 3.1.8b**). Moreover, functional group interactions profiles in different solvent environments were reported, e.g.

in DMSO ($\alpha_s = 0.8$ and $\beta_s = 8.9$) almost all functional group interactions are unfavorable (**Figure 3.1.8c**), making it one of the best solvents or in CHCl_3 ($\alpha_s = 2.2$ and $\beta_s = 0.8$), where a large zone of favorable solute-solute interaction is apparent (**Figure 3.1.8d**), corroborating its wide use in molecular recognition studies. Experiments on the complexation of one of the most polar hydrogen-bond donors (perfluoro-*t*-butyl alcohol) and one of the best hydrogen-bond acceptors (tri-*n*-butylphosphine oxide) were performed in 13 different solvents covering a range of properties.²⁵² Depending on the solvent, the association constants spanned over 5 orders of magnitude (10^{-1} to $> 10^5 \text{ M}^{-1}$), ranging from barely detectable complex in the most polar solvents (DMF and DMSO), through relatively stable formation in competitive hydrogen-bonding solvents (acetone and THF) to very stable complexes in non-competitive solvents (CHX). Some correlation was found between the solvent polarity parameter $E_T(30)$ (and other solvent descriptors) and the association constant, but it was insufficient to account for the variations in this system. It was possible however to apply a solvent competition model that accurately accounted for the system and obtain a LFER by a combination of some parameters (α , α_s , β and β_s). The results suggested that the solvents simply compete for the binding sites, with the other properties of the solvent having only minor significance.

Various hydrogen bonded arrays have been used to construct a variety of supramolecular system.^{255–259} Even though a numbers of systems have been reported not only in organic media but also in aqueous environments,^{169,170} surprisingly few contributions considered the effect of solvent on the supramolecular adduct.^{260–269}

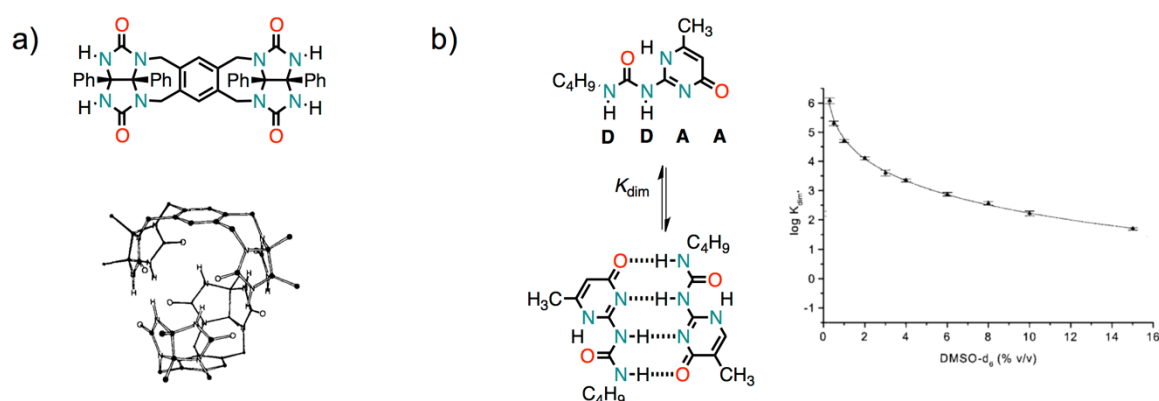


Figure 3.1.9. a) Self-complementary monomer with its self-assembled dimer (calculated) below; b) ureidopyrimidone monomer dimerization along plot of K_{dim} vs. solvent composition $\text{CDCl}_3/\text{DMSO-}d_6$.

For example, the self-assembly of a synthetic cavity through complementary hydrogen-bonding of a monomer into dimers was found dependent on the solvent: the dimer was present in CDCl_3 and Ph-H, while not in $\text{DMSO}-d_6$ (**Figure 3.1.9a**).²⁵⁰ In another study, the dimerization of ureidopyrimidones in solution was reported to be solvent-, substituent- and concentration-dependent (**Figure 3.1.9b**).²⁷⁰ In CHCl_3 , the dimerization is too strong to perceive dissociation ($K_d > 10^6 \text{ M}^{-1}$) and therefore it was studied in mixtures of CDCl_3 with $\text{DMSO}-d_6$, where the dimerization constant is strongly affected by the ratio of the two solvents. Furthermore, the ureidopyrimidones present a complex equilibrium of three tautomers that coexist in solution and their equilibria are affected both by the solvent polarity and concentration.

3.1.1.5. Hydrogen Bonding and π -Stacking

While the few examples of hydrogen bonding above report successful pairing of complementary hydrogen bonds, in order to obtain nano- and micro-structures multiple recognition events along with secondary interactions are necessary, usually aromatic stacking or solvophobic effect. Such an approach was used to prepare helical supramolecular fibers by using oligo(*p*-phenylenevinylene) ureidotriazine complementary fourfold hydrogen bonding motif (**Figure 3.1.10a**).²⁶² In CHCl_3 they dimerize with $K_{\text{dim}} = 2 \times 10^4 \text{ M}^{-1}$ and were present as random coil polymers. In more apolar solvents (dodecane), the H-bonded dimers aggregate into helical stacks by following a nucleation-elongation pathway. Further studies were performed in a variety of hydrocarbon solvents, by changing the length of the hydrocarbon chain ($\text{C}_n\text{H}_{2n+2}$ with $n = 7-13$), showed that the stability of the nuclei and stacks were affected (**Figure 3.1.10b**). The co-organization of the solvent at the outside of the nuclei and stacks play a direct role in the assembly process.

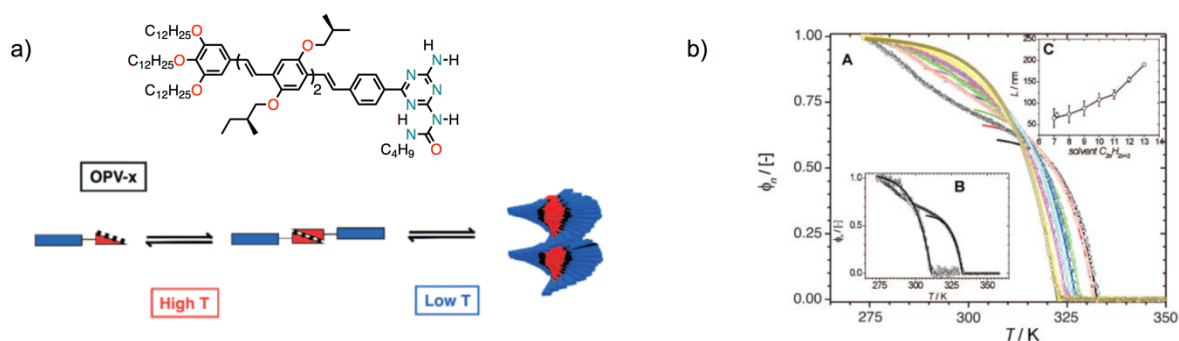


Figure 3.1.10. a) Chemical structure of OPV ureidotriazine along with schematic representation of H-bonding followed by stacking into helical supramolecular fibers; b) solvent-dependent CD measurements in eight alkane solvents.

Subsequent studies further probed the stability and dynamics of the oligo(*p*-phenylene vinylene) ureidotriazine by stepwise addition of a ‘good’ solvent (CHCl_3) to a poor solvent (MCH).²⁶³ This resulted in a depolymerization that occurs at a critical solvent composition, as predicted for this polymer assembled via cooperative mechanism. Additionally, this study showed that it is possible to form one-dimensional materials by choice of solvents and their ratio, avoiding the usual rapid dispersion of molecules into a ‘poor’ solvent, which often produced large agglomerates that precipitate.²²²

Ureidotriazine dimer, connected with an alkyl spacer, were found to dimerize through self-complementary quadruple hydrogen bonding and stack dimers into columnar architectures (**Figure 3.1.11**).²⁷¹ By varying the peripheral solubilizing groups it was possible to obtain stacks both in dodecane (with alkyl chains) and water (with ethylene oxide), the latter one creating a hydrophobic microenvironment, showing the generality of the system.

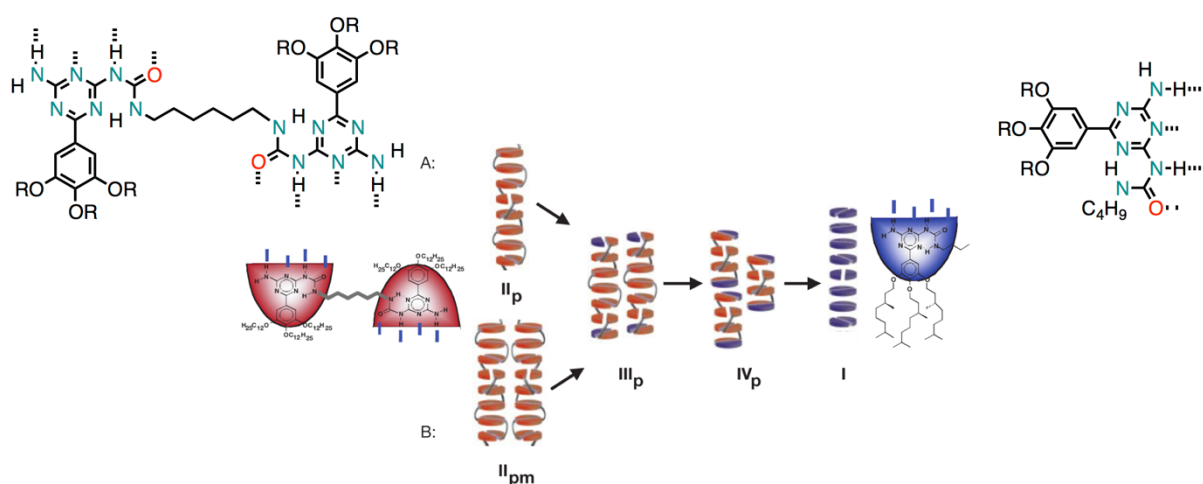


Figure 3.1.11. Chemical structure of bifunctional (left) and monofunctional (right) ureidotriazines and a schematic representation of the organization of mixtures of mono- and bifunctional compounds upon increasing the fraction of monofunctional compound.

Another very popular motif in supramolecular chemistry is the benzene-1,3,5-tricarboxiamide (BTA) that is able to form supramolecular polymers through hydrogen-bonding and stacking between the aromatic units.²⁷² BTAs were found to self-assemble into helical one-dimensional aggregates by threefold intermolecular hydrogen bonding (**Figure 3.1.12**). Therefore, addition of competing solvents with H-bonding, such as CH_3CN , resulted in disassembly of the aggregates.²⁷³ The role that

the solvent plays in the self-assembly process of BTAs was followed by CD, a technique that has a high sensitivity to the conformation of molecule.²⁷⁴ A pronounced effect of the different alkane solvents was observed on the shape of the Cotton effects and therefore on the thermodynamic parameters. A linear (*n*-heptane) and a cyclic (MCH) alkane solvents influenced differently the BTA conformation and more specifically the dihedral angle (θ) between the C=O group and the benzene central core. In linear alkanes, capable of intercalation between the BTA molecules, the θ is larger (around 45°) and in cyclic, bulky solvents the θ is smaller.

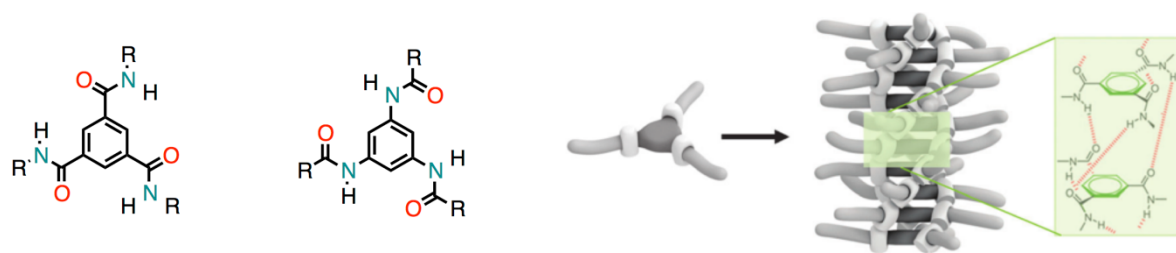


Figure 3.1.12. General chemical structures of C=O- and N- centered BTAs along with a schematic representation of the self-assembly into helical one-dimensional aggregates by three-fold hydrogen bonding.

Several BTA analogues, substituted also at the 2,4,6 position have been reported.^{275–277} These hexasubstituted BTAs showed a larger dihedral angle (amide-benzene), most probably due to the steric congestion, and their self-assembly was probed by fluorescence in various solvents. Surprisingly and in sharp contrast to trialkyl BTAs, due to the increased aromatic surface they aggregated mostly in CH_2Cl_2 , while no aggregation was observed in dodecane. This was rationalized by taking into account strong solvophobic interactions between the solvent and the long alkyl chains on the BTA, that should stabilize the monomer and therefore interfere with the aggregation. Other π -extended BTAs, such as three-substituted porphyrin (carrying chiral chains) was thoroughly studied for nanostructuration at the solid-liquid interfaces and will be described in more detail afterwards.^{266–268} Contrary to previous reports on chiral amplification (‘sergeants and soldiers’), BTA carrying three porphyrins did not behave according to this mechanism. It was shown that, in apolar alkanes like *n*-heptane, they form kinetically stable stacks that did not allow dynamic exchange of chiral and achiral components. However, when using Ph-CH_3 , a situation between stacks (*n*-heptane) and molecularly dissolved monomers (CHCl_3) was found, with the chiral monomers successfully incorporated into achiral stacks.

While most BTAs were found to aggregate through H-bonds and stacking between aromatic units, several examples showed that amide H-bonding does not play a dominant role in the intramolecular aggregation. An example of such behavior is the 3,3'-bis(acylamino)-2,2'-bipyridine substituted benzene-1,3,5-tricarboxamide (BiPy-BTA) motif, that was extensively studied (**Figure 3.1.13a**).^{264,278–280} It was observed that the amide hydrogen-bonding does not play a role in the aggregation process since strong intramolecular bonds are formed between the amide and the BiPy. Consequently, the BiPy-BTA adopts a planar geometry with the dihedral angle (amide-benzene) approaching zero. Therefore, the intermolecular forces that guide the self-assembly are strong π - π interactions and solvophobic forces. More recently, chiral, amphiphilic BiPy-BTA discotic molecules were self-assembled to form fibers made of either one (pure *i*PrOH, only π - π interactions present) or three molecules in the fiber cross-section (H_2O -*i*PrOH mixtures, where the hydrophobic effect steps in) (**Figure 3.1.13b**).²⁶⁴

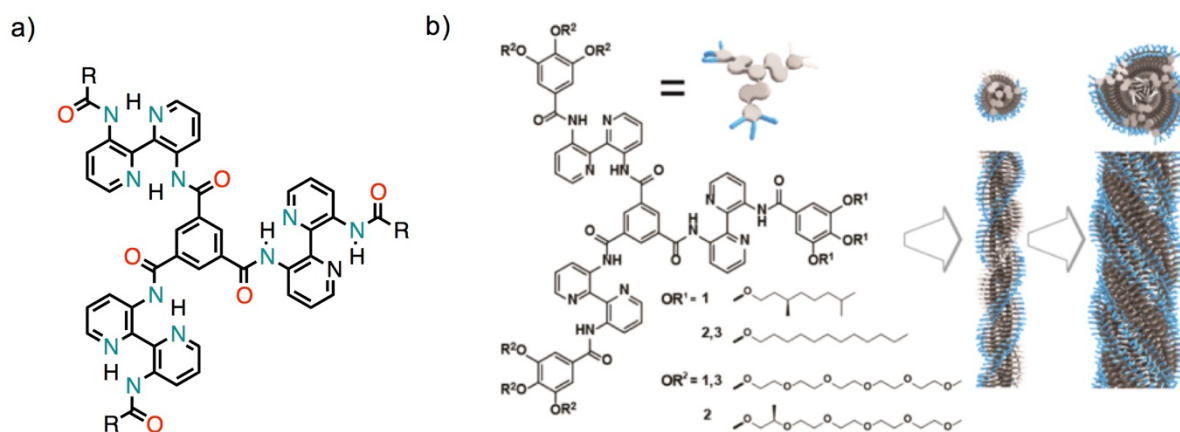


Figure 3.1.13. a) Chemical structure of 3,3'-bis(acylamino)-2,2'-bipyridine substituted benzene-1,3,5-tricarboxamide (BiPy-BTA); b) chemical structures of amphiphilic BiPy-BTA discotics and their hierarchical self-assembly first into a supramolecular fiber, followed by a triple helical bundle.

Interestingly, the self-assembly mechanism of the self-assembling system changes from cooperative (trialkyl BTAs) to isodesmic (BiPy-BTA) (**Figure 3.1.14**).^{272,281,282} It is expected that a self-assembled stack formed through intermolecular hydrogen-bonding, along the growth direction, leads to a permanent dipole in the complex, that in turn could lead to larger aggregates by further interaction through long-range dipole-dipole interactions. Computational studies were performed and showed that a BTA tetramer possesses large dipole moments, with charge polarizability along the direction of the stacks, while a BiPy-BTA tetramer does not show significant polarization.²⁸¹ This was confirmed

by designing and synthesizing PBIs carrying different linkers and self-assembling moieties.²⁸³ Molecules that present a significant macro-dipole or polarization were found to follow a cooperative mechanism of self-assembly, while absence of such dipolar groups resulted in isodesmic self-assembly.

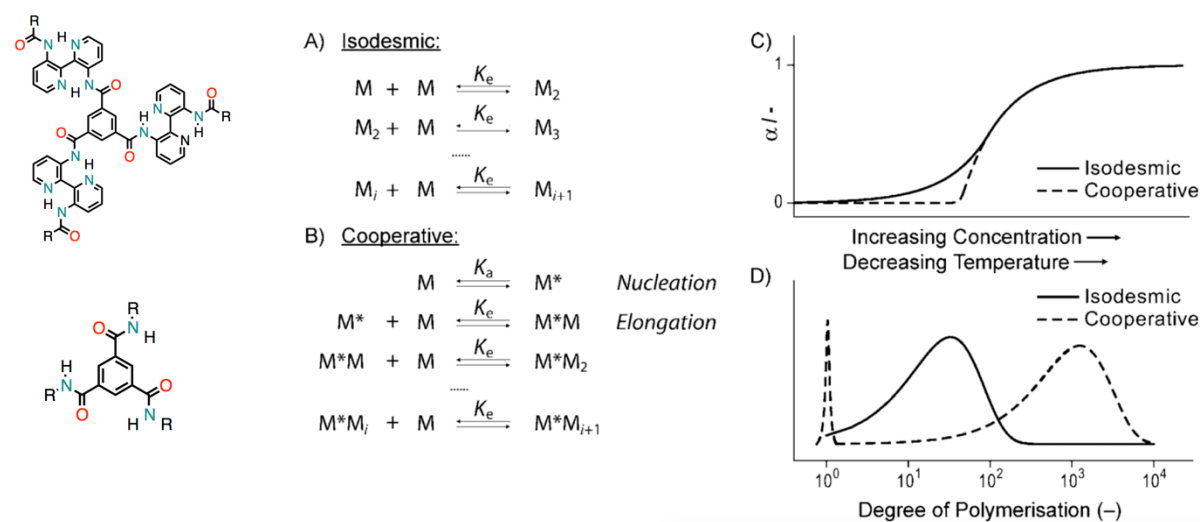


Figure 3.1.14. Schematic representation for the isodesmic (A) and cooperative (B) self-assembly mechanism for monomers M; schematic representation of the degree of aggregation vs. concentration and temperature (C); schematic molecular weight distribution (D).²³⁶

As the combination of different interactions was used to construct other PBI superstructures.^{179,284–288} Orthogonal intermolecular forces were used between perylene bisimide bearing four phenoxy substituents at the bay position and complementary melamine moieties. NMR complexation studies showed the independence of the two imide sites towards hydrogen bonding. Further complexation studies showed that a non-competitive environment (such as alkanes) is necessary for high degrees of complexation, with the association constants ranging from 240 M^{-1} in CDCl_3 to $5.4 \times 10^4 \text{ M}^{-1}$ in MCH.^{284,285} However, strong hydrogen bonding is not enough to form extended three-dimensional structures, as evidenced by lack of superstructures when very bulky phenoxy substitutes (that thus prevent π - π stacking) were used. Similar perylene bisimides, containing long alkyl chains on the tetraaryloxy bay substitutions, were reported to self-assemble into *J*-type aggregates through two-fold hydrogen-bonding and aromatic stacking, without the need of intermolecular hydrogen-bonding with complementary melamine units.^{289,290} PBIs functionalized at the imide position and carrying amides, connected with spacers of various lengths, were reported to polymerize in a solvent-dependent fashion.^{287,288} Temperature-dependent experiments revealed a non-sigmoidal transition that implied a

cooperative aggregation with a thermal hysteresis observed with different critical temperatures in the cooling and heating processes. Both critical temperatures were found lower in Ph-CH₃ when compared to MCH/Ph-CH₃ (2:1 v/v), showing that the polymerization is less stable thermodynamically in pure Ph-CH₃ (a more polarizable solvent with higher refractive index). Interestingly, it was found that the monomeric state is conformationally locked and kinetically trapped, being inactivated between the critical cooling and heating temperatures. This kinetical species is trapped by the intramolecular hydrogen bonded state after cooling, slowing down the formation of supramolecular fibers over time. By varying the alkyl spacer length from ethylene to propylene and pentylene the supramolecular polymerization behaved in a similar fashion, while butylene-tether PBI showed an off-pathway where the monomers self-assemble into nanoparticles, and turn slowly into fibrous polymers over time. Moreover, the controlled choice of solvent had a strong effect on the electron transfer and hence fluorescence quantum yield: and equilibrium between a 'closed' and 'open' conformation is preferred in MCH and DMF, respectively.

3.1.2. Solvent Effects on Surfaces

The control of supramolecular constructs over multiple lengths scale is of great interest for application in various fields including catalysis, (opto)electronics, magnetism and medicine.^{3,12,178,185,291} Particularly, supramolecular chemistry on metallic and insulating surfaces has become a model of choice for characterization, catalytic behavior, patterning, charge-transfer process and reaction dynamics, among others.^{292–295} Molecular design and choice of intermolecular forces has resulted in numerous supramolecular structures along with a variety of properties. Additionally, in view of the numerous molecular building blocks, it is not surprising that a number of different routes for the preparation of molecular nanostructures was reported.²⁹⁶ **Figure 3.1.15** schematically shows some of the most common nanostructuration methods, both solution-based (pre-deposition) and on-surface. Solution-based methods (**Figure 3.1.15** top) usually include the use of a 'poor' solvent, in which the molecule has limited solubility in order to maximize the intermolecular forces, especially in cases where the intermolecular forces are not strong (e.g. π - π stacking). Additionally, both fast processes like fast dispersion, or slow ones like crystallization can be employed. In the case of fast processes, *rapid solution dispersion* (*fast injection*) denotes injection of molecules in a 'good' solvent to a 'poor' solvent and thus the self-assembly is expected to occur simultaneously. For other molecules, where the precipitation (or crystallization) proceeds too rapidly (*i.e.* when the association between

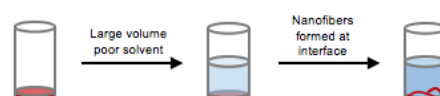
molecules in a ‘poor’ solvent is too strong) and yield large and uncontrollable aggregates, slow crystallization methods are better suited. Slow crystallizations include *phase transfer* and *vapor diffusion*. Phase transfer occurs when the ‘good’ and ‘poor’ solvent are quite different in density and polarity and the crystallization is induced by phase transfer at a bisolvent interface. Vapor diffusion is an even slower, but more complex process. The exchange via vapor diffusion between the two solvents allows a slow decrease in solubility and provides enough time for arranging in a favorable way.

Solution-based nanostructuration

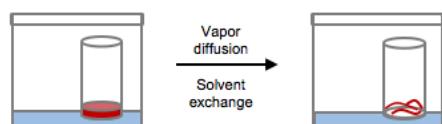
a) Fast injection: bulk phase self-assembly



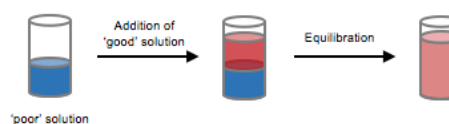
b) Bisolvent phase transfer: self-assembly at interface



c) Vapor diffusion

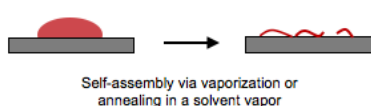


d) Addition of good solvent

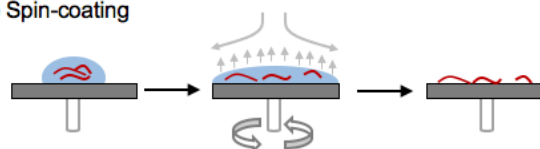


Surface-based nanostructuration

a) Drop-casting



b) Spin-coating



c) Zone-casting



d) Dip-coating

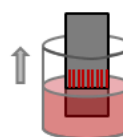


Figure 3.1.15. Schematic representation of nanostructured processes in solution and on surface. Adapted from references.^{222,296}

On the other hand, surface-based nanostructuration include a number of deposition methods, with the most common ones depicted in **Figure 3.1.15** (bottom) and are based mostly on solvent evaporation.²⁹⁶ Controlled evaporation methods include:

- *Drop-casting.* A small volume of a solution is deposited on a substrate as a drop and is left to dry either in air or in atmosphere of solvent (in order to slow down the evaporation), with the self-assembly highly influenced by *dewetting* or thin liquid film rupture on the surface. Dewetting is dependent on the solvent, the substrate nature and the solution concentration. However, its contribution can be minimized by employing low volatility solvents and thus decreasing the rate of solvent evaporation.
- *Spin-coating.* The solution is first applied on a substrate and then is rotated at high speed on a spinning wheel, with the centrifugal forces pushing the excess solution to the edges of the substrate, with a residue remaining in the substrate thank to surface tension.
- *Zone-casting.* The solution is continuously dispensed through a nozzle onto a moving substrate with the evaporation taking place from the surface meniscus formed between the nozzle and the substrate. This technique was used in order to produce aligned and anisotropic layers of molecular materials on substrates that have not been pre-oriented.
- *Dip-coating.* A substrate is dipped into a coating solution and then vertically pulled (at a constant speed) from the solution. In this manner, a stripe of pattern perpendicular to the withdrawal directions is obtained.

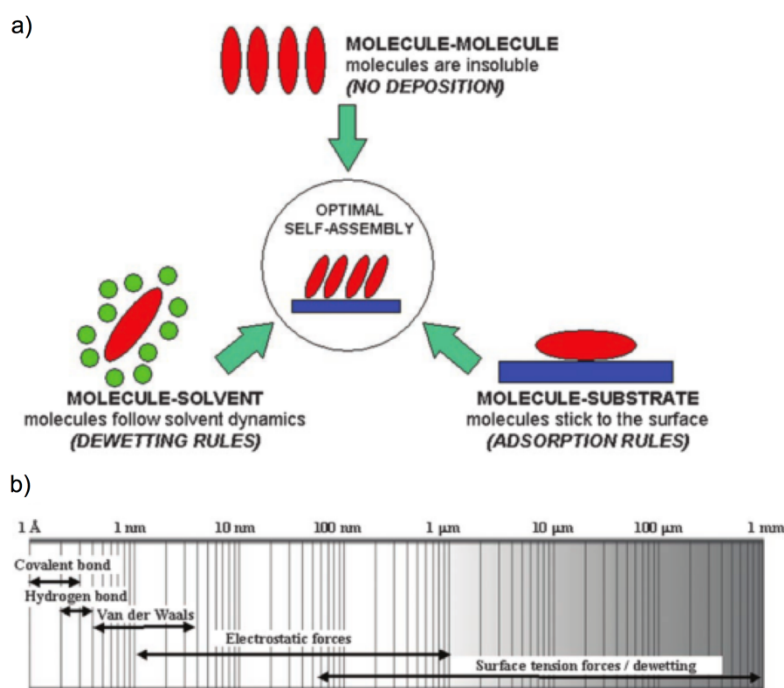


Figure 3.1.16. a) Three major types of interaction involved during solvent-assisted deposition; b) qualitative comparison of the relevant length scale over which each type of force dominates self-assembly.²⁹²

Generally, during solvent-assisted deposition, three major interactions have to be considered and a misproportion between them can lead to three different scenarios (**Figure 3.1.16**): (i) too strong molecule-molecule interactions can lead to insoluble or aggregated material; (ii) too strong molecule-substrate interactions lead to kinetically trapped molecules on the surface instead of interacting with each other and (iii) molecule-solvent interactions will prevent interaction with other molecules and most probably, amorphous structures guided by physical processes (such as dewetting) are obtained. Molecule-molecule and molecule-solvent interactions have been covered before and therefore, in this section, only molecule-substrate interactions and physical forces (e.g. coffee-stain^{297,298} and spinodal dewetting mechanisms²⁹⁹⁻³⁰²) will be considered. In this regard, coffee stains are formed when a drop of spilled coffee dries on a solid surface, leaving a ring-like deposit along the perimeter (**Figure 3.1.17ab**).^{297,298} This characteristic pattern is due to the pinned contact line of the drop where a capillary flow replenishes the evaporated liquid from the interior. Another important physical process on surface is dewetting, or the spontaneous rupture of a thin film on a solid surface into ensembles of characteristic and separated objects, leading to regular motifs with long-range order (**Figure 3.1.17cde**).³⁰²

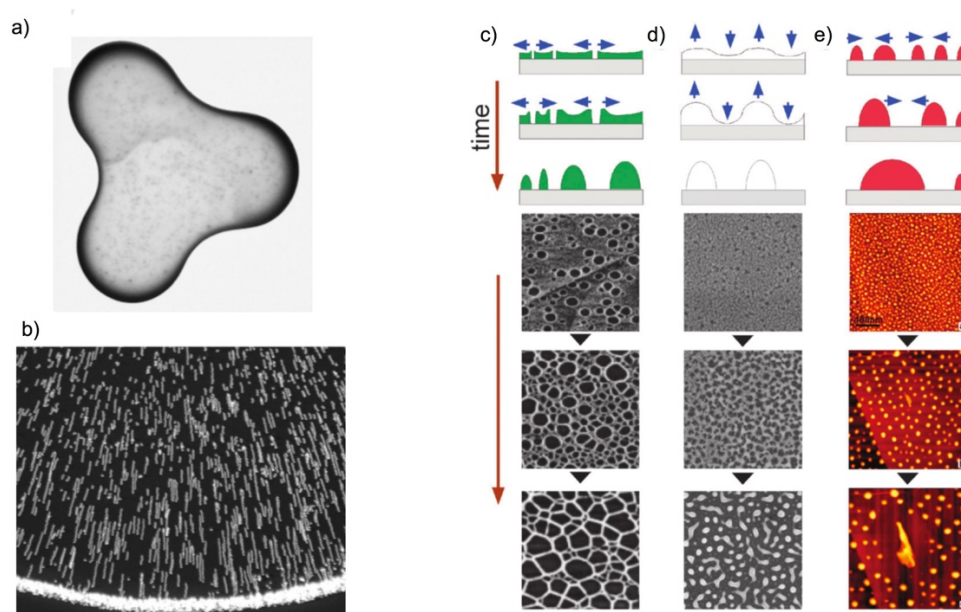


Figure 3.1.17. Common physical processes observed when solvent is evaporated from the surface. a,b) A coffee-stain and a demonstration of the physical processes involved with particles moving to the ring, multiple exposures superimposed;²⁹⁷ c,d,e) schematic representation and experimental examples of dewetting processes;³⁰² c) dewetting by nucleation, growth and coalescence of holes; d) spinodal dewetting; e) evolution of a dewetted film by Oswald ripening, followed by crystallization.

These physical processes were involved and were responsible for some of the morphologies reported below and will be described in detail in specific examples. Rather than reporting the different morphologies and listing the molecules used in those studies, the next section has been organized by different classes of building blocks and the recent progress that has been done in their soft matter nanostructuration.

3.1.2.1. Nanographenes

The self-assembly of hexabenzocoronene (HBC) and other polycyclic aromatic hydrocarbons have attracted much attention since they possess interesting properties (**Figure 3.1.18**).^{303–305}

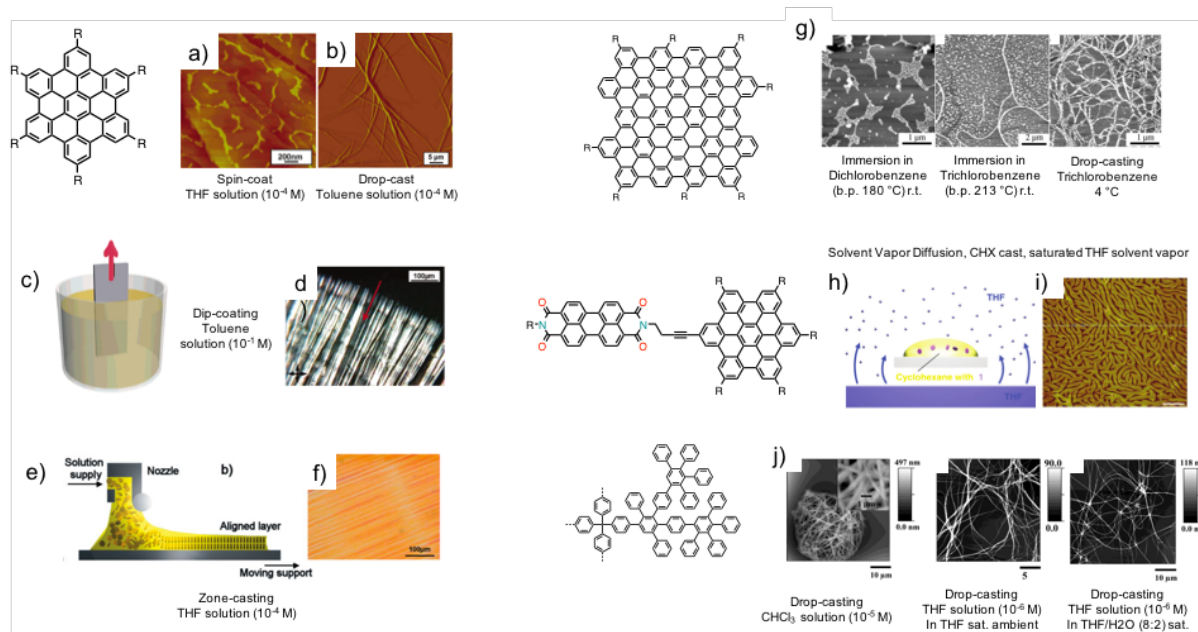


Figure 3.1.18. Self-organized polycyclic aromatic hydrocarbons with the deposition method and solvent: a-f) HBC deposited by spin-coating, drop-casting, dip-coating and zone-casting; g) giant nanographene (C132) morphologies obtained in different solvent and different temperature; h,i) solvent vapor diffusion scheme and morphology obtained from PBI-HBC hybrid and j) morphologies obtained by drop-casting a polyphenylene dendrimer in different conditions.

The self-organization of HBCs was systematically studied both in solution and on surface by chemical modification (varying the side-chains) and experimental conditions (solvents, concentrations and

substrates) (**Figure 3.1.18a-f**).^{303,304,306-309} Spin-coating a THF solution of hexa-dodecyl-hexa-*peri*-hexabenzocoronene HBC-C₁₂ ($K_a = 5.5 \times 10^3 \text{ M}^{-1}$ in this solvent) was found to give wide blobs randomly distributed over the surface (**Figure 3.1.18a**). By drop-casting from Ph-CH₃ and xylene solutions (surprisingly high $K_a = 1.5 \times 10^4 \text{ M}^{-1}$ in Ph-H) single long nanofibers were formed, with the difference in morphology attributed to the slower evaporation times for aromatic solvents (**Figure 3.1.18b**). Subsequently, the HBC-C₁₂ was processed by zone-casting technique by depositing a THF solution through a flat nozzle into a moving glass support, with the rates of motion support and solution deposition optimized, to obtain exceptionally long and uniaxially aligned columns (**Figure 3.1.18ef**).³⁰⁶ Alternatively, dipping into a relatively concentrated PhCH₃ solution (10⁻¹ M) and at a low moving velocity of the support, a homogenous film with oriented fibers made of uniaxially aligned HBC columns was obtained (**Figure 3.1.18cd**). Another way to minimize wetting effects was achieved by solvent vapor deposition of a PBI-HBC dyad (**Figure 3.1.18hi**).³⁰⁹ The drop-casted CHX dyad solution was placed in an ambient of saturated solvent vapor (THF). The evaporation rate can be tuned by different solvents, thus minimizing dewetting effects. Moreover, the active solvent vapor can be adjusted, *i.e.* a polar co-solvent will induce solvophobic association.

The self-organization of a giant nanographene fragment (C132) was studied under various conditions, by trying to minimize the dewetting effects that were found to be detrimental for definite morphologies (**Figure 3.1.18g**).³¹⁰ Immersion in a *o*-DCB solution, with various concentrations, yielded globular isolated aggregates, a situation that is strongly influenced by dewetting, according to an earlier model for drying-mediated self-assembly of nanoparticles solutions.³¹¹ It was shown that, by varying systematically the experimental conditions, it was possible to drive the self-organization from kinetically driven irregular aggregates to thermodynamically favored fibers. The latter ones were obtained from drop-casting a dilute trichlorobenzene solution onto a cold mica surface.

Polyphenylene dendrimers were found to organize into various morphologies when deposited on surfaces (**Figure 3.1.18j**).^{312,313} Although it is possible to obtain individual dendrimer molecules³¹³ on mica (when spin-coated under very diluted CH₂Cl₂ solutions) or undefined aggregates due to dewetting properties of the surface,^{312,313} more defined nanofibers were obtained when drop-casting on various substrates under a saturated solvent atmosphere (HOPG, silicon, mica and glass).³¹⁴ Clusters of fibers were found on HOPG substrate from a CHCl₃ solution, while nanofiber networks were obtained from THF solution on silicon, glass or mica. Addition of small amount of H₂O to the THF saturated atmosphere suppressed such aggregation of the nanofibers and yielded single

individual curved nanofibers, probably due to the presence of H₂O that improves the wetting properties and thus decreased the shear force of the lateral flow of the solvent.

3.1.2.2. [60]Fullerene

Solvent vapor annealing (SVA) was recently used for controlled vertical or lateral crystallization of C₆₀ nanowires (**Figure 3.1.19**).³¹⁵ Although the formation of various morphologies through drop-drying process of C₆₀ in various solvents was already reported,³¹⁶ mastering forces inside an evaporating droplet is critical for the fine control of the morphology. The edges of a droplet are pinned onto a substrate and therefore the capillary flow is going outward in order to replenish the evaporating solvent at the edges, as seen for the ‘coffee-ring’ effect. However, in presence of thermal and concentration gradients, the ‘Marangoni flow’ or a circulatory flow is generated and competes with the capillary flow (**Figure 3.1.19b**).

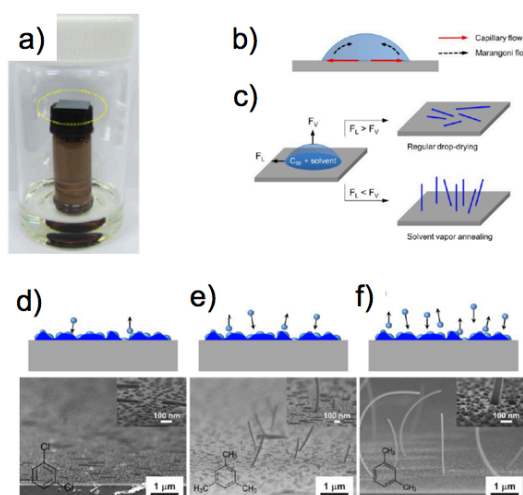


Figure 3.1.19. a) SVA apparatus and setup; b) scheme showing two main flows in the droplet; c) schematic representation of lateral and vertical forces in an evaporating droplet; d-f) SEM images of C₆₀ nanowires along with a schematic qualitative expression of relative degree of solvent wetting for 1,3-dichlorobenzene, mesitylene and *m*-xylene.³¹⁵

By employing a solvent with high vapor pressure (*m*-xylene), the droplet pinning is not happening due to rapid, massive lateral expansion and shrinkage of the droplet on the surface. Thus, vertically aligned nanowires are obtained along the direction of solution expansion. The SVA showed to be an ideal method in order to maximize the vertical flow over the lateral one.

C₆₀ aligned single crystals were prepared also by droplet-pinned crystallization (DPC) method.³¹⁷ The drying of a xylene solution on a silicon substrate showed the crystals to start nucleate near the contact line and were grown towards the center. This deposition method allowed to connect the source and the drain electrodes to measure a high electron mobility of this organic field-effect transistor (FET). This is a general method that allows fabrication with other organic semiconductors as well as co-deposition.³¹⁸

3.1.2.3. Porphyrin Derivatives

Porphyrin derivatives have attracted great attention for surface nanostructuring since they have interesting electronic properties and are (photo)catalytically active. Moreover, great efforts have been placed in mimicking natural assemblies of porphyrins, such as ring-shaped assemblies (in bacterial complex LH2). Formation of porphyrin rings, wheels or toroids has been reported (Figure 3.1.20a-d).³¹⁹⁻³²⁵

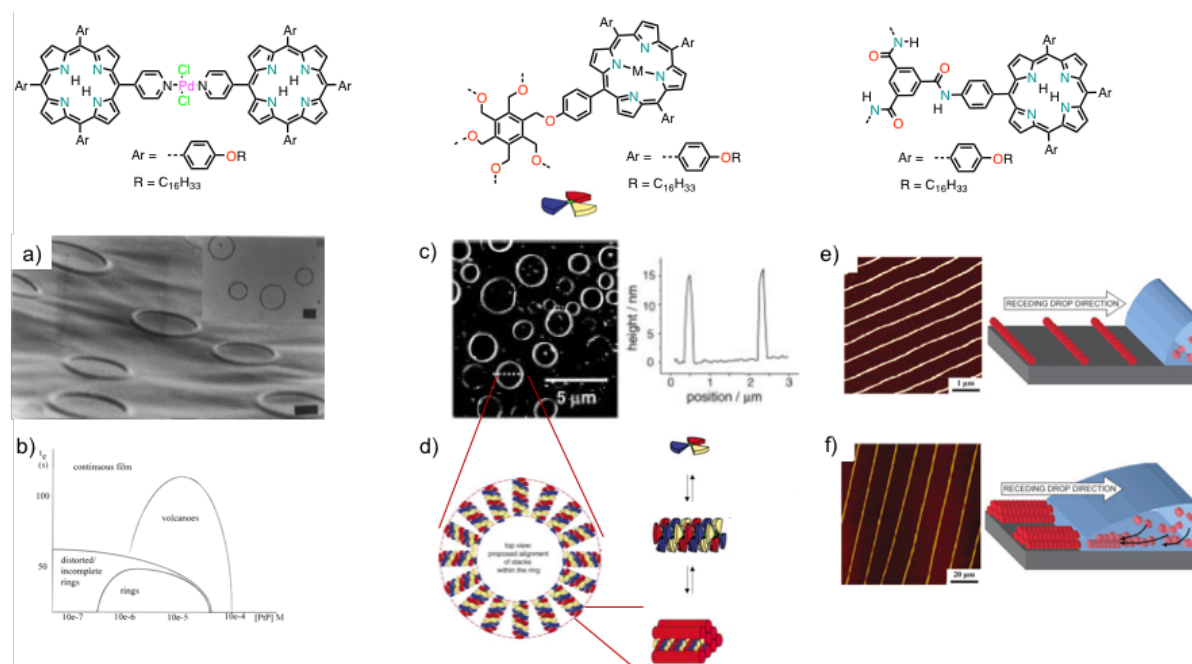


Figure 3.1.20. ab) Chemical structures and nanostructuring of porphyrin Pd dimer, cd) porphyrin hexamer and ef) porphyrin BTA trimer. a) Transmission electron micrograph (scale bar 1 μm);³¹⁹ b) nonequilibrium morphology diagram of substrate structures, evaporation time (y axis) and concentration (x axis); c) AFM image of hexa-porphyrin with a cross-section along the dotted line; d) schematic representation of the columnar stacks within the ring;³²³ e,f) AFM images of patterned mica after evaporation of a porphyrin trimer in chloroform along with the proposed mechanism of formation of patterned line during evaporation.^{266,267,292}

A porphyrin Pd dimer solution was deposited by using a variety of solvents, substrates and conditions (**Figure 3.1.20ab**). Deposition on a carbon-coated grid and glass showed CCl_4 to be the best solvent (compared to CHCl_3 and CH_2Cl_2) indicating that a higher boiling point is desirable, with slower evaporation stimulating the formation of well-defined rings. It was suggested that π - π stacking was occurring and that the aggregation was taking place already in solution. Consequently, by disruption aggregates with CH_3OH it was possible to avoid the formation of rings. Moreover, addition of CH_3OH altered not only the aggregation, but also increased the wettability of the glass substrate (with its more polar and hydrogen bonding character, when compared to CHCl_3) and finally affected also the thermodynamics of the liquid layer on the substrate. In order to probe the mechanism of ring formation, several measurements were performed by depositing CHCl_3 on glass under various conditions (of concentration, temperature and pressure). The results elucidated the ‘optimal’ conditions of evaporation rate and porphyrin concentration and yielded a morphology diagram (**Figure 3.1.20b**). Moreover, a three-step process has been proposed: (i) evaporation instability that causes rupture of the film and formation of sub-micrometer droplets (ii) coalescence of the small droplets, with the substrate controlling the pinning center for the evaporating droplets and (iii) material accumulates at the edges by particle flow inside the droplets and therefore forms the rings. Experiments supported an evaporation-driven solute transport mechanism since fast evaporation or low porphyrin concentration showed the poorly developed ring structures, while slow evaporation or too high concentration lead the system in a viscous dominated regime that hindered the formation of the rings.

In order to investigate more closely the self-assembly and surface dewetting processes, porphyrin hexamers and dodecamers were prepared (**Figure 3.1.20cd**).^{323,324} Since no fluorescence was observed inside the rings, the ‘coffee-stain’ mechanism was excluded and it was proposed that the ‘pinhole’ mechanism occurred instead (**Figure 3.1.21**). According to the pinhole mechanism, the films thin to a thickness at which holes are formed, which accounts for the ring formation. The rupture of the film, due to surface instability, can occur via two possible mechanisms, by spinodal dewetting or dewetting at heterogeneous nucleation sites. During the dewetting process, the material is deposited at the edges of the holes. Moreover, tandem processes occur during evaporation that depend on the surface (wettability) and molecular properties (solubility, stackability and adsorption) and all of those need to be considered when designing the experiments. Small, well-defined and relatively monodispersed rings were obtained on hydrophilic carbon coating glass substrate, with a high degree of fluorescence anisotropy. This suggested that the ring formation process was through spinodal dewetting, due to the

surface undulation that occurs at a later stage with the concentrated solution and the aggregation already occurred. Importantly, no rings were formed at low relative humidity (40-45 %) due to the H₂O molecules from air being physisorbed on the surface.

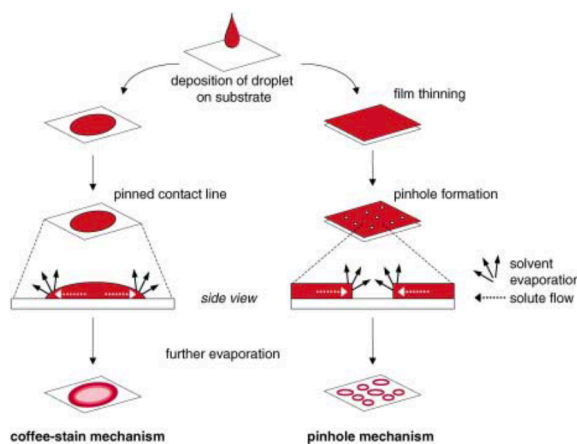


Figure 3.1.21. Schematic representation of the ring-formation process according to the coffee-stain mechanism and the pinhole mechanism.³²³

By further increasing the π -surface in a porphyrin dodecamer, a higher degree of molecular order was achieved.³²⁴ The formation of the rings was found to be independent of the wettability of the surface and a very high degree of optical polarization was observed. In a further attempt to increase stacking between modules, a disc-shaped porphyrin consisting of three porphyrin attached to a central benzene core with amide linkers (BTA) and intermolecular hydrogen bonding was sought (**Figure 3.1.22**).^{266-268,326} Indeed, drop-casting a dilute porphyrin-BTA solution formed highly uniform patterns of linear aggregates up to almost 1 mm (**Figure 3.1.22ac**). The mechanisms responsible for this macroscopic patterning and periodicity are governed by physical dewetting processes like 'coffee-stain' mechanism and spinodal dewetting. As a result of the 'coffee-stain' mechanism, there is a local increase in the concentration of the molecules near the contact-line of the evaporating droplet. Further evaporation gives unpinning and retraction of the contact line with deposition of porphyrin stacks onto the mica surface. The highly uniform periodicity, on the other hand, is attributed to the 'stackability' of porphyrin molecules along with the process of spinodal dewetting, causing an undulating pattern in the thin evaporating film. Moreover, there was a strict concentration range for the formation of this pattern (1-10 μM): lower concentrations gave small droplets with randomly deposited material, while higher concentrations gave AFM images typical of gels. Deposition from another, more apolar, solvent

such as *n*-hexane gave randomly oriented and intertwined fibers (Figure 3.1.22d). Formation of large aggregated species was observed also in the solution for this solvent, while in chloroform the porphyrins are molecularly dissolved (Figure 3.1.22e). Spinodal dewetting did not significantly impact deposition from *n*-hexane, most likely due to the limited mobility of the already formed supramolecular polymers in the thin film. Thus, most likely, upon drop-casting a dilute chloroform solution, supramolecular polymers do not precipitate, but are formed at the moment when the chloroform film undergoes spinodal dewetting.

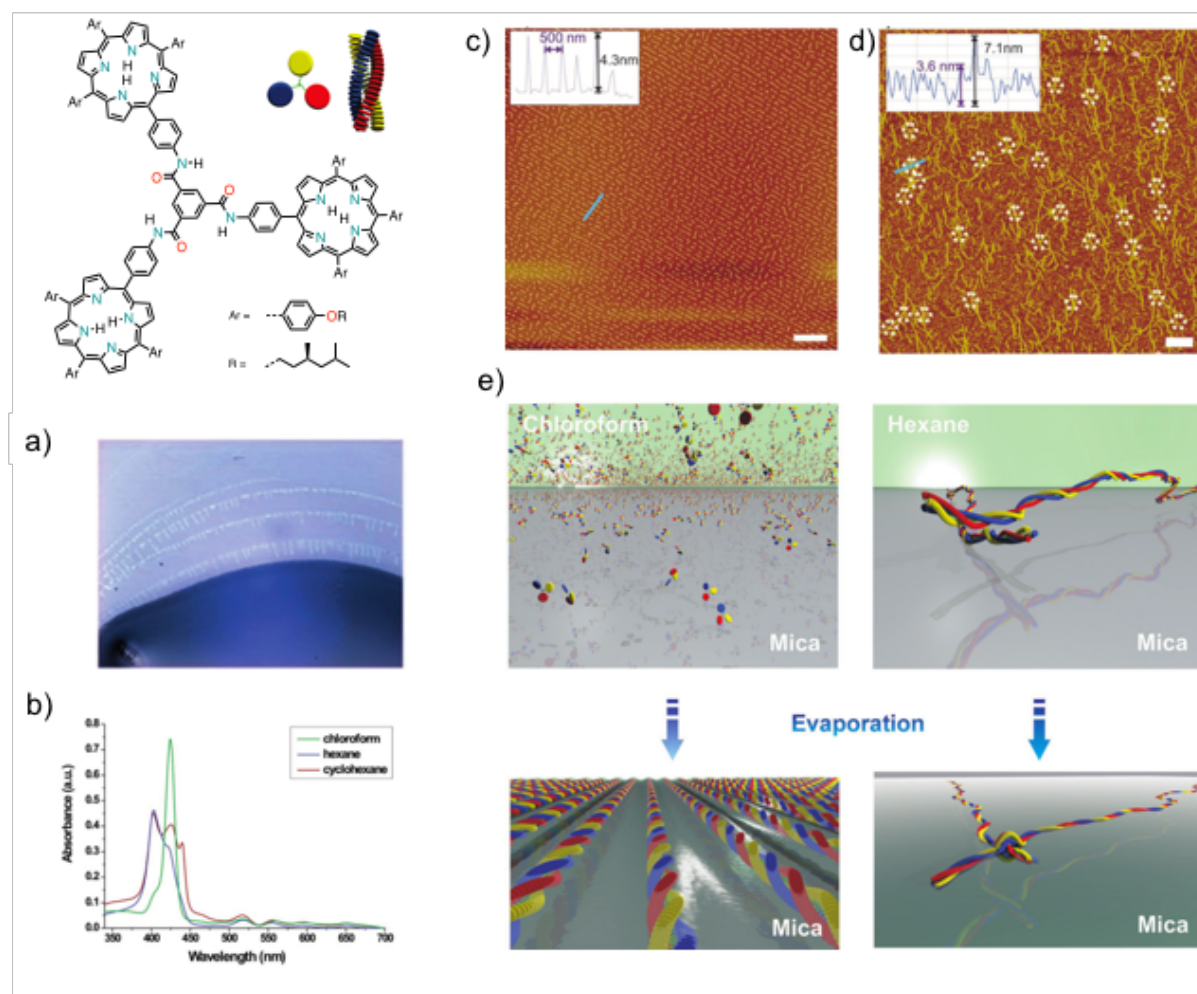


Figure 3.1.22. Self-assembly properties in solution and on surface for porphyrin BTA trimers. a) Optical micrographs of the coffee-like stain that forms during evaporation of a CHCl_3 solution on glass: the dark blue is solution, while the white stripes are the aggregates that remain after the retraction;²⁶⁶ b) UV-Vis spectra in CHCl_3 , hexane and CHX ; c,d) AFM images of drop-casted solution of CHCl_3 (c, scale bar 1 μm) and *n*-hexane (d, scale bar 2 μm), the dashed circles highlight the crossing points of the fibers; e) schematic representation of the aggregation behavior in chloroform and *n*-hexane.²⁶⁷

Porphyrin amphiphilic derivatives have also been prepared and studied (**Figure 3.1.23**).^{327,328} A chiral porphyrin-fullerene dyad showed a chiroselective assembly into photoconductive p-n heterojunction nanofibers. The racemic dyad co-assembled into nanospheres, whereas enantiopure dyad gave long nanofibers that showed a high ambipolar charge-carrier mobility ($\sim 10^{-1} \text{ cm}^2 \text{ V}^{-1} \text{ s}^{-1}$), far higher compared to the spherical assembly. Another amphiphilic tri-porphyrin assembles into vesicles in solution that gradually disappeared into nanowires on mica surface (**Figure 3.1.23b**). The adaptation to the mica surface is mainly due to the hydrophilic ethylene glycol chain, a hydrophobic dodecyl chain, secondary hydrogen-bonding or halogen-halogen interactions and finally the moisture that leads to the hydration of the mica.

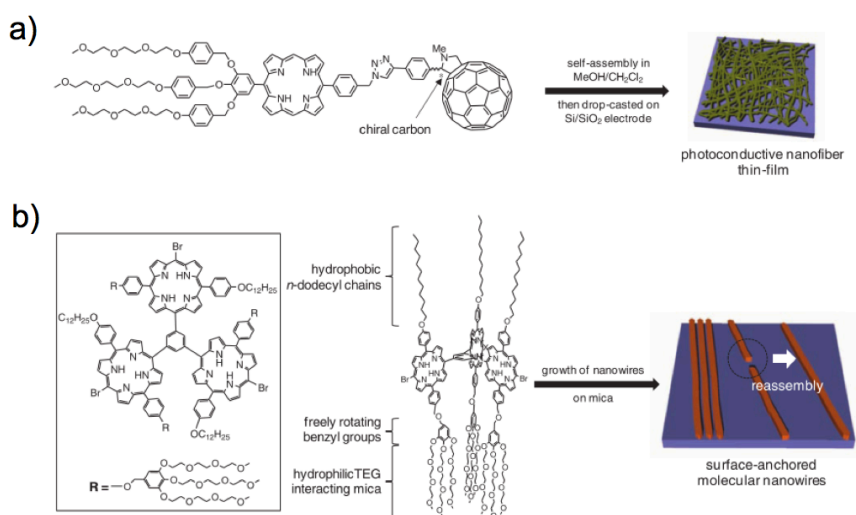


Figure 3.1.23. a) Molecular structure of a chiral D-A dyad assembled into nanofiber and b) trigeminal amphiphile porphyrins forming molecular nanowire through self-assembly and reassembly.³²⁹

3.1.2.4. Other π -Extended Molecules

Highly ordered, low-dimensional aggregates based on bis-urea-*n*-thiophene molecules were obtained on several substrates (SiO_2 , mica and graphite) (**Figure 3.1.24a**).³³⁰ It was found that thiophene moieties, in the same way of other hydrocarbons, are perpendicularly oriented when deposited on oxidic substrates (such as SiO_2 or mica), due to stacking interactions being energetically favored over substrate-molecule interactions. The latter interactions were enhanced drastically on molecularly-flat highly oriented pyrolytic graphite (HOPG) and therefore the molecules lied down. Subsequently, a set of experiments were performed with thwwhere the bis-urea-*n*-thiophene deposited in 1-octanol on

a SiO₂ surface and concentration/temperature were varied in order to obtain fibers of different lengths. It was observed that, at lowest temperature (20 °C), the growth occurred in a near-equilibrium type since evaporation is slowest and thus the mass transport towards the droplet is slowest. This led to a numerous nucleation centers yielding a large number of small fibers. At the highest temperature (120 °C), the mass transport is higher but the degree of super-saturation is lower, resulting in dendrites in a diffusion-dominated growth. At 70 °C, the growth does not follow neither diffusion nor nucleation, leading to longest fibers. The distribution of the aggregates was in agreement with the pinned contact line during droplet evaporation. The droplet did not move, but the evaporation continued and therefore the solution was driven outwards to compensate for evaporation losses near the edges. However, the presence of the fibers is in contrast with the coffee-stains. This was rationalized by the presence and directionality of strong intermolecular interactions (bis-urea), which were therefore responsible for the growth of fibers in the drying droplets.

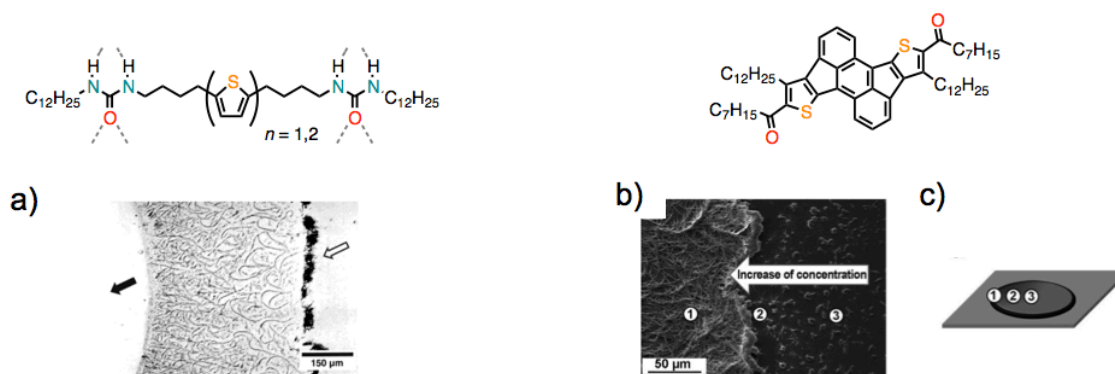


Figure 3.1.24. a) Chemical structure of bis-urea-*n*-thiophene with hydrogen bond interactions showed as dotted gray lines; the optical micrograph shows a typical aggregation pattern after the droplet is evaporated at 70 °C on SiO₂; the open arrows point at the outer edge of the droplet, while the solid arrow shows the optically empty center, (b) chemical structure of emeraldine derivative with SEM images of a drop-cast film of a dilute solution in THF showing a boundary between nanoribbons and nanobaskets corresponding to regions 1-3 of the 'coffee-ring' effect.

A heteroatomic π -conjugated emeraldine derivative (Figure 3.1.24b) was found to self-assemble from ribbons to vesicles and baskets, depending on the concentration of the drop-casted THF solution on a silicon substrate.³³¹

The critical role of the solvent has been reported on the morphology of oligophenylene ethynylene (OPE) and oligophenylene vinylene (OPV) derivatives (**Figure 3.1.25**).^{329,332} By playing with solvent polarity and drop-casting onto a mica surface 1-D nanorods (from Ph-H), 2-D networks (from CHCl_3) and 3-D hollow vesicles (from $\text{H}_2\text{O}/\text{CH}_3\text{CN}$) were prepared (**Figure 3.1.25a**). Amide-containing OPVs showed morphological formation from honeycombs to aligned fibers by change of solvent from CHCl_3 to Ph-CH₃ (**Figure 3.1.25b**).

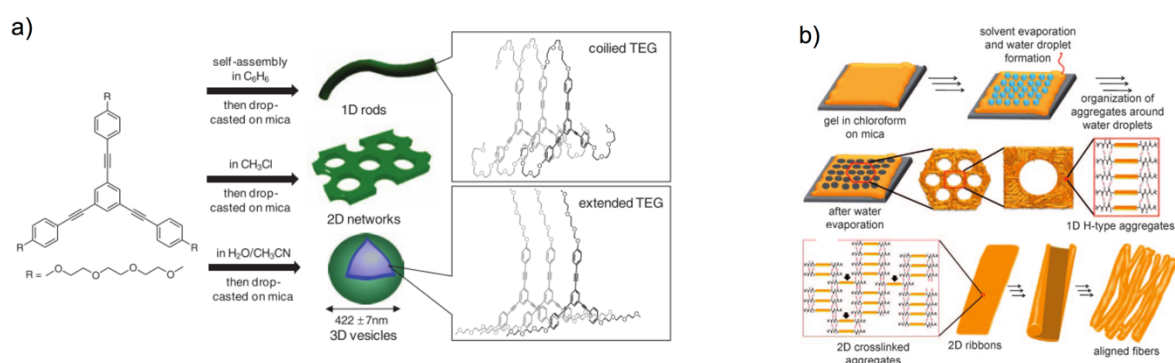


Figure 3.1.25. Schematic representation solvent-controlled self-assembly of assemblies of an a) OPE and an b) OPV derivatives.^{329,332}

The formation of honeycombs (as the one depicted in **Figure 3.1.25b**) is actually a very well-known phenomenon in nature and has been used as ‘breath figure’ (BF) technique for simple and robust bottom-up process consisting of evaporative cooling of a polymeric solution in volatile solvents in humid air.^{333–336} For example, it was possible to use a photo-responsive amphiphilic small molecules that formed supramolecular fibers and, by applied UV lithography, honeycomb patterns were formed.³³⁵

In order to obtain definite patterns on a surfaces an array of choices are present. For example, physical templates can be used, such as ‘sphere-on-flat evaporation’ or stamp template with an inclined slope that have been used in patterning organic semiconductor micro and nanocrystals.³³⁷ Moreover, post-deposition processing such as solvent vapor annealing can be used to generate morphologies.^{338–341} Finally, the quality of the solvent is of utmost importance since, for example, trace solvents have been found to be a predominant factor in a dipeptide-self-assembly.³⁴²

3.1.3. Aim of the Project

The aim of this project is to design and prepare novel building blocks for investigating soft matter nanostructuring both in solution and on surface. This work aims towards understating the preparation of functional materials that requires not only shaping the components of the system, but also control the organization of its building blocks. Although the toolkit of the chemist is helpful in tailoring with appropriate non-covalent interactions of the single pieces, achieving order on multiple length scales still remain a challenge. In particular, two approaches have been undertaken in this chapter. In the first case, a porphyrin derivative (**Figure 3.1.26**), featuring a flat central core (capable of π -stacking), hydroxy groups (capable of H-bonding) and a central metal ion (capable of coordination) was designed. This building block was inspired by naturally occurring chlorophylls, as a fully synthetically analogue in order to mimic light-harvesting chromophores

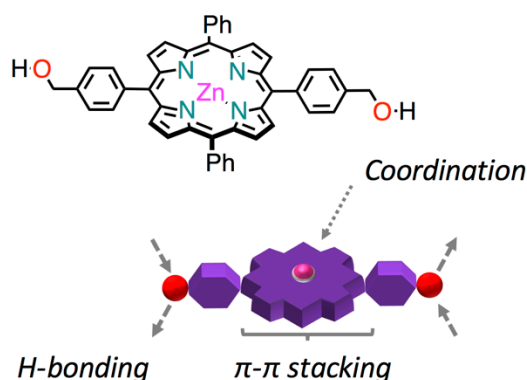


Figure 3.1.26. Target porphyrin **3-1-Zn** along with its cartoon representation highlighting the relevant functional units.

In the second case, two heterocomplementary units (**Figure 3.1.27**) were designed in order to bring a 'geometric core' (comprised of optically active BINOL) and a 'fluorescent core', containing a OPE (oligo-*p*-phenylene ethynylene) because of its high quantum yield. By three-fold hydrogen bonding between the uracil and diamidopyridine units, chiral supramolecular polymers should form. Additionally, the length of the supramolecular polymer should be tuned by appropriate choice of solvents. The transfer of chirality from molecular to higher length scale has been a topic of interest and was achieved by introducing chiral side chains in order to transfer chirality from the periphery to the central aromatic backbone. The interest in the BINOL core lies its use as a precursor for chiral ligands

in asymmetric catalysis. Accordingly, it is envisaged that carefully designed building blocks, together with appropriate control of conditions should lead to novel protocol in soft matter nanostructuring.

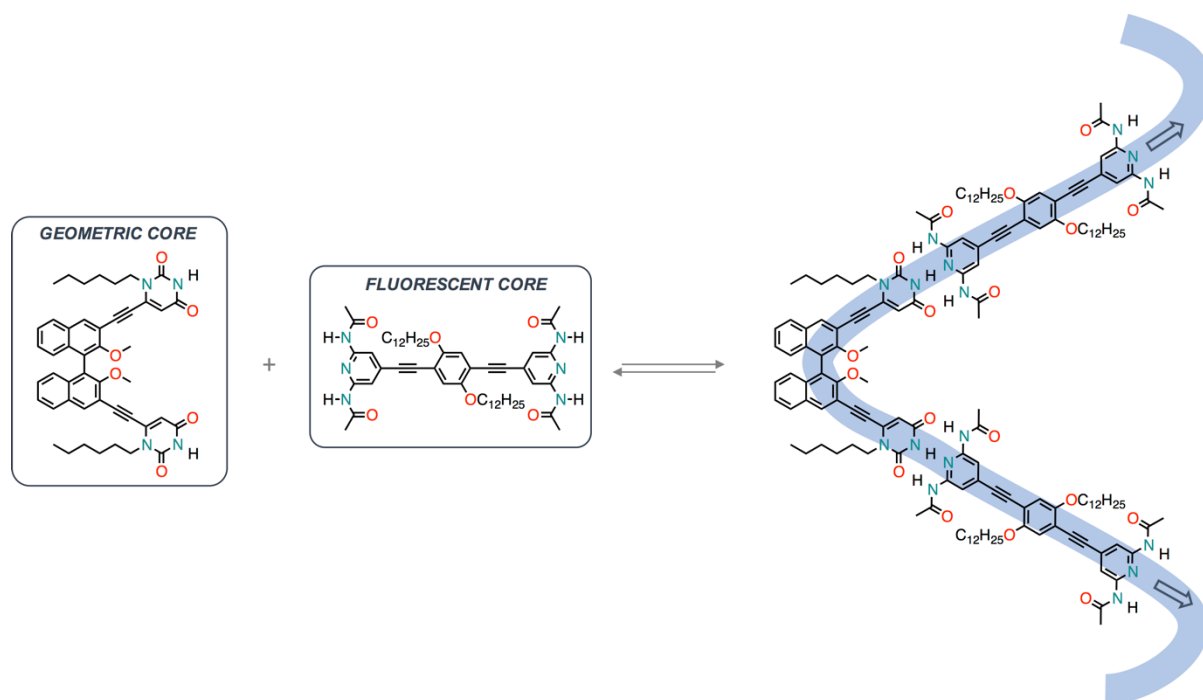


Figure 3.1.27. Target heterocomplementary geometric and fluorescent units capable of self-assembly through three-fold hydrogen-bonding.

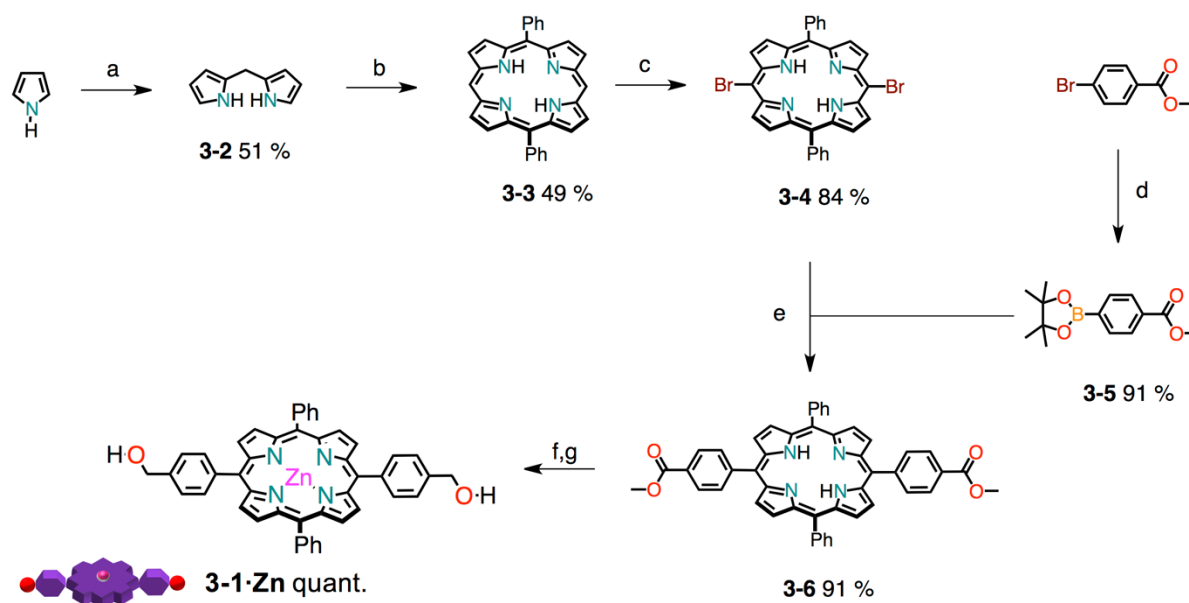
3.2. Solvent-Dependent Molding of Porphyrin-Based Nanostructures

In this section, we report a fully synthetic porphyrin **3-1-Zn**, a tetrapyrrolic macrocycle carrying a central zinc core (capable of ligation) and two hydroxymethyl groups that are *trans* to each other. The design of this macrocycle should enable self-assembly of the porphyrins in stacks and, owing to the second hydroxymethyl group, should give rise to novel nanostructures, other than the usual nanorods.^{343–346} The self-assembly property of **3-1-Zn** was evaluated by a variety of variable-temperature and concentration dependent UV-Vis spectroscopic measurements. Moreover, the formation of different nanostructures was evaluated under different solvent conditions, given the explicit role that the solvent plays in the formation of self-assembled nanostructures.^{252,262,266,269,347}

3.2.1. Synthesis and Characterization

Initially, we wanted to develop a high yielding route to synthesize the porphyrin derivative **3-1-Zn**

(Scheme 3.2.1). We reasoned that the best way to obtain the final benzyl alcohol would be the reduction of the porphyrin bis-ester. In order to obtain this key intermediate, it was desirable to avoid tedious chromatographic separations of porphyrin mixtures obtained by statistical Alder-Longo or Lindsey reactions (see also Chapter 1).^{348–350} The best route to the 5,15 substituted porphyrin is certainly through the MacDonald [2+2] condensation approach.^{351,352}



Scheme 3.2.1. Synthetic scheme for porphyrin **3-1·Zn**. Reagents and conditions: a) TFA, 70 °C; b) (i) TFA, CH₂Cl₂, r.t. (ii) DDQ, reflux (iii) Et₃N; b) NBS, CHCl₃/Py, 0 °C; c) B₂pin₂, Pd(dppf)Cl₂, KOAc, DMF, 90 °C; d) methyl 4-pinacolboranebenzoate **3-5**, Pd(PPh₃)₄ cat., K₃PO₄, THF, reflux; e) LiAlH₄, THF, 0 °C → r.t.; f) Zn(OAc)₂, CHCl₃, CH₃OH, r.t..

At first, the meso-unsubstituted dipyrromethane **3-2** was obtained by reaction of H₂CO with a large excess of pyrrole (as solvent) containing TFA (trifluoroacetic acid) as catalyst. The dipyrromethane was reacted with benzaldehyde (under TFA catalysis) in order to obtain 5,15-diphenylporphyrin derivative.³⁵³ The 10,20 meso-free positions were easily brominated with NBS (*N*-bromosuccinimide) in the presence of pyridine, an acid scavenger.³⁵⁴ The 5,15-dibromo-10,20-diphenylporphyrin **3-4** was then subjected to a Pd-catalyzed Suzuki-Miyaura cross coupling reaction³⁵⁵ with methyl pinacolboranebenzoate to yield exclusively the *trans*-porphyrin bis-ester **3-6**. Reduction from ester to benzyl alcohol in the presence of LiAlH₄ and subsequent metallation with Zn(OAc)₂·2H₂O yielded the final porphyrin **3-1·Zn** in a good overall yield. Notably, this sequence of

reactions gave products fairly different in polarity, making it easy to separate them by single column chromatography.

The porphyrin **3-1·Zn** was characterized by mono- (^1H and ^{13}C) and bi-dimensional (^1H - ^1H and ^1H - ^{13}C) NMR spectroscopies (**Figure 3.2.1**).

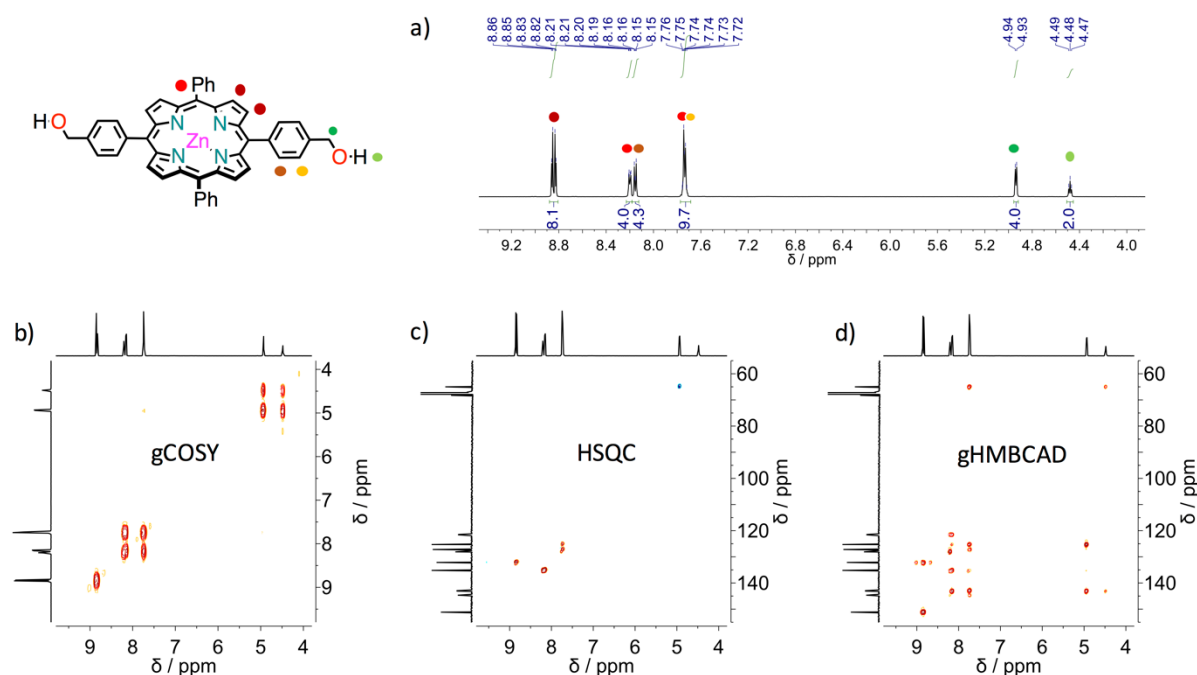


Figure 3.2.1. NMR spectroscopy experiments for porphyrin **3-1·Zn** (500 MHz, $\text{THF-}d_8$, 298 K, $c = 5.0 \times 10^{-3}$ M) – a) ^1H -NMR spectra; b) ^1H - ^1H correlation spectroscopy; c) ^1H - ^{13}C single quantum correlation and d) ^1H - ^{13}C multiple bond correlations.

Notably, in a polar aprotic solvent (such as $\text{THF-}d_8$) the O–H resonance appears as a triplet, due to the coupling to the benzylic $-\text{CH}_2-$ that, in turn, is a doublet (coupling constant ~ 6 Hz). Additionally, the β -pyrrolic resonances manifest as two doublets, probably due to the diminished symmetry in $\text{THF-}d_8$ induced by the $\text{Zn}\cdots\text{O}$ complexation. Protons that are part of the four phenyl rings (both unsubstituted and *para*-substituted ones) and are further away from the porphyrin macrocycle lie together in the 7.8–7.7 ppm region. Resonances from the phenyl rings close to the porphyrin macrocycle can be found at 8.2 ppm as a doublet of doublets (with coupling constants being 7 and 2 Hz for *ortho*- and *meta*- couplings, respectively) for the unsubstituted phenyl and at 8.15 ppm as a doublet (8 Hz for the only possible *ortho*- coupling) for the *para*-substituted phenyls. These findings

have been confirmed both by homonuclear (COSY) and heteronuclear correlations (on single quantum and multiple bond correlation, HSQC and HMBC, respectively).

Crystals suitable for X-ray spectroscopy were obtained for **3-1** (from THF/CHX vapor exchange) and **3-1·Zn** (slow evaporation of a THF solution). Solid structure and molecular packing of porphyrins **3-1** and **3-1·Zn** are shown in **Figure 3.2.2** and **Figure 3.2.3**.

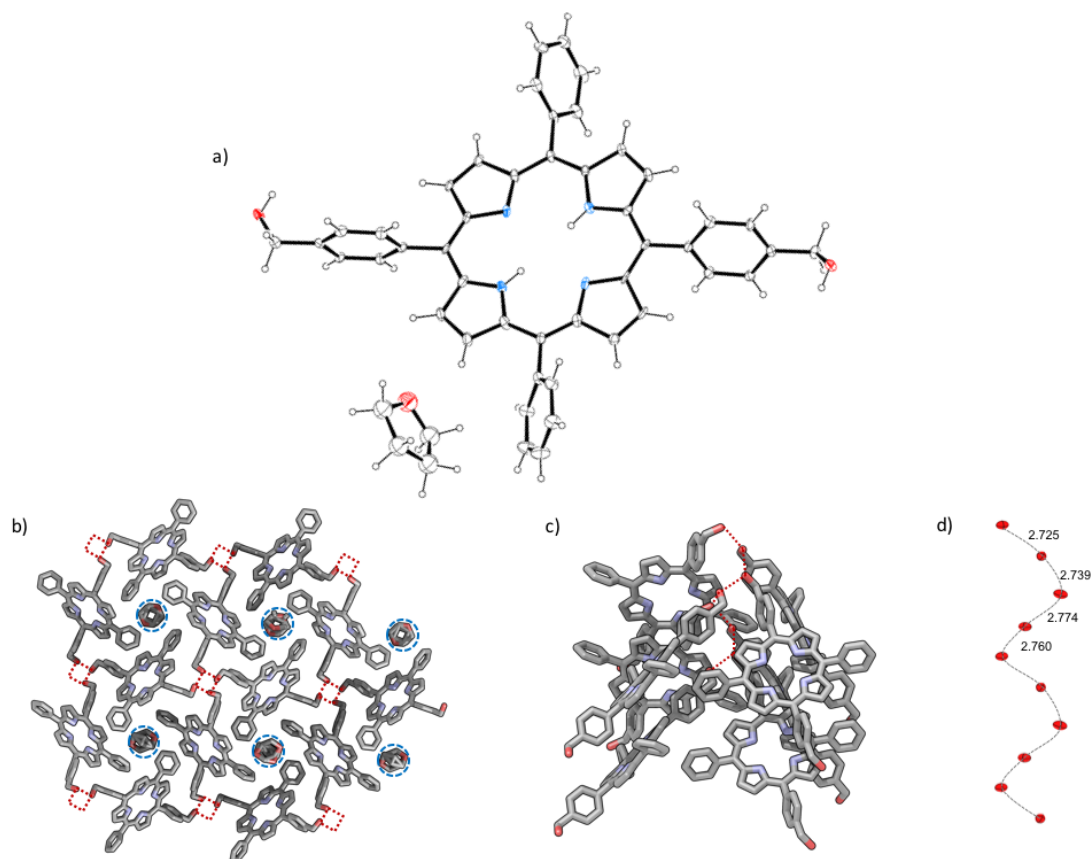


Figure 3.2.2. a) Crystallographic structure of porphyrin **3-1** (thermal ellipsoids are at 50% level; H atoms were omitted for clarity); molecular packing of **3-1** is shown: bc) top and side view of **3-1** with blue dashes showing solvent (THF) filled tubes and red dashes showing the H-bonding pores; d) helicoidal arrangement of the O atoms (50% thermal ellipsoids). See the ‘Crystallographic data’ section in the Experimental Section for more details.

In the asymmetric unit of crystals for **3-1**, one full and two half porphyrin molecules were found. Remarkably, a chiral helicoidal arrangement of hydrogen bonds connects 32 neighbor porphyrins ($d_{O-O} = 2.749(8) \text{ \AA}$), forming channels along the *a* axis occupied by the THF solvent molecules.^{356–358}

Finally, a slipped face-to-face stacking with an offset of 4.2 Å was observed, suggesting that this synthetic variant of chlorin forms *J*-aggregates. Although a similar ladder stacks are formed in an already reported bis[4-(hydroxymethyl)phenyl]porphyrin³⁵⁰, porphyrin **1** forms a different hydrogen bonded arrays (no hydrogen bonding is present between hydroxyl and pyrrolic NH) and includes also solvents in the solid state structure, contrarily to already reported porphyrin. Molecule **3-1·Zn** model (Figure 3.2.3) shows two crystallographically independent porphyrin molecules with differently coordinated ligands: one bound to a THF molecule, while the other is bound to a H₂O molecule. As also observed in the case of molecule **3-1**, neighbor porphyrins show intermolecular hydrogen bonds connections (average $d_{O-O} = 3.126(7)$ Å). Interstitial voids are filled by three additional THF molecules tightly connected to available hydroxyl groups (from porphyrins and H₂O).

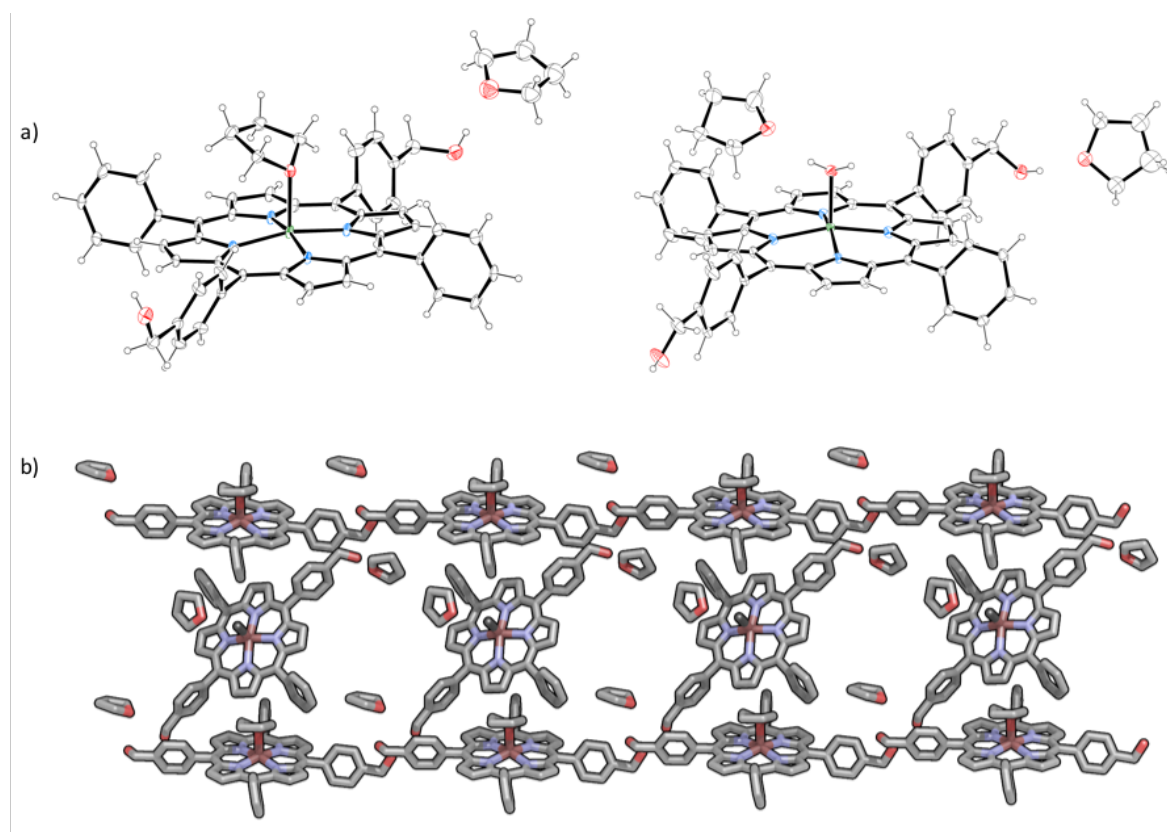


Figure 3.2.3. a) Crystallographic structures of porphyrin **3-1·Zn** (thermal ellipsoids are at 50% level; H atoms were omitted for clarity); b) molecular packing of **3-1·Zn** is shown: two crystallographically independent porphyrin molecules with differently coordinated ligands: one bound to a THF molecule, while the other is bound to a H₂O molecule. See the ‘Crystallographic data’ section in the Experimental Section for more details.

3.2.2. Self-Assembly in Solution

First of all, we evaluated the self-assembly through variable-temperature (VT)-NMR experiments (**Figure 3.2.4**). The best conditions were found in a 9:1 v/v CHX- d_{12} /THF- d_8 mixture since lower THF content resulted in precipitation of the porphyrin and higher resulted in a negligible chemical shift. By varying the temperature from 25 °C to 65 °C the most notable change is the upfield shift ($\delta = 3.97$ to 3.39 ppm) while a minor change is in the aromatic region (upfield shift of around 0.02 ppm). These changes suggest that at higher temperatures both hydrogen-bonding and π - π are disrupted. Therefore we proceeded with studying the system in more dilute solutions, allowing us to change the ‘good’/‘poor’ solvent ratio.

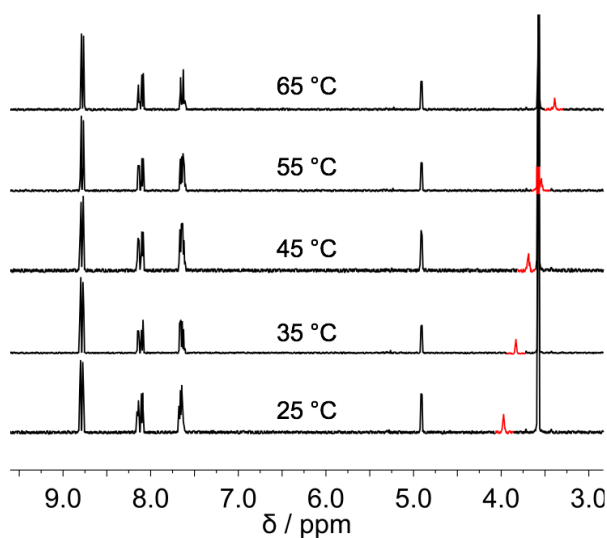


Figure 3.2.4. VT-NMR (500 MHz, CHX- d_{12} /THF- d_8 , $c = 1.0 \times 10^{-3}$ M) for porphyrin **3-1-Zn**.

The optical properties of **3-1-Zn** were investigated in THF, CHCl₃ and the combination of the two with methylcyclohexane (MCH). The latter solvent was used to trigger the self-assembly of the organic nanostructures (**Figure 3.2.5**). Fluorescence spectra were also acquired in the same solvent systems (**Figure 3.2.6**). At room temperature, **3-1-Zn** is dissolved in THF, with the UV-Vis spectrum displaying a sharp Soret band at $\lambda_{\max} = 424$ nm ($S_2 \leftarrow S_0$ transition) accompanied by Q-bands at $\lambda_{\max} = 556$ and 596 nm, typical of metal porphyrins where the increased symmetry causes the $S_1 \leftarrow S_0$ transition to reduce from four to two bands. In CHCl₃, the absorption spectrum presents changes with respect to that observed from the THF solution, with the Soret band showing hypso- and hypochromic shift.

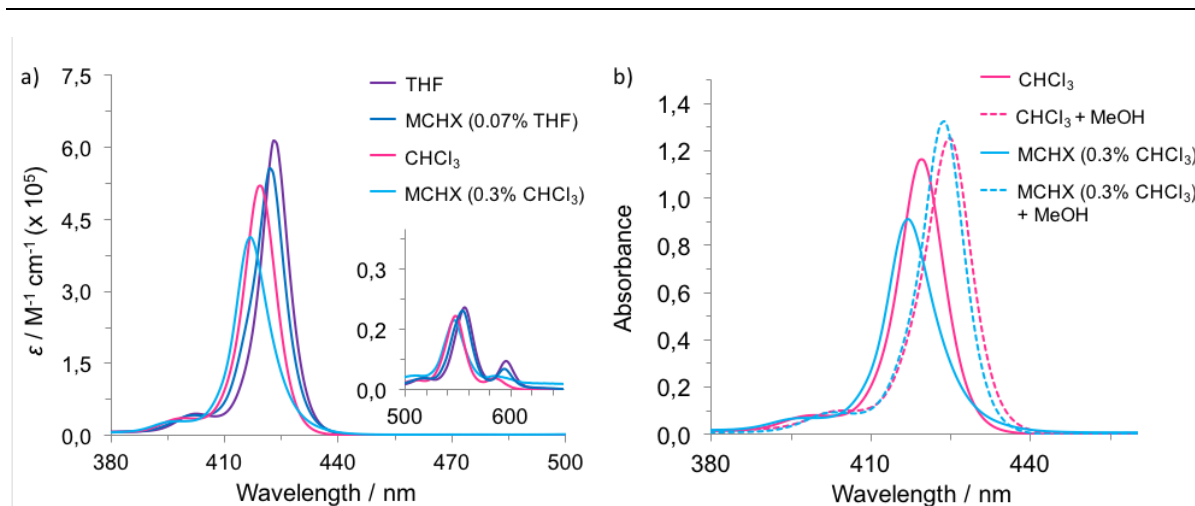


Figure 3.2.5. Absorbance profiles of **3-1-Zn** in different solvents that include THF (purple trace), CHCl_3 (pink), MCH (with THF, blue trace) and MCH (with CHCl_3 , light blue); inset shows enlarged region where the Q bands absorb; on the right are shown the absorption profiles after addition of a polar protic solvent such as MeOH.

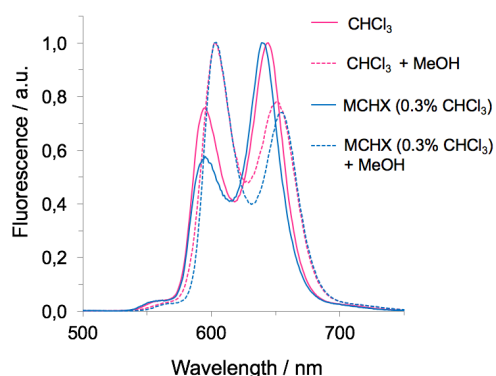


Figure 3.2.6. Fluorescence profiles of **3-1-Zn** before and after the addition of MeOH.

Only slight changes were discerned with variable temperature (VT) and concentration-dependent (**Figure 3.2.7**), such as narrowing of the Soret band. This suggests the formation of weakly-bonded supramolecular assemblies.³⁵⁹ To further investigate the formation of **3-1-Zn** assemblies in CHCl_3 , MeOH or pyridine were added to disrupt both hydrogen-bonding and axial zinc coordination interactions, respectively (**Figure 3.2.8**). By adding MeOH, the Soret band is steadily bathochromically shifted from $\lambda_{\text{max}} = 420$ to 425 nm, without the presence of a clear isosbestic point, most likely indicating the presence of sequential equilibria, from disaggregation to the $\text{MeO}\cdots\text{Zn}$

complexation. The pyridine UV-Vis titration in contrast, showed marked bathochromic shift from $\lambda_{\text{max}} = 420$ to 429 nm with a clear isosbestic point, recalling an equilibrium between the formation aggregates and the porphyrin-pyridine adduct.³⁴⁷

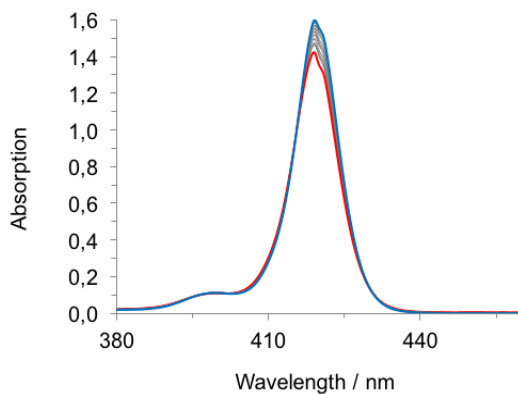


Figure 3.2.7. VT-UV-Vis of porphyrin **3.1-Zn** in CHCl_3 , showing only minor changes in the profile from 10 °C (blue line) to 60 °C (red line) with grey lines in the middle.

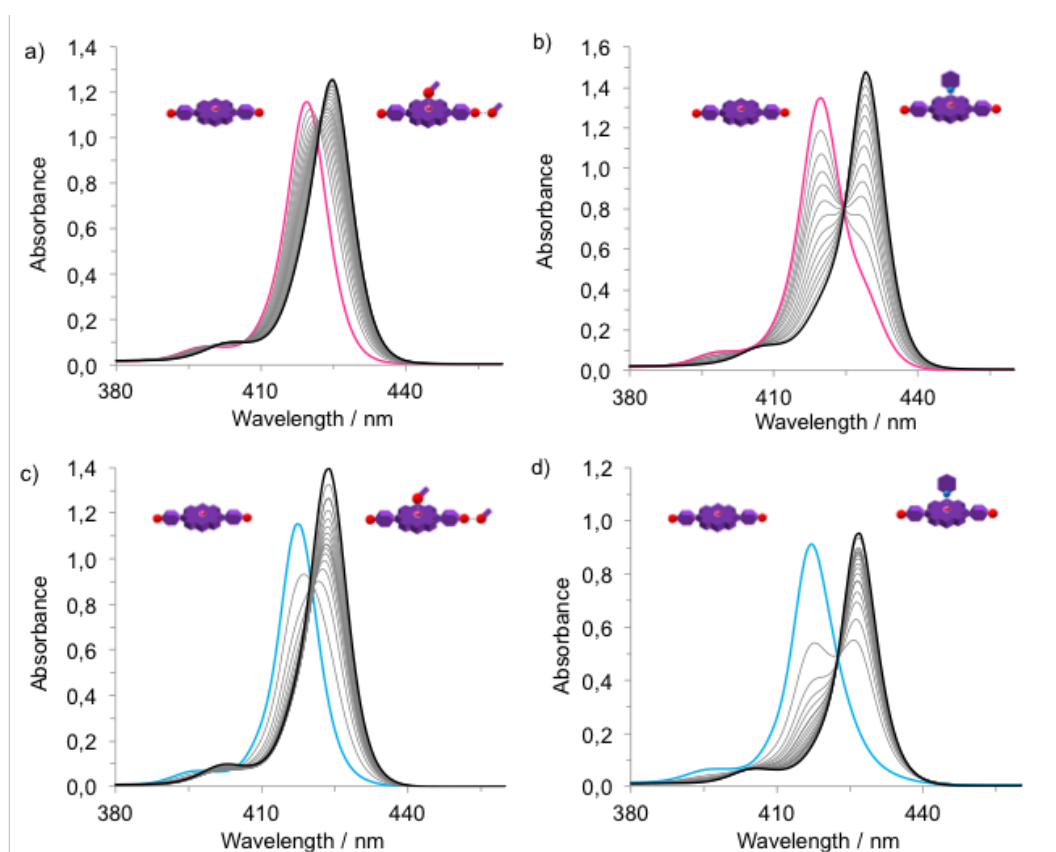


Figure 3.2.8. UV-Vis titration experiments for **3.1-Zn** with MeOH (a,c for CHCl_3 and MCH respectively) and pyridine (b,d for CHCl_3 and MCH respectively).

In order to further favor the formation of aggregates, a relatively concentrated solution of **3-1-Zn** in CHCl_3 was diluted in the apolar and non-coordinating MCH solvent (0.3 % CHCl_3 content). The resulting solution presents a broader Soret band with $\lambda_{\text{max}} = 417 \text{ nm}$, clearly indicating the formation of aggregates. Successive addition of different aliquots of MeOH or pyridine showed analogous behavior to that observed in CHCl_3 , namely restoring of the monomeric porphyrin species. However, temperature-dependent UV-Vis studies displayed a strong narrowing of the Soret band accompanied by a clear disappearing of the blue-shifted band centered at around 435 nm (**Figure 3.2.9**).

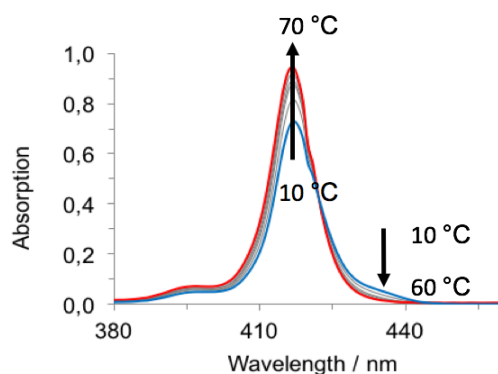


Figure 3.2.9. Temperature-dependented UV-Vis profiles of **3-1-Zn** in MCH (0.3% CHCl_3).

This result indicated the formation of weak aggregates, although stronger than in the case of CHCl_3 . Finally, in an attempt to further increase the content of apolar MCH, a more apolar solution of **3-1-Zn** could be prepared in a MCH-diluted THF solution (0.07% THF content). Notably, the absorption spectrum compared to that obtained in a THF solution, where **3-1-Zn** is molecularly dissolved, appears to be broadened exhibiting a loss in oscillator strength. Apparently, the energy of the absorption maximum does not shift and temperature-dependent and concentration-dependent studies were thus performed. VT-UV-Vis revealed that, by increasing temperature, the S-band of the aggregates at 422 nm decreases and the formation of the apparent monomer band at 417 nm appeared. Concentration-dependented studies showed the disappearance of the 422 nm band and the appearance of the absorption maximum at 417 nm, confirming the temperature-dependented behavior and the reversible nature of the aggregation phenomena (**Figure 3.2.10**).

Taken all together, these data suggest the formation of a bathochromically shifted bands that, when compared to that of the monomer, indicates the presence of slipped face-to-face stacking

arrangements, known also as *J*-aggregates. This is in line with previous studies in with zinc chlorins, as well with their semisynthetic and synthetic variants.³⁶⁰

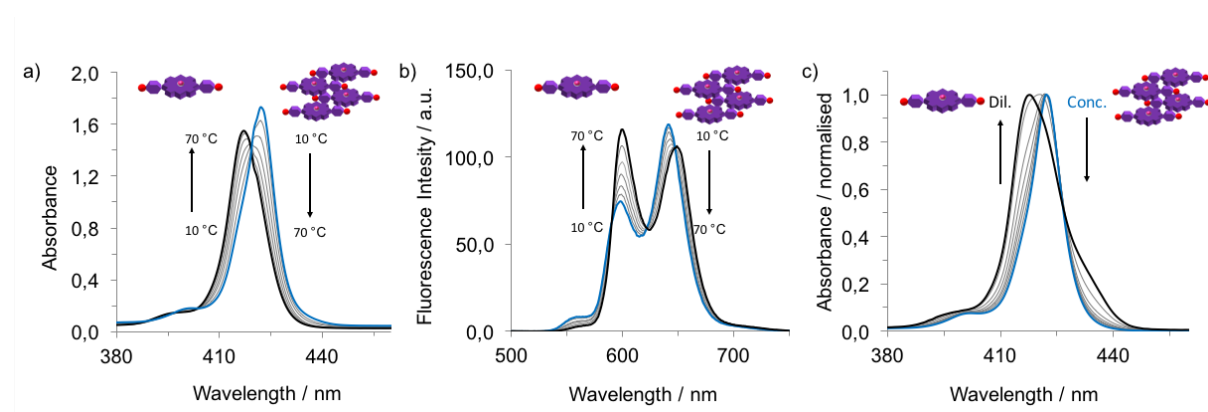


Figure 3.2.10. Absorption and fluorescence spectra of **3-1-Zn**. A) VT-UV-Vis experiment; b) VT-fluorescence experiment ($\lambda_{\text{ex}} = 419 \text{ nm}$) and c) concentration-depended experiment.

3.2.3. Self-Assembly on Surface

Prompted by these results, we carried out atomic force microscopy (AFM) studies to elucidate the morphology of the aggregates of **3-1-Zn** as deposited on a surface. In **Figure 3.2.11** are reported AFM height images of the **3-1-Zn** nanostructures as obtained from different solvents spin-coated onto a freshly cleaved mica surface. As it can be seen in the images, porphyrin **3-1-Zn** is able to form two-dimensional islands on the surface, with a typical height of 2 nm, in accordance with edge-on stacked height of the macrocycle onto the surface.^{266,347,361} Notably, the size of the islands is depended on the solvent used for the solution. For example, samples obtained from CHCl_3 (**Figure 3.2.11a**) show the formation of scattered islands, in agreement with the formation of weak non-covalent architectures that were observed by absorption experiments. From MCH (0.3 % CHCl_3) (**Figure 3.2.11b**), extended aggregates have been also observed. Finally, structures obtained from MCH (0.07 % THF content) shown in **Figure 3.2.11c** present themselves as heterogeneous structures, including islands displaying different sizes. As observed from spectroscopic studies, the presence of THF in the sample is responsible both for *H*-bonding disruption and the Zn complexation, the latter disrupting the formation of extended stacked nanostructures. However, since the amount of THF is very low (0.07 %) the formation of two-dimensional structures is still observed.

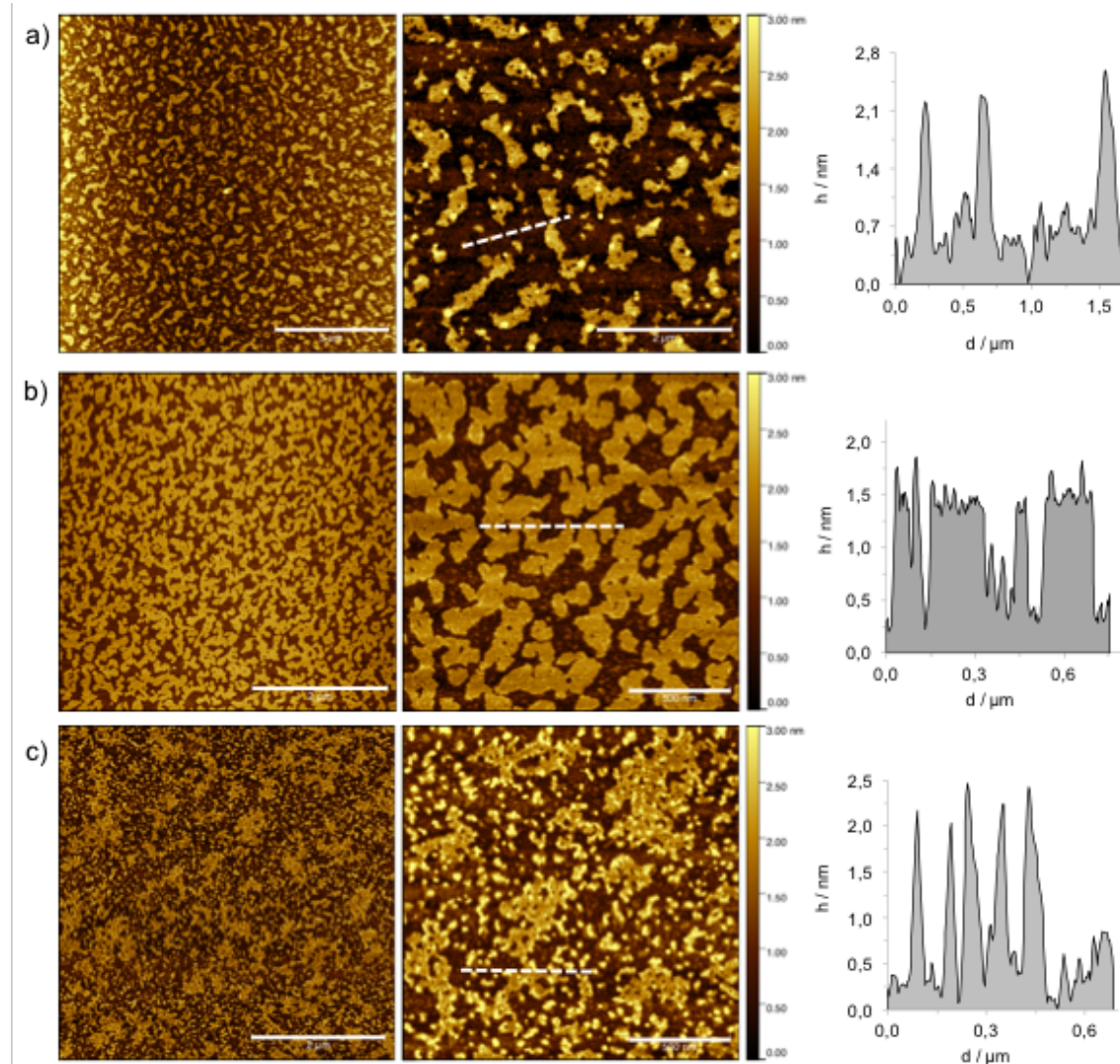
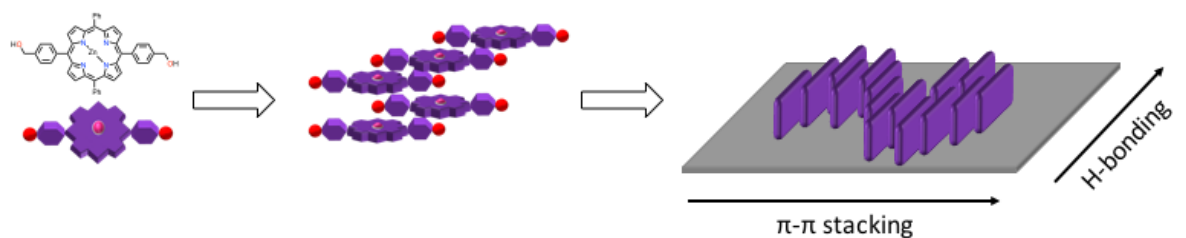


Figure 3.2.11. AFM height images in tapping mode with the profile of the white dashed lines. Samples were prepared by spin-coating a solution of **3-1-Zn** in a) CHCl_3 (scale bars 5 and 2 μm); b) in MCH (0.3 % CHCl_3 , scale bars 5 and 0.5 μm) and c) MCH (0.07% THF, scale bars 5 and 0.5 μm).



Scheme 3.2.2. Schematic representation of the aggregation of **3-1-Zn** in solution and when it is transferred onto the surface.

In order to appreciate the effect of *H*-bonding and zinc coordination, MeOH was added to the previously prepared CHCl₃ or MCH solutions. A typical AFM image is shown in **Figure 3.2.12**, where the formation of two-dimensional structures is not present. Most likely the presence of MeOH disrupts the formation of the aggregates favoring the presence of individual molecules on the surface, confirming the results observed from the spectroscopic measurements.

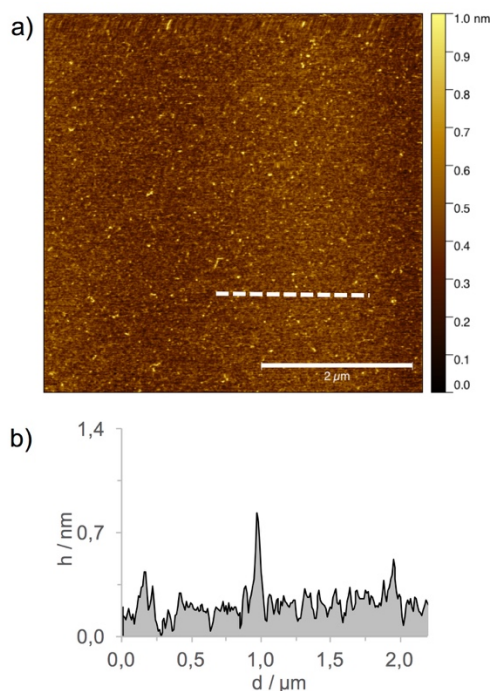
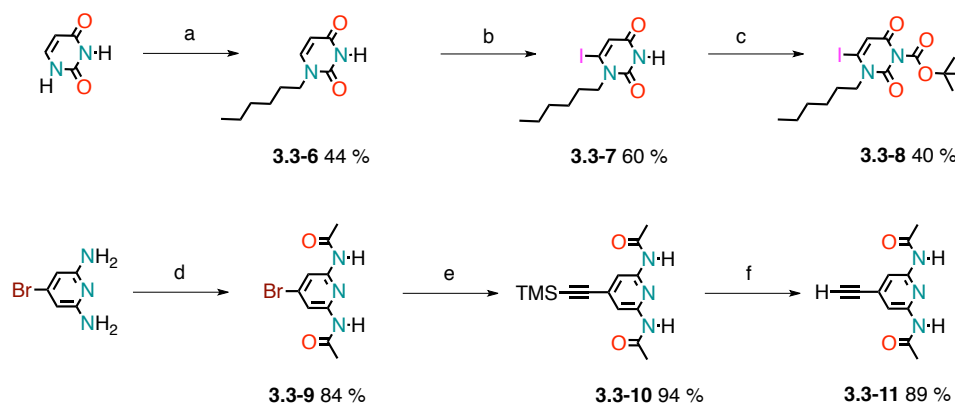


Figure 3.2.12. a) AFM height images in tapping mode (scale bar 2 μm) with the b) height profile of the white dashed line. Sample was prepared by spin-coating a solution of **3.1·Zn** in CHCl₃ + MeOH.

3.3. Solvent Molding of Organic Morphologies Made of Supramolecular Chiral Polymers

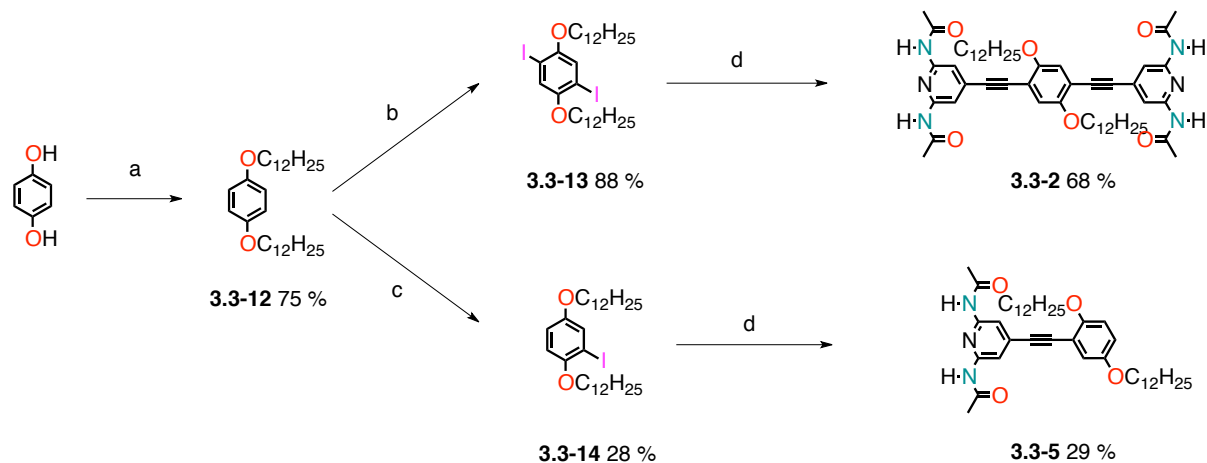
3.3.1. Syntheses

The complete synthetic pathway is reported in **Scheme 3.3.1**, **Scheme 3.3.2** and **Scheme 3.3.3**. Initially, we synthesized the molecular synthons (Ur and DAP) capable of three-fold hydrogen bonding that carry either a halogen or an ethynyl groups capable of subsequent Sonogashira cross-coupling reactions to the geometric or fluorescent unit. Uracil was alkylated with 1-bromohexane under basic condition at the N_1 position and iodinated at the 6 position, on the other side of the ADA hydrogen-bond motif. Part of 1-hexyl-6-iodouracil **3.3-7** was also *N*-BOC protected in order to have also reference compounds, not capable of forming hydrogen-bonding. On the other hand, 2,6-diamino-4-bromopyridine was acetylated, subjected to Pd-catalyzed Sonogashira cross-coupling with trimethylsilylacetylene that was finally deprotected in basic methanolic solution.

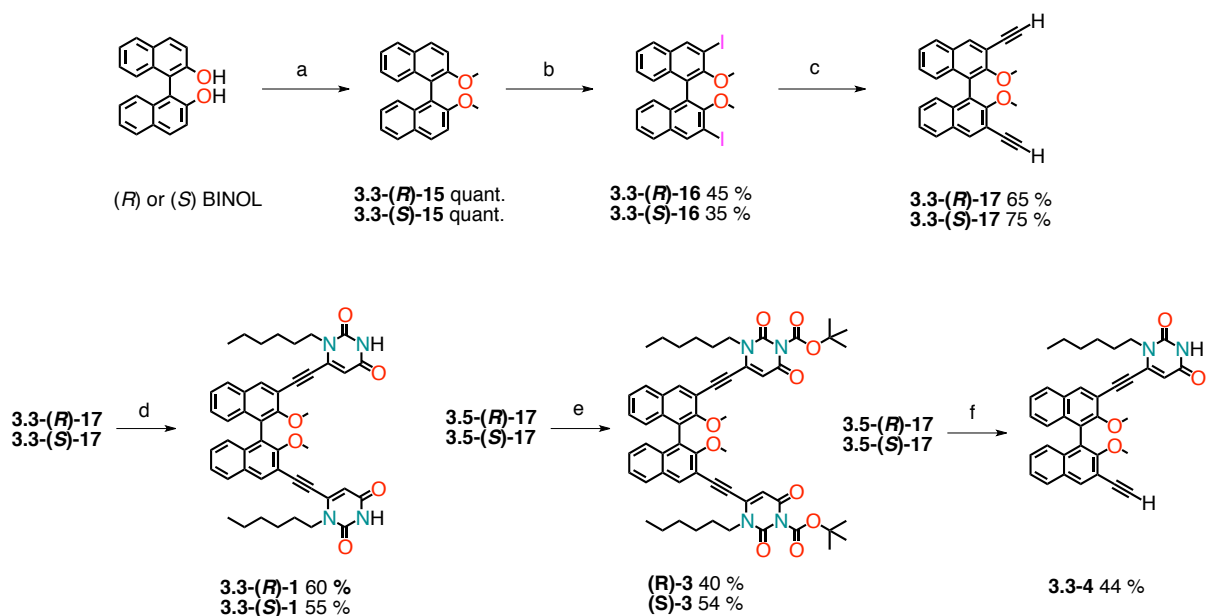


Scheme 3.3.1. Synthetic scheme for preparing molecular synthons capable of three-fold hydrogen bonding. Reagents and conditions: a) 1-bromohexane, K_2CO_3 , DMSO, 40 °C; b) i) LDA, THF, -78 °C, ii) I_2 , -78 °C, iii) AcOH, -78 °C \rightarrow r.t.; c) BOC_2O , pyridine, AcCN, 40 °C; d) Ac_2O , pyridine, r.t.; e) TMSA, $Pd(PPh_3)_4$, THF/ Et_3N /DMF, 85 °C; f) K_2CO_3 , THF/MeOH (1:1), r.t.

In order to obtain the mono- and di-topic OPE derivatives, hydroquinone was alkylated with 1-bromododecanol in basic media and then the bisdodecylbenzene was iodinated according to two different procedures, mostly differing in the equivalents of iodine. Finally, Pd-catalyzed Sonogashira cross-coupling with 2,6-diamido-4-ethynylpyridine gave OPE derivatives **3.3-2** and **3.3-5**.



Scheme 3.3.2. Synthetic pathway for the preparation of mono- and bis-diamidopyridine. Reagents and conditions: a) 1-bromododecane, K_2CO_3 , acetone, reflux; b) H_5IO_6 , I_2 , CH_3OH/CH_2Cl_2 (1:1), reflux; c) KIO_3 , I_2 , CH_3COOH , H_2SO_4 , H_2O , reflux; d) **3.3-11**, $Pd(PPh_3)_4$, CuI , DMF/Et_3N , THF , $120^\circ C$, μW irradiation.



Scheme 3.3.3. Synthetic pathway for the preparation of mono- and bis- and bis-BOC diuracil-BINOL. Reagents and conditions: a) CH_3I , K_2CO_3 , acetone, reflux; b) i) $nBuLi$, THF , $-78^\circ C$, ii) I_2 , THF ; c) i) $TMSA$, $Pd(PPh_3)_4$, CuI , Et_3N , $PhCH_3$, reflux, ii) K_2CO_3 , $THF/MeOH$ (1:1); d) **3.3-7**, $Pd(PPh_3)_4$, CuI , Et_3N , THF ; e) **3.3-8**, $Pd(PPh_3)_4$, CuI , Et_3N , THF ; f) **3.3-7** (1 eq.), $Pd(PPh_3)_4$, CuI , Et_3N , THF .

Starting from commercially available and (*R*)- or (*S*)-1,1'-bi-2-naphthols we carried out separate sequence of reactions in order to obtain the final enantiopure compounds. BINOL was methylated in

basic conditions with methyl iodide, then subjected to *ortho*-lithiation in order to introduce the iodine atoms in positions 2,2'. At this point it was possible to introduce the ethynyl group by Pd-catalyzed reaction and subsequent basic ambient deprotection. Final Sonogashira reaction with iodouracil **3.3-7** (in excess or defect) or BOC-protected iodouracil **3.3-8** gave the final compounds **3.3-(X)-1**, **3.3-(X)-3** and **3.3-4**. The compounds were fully characterized by ¹H- and ¹³C-NMR spectroscopies, IR, HRMS and by optical activity, which are reported in the Experimental Section.

3.3.2. NMR Investigations

The self-assembly of the hetero-complementary monotopic modules **4** and **5** was firstly studied to rationalize the influence of the lateral groups on the association behavior of the Ur • DAP recognition motif in solution. Titration experiments in CDCl₃ (**Figure 3.3.1ab**) showed a fast equilibrium, a progressive downfield shift of the uracil NH protons upon the incremental addition of **5**. The association constant was found to be 1296 (±3) M⁻¹ with a 1:1 stoichiometry (as evidenced by the continuous variation method, **Figure 3.3.1c**), a value which is comparable to that reported in the literature for similar systems.^{255,362} In more apolar solvents like Tol-*d*₈ and CDCl₃/CHX-*d*₁₂ (1:1 v/v), *K_a* values of 8737 (±627) and 14819 (±3820) M⁻¹ were measured, respectively (**Figure 3.3.1d-i**). As expected,²⁵² increasing the apolar character of the solvent mixture favored an enhancement of the binding strength. The solvent choice was also considered in case of self-complementary dimerization and was found to have only a negligible effect on the hetero-association complexes (**Figure 3.3.2**), as previously reported.³⁶³

Table 3.3.1. Calculated association constants (*K_a*) for the H-bonded heterodimer at 298 K for **4** + **5** ⇌ [**4·5**], dimerization constant (*K_{dim}*) for **4** and the corrected association constant (*K_c*) **4** + **5** ⇌ [**4·5**] taking into account the dimerization of **4** in the reported solvents along with the solvent polarity. Calculations performed with Scientist package from MicroMath.

Solvent	ε _r	Stoichiometry	<i>K_a</i> , M ⁻¹ (sd)	<i>K_{dim}</i> , M ⁻¹ (sd)	<i>K_c</i> , M ⁻¹ (sd)
CDCl ₃	4.81	1:1	1296 (3)	7.5 (0.1)	1300 (29)
Tol- <i>d</i> ₈	2.44	1:1	8737 (627)	60 (5)	8205 (564)
CDCl ₃ / CHX- <i>d</i> ₁₂	/	1:1	14819 (3820)	19 (4)	14427 (3980)

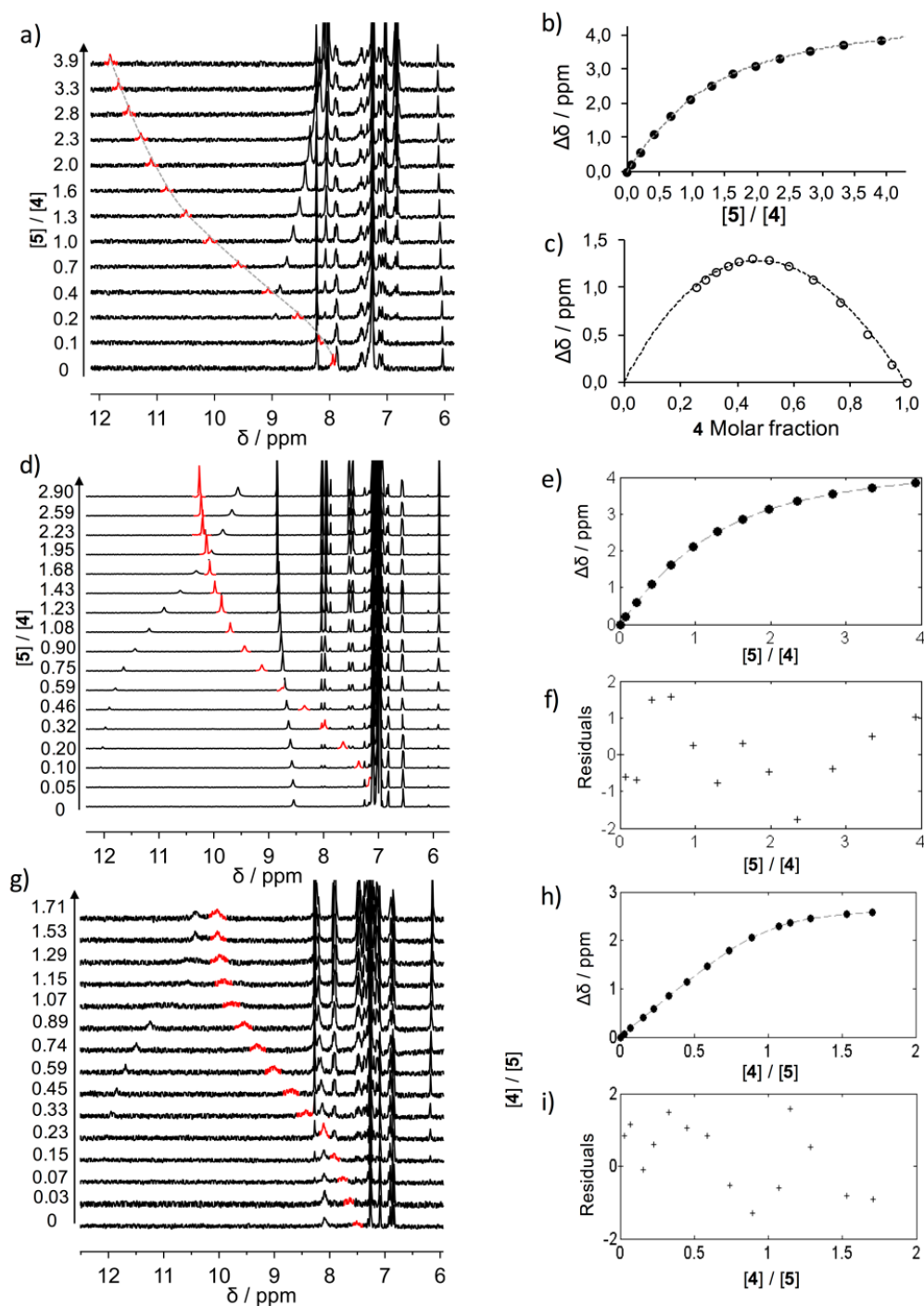


Figure 3.3.1. ¹H-NMR titration data a-c) in CDCl₃, d-f) Toluene and g-i) CDCl₃/CHX-*d*₁₂. a) ¹H-NMR (400 MHz, 298 K) titration data of **4** in CDCl₃ ($c = 1.3 \times 10^{-3}$ M) with different molar amounts of **5** (from 0 to 3.9 equiv.). NH peaks are highlighted in red; b) titration data and 1:1 nonlinear least-square fitting of the NH signals of **4** plotted against the molar ratio; c) Job's plot and fitting of the NH signals of **4** plotted against the molar fraction; d) ¹H-NMR (500 MHz, 298 K) titration data of **5** in Tol-*d*₈ ($c = 1.69 \times 10^{-3}$ M) with different molar equivalents of **4** (from 0 to 2.90 equiv.), R-NH peaks are highlighted in red; b) titration data and nonlinear least-square fitting of the NH signals of **5** plotted against the molar ratio; c) residuals after least-squares fitting; d) ¹H-NMR (400 MHz, 298 K) titration data of **5** in CDCl₃/CHX-*d*₁₂ (1:1 v/v) ($c = 1.52 \times 10^{-3}$ M) with different molar equivalents of **4** (from 0 to 1.71 equiv.), R-NH peaks are highlighted in red; e) titration data and nonlinear least-square fitting of the NH signals of **5** plotted against the molar ratio; f) residuals after least-squares fitting.

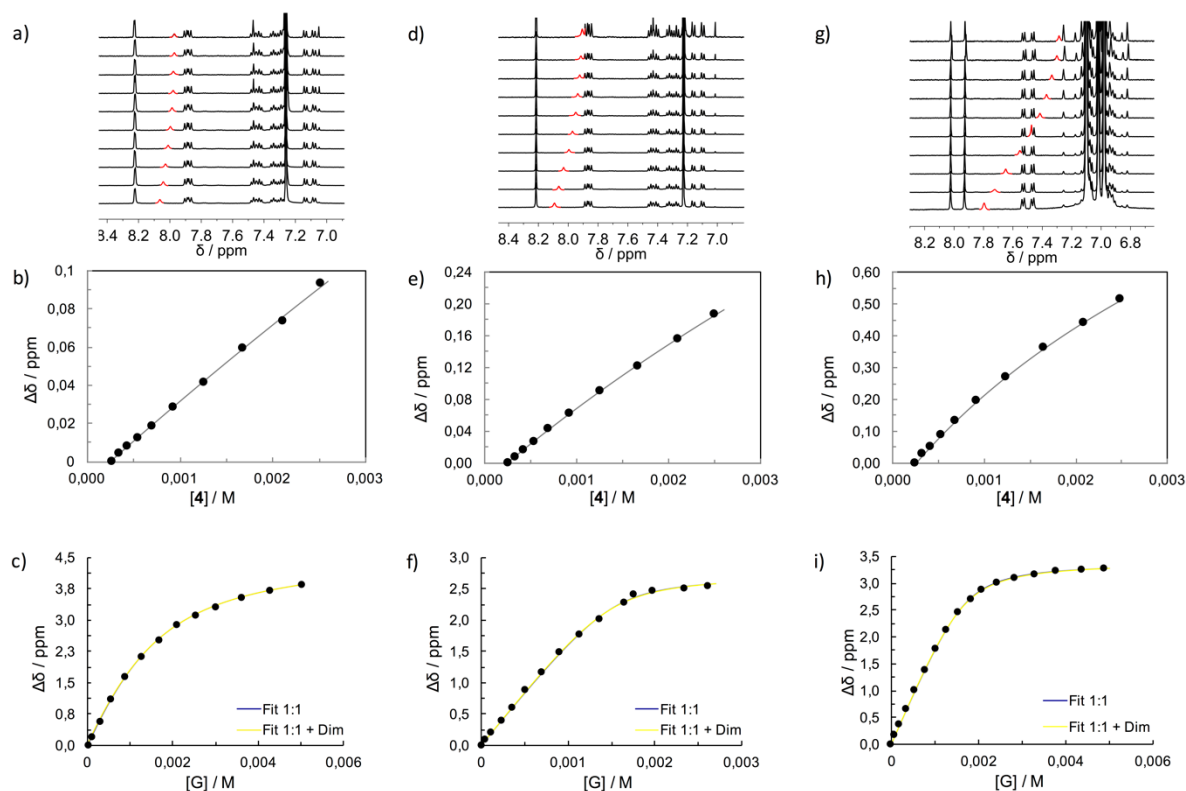


Figure 3.3.2. a) $^1\text{H-NMR}$ (500 MHz, 298 K) dilution data of **4** in CDCl_3 (from $c = 2.5 \times 10^{-3} \text{ M}$ to $\times 10^{-3} \text{ M}$) gave a dimerization constant of 7.5 M^{-1} ; d) $^1\text{H-NMR}$ (500 MHz, 298 K) dilution data of in $\text{CDCl}_3/\text{CHX-}d_{12}$ (1:1 v/v) (from $c = 2.5 \times 10^{-3} \text{ M}$ to $\times 10^{-3} \text{ M}$) gave a dimerization constant of 19 M^{-1} ; c) $^1\text{H-NMR}$ (500 MHz, 298 K) dilution data of **4** in $\text{Tol-}d_6$ (from $c = 2.5 \times 10^{-3} \text{ M}$ to $\times 10^{-3} \text{ M}$) gave a dimerization constant of 60 M^{-1} ; c,f,i) fitting of the experimental points **4** + **5** for 1:1 equilibrium with and without taking into account the dimerization constant obtained by the dilution experiments. Software employed - Scientist package from MicroMath.

Further NMR investigations confirmed the 1:2 and 2:1 binding stoichiometry for complexes $[\mathbf{1} \cdot (\mathbf{S})_2]$ and $[(\mathbf{4})_2 \cdot \mathbf{2}]$, respectively (Figure 3.3.3). By titrating monotopic **5** to a solution of $(\mathbf{S})\text{-1}$ and applying the data to a continuous variation model, maximum $\Delta\delta$ was observed around 0.66 molar fraction, corroborating the formation of a 1:2 complex. Analogous data was obtained by adding **2** to a solution of **4**, this time with the maximum $\Delta\delta$ around 0.33, indicative of a 2:1 complex. In all cases, NMR titrations in CHX/THF mixture (conditions later on used for diluted spectroscopic and microscopy studies) could not be performed due to the limited solubility of both molecular components in the concentration interval needed for NMR.

In order to corroborate the association of the supramolecular assemblies $[\mathbf{1} \cdot \mathbf{2}]_n$, $^1\text{H-NMR}$ spectroscopy was performed on a 1:1 mixture of molecular modules $(\mathbf{S})\text{-1}$ and **2** (Figure 3.3.4a, 500 MHz, 298 K) in CDCl_3 . The addition of an equimolar quantity of **2** to a solution of $(\mathbf{S})\text{-1}$ induced a

drastic downfield of the NH proton resonances suggesting the formation of the *H*-bonded complex (from 8.65 to 11.10 ppm and 8.15 to 9.75 ppm for (*S*)-1 and 2, respectively), whereas all the other signals remained unaltered.

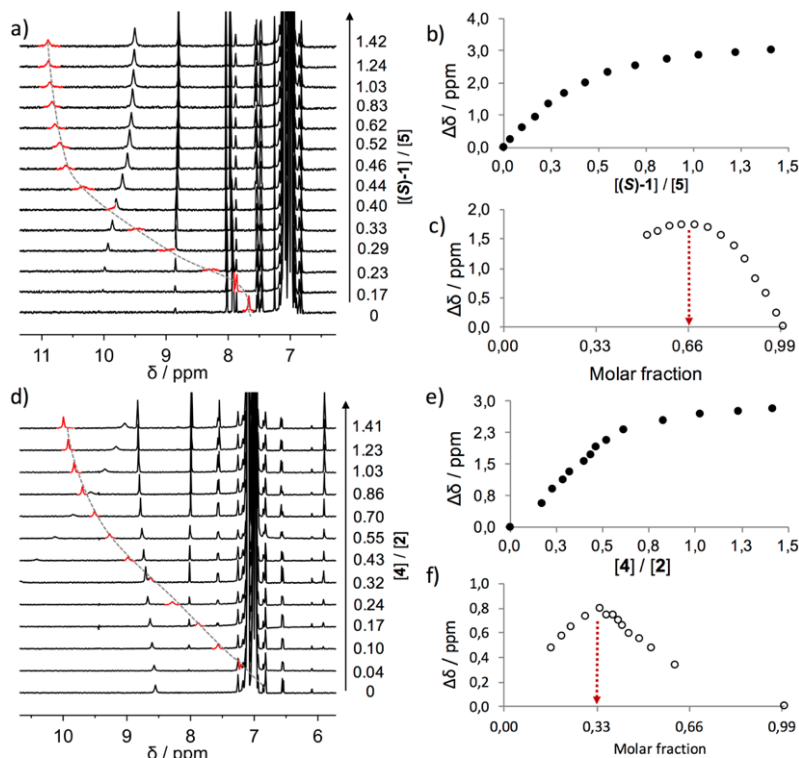


Figure 3.3.3. a) ¹H-NMR (500 MHz, 298 K) titration data of (*S*)-1 in Tol ($c = 1.27 \times 10^{-3}$ M) with different molar equivalents of 5 (from 0 to 1.42 equiv), NH peaks are highlighted in red; b) titration data fitting of the NH signals of 5 plotted against the molar ratio; c) Job's plot of the NH signals of 5 plotted against the molar fraction; d) ¹H-NMR (500 MHz, 298 K) titration data of 2 in Tol ($c = 0.65 \times 10^{-3}$ M) with different molar equivalents of (*S*)-4 (from 0 to 1.42 equiv), NH peaks are highlighted in red; e) titration data fitting of the NH signals of 2 plotted against the molar ratio; f) Job's plot of the NH signals of 2 plotted against the molar fraction.

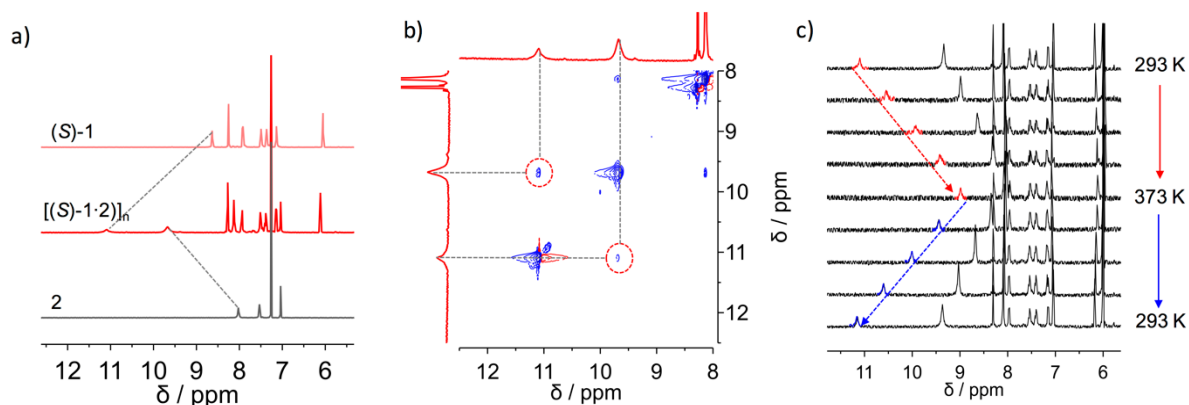


Figure 3.3.4. NMR characterization of supramolecular polymer [(*S*)-1-2]_n: a) ¹H-NMR (CDCl₃, 500 MHz, 298K) of (*S*)-1 (top), 2 (bottom) and supramolecular polymer [(*S*)-1-2]_n (middle); b) 2D-NOESY spectra (CDCl₃, 500 MHz, 298 K) of [(*S*)-1-2]_n; c) VT-NMR (C₂D₂Cl₄, 400 MHz) of [(*S*)-1-2]_n heating and cooling cycle.

^1H - ^1H NOESY (Figure 3.3.4b) analysis displayed the through-space interactions between the *NH* resonances arising from the adjacent protons (*NH*-Ur and *NH*-DAP, respectively) suggesting, as expected, a close spatial proximity ($< 5 \text{ \AA}$) between the Ur and DAP moieties. The non-covalent and reversible nature of the interaction was confirmed by variable temperature (VT)-NMR (400 MHz, $\text{C}_2\text{D}_2\text{Cl}_4$, Figure 3.3.4c). Indeed, upon increasing the temperature from 293 to 373 K, a gradual reinstatement of the *NH* chemical shifts characteristic of molecules (**S**)-1 and **2** alone were observed, clearly suggesting the gradual disruption of the *H*-bonded complex, and thus that of the supramolecular assembly. Finally, Diffusion Ordered Spectroscopy (DOSY) (CDCl_3 , 500 MHz, Figure 3.3.5) disclosed the presence of oligomeric species, in agreement with the predicted degree of polymerization N , featuring low diffusion coefficients $D_{[1-2]_n} = 2.00 \times 10^{-6} \text{ cm}^2 \text{ s}^{-1}$ (compared to $D_1 = 4.37 \times 10^{-6} \text{ cm}^2 \text{ s}^{-1}$ and $D_2 = 4.70 \times 10^{-6} \text{ cm}^2 \text{ s}^{-1}$) owing to the formation of high molecular-weight species, such as those deriving from the oligomeric assemblies.^{364,365}

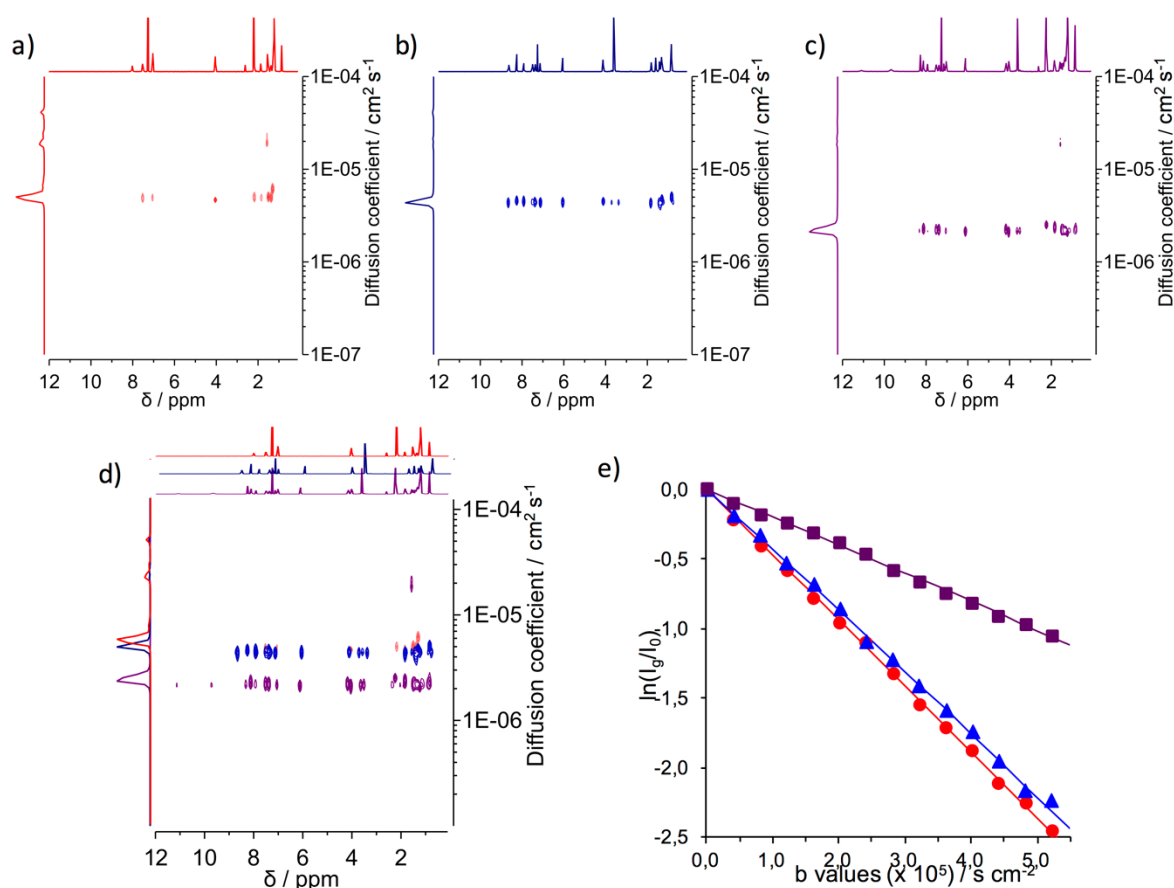


Figure 3.3.5. a-c) 2D-DOSY contour mode plots experiment in CDCl_3 of a) **2**, b) (**S**)-1 and c) $[(\text{S})\text{-1-2}]_n$; d) superimposed 2D-DOSY of compounds **2** and (**S**)-1 and supramolecular assembly $[(\text{S})\text{-1-2}]_n$; e) normalized logarithmic signal decay versus the diffusion weighing (b values) for (**S**)-1 (blue), **2** (red) and supramolecular polymer $[(\text{S})\text{-1-2}]_n$ (purple).

3.3.3. Molding of the Morphologies

3.3.3.1. Evaporation Induced Polymerization

As mentioned in the introductory section, the evaporation of a solvent plays a crucial role in the formation of various nanostructures. This effect is known as Evaporation-Induced Self-Assembly (EISA).^{366–368} As shown for inorganic architectures, one can also expect that in supramolecular polymerization, the vapor tension of a given liquid could play a dramatic role on the degree of polymerization. In a simplified model, this depends on the association strength of the recognition motif, the concentration of monomers and the liquid vapor pressure at a given temperature. To evaluate these effects on our system, we have investigated the polymerization behavior as a function of the evaporation rate of the solvent (Figure 3.3.6).

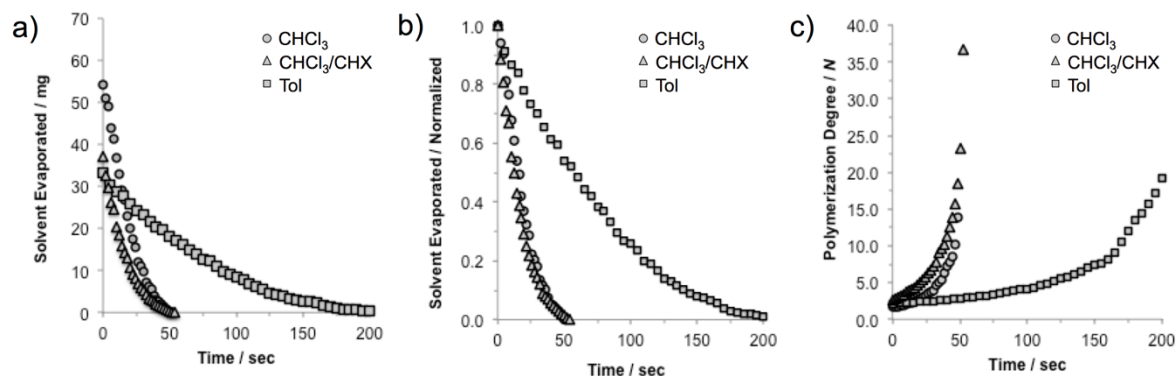


Figure 3.3.6. a) Solvent evaporation weight over time; b) normalized evaporation of the solvents reported as weight lost over time and c) estimated polymerization degree during evaporation. V and V_0 are the volume of the liquid at a t and 0 sec, respectively, calculated by measuring the weight divide by the liquid density. Vapor tension (p_A) values at 20 °C and ambient pressure: 22 mmHg for Tol, 159 mmHg for CHCl₃ and 118 for the 1:1 v/v CHCl₃/CHX mixture (the latter value was calculated from the Raoult's law).

Thus, we have measured the normalized time-dependent shrinking of a drop-casted liquid on an AFM support plate at room temperature in an open environment under ambient pressure. Depending on the vapor pressure of the liquid, a progressive increase in the concentration of the monomers is observed, thus dynamically affecting the degree of polymerisation.^{189,282,369} As outlined in Figure 3.3.6, the higher the liquid vapor pressure (p_A), the larger the maximum degree of polymerization; for instance, at the 50 sec timepoint, the estimated N is ~ 15 for a solvent with higher p_A (CHCl₃) and ~ 3

for a solvent with a lower p_A (Tol). This suggests that, in evaporating CHCl_3 solutions, the organic morphologies are mainly controlled by the formation of longer polymers, while in Tol very short oligomers are preferentially formed. On the other hand, solutions with similar evaporation rates give degrees of polymerization essentially controlled by the association strength of the recognition unit. For instance, in the 1:1 v/v CHCl_3 /CHX mixture higher degree of polymerization can be achieved (~ 40) than in CHCl_3 after 50 sec, due to stronger association of the $\text{Ur} \cdot \text{DAP}$ motif in apolar solutions. In this model, however, we did not consider the solvophobic and solvophilic properties of the solvent with respect to the monomers and the supramolecular assemblies. As previously observed for similar systems,³⁷⁰ the evaporation of the solvent can also lead to concentration-driven solutal instabilities, inducing precipitation phenomena, aggregation or polymerization termination. This effect will be qualitatively considered for each solvent in the discussions of the next paragraphs.

3.3.3.2. CHCl_3 : from Solution to Nanorods

Due to the chromophoric nature of the OPE spacer, UV-Vis spectra of dilute solutions were measured to gain insight into the self-assembly process. Under dilute conditions ($c = 2.5 \times 10^{-4} \text{ M}$) in CHCl_3 , no discernible changes in the absorption profiles of $[\mathbf{1} \cdot \mathbf{2}]_n$ compared to the individual compounds were noticed (Figure 3.3.7), due to the weak degree of association of the $\text{Ur} \cdot \text{DAP}$ complex.

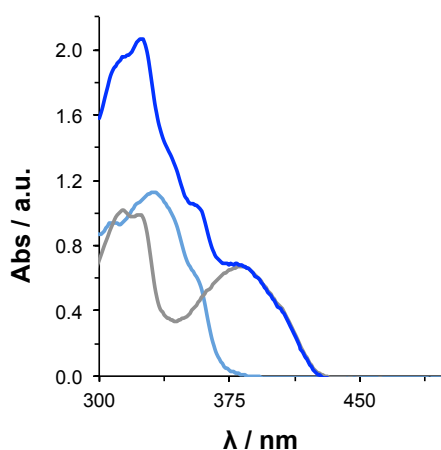


Figure 3.3.7. Absorption profiles in CHCl_3 ($c = 2.5 \times 10^{-4} \text{ M}$) of **2** (grey) and **(R)-1** (light blue) and a $[(\text{R})\text{-1} \cdot \mathbf{2}]_n$ (blue).

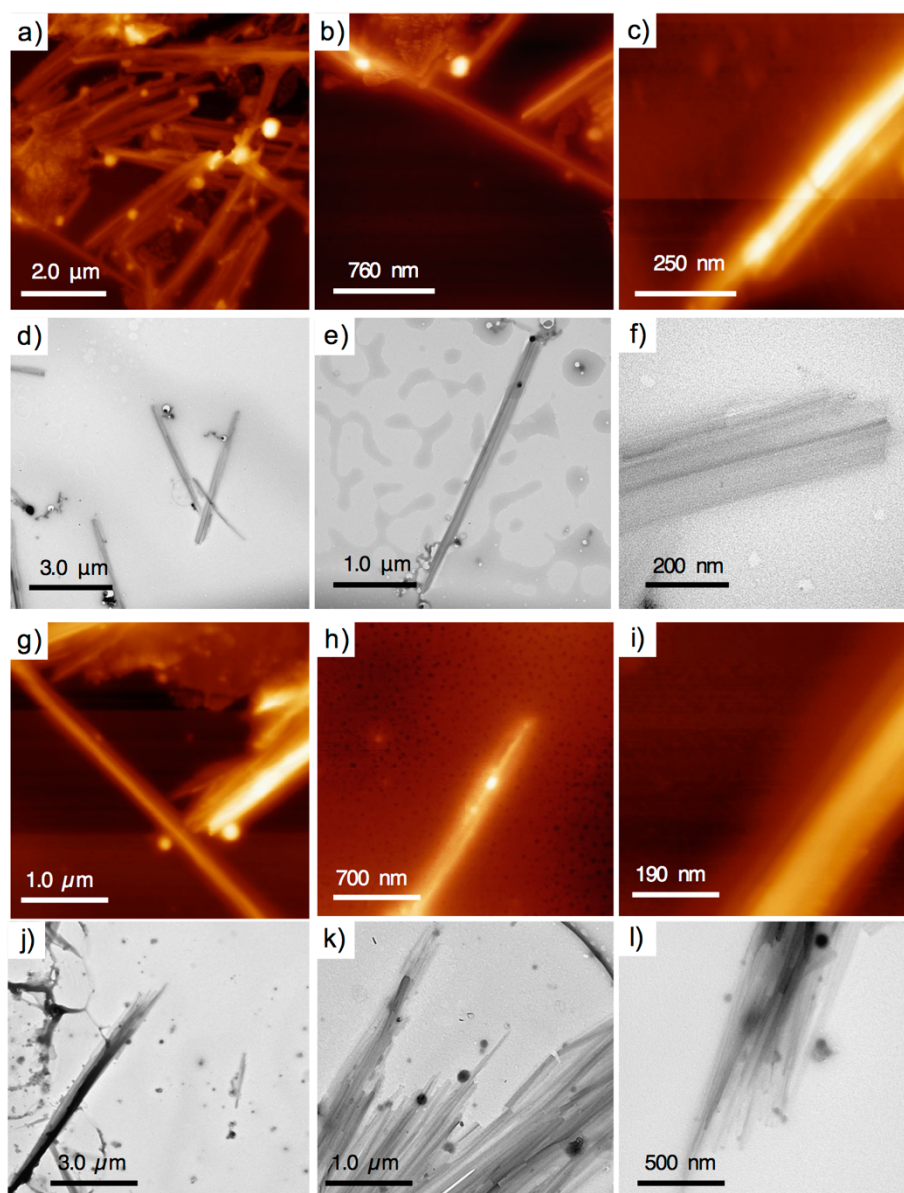


Figure 3.3.8. TM-AFM (a-c) and TEM (d-f) images of the morphologies obtained from a drop-casted CHCl_3 solution of $[(S)\text{-}1\cdot\mathbf{2}]_n$ ($c = 1.3 \times 10^{-3} \text{ M}$). TM-AFM (g-i) and TEM (j-l) images of the morphologies obtained from a drop-casted CHCl_3 solution of $[(R)\text{-}1\cdot\mathbf{2}]_n$ ($c = 1.3 \times 10^{-3} \text{ M}$).

However, when drop-casting a solution of $[1\cdot\mathbf{2}]_n$ ($c = 1.3 \times 10^{-3} \text{ M}$) onto freshly cleaved mica or carbon coated grids, aggregation was observed and different nanoscopic morphologies were visualized by TM-AFM and TEM. Both techniques confirmed the presence of rod-like microstructures featuring diameters between 150 and 500 nm and lengths ranging from 0.5 to 6.5 μm . Through the combined use of both TEM and AFM phase imaging (**Figure 3.3.8**), it was possible to discern rod-like structures composed of bundles of smaller fibers exhibiting a diameter of approximately 6 nm. Based on the

above considerations, we can interpret these fibers as formed by short supramolecular polymers ($N \simeq 15-20$) that upon formation undergo aggregation affording the macroscopic constitutional unit of the observed morphologies. Relying on the onset condition of a concentration-driven solutal instability,³⁷⁰ the extensive aggregation phenomenon seems to be governed by the solvophobic lateral alkoxy chains of compound **2**. It can be hypothesized that the $\text{OC}_{12}\text{H}_{25}$ chains are somewhat exposed on the external side of the polymeric assemblies forming a hydrophobic coat that enables extensive van der Waals interactions through chain-chain interdigitation, ultimately driving the formation of the aggregated morphologies.

3.3.3.3. Toluene: from Solution to Nanoparticles

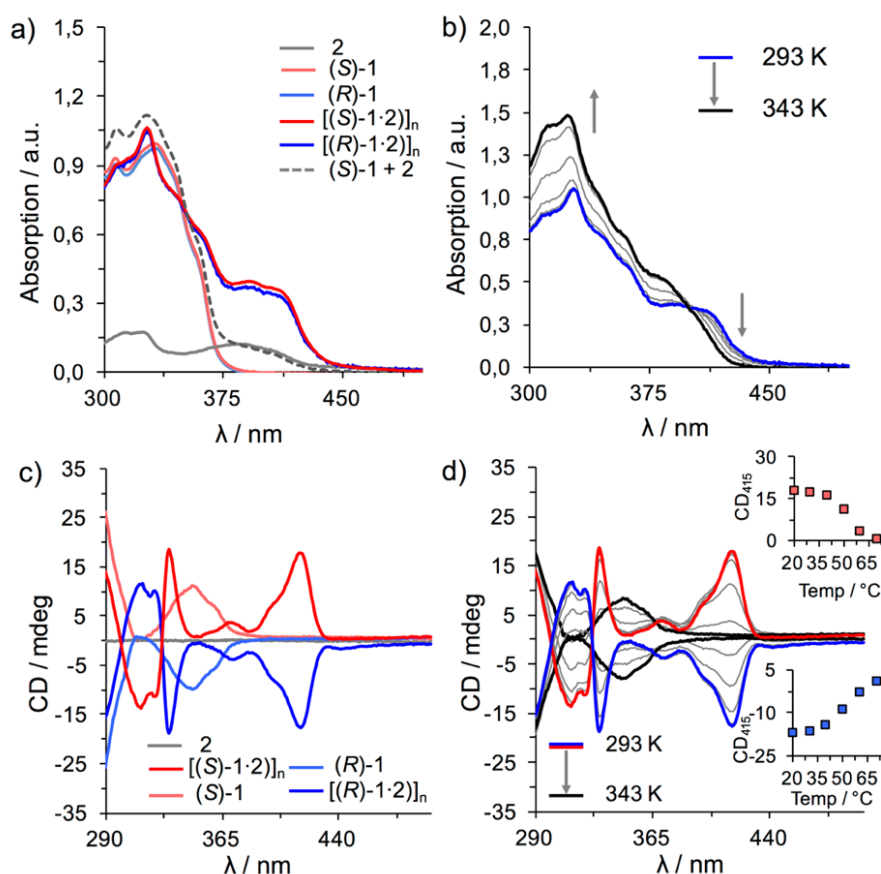


Figure 3.3.9. a) Electronic absorption spectra of (S)-**1**, (R)-**1**, **2**, [(S)-**1**·**2**]_n and [(R)-**1**·**2**]_n in Tol at 293 K ($c = 2.5 \times 10^{-4}$ M); b) VT absorption spectral changes in Tol from 293 to 343 K ($c = 2.5 \times 10^{-4}$ M, recorded each 5 K at a rate of 1 K/min); the same behavior was observed for the other enantiomer; c) CD spectra of (S)-**1**, (R)-**1**, **2**, [(S)-**1**·**2**]_n and [(R)-**1**·**2**]_n in toluene at 293 K ($c = 2.5 \times 10^{-4}$ M); d) VT-CD spectral changes of [(S)-**1**·**2**]_n and [(R)-**1**·**2**]_n in Tol from 293 to 343 K ($c = 2.5 \times 10^{-4}$ M) recorded each 10 K at a rate of 1 K/min); the inset shows the CD intensity (at $\lambda = 415$ nm) plotted versus temperature.

Subsequently, the influence of Tol on the self-assembly was studied. The UV-Vis profile of $[\mathbf{1}\cdot\mathbf{2}]_n$ ($c = 2.5 \times 10^{-4}$ M) showed a redshift ($\lambda = 388$ nm to $\lambda = 397$ nm) of the $\pi\text{-}\pi^*$ transition of the OPE derivative $\mathbf{2}$ and the formation of a shoulder at around 415 nm (**Figure 3.3.9a**).

Variable temperature measurements showed the appearance of an isosbestic point ($\lambda = 403$ nm) and an absorption profile that shifted towards the algebraic sum of the individual components (**Figure 3.3.9b**). Notably, the spectra were more intense at high temperatures, suggesting a scarce solubility or self-assembly of compound $\mathbf{2}$ in toluene solutions at room temperature (both scarce solubility and self-assembly of compound $\mathbf{2}$, was confirmed by VT-UV-Vis measurements, **Figure 3.3.10**).

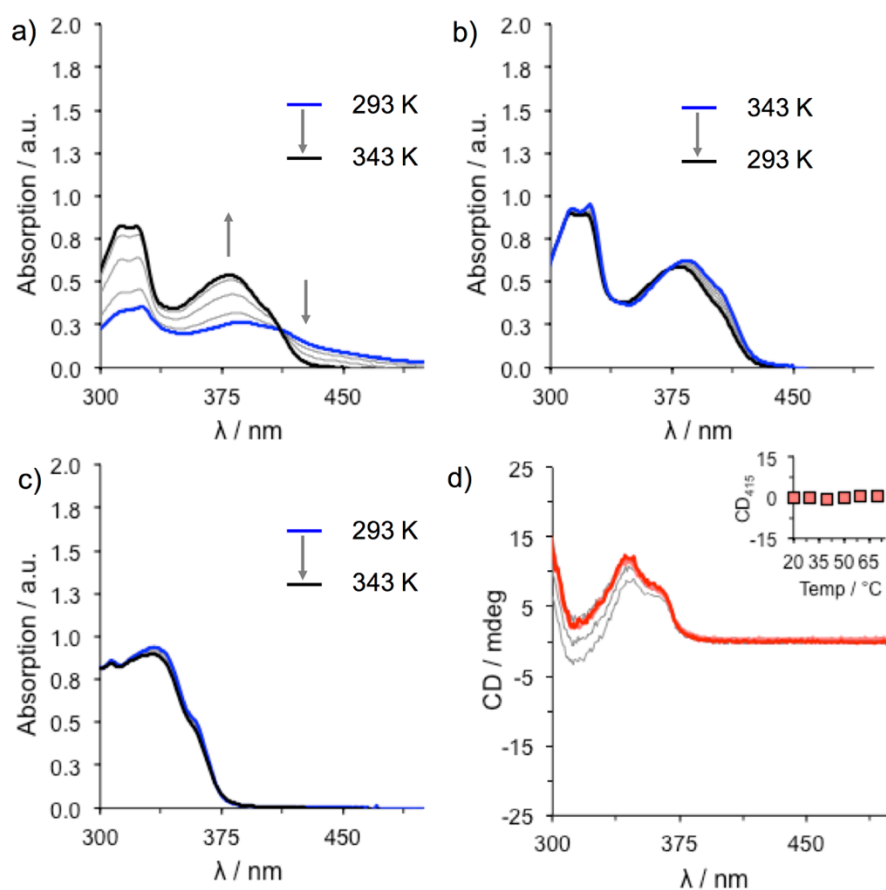


Figure 3.3.10. Variable temperature UV spectral changes (Tol, $c = 2.5 \times 10^{-4}$ M) of a) heating cycle only for $\mathbf{2}$; b) cooling cycle $\mathbf{2}$ and c) heating cycle for only $(R)\text{-}\mathbf{1}$ (cooling cycle showed identical changes); d) CD changes for $(S)\text{-}\mathbf{1}$ (heating cycle). All experiments are performed by steps of 10 K, at a rate of 1 K/min.

However, while the solubility of compound $\mathbf{2}$ in Tol is low, it increases once that 1 equiv. of compound $\mathbf{1}$ is added. Owing to the $(R)\text{-}\mathbf{1}$ or $(S)\text{-}\mathbf{1}$ intrinsic chirality and the favorable association of the Ur-DAP

complex in Tol, it was possible to study the chiral assemblies by Circular Dichroism (CD) spectroscopy on both the pure components and the relative assemblies. The CD spectra ($c = 2.5 \times 10^{-4}$ M) of the BINOL derivatives were characterized by a maximum at 352 nm and an overall CD effect, which takes place in the region between 290 and 380 nm (**Figure 3.3.9c**). When linear module **2** was added to a solution of (*R*)-**1** or (*S*)-**1**, a new band appeared in the region 390-435 nm with a peak around 415 nm and a shoulder around 400 nm (**Figure 3.3.9c**), a spectral region in which the BINOL derivatives are not CD active. To further investigate this induced CD effect in the region where achiral **2** absorbs, the CD spectra were recorded as a function of temperature and concentration for both [*(S)*-**1**·**2**]_n and [*(R)*-**1**·**2**]_n assemblies (**Figure 3.3.9d**). VT-CD experiments from 293 to 343 K for [**1**·**2**]_n showed a gradual decrease of the induced CD effect at 415 nm, which is in accordance with the VT-UV-Vis measurements. Surprisingly, drop-casting from a toluene solution of [**1**·**2**]_n ($c = 2.5 \times 10^{-4}$ M) onto mica showed only the presence of globular, yet undefined, aggregates (**Figure 3.3.11**). This suggests that as the solvent evaporates, the forming supramolecular assemblies undergo solutal instability already at short lengths, thus giving rise to non-structured morphologies most likely controlled by a fast matter-momentum transport in solution.

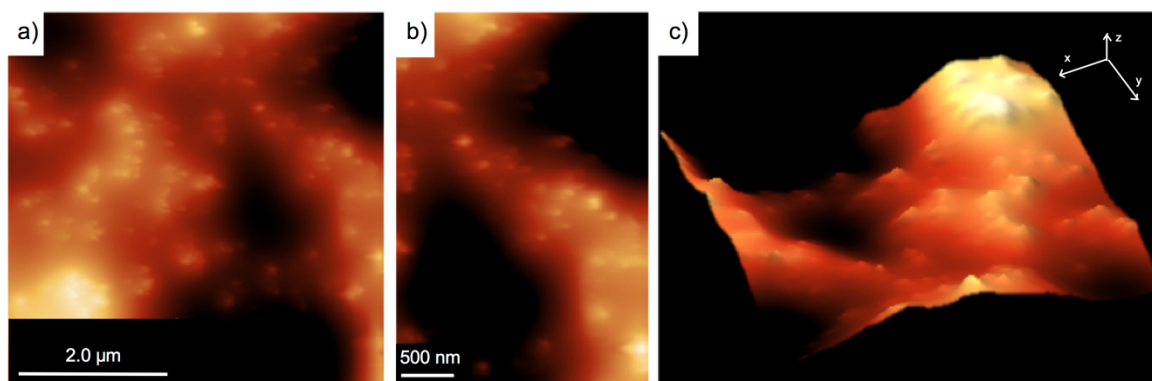


Figure 3.3.11. TM-AFM images of a drop-casted Tol solution of [**1**·**2**]_n ($c = 2.5 \times 10^{-4}$ M) on mica surface.

3.3.3.4. CHCl₃/CHX: from Solution to Nanofibers

The absorption profile of [**1**·**2**]_n in CHCl₃/CHX (1:1 v/v, $c = 2.5 \times 10^{-4}$ M) displayed a red-shift ($\lambda = 383$ nm to $\lambda = 390$ nm) of the π - π^* transition of compound **2** and the formation of a shoulder at $\lambda = 410$ nm (**Figure 3.3.12a**). Increasing the temperature from 293 to 333 K, the absorption spectra

underwent a gradual hypsochromic shift. The spectral shape at 333 K reminded that of the single components at room temperature, thus suggesting the disruption of the aggregates (Figure 3.3.13).

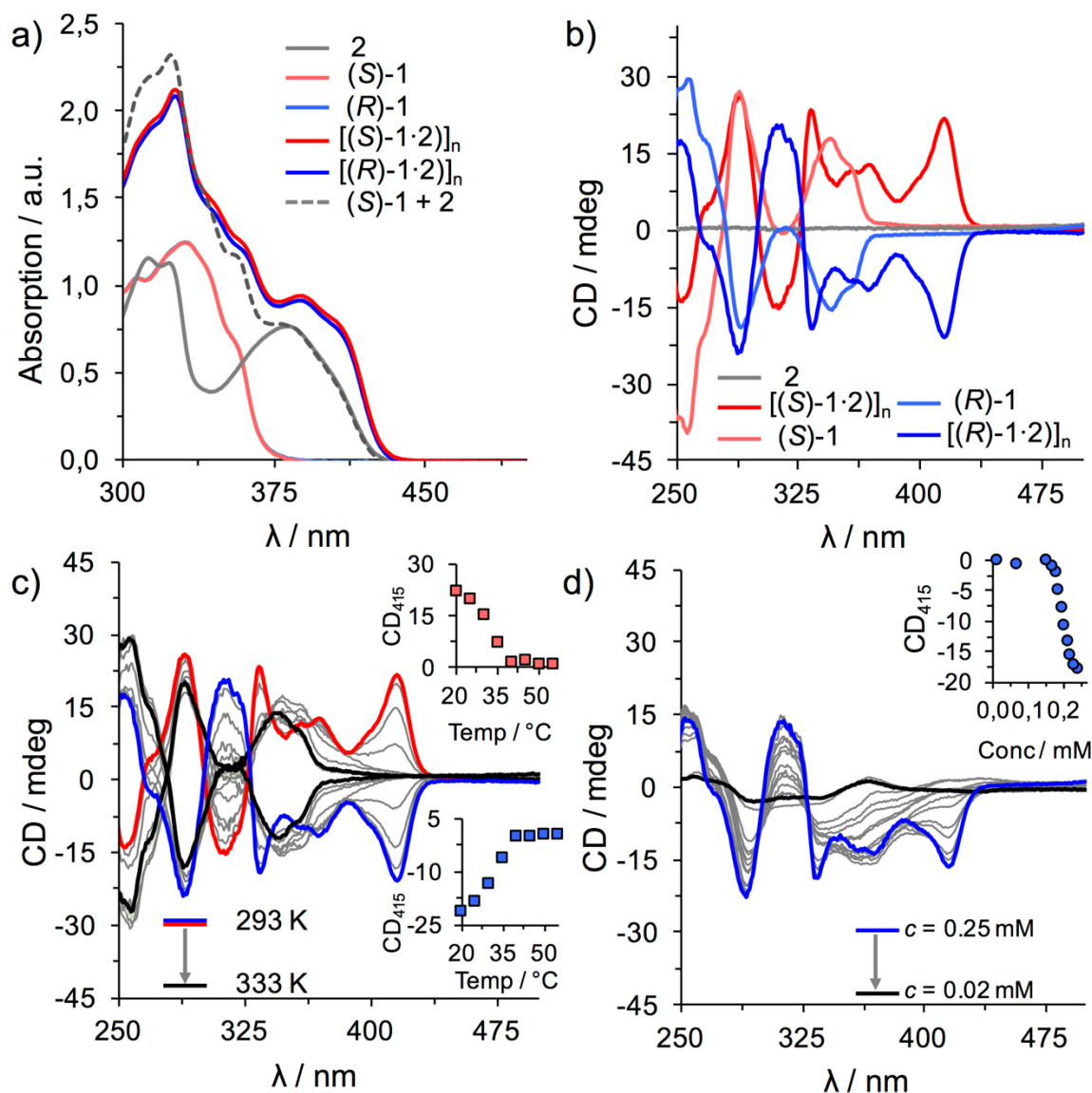


Figure 3.3.12. a) Electronic absorption spectra of (S)-1, (R)-1, 2, [(S)-1·2]_n and [(R)-1·2]_n in CHCl₃/CHX (1:1 v/v) at 293 K ($c = 2.5 \times 10^{-4} \text{ M}$); b) CD spectra of (S)-1, (R)-1, 2, [(S)-1·2]_n and [(R)-1·2]_n in CHCl₃/CHX (1:1 v/v) at 293 K ($c = 2.5 \times 10^{-4} \text{ M}$); c) VT-CD spectral changes of [(S)-1·2]_n and [(R)-1·2]_n in CHCl₃/CHX (1:1 v/v) from 293 to 333 K ($c = 2.5 \times 10^{-4} \text{ M}$, recorded each 5 K at a rate of 1 K/min); insets show plot CD intensity ($\lambda = 415 \text{ nm}$) versus temperature; d) variable concentration CD spectral changes of [(R)-1·2]_n in CHCl₃/CHX (1:1 v/v) at 293 K; inset shows plot CD intensity ($\lambda = 415 \text{ nm}$) versus concentration. The same behavior was also observed with the other enantiomer.

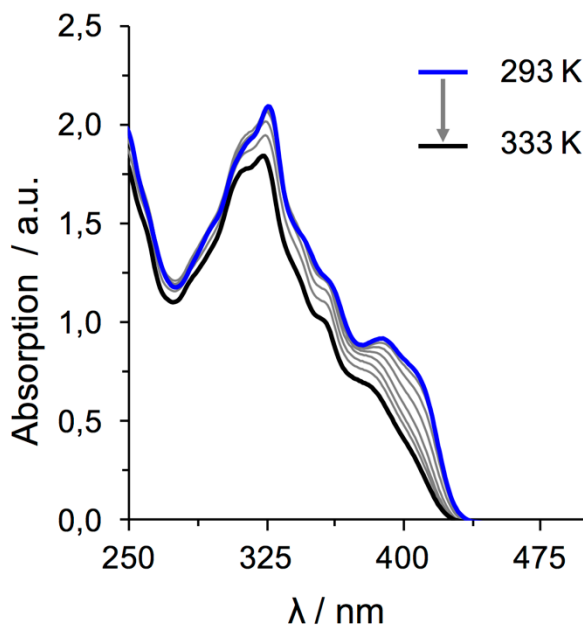


Figure 3.3.13. VT-UV spectral changes of a 1:1 ($c = 2.5 \times 10^{-4}$ M) mixture of (*R*)-**1** and **2** from 293 K (blue) to 333 K (black) in CHCl_3/CHX (1:1 v/v) by steps of 5°C at a rate of $1^\circ\text{C}/\text{min}$.

As expected, the absorption profiles were identical when performing the experiments with (*R*)-**1** or (*S*)-**1**. Additional experiments (VT-UV-Vis and CD) with reference molecules **4** and **5**, BOC-protected molecules **3**, and molecules **1** and **2** alone, did not show any significant changes in the absorption profile (Figure 3.3.14 shows VT experiments of compounds **1** and **2**, that were almost identical profiles obtained with reference molecules **4**, **5** and BOC-protected **3**), indicating that the spectral changes in $[\mathbf{1}\cdot\mathbf{2}]_n$ are attributed to that on of the supramolecular assembly. The same behavior was also observed by CD spectroscopy.

In CHCl_3/CHX (1:1 v/v), the CD spectra ($c = 2.5 \times 10^{-4}$ M) of the BINOL derivatives were characterized by CD signals between 250 and 390 nm (Fig. 6b). When a linear module **2** is added to a solution of (*R*)-**1** or (*S*)-**1**, a new band appeared in the region 390-440 nm with a maximum at around 415 nm and a shoulder around 400 nm (Figure 3.3.12b), again showing an induced CD effect in the region where achiral OPE **2** absorbs. The variation of the induced CD effect was recorded as a function of temperature and concentration for both $[(\mathbf{S})\text{-}\mathbf{1}\cdot\mathbf{2}]_n$ and $[(\mathbf{R})\text{-}\mathbf{1}\cdot\mathbf{2}]_n$ assemblies. As expected, both enantiomers displayed analogous spectroscopic trends (Figure 3.3.12c). VT-CD experiments from 293 to 333 K on a solution of $[\mathbf{1}\cdot\mathbf{2}]_n$ showed a gradual reduction of the induced CD signal at 415 nm, which is in accordance with the VT-UV-Vis measurements (Figure 3.3.13).

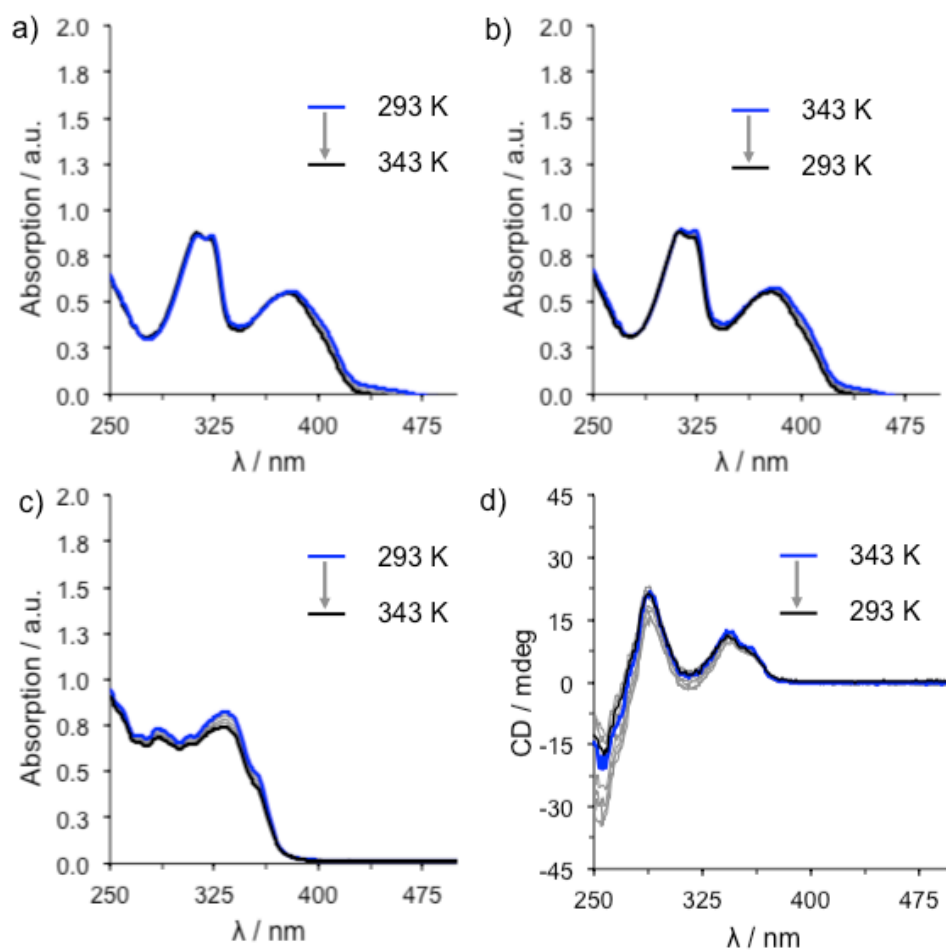


Figure 3.3.14. Variable temperature UV spectral changes of (CHCl_3/CHX , 1:1 v/v, $c = 2.5 \times 10^{-4}$ M) of a) heating cycle only for **2**; b) cooling cycle **2** and c) heating cycle for only **(R)-1** (cooling cycle showed identical changes); d) CD changes for **(R)-1** (cooling cycles). All experiments are performed by steps of 10 °K, at a rate of 1 K/min.

Similar results were also obtained when monitoring the CD profile during dilution experiments (**Figure 3.3.12d**, from $c = 2.5 \times 10^{-4}$ M to $c = 1.9 \times 10^{-5}$ M). The effect of concentration on the intensity of the induced CD at 415 nm shows a sigmoidal dependence (inset of **Figure 3.3.12d**), which suggests that the $\text{Ur} \cdot \text{DAP}$ complex governs the formation of the supramolecular architectures. Appreciably, when performing the experiments on $[(\mathbf{R})\text{-1}\cdot\mathbf{2}]_n$ and $[(\mathbf{S})\text{-1}\cdot\mathbf{2}]_n$ assemblies, the spectra were mirror images of each other (**Figure 3.3.12c**).

Subsequently, the morphology of the supramolecular aggregates made of $[\mathbf{1}\cdot\mathbf{2}]_n$ on mica surface (transferred from a CHCl_3/CHX (1:1 v/v) solution, $c = 2.5 \times 10^{-4}$ M) was studied. The TM-AFM and TEM images in **Figure 3.3.15** showed the formation of an entangled network of fibers displaying

heights ranging from 20 to 80 nm and lengths up to several μm . Although the CD spectra suggested the formation of a chiral secondary structure in a CHCl_3/CHX (1:1 v/v) solution, a microscopic helicity was not observed using AFM or TEM, even though it might be present at the nanoscopic level. This was also noticed for other supramolecular systems.^{371,372} The formation of fibers suggested that, the higher degree of polymerization in the 1:1 v/v CHCl_3/CHX solution favors the development of fibers. Most likely, the solvophilic character of this solvent mixture disfavors aggregation phenomena and thus solutal instabilities.

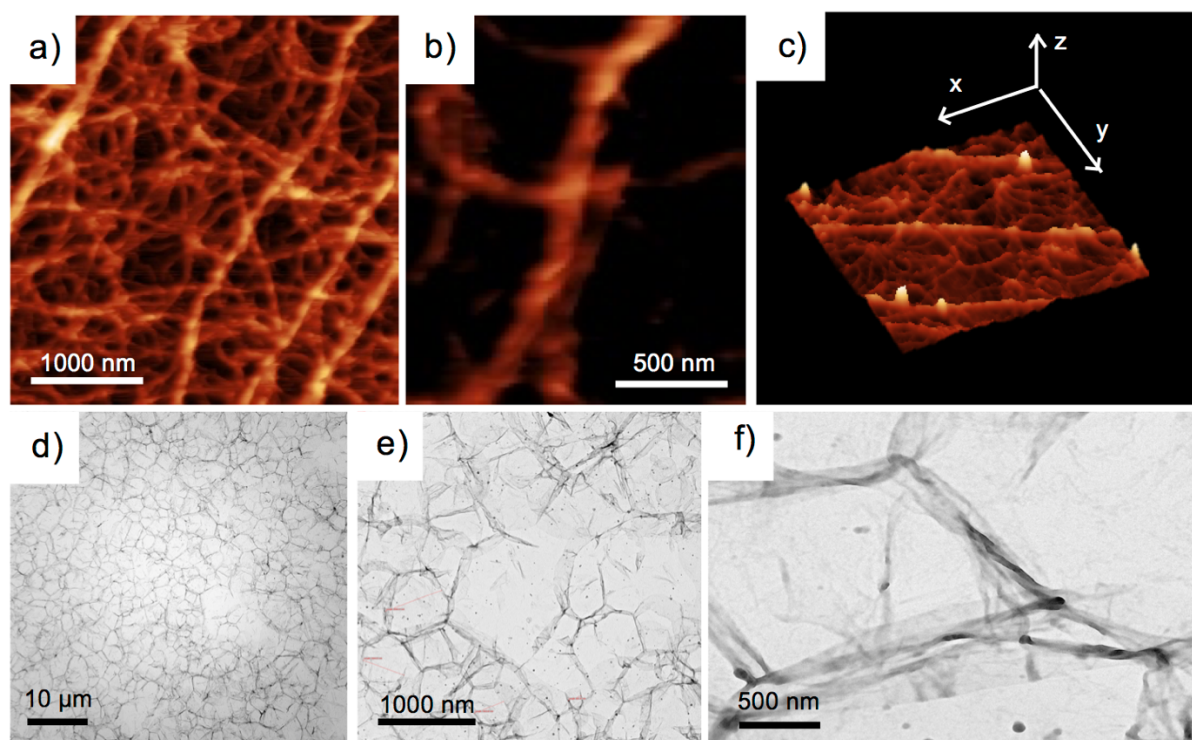


Figure 3.3.15. a-c) TM-AFM and d-f) TEM images of the morphologies obtained from a drop-casted CHCl_3/CHX (1:1 v/v) solution of $[(S)\text{-}1\cdot 2]_n$ ($c = 2.5 \times 10^{-4} \text{ M}$) on mica surface and on a carbon coated grid, respectively.

3.3.3.5. CHX/THF: from Solution to Chiral Helices

A good compromise between solubility and nanostructuration was found in a CHX/THF (95:5 v/v) solvent mixture. Although we could not estimate the degree of association in this solvent mixture because of the presence of precipitate at the typical concentration conditions for $^1\text{H-NMR}$, a chiroptical profile similar to that obtained in CHCl_3/CHX (1:1 v/v) and toluene solutions was also observed for a 1:1 mixture of **1** and **2** (Figure 3.3.16d).

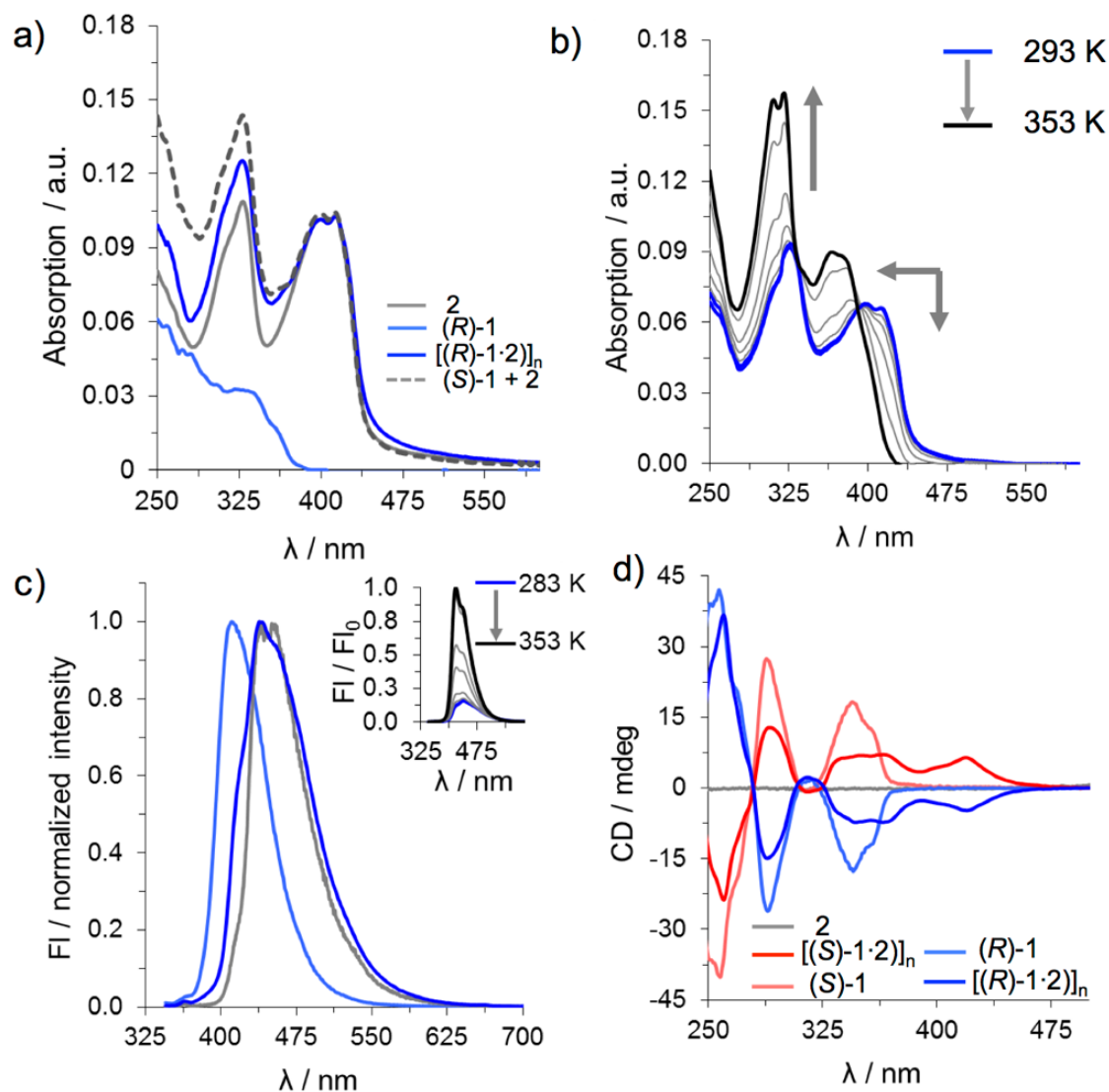


Figure 3.3.16. a) Electronic absorption of (R)-1 (light blue), 2 (grey), [(R)-1·2]_n (blue) and algebraic sum of (R)-1 and 2 (dash grey) in CHX/THF (95:5 v/v), $c = 3.5 \times 10^{-6}$ M; b) absorption spectral changes of 1:1 ($c = 3.5 \times 10^{-6}$ M) mixture of [(R)-1·2]_n during VT measurement; c) normalized fluorescence spectra of (R)-1 (light blue), 2 (grey), [(R)-1·2]_n (blue) and (inset) VT-emission spectral changes of [(R)-1·2]_n recorded each 10 K, at a rate of 1 K/min; d) CD spectra of (S)-1, (R)-1, 2, [(S)-1·2]_n and [(R)-1·2]_n in CHX/THF (95:5 v/v) at 293 K ($c = 3.5 \times 10^{-6}$ M).

Luminescence spectra were obtained at even more dilute concentrations ($c = 3.5 \times 10^{-6}$ M). Both molecules exhibited strong fluorescence, with related quantum yields (Φ_n) of 0.12 and ≈ 1.0 for 1 and 2, respectively. The absorption and emission features of OPE derivative 2 alone in the CHX/THF (95:5 v/v) mixture were red-shifted compared to more polar solvents such as MeOH and THF,^{373,374}

indicating a strong solvophobic-driven self-aggregation of **2**, most likely through J-type association.³⁴ Moreover, the emission of $[(\mathbf{R})\text{-1}\cdot\mathbf{2}]_n$ showed a weak shoulder at longer wavelengths and, compared to a solution containing only **2**, a lower quantum yield ($\Phi_{\text{fl}} = 0.18$) and a higher full width at half maximum (FWHM), i.e. 80 nm (**2**: 62 nm, **Figure 3.3.16c**). The slight changes observed in the absorption and emission spectra of $[(\mathbf{R})\text{-1}\cdot\mathbf{2}]_n$ along with the lifetime values (3.4 ns for **(R)**-1; $\tau_1 = 1.5$ ns; $\tau_2 = 3.7$ ns for **2**; $\tau_1 = 1.2$ ns; $\tau_2 = 4.2$ ns for $[(\mathbf{R})\text{-1}\cdot\mathbf{2}]_n$) were ascribed to the presence of H-bonded self-organized structures in CHX/THF (95:5 v/v) (**Figure 3.3.16a-c**). Notably, the emission at high temperature showed a blue shifted maximum with substantially reduced FWHM (52 nm) and the disappearance of the extended shoulder at longer wavelengths (**Figure 3.3.16c**). This indicated the presence of isolated units of molecule **2** in the sample, which also exhibited much higher intensity. Owing to the high quantum yield of the monomer unit **2** ($\Phi_{\text{fl}} \approx 1.0$), its emission peak masked the signal from weakly emissive molecular species (i.e., **(R)**-1, $\Phi_{\text{fl}} = 0.12$). In order to corroborate the presence of H-bonds between molecular species **(R)**-1 and **2**, a H-bond disrupting polar solvent such as DMSO was added (5 % v/v) to a solution of $[(\mathbf{R})\text{-1}\cdot\mathbf{2}]_n$ (**Figure 3.3.17ab**). Upon addition of DMSO, the absorption spectrum of $[(\mathbf{R})\text{-1}\cdot\mathbf{2}]_n$ shows the appearance of blue shifted bands with discernible signatures of the individual molecular units, **(R)**-1 and **2** (**Figure 3.3.17**). The disruption of the assembly by DMSO was also observed with the VT-fluorescence experiments.

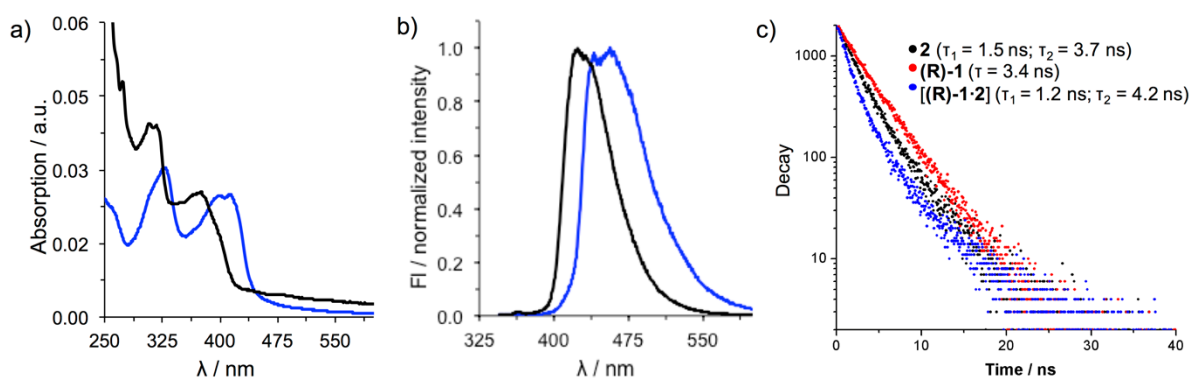


Figure 3.3.17. a) Absorption and b) normalized fluorescence spectra of $[(\mathbf{R})\text{-1}\cdot\mathbf{2}]_n$ in CHX/THF (95:5 v/v) before (blue) and after (black) addition of DMSO. Same results were obtained with molecule **(S)**-1; c) lifetime comparison of **2** (black), **(R)**-1 (red) and $[(\mathbf{R})\text{-1}\cdot\mathbf{2}]_n$ (blue) in CHX/THF (95:5 v/v), $\lambda_{\text{ex}} = 331$ nm; lifetimes reported on the graph.

Microscopic analysis of the deposition of CHX/THF (95:5 v/v) solutions containing $[(R)\text{-}1\cdot\mathbf{2}]_n$, also displayed the formation of fiber-like morphologies (Figure 3.3.18). The fibrous structures displayed small diameters ranging from 5 to 10 nm and average lengths between 0.8 μm to 3 μm . The same morphologies were also obtained upon deposition of the chiral supramolecular systems $[(S)\text{-}1\cdot\mathbf{2}]_n$.

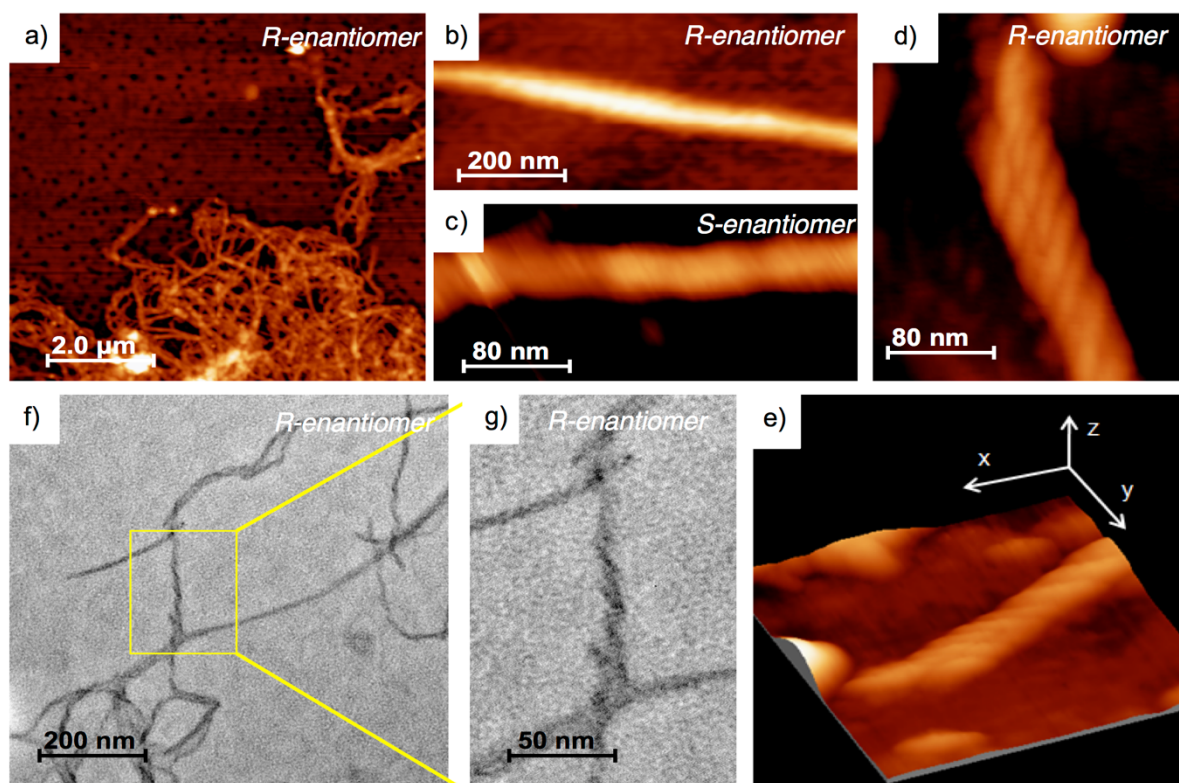


Figure 3.3.18. a-e) TM-AFM and fg) TEM images of nanofibers as obtained from drop casting a CHX/THF (95:5 v/v) solution of $[(R)\text{-}1\cdot\mathbf{2}]_n$ on mica surface and on a carbon coated grid, respectively ($c = 1.7 \times 10^{-3}$ M).

Additional experiments revealed the formation of nanofibers that lacked apparent chirality by AFM investigation of racemic $[1\cdot\mathbf{2}]$, giving further importance to the intrinsic chirality of the BINOL core (Figure 3.3.19). As previously mentioned, CD investigations of dilute solutions containing $[(R)\text{-}1\cdot\mathbf{2}]_n$ and $[(S)\text{-}1\cdot\mathbf{2}]_n$ under the same experimental conditions showed the formation of a new band, centered at around 420 nm but presenting opposite signs (Figure 3.3.16d). This observation, together with the formation of fibrous morphologies, can be considered as a clear proof of the transfer of chirality from the molecular scale to nanostructured nano-objects, in which the different single polymeric structures are held together by the combination of non-covalent interactions. Similarly to the case of the CHCl_3/CHX (1:1 v/v) solution, the formation of narrow fibers from CHX/THF (95:5 v/v)

suggested that under these conditions higher degree of polymerization are achieved and no extensive aggregation is observed. This is probably caused by the solvophilic character of these supramolecular polymers in this solvent mixture.

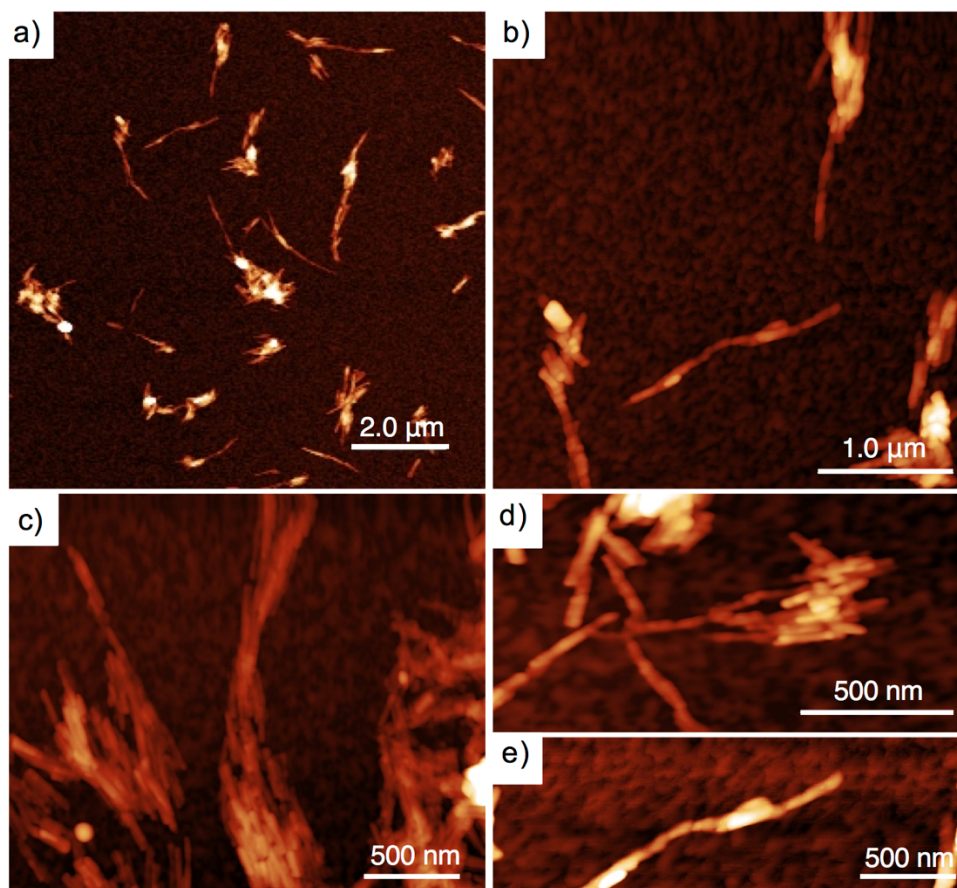


Figure 3.3.19. TM-AFM images (a-e) of a drop-casted CHX/THF (95:5 v/v) solution of $[(\text{racemic})\text{-}2]_n$ ($c = 1.7 \text{ mM}$) on mica surface.

3.3.3.6. Nanostructuration of the Chiral Helices

Additional evidences for the formation of the fibrous aggregates in solution were obtained from SAXS, a powerful technique to determine the shape and size of colloidal, diluted, and particulate systems.^{375,376} The SAXS pattern of a solution of $[(R)\text{-}1\cdot 2]_n$ in CHX-THF (95:5 v/v, $c = 1.7 \times 10^{-6} \text{ M}$) is reported in **Figure 3.3.20**. In order to reconstruct the three-dimensional structure adopted by the supramolecular polymer, the data have been fitted by assuming homogeneous monodisperse structural models, such as cylinders, hollow cylinders and helical bundles. The best fitting result (**Figure 3.3.20a**, red line) were obtained using helical superstructure models³⁷⁷ resulting from the

topological twisting (angle of 36°) of a 1D nanostructure featuring a ribbon-like structure (width of 8 nm).

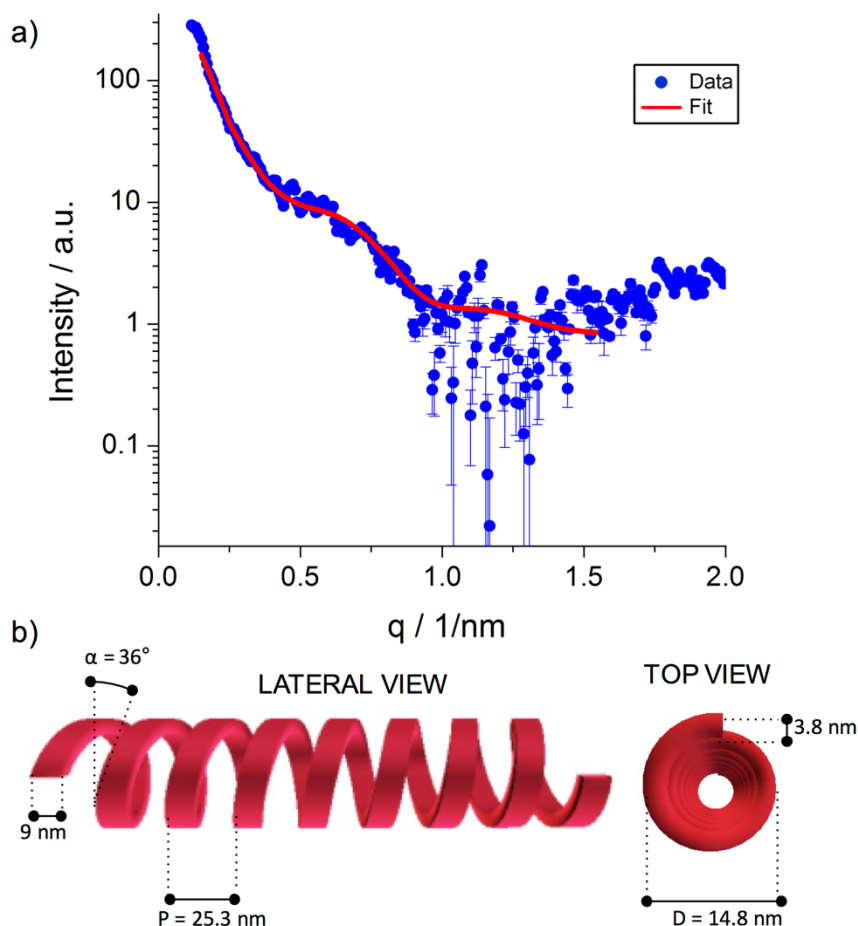


Figure 3.3.20. a) Experimental SAXS data (blue) obtained from a solution of $[(R)\text{-}1\text{-}2]_n$ in CHX/THF (95:5 v/v) (298 K, $c = 1.7 \times 10^{-6}$ M) superimposed with a fitting model (red line) of a helical tape; b) schematic representation of the supramolecular helicoidal fibers as obtained from $[(R)\text{-}1\text{-}2]_n$.

Their structural and geometrical features of which are depicted in **Figure 3.3.20b**. In order to elucidate the geometric organization of the self-assembled molecular models along the twisted ribbon system, more complex fitting models taking into account also its possible internal structure were also used. However, the results were not statistically significant, and thus they were not considered.

In order to gain insight into the molecular organization of the nanofibers, molecular modeling simulations were also carried out at the atomistic level using Molecular Mechanics (MM). MM studies were performed using the COMPASS force field, which accurately describe the geometry and torsion potentials of phenylene ethynylene oligomers, alkyl groups, BINOL, and is appropriately optimized

for modeling organic condensed phase and H-bonded structures.³⁸ **Figure 3.3.21** shows the structures of the studied compounds and the molecular modeling of the *H*-bonded bi-component supramolecular networks. Conformers of (*R*)-**1** and (*S*)-**1** possess a torsional angle between the naphthalenes planes of around 96° for the *transoid* conformer (see **Figure 3.3.21a** for the *transoid* conformation, where the 2,2'-methoxy groups are pointing in opposite directions) and 72° for the *cisoid* conformers. For linear module **2**, the *para*-phenylene ethynylene moiety has a flat torsion potential between the phenylenes (2.1 kJ mol⁻¹ barrier), which dictate through the torsional angle of the BINOL units the geometrical properties of supramolecular polymers [(*R*)-**1·2**]_n and [(*S*)-**1·2**]_n. Depending on whether one naphthyl substituent of the (*R*)-**1** or (*S*)-**1** module is facing the neighbouring naphthyl at each side of the linear linker (see sketch in **Figure 3.3.21b** where equivalent naphthalenes are depicted with the same black tonality), the complementary *H*-bonding arrangement yields two possible types of bi-component networks, namely helix or zig-zag patterns (**Figure 3.3.21b**). Based on a series of modeled assemblies obtained by different cycles of MM simulations, we found that square-shaped networks are indeed forming a helical assembly at the supramolecular level with a pitch made of tetrameric units of [(*R*)-**1·2**]_n (**Figure 3.3.21c**). In contrast, the zig-zag arrangement yields the formation of one-dimensional polymer, because in this setting two equivalent naphthyl substituents face each other at each termini of the linear unit (**Figure 3.3.21b**). Although this type of supramolecular organization would leave large voids in the arrangement, the presence of the C₁₂ alkyl groups stabilizes the formation of supercoiled double helical cables (**Figure 3.3.21c**) by lateral alkyl-alkyl interdigitation. In the geometry-optimized model of [(*R*)-**1·2**]_n shown in **Figure 3.3.21c**, both molecular geometries and length of the alkyl groups govern the formation of compact double helicoidal arrangement, with a single-helix pitch of around 3.8 nm (i.e. 1.9 nm from helix blue to helix yellow in **Figure 3.3.21c**). The geometry of the double helix has a rectangular cross section, with a minimum distance of around 2.8 nm from side to side and a maximum distance of around 5.0 nm from corner to corner. Indeed, such compact packing is very likely more stable than the zig-zag arrangement in apolar solvents, as the alkyl groups point at the outer surface of the helix. Notably, the geometrical parameters obtained from the MM simulation are in strict relationship with the structural data obtained from the SAXS analysis of [(*R*)-**1·2**]_n in a CHX/THF (95:5 v/v) solution. Indeed, the supramolecular dimerization of one of these single rectangular units through van der Waals interactions, dictated most probably by multiple interdigitation of the solubilizing alkyl chains, would lead to the formation of a flat ribbon nanostructure with dimension comparable with the one reported by the SAXS results (4 nm of height and 8 nm of width, **Figure 3.3.21c**, model (i)). The consequent

twisting and dimerization (Figure 3.3.21c, (ii) and (iii) steps, respectively) of the resulting ribbon would allow the formation of the supercoiled fibrous structure observed at the microscale by both TEM and AFM analysis.

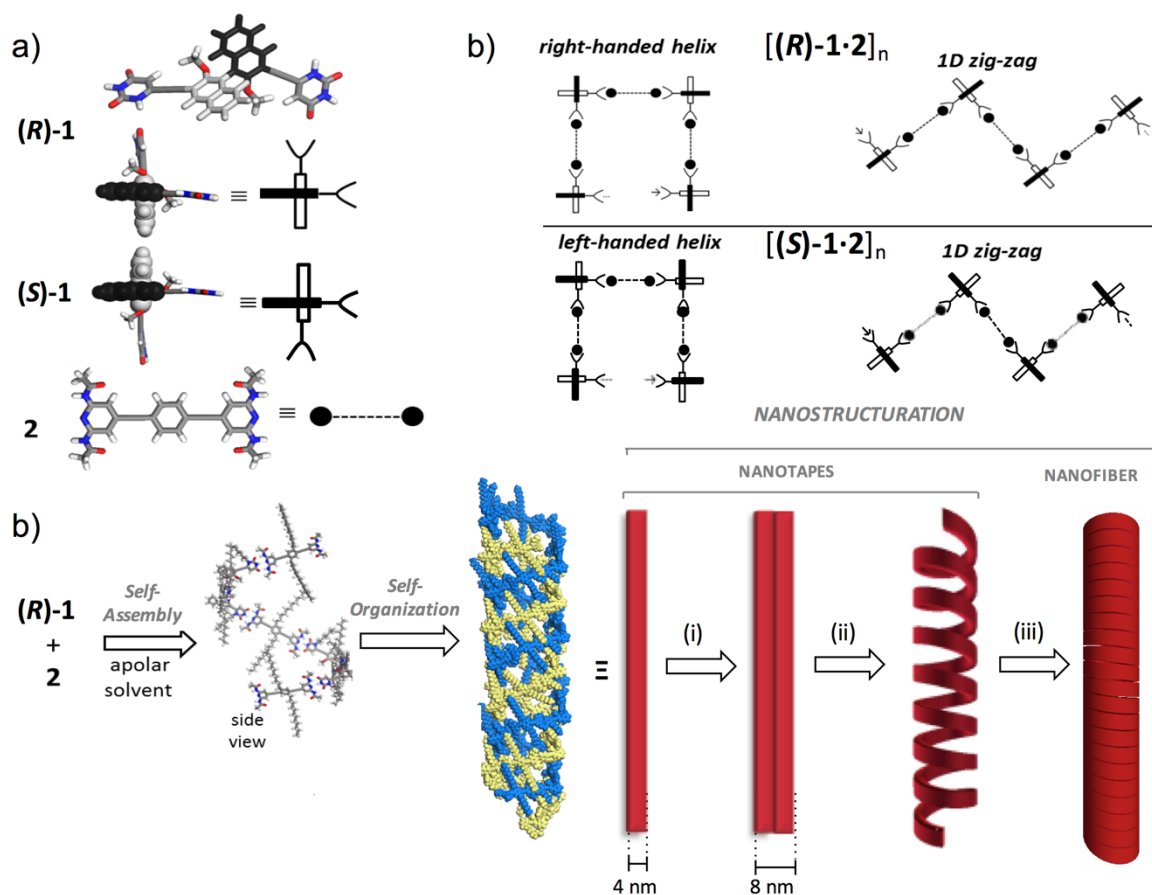


Figure 3.3.21. Molecular modeling of the supramolecular polymers of $[(R)-1\cdot 2]_n$ and $[(S)-1\cdot 2]_n$. a) Side and top views of conformers of (X) -1 along with their sketch representation (on the right); (b) sketch of the different possible assemblies considered for the molecular mechanics (MM) simulations; (c) proposed simulated model for self-organized nanofibers (CPK view, one helix in blue, the other in yellow ≈ 15 nm-long fiber as obtained through several MM simulations cycles of the superstructure): at first, the self-assembly occurs through H -bonding between the complementary modules in a helix-type arrangement, which is right- and left-handed for $[(R)-1\cdot 2]_n$ and $[(S)-1\cdot 2]_n$, respectively, followed by a self-interdigitation of the single helices yielding double helix nanofibers. As observed by SAXS analysis in solution and AFM images on surfaces, it is envisaged that the individual nanofibers are organized into the final superhelical nanofibers by a possible three step mechanism based on the formation of a tape structure (i) that will eventually twist into a single helical tape (ii) and finally dimerize into the final nanofibers structure (iii) observed by TEM and AFM.

3.3.3.7. From Nanospheres to Helices

To shed further light on the role of the solvent mixture giving the chiral morphologies, we investigated various solvent mixtures between CHX and THF. As in previous cases, an equimolar amount of molecular modules (*R*)-1 or (*S*)-1 and 2 were first dissolved into a minor volume of THF (solvent able to completely solubilize both compounds) and then diluted to the necessary volume with CHX. Aiming at favoring the formation of the most thermodynamically stable architectures, the resulting mixtures were heated and finally drop-casted onto mica surfaces for microscopic analysis and let to evaporate at room temperature. With the more polar mixture (CHX/THF 80:20 v/v), the formation of round shaped nanostructures was observed by TEM and TM-AFM investigations (Figure 3.3.22ad).

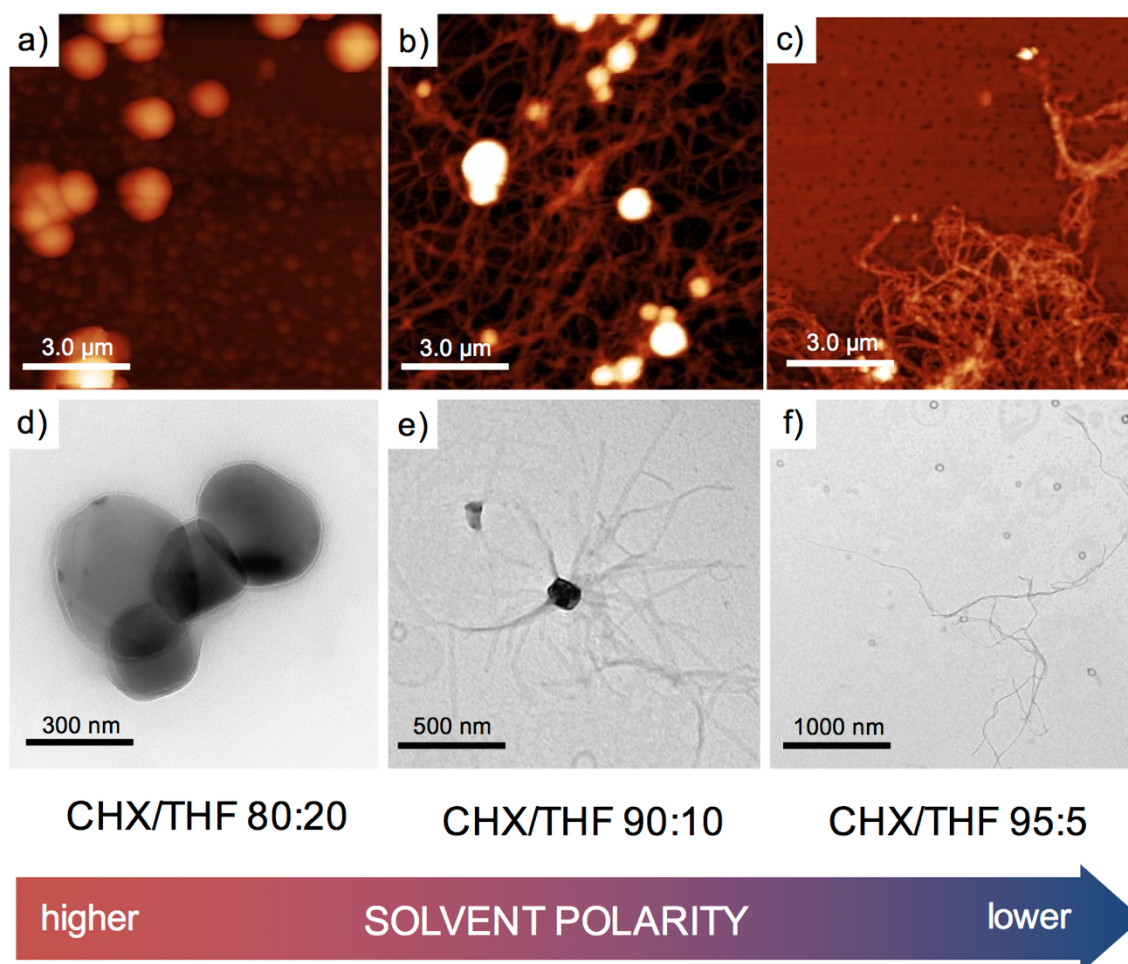


Figure 3.3.22. Nanostructuration of the supramolecular polymers into organic morphologies depending on the polarity of the drop-casted solution: a,d) TM-AFM and TEM images for CHX/THF (80:20 v/v); b,e) images for CHX/THF (90:10 v/v) and c,f) images for CHX/THF (95:5 v/v).

Through detailed TM-AFM analysis, spherical nanoparticles characterized by heights from 10 to 70 nm and thickness of nm to few tens of nm were obtained (**Figure 3.3.22a**). Interestingly, when a solution of $[1.2]_n$ was transferred from a CHX/THF (90:10 v/v) solution to the mica surface, globular aggregates were predominantly observed, but fibrous material also started to appear (**Figure 3.3.22be**). Specifically, the deposited material is characterized by the presence of spherical morphologies that peripherally exposes fibrous ramifications, with diameters between 5 and 50 nm and length up to several μm . With respect to the fibrous morphologies obtained from the CHX/THF (95:5 v/v) solutions, the ramifications displayed some substantial structural differences, as they appear as bamboo-like structures (**Figure 3.3.22cf**). In both cases, SAXS measurements did not reveal any periodicity or formation of homogenous structures. Whereas in the more polar solvent mixture (CHX/THF 80:20 v/v) the aggregation seems to be essentially governed by the concentration-driven solutal instability, increasing the apolar character of the solvent enhances the degree of polymerization, thus favoring the formation of long supramolecular polymers as the solvent evaporates, thus the formation of long fibers.

3.4. Conclusions

In view of precise and controlled preparation of functional supramolecular systems, this chapter focused on the nanostructuration of soft matter both in solution and on surface, with placing special attention to the choice of the solvent.

In the first part, porphyrin **3-1·Zn** was designed in order for the building block to have a flat core for π -stacking, lateral hydroxy groups capable of hydrogen bonding and finally a Zn(II) metal atom capable ligation. The porphyrin **3-1·Zn** was prepared according to a procedure that allowed us to avoid tidy and numerous column chromatographies. Then, the characterization through one- and bi-dimensional NMR techniques confirmed the structure of the product. Already in solid state, porphyrin **3-1·Zn** was found to self-assemble into stacks with central void created by a hydrogen bond network, which gave first validation of our system design. UV-Vis absorption studies showed hypso- and hypo-chromic shift of the Soret and Q-bands when more apolar solvent (CHCl_3 , MCH) are used instead of THF. Further titrations with either pyridine or CH_3OH showed breaking of both hydrogen bonding and axial zinc coordination interactions, respectively. Additional temperature- and concentration-dependent UV-Vis suggested that the porphyrin molecules are also able to form slipped stack arrangements (J-type aggregates). The solutions were then deposited by spin-coating on a mica

surface and AFM microscopy showed the formation of extended 2-D islands, suggesting that the aggregates were transferred from solution to the surface.

In the second part, novel molecular modules carrying hetero-complementary H-bonding recognition motifs were prepared and characterized. The building block is composed of a BINOL unit which, through its atropoisomers (*R*) and (*S*), served as a chiral unit. Together with a complementary H-bond partner, an achiral linear OPE chromophore, the modules underwent self-assembly through triple H-bonding interactions. The association strength of the three-fold H-bonded structures was determined in CDCl₃, CDCl₃/CHX-*d*₁₂ and Tol-*d*₈, together with their binding stoichiometry. Through a simple experimental model, we have shown that, together with the association strength, the vapor tension of a given solvent governs the degree of polymerization under evaporation conditions. In particular, solvents favoring strong H-bonded complexes and displaying high vapor pressures induce the formation of higher degrees of polymerization. Owing to the chromophore unit, it was possible to follow the self-assembly through UV-Vis, CD and fluorescence spectroscopies. Notably, through temperature- and concentration-dependent CD spectroscopies, an isodesmic polymerization mechanism was uncovered. The self-assembled supramolecular polymer has been transferred onto surface for microscopic investigations through AFM and TEM microscopy measurements. Nanostructuration afforded nanorods (from CHCl₃), nanofibers (CHCl₃/CHX), nanospheres (Tol, CHX/THF 80:20 v/v), hybrid nano-sphere/fibers (CHX/THF 90:10 v/v) and finally helical nanofibers (CHX/THF 95:5 v/v). The self-organization and the chiral transfer from solution to surface were also studied with the aid of SAXS analysis and molecular modeling in order to gain insights into the nanostructuration mechanism of the material into superhelical nanofibers. These results suggest that if high degrees of polymerization are achieved, fibrous structures apparently expressing chiral morphologies at the microscale can be obtained. The solvophilic character of a given solvent mixture disfavors aggregation phenomena, thus reducing solutal instability. Taken in concert, our experiments showed that the choice of solvent is crucial to dictate the polymorphism of the nanomaterial and the transmission of molecular chirality at higher scales. In particular, an optimal balance between high degree of association, solvent vapor pressure and the solvophobic/solvophilic properties needs to be accomplished in order to control the formation of organic morphologies.

4. Carbon-Based Templates for Photo-Active Materials

This chapter describes the organization of photo-active materials by using carbon-based templates, such as carbon nanotubes (CNTs) and carbon nanodots (CNDs). While carbon nanotubes hold great potential due to their extensively reported physical and electronic properties, carbon nanodots are the latest member of the nano-carbon family and their investigation is still limited. The chapter is divided in three sections: *i*) the introduction includes a general overview on common templates for arrangement of chromophores; *ii*) the hierarchical assembly of porphyrin arrays on carbon nanotubes, with the latter ones being able to get aligned under external stimulus, such as the magnetic field; *iii*) novel hybrids of carbon nanodots and porphyrins, however this being a system first of its kind both covalent and non-covalent approaches were employed.

The work presented in this chapter has been done in collaboration with Dr. *Mingjie Liu* from Dr. *Yasuhiro Ishida* group (RIKEN Center, Saitama, Japan) that performed the magnetic alignment experiments, Dr. *Andrea Minola* from the group of Prof. *Roberto Lazzaroni* (Université de Mons, Mons, Belgium) that performed the molecular modeling and Dr. *Rita De Zorzi* and Prof. *Silvano Geremia* (Università di Trieste) for solving the crystal structure. The work done on CNDs has been accomplished in collaboration with Francesca Arcudi (Università di Trieste) that performed the synthesis, the optical, the structural and morphological characterization of the CNDs and the hybrid material, and Dr. *Volker Strauss* from Prof. *Dirk Guldi* group (Friedrich-Alexander-Universität, Erlangen-Nürnberg, Germany) that carried out photophysical characterization of the hybrid material. Part of the work in this chapter has been used in the preparation of the manuscript “Templating porphyrin anisotropy via magnetically-aligned carbon nanotubes”. Part of this chapter has been published as “Synthesis, Separation, and Characterization of Small and Highly Fluorescent Nitrogen-Doped Carbon NanoDots” *Angew. Chem. Int. Ed.* **2016**, *55*, 2107–2112.

4.1. Introduction

Great efforts have been accomplished in the careful and precise design of building block that assemble in functional nanostructures. An alternative approach involves implementation of a template in order to organize molecular motifs into nano-, meso- or macroscopic objects as an alternative bottom-up approach. This, template-aided, approach aims at overcoming some of the current challenges in the bottom-up fabrication that include low yields, restricted complexity and suboptimal reproducibility.³⁷⁸

In this context, most commonly exploited materials as templates (**Figure 4.1.1**) are: *i*) bio-mimetic deoxyribonucleic acid (DNA); *ii*) inorganic zeolites and *iii*) carbon nanomaterials.

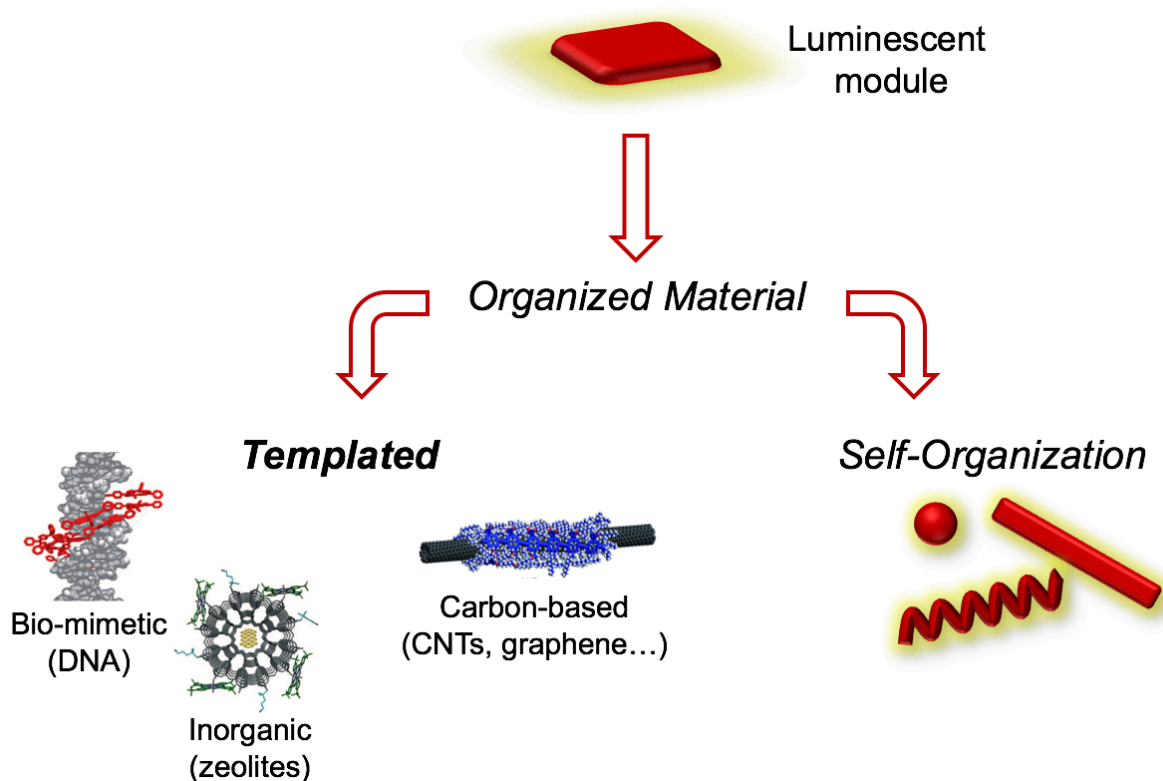


Figure 4.1.1. Approaches towards organized luminescent materials with templates such as DNA, zeolites or carbon-based materials.

4.1.1. Deoxyribonucleic Acid

DNA is a readily available biopolymer that nowadays can be prepared in almost any length, sequence or functionalization.^{379,380} It is thus an especially appealing template either for formation of programmed nanostructures with geometrical, size and positional control or for ordering precisely functional molecules.^{380–382}

An example of control on shapes and patterns that can be achieved is displayed by the so-called ‘DNA origami’, a single-strand DNA (ssDNA) that folds into predefined shapes and is held in place with short nucleotide ‘staple strands’ between the two segments of the ssDNA (**Figure 4.1.2**). DNA can be used as a scaffold for dyes and extended π -conjugated systems in several ways:

- Covalently linked π -conjugated systems to DNA;

- Supramolecular interactions resulting in intercalation, binding to the sugar-phosphate backbone and hydrogen-bonding to the bases.

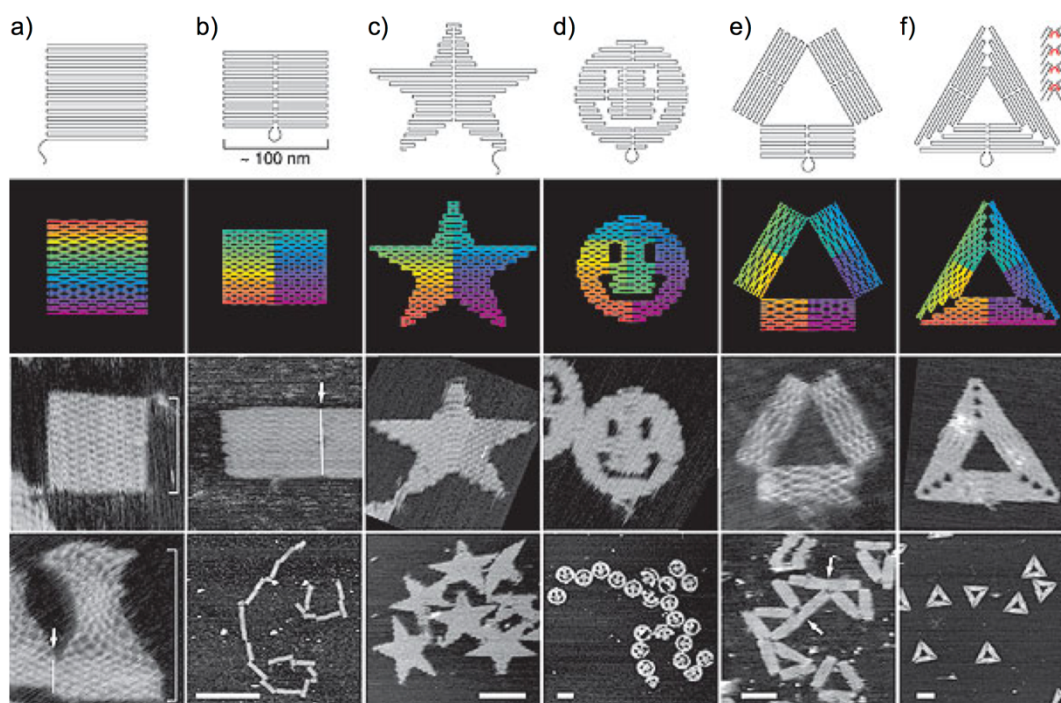


Figure 4.1.2. DNA origami shapes into: a) square, b) rectangle, c) star, d) smiley face, e) triangle with rectangular domains and f) sharp triangle. Second row, computer generated diagrams showing helix crossovers. Bottom two rows, AFM images of folded DNA specimens.^{378,383}

Several strategies that are usually employed as backbone modification of the DNA scaffold are shown in **Figure 4.1.3**. Modifications of natural nucleosides, such as functionalization of the nucleobase, replacement of the nucleobase or using surrogates are all options in the backbone modification. For example, porphyrins have been attached covalently to nucleobases on complementary strands of DNA (**Figure 4.1.3a-c**).³⁸⁴ Moreover, it is possible to create an array of mixed porphyrins by attaching, for example, a free-base porphyrin on one strand and a Zn(II) porphyrin on the other one. The formation of the double strand resulted in the formation of an alternated array that interacted and formed a zipper-like arrangement in the major groove of DNA. The DNA grooves were used to arrange several other π -systems by covalently linking dimers to the nucleobases. For example, pyrenes, biphenyls, bipyridyls, phenanthrolines and chrysenes among others showed the formation of excimers.^{385–388}

Another strategy is to replace various parts of the DNA structure, either the nucleobase, the (deoxy)ribose or the complete nucleoside. A popular strategy is removal of a natural nucleobase and replacement by an artificial one that allows a wide range of modifications.^{379,381,389} For example, fluorescent deoxyribosides (named ‘fluorosides’) were prepared by replacing the nucleobases with either pyrene, oxoperylene, dimethylaminostilbene and quinacridone as monomers that were subsequently used for automated synthesis of tetramers in a combinatorial set (Figure 4.1.3de).

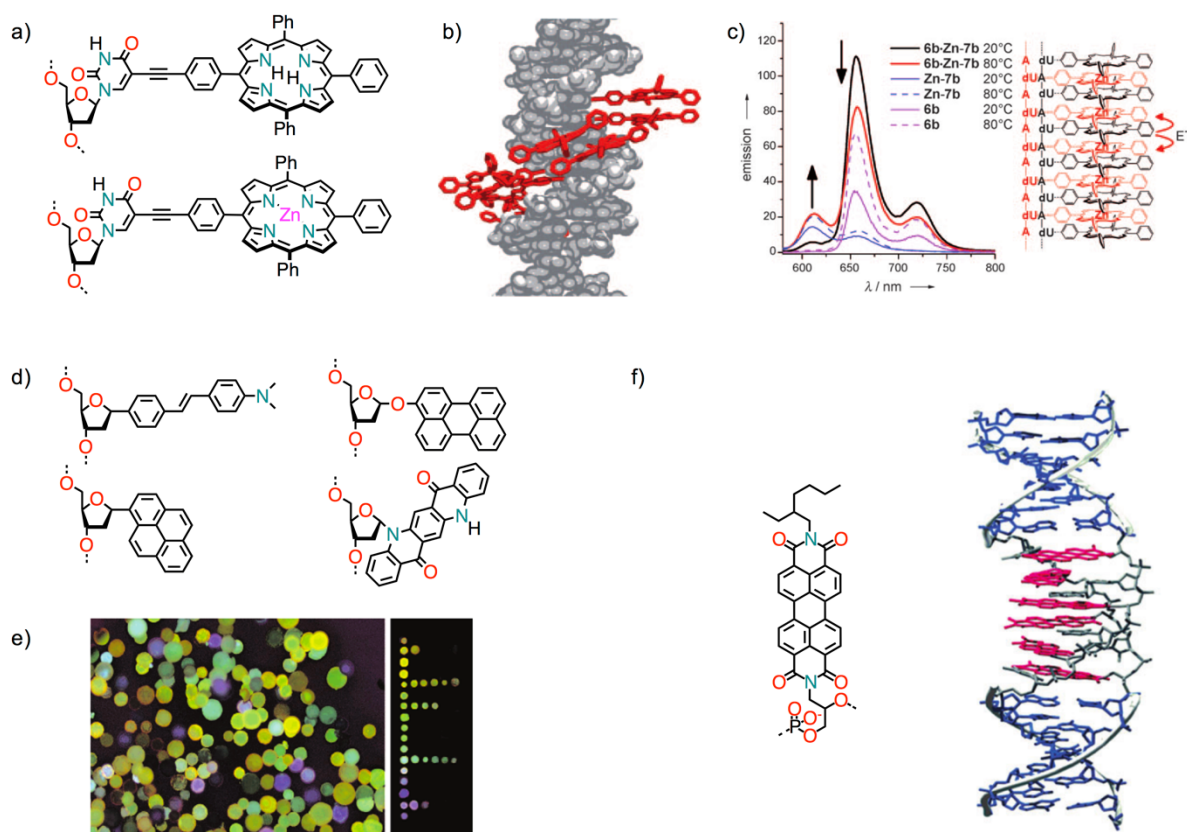


Figure 4.1.3. a-c) Modified base containing porphyrin dyes assembled in the major groove, with a part of calculated zipper structure and emission spectra of strands showing electron transfer; d-e) structures of artificial nucleosides monomers along with a fluorescence microscope image of a 256-member combinatorial library of all possible tetramers; f) perylene base surrogate along with the schematic view of the double helix.

The ribose in the DNA backbone was replaced with a short alkyl chain, resembling the distance between adjacent phosphates in natural oligonucleotides, carrying a PBI unit.^{390,391} The PBIs were incorporated in the strand in order to form zipper-like structures in the corresponding double helix. With the correct stereochemistry on the short alkyl linker and with the presence of Watson–Crick base

pairs at both termini, the strand adopted a right handed helix. Therefore, with this method it was possible to assemble molecules into a helical array and form the double helix even if the nucleotides were replaced by organic chromophores.

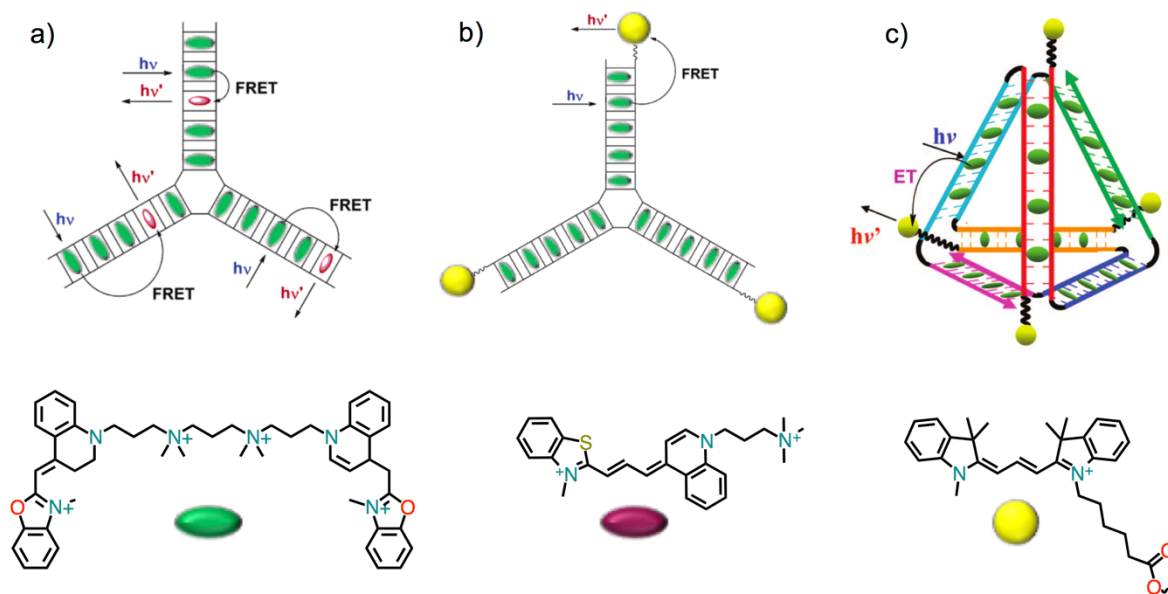


Figure 4.1.4. a) Schematic representation of branched DNA with both donor and acceptor molecules intercalated; b) branched DNA with intercalated donor molecules and covalently attached acceptor moieties; c) tetrahedron DNA nanotag with the representation of energy transfer between intercalated donor and covalently attached acceptor.

Intercalation, the insertion of a molecule between the base pairs of the DNA, has been extensively used in biology in form of drugs or tags. In addition, intercalation of the dyes was also used for assembling multichromophoric arrays (**Figure 4.1.4**).^{392,393} In order to mimic light-harvesting complex of plants, bacteria and algae, the protein structure was replaced by branched double-helical DNA nanostructures that could serve as scaffold for supramolecular binding (by intercalation) of chromophores. The presence of efficient fluorescence resonance energy transfer (FRET) in two different multichromophoric systems was demonstrated. In the first one, both donor and acceptor dyes were intercalated, while in the second one the donor was intercalated while the acceptor dyes covalently attached in order avoid donor dyes being displaced by acceptor one.

Electrostatic forces were also exploited in order to interact with the electron-rich and negatively charged sugar-phosphate backbone. For this reason, a series of water-soluble polymers

(polyfluorenone polymers and co-polymers) were prepared and tested as optical reporters thanks to the electrostatic interactions. Moreover, FRET was observed when dyes were intercalated within dsDNA.^{394–397} A tetranionic Ni(II) porphyrin was found capable of sensing the spermine induced Z-form of DNA.³⁹⁸ While no interaction is possible without the spermine, interaction with DNA is possible when the shielding action of protonated spermine is present.

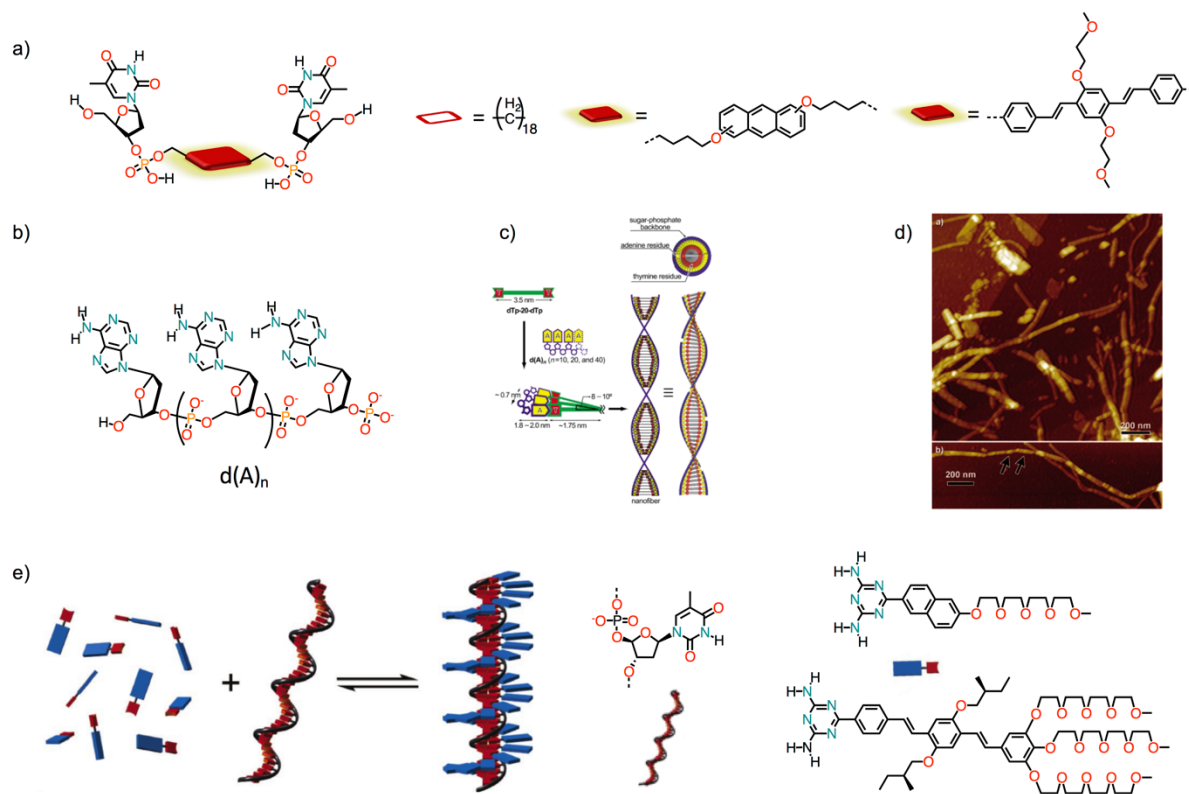


Figure 4.1.5. a) Structure of the thymidine appended amphiphiles, b) the oligoadenine template for the thymidine guests, c) proposed mechanism of formation of the oligoadenylic acid templated self-assembly, d) AFM image of self-assembled nanofibers; e) schematic representation of supramolecular complex formation between oligothymine ssDNA template and π -conjugated molecules.

Base pairing using ssDNA as templates for organic components is another possible strategy (**Figure 4.1.5**). Using oligoadenine as DNA template and thymine appended guest molecules the formation of fibers, hydrogels and helical stacks has been reported.^{399–403} By incorporation of anthracene in the di-thymine guest it was observed the formation of helical J-type aggregates. Helical stacks were also observed by using oligo(*p*-phenylenevinylene) carrying two thymines. In a similar approach, a single strand of oligodeoxythymidine was used in order to form three-fold hydrogen bonding with complementary diaminotriazines or diaminopurine guest dye molecules.^{404–409} Notably, the chirality

of the DNA template was transferred to the templated guest molecules into supramolecular helical structures.

4.1.2. Zeolites

Zeolites are framework silicates made of interlocking tetrahedrons of SiO_4 and AlO_4 , with each Al contributing with a negative charge compensated with cations (such as Na^+ , Ca^{2+} and others). For example, Zeolite L contains one-dimensional channels that run through the whole crystals, have an opening of around 0.7 nm and a center-to-center distance between channels of around 1.8 nm.^{410,411}

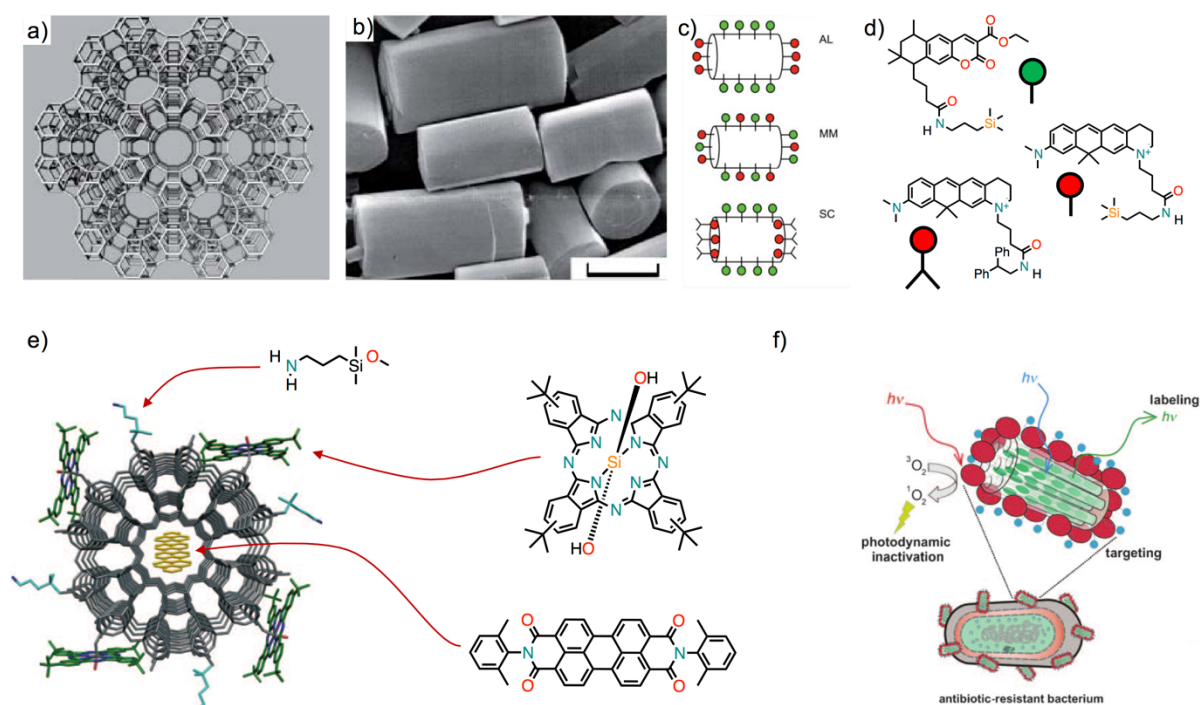


Figure 4.1.6. a) Zeolite crystal with parallel channels that run through the crystal; b) scanning electron microscopy image of zeolite crystals; c) schematic representation of bifunctional zeolite systems; d) chemical structure of the dyes; e) model of connection of the functional groups to the zeolite framework along with chemical structures of the indicated with the arrow on the zeolite; f) schematic representation of the zeolites used to target, label, and photoinactivate antibiotic-resistant bacteria.

Zeolites were found to include into their channels neutral or cationic molecules and can be further functionalized externally or internally with silane chemistry.⁴¹² Exploiting the orthogonal functionalization protocols for zeolites, green- and red-emitters were placed on the coat and at the

channel entrances, respectively (**Figure 4.1.6a-d**).⁴¹³ In this way, no unwanted energy transfer processes were observed, due to enough spatial separation between the dyes. Tri-functional zeolites were also prepared (**Figure 4.1.6ef**).⁴¹⁴ At first, a green-luminescent dye (*N,N'*-bis(2,6-dimethylphenyl)perylene-3,4,9,10-tetracarboindimide) was inserted in the zeolites channels by gas-phase inversion. The nanocrystals were then functionalized with a Si(IV) phthalocyanine by axial attachment of Si to the hydroxy groups present on the zeolites surfaces. Finally, the zeolites were coated with amino groups, since it was previously observed that bacteria adhere to amino-carrying zeolites. By exciting the phthalocyanine at 670 nm, an intense emission characteristic of ¹O₂ phosphoresce (at 1275 nm) was observed. The tri-functional zeolite was used for photodynamic inactivation of bacterial cells and was found to completely inactivate *E. coli* after 2 hours.

4.1.3. Carbon Nanotubes

In the carbon allotropes family, carbon nanotubes (CNTs) are conceptually made from rolled up graphene sheets. CNTs have attracted much attention due to their electronic properties,^{415,416} chemical and thermal stability,^{417,418} together with extremely high tensile strength and elasticity,^{419,420} to name a few. However, one of the major drawbacks is their tendency to strongly aggregate, making them very hard to process and use in applications. However, the functionalization of CNTs offers the opportunity to combine the properties of CNTs with those of other classes of materials for the desired application. To this end, two general strategies have been exploited: *i*) covalent functionalization or derivatization of oxygenated functions introduced by oxidative treatment or the functionalization of the sp² framework; *ii*) non-covalent functionalization through supramolecular interaction with other chemical species. While the first one transforms sp² carbons into sp³ and therefore interrupts conjugation, the latter one does not interfere with the π-electron system.

4.1.3.1. Surfactants and Biomolecules

As-produced CNTs usually display a distribution both in diameter and in chirality. Moreover, their separation and characterization is troublesome due to their tendency to aggregate into bundles, due to van der Waals tube-tube interactions. Surfactants are a non-aggressive and effective method for debundling nanotubes, dispersing and suspending them through supramolecular interactions, without affecting their electronic properties.⁴²¹ Anionic sodium dodecylsulfate (SDS) or nonionic triton (TX100) were among the first surfactants used to create colloidal suspensions.⁴²² Soon after, systematic studies of dispersion efficiency for nanotubes with various surfactants were reported by

preparing the dispersions with high-shear mixing, ultrasonication and followed by ultracentrifugation.⁴²³ Among the ionic surfactants investigated, sodium dodecylbenzenesulfonate (SDBS) gave the most resolved spectral features, while for non-ionic systems, higher molecular weight surfactants were found to suspend more SWNT material. In another set of experiments, with suspensions prepared under milder condition, *i.e.* gentle stirring for 3 days followed by centrifugation, bile salts (*e.g.* DOC, sodium deoxycholate) were found to be particularly effective in dispersing individual nanotubes.⁴²⁴ While numerous reports found efficient debundling and dispersion of nanotubes for quite a few surfactants, the supramolecular organization of the surfactants round the nanotubes has been under debate. However, it is believed that the organization is dependent on the surfactant concentration.⁴²⁵ Specifically, at low surfactant concentration, the micelles should interact dynamically and spread randomly around the tube, while with increasing concentration the micelle start to absorb and cover the nanotube.

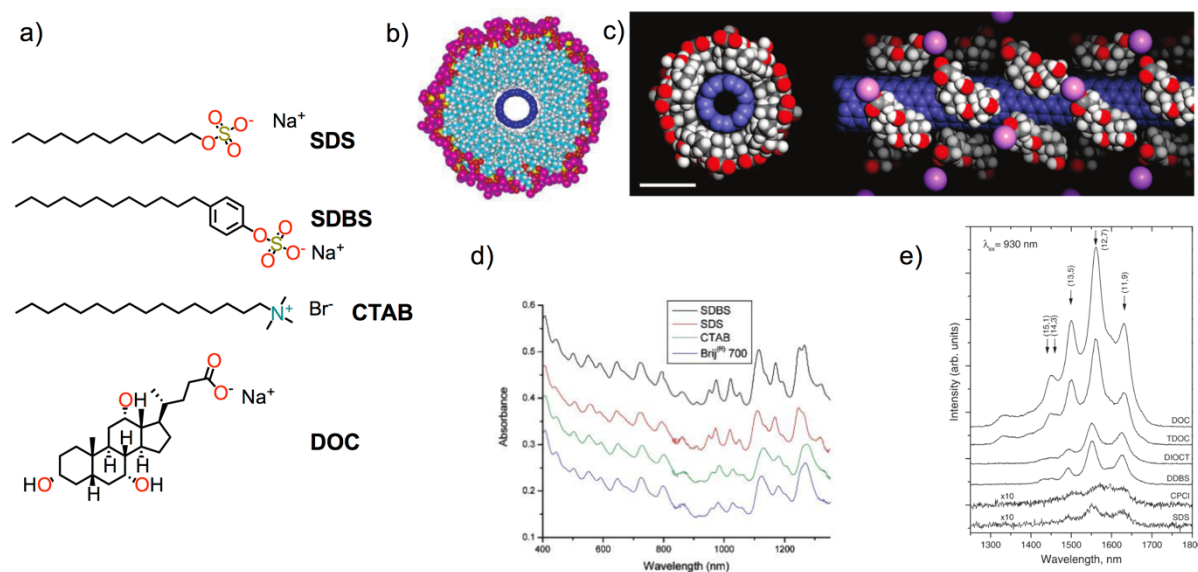


Figure 4.1.7. a) Commonly used surfactants for dispersing carbon nanotubes; b) cross-section model of individual nanotube in a cylindrical SDS micelle;⁴²⁶ c) arrangement of sodium cholate around CNTs;⁴²⁷ d) absorption spectra of nanotubes suspended in selected surfactants;⁴²⁷ e) fluorescence spectra (930 nm excitation) for CNTs dispersion in selected surfactants.⁴²⁴

Biomolecules were also found to be efficient in preparing high-quality dispersion of nanotubes, particularly DNA. At first, the ssDNA was found to wrap helically around the DNA, presumably with

the aromatic nucleobases stacking on the nanotube and the negatively rich phosphate backbone exposed to the water, ensuring the efficient suspension in water.⁴²⁸

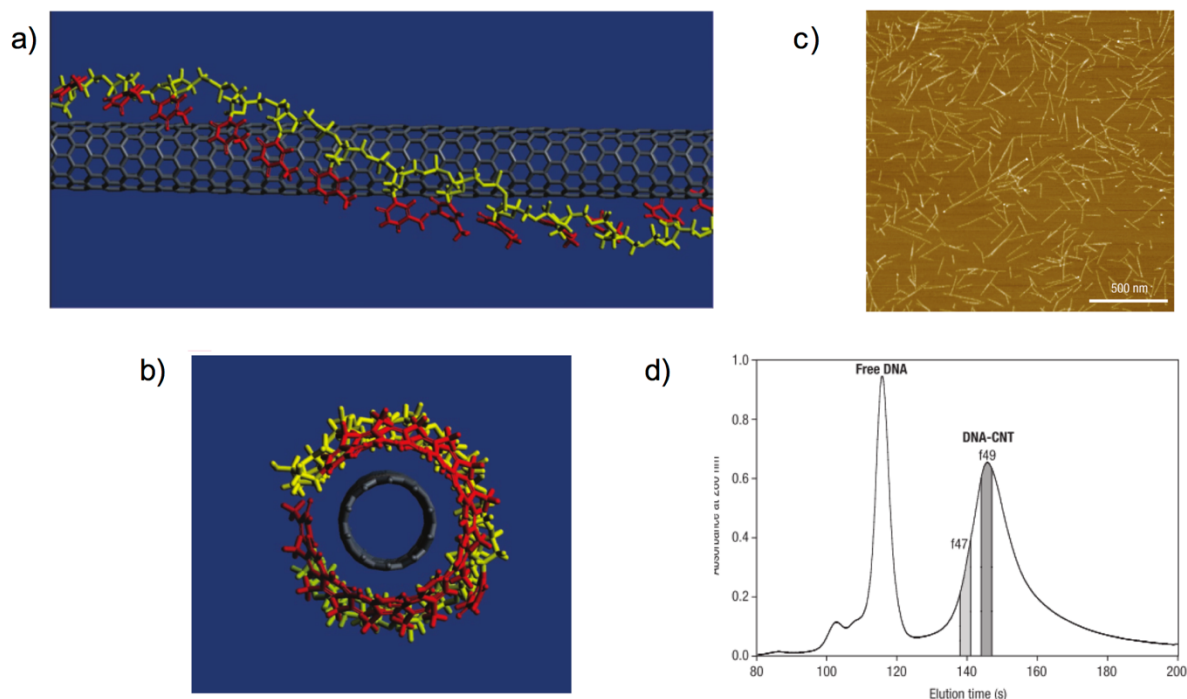


Figure 4.1.8. ab) Carbon nanotubes wrapped by a poly(T) sequence; c) AFM image of a DNA-CNT fractions and d) separation of free DNA and DNA-CNT by anion exchange chromatography.⁴²⁸

The individualization and dispersion of CNTs is important for their separation, with different approaches reported for sorting in length,^{429–431} diameter,^{432–434} chirality,^{435–437} semiconducting/metallic character^{438,439} and handedness.^{440,441} The dispersed CNTs with surfactant or DNA, exposing a negative charge on the surface, were further exploited in order to prepare donor-acceptor hybrids. CNTs wrapped with ssDNA were ion-paired with a Zn(II) porphyrin carrying four pyridinium peripheral groups and the newly assembled donor-acceptor system showed photoinduced electron transfer from the porphyrin to the CNT.⁴⁴² A similarly designed system was also shown to harvest light and generate photocurrent.⁴⁴³

4.1.3.2. Anchoring Group - Pyrenes

Pyrene and its derivatives, as polycyclic aromatic molecules, have been prepared and used as anchors for the nanotube sidewalls to bring new functionalities to the nanotubes. Common strategies used in

preparing supramolecular CNTs/pyrene/chromophore composite systems are depicted in **Figure 4.1.9**.

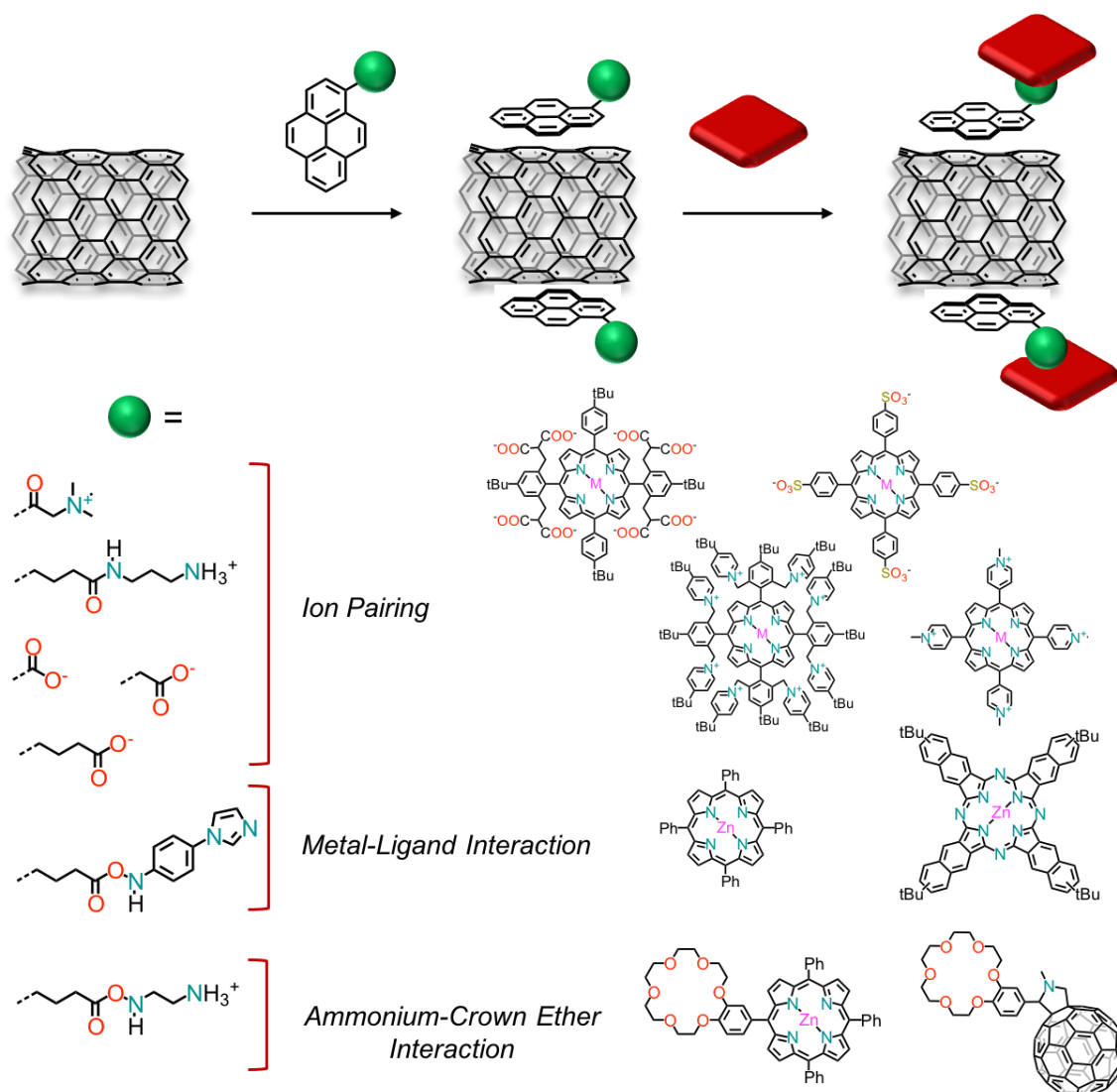


Figure 4.1.9. Common strategies for preparing non-covalent CNTs/pyrene/chromophore composite systems.

Pyrenes containing polar heads were found to disperse efficiently CNTs in H_2O , with the aromatic system interacting with the nanotube walls and the polar head (trimethylammonium group) ensuring the solubility in H_2O .^{444,445} This positively charged CNT/pyrene hybrid was then exploited to anchor chromophores such as negatively charged porphyrins and polythiophenes.^{446–449} This composite CNTs/pyrene/porphyrin material showed fast intrahybrid electron transfer with creation of long-lived radical-ion pairs. Similar assemblies could be achieved by inverting charges, *i.e.* using pyrene carboxylic acids derivatives and positively charged porphyrins.^{450,451}

Apart from creating assemblies by electrostatic interactions, other supramolecular systems have been constructed through metal-ligand interactions or crown ether/ammonium cation recognitions. CNTs dispersed with pyrene imidazole derivatives were used to axially coordinate Zn(II) porphyrins or phthalocyanines in solution.⁴⁵² Efficient quenching of the singlet excited states of porphyrins was also achieved by using pyrene derivatives carrying an ammonium cation and porphyrins equipped with benzo-18-crown-6 ether.⁴⁵³

Addition of new moieties through pyrene-nanotube π - π interactions was also realized by covalently linking the chromophore to the pyrene core and then dispersing the carbon nanotubes. Numerous examples involving, for example, porphyrins,⁴⁵⁴⁻⁴⁵⁶ phthalocyanines,⁴⁵⁷ tiophenes,⁴⁵⁸ fullerenes,⁴⁵⁹ and others, were used to bring more robust pyrene-based derivatives with better control of the final structures, even if each pyrene derivative had to be prepared independently.

4.1.3.3. Electron-Donor Molecules - Porphyrins and Other π -Conjugated Systems

Other polycyclic aromatic compounds have been used, *e.g.* anthracenes, phenanthrenes and coronenes, but were found generally less efficient than pyrenes in dispersing nanotubes.^{445,460,461}

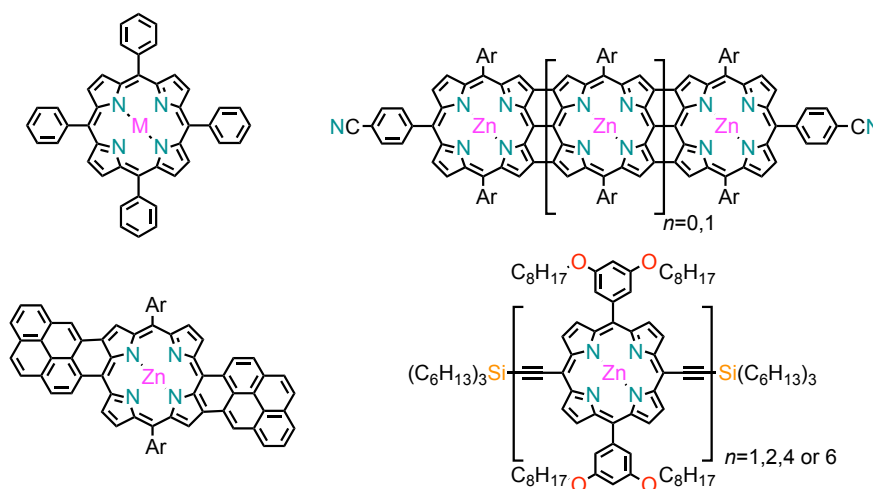


Figure 4.1.10. Porphyrin and their derivatives such as extended porphyrins, porphyrin tapes or porphyrin oligomers used for dispersion of carbon nanotubes.

Porphyrins were also found useful for dispersing carbon nanotubes. Tetraphenylporphyrin and other monomeric porphyrins were found to form π -stacking interactions with the nanotubes.⁴⁶²⁻⁴⁶⁶ However, simple porphyrin derivatives were not be as efficient in debundling and dispersing

nanotubes, thus novel methods^{466,467} or extended porphyrins⁴⁶⁸ or porphyrin oligomers were used (Figure 4.1.10).^{469,470} Other π -conjugated materials that were used to efficiently disperse carbon nanotubes include perylene bismides,^{471,472} tetrathiafulvalenes,^{473,474} oligo(*p*-phenylene ethynylenes),⁴⁷⁵⁻⁴⁷⁷ and alkylated fullerenes^{478,479} among others.

4.1.4. Carbon NanoDots

The large popularity of carbon nanostructures is due to fullerenes, carbon nanotubes and graphene. Thanks to the developments made in nanotechnology and in material synthetic methods, other materials joined the nanocarbon family. The latest member to join this class are Carbon NanoDots (CNDs), nanocarbons that comprise discrete, quasispherical nanoparticles with size below 10 nm.⁴⁸⁰ Since their accidental discovery during the purification of CNTs in 2004,⁴⁸¹ CNDs have emerged as very promising class of carbon nanomaterials. When compared to their ‘carbon cousins’, they possess even more intriguing properties and, with their fascinating photoluminescence, are attracting considerable attention. Labeled as ‘carbon nanolight’,⁴⁸² these small carbon nanoparticles have gradually become a rising star. Specifically, they can be promising substitutes to conventional semiconductor quantum dots (QDs), considered as superior fluorescent material over organic dyes, which toxicity is still a matter of debate.

One of their unique property is the tunable fluorescence emission.⁴⁸²⁻⁴⁸⁴ They afford multi-fluorescence colors under different excitation wavelengths. Although the fluorescence mechanism is complicated and further clarifications are needed, the excitation wavelength dependence is generally ascribed to effects from particles with different emissive sites on each CNDs.

Over the last decade a variety of synthetic methods in order to prepare CNDs have been explored.^{484,485} CNDs can be produced mainly from molecular precursors through ‘bottom-up’ approaches or by ‘top-down’ cutting routes. Many researchers are attempting to achieve high quality CNDs via simple, low-cost, green and efficient synthetic methods. Avoiding costly precursors, complex instrumental set-up, post-treatment or time-consuming procedures are definitively the main challenges in order to outperform the inorganic QDs. Solvothermal and hydrothermal synthesis are widely used due to their cheap and simple devices.^{484,485} However, they suffer of lengthy operational procedures and increasing efforts have been paid to high-energy technologies such as microwave (MW)-assisted techniques. Usually the quantum yields (QYs) are around 10 %, but they have been increased thanks to the recent advancements in synthetic methods.⁴⁸⁴ Further modifications to improve the fluorescent (FL)

performance are typically required and, the most common, include surface passivation or element doping.^{480,486,487} Nitrogen doping has been reported to give excellent optical properties and usually blue-shifted fluorescence, although usually introduction of nitrogen atoms requires harsh conditions.^{488,489} To overcome post-synthetic treatments, strategies such as the incorporation of passivation agents into the synthetic process were successfully adopted.⁴⁸⁴

Despite considerable advances, several challenges still remain and should be addressed in future works. To improve QYs so as to achieve highly controllable composition and structure, the development of reproducible and competitive synthetic methods is still needed.

Even if a plethora of applications are currently under investigation, many of them are still in their infancy. Features such as water solubility, biocompatibility, low cytotoxicity and *in vivo* toxicity were responsible since the beginning for bioapplications of CNDs.^{490,491} They are now the most explored and, except strong fluorescence, their photostability and high two-photon cross section in the therapeutic near-infrared region give clear advantages for *in vivo* bionanotechnology.

Nevertheless, many efforts have been done in their application to lighting and energy related fields.⁴⁹² CNDs also own other properties such as photoinduced electron transfer property, which extend their applications in light energy conversion and related applications. CNDs can act either as electron donors or as electron acceptors depending on the counterpart. Pioneering work showed that CNDs luminescence is quenched by electron acceptors, such as 4-nitrotoluene and 2,4-dinitrotoluene, or the electron donors, such as *N,N*-diethyl-aniline, through an electron transfer quenching mechanism.⁴⁹³ CNDs-based hybrids are beginning to emerge, for example, supramolecular nanohybrids SWCNTs/CNDs,⁴⁹⁴ PBI/CNDs,⁴⁹⁵ graphene oxide/CNDs⁴⁹⁶ have been found to feature remarkable charge-transfer activity, suggesting that CNDs are a valuable building-block for the design of electro- and photo-active hybrids for optoelectronic devices.

4.1.5. Aim of the Project

The two main objectives in this project are governed by the type of carbon-based templates, CNTs and CNDs and the knowledge we have of these two classes of carbon nanomaterials (**Figure 4.1.11**). CNTs can be functionalized in a supramolecular fashion and this achieves a dual goal: easier processability by improving their dispersibility as well as bringing new functionalities depending on the molecules used. Although this approach has been extensively employed in order to arrange organic

materials around the nanotube walls, herein we want to further exploit the response of CNTs to the magnetic fields in aligning their long-axis parallel to the field direction (**Figure 4.1.12**).

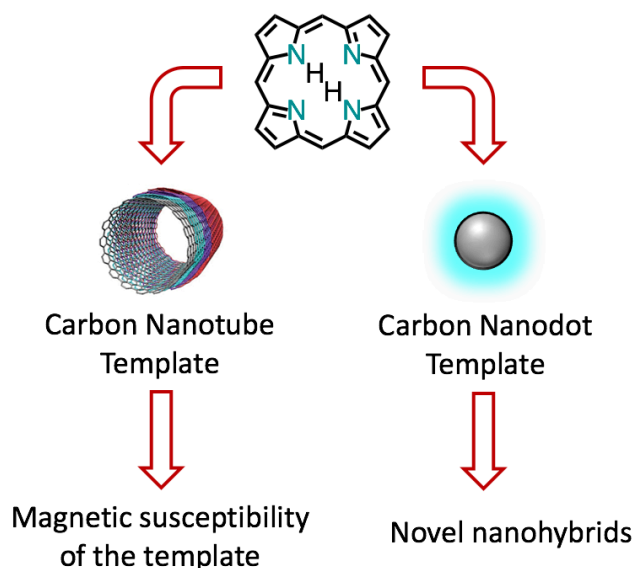


Figure 4.1.11. Schematic approach in template assisted assembly of porphyrin derivatives in this chapter.

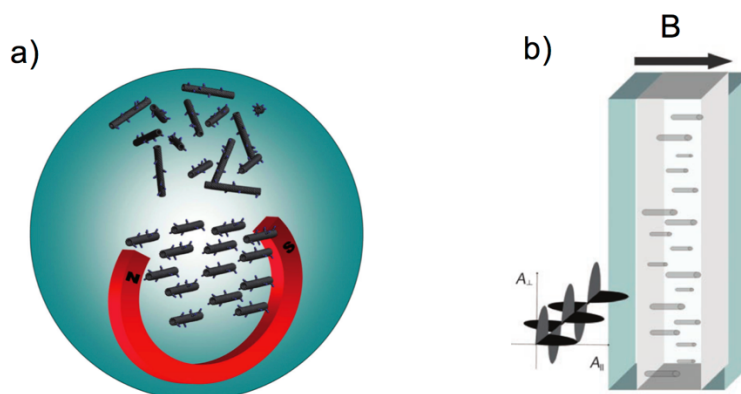


Figure 4.1.12. a) Schematic representation of aligned carbon nanotubes by magnetic fields and b) nanotubes align parallel to the magnetic field (B), which is at right angles to the incident light.⁴⁹⁷

Thus, by functionalizing nanotubes with photoactive chromophores, such as porphyrins, we should be able not only to arrange the chromophores around the nanotubes walls but also align them preferentially in one direction, achieving a high degree of order in our system. Furthermore, we envisage using organogels in order to preserve the information of our hybrid system even when the magnetic field is turned off. Although the magnetic susceptibility of carbon nanotubes depends on their helicity and on the angle between the magnetic field and the tube main axis, in any case the

magnetic susceptibility anisotropy is higher than zero, thus sufficient to direct their alignment in a magnetic field.

In the second part, a different approach is required since carbon nanodots are the latest class of carbon-based nanomaterials and their optical and electronic properties have not yet been explored as in the case of carbon nanotubes. Additionally, since this is a new material, reproducible, reliable and scalable methods first need to be developed before exploring their properties and potential applications. Therefore, we propose a novel synthetic method using microwave irradiations of cheap and abundant starting materials such as amino acids (arginine) and dopants (ethylenediamine). This material first needs to be thoroughly characterized before being functionalized in order to probe its properties in hybrid materials. Subsequently, we propose both a covalent and non-covalent approach in order to arrange chromophores, which (opto)electronic properties are well understood, around these nanoparticles.

4.2. Magnetically Aligned Carbon Nanotubes as Templates

The chemical structures, along with the schematic representation of the formation of the hybrid material is depicted in **Figure 4.2.1**.

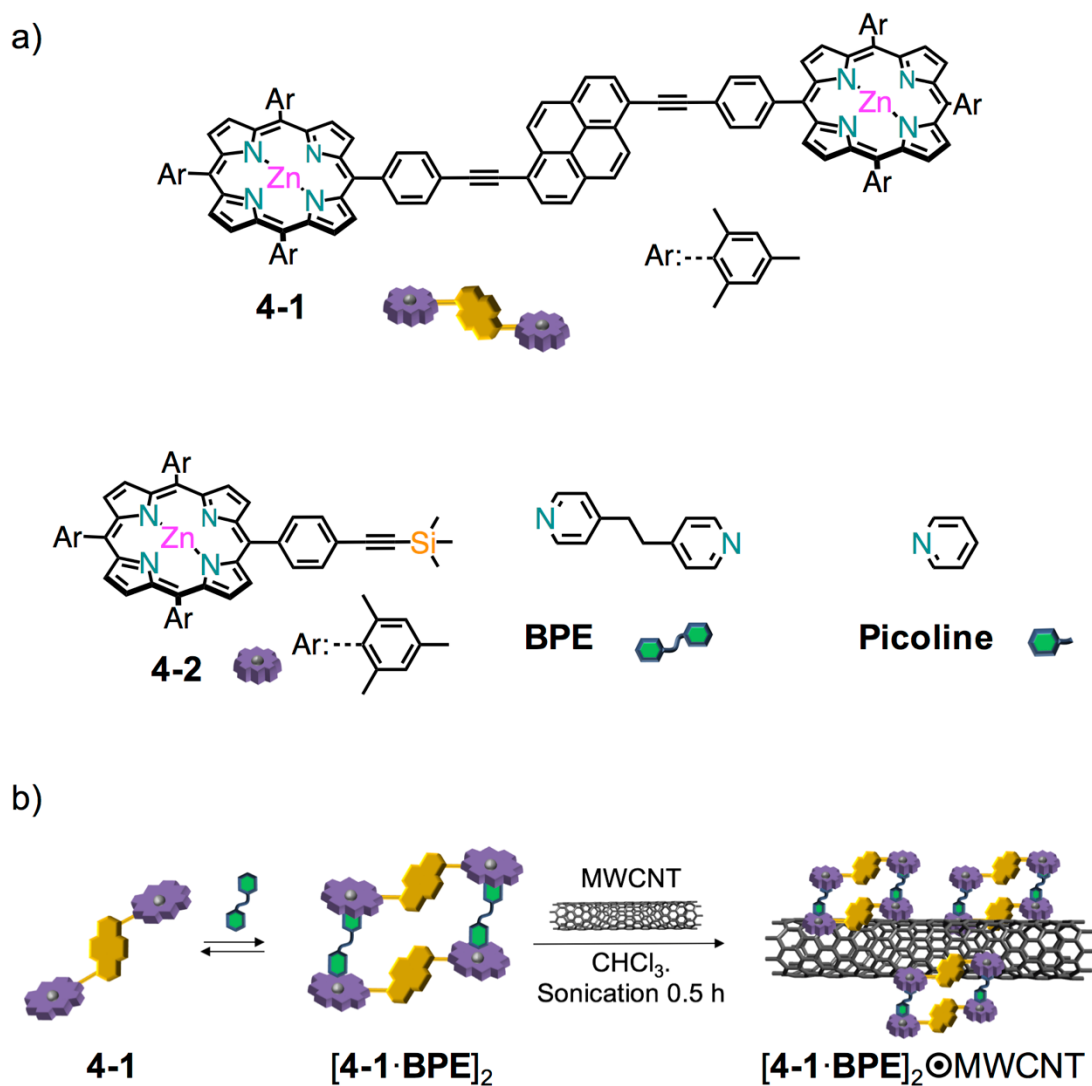
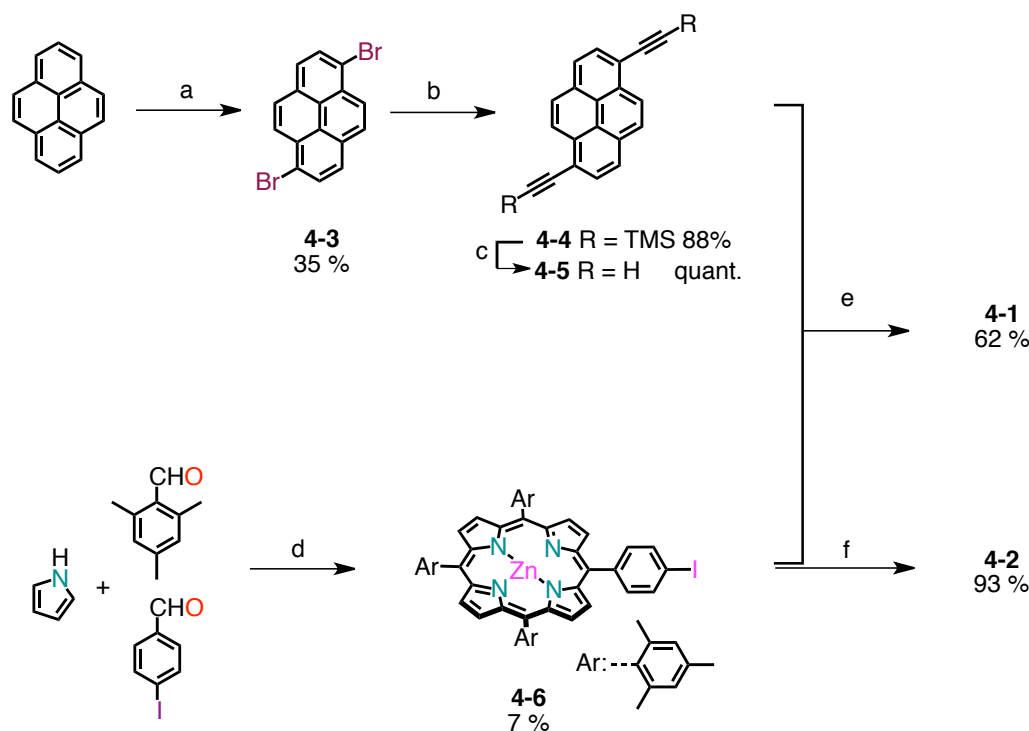


Figure 4.2.1.a) Chemical structures along with cartoon representation of the Zn(II) porphyrins and ligands used in this section; b) schematic representation of porphyrin array/carbon nanotube hybrid.

4.2.1. Synthesis and Characterization

The synthetic pathway undertaken to obtain compounds **4-1** and **4-2** is reported in **Scheme 4.2.1**.



Scheme 4.2.1. Synthetic scheme used in order to prepare compounds **4-1** and **4-2**. Reagents and conditions: a) Br_2 , CCl_4 , r.t.; b) TMSA, $\text{Pd}(\text{PPh}_3)_2\text{Cl}_2$, PPh_3 , CuI , $\text{THF}/\text{PhCH}_3/\text{Et}_3\text{N}$, 120°C , 1 h, μW irradiation; c) K_2CO_3 , $\text{CHCl}_3/\text{MeOH}$, r.t.; d) 1. $\text{BF}_3\cdot\text{Et}_2\text{O}$, CHCl_3 , 1 h, r.t.; 2. DDQ , 1 h, r.t.; 3. Et_3N , 15 min, r.t.; 4. $\text{Zn}(\text{OAc})_2\cdot 2\text{H}_2\text{O}$, $\text{CHCl}_3/\text{MeOH}$, r.t.; e) $\text{Pd}_2(\text{dba})_3$, AsPh_3 , $\text{PhCH}_3/\text{Et}_3\text{N}$, r.t.; f) TMSA, $\text{Pd}_2(\text{dba})_3$, AsPh_3 , $\text{PhCH}_3/\text{Et}_3\text{N}$, r.t.

Compound **4-1** is comprised of a central aromatic core, 1,6-disubstituted pyrene, and two peripheral Zn(II)-porphyrin units. Moreover, the Zn(II)-porphyrin bears three mesityl units around its core in order to avoid possible π - π interactions with the MWCNTs. Bromination of pyrene yielded 1,6-dibromo pyrene **4-3** that was subsequently reacted with TMSA under Pd-catalyzed conditions and finally the TMS groups was removed in basic conditions. The iodophenyl-porphyrin **4-6**, on the other hand, was prepared through a mixed aldehyde condensation under Lindsey conditions. The mixture of porphyrins that was obtained proved to have very little difference in polarity to be separated on SiO_2 column chromatography and therefore the porphyrin mixture was reacted with $\text{Zn}(\text{OAc})_2\cdot\text{H}_2\text{O}$. The difference in polarity, albeit low, was enough to separate the mixture with several column chromatographies. The two synthons, pyrene and porphyrins, were connected with a Pd(0)-catalysed copper-free Sonogashira cross-coupling reaction in good yield. Suitable crystals for X-ray crystallography were grown by vapor diffusion of MeOH into a CHCl_3 solution of **4-1**: the 3D structure in the

crystal is shown in **Figure 4.2.2**. Additionally, the monotopic porphyrin **4-2**, was analogously prepared through Pd(0)-catalysed cross-coupling reaction between porphyrin **4-6** and trimethylsilylacetylene in excellent yield. Notably, solid state structure of porphyrin **4-2** (obtained from slow evaporation of a pyridine solution) showed that the axial coordination with the Zn(II) is possible.

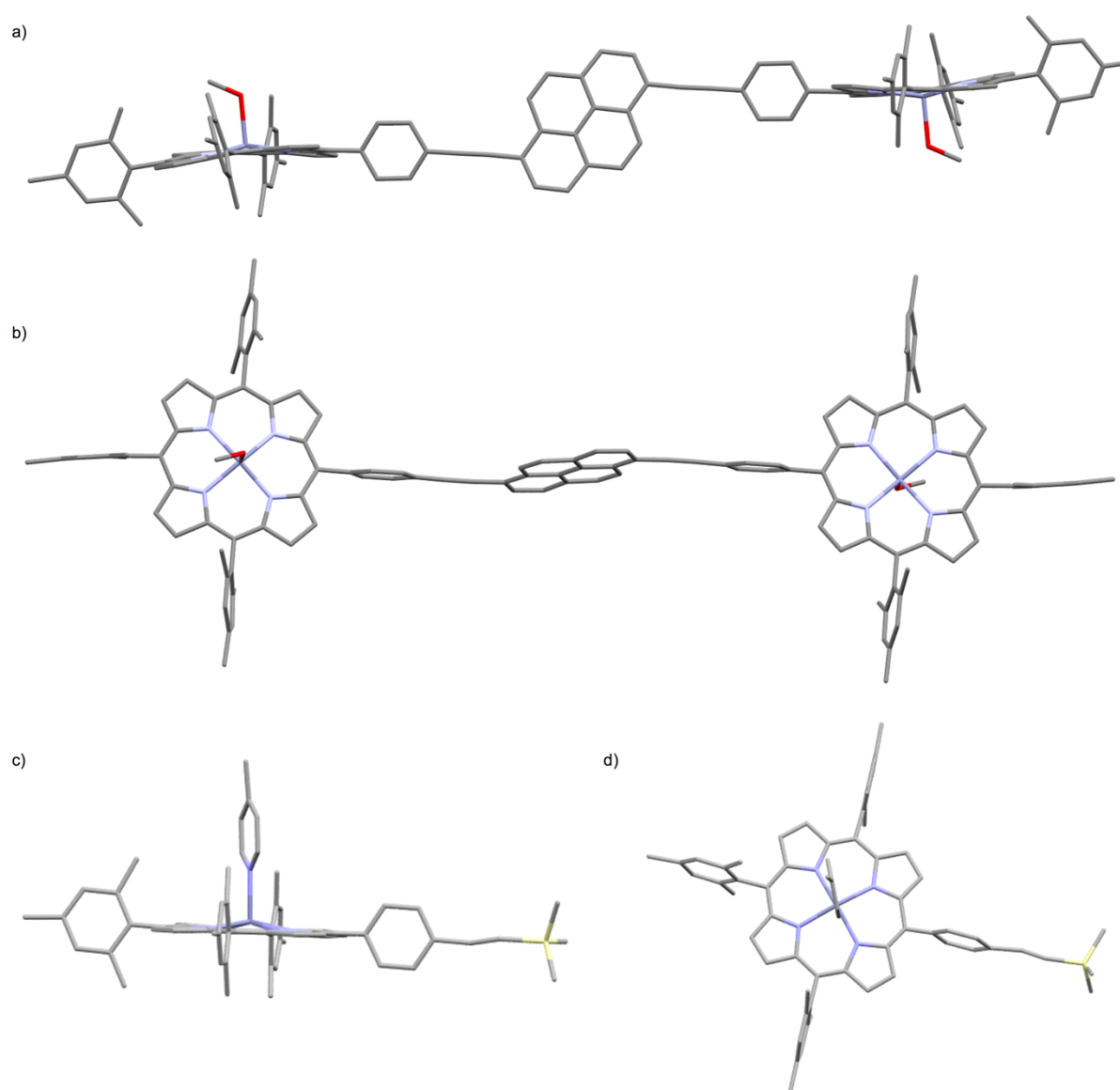


Figure 4.2.2. X-ray structures of a) side and b) top view of compound **4-1** (solvent molecules were omitted) and c) side and d) top view of porphyrin **4-2**.

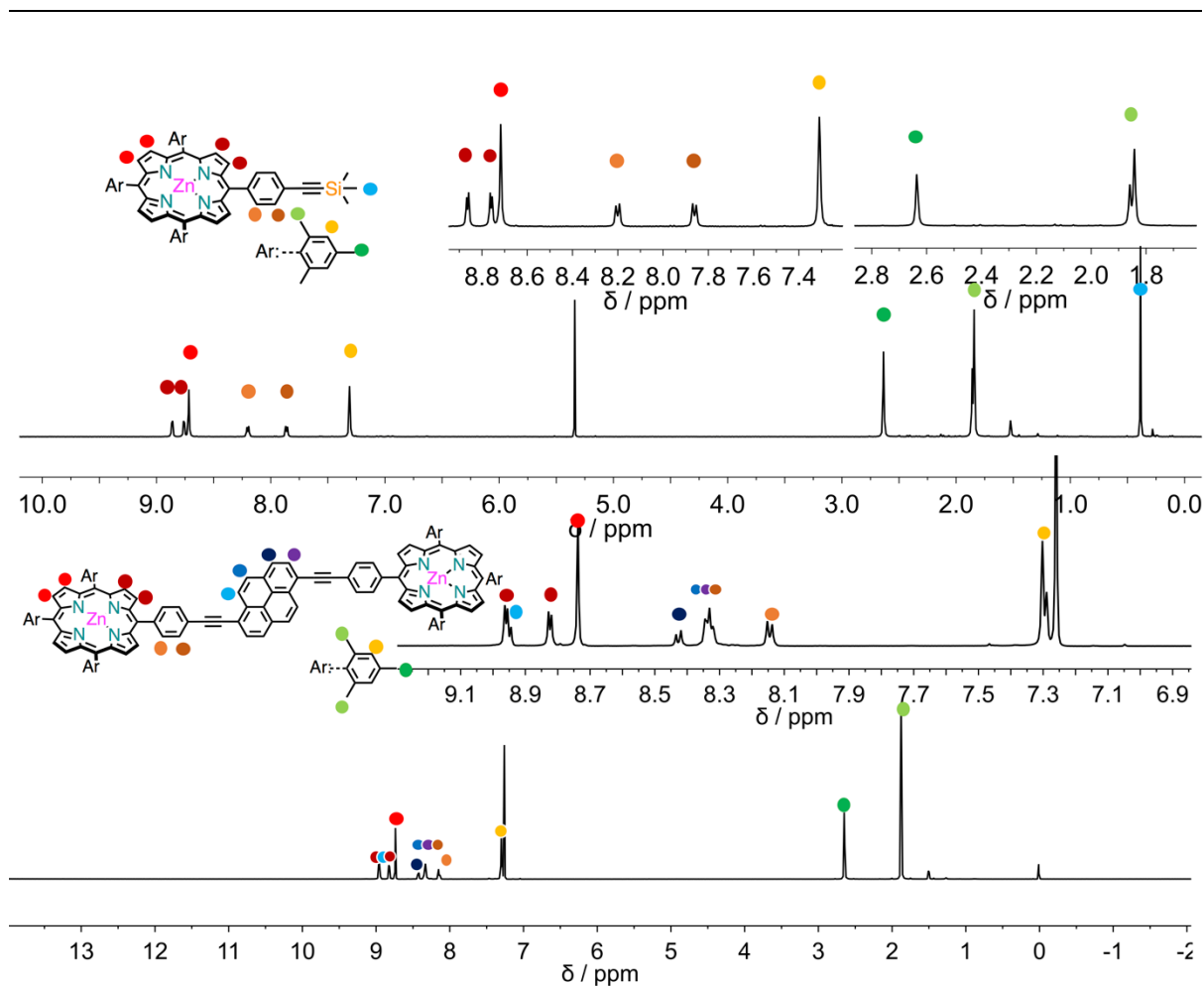


Figure 4.2.3. $^1\text{H-NMR}$ spectra (500 MHz, 298 K) for compound **4-2** (CD_2Cl_2) and compound **4-1** (CDCl_3).

4.2.2. Porphyrin Array Formation

First of all, we set to study the formation of the porphyrin array $[\mathbf{4-1}\cdot\text{BPE}]_2$ in a CHCl_3 solution. While the coordination chemistry of Zn(II) porphyrins has been studied in detail,^{498,499} there are no reports on the influence of mesityl peripheral groups on the metal coordination ($\text{N}\cdots\text{Zn}$). In order to appreciate the impact of the peripheral groups on the coordination, we performed an UV-Vis titration ($c = 3.0 \times 10^{-6}$ M, CHCl_3 , 298 K) of porphyrin **4-2** with **4-methylpyridine (Picoline)** (**Figure 4.2.4a**). The progressive addition of **Picoline** into a solution of **4-2**, resulted in a bathochromic shift of the Soret band from 421 to 431 nm. Non-linear global regression analysis, gave a microscopic binding constant $K_m = 1.8 \times 10^4 \text{ M}^{-1}$. This is in great agreement with the value obtained by $^1\text{H-NMR}$ titration for the same system ($K_m = 1.6 \times 10^4 \text{ M}^{-1}$, **Figure 4.2.4b**).

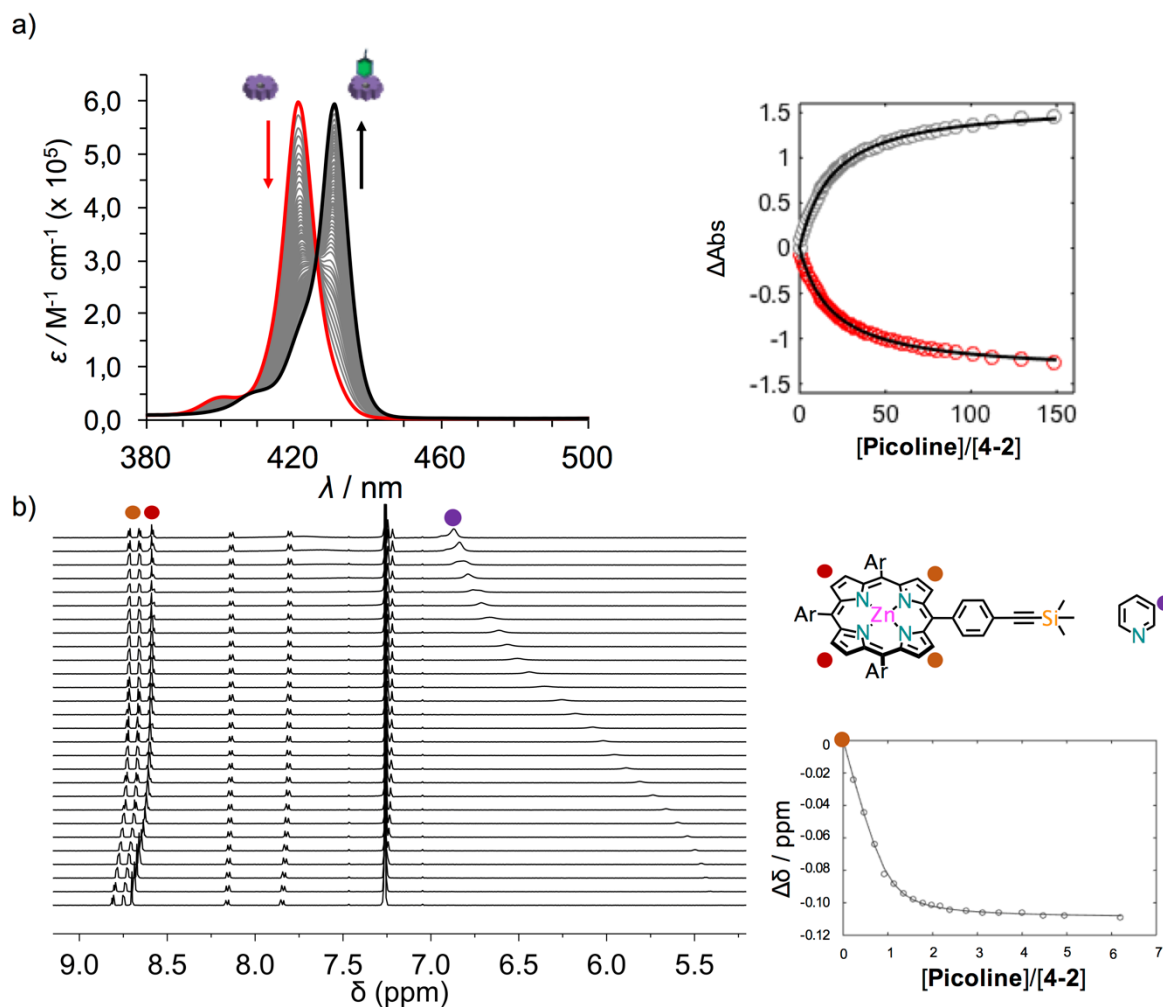


Figure 4.2.4. a) UV-Vis titration data (CHCl_3 , 298K) of compound **4-2** ($c = 3.0 \times 10^{-6} \text{ M}$) with different molar amounts of **Picoline** (from 0 to 150 equivalents); on the right the variation in absorbance at 421 nm (red circles) and 431 nm (black circles) plotted against the molar ratio with the corresponding 1:1 non-linear least-square fitting; b) $^1\text{H-NMR}$ titration experiment (CHCl_3 , 298K) of compound **4-2** ($c = 0.9 \times 10^{-3} \text{ M}$) with different molar amounts of **Picoline** (from 0 to 6 equivalents), on the right the 1:1 non-linear least-square fitting.

Then, variable-temperature UV-Vis and concentration-dependent $^1\text{H-NMR}$ experiments were performed for compound **4-1** that showed no appreciable self-aggregation phenomena (**Figure 4.2.5**). Subsequently, in order to prove the interaction between compound **4-1** and **BPE** we performed an UV-Vis titration ($c = 1.8 \times 10^{-5} \text{ M}$, CHCl_3 , 298 K) following the Q bands (**Figure 4.2.6a**). A bathochromic shift (from 550 to 565 nm) accompanied with a hypochromic effect and a second bathochromic shift (from 590 to 605 nm) together with a hyperchromic effect, were observed, confirming the $\text{N} \cdots \text{Zn}$ coordination. To gain further insights into the structural

changes upon the binding of the ligand to compound **4-1**, $^1\text{H-NMR}$ of a 1:1 mixture ($c = 1.1 \times 10^{-3} \text{ M}$, CHCl_3 , 298 K) was performed (**Figure 4.2.6b**). The most obvious change upon addition of 1 equiv. of **BPE** is the appearance of three additional peaks at 5.05, 3.05 and 1.25 ppm, attributed to the bispyridyl protons that show a significant upfield shift (compared to the free **BPE**) due to the combined anisotropy of the porphyrin ring current. Changes were also observed in the chemical shift and multiplicity of the porphyrin protons: an upfield shift for all β -pyrrolic signals of around 0.15 ppm was observed.

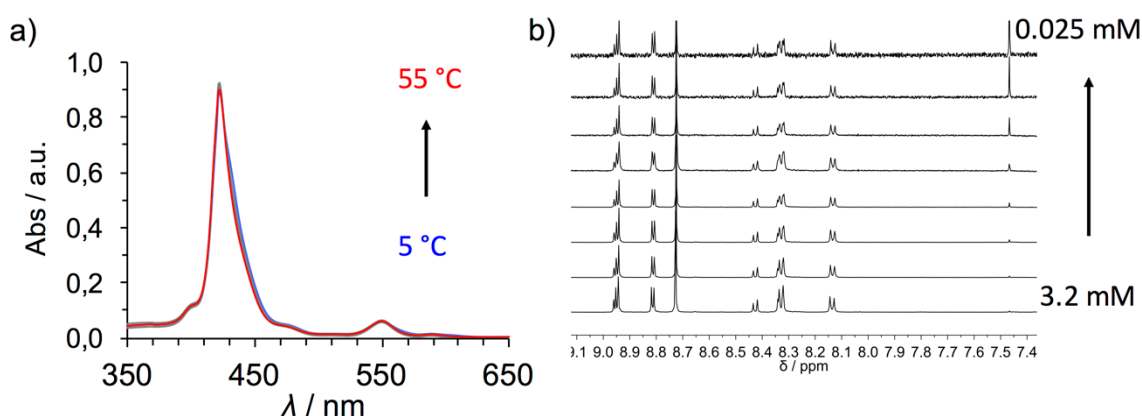


Figure 4.2.5. UV-Vis temperature experiment (CHCl_3) and $^1\text{H-NMR}$ dilution experiment of compound **4-1** alone in order to investigate its self-aggregation.

These changes prompted us to perform $^1\text{H-NMR}$ titrations ($c = 1.1 \times 10^{-3} \text{ M}$, CHCl_3 , 298 K, **Figure 4.2.6cd**) in order to elucidate the structural changes that occur upon binding. The addition from 0 to 1 equivalent (eq.) of **BPE** showed the upfield shift of the α , β and $-(\text{CH}_2)_2-$ signals of the ditopic pyridine ligand at 5.05, 3.05 and 1.25 ppm. Addition of more than 1 eq. of ligand showed the progressive downfield shift of the ligand signals toward those of the free species, indicating a fast equilibrium. More useful structural information was obtained by observing the evolution of β -pyrrolic signals upon addition of the ligand. From 0 to 1 eq. of **BPE**, the β -pyrrolic protons showed a progressive upfield shift and an increased multiplicity due to the diminished symmetry of compound **4-1** upon coordination. Addition of more than 1 eq. of the ligand maintained the increased multiplicity of the β -pyrrolic signals, but a downfield shift was observed. The experimental data in **Figure 4.2.6d** are diagnostic of a closed 2:2 sandwich that progressively moves toward the $[\text{1} \cdot (\text{BPE})_2]$ complex.^{500,501} Unfortunately,

precipitation of the complex, which occurs upon progressive addition of ligand to the solution made it impossible to obtain a good fit (Figure 4.2.6d, Figure 4.2.6c note the baseline changes even if n scans remains constant).

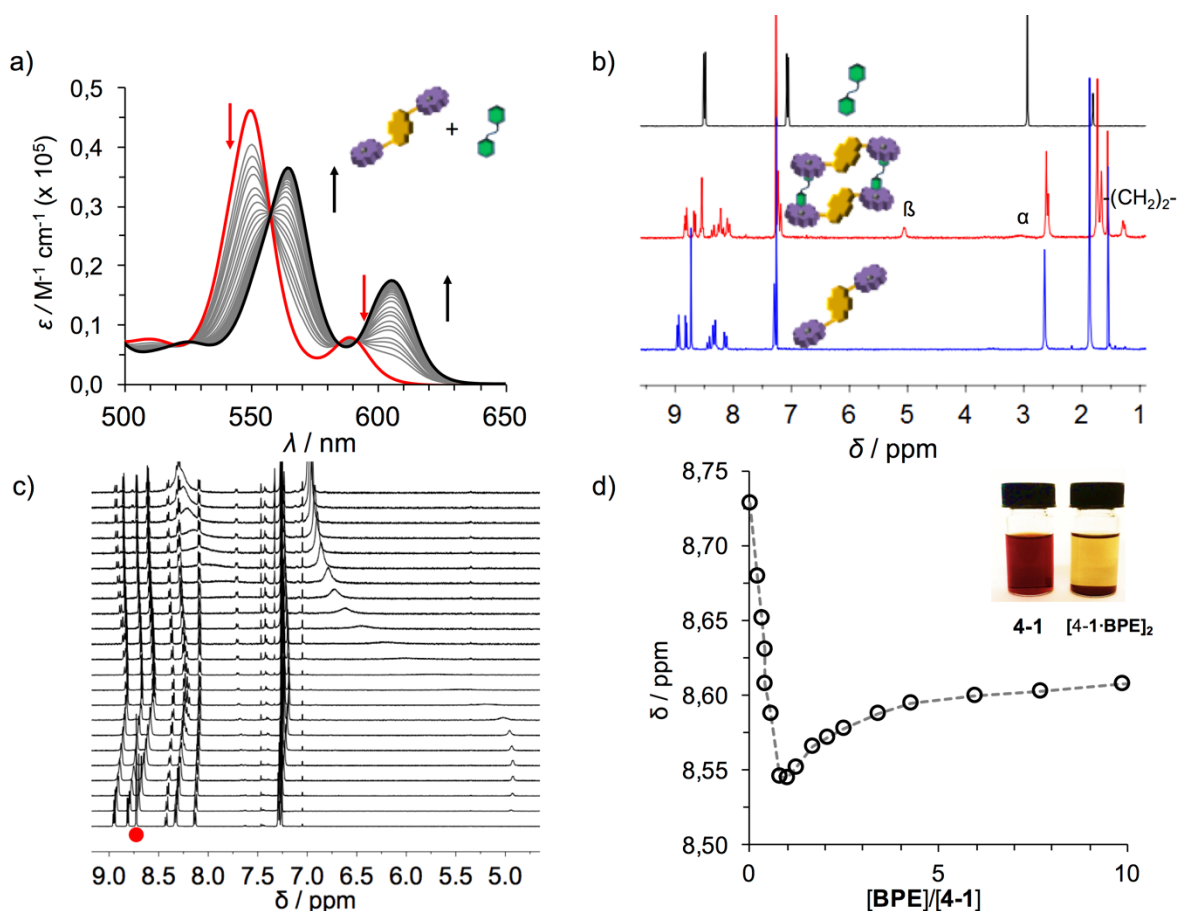


Figure 4.2.6. a) UV-Vis titration data (CHCl_3 , 298 K) of compound **4-1** ($c = 1.8 \times 10^{-5} \text{ M}$) with different molar amounts of **BPE** (from 0 to 36 equivalents); b) $^1\text{H-NMR}$ (CDCl_3 , 298 K, $c = 1.1 \times 10^{-3} \text{ M}$) of **BPE** (top), compound **4-1** (bottom) and their 1:1 mixture (middle), α , β and $-(\text{CH}_2)_2-$ indicate the signals of complexed **BPE**; cd) $^1\text{H-NMR}$ (CDCl_3 , 298K) titration of compound **4-1** ($c = 1.1 \times 10^{-3} \text{ M}$) with **BPE**, experimental data for β -pyrrole protons ppm shift against **BPE** equiv.; the grey line is intended as guide for the eye; inset shows a solution of **4-1** before (left) and after (right) the titration experiment; inset shows a $1.1 \times 10^{-3} \text{ M}$ solution of **4-1** before (left) and after (12 h, right) the titration experiment.

In order to further characterize the structure of the coordination complex, Diffusion-Order Spectroscopy (DOSY) measurements of solution containing the single components or the 1:1 mixture were performed (Figure 4.2.7). This powerful technique has become the method of choice for multi-component systems in order to gain insights of their effective size and

shape.^{364,365} In this context, diffusion NMR spectroscopy would help us to determine the species in solution even if some precipitate is formed.

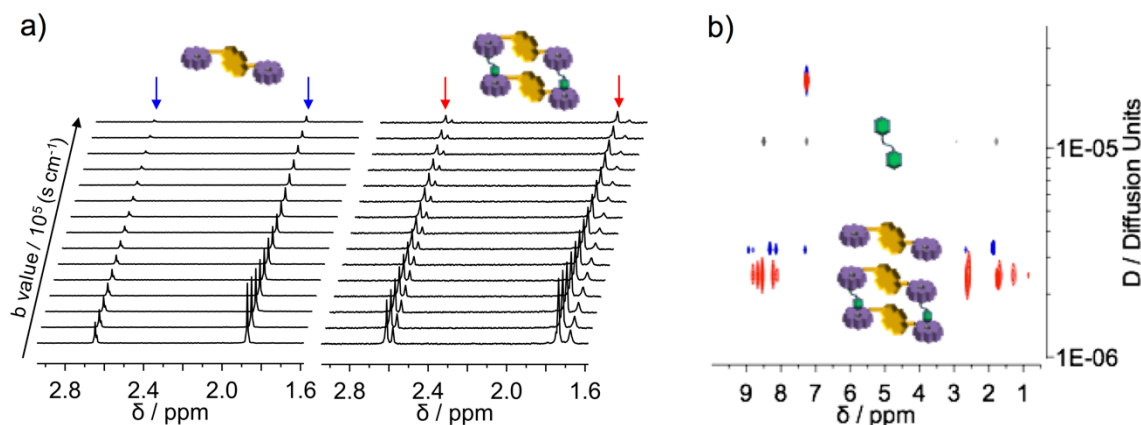


Figure 4.2.7. DOSY investigation a) stack plot showing the signal decays as a function of gradient strength (G) for compounds **4-1** and $[4-1.BPE]_2$; b) overlay of three 2D-DOSY experiments – **BPE** (black), compound **4-1** (blue) and $[4-1.BPE]_2$ (red).

The diffusion coefficient (D_f) of the species showed a slightly decrease of the D_{exp} of a 1:1 mixture when compared to compound **4-1** alone (**Figure 4.2.7**). This observation alone would exclude the formation of oligomeric/polymeric species in solution. Additional analysis of the DOSY data allowed us to compare the D_f with the respective molecular weights (MW). For rod-like species, such as those considered here, the ratio of the diffusion coefficients for two different molecular species (D_1/D_2) is inversely proportional to the square root of the ratio of their molecular weights (M_2/M_1):^{502,503}

$$\frac{D_1}{D_2} = \sqrt[2]{\frac{M_2}{M_1}}$$

Thus, by comparing these ratios, as reported in **Table 4.2.1** and **Figure 4.2.8**, we can confirm the formation of $[4-1.BPE]_2$ in solution. Moreover, the NMR diffusion coefficients allowed us to obtain the hydrodynamic radius (r_h), through the Stokes-Einstein equation (**Figure 4.2.8**, **Table 4.2.1**), which was in great agreement with its size and shape.

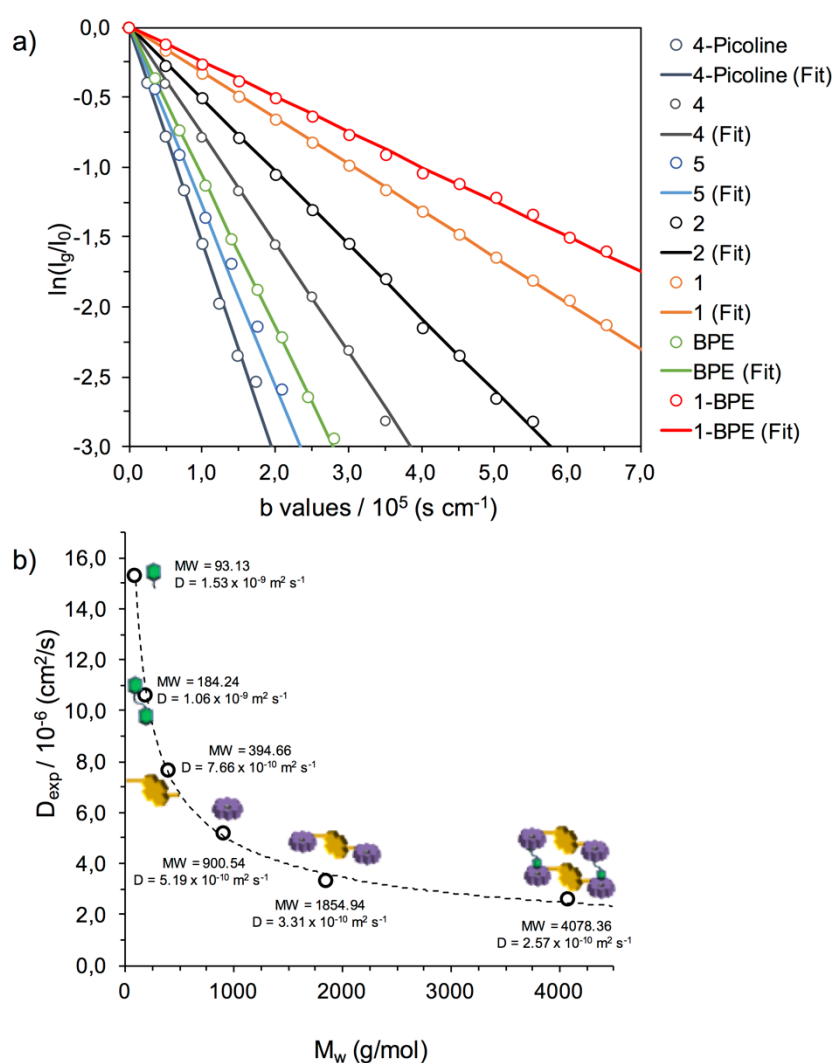


Figure 4.2.8. a) Normalized signal decays ($\ln(I/I_0)$) versus the diffusion weighing (b values) of representative peaks of **BPE** (black), **4-1** (blue) and **[4-1.BPE]₂** (red) among others with the corresponding linear fits; b) graphical analysis of D_{exp} values for different molecules used in this study, with **BPE** as reference; the dotted lines represent the calculated correlation of diffusion coefficients and molecular weights assuming that the diffusion coefficients for two different molecular species (D_1/D_2) are inversely proportional to the square root of the ratio of their molecular weights M_2/M_1 for rod-like species.

Table 4.2.1. Diffusion coefficients (D_{exp}) determined by DOSY experiments. Molecular weights (MW) and the relation between diffusion coefficients and molecular weights (compared to **BPE**) for rod-like species is reported.

Molecule	Diff. Coeff. ($\times 10^{10} / \text{cm}^2 \text{ s}^{-1}$)	MW (g/mol)	$D_{\text{BPE}} / D_{\text{n}}$	$(MW_{\text{n}} / MW_{\text{BPE}})^{1/2}$
BPE	10.59	184.24	1.00	1.00
4-1	3.31	1854.94	0.31	0.32
[4-1·BPE]₂	2.57	4078.36	0.24	0.21

4.2.3. Solubilization of MWCNTs

Following a recently-reported procedure for the non-covalent functionalization of CNTs with organic molecules,⁵⁰⁴ it was possible to functionalize and solubilize MWCNTs with the **[4-1·BPE]₂** complex (**Figure 4.2.9.**) by means of multiple cycles of dispersion/centrifugation steps. Samples of **[1·BPE]₂⊙MWCNT** were prepared by sonication (room temperature, 30 min) of 10.0 mg of pristine MWCNTs into an equimolar solution of **4-1** and **BPE** in CHCl_3 ($c = 4.9 \times 10^{-5} \text{ M}$). The resulting black suspension was then centrifuged (at 5 krpm) for 30 min in order to separate the unfunctionalized and aggregated carbonaceous material from the solubilized CNTs. Finally, the supernatant solution was separated, filtered, and washed with CHCl_3 to remove the excess of the organic material. Multiple cycles were performed until the filtrate showed no UV-Vis absorption profiles. The same procedure was used in order to determine whether other compounds used in this study could disperse the MWCNTs. With compounds **4-1**, **4-2** and **4-4** only traces ($< 5 \%$) of the hybrid material were detected; in contrast, the **[4-1·BPE]₂** complex gave a high dispersibility to the carbon material.

The dispersibility was also confirmed by means of tapping mode atomic force microscopy. Indeed, a drop-casted solution of **[4-1·BPE]₂⊙MWCNT** showed the presence of only

individualized CNT structures (**Figure 4.2.10bc**), indicating the efficient de-bundling action by $[4-1\cdot\text{BPE}]_2$.

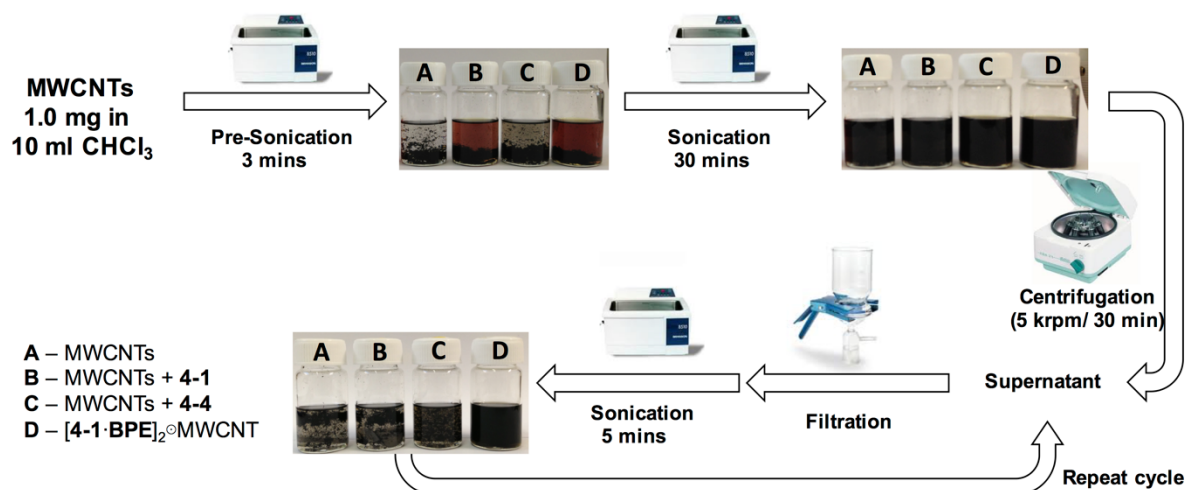


Figure 4.2.9. Protocol adopted for the non-covalent solubilization of CNTs: a suspension of MWCNTs in CHCl_3 (1.0 mg in 10 mL) was pre-sonicated and organic material was added ($c = 4.9 \times 10^{-5}$ M). This suspension was sonicated for 30 minutes, centrifuged for 30 minutes, the solubilized nanotubes were taken from the supernatant and this solution was filtered to remove excess organic material. The solid was redissolved in 10 ml CHCl_3 and sonicated for 5 minutes to obtain a stable suspension. This process was repeated until UV-Vis absorption showed no excess organic material in the filtrate.

A closer analysis of the $[4-1\cdot\text{BPE}]_2^{\circ}\text{MWCNT}$ material clearly showed the presence of tubular structures having lumps along the nanotubes (**Figure 4.2.10bc**) that were not present in the case of the pristine MWCNTs (**Figure 4.2.11**). These periodic structures can be possibly attributed to the sandwiched $[4-1\cdot\text{BPE}]_2$ complex, that is absorbed around MWCNTs thus enhancing their solubility. Furthermore, the presence of soft-organic material onto the CNT surface was observed by phase imaging of $[4-1\cdot\text{BPE}]_2^{\circ}\text{MWCNT}$ (**Figure 4.2.10c**). Indeed, phase analysis revealed the presence of areas of the sample possessing different contrast which could be ascribed to the adsorption of organic material possessing different physical and viscoelastic properties than that of the graphitic CNTs.

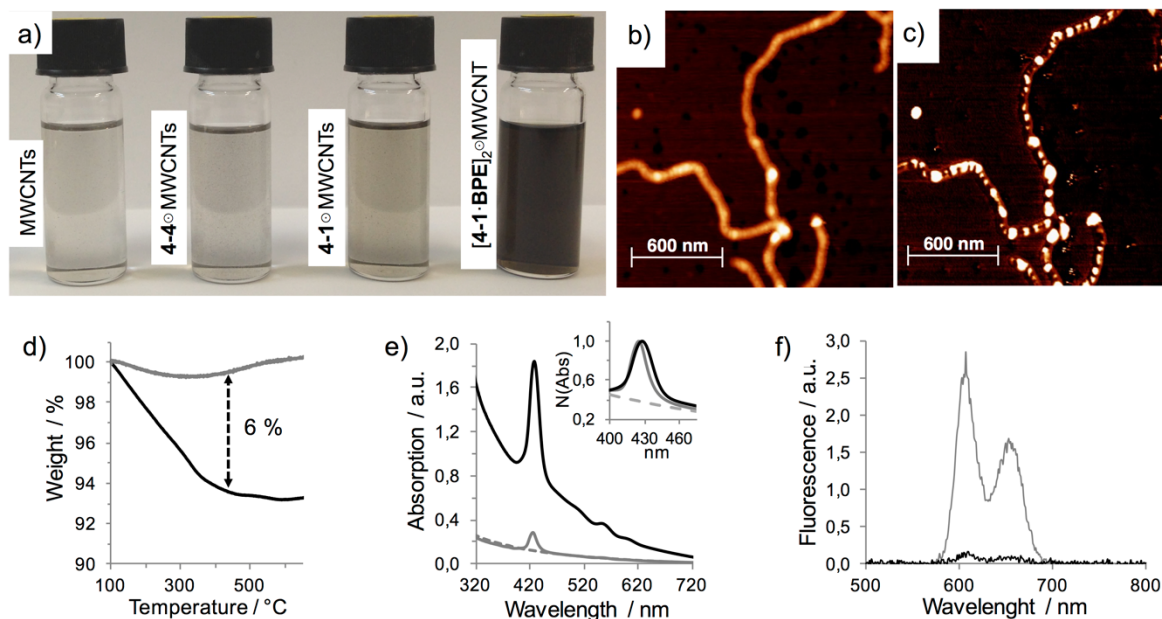


Figure 4.2.10. a) Photograph of the suspension obtained from the non-covalent solubilization protocol; b,c) topography and phase TM-AFM images of the $[4-1\text{-BPE}]_2\odot\text{MWCNT}$; d) thermogravimetric analysis of the $[4-1\text{-BPE}]_2\odot\text{MWCNT}$ (black line) in comparison to the pristine MWCNTs (grey line) showing a weight loss of 6 % at 450 °C; e) UV-Vis spectra of the $[4-1\text{-BPE}]_2\odot\text{MWCNT}$ (black), $4-1\odot\text{MWCNT}$ (grey) and $4-4\odot\text{MWCNT}$ (dashed), the inset shows the normalized absorption of the 3 hybrids; f) fluorescence profile of $[4-1\text{-BPE}]_2\odot\text{MWCNTs}$ (black line, concentrated) and $[4-1\text{-BPE}]_2\odot\text{MWCNTs}$ (grey line, diluted).

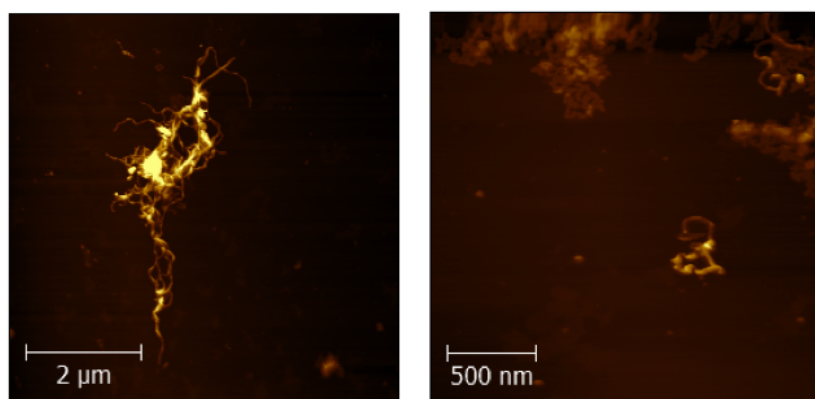


Figure 4.2.11. TM-AFM images of pristine MWCNTs.

The presence of the organic compound on the nanotubes was also investigated by recording the UV-Vis absorption and emission profiles. The UV-Vis spectra of $[4-1-BPE]_2 \odot MWCNT$ showed the characteristic absorption profiles of dispersed nanotubes, along with the typical electronic Soret and Q transitions of the porphyrin macrocycle (**Figure 4.2.10e**). Fluorescence spectroscopy (**Figure 4.2.10f**) showed a weak emission profile, suggesting a certain degree of quenching in the hybrid material that, as could be expected, was due to the adsorption on the nanotubes. Final evidence of the formation of the hybrid material was obtained through thermogravimetric analysis (TGA). At 450 °C the hybrid material presents a 6 % loss in weight when compared to the pristine MWCNTs (**Figure 4.2.10d**), with the weight loss attributed to the presence of the organic material. Finally, we proved that the functionalization of the MWCNTs is reversible (**Figure 4.2.12**) by employing a strong acid (trifluoroacetic acid, TFA, capable of protonating both the porphyrin and the ligand) or by heating.

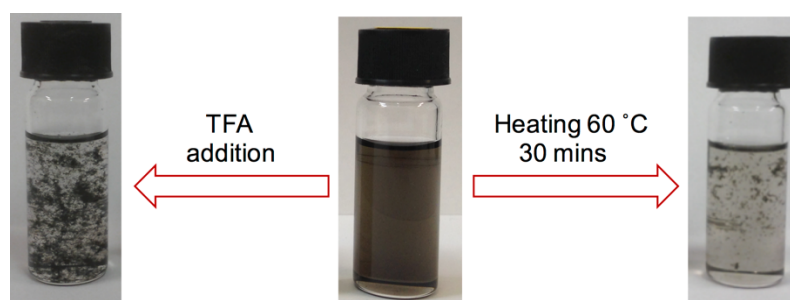


Figure 4.2.12. Reversibility of the functionalization; photograph of acid addition and heating experiment.

4.2.4. Molecular Modeling

Molecular modeling simulations have been performed in order to gain some understanding on the morphology of the $[4-1-BPE]_2/CNT$ interface in the $[4-1-BPE]_2 \odot MWCNT$ hybrid material. The Biovia molecular modeling package Materials Studio 7⁵⁰⁵ has been used to perform such modeling, using its implementation of the COMPASS force field.⁵⁰⁶ Only the outermost tube of the MWCNTs has been considered for the modeling, assuming that the main contribution to the stability of the $[4-1-BPE]_2 \odot MWCNT$ interface is coming from the adsorption on the MWCNTs external wall, which we represent as an infinite, rigid carbon nanotube having a diameter of about 10 nm.

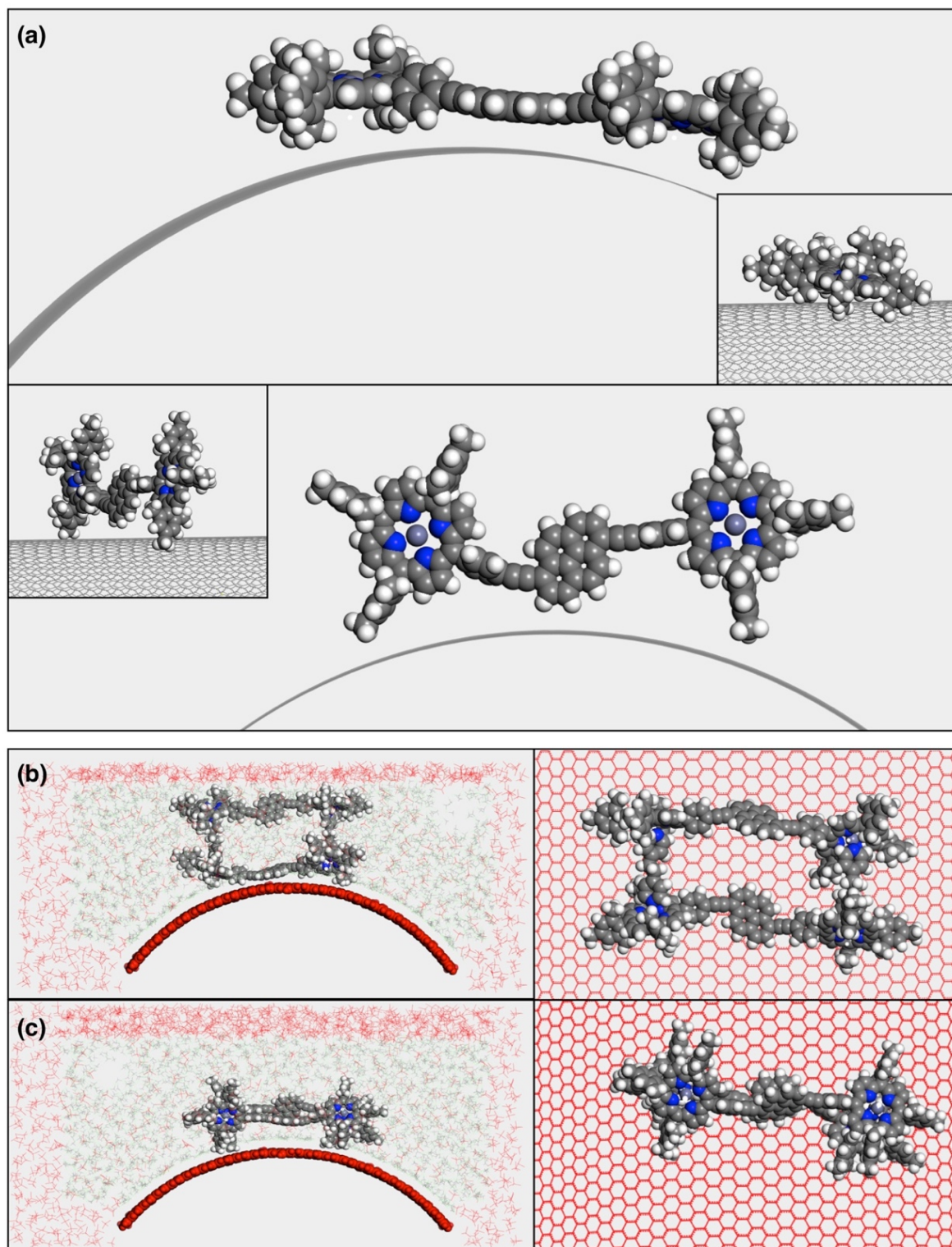


Figure 4.2.13. a) Front and side view of compound 4-1 adsorbed flat (top) and edge-on (bottom) on the nanotube; b) most stable conformations for $[4-1-BPE]_2@MWCNT$ complex adsorbed flat and c) edge-on on the nanotube; figures b,c left show the full system where the fixed molecules are shown in red. Figures b/c right show the top views of the adsorbed geometries.

The first step in building the molecular model for the [4-1·BPE]₂/CNT interface was to compare the interaction between the nanotube wall and compound 4-1 when adsorbed in flat and edge-on geometries. The 4-1[⊙]MWCNT interaction energy, $E(4-1^{\odot}\text{MWCNT})$, is calculated as the sum of the electrostatic and dispersion (vdW) energies between compound 4-1 and the nanotube. The results showed that compound 1 is about 67 kcal mol⁻¹ more stable when adsorbed flat on the nanotube (Figure 4.2.13a top) than when it is adsorbed in an edge-on orientation (Figure 4.2.13a bottom). This is due to the fact that when compound 4-1 is adsorbed flat, (i) favorable π - π interactions can be formed between its pyrene fragment and the nanotube wall, and (ii) less torsional stress is present in its molecular structure. The much higher stability of the flat orientation is also reflected in the observation that when in the edge-on orientation, compound 4-1 will spontaneously go flat on the nanotube in just a few ps of MD simulation. Next, we built the [4-1·BPE]₂ complex and made it interact with the surface of the nanotube in a bath of CHCl₃. The adsorption on the CNT surface of the [4-1·BPE]₂ complex was investigated during 100-ps long molecular dynamic simulations, both in the flat (Figure 4.2.13b left) and edge-on (Figure 4.2.13c left) geometries. Finally, an iterative MD/Quench scheme,⁵⁰⁷ consisting in a series of short (20-ps) MD, followed by a geometry optimization of the system, is used to obtain the most stable conformations of the [4-1·BPE]₂ complex in the flat and edge-on geometries (Figure 4.2.13b,c right). The stability of the interfaces is then estimated by comparing the [4-1·BPE]₂[⊙]MWCNT interaction energies, and the results showed that the interface where the [4-1·BPE]₂ complex is adsorbed flat on the nanotube is about 42 kcal mol⁻¹ more stable than that where the complex is adsorbed edge-on. This difference can be rationalized considering the complete adsorption of one pyrene unit on the nanotube, whereas the only interactions between the complex and the carbon surface are present through some methyl groups on the mesityl arms in the edge-on geometry. These results indicate that the [4-1·BPE]₂ complex prefers to interact with the nanotube by having one porphyrin fully adsorbed on the surface and the other one solvated.

4.2.5. Magnetic Alignment

At this point, the CNTs, through their magnetic susceptibility,^{497,508-511} could be used for the templated alignment of the adsorbed organic material as a top-down approach.⁵¹²⁻⁵¹⁴ However, the alignment can hold only when a magnetic field is applied, thus using only a solution of

hybrid material would be unpractical. To this end, we used an organic polymer that, in the presence of organic solvent, would swell and gelate relatively fast (**Figure 4.2.14**). The optimized procedure for the formation of the aligned hybrid material is depicted in **Figure 4.2.14a**: to the solid poly(hydroxybutyrate-co-hydroxyvalerate) (PHBV) (10 mg) was added a solution of hybrid $[4\text{-}1\text{-BPE}]_2\text{MWCNT}$ (1 mL) and the mixture was briefly heated to solubilize the organogel. At this point, toluene (2 mL) was added to the heated solution and the whole system was placed under a magnetic field (B , 10 T) and left until gelation was complete. Considering the direction of the magnetic field, one could imagine a “side-wall” face of the hybrid gel perpendicular to the B and a “tip” was in the same direction of the magnetic field. By employing different amounts of organogel, the time needed to achieve complete gelation could be tuned. The best results were obtained for 10 mg of PHVB and applying the magnetic field for 60 minutes. This procedure was performed also for PHVB alone and PHVB with only the $[4\text{-}1\text{-BPE}]_2$ complex in order to pinpoint the templating effect of carbon nanotubes.

The first evidence of anisotropic absorption due to aligned CNTs was observed with the polarized optical microscope (POM) under a crossed Nicols (**Figure 4.2.14c**). The microscope displayed very different image brightness depending on the rotation of the sample. When the “side-wall” face of the aligned hybrid organogel was rotated in an in-plane manner, its POM showed a contrast every 45° , giving a dark image when the light polarization angle with respect the applied magnetic field was 0° or 90° . When performing reference measurements on the “tip” edge of the aligned hybrid organogel no difference in brightness was perceived (**Figure 4.2.15a**). Whether the goal of building a three-dimensional templated porphyrin arrays was achieved, polarized UV-Vis absorption spectroscopy was performed (**Figure 4.2.14de**). When rotating the “side-wall” face and measuring the absorption spectra every $\theta = 15^\circ$ (**Figure 4.2.14d**), a stepwise reduction in overall absorbance (including the Soret and Q-bands of the porphyrin) was observed from $\theta = 0^\circ$ (maximum absorbance) to $\theta = 90^\circ$ (minimum absorbance). This effectively proved that the templated material is aligned and exhibits anisotropic absorbance. Additional experiments at the “tip” face (**Figure 4.2.14e**) showed an optical isotropic behavior: no changes in absorption intensity were detected at different incident angles ($\theta =$ from $0^\circ \rightarrow 90^\circ$ by 15° steps). Similar results were obtained when performing UV-Vis absorption measurements on the PHVB-alone organogel and the hybrid

organogel containing only the $[4-1\text{-BPE}]_2$ (Figure 4.2.15b-e) thus confirming once again the importance of the templating exercised by the carbon nanotubes.

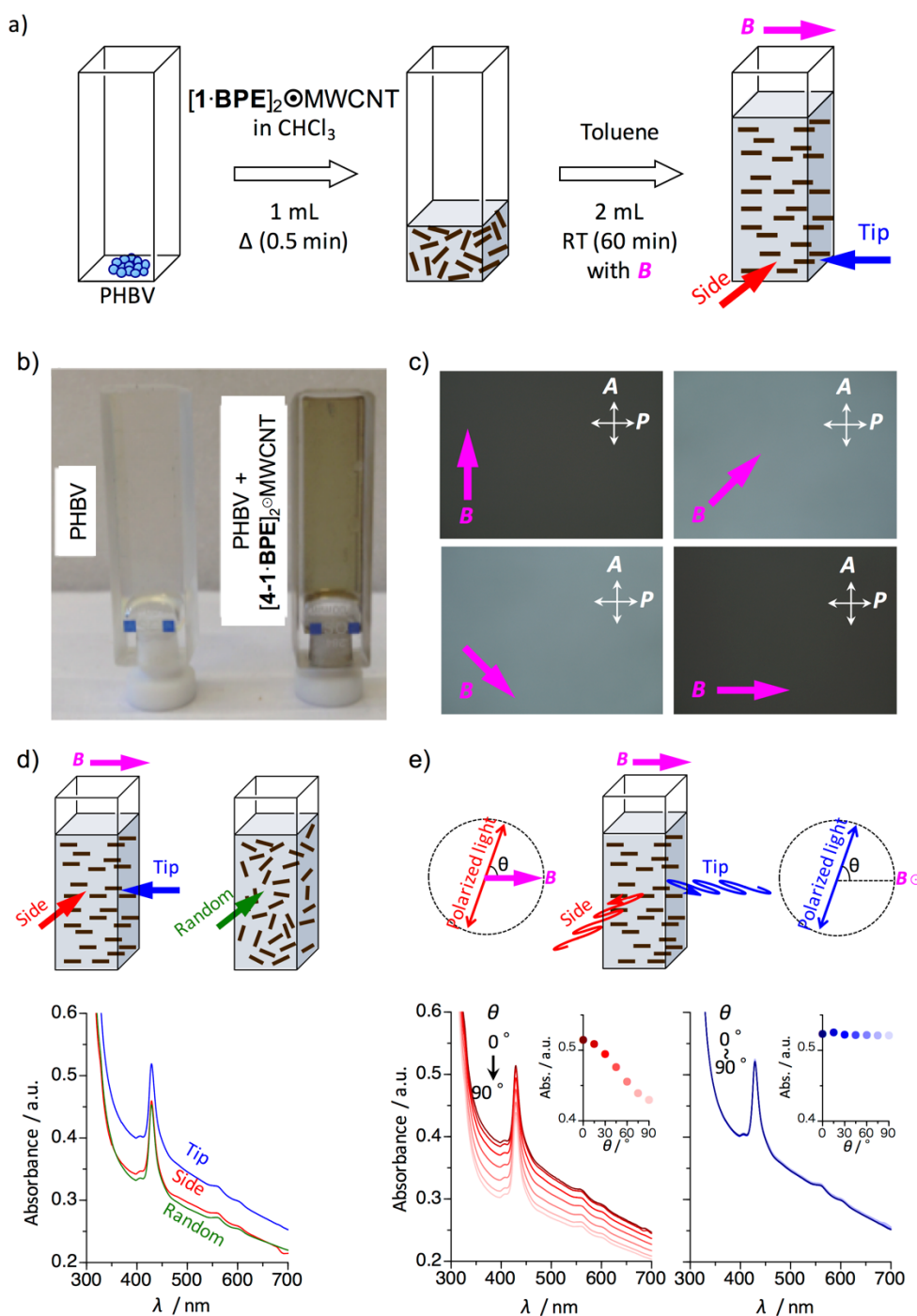


Figure 4.2.14. a) Steps adopted in the preparation of the aligned hybrid organogel containing $[4-1\text{-BPE}]_2$ @MWCNT; b) photograph of the PHBV-alone organogel (left) and aligned hybrid organogel (right); c) POM images of the "side-wall" face of the aligned hybrid organogel; de) UV-Vis absorption profiles recorded at different polarized angles ($\theta =$ from $0^\circ \rightarrow 90^\circ$ by 15° steps) of the "side-wall" face d) and the "tip" face e).

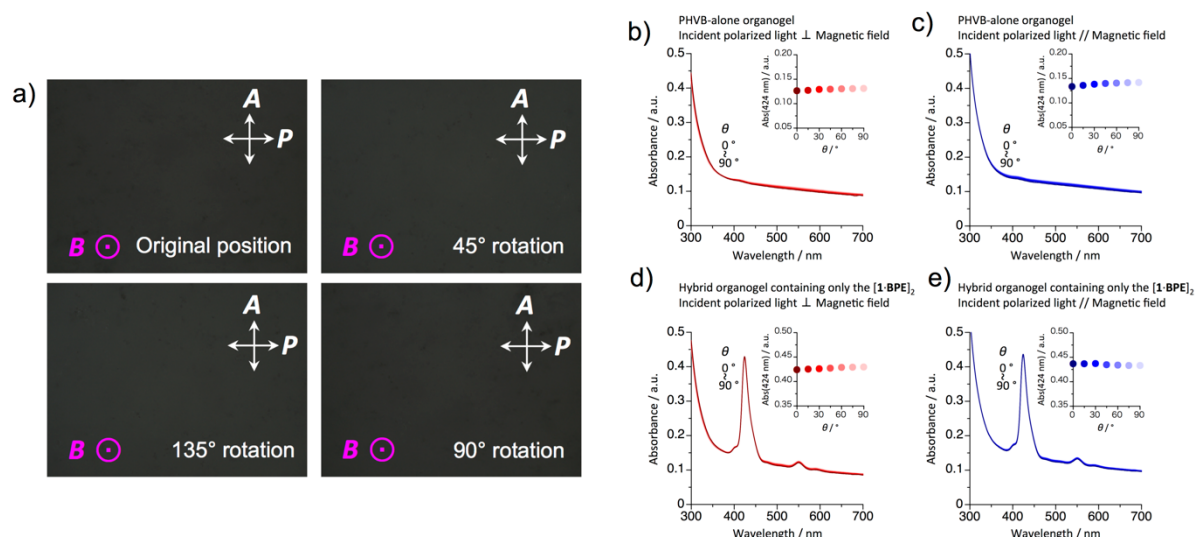


Figure 4.2.15. a) POM images of the “tip” face of the aligned hybrid organogel containing [4-1-BPE]₂⊙MWCNT; UV-Vis absorption profiles of organogels recorded at different polarization angles ($\theta =$ from $0^\circ \rightarrow 90^\circ$ by 15° steps); bc) PHVB-alone organogel irradiated with an incident polarized light perpendicular (b) and parallel (c) to the applied magnetic field; de) hybrid organogel containing only the [1-BPE]₂ irradiated with an incident polarized light perpendicular (d) and parallel (e) to the applied magnetic field.

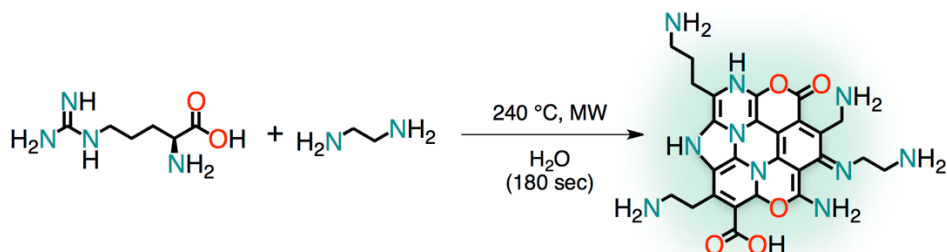
4.3. Towards Porphyrin-Carbon Nanodots Nanohybrids

4.3.1. Synthesis and Characterization

We performed a simple bottom-up method for highly fluorescent nitrogen-doped CNDs (NCNDs) with among the smallest size and the highest FLQYs reported so far.^{484,485} Using this approach, followed by simple dialysis, NCNDs could be obtained within three minutes without the need of sophisticated equipment or additional surface passivation. The use of microwaves (MW) as possible alternative synthetic approach allowed us to avoid multi-step synthesis and provided benefits such as faster rates, milder conditions, and low energy consumption. Moreover, microwave irradiation provided simultaneous, homogeneous, and fast heating, leading to uniform size distribution of nanodots.

Arginine (Arg) and ethylenediamine (EDA) were used as carbon and nitrogen sources (**Scheme 4.3.1**). Amino acids are ideal carbon and nitrogen sources for CNDs owing to their low cost and

abundance. Moreover, molecules containing primary amines allow simultaneous nitrogen doping and surface passivation during the synthetic process.



Scheme 4.3.1. Reaction scheme for preparing NCNDs, with a product drawn as a tentative representation of a representative structural unit.

The heterogeneous solution underwent thermal carbonization of the precursors and led to nucleation. Finally, the nuclei grew by diffusion of other molecules towards the surface of the nanoparticles.

The MW parameters were optimized to obtain the desired properties of the final material, in terms of optical performance. Appropriate viscosity and temperature control were needed for a uniform carbonization process that leads to the formation of NCNDs. Fluorescent NCNDs were obtained at 240 °C, 26 bar, 200 W with a MW heating time of 180 seconds using H₂O as reaction medium. The obtained NCNDs exhibited a high solubility in water (up to 80 mg mL⁻¹) and in common polar organic solvents.

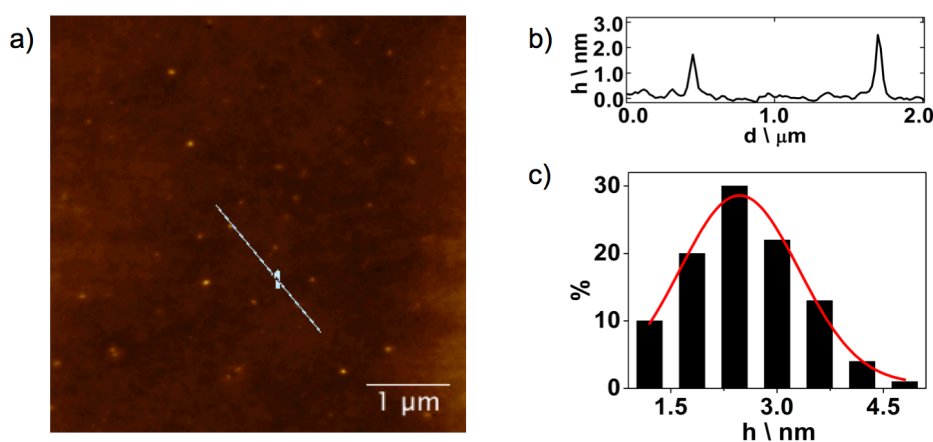


Figure 4.3.1. a) TM-AFM images of NCNDs (5.0 × 5.0 μm) on a mica substrate; b) height profile of NCNDs; c) size histograms of NCNDs with curve fit to the data using a Gaussian model.

Atomic force microscopy confirmed the round shape and showed that NCNDs have a rather homogeneous size distribution (**Figure 4.3.1**). By statistical analysis of the height of about one hundred nanoparticles, we determined an average size of 2.47 ± 0.84 (full width at half-maximum (FWHM): 1.977).

FT-IR spectroscopy and X-ray photoelectron spectroscopy (XPS) were useful tools for the investigation of the structure and composition of NCNDs and showed the presence of multiple oxygen and nitrogen functional groups on their surface. Moreover, the presence of amino groups amenable to further functionalization, allows easy insertion of further functional groups and/or appealing molecules/ions through standard organic chemistry procedures.

In addition, we gained unprecedented structural information reporting the first detailed NMR study. For this purpose, we prepared ^{13}C -enriched NCNDs (N^{13}CNDs) for ^{13}C -NMR investigations (**Figure 4.3.2**, middle), starting with fully ^{13}C -enriched Arg and EDA. A tentative interpretation of a representative structural unit of NCNDs is reported in **Figure 4.3.3**, with a general peak assignment. Typically, ^{13}C -NMR spectra of N^{13}CNDs consist of an aliphatic region (**Figure 4.3.3**, C_a), with carbon atoms connected to heteroatoms (C_b) or to an aromatic core (C_c) and an aromatic region (C_{d-h}). Moreover, the contribution of each component was evaluated, using separated and combined ^{13}C -Arg and ^{13}C -EDA (**Figure 4.3.2**, top and bottom).

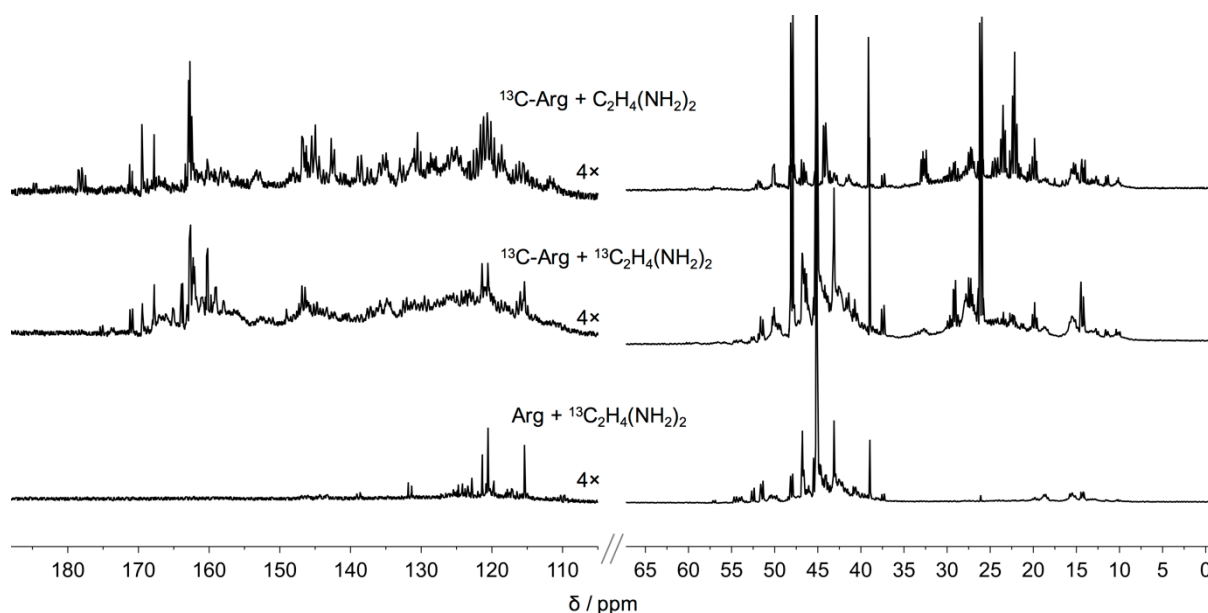


Figure 4.3.2. ^{13}C -NMR spectra (126 MHz, D_2O) of N^{13}CNDs prepared starting from ^{13}C -Arg and EDA (top), ^{13}C -Arg and ^{13}C -EDA (middle) and Arg and ^{13}C -EDA (bottom). The intensity of the aromatic region was increased 4.0 times in order to facilitate the visualization.

Figure 4.3.2-top shows the ^{13}C -NMR spectrum of NCNDs produced using only ^{13}C enriched Arg. It is clear that the aromatic core and the aliphatic carbons as well as the carbonyl regions mainly originate from Arg. While EDA (**Figure 4.3.2-bottom**) mostly contributes to the typical region of aliphatic carbon atoms connected to heteroatoms, signals arising from EDA were also found in the aromatic core of N^{13}CNDs .

Further bidimensional experiments (^1H - ^{13}C) revealed numerous H-C correlations both by direct (HSQC, **Figure 4.3.3** H_a - C_a H_b - C_b H_c - C_c ; **Figure 4.3.4**) or through multiple-bond correlations (HMBC, **Figure 4.3.3** H_a - C_b - C_c H_c - C_d - C_e ; **Figure 4.3.5**). Remarkably, protons that lie in the aliphatic region and close to heteroatoms were found to correlate with the aromatic sp^2 -carbon core (**Figure 4.3.5**). Analogous data was obtained from ^{13}C - ^{13}C one bond correlation (INADEQUATE, **Figure 4.3.3** C_a - C_c C_c - C_d C_f - C_g - C_h ; **Figure 4.3.6**). Additionally, diffusion-ordered spectroscopy (DOSY, **Figure 4.3.7**) was performed through ^1H - ^{13}C multiple-bond correlation to unambiguously assign the signals to macromolecular species.

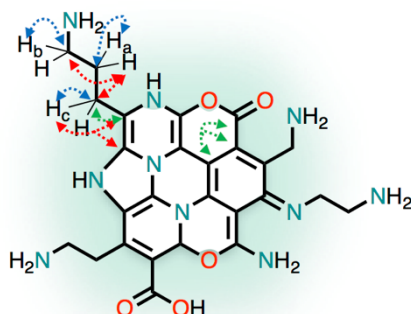


Figure 4.3.3. Representative structural correlations found in NMR experiments are reported in dashed arrows (HSQC blue lines, HMBC red lines and INADEQUATE green lines).

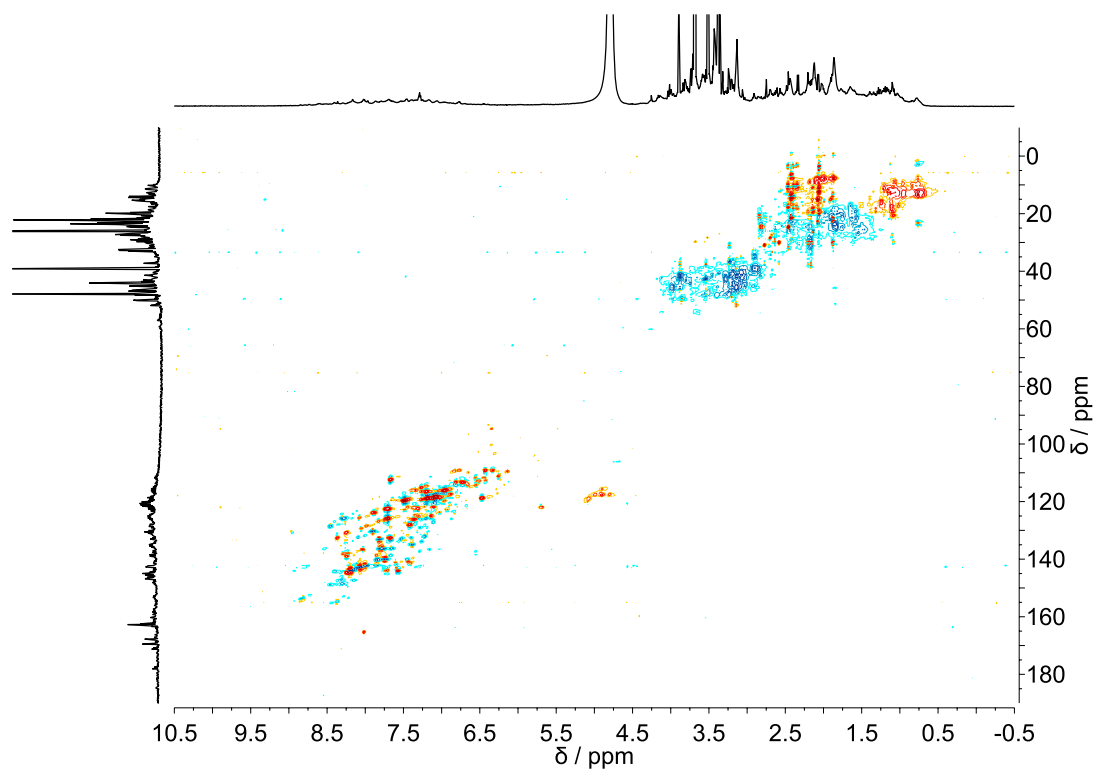


Figure 4.3.4. HSQC spectra of N^{13}CNDs prepared starting from ^{13}C -Arg and EDA (scan t1 increment = 16, t1 increments = 256, one-bond J_{1xh} = 146.0 Hz).

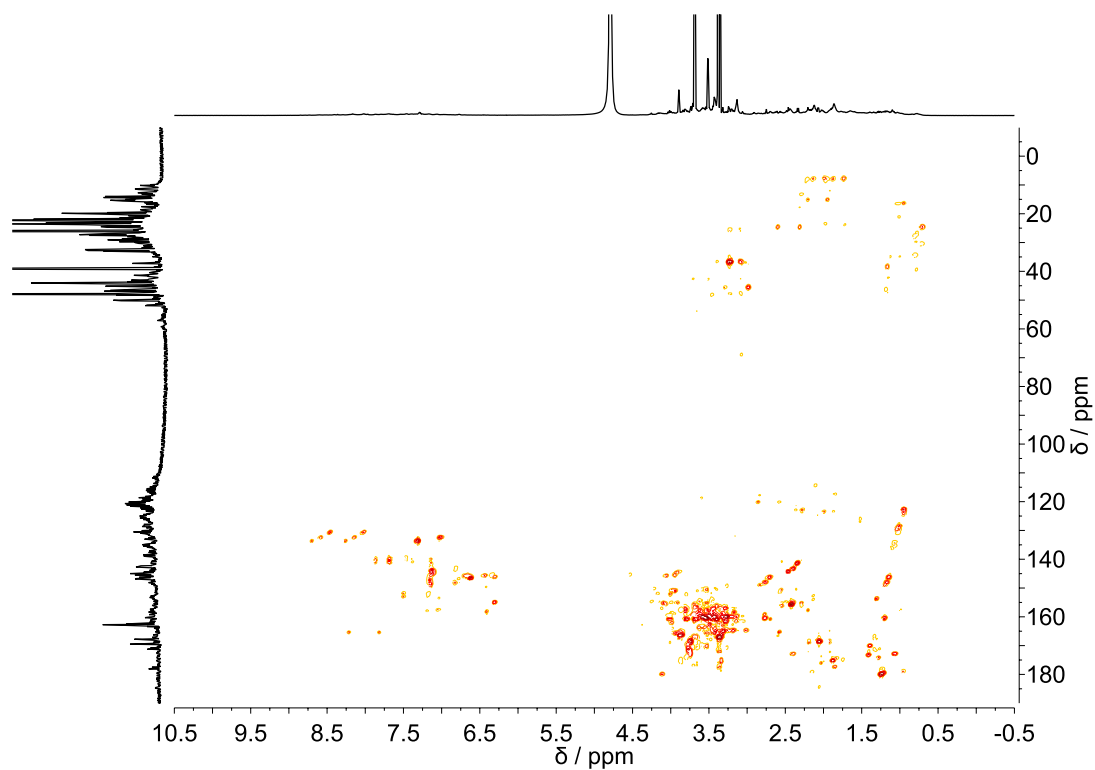


Figure 4.3.5. HMBC spectra of N^{13}CNDs prepared starting from ^{13}C -Arg and EDA (scan t1 increment = 16, t1 increments = 400, multiple bond $J_{n\text{hx}}$ = 8.0 Hz).

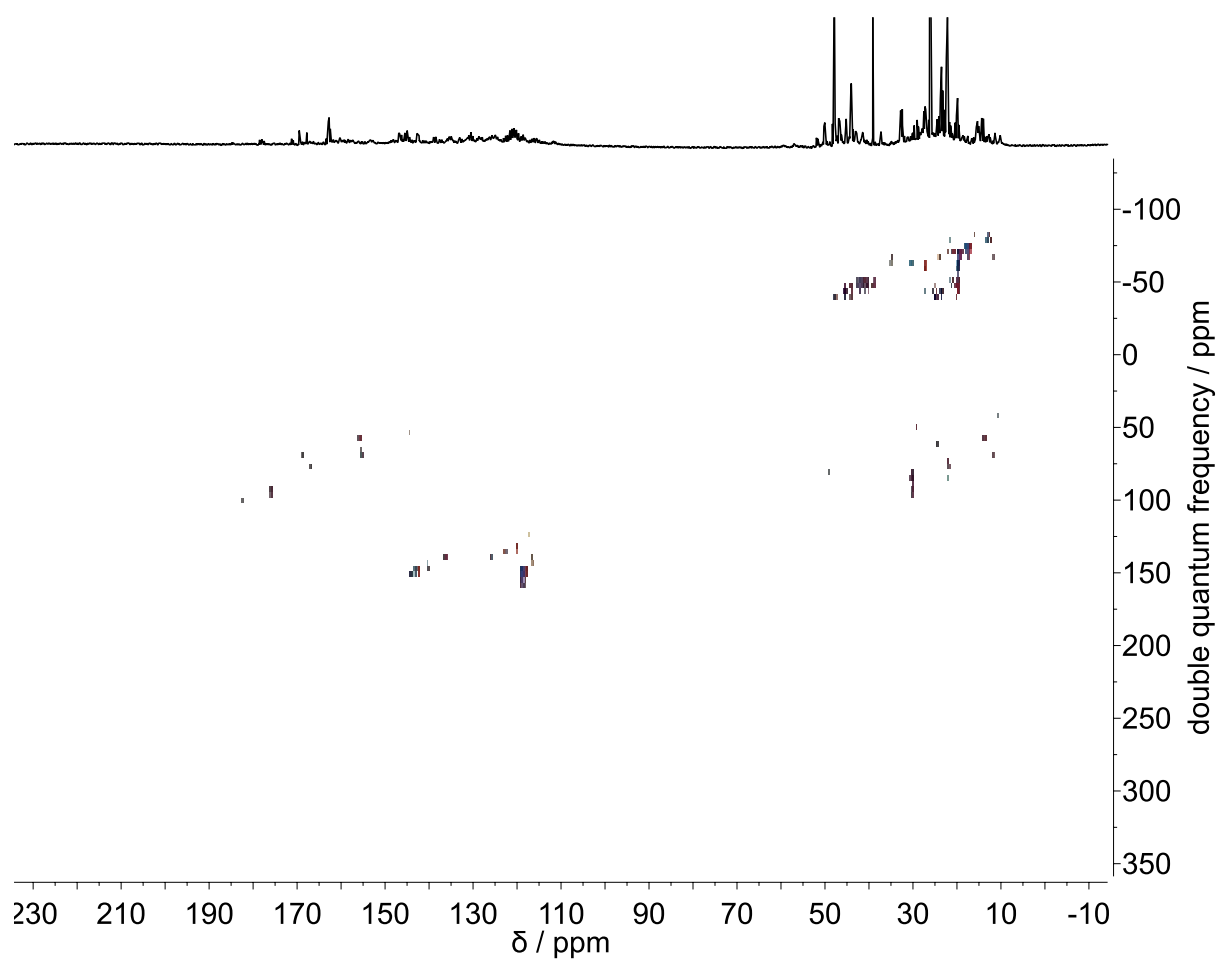


Figure 4.3.6. INADEQUATE spectra of $N^{13}CNDs$ prepared starting from ^{13}C -Arg and EDA (scans = 256, $J = 55$ Hz).

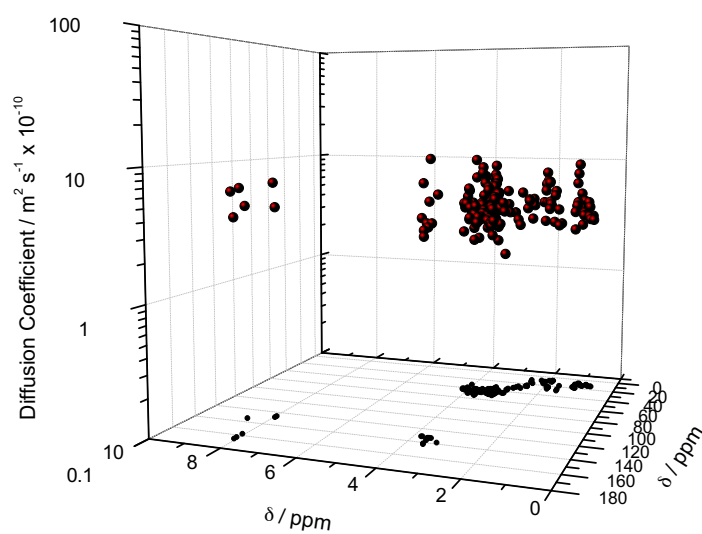


Figure 4.3.7. 3D-DOSY spectra of $N^{13}CNDs$ prepared starting from ^{13}C -Arg and EDA.

In light of this results, we argued that NCNDs are rounded-shaped nanomaterials, containing both aliphatic and aromatic regions with abundant functional groups located at the surface. These groups act as a passivation layer, which improves their hydrophilicity and stability in aqueous systems, as well as their efficient photoluminescence properties. NCNDs produce multi-fluorescence colors under different excitation wavelengths, and this behavior may arise not only from particles of different size but also from a distribution of different emissive domains on each carbon dot. The fluorescence spectra of NCNDs show a broad emission peak at 356 nm when the sample is excited at the optimal excitation wavelength (300 nm, **Figure 4.3.8**). The fluorescence peaks shift from 356 nm to 474 nm when the excitation wavelength changes from 300 to 420 nm and the fluorescence intensity decreased as the peak red shift.

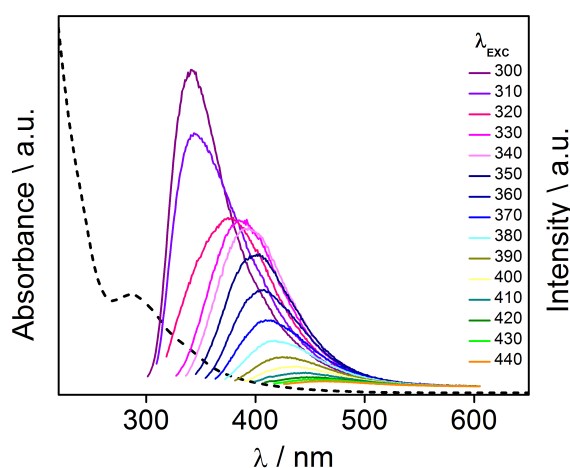


Figure 4.3.8. FL and UV-Vis absorption spectra and FL spectra in water (298 K) at different excitation wavelengths.

4.3.2. CNDs-Porphyrin Nanohybrids

As mentioned beforehand, porphyrinoids, due to their preeminent role in nature, are the chromophores of choice to employ as components of photovoltaic and artificial photosynthetic devices. Porphyrins hold some advantages with respect to other types of electro- and photoactive compounds which arise from their 18 π -electron aromatic structure, high molar absorption coefficients and fast energy and/or electron transfer donor abilities to electron acceptor counterparts. Thus, porphyrins are widely used as molecular components in artificial photosynthetic systems, both for energy-transfer and electron-transfer processes. Moreover, the possibility of tailoring their redox

potentials through peripheral functionalization represents an appealing feature for their use in the above-mentioned energy-related areas.

Until now, a large variety of covalent and supramolecular systems based on porphyrins and carbon nanostructures have been described and the photophysical properties of some of these D–A materials studied both in solution and/or in the solid state as well as their use as active components in photovoltaic devices.^{515,516} Moreover, chemically functionalized carbon nanomaterials, such as fullerenes and SWCNTs, with photoactive molecules, such as light-harvesting donors, have been recognized as useful materials for photocatalytic and light-energy conversion applications.^{127,517}

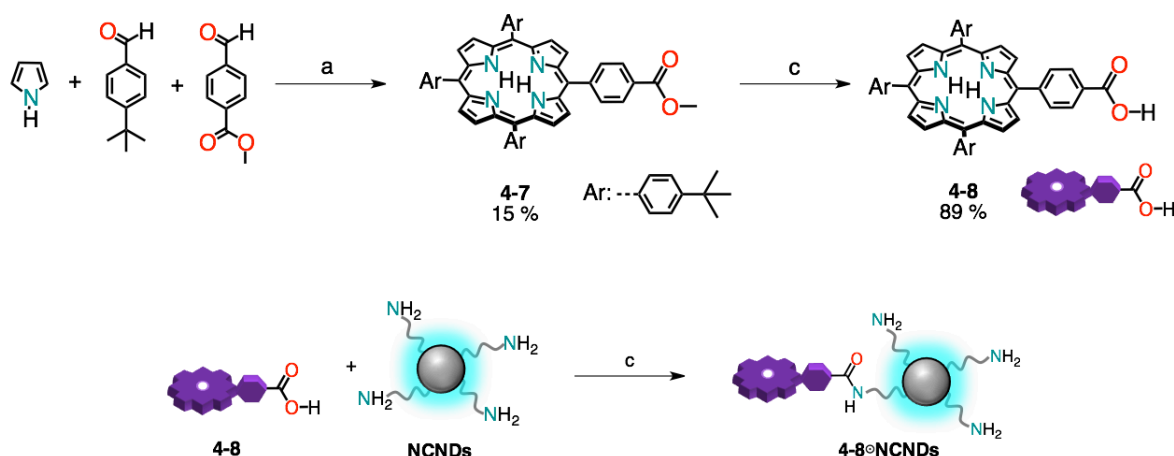
Covalently linked systems have been found to exert a substantial impact on the interactions between the porphyrins and nanocarbons in the excited and ground states.^{127,518,519} However, in most cases, the covalent functionalization is a multi-step synthetic process and nanocarbons display poor solubility in organic solvents used for the synthesis. Furthermore, direct covalent functionalization converts the sp^2 carbons of some of the double bonds of SWCNTs to sp^3 carbons, cutting-off the π -conjugations and altering their electronic properties.

On the contrary, ease of labeling through the functional groups already present on the surface after the synthesis, together with a high solubility and the ability to form stable charge-transfer hybrids with either electron donors or acceptors, make CNDs ideal candidates for the covalent grafting of photo- and/or electro-active organic units towards CNDs-based hybrid materials.

Therefore, the intriguing photophysical properties of porphyrins have inspired us to explore, for the first time, their behavior when covalently attached to NCNDs. To this end, a porphyrin carrying a carboxyphenyl peripheral moiety was first prepared through a mixed aldehyde condensation reaction under Lindsey conditions and was subsequently saponified with aq. KOH to obtain the free carboxy group. The porphyrin and the NCNDs could now be coupled through a carbodiimide condensation reaction (**Scheme 4.3.2**).

The resulting conjugate (**4-8^oNCNDs**) was found to be highly soluble in H_2O . Thus, the coupling of porphyrin to NCNDs results in its solubility in water media that could be not achieved for the porphyrin alone. Therefore, NCNDs can be easily functionalized and, more importantly, they can be used as water-soluble carriers.

Promising results indicating that NCNDs serve as electron acceptors and the photoexcited porphyrins moieties serve as electron donors have been obtained. However, detailed photophysical studies to shed light on the dynamics of the resulting hybrid nanosystem are currently underway.



Scheme 4.3.2. Reaction scheme for preparing the carboxy-porphyrin and its subsequent amide coupling with NCNDs. Reagents and conditions: a) i) $\text{BF}_3 \cdot \text{OEt}_2$, CHCl_3 , r.t.; ii) chloranil; b) aq. KOH, EtOH, reflux; c) EDC, NHS, DMF, r.t.

Steady state absorption of the references **4-8**, **NCNDs** and their conjugate (**4-8°NCNDs**) were conducted either in MeOH or $\text{H}_2\text{O}/\text{THF}$ (1:1). The absorption spectra of **4-8** in MeOH (**Figure 4.1.2** left) shows the five maxima at 415, 514, 549, 590, and 646 nm assigned to the Soret and the four Q-bands. **4-8°NCNDs** shows the characteristic porphyrin Soret and Q-bands marginally red-shifted, suggesting the occurrence of electronic communication between the porphyrin moieties and the nanodots in the ground state. In $\text{H}_2\text{O}/\text{THF}$ (**Figure 4.1.2** right) the absorption maxima appear at 419, 515, 551, 593, and 649 nm for both **4-8** and **4-8°NCNDs**. The absorption spectrum of NCNDs is governed by two rather weakly defined maxima at 285 and 302 nm in MeOH and 285 and 318 nm in $\text{H}_2\text{O}/\text{THF}$ with a broad absorption trailing into the visible.

Fluorescence spectroscopy was a useful tool for extending the investigation of electronic interactions of the porphyrin units with the nanodots in the excited state of the **4-8°NCNDs** nano hybrid (**Figure 4.3.10**). CNDs or porphyrins were selectively excited at 290 nm or 550 nm in $\text{H}_2\text{O}/\text{THF}$ (1:1), respectively. The fluorescence spectra of **4-8°NCNDs** in $\text{H}_2\text{O}/\text{THF}$ (1:1) upon excitation at 290 nm

and 550 nm were compared to the fluorescence of the corresponding references. The fluorescence spectrum of NCNDs is best described as a broad, asymmetric emission peak with a maximum at 370 nm and in the **4-8^oNCNDs** conjugate appears shifted by 4 nm to 374 (Figure 4.3.10 left). In addition, the fluorescence intensity is quenched by a factor of 2/3 confirming the occurrence of electronic communication between the porphyrin moieties and the nanodotots. When excited at 550 nm, the fluorescence maxima of **4-8^oNCNDs** appear at 653 and 718 nm and are not shifted with respect to the references (Figure 4.3.10 right). In any case, the fluorescence emission of photoexcited porphyrin is significantly quenched (40 %) in the covalently associated **4-8^oNCNDs** nano hybrids.

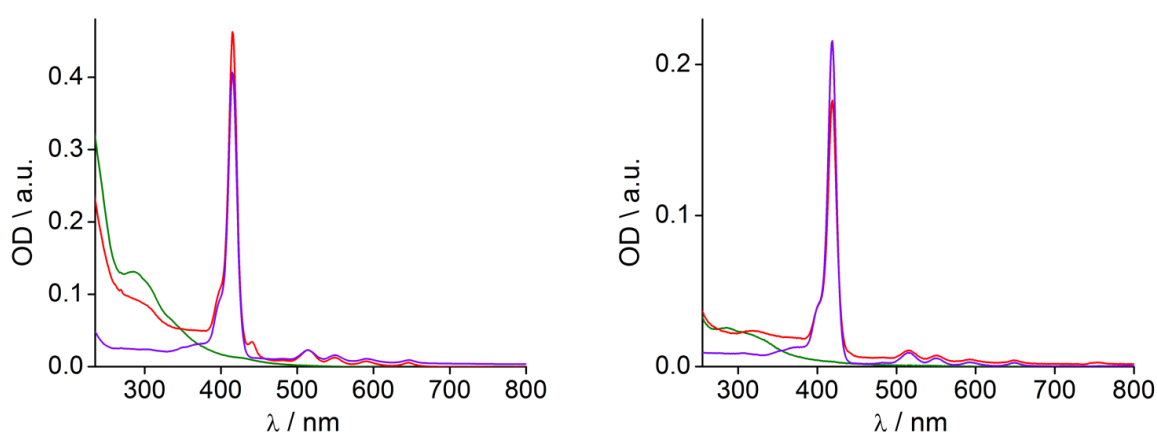


Figure 4.3.9. Steady state absorption spectra of **4-8** (violet), **NCNDs** (green) and **4-8^oNCNDs** (red) in MeOH (left) and H₂O/THF (1:1) (right).

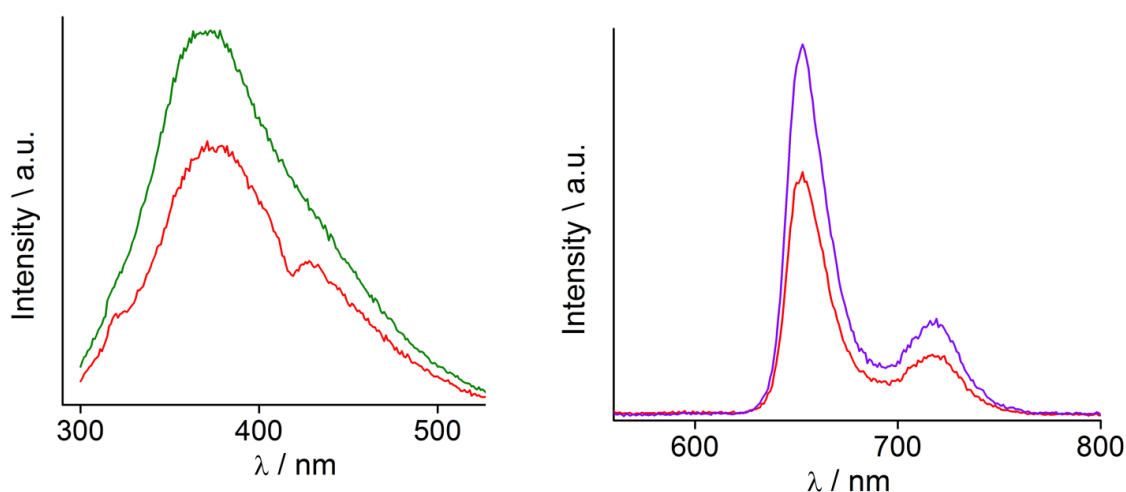


Figure 4.3.10. Steady state fluorescence spectra upon excitation at 290 nm of **NCNDs** (green) and **4-8^oNCNDs** (red) on the left and upon excitation at 550 nm of **4-8** (violet) and **4-8^oNCNDs** (red) in H₂O/THF (1:1) on the right.

First clues show that a covalently linked porphyrin with NCNDs can act as an energy absorbing and electron donating antennae, while NCNDs acts as electron acceptor units, in a hybrid system where the porphyrin moiety resides near to the surface of the CNDs framework.

These promising results for the covalent porphyrin^oNCNDs hybrid prompted us to prepare water-soluble porphyrins (**Figure 4.3.11**) in order to probe and compare the covalent and supramolecular hybrid materials. This results will be reported elsewhere.

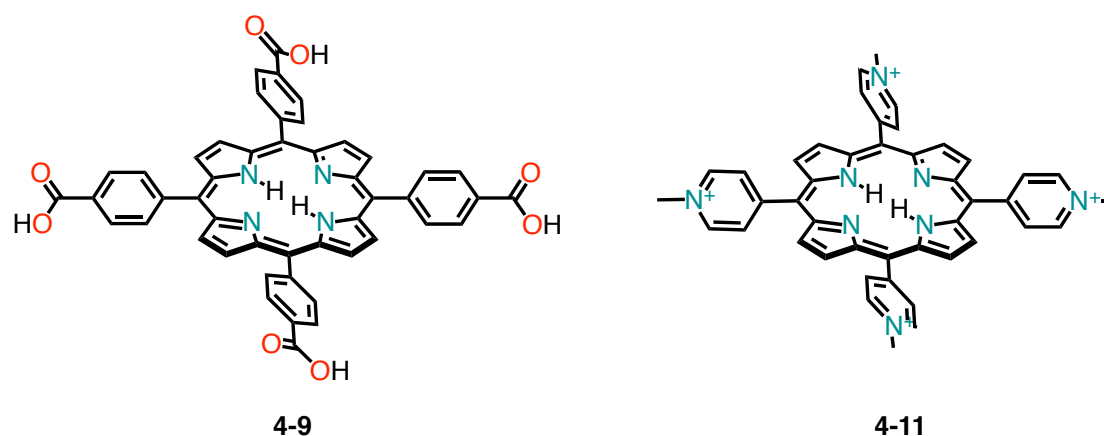


Figure 4.3.11. Water-soluble porphyrins for non-covalent porphyrin^oNCNDs nanohybrids.

4.4. Conclusion

This chapter focused on preparation of novel hybrid materials using carbon-based templates for arranging chromophores. In the first part, a porphyrin array was prepared and was used to disperse otherwise insoluble carbon nanotubes, in order to prepare a 1-D hybrid material. Then, due to the magnetic susceptibility of the CNTs, it was possible to arrange the hybrid material parallel to the magnetic field. The arrangement was 'blocked' by gelating the sample during application of the magnetic field. The final system was then characterized in order to prove that the hybrid material was arranged. Since the composite material showed higher absorption in 'sidewall' face compared to the 'tip' face we can envisage applications as light-harvesting systems, where the arrangement and absorption play a very important role.

The second part focused on the preparation of a carbon nanodots-based donor-acceptor system. In particular, a porphyrin-CNDs linked composite and its pioneering photophysical investigation were

discussed. We believe that our key finding of photoinduced charge separation (CS) between CNDs and porphyrins will give a significant contribution to scientists working in the arising field of CNDs. Thus, for efficient photoinduced charge separation, optimization of the coupling in the porphyrin–CNDs composites is far behind that in the porphyrin–fullerene or SWCNTs composites, but on the other hand this leaves plenty of room for improvement. Moreover, these results are leading us to the supramolecular constructions of nano-architectures using multiple combinations of these two moieties being able to generate large libraries of electron-donor/electron-acceptor ensembles. Thus, the newest nanocarbons CNDs may open the door to a number of applications and could be a target of choice for the development of novel photoactive materials.

5. Patterning Metal Surfaces

In this chapter, the design, syntheses and surface self-assembly of polycyclic aromatic hydrocarbons (PAHs) is described. The first part addresses the self-assembly of pyridyl furnished pyrenes on a metal surface, notably with the formation of porous networks that could accommodate guests. The second part deals with the formation of organo-metallic networks on surface using two different approaches. Finally, an overview on future directions is presented, including the work undergoing on O-doped systems and their self-assembly.

The work presented in this chapter is part of several collaborations. The first part presented in this chapter is a collaborative work done with *Tobias Kaposi*, *Dr. David Écija*, *Prof. Willi Auwärter* from the group of *Prof. Johannes Barth* (TUM München, Germany). The second part of this work was done in collaboration with *Borja Cirera* and *Dr. David Écija* (IMDEA Nanoscience, Madrid, Spain). Finally, the work on O-doped systems is part of collaborative work with *James Lawrence* and *Prof. Giovanni Costantini* (University of Warwick, Coventry, United Kingdom). Part of the work from this chapter has been *submitted* as ‘Supramolecular spangling, crocheting and knitting of functionalized pyrene molecules on a silver surface’. Another part of this chapter has been used to prepare a manuscript entitled ‘Lanthanide-carboxylate nanomeshes with tunable cavity size and coordination node’.

5.1. Introduction

5.1.1. Overview on Scanning Tunneling Microscopy

The development of *nanomaterials* – systems, structures and devices characterized with one dimension ranging from 0.1 to 100 nm – aims to take advantage of the properties that can arise at the nanoscale level and that can considerably vary from the corresponding bulk material.¹⁹⁰ For instance, silver metal possesses no biological activity while silver nanoparticles are antimicrobial.⁵²⁰ In a similar fashion, the size of metal nanoparticles impacts its conductivity inorganic semiconducting nanoparticles influences its optical and electronic properties.^{521,522} Industries that have flourished on miniaturization, such as microelectronics and magnetic data storage, look up to nanotechnology to find practical solutions.

The two main approaches to create such miniaturization in a reproducible and accurate fashion are the ‘top-down’ and ‘bottom-up’ techniques’ (**Figure 5.1.1**).⁵²³ The ‘top-down’ approach⁵²⁴ is basically

an advancement of early techniques such as writing, printing or lithography and is capable of producing elements down to 100 or less nm. Modern tools include electron-beam writing and UV or hard X-ray lithography,⁵²⁵ but further improvement will require more investments and substantial equipment evolution.

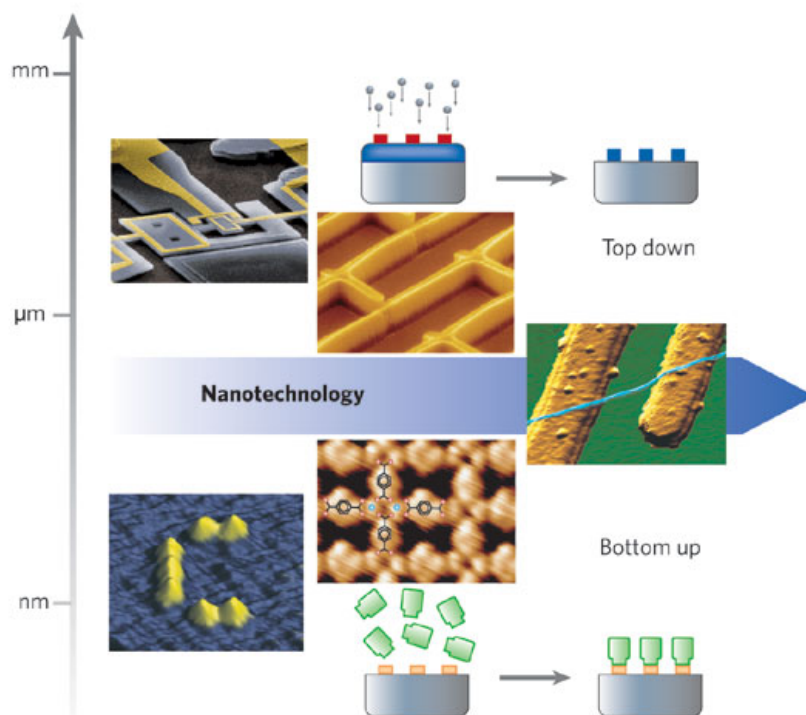


Figure 5.1.1. Two approaches to control matter at the nanoscale. For top-down fabrication, methods such as lithography, writing or stamping are used to define the desired features. The bottom-up techniques make use of self-processes for ordering of supramolecular or solid-state architectures from the atomic to the mesoscopic scale.⁵²³

Contrary to the top-down method, the 'bottom-up' approach is based on growth phenomena and aims to assemble atoms or molecular components into well-ordered surface structures. The bottom-up methods introduce several advantages such as long-range order, high convergence in the nanostructuring protocol, easy formation of the final nanostructures, defect free architectures due to the reversible nature of the interactions involved which can induce the most thermodynamically stable phase.^{291,526,527} The span of structures in the nanometer scale, that can be build from metallic or

semiconducting materials, is to a certain extent limited since the design and fabrication have to be based on structural and functional features in these materials. As a consequence, organic chemistry provides access to an extensive number of building blocks that can be linked for the most part through hydrogen bonds and metal-ligand interactions to furnish fine-tuned supramolecular architectures. In this context, the surface of a bulk material can represent a solid support playing the part of a counter electrode or mechanical support.^{523,528,529} In particular, Scanning Probe Microscopies (SPM) are unique tools for the nanoscale, since they allow not only imaging but also structuring matter on the nanoscale (same cases even on the atomic scale). Among the different techniques, the scanning tunneling microscope (STM) revolutionized modern nanosciences and nanotechnologies and earned the Nobel Prize in Physics in 1986 to its inventors, Gerd Binnig and Heinrich Rohrer.^{294,530,531}

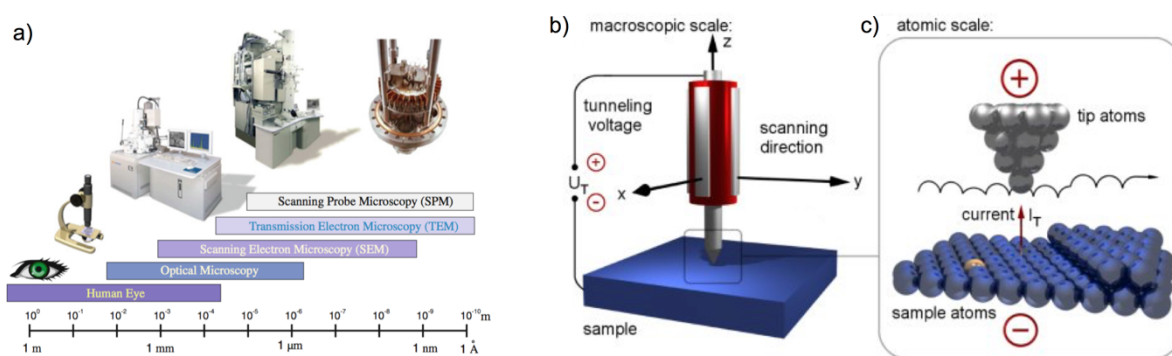


Figure 5.1.2. a) Comparison of imaging ranges for different microscopy techniques⁵³¹ and bc) macroscopic and atomic schematic view of a STM.⁵³²

A schematic representation of an STM, with a fine metal tip as probe, is shown in **Figure 5.1.2.**⁵³¹ When a bias voltage is applied and the tip is brought to within about 10 Å of the sample, electron can ‘tunnel’ through the gap from the sample into the tip, or the other way around, depending on the sign of the bias voltage. This current (tunneling current) is detected and increases with decreasing distance between the tip and the sample. Therefore, specific tip-sample distance corresponds to a specific measured tunneling current and is used to create a STM image. The tunneling current is an exponential function of the distance, *i.e.* a change in tunneling current by an order of magnitude changes if the separation between the tip and the sample changes by 10 % (around 1 Å). STMs usually scan samples in one of the following two modes: *constant-current* or *constant-height* mode. In constant-current mode, the tunneling current is kept constant by adjusting the height of the tip at each

measurement point. While in constant-height, the tip travels horizontally above the sample with the tunneling current varying based on the topography and electronic properties of the sample. Even though it seems that an STM image corresponds to the topography of the sample, it equates to the electronic density of states at the surface. STM experiments are usually performed either at solid-liquid interfaces at room temperature under atmospheric condition⁵³³ or under ultra-high vacuum (UHV)⁵²⁹. In the case of solid-liquid imaging, the tip is immersed in a saturated organic solution of apolar solvent and, since the solvent can interact with the tip, this technique can lack spatial resolution. On other hand, UHV technique can yield better resolution, especially when performed at low temperatures and therefore reducing electronic noise and free movement of molecules. However, this method requires evaporation of the molecule from quartz crucible with the microscope placed into an UHV environment (10^{-10} mbar).

Scanning tunneling microscopies and spectroscopies were used to map different properties of molecules with submolecular resolution, e.g. molecular orbitals.⁵³⁴ As examples, two molecules in **Figure 5.1.3** are reported, naphthalocyanine and pentacene, and their acquired STM images.^{535,536} The molecules were electronically decoupled from the metal surface Cu(111) using an ultrathin insulating NaCl film and different bias voltages were applied to map the molecular orbitals.

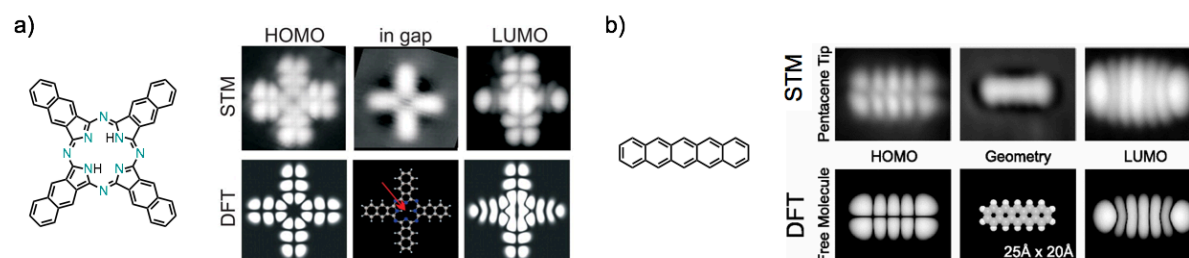


Figure 5.1.3. Orbital images obtained from STM and DFT for a) naphthalocyanine and b) pentacene. STM images are obtained at different bias voltages (usually exceeding HOMO or LUMO).

STM technique has not been used only to map molecular properties with submolecular resolution, both it is also the technique of choice for studying patterned surface, build using the bottom-up approach, as evidenced by examples reported here below.^{294,537,538}

5.1.2. Self-Assembly on Solid Surfaces

Even though much effort has been made in the last decades, the transfer of geometric features from the molecular to the final level remain a laborious and partially unresolved task. Another potential issue is that the supramolecular knowledge from solution cannot be directly transferred to the surface^{528,539} and the influence on the non-covalent bonds need to be fully understood. Most common types of non-covalent bonding used to join molecular components are: *i*) H-bonding interactions, *ii*) metal-ligand coordination, *iii*) van der Waals contacts, *iv*) dipole-dipole interactions and *v*) halogen bonds. In the next sections notable examples of these interaction on surface will be discussed.

5.1.2.1. Hydrogen Bonding

Porous networks were obtained from mono-component systems that self-assemble through complementary hydrogen bonding (**Figure 5.1.4**). In this regard, dimerization of carboxylic acid through two-fold hydrogen bonding represents a simple approach for supramolecular chemistry on surfaces. As an example of this approach, tricarboxylic acid derivatives were found to form porous networks on various surfaces (graphite, Ag(111), ...) due to its planar structure and the dimerization of the carboxylic groups.⁵⁴⁰⁻⁵⁴² Trimesic acid (TMA, 1,3,5-benzenetricarboxylic acid) was found to form honeycombs on Ag(111), with every pore being surrounded by six TMA molecules, each connected via double hydrogen bonding interactions. Another tricarboxylic derivative, benzene-1,3,5-triyl-tribenzoic acid (**Figure 5.1.4a**) was found to display a more complex behavior than its TMA analogue, with three distinct phases on Ag(111). Sublimation, followed by thermal annealing (270-300 K) yielded a phase structurally similar to that of TMA systems, with pores significantly enlarged to 2.95 nm, that were shown to be capable of trapping other guest molecules. Annealing at higher temperatures resulted in sequential phase transformations into arrangements of closer-packed molecules. Hexagonal assembly was observed for 4,9-diamonoperylene-quinone-3-10-diimine (DPDI, **Figure 5.1.4b**) after its recognition sites were activated on Cu(111) surface.⁵⁴³ Thermal dehydrogenation lead to the 'activated' molecular modules to form a porous network through hydrogen bonds with high stability and structural regularity. This grid was then used to position single molecules, in particular for the stepwise assembly of Zn octaethylporphyrin and C₆₀ complex.⁵⁴⁴ A long range order of honeycomb networks by hydrogen bonded spontaneous arrangement of anthraquinone on a Cu(111) surface was reported (**Figure 5.1.4a**).⁵⁴⁵ The formation of the network is driven by hydrogen bonding between carbonyl groups and aromatic protons. Moreover, the formed

cavities (around 50 Å) were more than five times the individual anthraquinone units, and were found to be a balance between intermolecular interactions and substrate-mediated adsorbate-adsorbate repulsion.

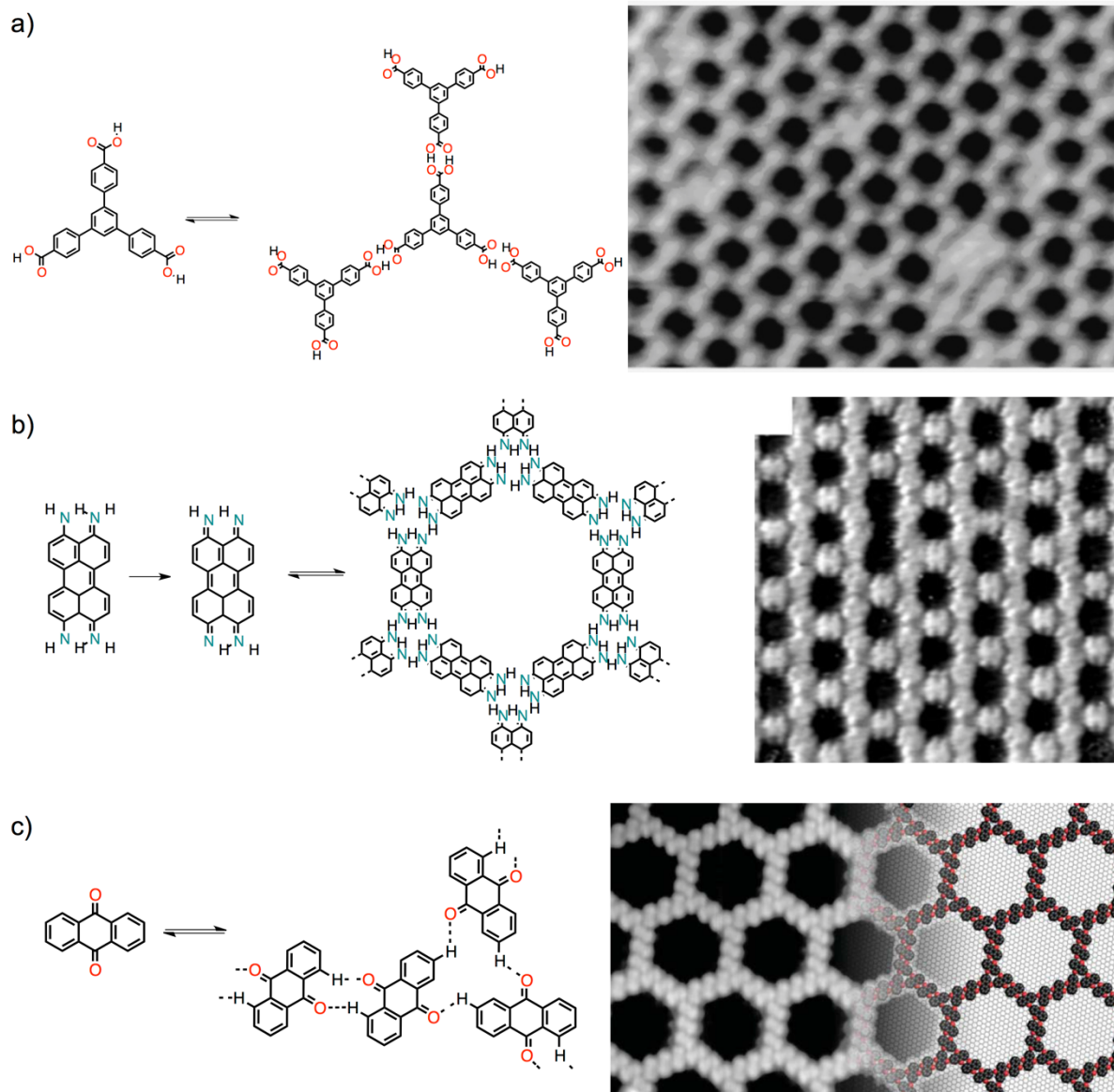


Figure 5.1.4. Self-assembled homo-molecular porous honeycomb networks; a) 4,4',4''-benzene-1,3,5-triyltribenzoic acid on Ag(111) surface (30 × 20 nm, annealing at 270-300 K); b) 4,9-diaminoperylene-quinone-3,10-diimine on a Cu(111) surface (15 nm × 15 nm); c) anthraquinone molecules on a Cu(111) surface (260 Å × 150 Å image size).

Multi-component systems were also prepared in order to design porous sites in a more rational way. Perylene bisimide and melamine were found to form two-component hexagonal networks array

(Figure 5.1.5a) on Ag/Si(111) $\sqrt{3} \times \sqrt{3}$ R30° substrate surface under UHV conditions.⁵⁴⁶ The melamine is able to form nine hydrogen bonds in total and was found to position itself at the vertices, while the PBI modules constituted straight edges of the hexagonal domains. This three-fold symmetry is obtained after stepwise deposition of the components and annealing at 100 °C and was subsequently shown to host in its cavities C₆₀ heptamers.

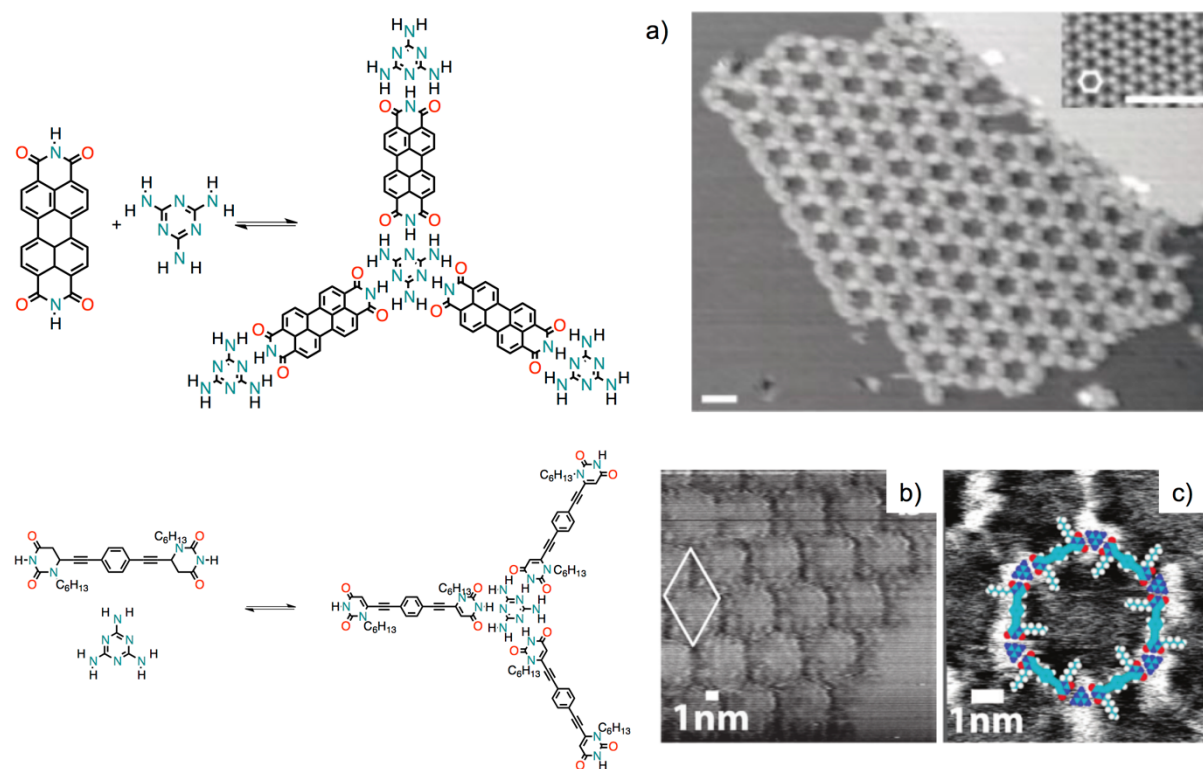


Figure 5.1.5. Two-components porous networks; a) PBI and melamine three-fold hydrogen bonds generate a regular hexagonal network on Au(111); b) bis-uracyl and melamine modules form a hexagonal porous network deposited in 1,2,4-trichlorobenzene on HOPG surfaces.

The PBI/melamine supramolecular patterning was complemented with self-assembled monolayers (SAMs).⁵⁴⁷ First, the same PBI-hexagonal network on Au(111) surface (from a DMF solution) was formed and subsequently, by working on a gold surface, SAMs of alkane thiols in the honeycomb cavities were formed.⁵⁴⁷ Further studies showed the PBI/melamine network to act as diffusion barrier to deposited Cu adatoms, limiting their residence to the 3.5 nm pore.⁵⁴⁸ The PBI/melamine two-component system was also found to be highly dependent on temperature annealing of the Ag(111) substrate (under UHV). The deposition of the molecules was followed by various steps of thermal

annealing: 50 °C gave melamine islands with PBIs adsorbed on their edges,⁵⁴⁹ 60-80 °C yielded hexagonal networks described above,⁵⁴⁹ while annealing at higher temperatures converted the hexagonal into parallelogram arrangements.⁵⁵⁰ Our group, in a collaborative project, reported the formation of two-component porous network based on bis-uracil compounds and melamine, at the solid-liquid (HOPG/1,2,4-trichlorobenzene) interface (**Figure 5.1.5**).⁵⁵¹ As in the case with PBI/melamine patterning, the melamine is at the vertices and forms three three-fold hydrogen bonding with bis-uracil linkers. Notably, at higher concentration ($\sim 20 \mu\text{M}$) tightly packed monolayers of melamine are formed, while at lower concentration regime ($\sim 2 \mu\text{M}$) no competitive physisorption between melamine and bis-uracil modules at the HOPG/TCB interface is observed and sub-monolayer coverage is achieved. In another study, ‘Lander-type’ molecules were designed due to a pronounced three-dimensional structure that leads to the decoupling of the central aromatic core from the underlying substrate, with the assembly guided by hydrogen bonding interactions (**Figure 5.1.6**).⁵⁵²⁻

554

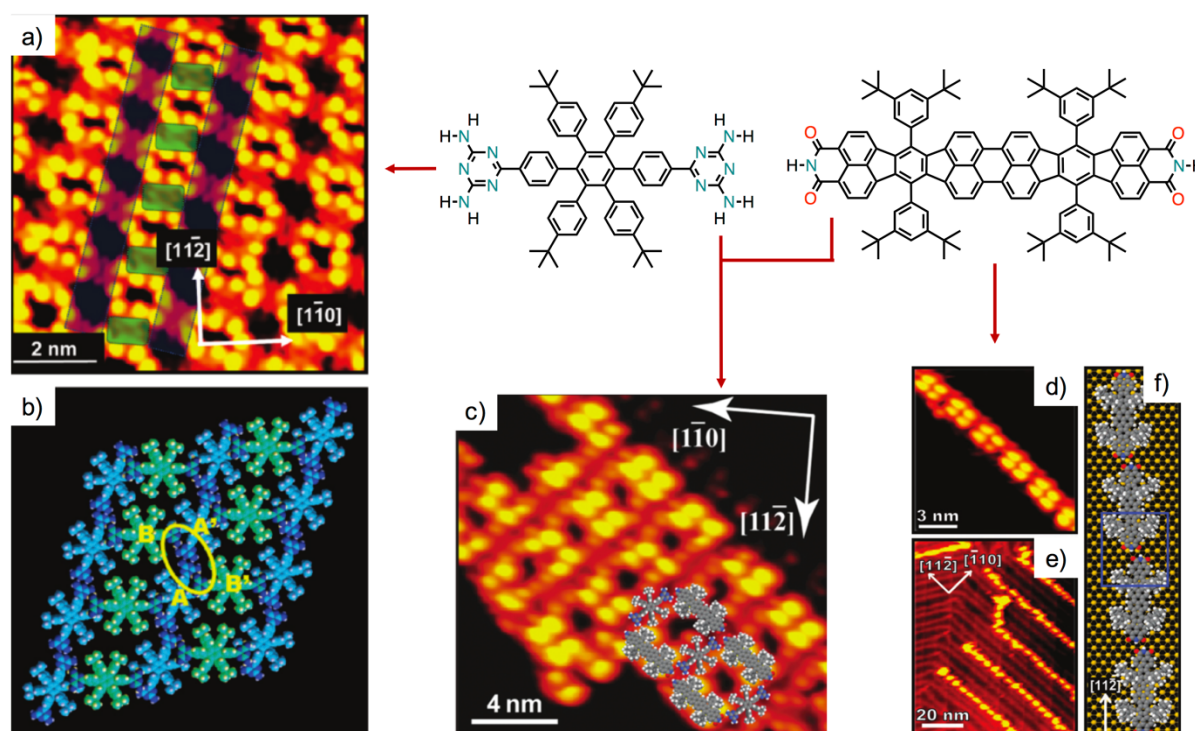


Figure 5.1.6. Lander-type patterning of Au(111) surfaces; ab) Lander-DAT, STM image of ‘grid’ phase with high-symmetry directions of the Au(111) substrate superimposed and its space-filling model showing ‘head-on’ and ‘sideways’ coupling; c) bi-component Lander-DAT and Lander-DCI two-dimension islands formed with superimposed space-filling models; d-f) Lander-DCI chains on Au(111) terraces along with the model.

Lander-DCI (carrying two-di-carboxylic imide, DCI, functionalities) two-fold double N–H··O hydrogen bonding showed to guide the formation of 1-D chains, but the molecule-substrate interaction was found central in the alignment of the resultant chains (**Figure 5.1.6d-f**). Another Lander-type molecule, Lander-DTA (carrying dual diamino-triazine, DAT, moieties), was able to self-assemble both in 1-D and a range of distinct 2-D nanostructures (**Figure 5.1.6ab**). The conformational flexibility (from the decoupled aromatic core from the surface) of this compound resulted in different types of hydrogen bonding (‘sideways’ and ‘head-on’) that would not have been possible using planar compounds. Additional experiments with the co-deposition of the Lander-DTA and –DCI molecule yielded extended 2-D structures (**Figure 5.1.6c**).⁵⁵⁴ Since the rotation of the DAT group is not favorable for complementary DAT-DCI interaction, the formation of Lander-DCI chains interconnect by Lander-DAT molecules by optimized three-dimensional interaction nodes is observed.

5.1.2.2. Dipole-Dipole Interactions

The cyanophenyl moiety, with its simple and asymmetric charge distribution, has been exploited in order to introduce dipole-dipole interactions (**Figure 5.1.7**). Three typical arrangements were found with cyanophenyl groups: *i*) antiparallel dipole-dipole bonding, *ii*) trimeric bonding and *iii*) a hydrogen bonding-type of association.

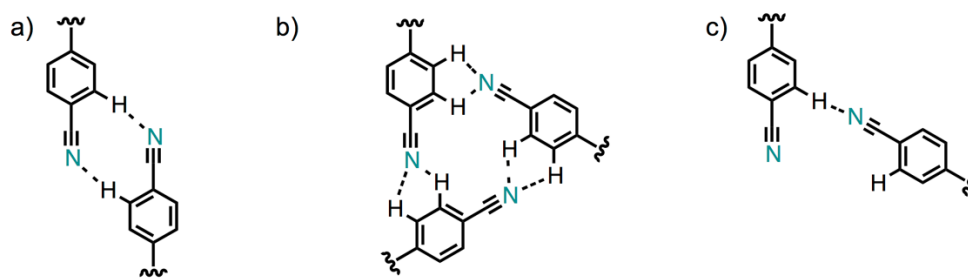


Figure 5.1.7. Typical cyanophenyl C–H··NC interactions between cyanophenyl groups: a) antiparallel dipole-dipole bonding, b) trimeric bonding and c) hydrogen bonding-type association (with variable angle).⁵⁵⁵

Porphyrins equipped with one or two cyanophenyl groups were shown to selectively aggregate on Au(111) into trimers, tetramers or extended supramolecular wire-like structures.⁵⁵⁶ From STM images, the estimated CH··NC contact was 2.5 Å for cyclic structures (**Figure 5.1.8a** i-iii) and 2.6 Å

for antiparallel (**Figure 5.1.8a** iv-ix), that were in good agreement for the calculated cyanophenyl supramolecular structures. The A_2B_2 porphyrins were prepared also with elongated cyanophenyl by one phenylene unit – cyanobiphenyl units (**Figure 5.1.8cd**).⁵⁵⁵

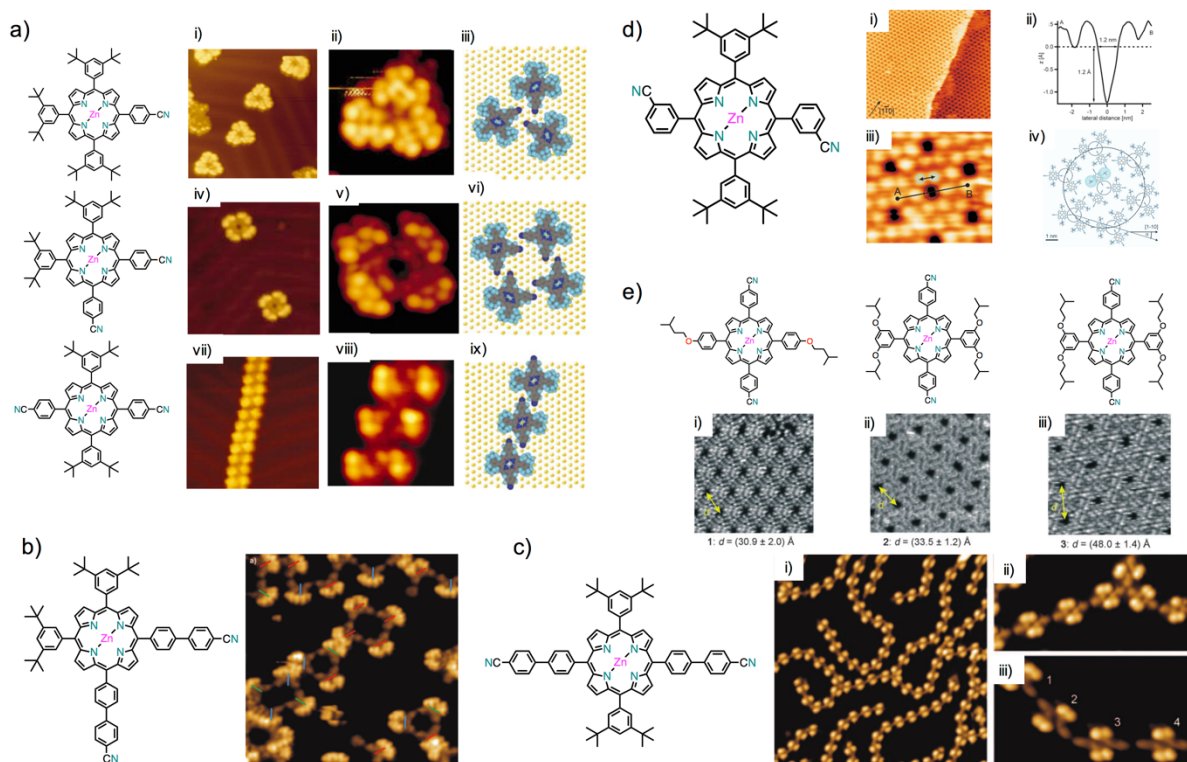


Figure 5.1.8. Cyanophenyl guided porphyrin aggregation; a) cyanophenyl porphyrins on Au(111) surface ($20 \times 20 \text{ nm}^2$) along with enlarged area ($5.3 \times 5.3 \text{ nm}^2$) and the molecular models; b) *cis*-porphyrin on Cu(111) ($18 \times 18 \text{ nm}^2$) showing different oligomeric structure; c) *trans*-porphyrin STM images ($50 \times 50 \text{ nm}^2$) along with cut-outs ($15 \times 7 \text{ nm}^2$) of the trimeric branching site and of the wire-like oligomer ($10.4 \times 5.7 \text{ nm}^2$); d) formation of a porous network on Ag(111) surface along with a zoom-in and a profile scan; finally the proposed model for self-assembled network; e) STM images ($15 \times 15 \text{ nm}^2$) of porous networks formed on Cu(111) from the above drawn porphyrin, with coverage close to one monolayer in each case.

The *cis*-cyanobiphenyl porphyrin, for a coverage up to one monolayer, assembled into oligomeric macrocycles held by antiparallel $\text{CN}\cdots\text{CN}$ dipolar interactions and additional $\text{CH}\cdots\text{NC}$ hydrogen bonding (**Figure 5.1.8b**). The *trans* regioisomers behaved very differently on Cu(111), compared to the above mentioned system on less reactive surface such as Au(111) (**Figure 5.1.8c**). At low coverage, it was observed the formation of both antiparallel dipole-dipole interactions along the supramolecular chain and scatter formation of non-covalent trimers. At high surface coverage, the *trans*-isomer

formed a very dense non-porous network due to antiparallel dipole-dipole bonding along one direction and van der Waals interactions in the other. Moreover, on a Cu(111) surface a strong adsorbate-substrate interaction was observed, which enabled the formation of others type of interactions, such as interlocked chains by additional van der Waals interactions by voluminous 3,5-di(*tert*-butyl)phenyl side chains. A 2-D porous network could be prepared for the 3-cyanophenyl *trans*-isomer (**Figure 5.1.8d**) on Ag(111) surface by an interplay of dipole-dipole and van der Waals interactions.⁵⁵⁷ Formation of cavities (diameter of about 1.2 nm) by trimeric units, guided into hexagonal pores possibly due to interaction with Ag(111) substrates as the cyano functional groups can act as donating ligands. The 1.2 nm cavities were found to host C₆₀ molecules, as could be predicted due to the compatible size of the fullerene cage. Further work, on 4-cyanophenyl *trans*-isomer, was undertaken to understand the influence of different alkoxyphenyl substituents on the porosity of porphyrin assemblies at UHV on a Cu(111) substrate (**Figure 5.1.8e**).⁵⁵⁸ It was observed that, by keeping the same 4-cyanophenyl substituents in 5,15- and changing the alkoxy chains on the 10,20-diphenylsubstituents, a control on the structure dimensionality and the pore-to-pore distances could be achieved, without significantly affecting the pore size.

5.1.2.3. Metal-Coordination Networks

The donating property of the cyanophenyl moieties was recently exploited by our group, working with tetra[(4-cyanophenyl)phen-4-yl]porphyrin (2H-TPCN) (**Figure 5.1.9**).^{559,560} 2H-TPCN self-assembles on Ag(111) into tetragonal close-packed network. Exposure of the network to gadolinium (Gd) atoms gave rise to nanoporous grid-like network stabilized by Gd...NC coordination and subsequent exposure to cobalt (Co) atoms was found to selectively metalate the central porphyrin core, with preservation of the lanthanide coordination network and thus forming a distinct d-f array.

Metal-ligand coordination chemistry of nitrile was also exploited in constructing bi-component networks. Metal-Organic Networks (MON) are formed by exploiting highly specific and directional interaction between organic ligand and transition metal centers. Notably, honeycombs could be formed by using oligo-phenyldicarbonitrile molecules (with 3,4, or 5 phenyl rings) with Co^{III} that has the ability to coordinate three nitrile groups at 120° with respect to each other (**Figure 5.1.10a**).⁵⁶¹⁻⁵⁶⁴ Highly regular and extended hexagonal arrays were obtained with pore size depending on the used organic linker (10, 15, 20 and 24 nm² for NC-Ph₃-CN, NC-Ph₄-CN, NC-Ph₅-CN and NC-Ph₆-CN, respectively).

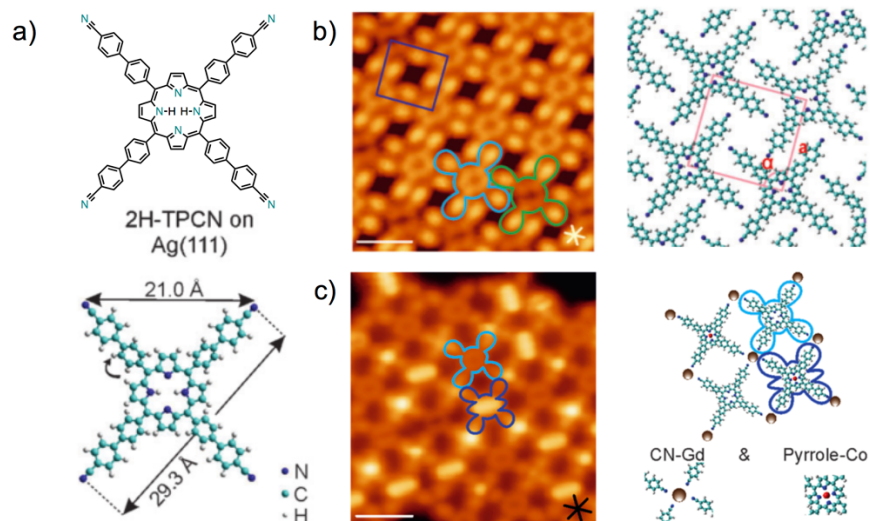


Figure 5.1.9. a) Chemical structure along with ball-and-stick model of 2H-TPCN from semi-empirical AM1 calculations in Hyperchem; b) tetragonal network formed upon self-assembly of 2H-TPCN on Ag(111), high-resolution STM image where submolecular features can be identified, the colored contours (green and blue) indicate the two tautomers, scale bar 2 nm; c) free-base and Co-metallated macrocycles appear as ring-shaped cores and elongated protrusions along two different orientations, respectively (highlighted by light blue and dark blue contours, respectively). Gd atoms are visualized as round dots irrespective of the applied bias voltage.

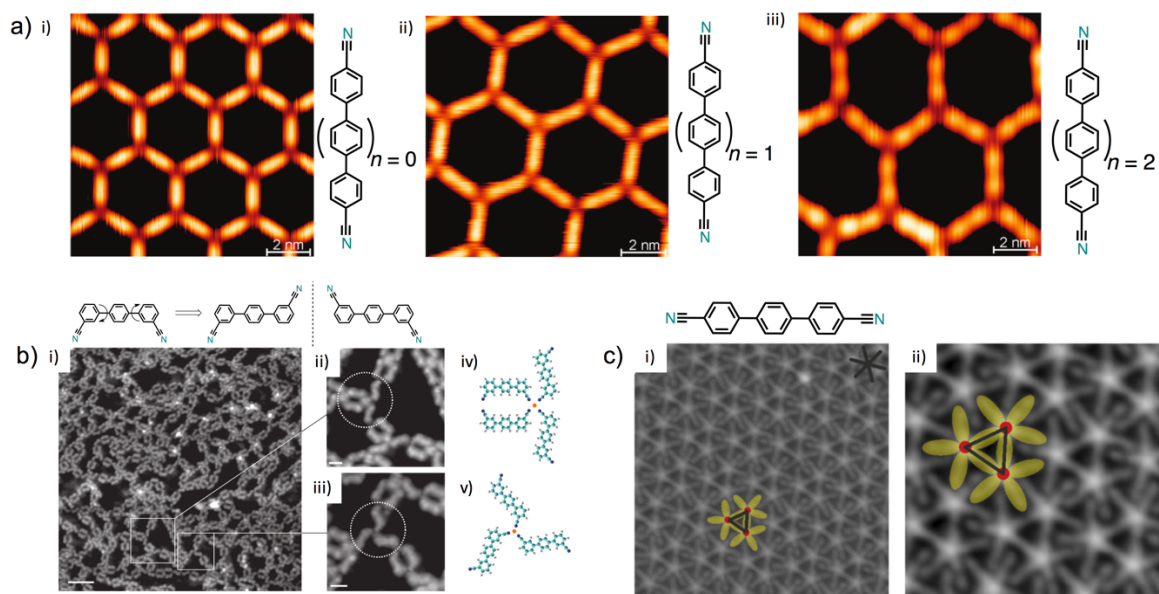


Figure 5.1.10. UHV STM image of the linear and non-linear dicarbonitrile linkers; a) extended nanomesh formed using linkers and Co atoms on a Ag (111) surface by extending the linker length, with along the chemical structures of molecules; b) non-linear pro-chiral linker disordered coordination network on Ag(111) showing three-fold and four-fold coordination nodes with their corresponding models (scale bar 5 nm); c) Ce-directed assembly of linear NC-Ph₃-CN on Ag(111) surface showing five-fold coordination and lateral CN...phenyl interactions.

A more complex system could be obtained by employing a non-linear pro-chiral linker.⁵⁶⁵ With diminished symmetry of the molecules, the number of conformation states accessible becomes larger and thus more complex binding schemes were observed. By incorporating a transition-metal center and a non-linear linker, the formation of a robust and random coordination networks as a new route towards a divergent assembly scenario (**Figure 5.1.10b**). More recently, using a linear NC-Ph₃-CN linker on Ag(111) it was reported the coordination with f-block metal centers (such as cerium or gadolinium) into networks that involve five-fold carbonitrile-lanthanide coordination (**Figure 5.1.10c**).^{566,567}

Numerous other architectures of MOC were reported.^{568,569} For example, 2-D metal-organic networks from iron (Fe) atoms and trimesic acid (TMA) on Cu(100) were found to form mononuclear chiral complexes at room temperature (**Figure 5.1.11a**).^{570–572}

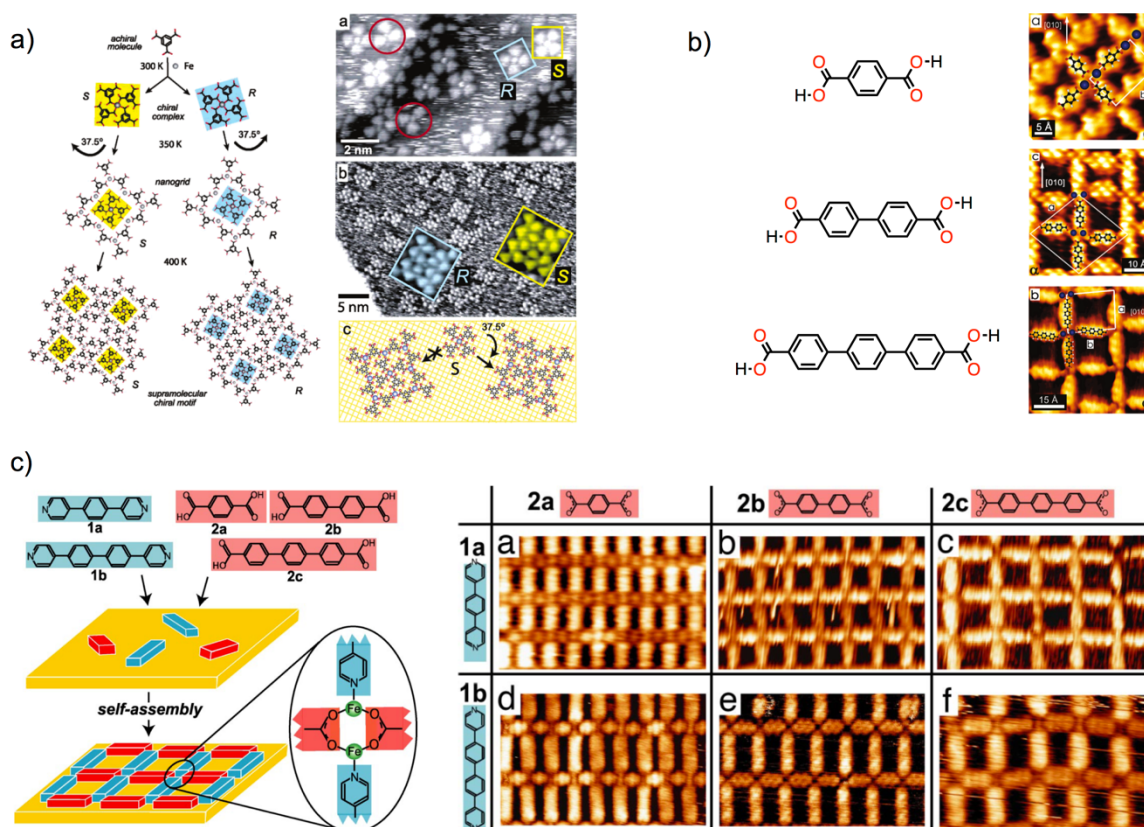


Figure 5.1.11. 2-D metal coordination networks; a) schematic representation of trimesic acid (TMA) and Fe atoms that form the secondary chiral mononuclear $\text{Fe}(\text{TMA})_4$ complex that are antecedents for tertiary polynuclear nanogrids, supramolecular motifs for the assembly of homochiral nanocavity arrays; b) reticular nanoporous Fe-carboxylate networks with diiron centers as coordination motif with different length linkers; c) schematic representation of the complementary molecular ligands deposited with Fe atoms on Cu(100) and the ‘library’ of corresponding self-assembled coordination networks.

From the building blocks (tricarboxylate and Fe atoms) a secondary mononuclear chiral complex was formed that is the precursor to tertiary polynuclear metal-organic nanogrids. Additional experiments with rod-like dicarboxylic acids (*p*-phenylene to *p*-terphenylene) as organic linkers and Fe, showed the formation of topologically rectangular networks, all comprising iron pairs as the networks nodes (**Figure 5.1.11b**).⁵⁷³ Accordingly, the size of the cavities was found to increase almost one order of magnitude. Furthermore, linker and Fe were found to interact with the substrate, which affected the structural details such as orientation, geometry and iron-iron spacing. Further evolution in complexity was achieved in a self-recognizing and self-selecting coordination network (two Fe atoms in a node made of two carboxylate and two pyridines) on a Cu(100) surface (**Figure 5.1.11c**).⁵⁷⁴ The ligands were found to coordinate with Fe atoms in order to form regular arrays or rectangular multicomponent compartments with adjustable size and shapes.

The metal-ligand coordination was taken advantage also by our group in preparing metallo-organic porphyrin assemblies (**Figure 5.1.12**).⁵⁷⁵⁻⁵⁷⁷ Deposition of A₃B porphyrin carrying pyrid-4-ylethynylphenyl substituent on a Cu(111) surface revealed the formation of dimers, that are connect through one Cu adatom coordinated by two pyridines facing each other, in an anti parallel head-on configuration. The A₂B₂ *cis*-isomer displayed the formation of different aggregates with well-defined shape and orientation (mostly triangular and rhombic species made of three or four molecules, respectively) and, on increased coverage, pentamers and hexamers were observed. As for mono-substituted porphyrin above, the interaction was found to occur through head-on pyridyl functions. Finally, *trans*-like porphyrin was investigated. At the coverage of 0.4 ML (substrate temperature 350 K) extended supramolecular chains, that are not interconnected, were observed. Specifically, the intermolecular center-to-center distance between two connected molecules was 32.7 Å, and considering a molecular dimension of the porphyrin monomer to be 29.1 Å, this gave a spacing distance of 3.6 Å between two pyridyl nitrogen atoms. This distance is enough to accommodate the two-fold Py...Cu...Py interaction (**Figure 5.1.12c-f**).

Additionally, the presence of two 3,5-di-*tert*-butylphenyl groups at the 10,20 *meso*-position, upon deposition (at low coverage) on a atomically flat and inert Ag(111) surface, was found to give two chiral configurations of the porphyrin modules. By increasing the coverage, a trimeric aggregate was observed as enantiopure cluster consisting of the same conformations. This unit was a secondary supramolecular building block that formed large aggregates, up to a highly regular hexagonal supramolecular porous network (**Figure 5.1.12gh**).

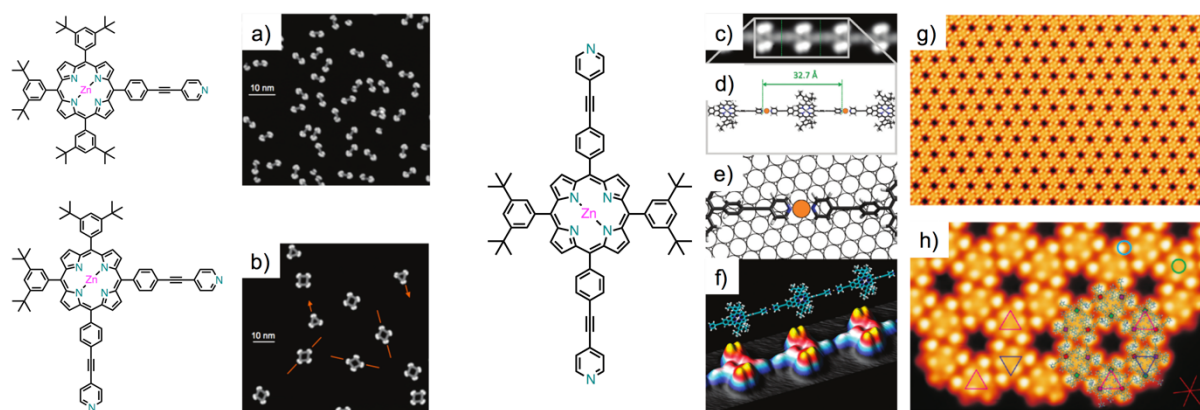


Figure 5.1.12. Chemical structures of porphyrins with *t*-Bu₂Ph groups and pyridyl substituents; a) STM image of self-assembled dimer on a Cu(111) surface; b) coexistence of triangular and rhombic supramolecules after deposition of porphyrin on Cu(111) surface; c) high-resolution STM image of straight coordination chain segment on Cu(111); d) schematic view of pyridil-Cu-pyridyl linear chain; e) top-view model of the Py-Cu-Py coupling motif; f) three-dimensional and computer view of a string chain; g) STM overview image of *trans*-isomer on a Ag(111) surface; h) close-up with superimposed model of the assembly.

5.1.2.4. Halogen-Bonding

Recently, few examples have reported the formation of patterned surfaces through halogen bonding (XB), a non-covalent interaction between an electrophilic cap on a halogen atom (σ -hole) and a nucleophile side on an adjacent molecule.¹⁰ Binary supramolecular structures based on halogen bond between ethynylpyridines and aryl-halides building blocks on graphite were prepared (**Figure 5.1.13a**).⁵⁷⁸ It was observed that electrical stimuli of the STM tip induced the formation of porous and linear networks, with the direction interactions between designed building block guiding the structural outcome.

Fully fluoro-substituted aromatics were generally believed not to form halogen bonds due to the absence of the σ -hole. However, a fluorine homocontact was reported in fully fluoro-substituted aromatic molecule, capable of forming two-dimensional supramolecular structures on Ag(111) surface (**Figure 5.1.13b**).⁵⁷⁹ Although dispersion forces play an important role in the interaction, the driving force was found to be the anisotropically distributed electrostatic potential around the fluorine atoms.

The self-assembly of pyrene derivatives and their role in the Ullmann coupling was explored (**Figure 5.1.13c**).^{580,581} On a Au(111) surface under UHV conditions, 1,3,6,8-tetrabromopyrene molecules arrange into two different 2-D patterns that are stabilized by XB and Br...H bonds at the same time.

The same pyrene derivative was also studied on Cu(111) and Au(111) surfaces. Deposition on Cu(111) at 300 K generated branched coordination polymer due to debromination reaction and formation of C-Cu-C bond. Annealing at 473 K formed short and covalently linked oligomers. Upon deposition on Au(111) at 300 K gave, in contrast, a 2-D pattern stabilized by C-Br...Br-C halogen and C-Br...H-C hydrogen bonds. Thermal annealing at 473 K lead to debromination, followed by formation of metal-coordinated networks. Further annealing gave covalently linked disordered networks.

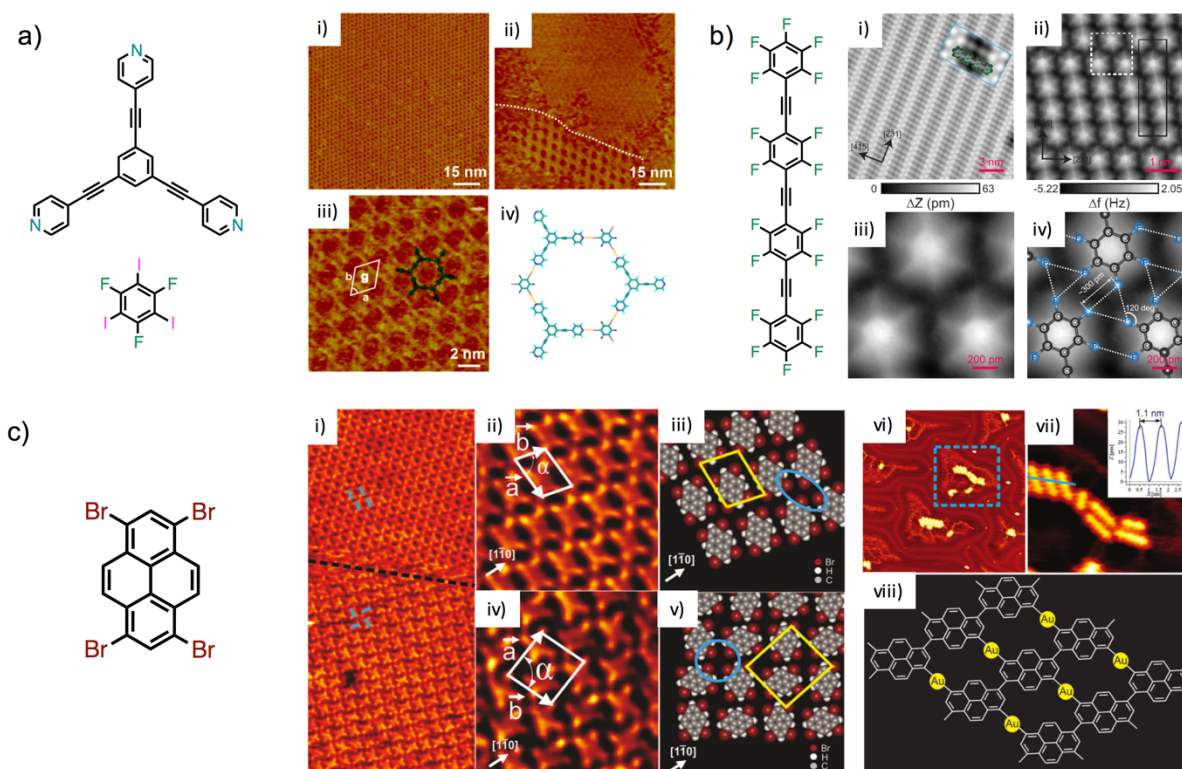


Figure 5.1.13. Halogen guided self-assembly on surfaces; a) tritopic XB acceptor and donor results in honeycomb structure, (i) large-scale STM image of the honeycomb structure; (ii) STM image shows the coexistence of a close-packed structure and network; (iii) high-resolution STM image of the 3N/3F3I honeycomb structure; (iv) structural model of the honeycomb structure; b) i) STM topography of the self-assembled molecule on Ag(111), ii) frequency shift map Δf of the self-assembly at a constant height mode; iii) magnified Δf map of the white square and iv) same as before with superimposed mode; c) tetrabromopyrene on Au(111) i) overview STM image showing co-existence of two different molecular arrangements with ii,iii) and iv,v) the magnified regions along with proposed molecular models for the two phases; vi-viii) tetrabromopyrene on Au(111) annealed at 523 K that formed ordered 1-D polymer chains arranged in 2-D islands.

5.1.2.5. Charge-Transfer on Surfaces

Self-assembly guided by interfacial (molecule-substrate) charge transfer was also reported.^{582–584} Rubrene, a fluorescent polycene with promising electronic properties for organic electronic materials was expected to cluster, as it is a nonpolar molecule, through van der Waals forces (**Figure 5.1.14a-c**) However, on a Au(111) surface homochiral assemblies were found to evolve with increasing rubrene coverage from very small structures composed of a few molecules, to honeycomb islets, and to 1-D chains of supramolecular pentamers, and occasionally into regular decagons. The evolution of 1-D structures came as surprise and suggested that the assembly was governed by a competition of attractive and repulsive forces.⁵⁸²

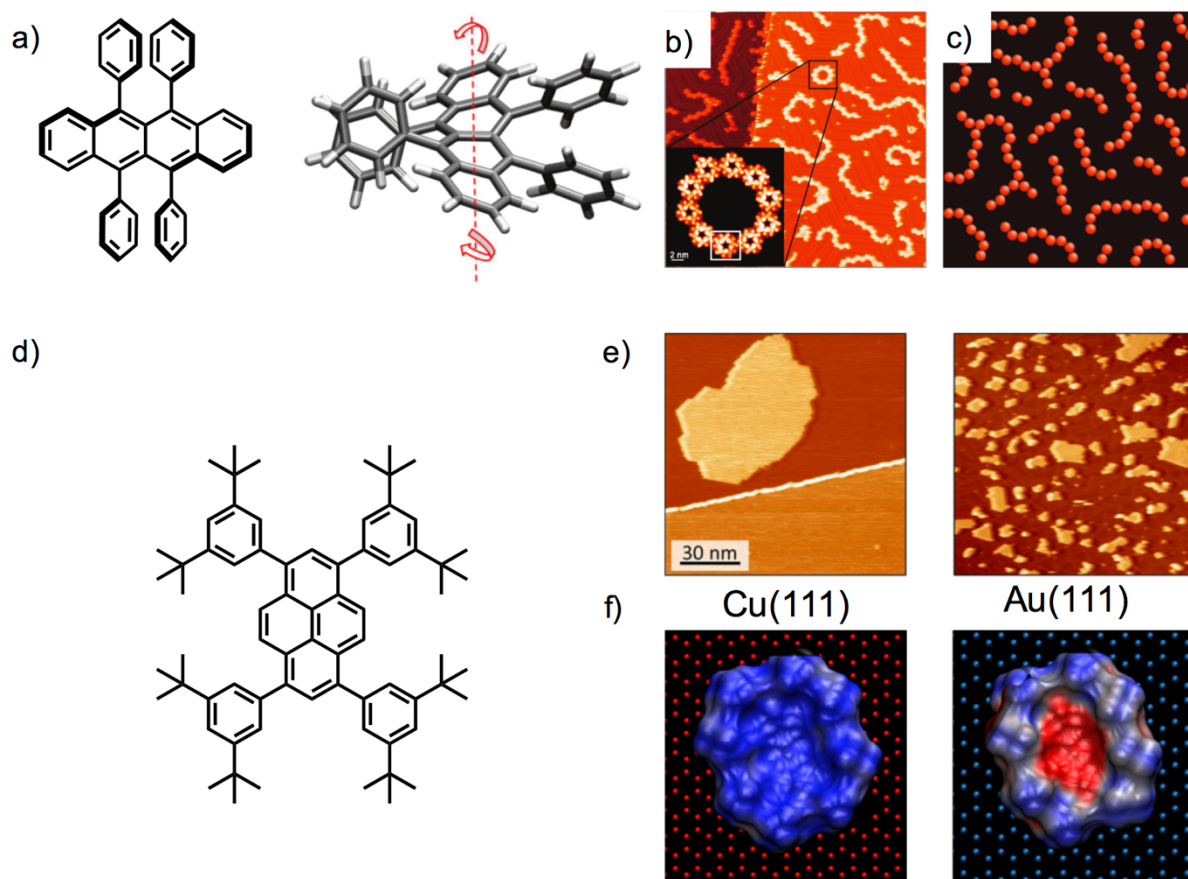


Figure 5.1.14. a-c) Rubrene chemical structure, its optimized model along with the STM images showing sequences of rubrene pentagons (inset is a decagon of pentagons) and a snapshot of the MD simulation; d-f) TBP molecule self-assembly on Cu(111) and Au(111) surface at low molecular coverage, bottom is the DFT calculated distribution of electrostatic potential energy shift with respect to the bare substrate for a TBP molecules.

The results were rationalized through molecular dynamic simulations and spectroscopic measurements.⁵⁸² Rubrene pentagons can be transformed into positive supramolecular ion, since absorbed rubrene HOMO level can rise above the Au(111) Fermi level, giving a charge transfer (hole formation) mechanism. The charged rubrene pentagons on Au(111) are therefore electrostatically repulsed between them. ‘Long-range’ repulsion therefore prevails over ‘short-range’ attractive van der Waals forces at distances exceeding the nearest neighbor linkage length. The interplay between these two forces is responsible for maximizing second neighbor distances within linked pentamers structure, leading to 1-D assembly. Moreover, striking resemblance between MD simulations and experimental STM images was observed, proving that the proposed model support the experimental observations. With these results, specifically designed molecules were synthesized in order to balance the two effects (**Figure 5.1.14d-f**).⁵⁸⁴ A tetra[1,3-di(*tert*-butyl)phenyl]pyrene (TBP) was made in order to weakly interact with transition metal substrates and have a smaller effective ionization potential than the substrate work function, but very close to it. On a Au(111) surface, the molecules underwent a rather peculiar organization, characterized by formation of several separated small island instead of a single large one, an anomalous coarsening.

The substrate was found to affect another molecule, and consequently the self-assembly, such as tetracyanoethylene (TCNE), a strong electron acceptor (**Figure 5.1.15a-c**).^{585,586} Three different substrates were investigated: Au(111), Ag(100) and Cu(100) and showed remarkable differences in TCNE behavior in the ML limit. The results were rationalized by a combination of charge-transfer and lattice-matching properties of TCNE with the different substrates. This causes in a variation of the molecule-molecule and molecule-substrate interactions. Further experiments showed that adsorption of TCNE on Cu(100) is accompanied by a reconstruction of the topmost Cu surface layer, with Cu atoms bound directly to nitrile groups strongly buckled out (protruded) of the surface. Moving from Au(111), to Ag(100) and finally to Cu(100) surface a stronger molecular-substrate binding is observed.

Tetracyano-*p*-quinodimethane (TCNQ, **Figure 5.1.15d-f**) on a Cu(100) surface was found to undergo electron-transfer that lead to significant structural rearrangement both on the metallic and on the organic side of the interface.⁵⁸⁷ The dicyano moieties were found to bend towards the surface that enabled a strong chemical interaction with copper, leading to high adsorption energy (2.23 eV) and rearrangement of the copper surface.

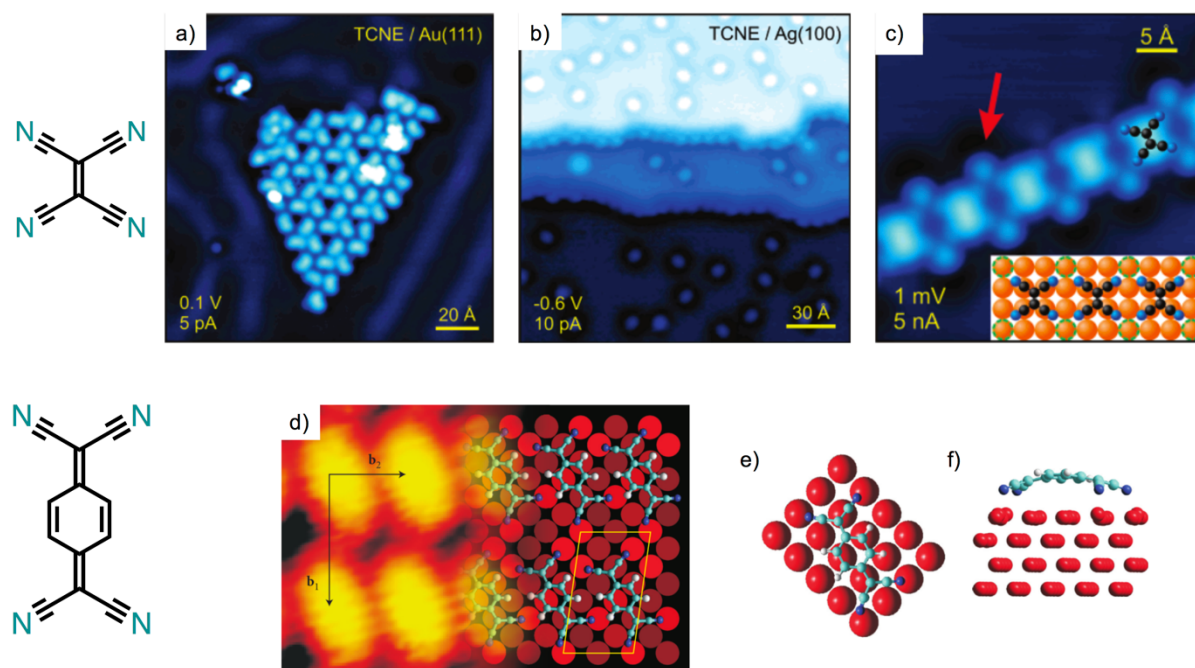


Figure 5.1.15. a-c) STM images of TCNE adsorption on Au(111) with a) order in loose hexagonal pattern, b) TCNE on Ag(100) terraces as isolated molecules; c) TCNE on Cu(100) results in long chains and islands with square symmetry, with Cu-substrate reconstruction indicating formation of a metal-organic coordination network; d-f) TCNQ/Cu(111) interface from experiments and DFT calculations showed structural rearrangements.

5.1.3. Chemical Reactions on Surfaces

Among low-dimensional nanostructured materials that exhibit attractive dimensional-related properties compared to their bulk materials, carbon-based derivatives have merged as light, versatile and low cost alternative.⁵⁸⁸ The rising star among low-dimensional carbon nanomaterials is graphene, characterized by long-range π -conjugation and zero band-gap, a promising candidate for electronic devices.⁵⁸⁹ Tailored macromolecules with semiconducting properties have therefore attracted much attention and have been fabricated. In order to achieve a high degree of atomic and therefore band-gap precision for molecular devices lately C-C coupling of molecular aromatic precursors has opened almost limitless possibilities.²⁹³ Moreover, after mastering the principles of heterogenous reactions and catalysis, on-surface reactions seemed feasible. In this respect, UHV offers some advantages: clean conditions, use of a wide range of temperatures (4-600 K), 2-D confined geometry and the reaction can be followed by STM imaging, allowing also spectroscopic measurements.

The conductance of on-surface produced single polymer was reported (**Figure 5.1.16a-d**).^{590,591} Dibromoterfluorene (DBTF) monomers were deposited on a Au(111) surface that was annealed at 520 K for 5 minutes, the bromine atoms dissociate and covalent bonds can be formed between activated TF monomers that diffuse on the surface. The conducting and mechanical characteristics of the 1-D wire were measured by pulling it up from the Au(111) surface with the STM tip and showed conductance of a single and same molecular wire with 20 nm length.

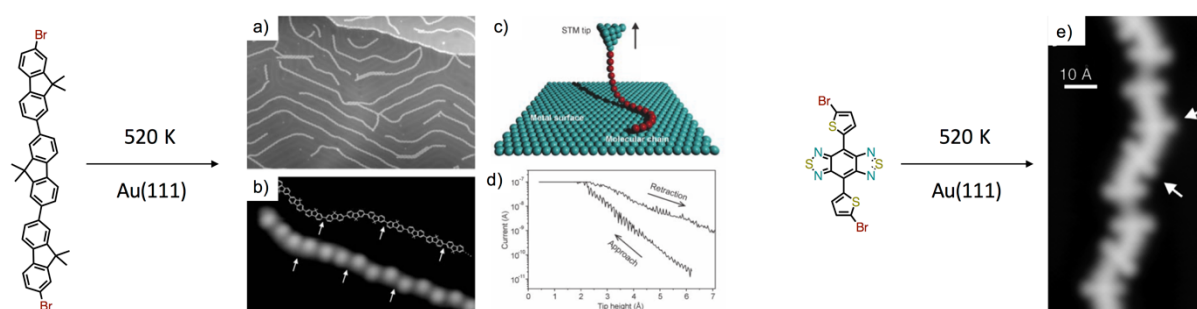


Figure 5.1.16. On-surface polymerization of monomers to conjugated molecular chains; a-d) polyfluorene chains from TBDF: a) overview STM image (80 by 120 nm) after the polymerization and b) STM image of polyfluorene chain (5.9 by 3.6 nm), c) scheme of chain pulling from the surface in rope-like manner and d) tunneling current as a function of the tip height during vertical manipulation; e) DAD polymer synthesized on-surface with an STM image 4.9 by 9 nm.

Flexible molecular wires made of donor-acceptor units were also prepared in a similar fashion and their conductance was measured.⁵⁹² A bis(5-bromo-2-thienyl)-benzobis(1,2,5-thiadiazole) as the Br-DAD-Br monomer (**Figure 5.1.16e**) was prepared and polymerized at 520 K on a Au(111) surface in order to obtain a polymer that alternates donor and acceptor units. It was observed that the D-A-D turns are key for high conductance when compared to homogenous polymers (e.g. made of only thiophene units), with the latter showing a much larger band gap and reduced conductance.

The on-surface C-C coupling was successfully employed in order to construct porphyrin nano-architectures (**Figure 5.1.17**).^{593,594} 5,10,15,20-Tetrakis(4'-bromophenyl)porphyrin (Br₄TPP) was adsorbed on a Au(111) that, with sufficient heating, becomes activated (*i.e.* forms radical fragments) and upon thermal diffusion is able to react with other radicals, resulting in intermolecular chemical bonds. Selective and sequential thermal dissociation was achieved on a similar porphyrin scaffold, a A₂B₂ 5,15-bis(4'-bromophenyl)-10,20-bis(4'-iodophenyl)porphyrin (*trans*-Br₂I₂TPP). At 120 °C

efficient polymerization was induced with selective activation of the iodine substituent into formation of linear chains, leaving the bromine groups intact, ready to be activated in the subsequent step. In the next growth step (heating to 250 °C), 2-D architectures are formed from the 1-D chains.

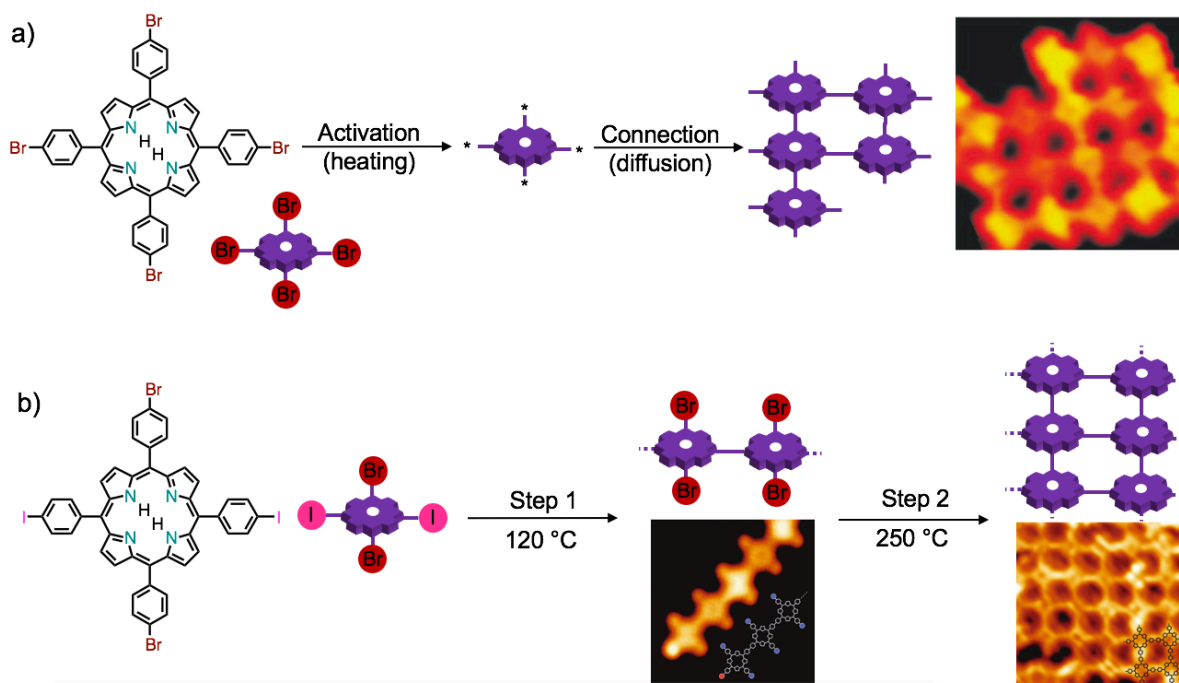


Figure 5.1.17. a) Schematic formation of covalently bound networks along with STM image ($8.5 \times 8.5 \text{ nm}^2$) on Au(111) surface; b) hierarchical growth following sequential thermal activation of iodine ($8 \times 8 \text{ nm}^2$) and bromine ($10 \times 10 \text{ nm}^2$).

Graphene nanoribbons (GNRs), *i.e.* cutting graphene into narrow ribbons, is a topic of major interest since it gives the possibility to tune the value of the bandgap to the desired value for the intended applications.⁵⁹⁵ This path however presents major challenges by top-down approaches (**Figure 5.1.18a**), since it is not feasible with lithographic methods and the presence of even weak defects could give rise to scattering and localization of electrons.^{596–598} An alternative approach, by stitching up molecular precursors into graphene nanoribbons in a ‘bottom-up’ manner (**Figure 5.1.18b**), was proposed through on-surface reaction of 10,10'-dibromo-9,9'-bianthryl (DBBA) precursor. The precursor molecule first is evaporated on a crystalline surface of a noble metal, such as Au(111) and Ag(111) under UHV conditions. Next, annealing allows the formation of radicals that diffuse and meet on the surface, leading to polymer chains through aryl-aryl coupling, similar to the classical Ullmann reaction.^{599,600} The sample is then annealed a second time in order to induce

cyclodehydrogenation reactions that turn the polymer into an atomically precise GNRs with a width N of seven carbon atoms.

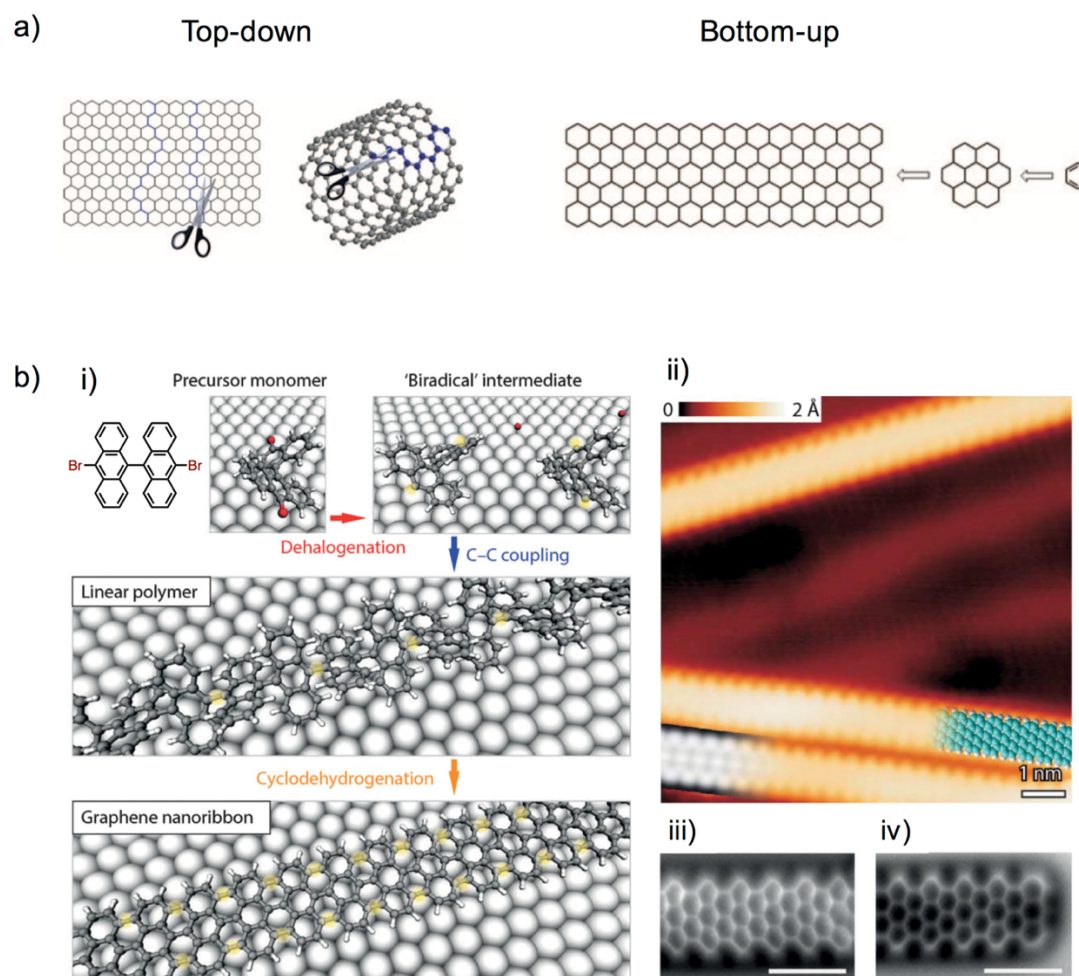


Figure 5.1.18. a) Schematic overview of the top-down and bottom-up fabrication of GNRs;⁶⁰¹ b) on-surface synthesis of $N = 7$ armchair graphene nanoribbons (7-AGNRs); i) synthesis steps including surface-assisted dehalogenation of DBBA monomers, polymer growth by radical addition at temperature and surface-assisted cyclodehydrogenation; ii) constant-current scanning tunneling microscopy (STM) image of 7-AGNRs on Au(111) with superimposed model (blue) and STM simulation (grey); iii-iv) non-contact atomic force microscopy images showing body and terminus of atomically precise 7-AGNR, recorded at constant height with CO-terminated tip.

After the first report of GNRs, much attention has been placed onto armchair GNRs. Starting with poly(*para*-phenylene), considered as 3-AGNR, 5,7,9 and 13-GNRs have been reported.^{602–605} The bottom-up approach is also not limited to armchair nanoribbons, but also ‘chevron-type’ and ‘zig-zag’

nanoribbons (ZGNRs), structures that are out of reach for the top-down approach, can be prepared by carefully designing the starting molecular precursor (**Figure 5.1.19**).^{603,606,607}

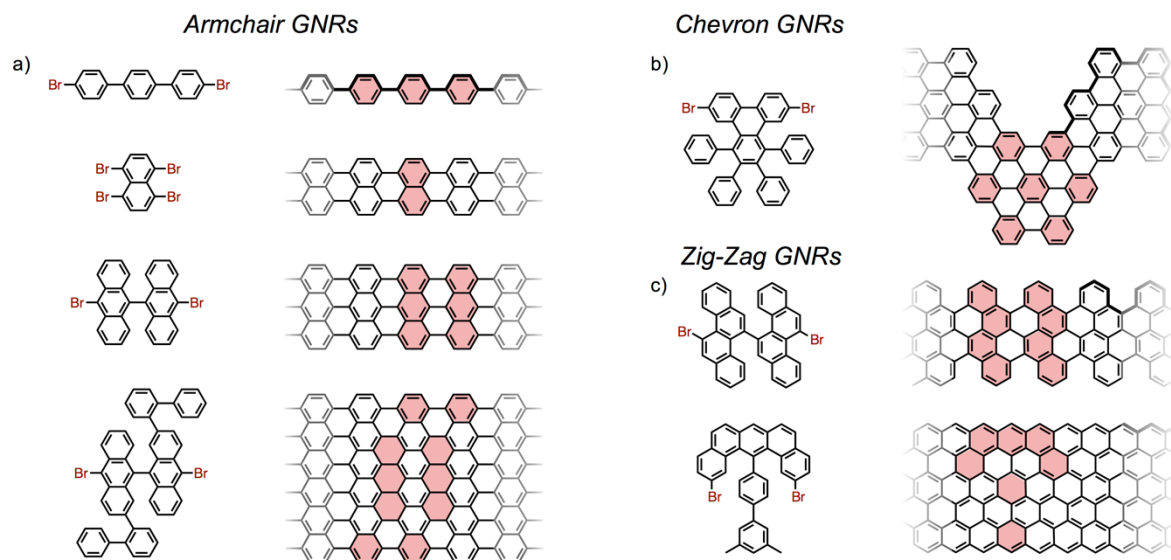


Figure 5.1.19. Molecular precursors for on-surface synthesis of atomically precise GNRs; a) armchair GNRs ($N = 1, 3, 4, 7, 13$); b) chevron GNR; c) zig-zag GNRs ($N = 5$ with cove defect and $N = 6$).

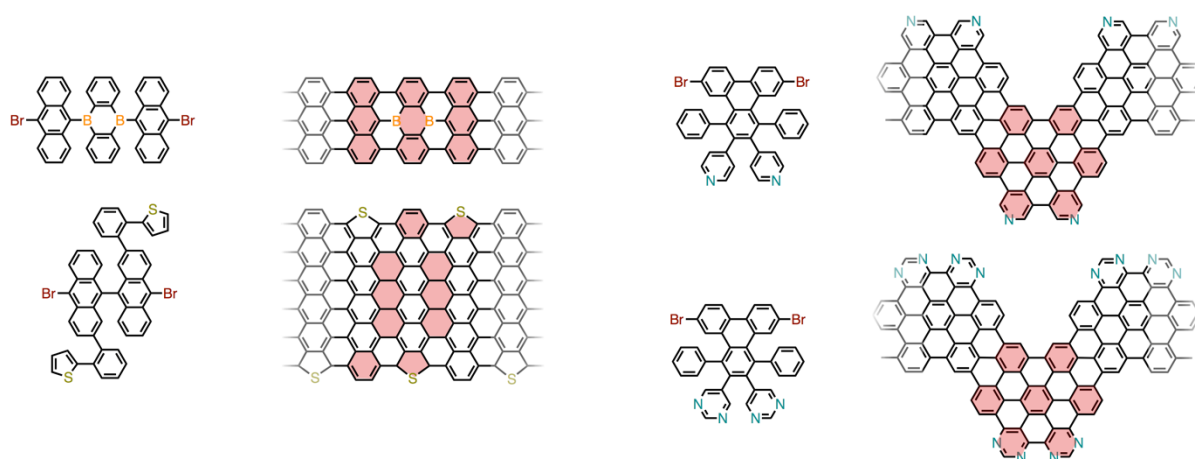


Figure 5.1.20. Site-specific doping with boron, nitrogen or sulfur of GNRs.

Additional benefits of the bottom-up approach include atomically controlled substitutional ‘doping’, by replacing carbon atoms with heteroatoms, such as boron, nitrogen or sulfur (**Figure 5.1.20**).^{608–611}

Despite the recent progress of the aryl-aryl couplings, there is still much to explore in the area of on-

surface organic chemistry, including dehydrogenative coupling, Glaser coupling, cycloaddition and cyclotrimerizations. Additionally, the reported bandgaps for AGNRs $N=5-13$ still exceed 1 eV, even while adsorbed on a metal substrate, thus showing the constant need for further bandgap tuning.

5.1.4. Aim of the Project

The main aim of this project is to investigate the bottom-up approach as precise patterning of metal surfaces. In order to create functional patterns, a polycyclic aromatic hydrocarbon such as pyrene has been established as a key building block. Pyrene has been defined as ‘the fruit fly of photochemists’⁶¹² due to some characteristics as excimer formation, long-lived excited state, high fluorescence quantum yield and the sensitivity of its excitation spectra to micro-environmental changes, making it one of the most studied organic molecules.⁶¹²

Patterning of metal surfaces can be achieved in a variety of ways. We reason that one approach, by using pyrenes carrying pyridine moieties, employing hydrogen bonding. Moreover, we aim towards creating different patterns through molecular design and introduction of pyridyls in specific sites of the pyrene core. In this regards, pyrene chemistry should allow us to play both on number and site of the pyridyl groups (Figure 5.1.21). Reference molecules, carrying phenyls instead of pyridyls, by not carrying information for self-assembling, should yield individualized molecules, rather than patterned surfaces.

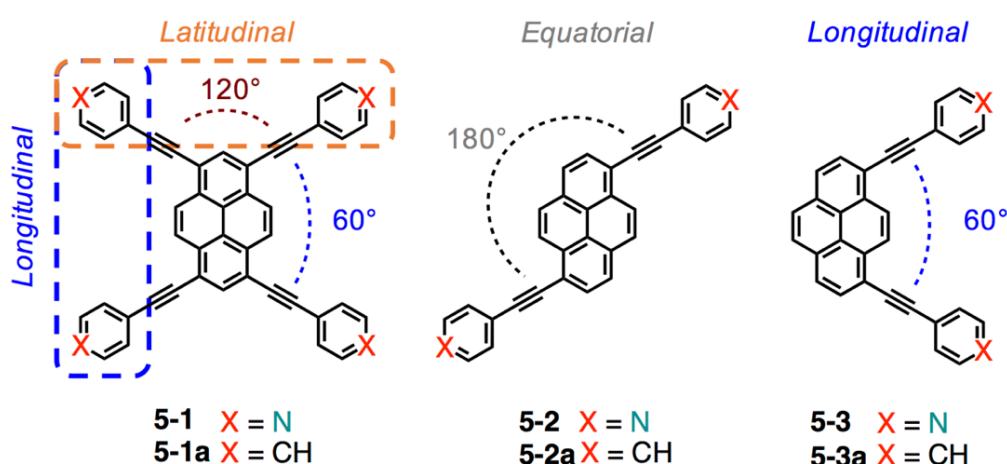


Figure 5.1.21. Target pyrenyl modules. X = N and = C-H for the pyridyl- (5-1, 5-2 and 5-3) and phenyl-derived (5-1a, 5-2a and 5-3a) modules, respectively.

Another bottom-up approach we intend to explore in structuring organic matter on metal surface is through the metal-organic approach (**Figure 5.1.22**). Metals should be coordinated through use of, for example carboxy groups or by introducing reactive sites on the molecule. The latter approach can be achieved by using bromo-derivatives, that are known to active by simple thermal treatment of the surface. To this end, both a bis-carboxy pyrene derivative and a bis-bromo derivatives will be prepared and, thanks to the presence of two groups coordinating or reactive groups, should lead to organo-metallic architectures on surfaces.

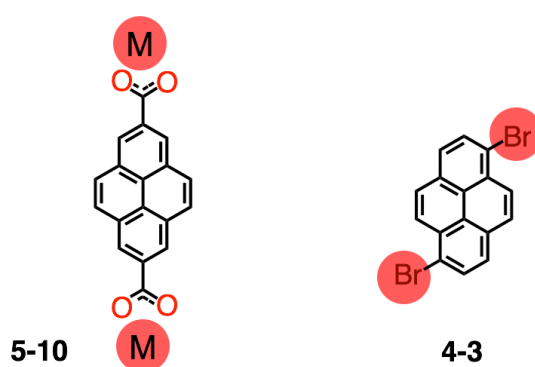


Figure 5.1.22. Two approaches towards metal-organic patterning of metal surfaces.

5.2. Syntheses of Pyrene Derivatives

Electrophilic substitution takes place preferentially at the 1-, 3-, 6-, 8-positions, with the *tert*-butylation the only exception (occurs at 2-, 7- positions). 1-substituted and 1,3,6,8-tetrasubstituted pyrene are easily accessible with relatively simple purification. Di-substituted pyrenes are accessible, although the yields can be lower due to formation of two regioisomers with very similar polarity, thus hampering purification. In any case, the introduction of halogen groups on the pyrene allows us further functionalization with, for example, palladium catalyzed cross coupling reactions. Exhaustive bromination of the pyrene core in the presence of Br_2 in nitrobenzene at 120 °C afforded 1,3,7,8-tetrabromopyrene **5-4**,³⁷⁴ that was hardly soluble in organic solvents, but the reaction was confirmed by MS and the reaction sequence could be carried on. Notably, to obtain 1,6- and 1,8-disubstituted pyrenes **4-3** and **5-8**, halogenation reactions with Br_2 in CCl_4 at room temperature or with I_2 and KIO_4 in H_2SO_4 and CH_3COOH at 40 °C were performed. Both 1,6-dibromopyrene and 1,8-diiodopyrene

could be isolated as pure products after multiple crystallization cycles and their purity was appreciated with $^1\text{H-NMR}$ (Figure 5.2.2 and Figure 5.2.3).

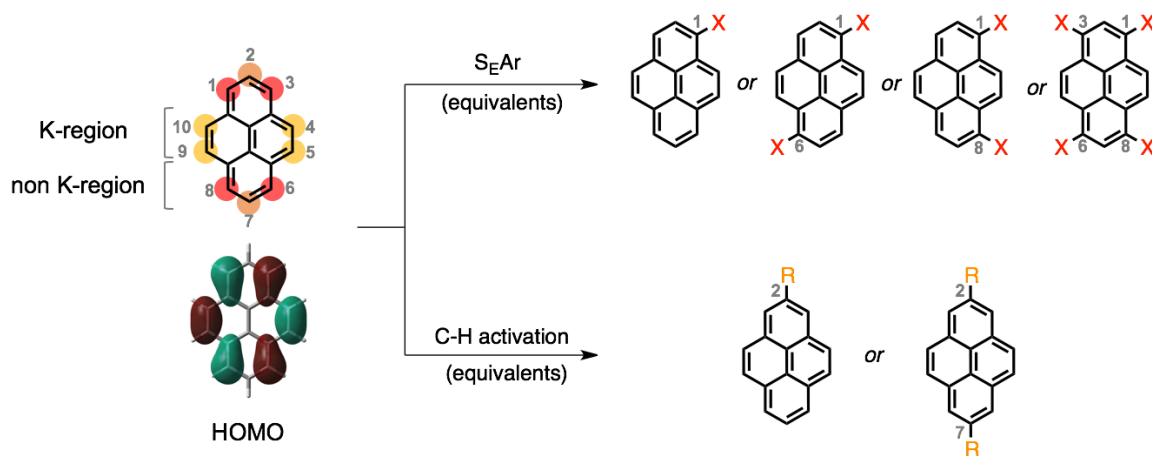
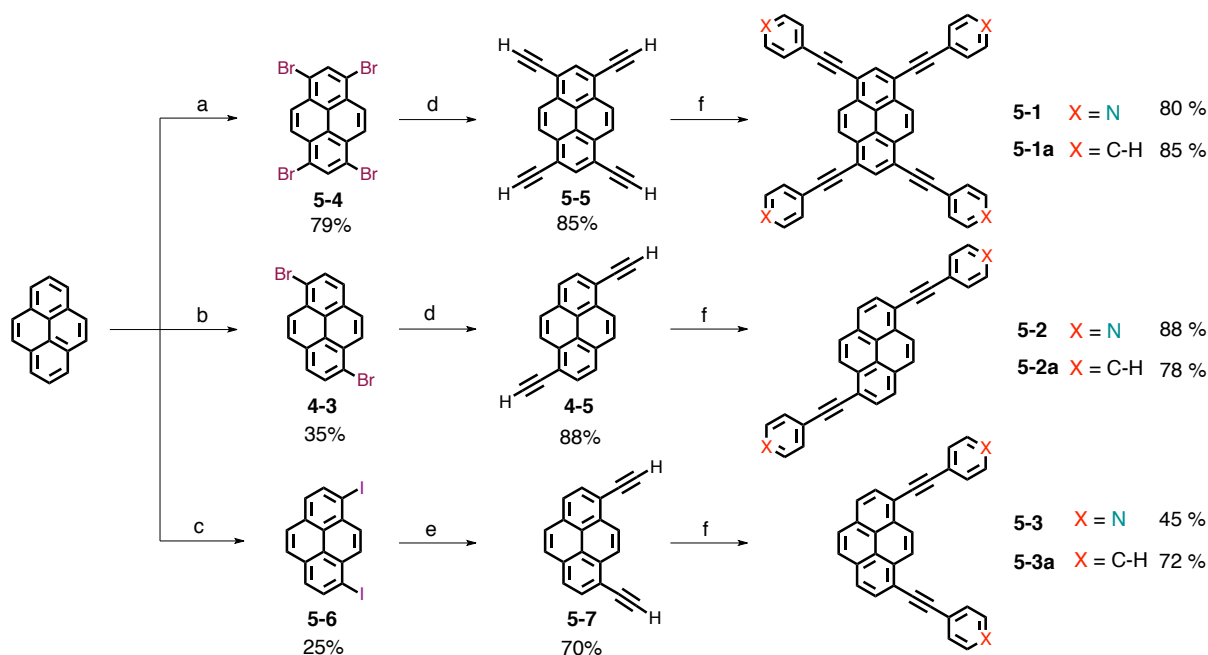
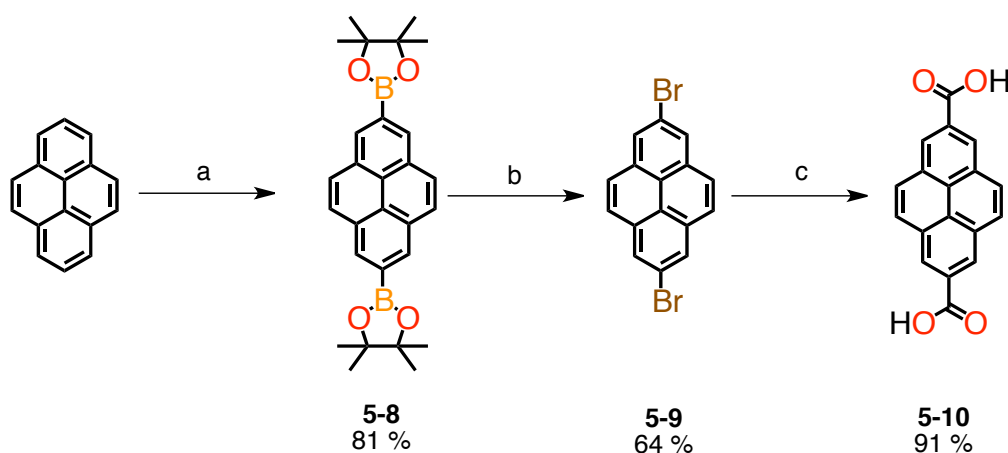


Figure 5.2.1. Pyrene with numbered position and HOMO orbital plot; positions 1-, 3-, 6-, 8- are accessible through electrophilic substitution reaction; position 2-, 7- can be functionalized through C-H activation.



Scheme 5.2.1. Synthetic pathways for the preparation of compounds **5-1(a)**, **5-2(a)** and **5-3(a)**. Reagents and conditions: a) Br_2 , nitrobenzene, $120\text{ }^\circ\text{C}$; b) Br_2 , CCl_4 , r.t.; c) I_2 , KIO_4 , H_2SO_4 , AcOH , $40\text{ }^\circ\text{C}$; d) 1. TMSA, $\text{Pd}(\text{PPh}_3)_2\text{Cl}_2$, CuI , PPh_3 , THF , $i\text{Pr}_2\text{NH}$, $80\text{ }^\circ\text{C}$; 2. KOH , MeOH , THF , r.t.; e) 1. TMSA, $\text{Pd}(\text{PPh}_3)_4$, CuI , THF , Et_3N , r.t.; 2. KOH , MeOH , THF , r.t.; f) 4-iodopyridine or iodobenzene, $\text{Pd}(\text{PPh}_3)_4$, CuI , THF , Et_3N . Note: the best result in order to synthesize compound **5-1a** has been obtained by reacting compound **5-4** with phenylacetylene in Pd-cross coupling conditions.

The halogen-derived pyrenes were subjected to Sonogashira-Hagihara Pd-catalyzed cross-coupling reaction to obtain the relevant TMS-protected ethynyl derivatives, that in the presence of a KOH solution in MeOH/THF (1:1) could be deprotected leading to the terminal acetylene derivatives (**5-5**, **4-5** and **5-7**). Subsequent Sonogashira-Hagihara cross coupling with 4-iodopyridine or iodobenzene afforded compounds **5-1**, **5-2** and **5-3** and reference molecules **5-1a**, **5-2a** and **5-3a** in good yields (**Figure 5.1.21**). While the introduction of the phenyl groups did not pose particular challenges (compounds **5-1a**, **5-2a** and **5-3a**), equipping the pyrene core with the pyridyl moieties proved to be particularly challenging because of the significant insolubility of final conjugates **5-1** and **5-2** in common organic solvents. Compound **5-2**, with the two pyridyl moieties in position 1 and 8, had a sufficient solubility in pyridine, which allowed its purification by column chromatography. On the other hand, compounds **5-1** and **5-2** were prepared following two different methods: *i*) following conventional protocols with Pd catalyst and CuI as co-catalyst at room temperature and *ii*) microwave assisted conditions. While classical conditions afforded precipitates within minutes from the onset of the reaction (that was extensively washed with MeOH, AcCN and PhCH₃) that were hardly processable in organic solvents, while microwave irradiation conditions yielded more soluble (*i.e.*, most likely less aggregated) materials soluble in organic solvents at high temperatures (*e.g.*, 1,1,2,2-tetrachloroethane, TCE). Accordingly, it was possible to obtain different materials that were subsequently sublimed on Ag(111): classical conditions yielded pyrene derivatives **5-1** and **5-2** contaminated with iodide species, presumably from the CuI co-catalyst, and microwave assisted reaction yielded uncontaminated molecules **5-1**, **5-2** and **5-3** that were thoroughly characterized (**Figure 5.2.4**).



Scheme 5.2.2. Synthetic scheme used for the synthesis of pyrene derivatives functionalized in 2-, and 7-. Reagents and conditions: a) B₂Pin₂, [Ir(μ-OMe)cod]₂, 4,4'-di-tert-butyl-2,2'-bipyridine, THF, 80 °C; b) CuBr₂, H₂O, THF/MeOH, 90 °C; c) i) ^tBuLi, THF, -78 °C, ii) CO₂, iii) H₂O.

Next, the pyrene derivatives functionalized in positions 2- and 7 were prepared (**Scheme 5.2.2****Scheme 5.2.2**. Synthetic scheme used for the synthesis of pyrene derivatives functionalized in 2-, and 7-. Reagents and conditions: a) B_2Pin_2 , $[Ir(\mu-Ome)cod]_2$, 4,4'-di-tert-butyl-2,2'-bipyridine, THF, 80 °C; b) $CuBr_2$, H_2O , THF/MeOH, 90 °C; c) i) $nBuLi$, THF, -78 °C, ii) CO_2 , iii) H_2O). Ir-catalyzed C-H activation and borylation at the least hindered positions were performed to obtain the 2,7-functionalized pyrene derivative.^{613,614} The boronate was reacted with $CuBr_2$ in order to obtain 2,7-dibromopyrene. The bromines were then exchanged with Li and the organolithium was reacted by bubbling CO_2 , followed by acidic work-up in order to obtain the 2,7-dicarboxypyrene, following a literature procedure.⁶¹⁵

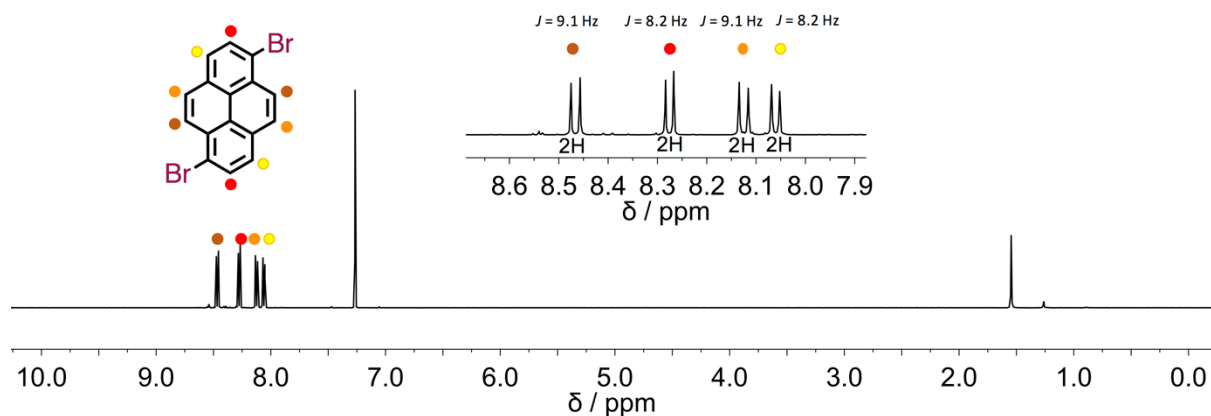


Figure 5.2.2. 1H -NMR (500 MHz, $CDCl_3$, 298 K) of 1,6-dibromopyrene **4-3**.

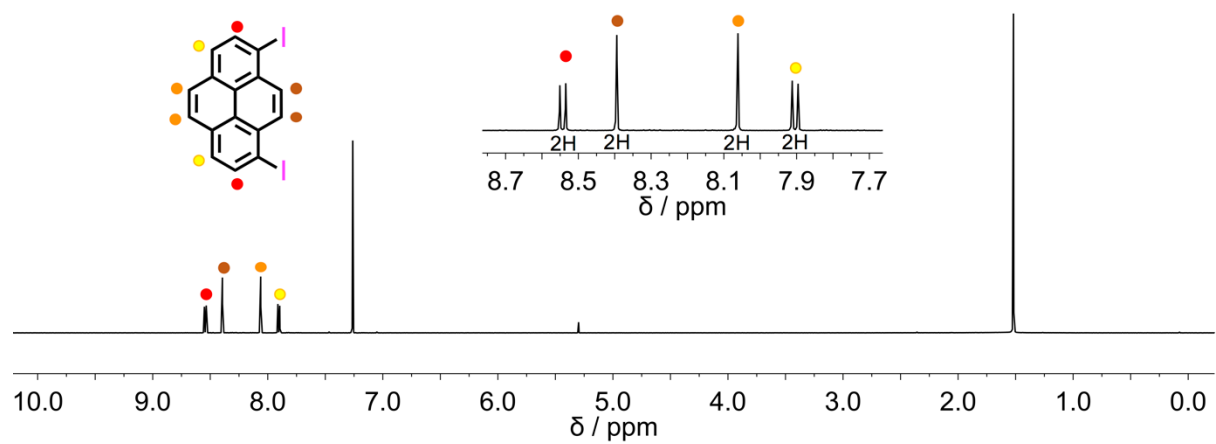


Figure 5.2.3. $^1\text{H-NMR}$ (500 MHz, CDCl_3 , 298 K) of 1,8-diiodopyrene **5-6**.

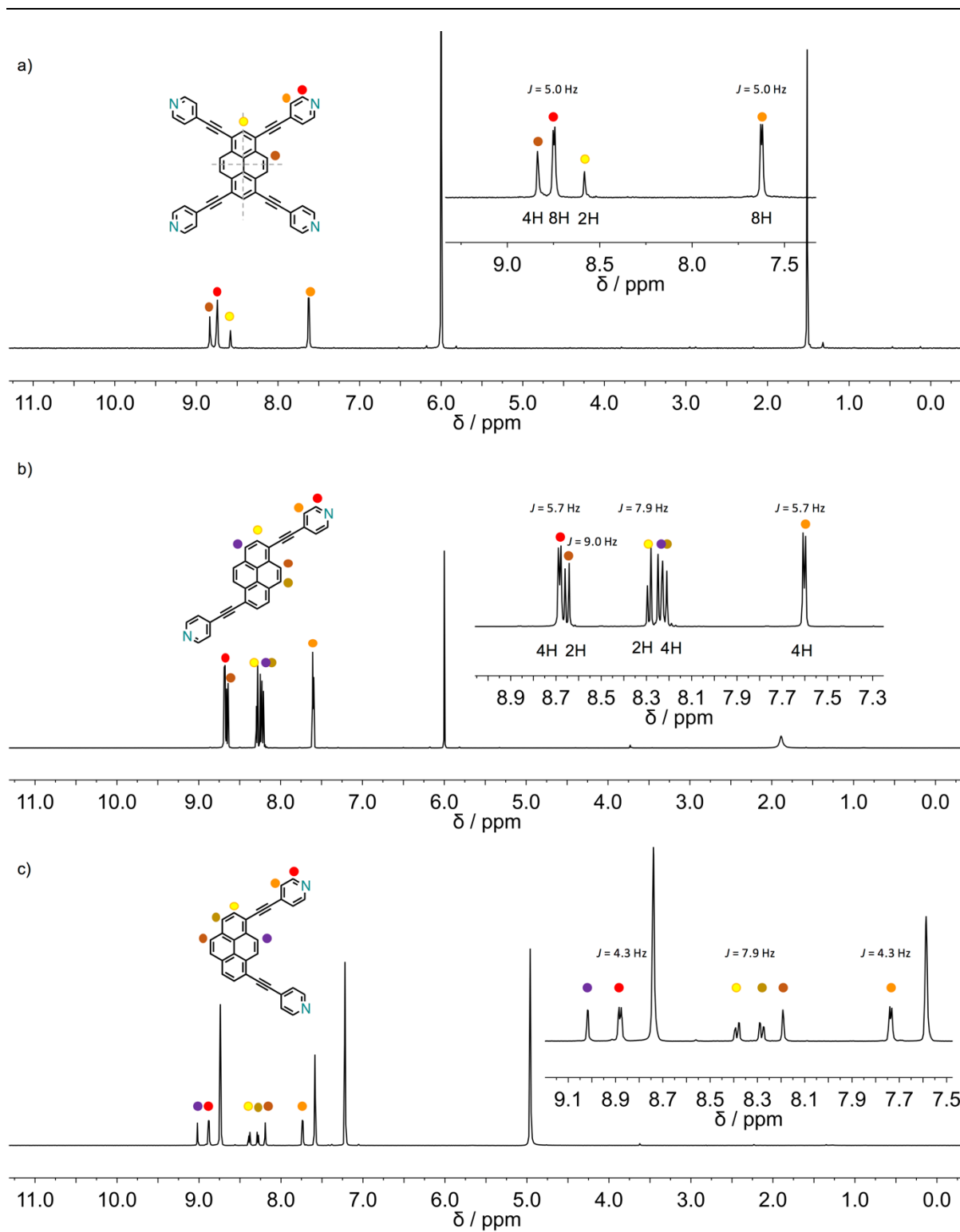


Figure 5.2.4. ^1H -NMR spectra (500 MHz) of pyrene derivatives a) **5-1** (TCE- d_2 , 353 K), **5-2** (TCE- d_2 , 298 K) and **5-3** (500 MHz, Pyridine- d_5 , 298 K).

5.3. Self-Assembly of Pyrenes on Ag(111)

The sublimation of a submonolayer coverage of tetrapyrindyl pyrene derivative **5-1** on Ag(111) gives rise to the formation of regular, extended islands (**Figure 5.3.1a**), presenting one border always pinned to the bottom side of crystal step edges, which hints to their role as nucleation centers. High resolution STM data (**Figure 5.3.1b**) reveals the layer organization and submolecular features. Each molecule exhibits a two-fold symmetric shape resembling a St. Andrew's cross, suggesting a flat adsorption on the surface with a bright central core attributed to the pyrenyl core, and four peripheral dim circular lobes assigned to the peripheral pyridin-4-ylethynyl functional groups.

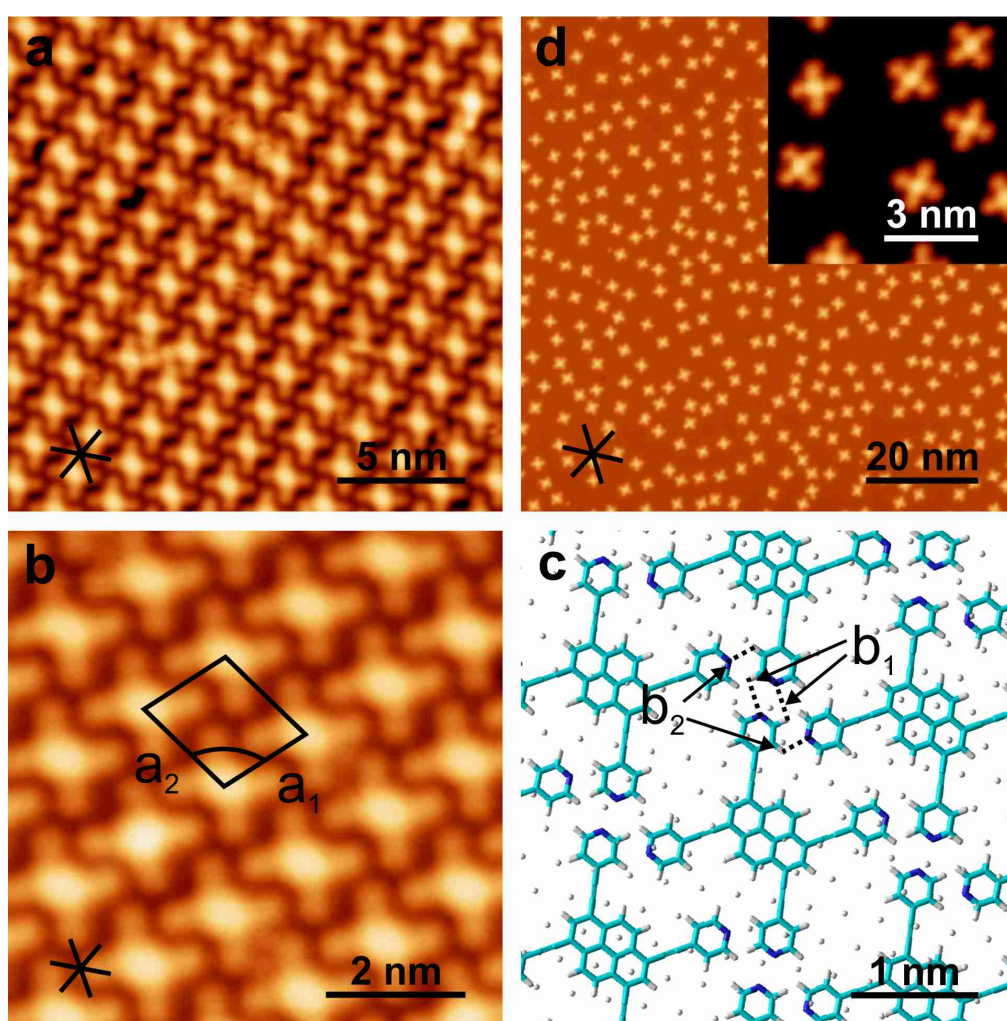


Figure 5.3.1. Self-assembled network of tetrapyrindyl pyrene **5-1** on Ag(111) as imaged by STM. a-c) Tetrapyrindylpyrene species on Ag(111). (a) Overview image (0.1 nA, -0.2 V). (b) High-resolution image (0.1 nA, -0.5 V). (c) Structural model. d) Tetraphenyl species **5-1a** on Ag(111): overview (0.5 nA, 1 V) and high-resolution insert (0.2 nA, 0.1 V). The stars indicate the dense-packed directions of the Ag(111) lattice.

The molecules are arranged forming a rhombic network defined by the lattice vectors $\mathbf{a}_1 = 15.4 \pm 0.5$ Å and $\mathbf{a}_2 = 18.0 \pm 0.5$ Å, with an opening angle γ equal to $100 \pm 2^\circ$ (cf. black rhombus in **Figure 5.3.1b**). As a result, molecules **5-1** interdigitate in the short direction a_1 , whereas they form a small rhombic cavity of approximately 6×6 Å² along direction a_2 . A tentative atomistic model of the assembly is depicted in **Figure 5.3.1c**. Within the accuracy of the STM calibration, the architecture appears as a superstructure semi-commensurate with the Ag(111) substrate with matrix:⁶¹⁶

$$M = \begin{pmatrix} 4.5 & 1.5 \\ \frac{1}{4} & 7 \end{pmatrix}$$

Although the exact binding site cannot be determined from this model, it becomes apparent that every row in a_2 -direction consists of molecules adsorbed on identical binding sites, with binding sites alternating between the rows aligned along the a_1 -direction. The majority of molecules align their short axis of symmetry slightly off the close-packed directions of the Ag(111) lattice (cf. **Figure 5.3.1bc**). Within one island the pyrene molecules present the same orientation. The rhombic network is mainly stabilized by two distinct intermolecular non-covalent N \cdots H bonds (indicated as b_1 and b_2 in **Figure 5.3.1c**) between the pyridyl functions of adjacent species, with projected N \cdots H lengths of 2.9 ± 0.3 Å and 2.4 ± 0.3 Å, respectively. Notably, the domains present organizational chirality based on two distinct interdigitation alignments of the achiral pyrene units. Accordingly, mirror domains of derivative **5-1** are resolved on the surface.

To elucidate the coordination aptitude of the pyridine-4-ylethynyl groups, reference tetraphenyl pyrene derivative **5-1a** (1,3,6,8-tetra(phenylethynyl)pyrene) was also deposited on Ag(111) (**Figure 5.3.1d**). Although the molecules are adsorbed flat on the surface as for pyrene derivative **5-1**, the absence of the peripheral pyridyl groups prevents the formation of N \cdots H bonds and, despite the possibility of aggregating through VdW interactions, only a scattered distribution of molecules **5-1a** is clearly observed on the surface. Statistical analysis of next-neighbor distances does not reveal counts at a separation closer than 20 Å. This suggests the presence of considerable intermolecular repulsion, possibly caused by molecule-substrate charge transfer.⁶¹⁷⁻⁶¹⁹

Molecule **5-1a** also aligns its short symmetry axis slightly off to the close-packed directions of the Ag(111) lattice, similarly to derivative **5-1**. The effect for both cases is comparable, with a magnitude of $(5.5 \pm 1)^\circ$ in the case of module **5-1** and a broader distribution in the case of phenyl-terminated molecule **5-1a**, which exhibits angles of about $(6 \pm 10)^\circ$. This suggests that the tilt is primarily induced by interactions between the surface and pyrene core rather than intermolecular interactions through the pyridyl moieties, but it is greatly stabilized by the rigidity of the assembly.

Next, the focus was set on the self-assembly of di-substituted pyrene derivatives **5-2**, **5-2a** and **5-3**, **5-3a**. 1,8-Di(pyridin-4-ylethynyl)pyrene (abbreviated as *cis*-like dipyridyl-pyrene) derivative **5-3** was sublimated on pristine Ag(111).

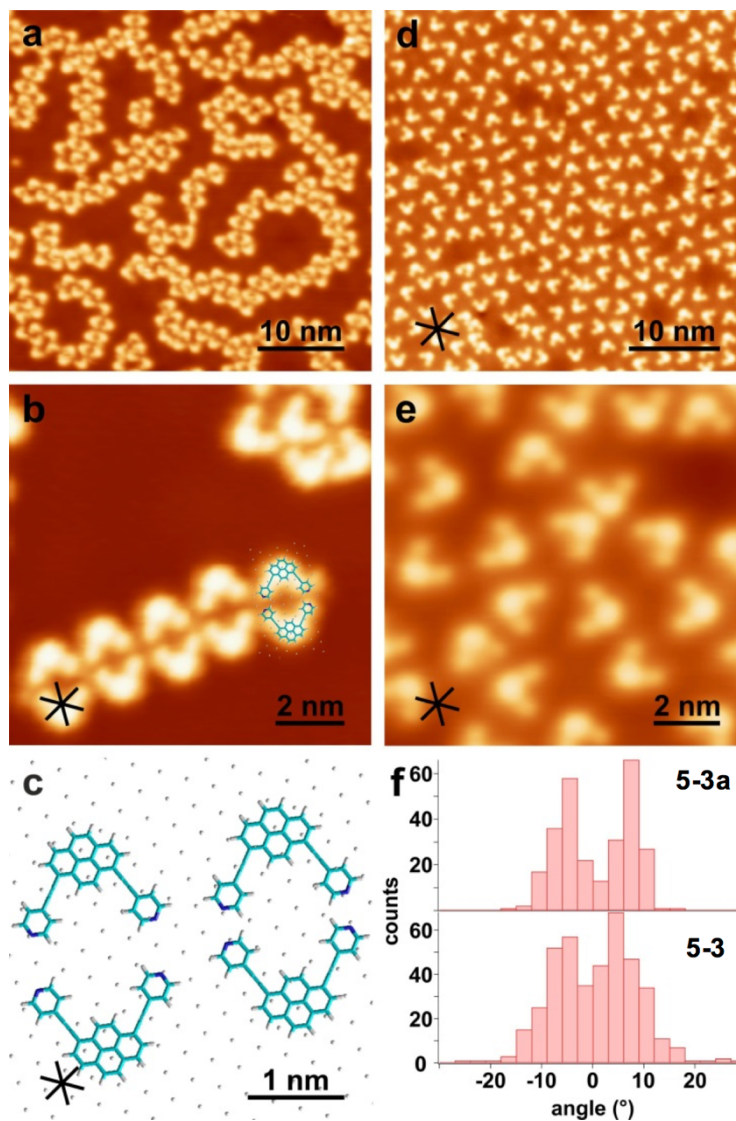


Figure 5.3.2. Self-assembly of *cis*-like bidentate pyrene modules **5-3** and **5-3a** on Ag(111). a-c) *cis*-like dipyridylpyrene **5-3** on Ag(111). a) Overview image (0.1 nA, -0.2 V). b) High-resolution image (0.15 nA, -0.2 V). c) Structural model showing two dimer configurations on the Ag(111) lattice. The projected N...N distances are 3.7 Å and 4.8 Å, respectively. d-e) *cis*-like Diphenylpyrene **5-3a** on Ag(111). d) Overview image (0.09 nA, 0.1 V). No assemblies are formed after room temperature deposition of reference species **5-3a**. e) High resolution image of **5-3a** highlighting the restricted number of orientations of the molecule on the Ag(111) lattice (0.1 nA, 0.1 V). f) Histograms showing the distribution of angular alignment deviation from close-packed lattice directions (equivalent to 0°) for molecules **5-3** and **5-3a** (406 and 275 molecules, respectively).

Figure 5.3.2a displays the resulting assembly for a submonolayer coverage, which consists of long chains, coexisting with some agglomerates. A high-resolution image allows us to discern the submolecular features (**Figure 5.3.2b**). Each molecule presents a two-fold pacman-like shape, exhibiting a bright center attributed to the pyrene core, and two dim peripheral lobes assigned to the pyridin-4-ylethynyl peripheral groups. Regarding the molecular organization, two supramolecular motifs are clearly identified: *i*) head-to-head contacts between oppositely oriented species, giving rise to pure chains (*cf.* bottom part of **Figure 5.3.2b**) and *ii*) intermolecular N \cdots H bonds between pyridin-4-ylethynyl moieties and the pyrene core of adjacent molecules with a projected N \cdots H length of 2.3 ± 0.5 Å, giving rise to the formation of agglomerates (*cf.* top part of **Figure 5.3.2b**). A tentative atomistic model of the molecular chains is depicted in **Figure 5.3.2c**, revealing a non-commensurate adsorption of the molecular species, which follows a fashion by which the axis of symmetry is again oriented slightly off the close-packed directions of the substrate. The nature of the head-to-head contacts (motif *i*) is still under debate and may involve Ag substrate atoms, probably slightly pulled up by the interaction with the pyridyl moieties. A statistical analysis of nearest neighbor separations for a coverage of 0.23 molecules/nm² reveals a preferred separation of 15 Å that is shorter than the head-to-head distance of roughly 18 Å. As in the assembly of species **5-1a**, the deposition of bidentate *cis*-diphenylpyrene species **5-3a** on Ag(111) results in a scattered distribution of molecules over the entire surface (**Figure 5.3.2de**). High-resolution STM images show that this molecular species presents a very similar appearance to **5-3**, *i.e.* they are adsorbed flat exhibiting a central bright core attributed to the pyrene backbone, and two peripheral dim lobes assigned to the phenyl functions. A statistical analysis of the nearest neighbor separations for coverage of 0.18 molecules/nm² reveals the absence of counts at small separations, pointing to a dominating repulsive molecule-molecule interaction, possibly originating from molecule-substrate charge transfer.⁵⁸⁴ In addition, a statistical analysis was made pertaining to the orientation of modules **5-3** and **5-3a** with respect to dense-packed lattice directions, which shows that both species tend to prefer a slightly tilted orientation of their short symmetry axis of about 5-10° off the closest high symmetry direction (*cf.* **Figure 5.3.2f** and model in **Figure 5.3.2c** for comparison). This is in perfect agreement with the distribution of orientations for pyrene module **5-1a**, again corroborating our assumption that the substrate-backbone interactions rather than the interactions between substrate and functional groups are governing the alignment. However, the distribution is slightly narrower in the case of phenyl-terminated module **5-3a**. We attribute this to a directional influence due to interactions between the pyridyl nitrogen atom and the

surface, stabilizing the molecule in orientations with even bigger misalignment with respect to the dense-packed crystal directions.

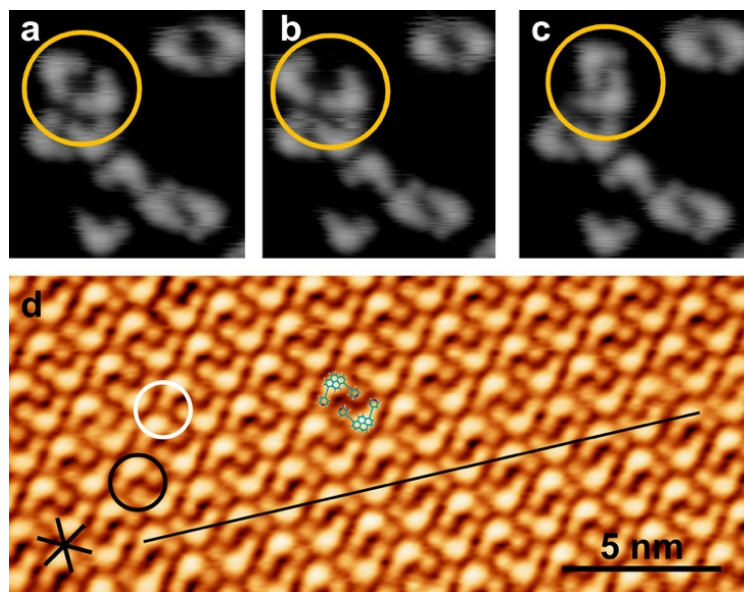


Figure 5.3.3. Meta-stability of the head-to-head coupling of *cis*-like pyrene **5-3** on Ag(111). Transformation of the head to head motif **a**) to a dense-packed dimer **c**) by lateral STM manipulation at 6 K. This process is reversible (0.08 nA, -1 V). **d**) An identical packing is achieved at a full coverage of the sample after room temperature deposition (0.1 nA, 0.1 V). The superimposed models represent the dimer motif.

The rather narrow distribution of misalignments leads to an almost uniform distribution of directions of chains in the case of low coverages of pyrene derivative **5-3**, which may be extracted from STM images by autocorrelation (2D Fourier analysis). This is in contrast with other systems where a more rigid alignment between neighboring molecules corresponds to directionality in the assembly of one-dimensional structures.⁵⁷⁷ Remarkably, as depicted in **Figure 5.3.3a-c**, by lateral STM manipulation of a head-to-head link of *cis*-like pyrene **5-3** one can reversibly convert the motif into an interdigitated dimeric complex (**Figure 5.3.3c**) with a separation of 15 Å, which involves N \cdots H bonds between opposite molecular units.

By drastically increasing the coverage up to the monolayer regime, a new phase arises (**Figure 5.3.3d**), which presents a one-dimensional long-range order and consists of parallel rows of two oppositely oriented molecules (*cf.* black line superimposed on a row in **Figure 5.3.3d**). The rows are interlocked with each other by two different N \cdots H H-bonds: *i*) the interdigitated dimer described above (*cf.* black circle in **Figure 5.3.3d**), and *ii*) that between the pyridin-4-ylethynyl moieties and the pyrene core of

identically-oriented species (*cf.* white circle in **Figure 5.3.3d**). Again, as a result of the interdigitated dimer, a surface organizational chirality arises in the form of two different synthons. This duality in turn gives rise to two possible domains within the dense-packed arrays (**Figure 5.3.3d** just above the black line). In a further set of experiments, the sublimation of *trans*-like pyrene derivative **5-3** on Ag(111) gives rise to a porous network, featuring a Kagome lattice architecture. An overview image is presented in **Figure 5.3.4a**, exhibiting cavities of two different diameters, about 6 and 18 Å, respectively. A high-resolution image allows us to discern some intramolecular features (**Figure 5.3.4b**). The molecular species exhibit a bright central lobe and two peripheral dims, again assigned to the pyrene core and pyridin-4-ylethynyl moieties, respectively.

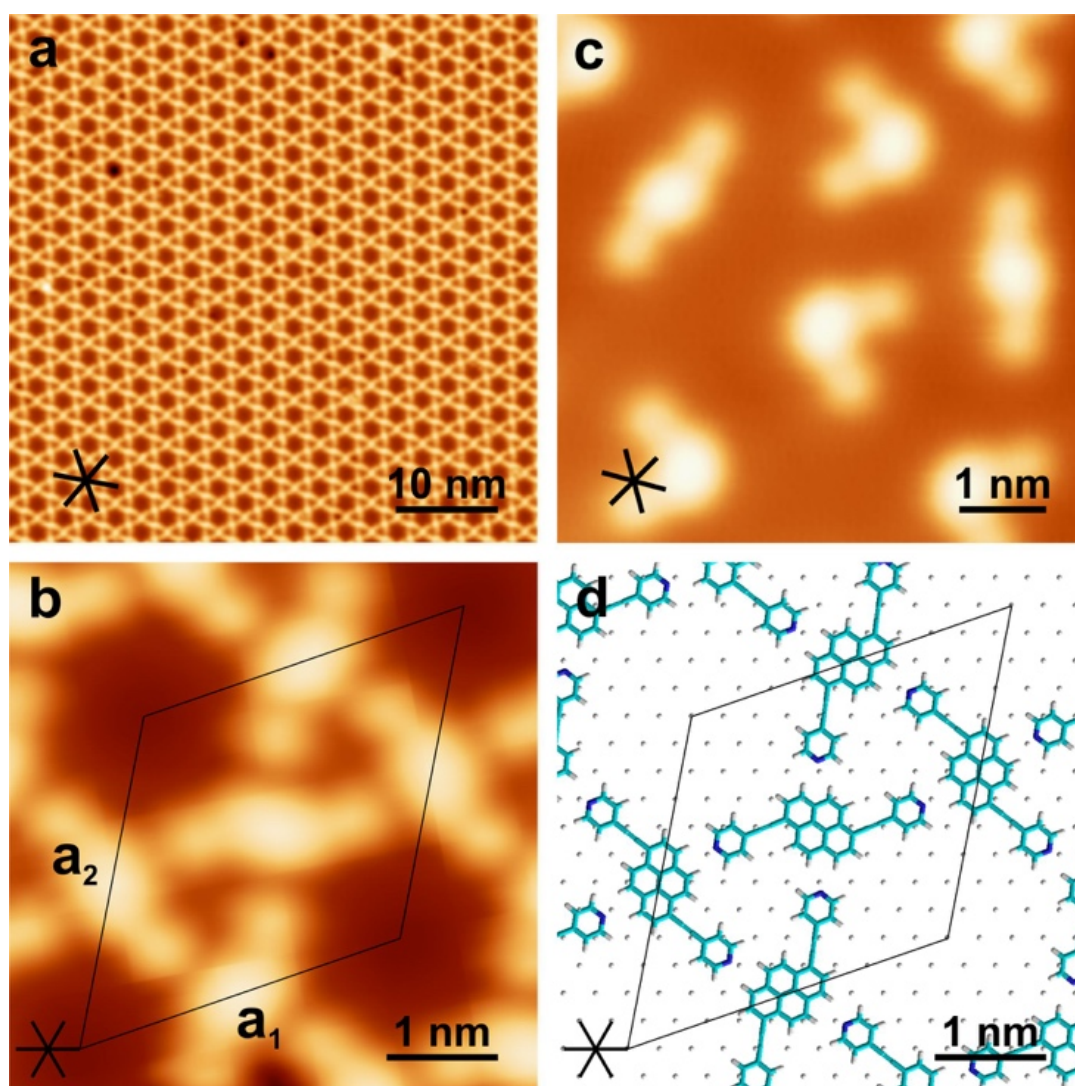


Figure 5.3.4. Self-assembly of *trans*-like bidentated pyrenes **5-2** and **5-2a** on Ag(111). a,b) Kagome lattice formed by molecule **5-2**. a) Overview image (0.1 nA, -0.2 V). b) High-resolution image (0.5 nA, -0.02 V) and superimposed unit cell of the Kagome lattice formed by **5-3**. c) Individual **5-2a** and **5-3a** reference molecules coexisting on Ag(111) (0.09 nA, 0.1 V). d) Structural model of the Kagome lattice and its unit cell.

Furthermore, since the *trans*-like isomers have pro-chiral faces, a different molecular chirality is exhibited upon adsorption on the metal surface. Hence, the supramolecular network features a chiral arrangement, which manifests in the presence of two enantiopure mirror-symmetric domains of the Kagome network, designated as α -*trans* and α' -*trans*. A tentative structural model reveals commensurability of both domains with the underlying substrate within the accuracy of the STM calibration (**Figure 5.3.4d**). In this model the unit-cell vectors of the Kagome lattice ($a_1 = a_2 = 30.6 \text{ \AA}$) form an angle of $\pm 19.1^\circ$ (negative for α -*trans*, positive for α' -*trans*) with respect to the close-packed directions of Ag(111). The model geometry is a perfect hexagonal lattice with an inscribed angle of 60° between a_1 and a_2 , the superstructure can thus be designated as $(\sqrt{112} \times \sqrt{112})R19.1^\circ$. Again, the formation of this network is glued by intermolecular N...H H-bonds between pyridyl ligands and adjacent pyrene cores, with a projected N...H bond length of $(2.7 \pm 0.5) \text{ \AA}$. These interactions along with the commensurability leads to the formation of highly regular and extended islands, some of which were found to exceed the 0.2 \mu m^2 regime. Finally, *trans*-like diphenylpyrene derivative **5-2a** presents a uniform distribution of single molecules on the Ag(111) surface, again suggesting the presence of repulsive intermolecular interactions. For comparison purposes, **Figure 5.3.4c** shows both molecules **5-2a** and **5-3a**. *Trans*-like pyrenes **5-2a** are adsorbed flat on the surface and exhibit similar appearance to that of molecule **5-2**, presenting a central bright lobe identified as the pyrene core and two peripheral features attributed to the phenyl substituents. Since the molecule also possesses two prochiral faces, two different chiral adsorption modes have been found and labeled as β -*trans* and β' -*trans*, respectively (see **Figure 5.3.4c**).

Iodine co-adsorption. To explore the hosting capabilities of the porous pyrene networks to monoatomic adsorbates, we analyzed samples of molecules **5-1** and **5-2** containing iodide contaminations. Halogens, and specifically iodine and bromine, currently attract considerable interest in self-assembly procedures, as halogen-bonding interactions might be used to tether the formation of surface-confined supramolecular assemblies and halogen-containing by-products are formed during surface-confined dehalogenation C-C coupling.^{602,620,621}

Indeed, after depositing iodine-containing species **5-1** and **5-2** we found a majority of the cavities formed by the supra-molecular networks to be occupied by circular protrusions (**Figure 5.3.5**), in brightness and thus apparent height similar to the surrounding molecules. The apparent extension of the protrusions in STM images is consistent with mononuclear iodine species. Indeed, XPS experiments yielding chemical sensitivity allow us to conclusively assign these protrusions to iodine

atoms interacting with Ag, *i.e.*, to iodide species (**Figure 5.3.5f**). In the iodine 3d XP spectra recorded after depositing a layer of the iodine-containing tetra-pyridyl-pyrene material on Ag(111) one can clearly observe two signals, reflecting the spin-orbit split $3d_{5/2}$ and $3d_{3/2}$ components. The most intense feature with binding energy of 618.6 eV corresponds to the $3d_{5/2}$ orbital while the second one is attributed to the $3d_{3/2}$ orbital with a binding energy of 630.1 eV.^{622,623}

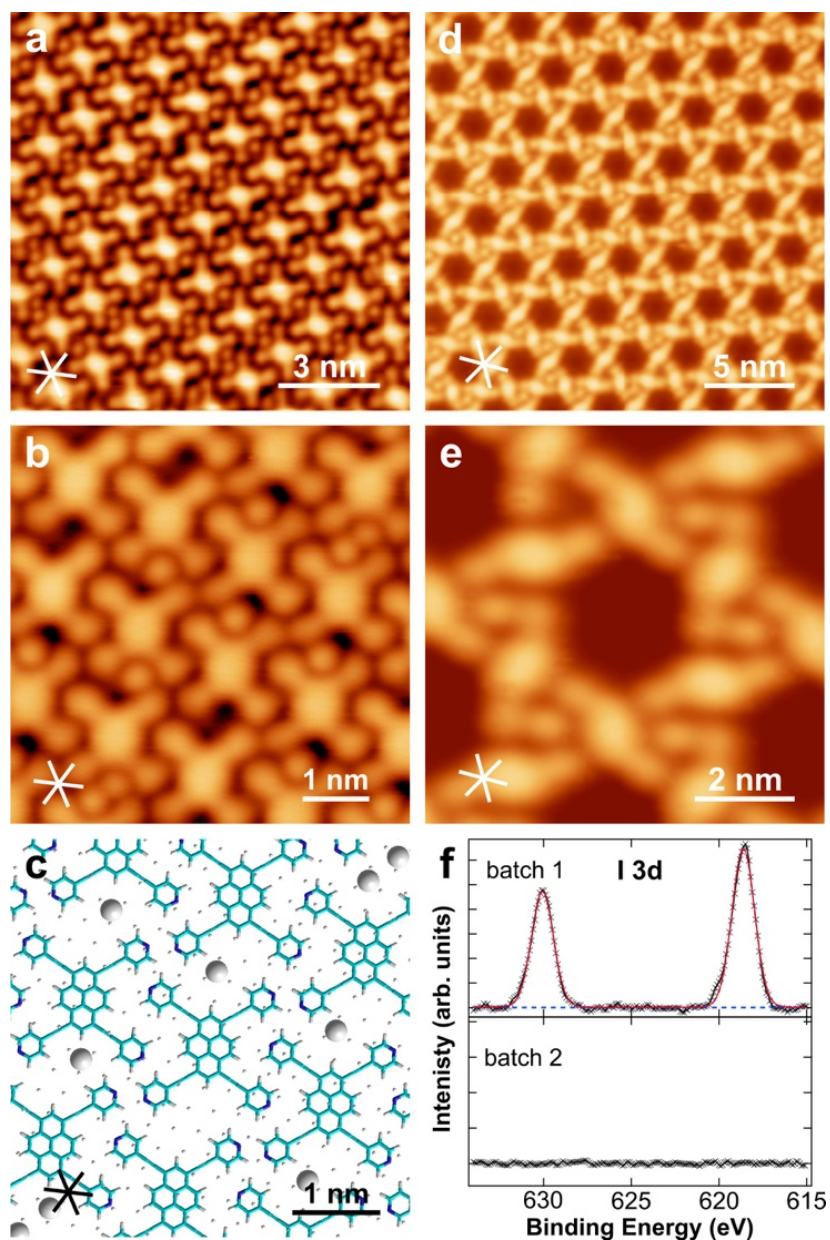


Figure 5.3.5. Self-assembly of pyridyl-terminated pyrene species **5-1** and **5-3** on Ag(111) showing decoration by co-adsorbed iodide. (a,b,c) Rhombic islands formed by species **5-1**. a) Overview image (0.05 nA, 1 V). b) High-resolution image showing the protrusions attributed to iodide species (0.05 nA, -1 V). c) Tentative model of a detail of b) highlighting the plausible hollow site adsorption of iodide. d,e) Kagome lattice formed by species **5-2**. d) Overview image (0.1 nA, -0.2 V). e) High resolution image (0.09 nA, 0.1 V). f) Iodine 3d XPS signature of the I-contaminated (top) and clean (bottom) samples of molecule **5-1**.

These binding energies are characteristic for iodide and are distinctly different from molecular iodine or iodine compounds on Ag(111).^{624,625} Samples containing no iodine, **Figure 5.3.5f**, show no such signature. Accordingly, Ag adatoms that were reported to stabilize organic assemblies on surfaces⁷³ and readily engage in coordination interaction with ethynylene triple bonds in organometallic complexes⁶²⁶ are ruled out as origin of the protrusions. Furthermore, carbon 1s signatures of both materials show no differences in chemical species or binding energies between the two cases, confirming the equivalence of the pyrene units. In the case of tetradentated module **5-1**, the small voids can be filled with either zero, one or two iodide species (**Figure 5.3.5ab**), whereas in the case of the Kagome lattice only one iodide unit can be accommodated (**Figure 5.3.5de**). The large cavities seldom exhibit a single protrusion tucked into one of the six corners. Island borders are not decorated in any case, which suggests that the iodide maximizes its interaction with adjacent pyrene molecules by occupying the pores. Below the saturation coverage of the small cavities (2 I per **5-1**; 2/3 I per **5-3**), the guested iodide has a minor influence on the porous architectures. While the rhombic network of module **5-1** shows unit cell vector a_2 to be slightly extended by less than 1 Å, the Kagome's unit cell appears not to be changed. Structural models based on the high-resolution STM data highlight the positions of the iodide atoms relative to the pyrenes (**Figure 5.3.5c**). The substrate registry was chosen in a way to accommodate the iodide on the well-known hollow adsorption sites of the Ag(111) lattice.⁶²⁷ The resulting average I...H distance amounts to (2.9 ± 0.5) Å, which is slightly smaller than the sum of the van der Waals radii of the two atoms (3.18 Å), consistent with attractive interactions. Indeed, differences in electronegativity between halogens⁶⁴ or diatomic adsorbates⁷⁶ and hydrogens are known to stabilize supramolecular architectures on surfaces. However, comparing the distances between two adjacent modules **1** separated by zero, one or two iodides, only a minute difference of less than 0.5 Å – well within the error bar of our measurements – is observed. This suggests that the iodide residence in the pore⁶²¹ is determined by the availability of preferred hollow adsorption sites within the voids. As visualized in **Figure 5.3.5c**, due to the non-commensurate overlayer structure, every pore exposes different bare Ag areas. In most pores, one hollow site is available within the steric constraints, while some pores offer two hollow sites with a separation exceeding twice the van der Waals radius of the iodide units. In the case of the Kagome lattice formed from **5-2**, the registry is consistent with small pores being centered on hollow sites (**Figure 5.3.5d**), thus hosting a maximum of one iodide each. A further increase of iodine yields to a rearrangement of the architectures featuring iodides on all four sides of the modules **5-1**. In agreement with the literature discussing the thermal

desorption of iodine from Ag(111),⁶²⁸ moderate annealing to 180° C did not induce a significant decrease of the iodide species in the pyrene architectures.

5.4. Organometallic Architectures from Pyrene Derivatives

Coordination chemistry on surfaces has emerged as a powerful strategy to design on-surface confined functional materials with prospects in sensing, catalysis, molecular electronics and magnetism.⁵⁶⁸ Surprisingly, despite the relevance of rare-earths in high technology,^{629,630} coordination chemistry of lanthanides on surfaces has mainly remained elusive. Only recently, the first lanthanide-directed architectures were reported on coinage metals.^{559,560,566,567} Importantly, it was shown that carboxylate moieties could be exploited to design a thermally robust gadolinium-driven reticular architecture, in which the nature of the bond indicated ionic characteristics.⁶³¹

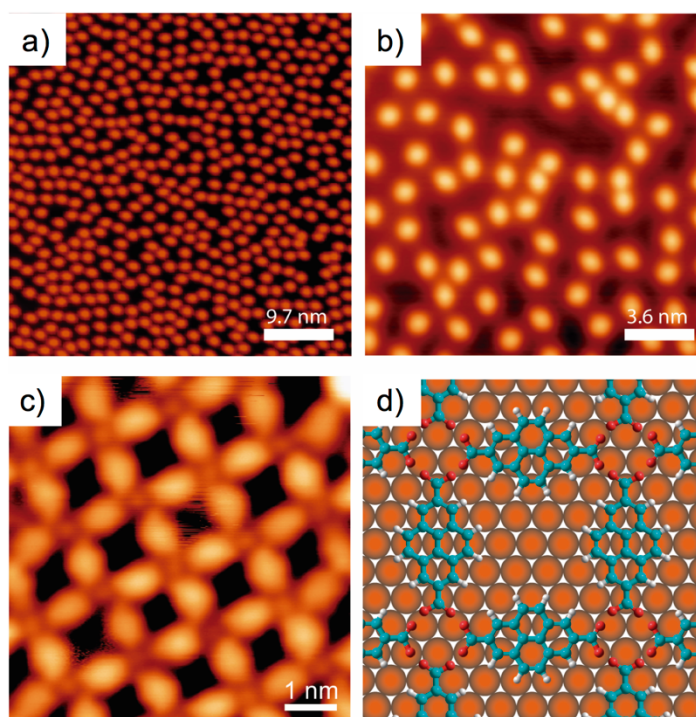


Figure 5.4.1. ab) Pyrene derivative **5-10** on Cu(111) surface without lanthanides and cd) lanthanide-directed Dy:**5-10** metallosupramolecular network (cd).

Figure 5.4.1ab show the individualized **5-10** molecules after it was deposited on Cu(111) and the temperature held at 100 °C to afford full deprotonation. With dysprosium (Dy), the situation is

notably different, with the formation of a porous grid formed (**Figure 5.4.1cd**). Pyrene species **5-10** are visualized as bright rods, whereas dysprosium centers are imaged as dim protrusions. The corresponding atomistic model **Figure 5.4.1d** reveals commensurability of the metallosupramolecular architecture with the substrate, in which the dysprosium centers occupy hollow sites and one of the linear directions of the reticular grid is aligned with the close-packed directions of the substrate, thus resulting in three orientational supramolecular domains. The metal-organic network is stabilized by an eight-fold Dy...O coordination with an average projected internodal distance of $15.4 \pm 0.5 \text{ \AA}$, thus resulting in an average projected Dy...O bond length of $2.3 \pm 0.5 \text{ \AA}$.

1,6-Dibromopyrene **4-3** was also used as another approach in patterning metal surfaces with organometallic architectures (**Figure 5.4.2**). Preliminary experiments showed that pyrene **4-3**, upon deposition on a Ag(111) surface held slightly below room temperature, presents a major phase of hexagonal porous network (**Figure 5.4.2ab**). Furthermore, since the *trans*-like isomer has pro-chiral faces, a different molecular chirality is exhibited upon adsorption on the metal surface. Hence, the supramolecular networks featured chiral arrangements, which manifest in the presence of two enantiopure mirror-symmetric domains.

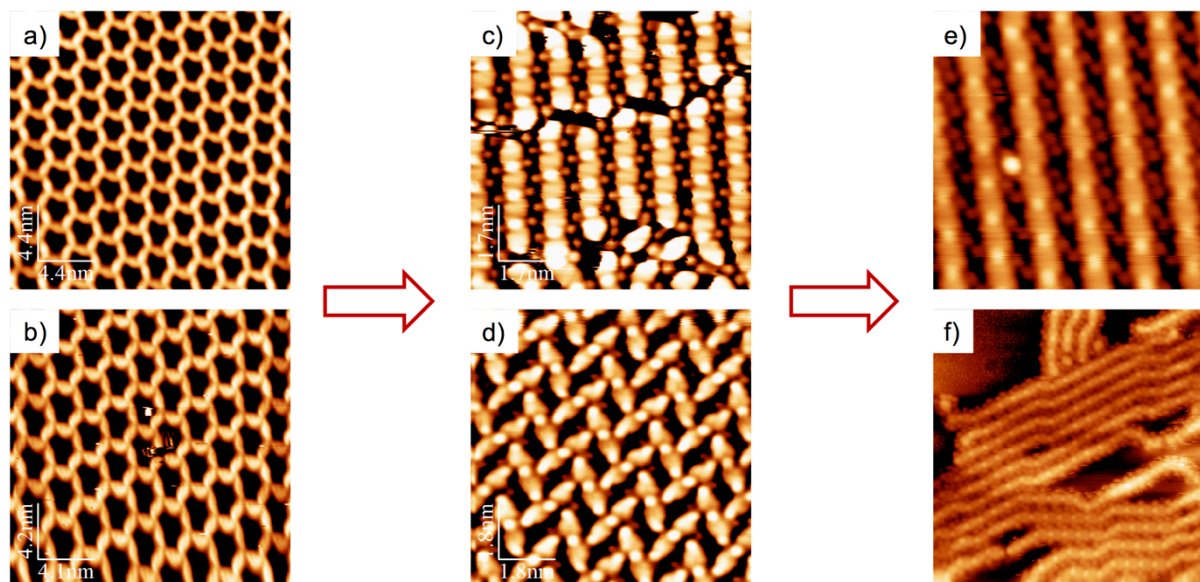


Figure 5.4.2. STM images for pyrene derivative **4-3** on Ag(111) surface: ab) deposition onto surface held at slightly below r.t. leads to a major phase of two chiral hexagonal porous networks; c) deposition onto surface held slightly above r.t. leads to partial debromination with no long-range order (c, at small coverage) and long-range ordered lattices (d, high coverage regime); ef) thermal annealing ($150 \text{ }^\circ\text{C}$) results in formation of organo-metallic chains.

Deposition of dibromopyrene **4-3** on surface held slightly above room temperature showed partial debromination (**Figure 5.4.2cd**). In a small coverage regime of the pyrene derivative, unordered motifs were observed with the majority of the molecules without any bromines (or only one in dimers, trimer, ...) with the Br atoms apparently bonded to Ag adatoms. On a high coverage regime, the formation of islands of dimeric units featuring long-range ordered lattices were observed. By thermal annealing (100 °C) almost total debromination is observed and the formation of long metallo-organic chains is apparent (**Figure 5.4.2ed**) with the Br atoms still present between the chains, in proximity to Ag adatoms. Further annealing did not seem to show the formation of C-C covalent bond. However, further experiments are underway.

5.5. Conclusions

In the context of creating patterned surface employing the bottom-up approach, this chapter reports the design, syntheses and STM investigations of a series of pyrene derivatives on metal surfaces. The attractive pyrene core was functionalized with a specific number of functional groups in specific positions in order to obtain our starting building block for patterning metal surfaces in a bottom-up approach.

In the first section, pyrenes equipped both with pyridylacetylene and phenylacetylene termini were prepared and deposited on a Ag(111) substrate and their self-assembly behavior was investigated. The deliberate geometrical positioning of the pyridyl recognition sites in a *tetra-* (**5-1**), *trans-* (**5-2**) or *cis-* like fashion (**5-3**) allowed the tailoring of different supramolecular architectures, giving rise to rhombic arrays (**5-1**), porous Kagome networks (**5-2**) and chain-like assemblies (**5-3**). The intermolecular N \cdots H bonds – enabled by the pyridyl termini - proved to be decisive for the formation of the supramolecular structures. For the phenyl-functionalized reference pyrenes (**5-1a**, **5-2a** and **5-3a**), repulsive intermolecular interactions dominated, resulting in individual modules at low coverage. On the other hand, the azimuthal alignment shows no significant dependency on the functionalization and thus is dictated by the geometrical properties of the pyrene core. Furthermore, we have exploited the robust, open porous architectures of modules **5-1** and **5-2** as templates for the positioning of individual monoatomic iodine guests, identified as iodides. Their positioning is tentatively assigned to a preferred absorption on the hollow sites of the Ag(111) substrate, where they do not interfere with the order of the pyrene arrays at moderate coverage. The decoration of supramolecular networks

with iodide units that bases on attractive interactions might thus be instrumental in stabilizing the selected organic architectures, displaying exceptional hosting capabilities of the porous network.

In the following section, pyrene derivatives were designed and prepared as targets for building metallo-organic architectures on metal surfaces. In one case, a metallo supramolecular coordination with lanthanides (Dy), rare earths that have recently attracted attention for on-surface coordination chemistry, was shown to form porous grids when a biscarboxy-pyrene **5-10** is present. The metal-organic network was found to be stabilized by an eight-fold Dy...O coordination with an average projected internodal distance of 15.4 ± 0.5 Å. As a second approach, 1,6-dibromopyrene **4-3** was deposited and showed the formation of a hexagonal porous network, that could be modified by thermal treatment of the surface. First, a partial debromination resulted in formation *n*-mers with no apparent long-range order at low coverage, while long-range ordered dimers were observed on high coverage regime. Further thermal annealing resulted in the formation of extended organo-metallic chains.

This chapter shows that, even though great efforts have been placed in the bottom-up preparation of patterned metal substrates, there is still a lot of undiscovered potential, part of which we are trying to reach in our laboratory.

5.6. Perspectives

5.6.1. Self-Assembly of *Peri-Xanthenoxanthene*

While a precise doping with nitrogen⁶⁰⁸ (and very recently with sulfur)⁶¹¹ has been achieved, very little work has been done on precise oxygen-doped π -extended conjugated system. In this respect, *peri-xanthenoxanthene* (PXX) (**Figure 5.6.1a**), the O-doped equivalent of anthanthrene, represents the core on which build a family of O-doped aromatic hydrocarbons.

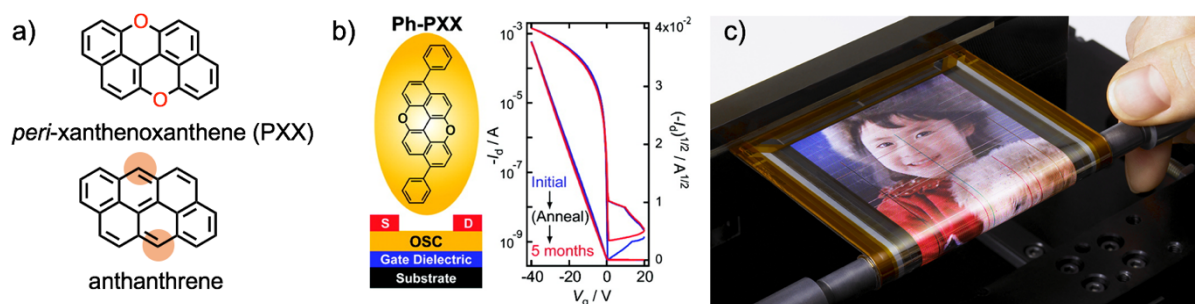
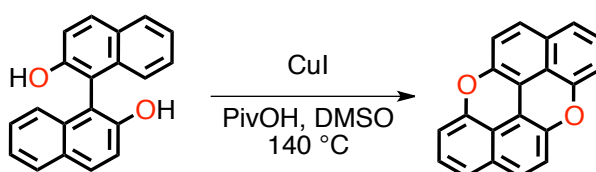


Figure 5.6.1. a) Chemical structure of *peri-xanthenoxanthene* (PXX), O-doped equivalent of anthanthrene; b) organic thin-film transistor (OTFT) developed with PXX⁶³² and c) OTFT (based on OPXX) driven OLED display.⁶³³

Diphenyl-PXX derivative was investigated as semiconductor (OSC) for organic thin-film transistor (OTFT) as stable π -system against oxidation (**Figure 5.6.1bc**).⁶³² An efficient carrier injection was achieved, with a HOMO level of PXX diphenyl derivative estimated to be only 5.1 eV below vacuum level. Moreover, OTFT achieved a high apparent mobility over $0.4 \text{ cm}^2/(\text{V s})$ and was stable for 5 months under ambient conditions. Additionally to its excellent carrier transport capacity, PXX has been found to be suitable for use in organic electroluminescent devices by increasing in the efficiency and lifetime of organic electronic devices compared to prior art back in 2010.⁶³⁴ A monomer precursor of PXX (7,7'-bis(2,2'-bithiophen-5-yl)-1,1'-bi-2,2'-naphthol) was subjected to electropolymerization into a highly conductive fully conjugated polymer containing PXX. Moreover, PXX has been used to prepare charge-transfer complexes with 2,4,6-trinitrophenol, I_3 , $[\text{Ni}(\text{maleontriledithiolate})_2]$ ⁶³⁵ and TCNQ.⁶³⁶ Due to all the abovementioned properties, along with its propensity to generate charge-transfer complexes, we were set to investigate the properties of PXX and its complexes (with TCNQ) on metal surfaces.

First, a scalable and simple protocol for synthesis and purification had to be applied. The original procedure dates back to 1905 through oxidation of binaphthols with $K_4[Fe(CN)_6]$ that yielded PXX and unidentified by-products.⁶³⁷ Some years later, Ag_2O was proposed as oxidant, giving PXX with other oxidized derivatives.⁶³⁸ The oxidative ring closure of binaphthols was found to occur in satisfactory yields with CuO and $Cu(OAc)_2$.^{639,640} More recently, the CuO and $Cu(OAc)_2$ have been revived and modifications of the original methodologies have been proposed.^{634,635}



Scheme 5.6.1. Optimized solution-based synthesis of PXX starting from binol molecule.

Recently, in our laboratories, Dr. Daphné Stassen applied a Cu-catalyzed oxidative C-H cycloetherification procedure^{641,642} on the 1,1'-bi-2-naphthol scaffold in order to prepare PXX in solution in very good yield (**Figure 5.6.1**). At this point, with a scalable procedure that yield product in a very good yield and high purity, STM investigations were sought (**Figure 5.6.2**, **Figure 5.6.3**).

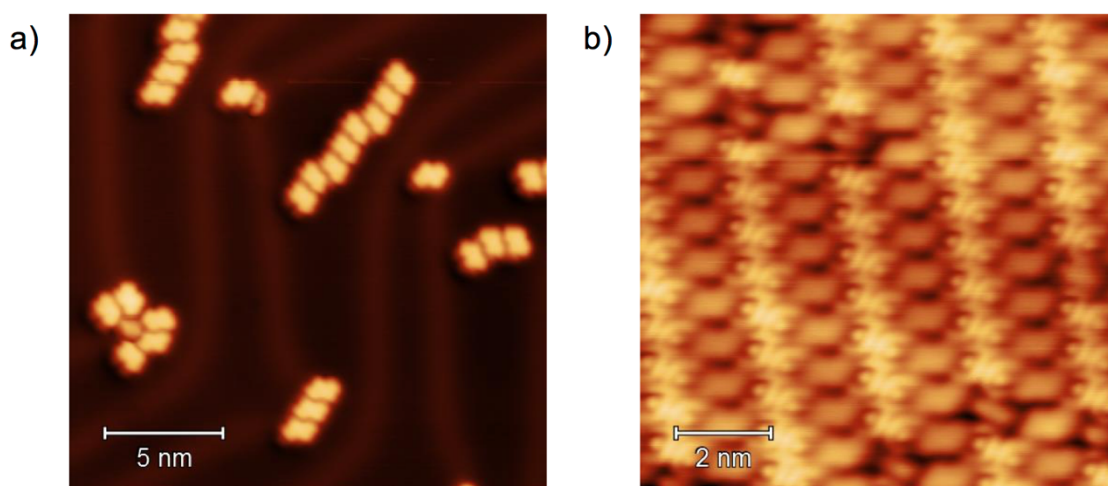


Figure 5.6.2. PXX deposited on a Au(111) surface with TCNQ at r.t. (STM taken at 5 K) with a) area of a terrace with mostly PXX molecules and b) an area of donor (PXX)-acceptor (TCNQ) row.

PXX was deposited, together with the TCNQ, both on Au(111) and Cu(111) surfaces, in order to investigate also possible variation in molecule-molecule and molecule-substrate interactions. **Figure 5.6.2b** shows that PXX and TCNQ are able to form rows of donor-acceptor assemblies, resembling charge-transfer monolayers of TTF-TCNQ previously reported.^{643–645}

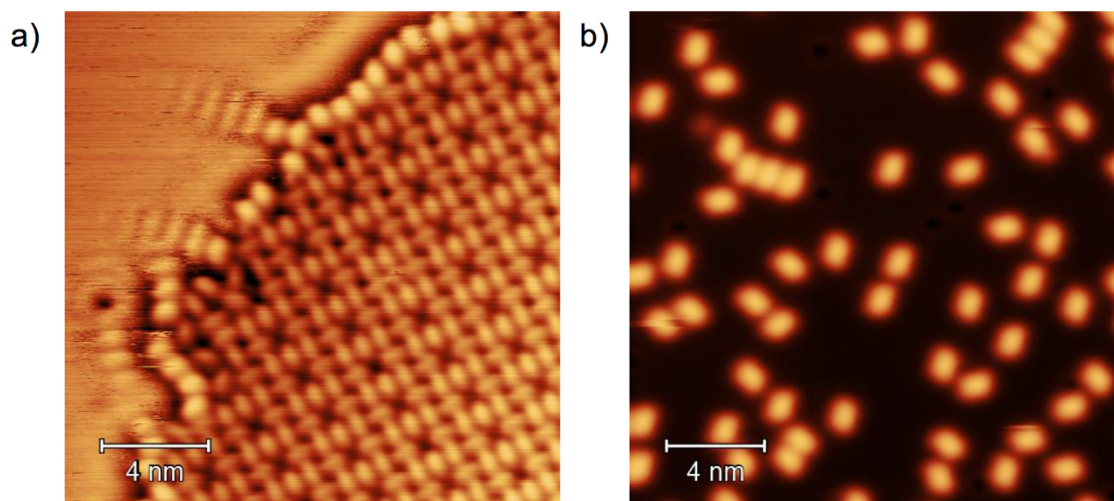


Figure 5.6.3. a) PXX/TCNQ deposited on a Cu(111) surface at r.t. (with STM taken at 77 K) and b) PXX deposited on Cu(111) at r.t. (STM taken at 5 K).

On the other hand, on a Cu(111) substrate (**Figure 5.6.3**), PXX has been found to assemble at the edges of a TCNQ island, while outside the islands the PXX (at 77 K and < 1 ML) is too mobile to be observed. PXX alone (on a Cu(111) surface and 5 K) presents itself as separated molecules, suggesting long-range repulsion as a charged molecule.⁵⁸⁴

5.6.2. Pyridine and Bipyridine Guided Self-Assembly

As a bottom-up approach in patterning surfaces that we achieved with pyrene derivatives, some issues need to be addressed, such as low solubility and regioselectivity in order to obtain di-substituted derivatives. To this end, we propose the use of pyridine and bipyridyl metal-ligand coordination complexes on anthracene and porphyrin scaffolds. While we already reported pyridyl coordination driven formation of metallocsupramolecular structures,^{575–577} we sought to expand this approach on

pyridylethynyl and pyridylethenyl derivatives, also in the light of the porous host-guest structure we reported in previous sections.

As an alternative polycyclic aromatic hydrocarbon, anthracene holds much promise (see also **Figure S6.7**). For example, anthracene was used in first experiments in order to generate light from organic materials (in the first OLED)⁶⁴⁶ and more generally in organic electronics.^{647–649}

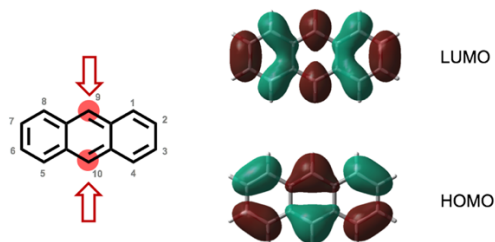
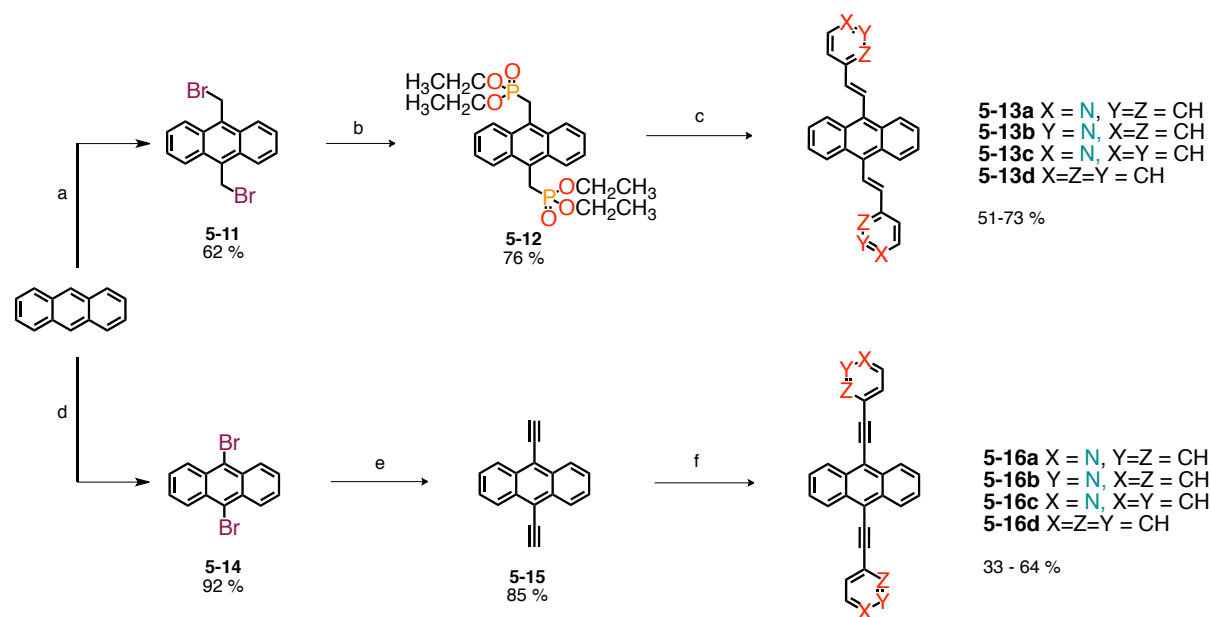


Figure 5.6.4. Chemical structure of anthracene along with its calculate HOMO and LUMO orbitals (Gaussian DFT B3LYP 6-311G).



Scheme 5.6.2. Synthetic scheme for the synthesis of anthracene derivatives. Reagents and condition: a) $(\text{CH}_2\text{O})_n$, HBr in AcOH, 50 °C; b) $\text{P}(\text{OEt})_3$, 150 °C; c) Ar-CHO, tBuOK , THF, r.t.; d) Br_2 , Ph- NO_2 , r.t.; e) 1. TMSA, $\text{Pd}(\text{PPh}_3)_2\text{Cl}_2$, CuI, THF/ Et_3N , 50 °C; 2. KOH, MeOH, THF, r.t.; f) Ar-I, $\text{Pd}(\text{PPh}_3)_4$, CuI, THF/ Et_3N , r.t.

Moreover, anthracene reacts towards electrophilic substitution exclusively in positions 9- and 10-, thus the HOMO and LUMO orbitals can be easily engaged (**Figure 5.6.4**). The complete synthetic

approach to anthracene derivatives is reported in **Scheme 5.6.2**. Anthracene was brominated with Br_2 or bromomethylated in presence of *para*-formaldehyde and HBr solution (in AcOH). The bis(bromomethyl)anthracene was transformed into ethyl phosphonate with triethyl phosphite in a Michaelis-Arbuzov reaction. The phosphonate, in presence of aldehydes and basic conditions, readily produced the *trans*-alkenes in a Horner-Wadsworth-Emmons reactions. On the other hand, the ethynyl series was prepared by a Sonogashira–Hagihara Pd-catalyzed cross coupling reaction between 9,10-dibromoanthracene and TMSA. The trimethylsilyl group was then removed under basic conditions and the free alkyne was coupled with the iodo-aryl compounds to obtain the final compounds.

In order to explore further metal-ligand coordination on the surface, we prepared porphyrins carrying either one or two 2,2'-bipyridyl (BiPy) groups, a popular ligand in supramolecular chemistry that has not yet been exploited for patterning surfaces.⁶⁵⁰

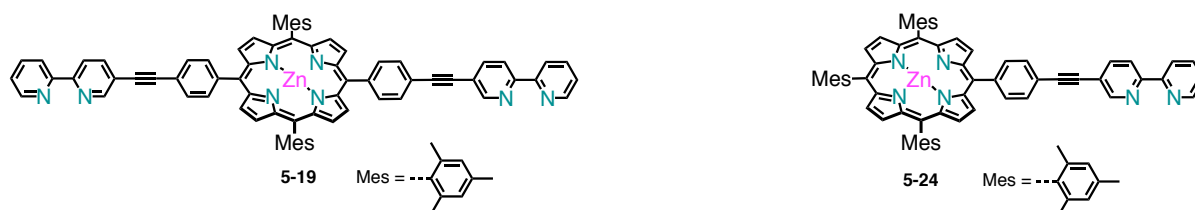
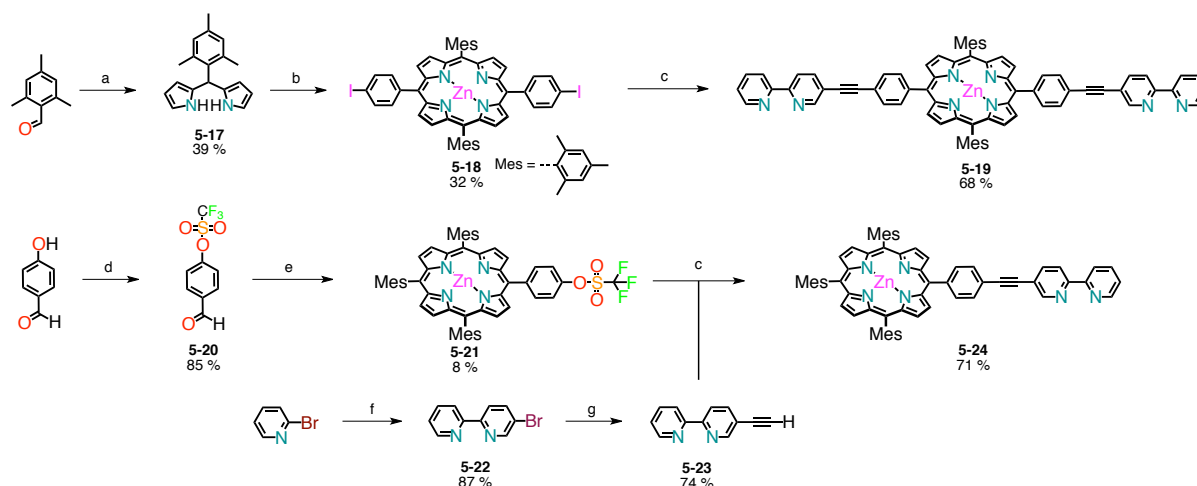


Figure 5.6.5. Porphyrins **5-23** and **5-24** carrying 2,2'-bipyridyl moieties.

The molecules were prepared according to **Scheme 5.6.3**. At first, we performed a mixed aldehyde condensation under Lindsey conditions that yielded a mixture of A_3B and *trans*- and *cis*- A_2B_2 porphyrins. Due to the very low difference in polarity between the iodophenyl and mesityl substituents, the purification of porphyrins could be achieved only after consecutive gravity-fed column chromatographies with cyclohexane/dichloromethane (85:15 v/v) as eluent mixture. In order to avoid time- and cost-consuming separations we investigated alternative approaches. While the *trans*- A_2B_2 porphyrin could be prepared through the 2+2 dipyrromethane approach, the mixed aldehyde approach is necessary for the A_3B porphyrin. However, we sought to replace the iodine group with another moiety that has the same (or similar) reactivity but very different polarity in order to facilitate the column chromatography separations. Thus, a trifluoromethanesulfonate (triflate) group

was used that indeed did show better separation of the porphyrins mixture. The triflate was also successfully used in Sonogashira cross-coupling, after addition of LiCl since, in presence of $\text{Pd}(\text{PPh}_3)_4$, the triflate is a counterion and not a ligand, and otherwise the reaction would not proceed.



Scheme 5.6.3. Synthetic scheme for the synthesis of porphyrin-BiPy derivatives. Reagents and conditions: a) pyrrole, $\text{BF}_3 \cdot \text{OEt}_2$, r.t.; b) i) 4-iodobenzaldehyde, $\text{BF}_3 \cdot \text{OEt}_2$, CHCl_3 , r.t., ii) DDQ, iii) Et_3N , iv) $\text{Zn}(\text{OAc})_2 \cdot \text{H}_2\text{O}$, $\text{CHCl}_3/\text{MeOH}$, r.t.; c) 5-ethynyl-2,2'-bipyridine, $\text{Pd}(\text{PPh}_3)_4$, (LiCl), $\text{DMF}/\text{Et}_3\text{N}$, 120°C , μW irradiation; d) Tf_2O , pyridine, 0°C to r.t.; e) i) meso-CHO, $\text{BF}_3 \cdot \text{OEt}_2$, CHCl_3 , r.t., ii) chloranil, iii) Et_3N , iv) $\text{Zn}(\text{OAc})_2 \cdot \text{H}_2\text{O}$, $\text{CHCl}_3/\text{MeOH}$; f) $n\text{-BuLi}$, THF, -78°C , Bu_3SnCl , ii) 2,6-dibromopyridine, $\text{Pd}(\text{PPh}_3)_4$, PhCH_3 , reflux; g) i) TMSA, $\text{Pd}(\text{PPh}_3)_2\text{Cl}_2$, PPh_3 , CuI , Et_3N , 80°C .

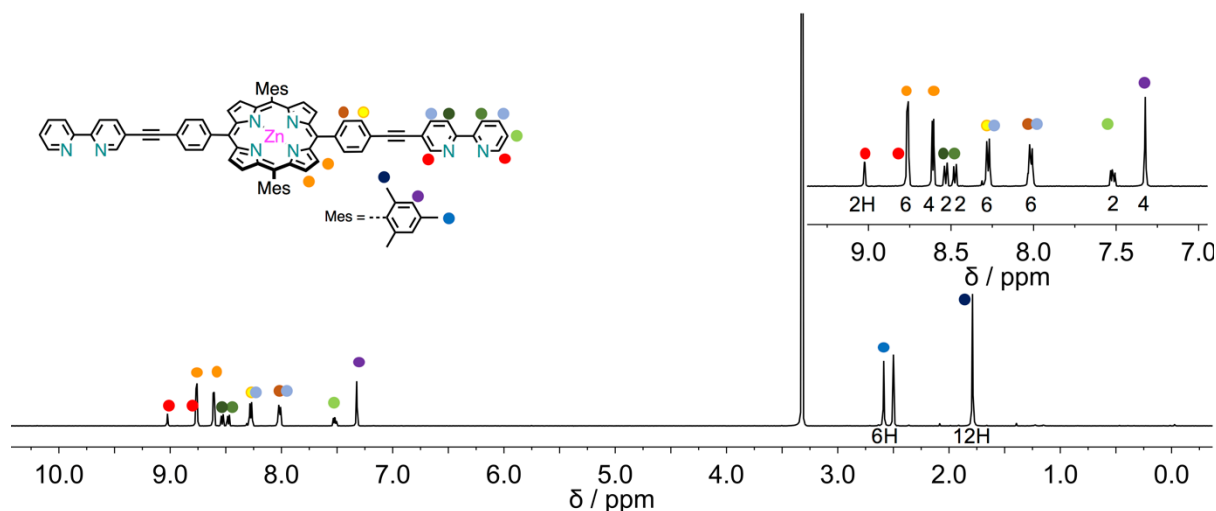


Figure 5.6.6. $^1\text{H-NMR}$ (500 MHz, 298K, $\text{DMSO}-d_6$) of bis-bipy-porphyrin derivative 5-19.

STM experiments of the BiPy-porphyrins will be performed and will be reported elsewhere.

5.6.3. On-Surface Reactions with Porphyrin Precursors

Conjugated porphyrin arrays, with delocalized electronic networks, have been prepared mostly by using alkene or alkyne type bridging or by connecting directly porphyrin with individual or multiple bonding to form fused porphyrin arrays.⁶⁵¹ These derivatives have been used in various applications such as near-infrared (NIR) dyes, non-linear optical materials and molecular wires. **Figure 5.6.7** show two examples on how extended conjugation affects some of their properties.

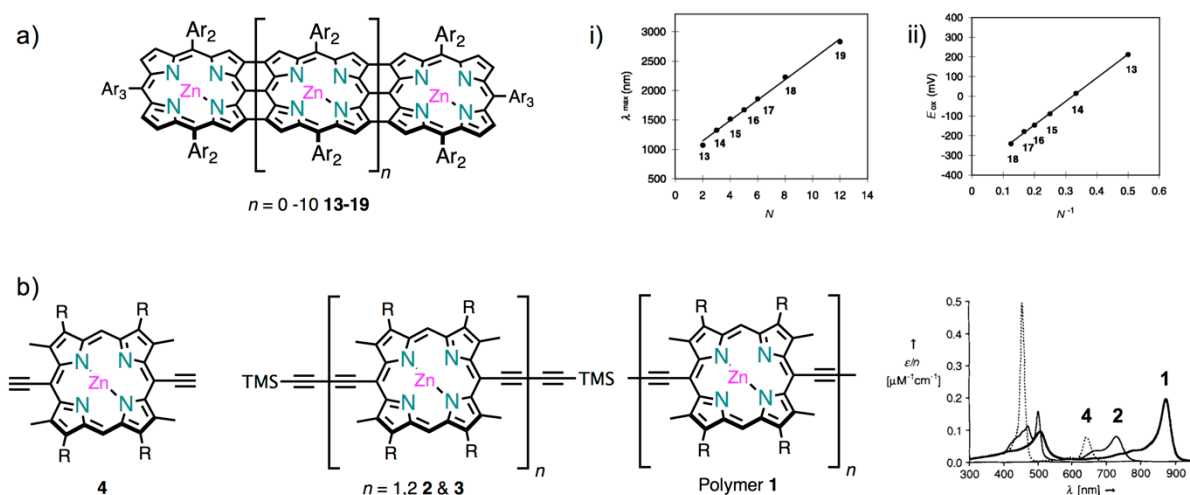


Figure 5.6.7. a) Fully conjugated porphyrin tapes (from dimer to dodecamer), i) plot of absorption peak versus number of porphyrin in the tape (N) and ii) plot of the first oxidation potential versus N ; b) butadiyne-bridged porphyrin oligomers and their absorption spectra.

Triply meso-meso-, β - β -, and β - β -linked zinc(II)-oligoporphyrins (**Figure 5.6.7a**) showed extremely red-shifted absorption bands with increasing number of porphyrins, reaching ~ 3500 wavenumber.⁶⁵² Progressive decrease of one-electron oxidation potential upon increasing of the porphyrin number was also observed. Butadiyne-linked conjugated porphyrins showed the red-shift of Q-bands with increasing chain-length, reaching ~ 900 nm in the case of polymers.⁶⁵³ Numerous other derivatives were also reported, but they pose synthetic and purification challenges, as well as difficulties in transferring high-molecular weight polymers onto metal surface. Therefore, an on-surface approach from porphyrin monomers was proposed (**Figure 5.6.8**).

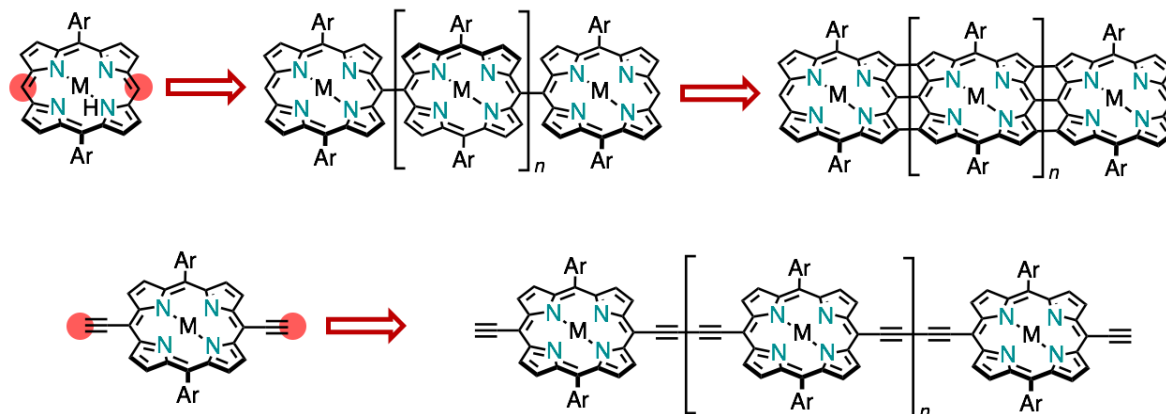


Figure 5.6.8. Schematic approach to creating conjugated porphyrin tapes and oligomers.

At first, we prepared meso-free and meso-brominated A_2B_2 porphyrin. The synthesis was accomplished through the 2+2 dipyrromethane condensation procedure with the desired porphyrins easily separated and in good yields. Bromination of the meso-free porphyrins usually proceeds > 85 % yields and the purification yielded pure porphyrin precursors.

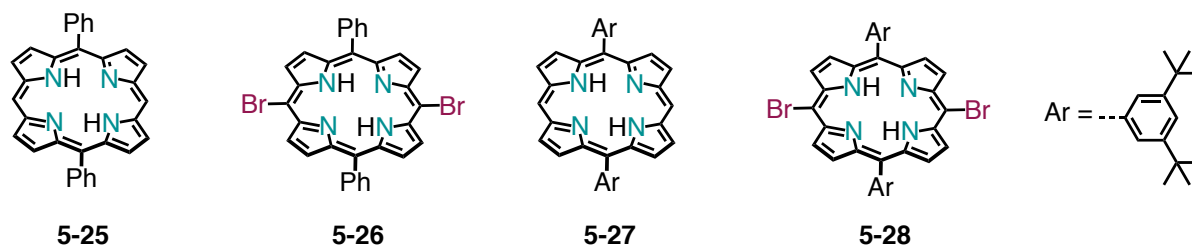


Figure 5.6.9. First-generation molecular precursors for on-surface synthesis.

In **Figure 5.6.10** can be observed that when 5,15-diphenylporphyrin is annealed on a Au(111) substrate⁶⁵⁴ unfortunately no intermolecular reaction takes place, leading to intramolecular cyclodehydrogenation products.

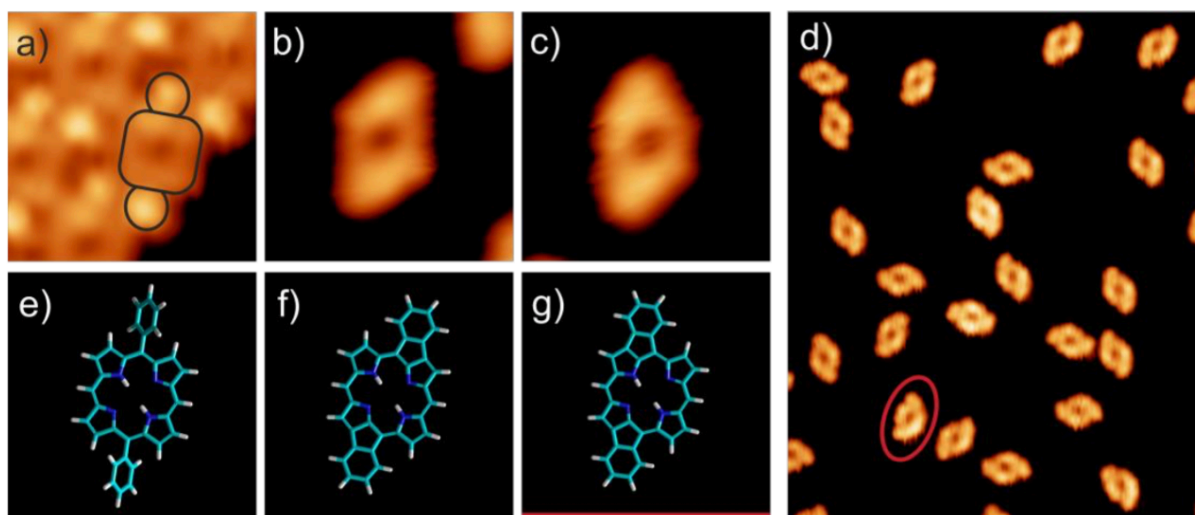


Figure 5.6.10. STM images of 5,15-diphenylporphyrin molecules on Ag(111), with structural models. After room temperature deposition, islands of 5,15-diphenylporphyrin molecules are found (a) single molecule and its respective structural model is shown in (e); after annealing this surface at 580 K only isolated molecules can be found (d), with the majority of these isolated molecules (91%) appears as (b) whereas a minority (9%) appears as (c).⁶⁵⁴

With this in mind, we prepared a 5,15-bis(pentafluorophenyl)porphyrin in order to remove the hydrogens that were involved in the cyclodehydrogenation side reaction.

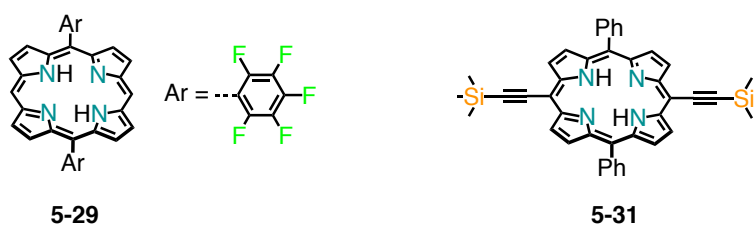


Figure 5.6.11. Second-generation molecular precursors for on-surface synthesis.

Part of the characterization is reported in **Figure 5.6.12** as $^1\text{H-NMR}$ spectra. 5,15-Bis(pentafluorophenyl)porphyrin (top, $\text{THF-}d_6$) show typical resonances of *meso*-free, β -pyrrole and inner *NH* protons. 5,15-Bis(trimethylsilyl ethynyl)-10,20-diphenylporphyrin (bottom, CDCl_3) shows resonances of β -pyrrole, phenyl substituents, trimethylsilyl and inner *NH* protons.

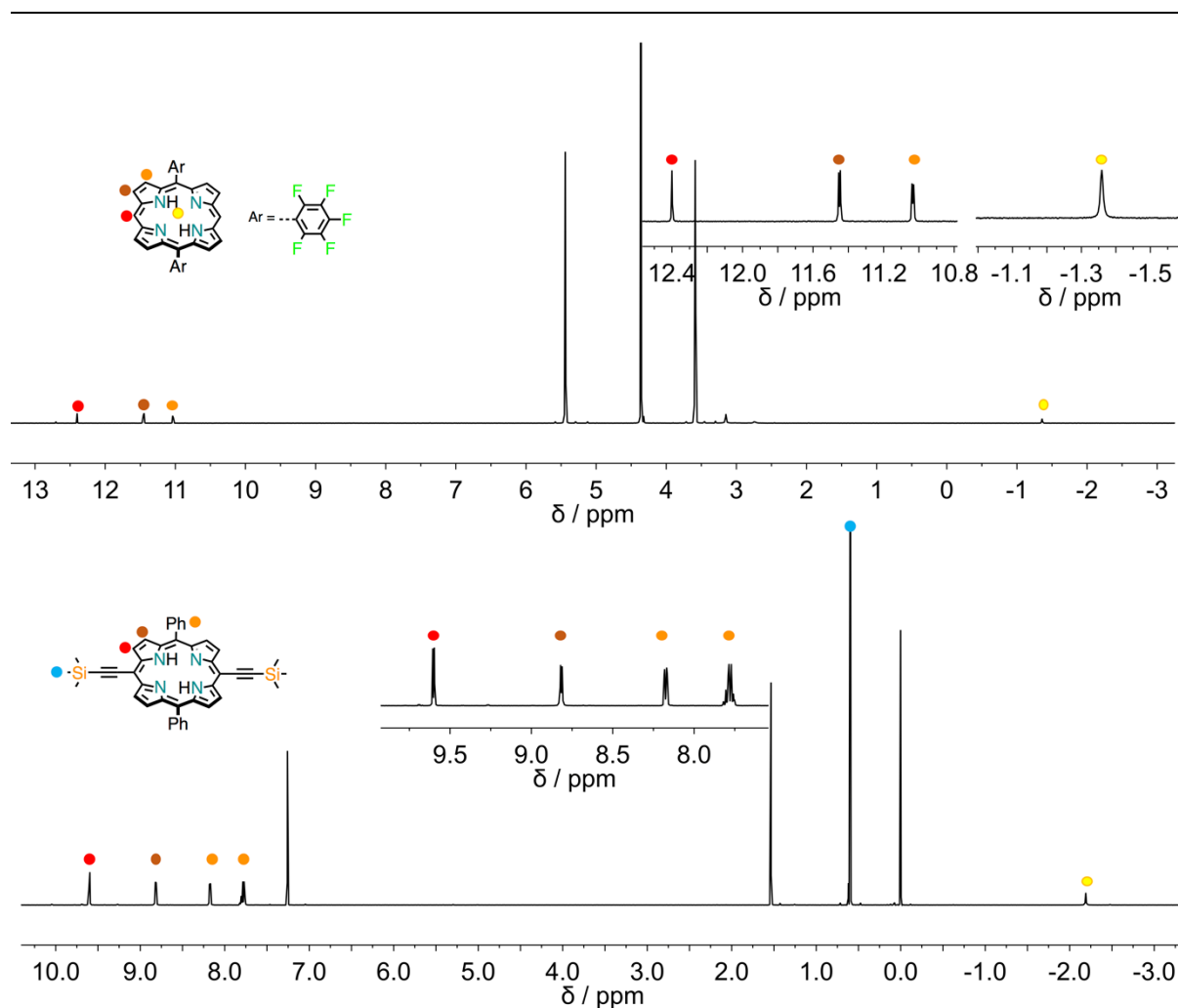


Figure 5.6.12. ¹H-NMR spectra (500 MHz, 298 K) of 5,15-bis(pentafluorophenyl)porphyrin (top, THF-*d*₈) and 5,15-bis(trimethylsilylethynyl)-10,20-diphenylporphyrin (bottom, CDCl₃).

5,15-Bis(pentafluorophenyl)porphyrin will be investigated for on-surface reactions, namely the *meso-meso* coupling followed by oxidation into a porphyrin tapes. On the other hand, 5,15-bis(trimethylsilylethynyl)-10,20-diphenylporphyrin will be de-protected right before performing on-surface experiments since the free alkyne can be unstable and undergo degradation.

In order to take advantage of already know on-surface reaction and condition, e.g. Ullmann aryl-aryl coupling followed by cyclodehydrogenation, porphyrin carrying bromo-naphthyl or bromo-anthracenyl groups were designed (**Figure 5.6.13**), with their syntheses posing some challenges.

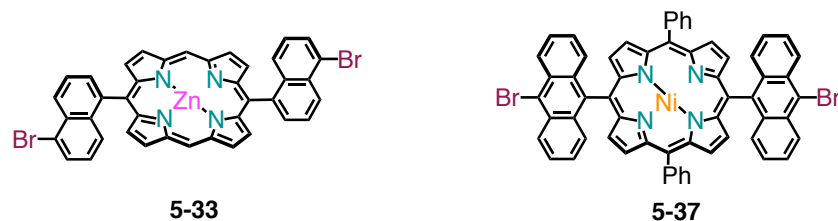
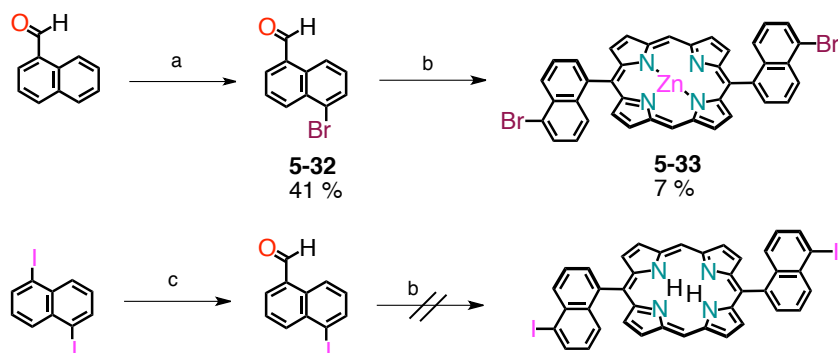


Figure 5.6.13. Third-generation molecular precursors for on-surface synthesis.

Initially, we wanted to prepare the 5,15-bis(5-iodo-1-naphthyl)porphyrin, but only traces of porphyrin was formed under TFA-catalyzed conditions (mostly starting aldehyde was found after 12 hours of reaction). Therefore, we prepared the bromo derivative and the condensation reaction proceeded much easier than in the case above. However, the product was not sufficiently pure due to presence of impurities that had the same polarity as our target product. The impure porphyrin was therefore metallated with $\text{Zn}(\text{OAc})_2 \cdot 2\text{H}_2\text{O}$ and the difference in polarity allowed us to purify the compound.

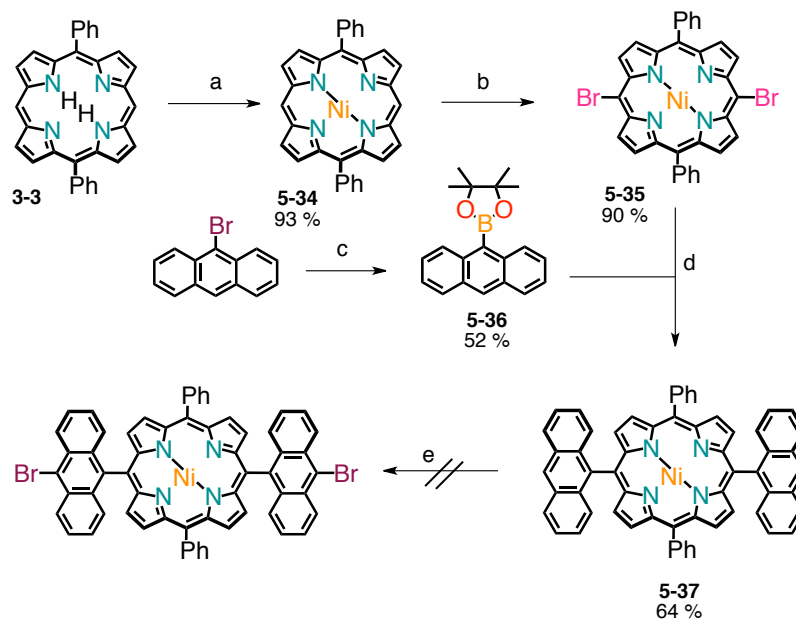


Scheme 5.6.4. Synthetic approach towards naphthyl substituted porphyrins.

The synthesis of bromo-anthracenyl substituted porphyrin was unsuccessful so far. The synthetic scheme is reported below (**Scheme 5.6.5**).

Although the 5,15-dianthracenyl-10,20-diphenylporphyrin was obtained through a Suzuki cross-coupling reaction between a Ni(II) dibromoporphyrin and anthracenoboronate in good yield, the bromination (using literature procedures for bromination of 9,9'-bianthracene⁶⁰⁵) of this anthracenylporphyrin showed to give a number of side-product with almost identical polarity, with

the bromination of electron rich Ni-porphyrin core competing with 10,10' bromination (Figure 5.6.14).



Scheme 5.6.5. Synthetic approach towards 5,15-dianthracenyl-10,20-diphenylporphyrin. Reagents and conditions: a) Ni(acac)₂, toluene, reflux; b) NBS, CH₂Cl₂/MeOH, r.t.; c) B₂pin₂, KOAc, PdCl₂(PPh₃)₂, 90 °C; d) PdCl₂(PPh₃)₂, AsPh₃, Cs₂CO₃, THF, reflux.

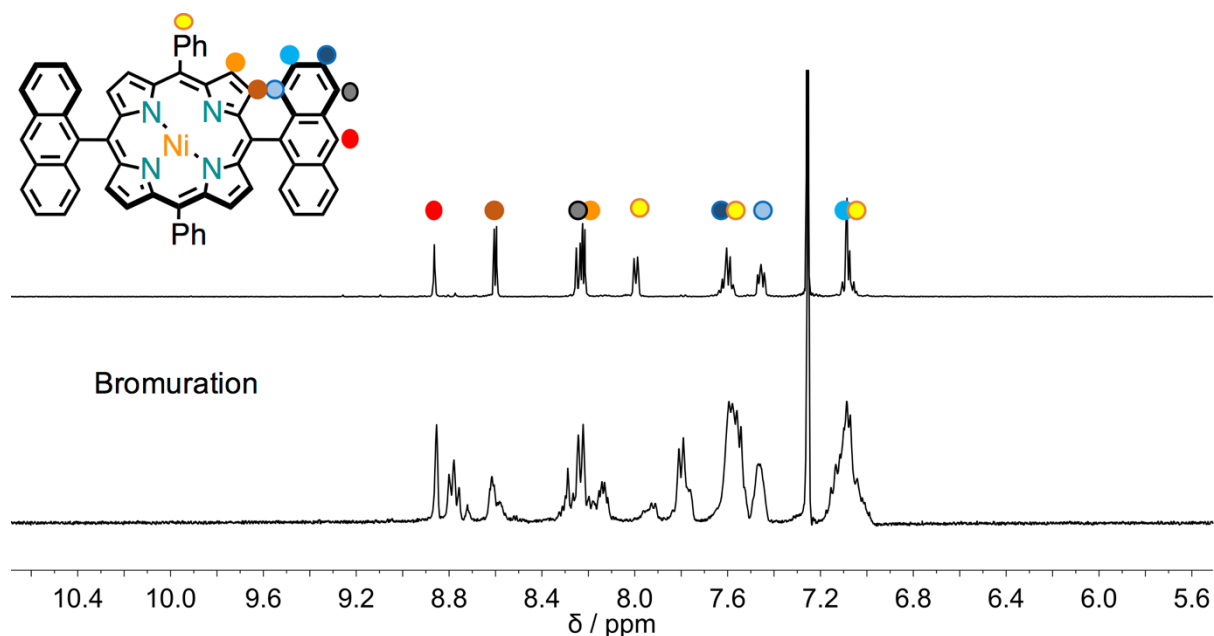


Figure 5.6.14. ¹H-NMR spectra (500 MHz, CDCl₃, 298 K) of 5,15-dianthracenyl-10,20-diphenylporphyrin and the bromination reaction.

6. Experimental Section

6.1. Instruments and Methods

Thin layer chromatography (TLC) was conducted on pre-coated aluminum sheets with 0.20 mm Merck Silica Gel F254.

Column chromatography was carried out using Merck silica gel 60 Å (particle size 40-63 µm or 60-200 µm).

Melting points (m.p.) were measured on a SMP-20 in open capillary tubes and have not been corrected.

Microwave reactions were performed on a CEM Discover Microwave Reactor.

NMR spectra were obtained on a *Varian Inova* spectrometer (500 MHz ¹H and 125 MHz ¹³C) or *Varian Gemini 200* spectrometer (200 MHz ¹H and 50 MHz ¹³C) or on a *JEOL Eclipse 400FT* (400 MHz ¹H). Chemical shifts are reported in ppm using the solvent residual signal as an internal reference (Chloroform-*d*: δ_H = 7.26 ppm, δ_C = 77.23 ppm; 1,1,2,2-Tetrachloroethane-*d*₂: δ_H = 6.00 ppm, δ_C = 73.78 ppm; Pyridine-*d*₅: δ_H = 8.74, 7.58, 7.22 and δ_C = 150.35, 135.91, 123.81, Dimethyl Sulfoxide-*d*₆: δ_H = 2.50 ppm, δ_C = 39.51 ppm; Methylene Chloride-*d*₂: δ_H = 5.32 ppm, δ_C = 54.00 ppm; Acetonitrile-*d*₃: δ_H = 1.94 ppm; Toluene-*d*₈: δ_H = 7.09, 7.00, 6.98 ppm; Deuterium Oxide: δ_H = 4.80 ppm). The resonance multiplicity is described as *s* (singlet), *d* (doublet), *t* (triplet), *q* (quartet), *m* (multiplet), *br* (broad signal).

DOSY self-diffusion coefficient evaluations were carried out using *Varian Inova* (500 MHz) NMR spectrometer equipped with Performa II-Z gradient coils (Varian, Palo Alto, CA, USA).

IR spectra (KBr) were recorded on a Perkin Elmer 2000 spectrometer.

Optical rotations were measured on a polarimeter with a sodium lamp (*l* = 589 nm) and are reported as follows: $[\alpha]^{25}_{\text{D}}$ (*c* = g (100 mL)⁻¹, solvent).

Optical and Chiroptical spectroscopy. UV-Vis measurements were performed on Cary 5000 Spectrophotometer (Varian) and on a ChirascanTM Plus CD Spectrometer from Applied Photophysics, using 1 mm path quartz cuvettes; Fluorescence measurements on Cary Eclipse Fluorescence Spectrophotometer (Agilent *Technologies*), using 1 cm path quartz cuvettes; CD spectroscopy was performed using a Jasco J-815 spectropolarimeter and using a ChirascanTM Plus CD

Spectrometer from Applied Photophysics. The measurements were carried out using 1 mm suprasil quartz cells from Hellma Analytics. The spectra were recorded between 250 and 500 nm, with a bandwidth of 1 nm, time per point 1 s and two repetitions. The solvent reference spectra were used as baselines and were automatically subtracted from the UV-Vis and CD spectra of the samples. The variable temperature experiments (VT-CD) were performed using a TC125 Temperature Controller from Quantum Northwestern running on the Chirascan™ Spectrometer. The temperatures were varied with heating/cooling cycles by steps of 5 K at a rate of 1 K/min. The temperature of the solution was determined using a temperature probe immersed in the quartz cuvettes.

Microscopy. The samples for AFM were prepared by drop-casting about 40 μL of solution onto mica substrates, air dried in open ambient at 293 K. Tapping-mode AFM measurements were carried out in air at 293 K by using a Nanoscope IIIa (Digital Instruments Metrology Group, USA) instrument, model MMAFMLN. The collected images were then analyzed with WsXm 4.0 software (Nanotec Electronica S. L.), and Gwyddion 2.39. The samples for TEM studies were prepared by drop-casting about 20 μL of solution onto a carbon-coated nickel grid (3.00 mm, 200 mesh), air dried, and imaged on a Philips EM 208 TEM microscope (accelerating voltage of 100 kV).

Mass spectroscopy. ESI-MS (5600 eV; MeOH) were performed on a Perkin-Elmer API1 by Dr. Fabio Hollan (University of Trieste) and High resolution mass spectrometry (HRMS) was performed by the “Fédération de Recherche”; ICOA/CBM (FR2708) platform of Orléans in France, on a Bruker maXis Q-TOF in the positive ion mode. The analytes were dissolved in a suitable solvent at a concentration of 1 mg/mL and diluted 200 times in methanol (≈ 5 ng/mL). The diluted solutions (1 μL) were delivered to the ESI source by a Dionex Ultimate 3000 RSLC chain used in FIA (Flow Injection Analysis) mode at a flow rate of 200 $\mu\text{L}/\text{min}$ with a mixture of $\text{CH}_3\text{CN}/\text{H}_2\text{O} + 0.1\%$ of HCO_2H (65/35). ESI conditions were as follows: capillary voltage was set at 4.5 kV; dry nitrogen was used as nebulizing gas at 0.6 bars and as drying gas set at 200 °C and 7.0 L/min. ESI-MS spectra were recorded at 1 Hz in the range of 50-3000 m/z. Calibration was performed with ESI-TOF Tuning mix from Agilent and corrected using lock masses at m/z 299.294457 (methyl stearate) and 1221.990638 (HP-1221). Data were processed using Bruker Data Analysis 4.1 software. **MALDI-MS** were recorded using a Waters QToF Premier mass spectrometer equipped with a nitrogen laser, operating at 337 nm with a maximum output of 500 mW delivered to the sample in 4 ns pulses at 20 Hz repeating rate. Time-of-flight analyses were performed in the reflectron mode at a resolution of about 10,000. The matrix solution (1 μl) was applied to a stainless steel target and air dried. Analyte samples were dissolved in a suitable solvent to obtain 1 mg/mL solutions. 1 μl aliquots of these solutions were

applied onto the target area already bearing the matrix crystals, and air dried. For the recording of the single-stage MS spectra, the quadrupole (rf-only mode) was set to pass ions from 100 to 1000 THz and all ions were transmitted into the pusher region of the time-of-flight analyzer where they were analyzed with 1 s integration time.

Titration experiments. When carrying out NMR or UV-Vis titration experiments a lot of attention has been placed in the preparation, experiment and processing. Some excellent texts were followed that include above all: (1) Thordarson, P. Determining Association Constants from Titration Experiments in Supramolecular Chemistry. *Chem. Soc. Rev.* **2011**, *40*, 1305–1323 (Matlab scripts used for non-linear fitting were downloaded from this reference, together with online tools found on <http://supramolecular.org>), (2) Analytical Methods in Supramolecular Chemistry, Schalley, C. A. Ed, Wiley-VCH, 2007 and (3) Supramolecular Chemistry: From Molecules to Nanomaterials, Steed, J. W. and Gale P. A. Eds, Wiley, 2012.s

Chemicals were purchased from Sigma Aldrich, TCI, Acros, Fluorochem and Alfa Aesar and used as received. **Solvents** were purchased from Sigma Aldrich, VWR and Acros, and **deuterated solvents** from Sigma Aldrich, Cambridge Isotope Laboratories and VWR. General solvents such as THF and Et₃N were distilled from Na, Na/benzophenone, and CaH₂ respectively.

6.2. Specific Instrumentation and Techniques

6.2.1. Diffusion NMR Measurements

The gradient strength was calibrated with pure water ($D = 2.229 \times 10^{-9} \text{ m}^2 \text{ s}^{-1}$ at 298.2 K) and the maximum gradient strength was about $53 \text{ G}\cdot\text{cm}^{-1}$. ‘The Dbpsste_cc’ pulse sequence was used for the measurements of diffusion coefficient. Samples were weighted, transferred in 5-mm diameter NMR tubes and dissolved in the solvent appropriate solvent and then allowed to stand for at least one hour before starting measurements. Experiments were performed by keeping the z-gradient pulse length constant and gradually increasing the gradient strength in 15 steps. The gradient pulse length was in the appropriate ms to measure the diffusion coefficient of all components. The diffusion coefficients (D) were obtained from the slope of the following equation:

$$\ln(I_g/I_0) = -(\gamma^2 \delta^2 G^2 (\Delta - \delta/3))D$$

Where I_g and I_0 are intensities of the NMR signal in the presence and absence of field gradient pulses; γ is the gyromagnetic constant for ¹H; δ is the duration of the z-gradient pulse; G is the gradient

strength; and Δ is the time interval between the gradient pulses (diffusion time). The D was obtained by fitting the experimental data (peak intensity with increasing gradient strength) by a multi-exponential function (least square fitting according the algorithm of Levenberg, 1944; Marquardt, 1963).

$$\sum_{k=1}^{N_e} \frac{I_k}{I_0} e^{-\left(\gamma^2 \delta^2 G^2 \left(\Delta - \frac{\delta}{3}\right)\right) D^k}$$

Where I_k is the k th pre-exponential factor and D_k is the k th diffusion coefficient. The number of N_e of exponentials considered was that minimizing the product (N_e, χ) , where χ is the sum of squared differences referred to the equation fitting to experimental data.

Finally, D was placed in the Stokes-Einstein equation to obtain r_s , the hydrodynamic radius (or Stokes' radius) of the molecular species:

$$D = k_b T / 6 \pi \eta r_s$$

Where k_b is the Boltzmann constant, T is the absolute temperature and η is the viscosity of the medium. The viscosity of the solvent mixtures (when needed) was estimated using the Refutas equation.

6.2.2. Chapter 2

6.2.2.1. Molecular Modeling

The calculations were performed using the Gaussian 09 package. Geometry optimization of porphyrins 2-1 and 2-2, fullerenes 2-3 and 2-4 and the pseudorotaxanes was carried and the molecular volume was computed. Then the hydrodynamic radius (r_h) of an ideal sphere including the molecules was also derived. Dealing with such large systems, the semi-empirical method PM6⁶⁵⁵ was chosen as appropriate to obtain qualitative information about these molecules.

6.2.2.2. Z-Scan Measurements

The nonlinear optical (NLO) parameters, *i.e.* the nonlinear absorption coefficient β and the nonlinear refractive index parameter γ' of the pseudorotaxane assemblies and all the individual molecular components (*i.e.*, reference compounds), were determined using the Z-scan technique employing 532 nm, 35 ps laser pulses from a mode-locked Nd:YAG laser (Quantel YG900) operating at 10 Hz.

The laser beam was focused into the sample by means of a 20 cm focal length quartz lens and its energy was measured by an energy meter (Coherent J-10MB-LE). The samples were placed into 1mm thick quartz cells. The beam waist w_0 of the laser beam was determined using a CCD camera (Watec LCL-903HS) and was determined to be $17.4 \pm 0.5 \mu\text{m}$ at 532 nm. The transmitted through the sample laser light was detected by a photomultiplier (Hamamatsu R5108) and the electrical signal was further processed by a boxcar integrator (Stanford Research Systems, SR 250). The optical absorption spectra of the prepared solutions were measured on a Hitachi U-3010 spectrophotometer. So briefly, according to this technique, a sample is moving along the propagation direction of a focused laser beam (*i.e.*, along the z -axis), thus experiencing different laser intensity at each z -position. Then, two types of transmission measurements are performed, the so-called “open-” and “closed-aperture” Z-scans. During the former transmission measurement, the transmitted laser light is measured just after the sample, as a function of the sample z -position. The nonlinear absorption coefficient β can be determined from the fitting of the “open-aperture” Z-scan transmission recording with the following equation:

$$T = \frac{1}{\sqrt{\pi} \left[\frac{\beta I_0 L_{\text{eff}}}{1 + z^2 / z_0^2} \right]} \int_{-\infty}^{\infty} \ln \left[1 + \frac{\beta I_0 L_{\text{eff}}}{1 + z^2 / z_0^2} \exp(-t^2) \right] dt \quad (1)$$

where $L_{\text{eff}} = [1 - \exp(-a_0 L)] / a_0$ is the effective sample thickness, a_0 is the linear absorption coefficient, L is the sample length, z_0 is the Rayleigh length, z is the position of the sample and I_0 is the on-axis peak irradiance at the focal plane.

From the division of the “open-” by the “closed-aperture” Z-scan recordings, the “divided” Z-scan is obtained. In the case of low nonlinear absorption, the nonlinear refractive index parameter γ' can be obtained from the “divided” Z-scan using the following relation:

$$\gamma' = \frac{\lambda \alpha_0}{1 - e^{-a_0 L}} \frac{\Delta T_{p-v}}{0.812 \pi I_0 (1 - S)^{0.25}} \quad (2)$$

where: ΔT_{p-v} is the difference of the normalized transmission between the peak and the valley of the “divided” Z-scan curve, $S = 1 - \exp(-2r_\alpha^2 / w_\alpha^2)$ is the linear aperture transmission with r_α and w_α being the aperture radius and the beam radius on the aperture respectively and λ is the excitation laser wavelength.

The imaginary ($\text{Im } \chi^{(3)}$) and real ($\text{Re } \chi^{(3)}$) parts of the third-order susceptibility $\chi^{(3)}$ can be easily calculated from the following relations:

$$\text{Re } \chi^{(3)}(esu) = \frac{c(m/s)n_0^2 \gamma'(m^2/W)}{480\pi^2} \quad (3)$$

$$\text{Im } \chi^{(3)}(esu) = \frac{c^2(m/s)^2 n_0^2 \beta(m/W)}{960\pi^2 \omega(s^{-1})} \quad (4)$$

where c is the light velocity in m/s, ω is the excitation frequency in cycles/s and n_0 is the linear refractive index of the solvent.

Finally, the value of the second hyperpolarizability γ can be obtained from the following relation^[4]:

$$\gamma = \chi^{(3)} / NL^4 \quad \gamma = \chi^{(3)} / NL^4 \quad (5)$$

where N is the number of molecules per cm^3 and $L = (n_0^2 + 2) / 3$ is the Lorenz-Lorentz local field correction factor. The second hyperpolarizability, γ , designates the magnitude of the nonlinearity per molecule, thus being a molecular constant.

For the determination of the NLO parameters measurements of the different molecular systems investigated in this work, several solutions with different concentrations were prepared for each molecule and were measured using different laser energies. In all cases, in order to check for contribution(s) of the neat solvents, i.e. $\text{CH}_2\text{Cl}_2/\text{CH}_3\text{CN}$ and/or Et_3N , to the NLO response of the solutions, separate measurements of the solvents were performed under identical experimental conditions to those employed for the solutions. In all cases, it was confirmed that the solvents did not exhibit any contribution for the range of laser energies used for the measurements of the solutions. Therefore, the shape of the Z-scan recording was reflecting straightforwardly the sign of the NLO response of the solute. In **Figure 2.4.1**, some representative “open-” and “divided-” Z-scans of solutions of the pseudorotaxanes in $\text{CH}_2\text{Cl}_2/\text{CH}_3\text{CN}$ (9:1) are presented, obtained under 35 ps, 532 nm laser excitation. As shown, the “open-aperture” Z-scans of all pseudorotaxanes were found exhibiting reverse saturable absorption (RSA) behavior, as indicated by the transmission minimum exhibited. From the fitting of these transmission recordings with equation (1), the nonlinear absorption coefficient β was determined and next the imaginary part of the third-order susceptibility was obtained from equation (4). In addition, the corresponding “divided” Z-scans were exhibiting a pre-focal

transmission peak followed by a post-focal transmission valley, suggesting defocusing behavior (i.e., negative sign NLO refractive index parameter γ').

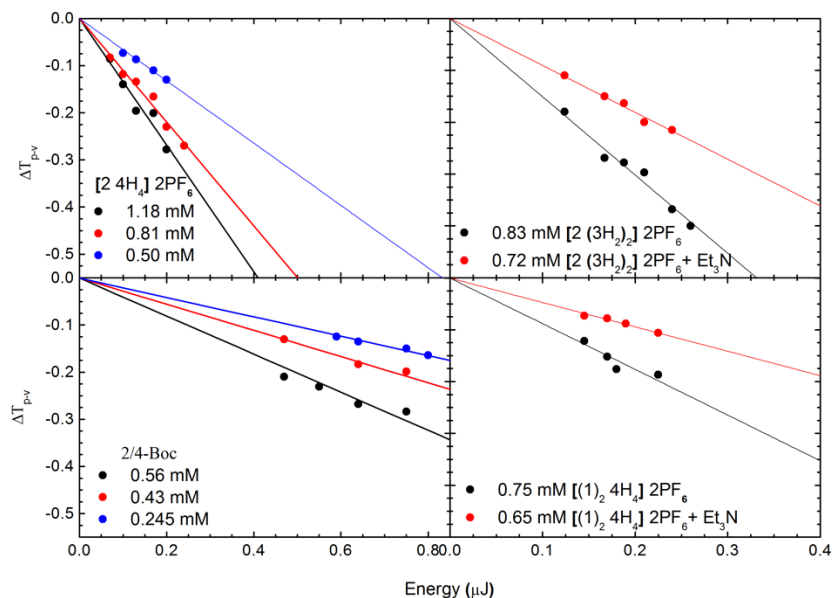


Figure S6.1. Variation of the ΔT_{p-v} parameter versus the laser energy, under 35 ps, 532 nm laser excitation.

The variation of the ΔT_{p-v} parameter, obtained from the “divided” Z-scans, as a function of the laser energy is presented in **Figure S6.1**. As shown, a good linear variation was found to hold in all cases, the straight lines of **Figure S6.1**, corresponding to the best linear fits of the experimental data points. From the slopes of these best fits lines the nonlinear refractive index parameter γ' was determined using equation (2), while the real part of the third-order susceptibility ($\text{Re } \chi^{(3)}$) was then calculated from equation (3). The second hyperpolarizability γ values of all molecular systems studied in this work are reported in **Table S6.1**, together with the corresponding value for [60]fullerene for comparison purposes.

As can be seen, the fullerene derivatives **2-3-** and **2-4-Boc**, **2-3H₂** and **2-4H₄** (i.e., entries 2, 3, 4 and 5) exhibited similar NLO response to that of [60]fullerene (i.e., entry 1), having negligible NLO refraction and substantial NLO absorption of positive sign (i.e., RSA). The two porphyrin crown ether complexes, namely **2-1** and **2-2** (i.e., entries 6, 7), were found to exhibit a 20-fold larger NLO response than that of [60]fullerene derivatives, exhibiting both strong NLO absorption and refraction, the latter of negative sign, corresponding to self-defocusing. Then, the **2-1/2-3-BOC**, the **2-2/2-3-BOC**, the **2-1/2-4-BOC** and the **2-2/2-4-BOC** (i.e., entries 8, 9, 10 and 11) 1:1 mixtures of the [60]fullerene

derivatives with the porphyrin crown ether complexes were all found to exhibit very similar NLO response within the experimental uncertainties. In fact, their second hyperpolarizability values were found to be very close to the values of porphyrin crown ether complexes, as the [60]fullerene nonlinearity was much weaker to influence considerably the NLO response of the mixtures.

Table S6.1. Second hyperpolarizability, γ , values of the [60]fullerene, the 3- and 4-BOC, the 3H₂ and 4H₄ fullerene based molecular systems, the 1 and 2 porphyrins crown ether complexes, the 1/3-BOC, 2/3-BOC, 1/4-BOC and 2/4-BOC in 1:1 mixtures, and the pseudorotaxanes assemblies [1·3H₂]-PF₆, [(1)₂·4H₄]-2PF₆, [2·(3H₂)₂]-2PF₆ and [2·4H₄]-2PF₆, obtained under 35 ps, 532 nm laser excitation.

Entry	Sample	$\epsilon@532\text{nm}$ (L mol ⁻¹ cm ⁻¹)	Re γ ($\times 10^{-31}$ esu)	Im γ ($\times 10^{-31}$ esu)	γ ($\times 10^{-31}$ esu)
1	C ₆₀	811.7	<0.08	0.28±0.01	0.28±0.01
2	2-3-BOC	920	-	0.30±0.02	0.30±0.02
3	2-4-BOC	1054	-	0.35±0.05	0.35±0.05
4	2-3H ₂	1171	-	0.32±0.05	0.32±0.05
5	2-4H ₄	1403	-	0.28±0.02	0.28±0.02
6	2-1	3426	-(5.1±0.2)	3.0±0.2	5.9±0.3
7	2-2	3693	-(4.0±0.3)	3.9±0.2	5.6±0.4
8	2-1/2-3-BOC	4671	-(4.4±0.2)	5.3±0.9	6.8±0.9
9	2-2/2-3-BOC	4556	-(3.9±0.4)	5.7±0.4	6.9±0.6
10	2-1/2-4-BOC	4581	-(4.0±0.6)	4.0±0.3	6.0±0.6
11	2-2/2-5-BOC	4562	-(3.8±0.2)	4.0±1.0	5.4±1.0

6.2.3. Chapter 3

6.2.3.1. Evaporation Experiments

40 μL of solvent was drop-casted onto an AFM support plate on a zeroed balance (293 K, open ambient in order to avoid slowing down of the evaporation). The decrease in weight was followed with a camera and the weight values measured with a high precision balance. The estimated loss ratio (weight/weight₀ or volume/volume₀) was multiplied with the initial concentration to obtain the value at a given time. The initial concentration is the same as that used for the microscopic studies, namely: 1.1 mM (CDCl_3), 0.25 mM (PhCH_3) and 0.25 mM (CDCl_3/CHX). In this way, it was possible to estimate the polymerization degree (N), $N \approx (K_a [\text{monomer}])^{1/2}$ as a function of the solvent evaporation.

6.2.3.2. Titration Experiments

Representative procedure: **3.3-(S)-4** (1.09 mg, 1.90×10^{-3} mmol) was dissolved in 1.50 mL of CDCl_3 to obtain solution A of 1.27×10^{-3} M. This solution A was transferred to an NMR tube (0.50 mL) and the rest (0.75 mL) was used to dissolve **3.3-5** (4.71 mg, 7.12×10^{-3} mmol) to obtain solution B with concentration 9.49×10^{-3} M. Solution B was added to the NMR tube in aliquots of 5, 10, 20, 25, 30, 35, 40, 50, 75, 100 and 150 μL . The titration data was fitted using nonlinear least-square fitting Matlab script by Prof. Thordarson.

6.2.4. Chapter 4

6.2.4.1. Molecular Methodology

When modeling compound **4-1**, all the coordination bonds between the Zn atoms and the porphyrins have been taken into account using harmonic restraints on the distances and angles between the Zn atoms and the nitrogen atoms of the porphyrins.

When we built the $[\mathbf{4-1 \cdot BPE}]_2$ complex, we added the necessary harmonic constraints to ensure all coordination bonds are considered and that the complex stays in the closed form geometry suggested by the experimental findings. When modeling the $[\mathbf{4-1 \cdot BPE}]_2$ complex, the interactions between the molecules forming it and with the nanotubes are strong enough to overcome the restraints and deform the complex structure. To avoid such deformation, we explicitly introduce the solvent in the model, so that the complex is solvated and retains its actual structure. To do this, the complex is soaked and equilibrated into a periodic simulation box of chloroform, which was previously equilibrated at room temperature and pressure. In order to gain information on the way a single $[\mathbf{4-1 \cdot BPE}]_2$ complex

adsorbs on the nanotube, ideally we should soak the nanotube and the complex in a solvent box large enough to contain both: this would hugely increase the computational time of the simulation due to the large number of solvent molecules required to fill such modeling box. To reduce the computational cost of the model, we consider that because of the use of a cut-off for the non-bonding interaction of 1.2 nm, most of the system will not contribute to the stability of the interface. Therefore, we replace the ideal model with the following system: the solvent box containing the solvated [4-1-BPE]₂ complex, has been placed in contact with a portion of the original nanotube wall having a surface area of about 140 nm². This slab of the nanotube wall is kept rigid during the simulations. Also, all the solvent molecules defining the edge of the solvent box have been frozen, to avoid their dispersion in the non-periodic modeling box. Few solvent molecules have been removed to reduce the liquid density and help the diffusion.

6.2.4.2. Preparation of the Hybrid and Alignment

The samples of [1-BPE]₂⊙MWCNTs, as well as the control samples (4-1⊙CNTs, 4-4⊙CNTs, 4-2⊙CNTs) were prepared according to this procedure. The organic molecule (4.9×10^{-5} M, 1 mL CHCl₃) was added to a pre-sonicated (room temperature, 3 min) dispersion of 1.0 mg of pristine MWCNT (Nanocyl 7000, batch 318-25) in 10 mL CHCl₃. The dispersion was then sonicated (room temperature, 30 min). The resulting black suspension, was then centrifugated at 5 krpm for 30 min in order to separate the unfunctionalized and aggregate carbonaceous material, from the solubilized CNT. The supernatant solution was separated and filtered through a Teflon(JH)Millipore® (0.45 μm) filter and washed with CHCl₃ (20 mL) to remove the organic excess. The sonication-centrifugation-filtration cycle was repeated. Finally, the solubilized CNT were recovered from the Millipore filter (sonication, 5 min) and the solutions were analyzed by absorption and emission spectroscopies.

Magnetic alignment was performed on a superconducting magnet JASTEC 10T100 with a vertical bore of 100 mm was used for magneto-induced orientation of MWCNTs. Polarized optical microscopy (POM) was performed on a Nikon model Eclipse LV100POL optical polarizing microscope. Polarized UV-Vis spectra were recorded on a JASCO V-670 UV-VIS-NIR spectrophotometer.

The organogel used was poly(3-hydroxybutyric acid-co-3-hydroxyvaleric acid) (PHVB) with PHV content 4 mol %, bought from Sigma Aldrich.

6.2.5. Chapter 5

6.2.5.1. STM Experiments

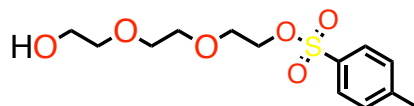
All experiments were performed using a custom-built ultrahigh vacuum system housing an SPS-CreaTec low-temperature STM operated at 6 K. The base pressure was in the range of $\sim 8 \times 10^{-10}$ mbar during the experiments. The Ag(111) single crystal was cleaned by repeated Ar⁺ sputtering cycles at 800 eV and subsequent annealing at 723 K for 10 minutes. Subsequently, the pyrene derivatives were deposited by organic molecular beam epitaxy from a thoroughly degassed quartz crucible held at varying temperatures onto the Ag(111) surface held at ~ 300 K. STM images were acquired in constant current mode using an electrochemically etched tungsten tip prepared by Ar⁺ sputtering at 1 keV and controlled tip-formings into the bare Ag(111) surface. The structural models were generated using the HyperChem 7.5 Software package, whereas the WSxM software was used represent the STM images.

6.2.5.2. Surface XPS

The XP spectra were taken under UHV conditions with a base pressure in the low 10^{-9} mbar regime. The single crystal Ag(111) surface was cleaned by combination of Ar⁺ sputtering (1 keV) and annealing at 720 K. The pyrene derivate was deposited by organic molecule beam epitaxy from a boron nitride crucible held at 590 K onto the substrate, which was held at room temperature. All measurements were performed at room temperature. The spectra were taken in normal electron emission geometry and the pass energy for the hemispherical analyzer was set to 20 eV. The electrons were excited by X-ray emission from a polychromic Al K_α source. All binding energies were calibrated according to the Ag 3d_{5/2} line (368.3 eV) of the substrate. The linear background was subtracted from the raw data using either a Shirley background (C 1s) or polynomial functions (I 3d) and afterwards the spectra were fitted using a Voigt function.

6.3. Synthetic Procedures

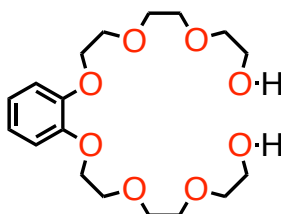
2-5 2-(2-(2-hydroxyethoxy)ethoxy)ethyl 4-methylbenzenesulfonate



To a solution of triethylene glycol (35.0 mL, 0.3 mol) and NaOH (8.0 g, 0.2 mol) in THF/H₂O (1:1 80 mL) in an ice bath was added dropwise tosyl chloride (24.0 g, 0.1 mmol) in THF (80 mL) over 3 h. The reaction mixture was stirred overnight. The mixture was concentrated under reduced pressure. The residue was extracted with EtOAc and dried over Na₂SO₄. After the solvent was removed under reduced pressure, the crude was purified by column chromatography (SiO₂, EtOAc) to afford product (13.1 g, 34 % yield).

¹H NMR (200 MHz, Chloroform-*d*): δ 7.75 (d, *J* = 8.3 Hz, 2H, Ar-*H*), 7.30 (d, *J* = 8.0 Hz, 2H, Ar-*H*), 4.24 – 3.99 (m, 2H, -SO₃-CH₂-CH₂-O-), 3.78 – 3.38 (m, 10H, -O-CH₂-CH₂-O-), 2.67 (bs, 1H, -O-*H*), 2.40 (s, 3H, Ar-CH₃). ¹³C NMR (50 MHz, Chloroform-*d*): δ 144.91, 132.91, 129.88, 127.97, 72.58, 70.81, 70.35, 69.31, 68.74, 61.76, 21.77. ESI-MS (+): expected 304.10 for C₁₃H₂₀O₆S, found 327.1 (M + H⁺). Characterization in accordance with literature.⁶⁵⁶

2-6 1,2-Bis{2-[2-(2-hydroxyethoxy)ethoxy]ethoxy}benzene

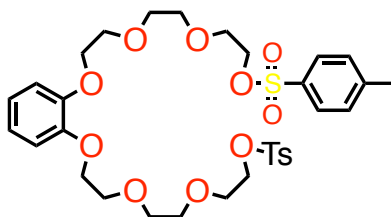


To a solution of pyrocatechol (2.28 g, 0.02 mol) in dry CH₃CN (150 mL), were added compound 2-5 (12.60 g, 0.04 mol) and K₂CO₃ (13.16 g, 0.09 mol) was added and the mixture was refluxed for 60

h. The reaction mixture was filtered and then concentrated under reduced pressure. The crude was purified by column chromatography (SiO₂, EtOAc → EtOAc/MeOH 9:1) to afford the desired product (4.21 g, 56 % yield).

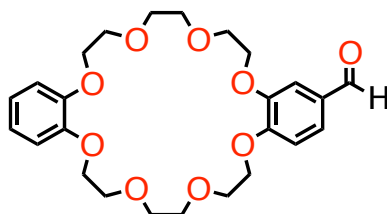
¹H NMR (500 MHz, Chloroform-*d*): δ 6.91 (s, 4H, Ar-*H*), 4.23 – 4.09 (m, 4H, -O-CH₂CH₂-O-), 3.94 – 3.81 (m, 8H, O-CH₂CH₂-O), 3.75 – 3.65 (m, 8H, -O-CH₂CH₂-O), 3.65 – 3.53 (m, 4H, -O-CH₂CH₂-O-). ¹³C NMR (50 MHz, Chloroform-*d*): δ 148.91, 121.85, 114.53, 72.96, 71.05, 70.55, 69.94, 68.83, 61.91. ESI-MS (+): expected 374.19 for C₁₈H₃₀O₈, found 397.3 (M + H⁺). Characterization in accordance with literature.⁶⁵⁶

2-7 1,2-Bis[2-[2-(2-tosyloxyethoxy)ethoxy]ethoxy]benzene



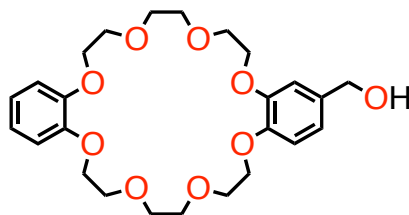
To a mixture of compound **2-6** (4.00 g, 0.01 mol) and NaOH (1.64 g, 0.04 mol) in THF/H₂O (1:1, 22 mL), in an ice bath, was added dropwise tosyl chloride (4.06 g, 0.02 mol) in THF (32 mL), over 3 h. The mixture was stirred overnight, then was concentrated under reduced pressure. The residue was extracted with EtOAc and the organic phases were dried over Na₂SO₄. After the solvent was removed under reduced pressure, the crude was purified by column chromatography (SiO₂, Pet. Et./AcOEt 1:1 → 2:8) to afford the desired product (3.07 g, 42 % yield).

¹H NMR (500 MHz, Chloroform-*d*): δ 7.79 (d, *J* = 8.3 Hz, 4H, tosyl-*H*), 7.32 (d, *J* = 7.8 Hz, 4H, tosyl-*H*), 6.91 (s, 4H, Ar-*H*), 4.23 – 4.05 (m, 8H, O-CH₂CH₂-O), 3.91 – 3.78 (m, 4H, -O-CH₂CH₂-O-), 3.74 – 3.64 (m, 8H, -O-CH₂CH₂-O-), 3.63 – 3.54 (m, 4H, -O-CH₂CH₂-O-), 2.42 (s, 6H, Ar-CH₃). ¹³C NMR (126 MHz, Chloroform-*d*): δ 149.20, 144.99, 133.22, 130.03, 128.18, 121.89, 115.17, 71.03, 70.98, 70.06, 69.48, 69.08, 68.93, 21.84. ESI-MS (+): expected 682.21 for C₃₂H₄₂O₁₂S₂, found 705.3 (M + H⁺). Characterization in accordance with literature.⁶⁵⁶

2-8 (2-Formyl)dibenzo[24]crown-8

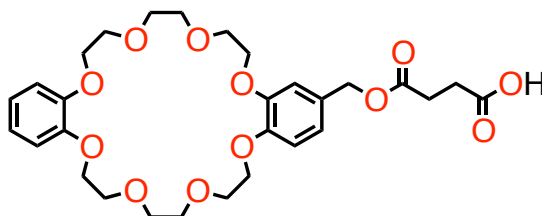
A mixture of 3,4-dihydroxybenzaldehyde (1.2 g, 9.0 mmol), K_2CO_3 (6.0 g, 43.4 mmol) and a catalytic amount of LiBr in MeCN (1.0 L) was heated to reflux for 1 h, under Ar. A solution of **2-7** (6.1 g, 9.0 mmol) in MeCN (0.5 L) was added dropwise over 12 h and the mixture was heated to reflux for another 48 h. Filtration and concentration of the filtrate under reduced pressure left an oil which was taken up in CH_2Cl_2 (300 mL) and washed with 0.1 M aq. HCl solution and brine. The organic phase was dried (Na_2SO_4) and removed under reduced pressure. The crude was purified by column chromatography (SiO_2 , AcOEt/MeOH 1 \rightarrow 95:5) to afford a white powder as product (2.0 g, 47 % yield).

m.p. 104-105 °C. 1H NMR (500 MHz, Chloroform-*d*): δ 9.81 (d, $J=0.7$ Hz, 1H, Ar-CHO), 7.41 (dd, $J=8.1, 1.8$ Hz, 1H, Ar-*H*), 7.37 (d, $J=1.8$ Hz, 1H, Ar-*H*), 6.93 (d, $J=8.2$ Hz, 1H, Ar-*H*), 6.91 – 6.80 (m, 4H, Ar-*H*), 4.21 (dt, $J=8.8, 4.1$ Hz, 4H, -O- CH_2CH_2 -O-), 4.18 – 4.11 (m, 4H, -O- CH_2CH_2 -O-), 3.97 – 3.89 (m, 8H, -O- CH_2CH_2 -O-), 3.84 (s, 4H, -O- CH_2CH_2 -O-), 3.83 (s, 4H, -O- CH_2CH_2 -O-). ^{13}C NMR (126 MHz, Chloroform-*d*): δ 191.04, 154.50, 149.38, 149.10, 149.08, 130.39, 126.99, 121.62, 121.59, 114.18, 112.09, 111.27, 71.75, 71.64, 71.52, 71.50, 70.15, 70.15, 69.89, 69.73, 69.66, 69.62, 69.61, 69.54. ESI-MS (+): expected 476.20 for $C_{25}H_{32}O_9$, found 499.3 (M + H^+). Characterization in accordance with literature.⁶⁵⁷

2-9 (2-Hydroxymethyl)dibenzo[24]crown-8

To a solution of **2-8** (0.550 g, 1.154 mmol) in CH₃OH/CH₂Cl₂ (1:1, 24 mL), cooled to 0 °C, was added portionwise NaBH₄ (0.131 g, 3.462 mmol) and the resulting solution was allowed to warm to r.t. and then left stirring overnight. The reaction mixture was acidified with 1 M aq. HCl and extracted with CH₂Cl₂. The organic layer was washed with 1 M aq. NaHCO₃ and H₂O, dried (Na₂SO₄) and evaporated to yield a white solid, as product (0.550 g, quantitative yield).

m.p. 94-96 °C. ¹H NMR (500 MHz, Chloroform-*d*): δ 6.93 – 6.79 (m, 7H, Ar-*H*), 4.59 (s, 2H, Ar-CH₂-OH), 4.15 (m, 8H, -O-CH₂CH₂-O-), 3.96 – 3.87 (m, 8H, -O-CH₂CH₂-O-), 3.83 (s, 8H, -O-CH₂CH₂-O-). ¹³C NMR (126 MHz Chloroform-*d*): δ 149.18, 121.65, 120.17, 114.33, 114.15, 113.26, 110.20, 71.51, 70.14, 69.81, 69.65, 65.46. ESI-MS (+): expected 476.20 for C₂₅H₃₂O₉, found 499.3 (M + H⁺). Characterization in accordance with literature.⁶⁵⁸

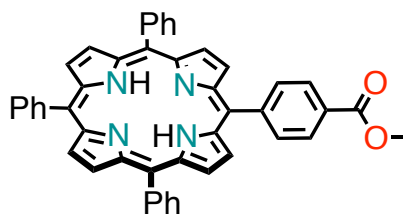
2-10 {[(3-carboxypropanoyl)oxy]methyl}dibenzo[24]crown-8

A solution of **2-9** (200 mg, 0.418 mmol), succinic anhydride (44 mg, 0.443 mmol) and 4-DMAP (catalytic amount) in dry PhCH₃ (30 mL) was refluxed overnight. The solution was left to cool to room temperature and the solvent was removed under reduced pressure. The crude product was

precipitated from CH₂Cl₂ with CHX, pentane and Et₂O to obtain the product as a white solid (205 mg, 85 % yield).

m.p. 112-112.5 °C. ¹H NMR (500 MHz, Chloroform-*d*): δ 6.88-6.82 (m, 7H, Ar-*H*), 5.03 (s, 2H, Ar-CH₂-O), 4.21-4.09 (m, 8H, O-CH₂CH₂-O), 3.92-3.87 (m, 8H, O-CH₂CH₂-O), 3.82 (s, 8H, O-CH₂CH₂-O), 2.64 (s, 4H, -OOC-CH₂CH₂-COOH). ¹³C NMR (126 MHz Chloroform-*d*): δ 176.75, 172.24, 149.19, 149.09, 149.05, 129.01, 121.86, 121.62, 114.56, 114.26, 113.77, 71.45, 71.39, 70.11, 70.08, 70.01, 69.63, 69.56, 69.55, 66.72, 29.27, 29.01. IR (KBr): cm⁻¹ 2929, 2922, 1733, 1714, 1593, 1521, 1506, 1451, 1432, 1331, 1309, 1258, 1128, 1098, 1056, 941, 804. ESI-MS (-): found 577.2 (M - H⁺), C₂₉H₃₈O₁₂ requires = 578.2.

2-11 5,10,15-Triphenyl-20-(4-methylbenzoate) porphyrin

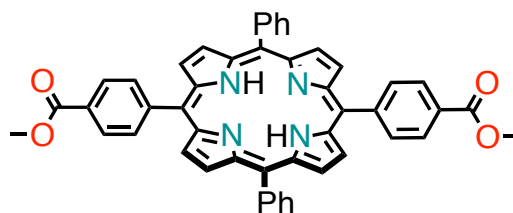


To a solution of benzaldehyde (0.22 mL, 2.19 mmol), methyl 4-formylbenzoate (0.33 g, 2.19 mmol) and freshly distilled pyrrole (0.30 mL, 4.38 mmol) in CHCl₃ (1.0 L) was added BF₃·OEt₂ (0.36 mL), under Ar. The solution was stirred for 1 h before adding *p*-chloranil (0.40 g, 1.68 mmol) and was left stirring for another hour. Finally, Et₃N (0.28 mL) was added and all was stirred for 15 min. The solution was concentrated under reduced pressure and passed through a short silica plug (Pet. Et./CH₂Cl₂ 1:1) to obtain a dark purple solid as a mixture of TPP and porphyrin esters. Compound **2-11** was purified by column chromatography as the second band (SiO₂, CHX/AcOEt from 95:5) and finally precipitated from CH₂Cl₂ with CHX (0.15 g, 10 % yield).

m.p. > 300 °C. ¹H NMR (200 MHz, Chloroform-*d*): δ 8.88 (m, 8H, Pyr-*H*), 8.49-8.30 (dd, 4H, *J* = 26.8, 8.4 Hz, Ar-*H*), 8.27-8.17 (m, 6H, Ph-*H*), 7.81-7.73 (m, 9H, Ph-*H*), 4.12 (s, 3H, -COO-CH₃), -2.78 (bs, 2H, Pyr-NH). ¹³C NMR (50 MHz Chloroform-*d*): δ 167.48, 147.22, 142.20, 134.71, 131.37, 129.73, 128.09, 127.96, 126.89, 120.76, 120.56, 118.71, 52.67. IR (KBr): cm⁻¹ 2925, 2920, 1722, 1606,

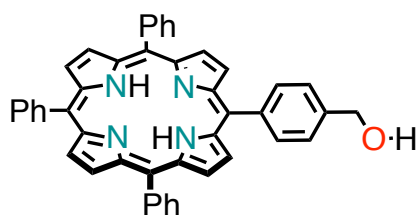
1437, 1491, 1279, 1178, 1112, 965, 799, 726, 707. **ESI-MS** (+): found 673.4 ($M + H^+$), $C_{46}H_{32}N_4O_2$ requires = 672.3.

2-12 5,15-Bis(4-methylbenzoate)-15,20-diphenylporphyrin



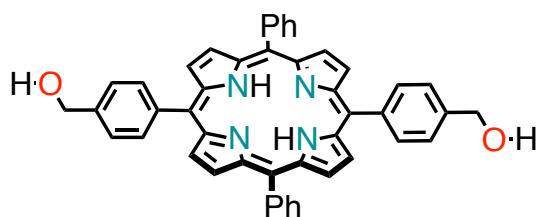
To a solution of benzaldehyde (0.22 mL, 2.19 mmol), methyl 4-formylbenzoate (0.33 g, 2.19 mmol) and pyrrole (0.30 mL, 4.38 mmol) in $CHCl_3$ (1.0 L) was added $BF_3 \cdot OEt_2$ (0.36 mL), under Ar. The solution was stirred for 1 hour before adding Chloranil (0.40 g, 1.68 mmol) and was left stirring for another hour. Finally, Et_3N (0.28 mL) was added and all was stirred for 15 min. The solution was concentrated under reduced pressure and passed through a short silica plug (Pet. Et./ CH_2Cl_2 1:1) to obtain a dark purple solid as a mixture of TPP and porphyrin esters. Compound **2-12** was purified by column chromatography as the third band (eluent: CHX/AcOEt from 9:1) and finally precipitated from CH_2Cl_2 with CHX (0.14 g, 9 % yield).

m.p. > 300 °C. 1H NMR (200 MHz, Chloroform-*d*): δ 8.85 (dd, 8H, $J = 15.8, 5.0$ Hz, Pyr-*H*), 8.39 (dd, 8H, $J = 28.6, 8.2$ Hz, Ar-*H*), 8.25-8.19 (m, 4H, Ph-*H*), 7.81-7.73 (m, 6H, Ph-*H*), 4.12 (s, 6H, -COOCH₃), -2.78 (bs, 2H, Pyr-NH). ^{13}C NMR (50 MHz Chloroform-*d*): δ 167.43, 147.08, 142.10, 134.72, 131.69, 131.08, 130.85, 129.82, 128.13, 128.05, 126.94, 121.00, 120.80, 119.15, 118.96, 52.67. IR (KBr): cm^{-1} 2926, 2921, 1724, 1604, 1435, 1489, 1275, 1175, 1112, 962, 802, 738. **ESI-MS** (+): found 731.4 ($M+H^+$), $C_{48}H_{34}N_4O_4$ requires = 730.3.

2-13 5,10,15-Triphenyl-20-[(4-hydroxybenzyl)]-porphyrin

A solution of **2-11** (0.050 g, 0.068 mmol) in dry THF (5.0 mL) was added dropwise to a suspension of LiAlH_4 (0.003 g, 0.081 mmol) in dry THF (2.0 mL) at 0 °C, under Ar. The reaction was left to stir for 30 min at room temperature before being quenched with EtOH (9 mL) and H_2O (1 mL). The mixture was diluted with CH_2Cl_2 (50 mL) and the organic layer was washed with H_2O and brine, dried (Na_2SO_4) and concentrated under reduced pressure. The crude product was purified by column chromatography (SiO_2 , CHX/AcOEt 1:1) and finally precipitated from THF with CHX to obtain **2-13** (0.038 g, 81 % yield).

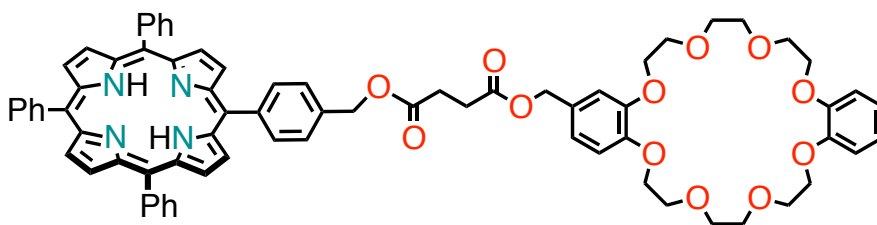
m.p. > 300 °C. $^1\text{H NMR}$ (500 MHz, Chloroform-*d*): δ 8.89 (s, 8H, Pyr-*H*), 8.26-8.21 (m, 8H, Ph-*H*), 7.80-7.72 (m, 11H, Ph-*H*), 5.02 (s, 2H, Ar- $\text{CH}_2\text{-O}$), 1.96 (bs, 1H, $\text{-CH}_2\text{OH}$), -2.71 (bs, 2H, Pyr-NH). $^{13}\text{C NMR}$ (50 MHz Chloroform-*d*): δ 142.38, 141.78, 140.46, 134.95, 134.76, 127.93, 126.90, 125.52, 120.40, 120.38, 119.96, 65.62. IR (KBr): cm^{-1} 2919, 2911, 1631, 1468, 1440, 1257, 1118, 966, 1112, 965, 799, 736, 702. ESI-MS (+): found 643.3 ($\text{M} - \text{H}^+$), $\text{C}_{45}\text{H}_{32}\text{N}_4\text{O}$ requires = 644.3.

2-14 5,15-Bis(4-hydroxybenzyl)-15,20-diphenylporphyrin

A solution of **2-12** (0.127 g, 0.174 mmol) in dry THF (10.0 mL) was added dropwise to a suspension of LiAlH₄ (0.008 g, 0.209 mmol) in dry THF (5.0 mL) at 0 °C, under Ar. The reaction was left to stir for 30 min at room temperature before being quenched with EtOH (9 mL) and H₂O (1 mL). The mixture was diluted with CHCl₃ and the organic layer was washed with H₂O and brine, dried (Na₂SO₄) and removed under reduced pressure. The crude was purified by column chromatography (SiO₂, CHX/AcOEt 1:1), precipitated from THF with CHX to obtain **2-14** (0.082 g, 70 % yield).

m.p. > 300 °C. ¹H NMR (500 MHz, Chloroform-*d*): δ 8.85 (s, 8H, Pyr-*H*), 8.25-8.19 (m, 8H, Ar-*H*), 7.79-7.73 (m, 10H, Ar-*H*), 5.05 (s, 4H, ArCH₂OH), 2.00 (bs, 2H, ArCH₂OH), -2.76 (bs, 2H, Pyr-NH). ¹³C NMR (50 MHz Chloroform-*d*): δ 142.35, 141.75, 140.47, 134.94, 134.76, 127.94, 126.91, 125.52, 120.43, 119.99, 65.61. IR (KBr): cm⁻¹ 2941, 2852, 1627, 1572, 1489, 1445, 1383, 1339, 1200, 1061, 965, 797, 713, 702. ESI-MS (+): found 675.4 (M+H⁺), C₄₆H₃₄N₄O₂ requires = 674.8.

2-1 5,10,15-Triphenyl-20-[[[(3-carboxypropanoyl)oxy]methyl]dibenzo[24]crown-8 porphyrin

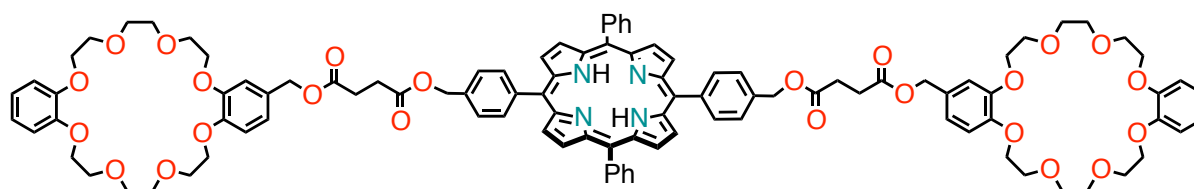


To a solution of **2-13** (75 mg, 0.130 mmol), **2-10** (40 mg, 0.062 mmol) and 4-DMAP (16 mg, 0.130 mmol) in CH₂Cl₂ (7 mL) was added EDC·HCl (25 mg, 0.130 mmol) at 0 °C, under Ar. The reaction was left to warm up to r.t. and was left stirring overnight, under Ar. The reaction mixture was diluted with CH₂Cl₂ and the organic layer was washed with 0.1 M aq. HCl, sat. aq. K₂CO₃ solution and H₂O, dried (Na₂SO₄) and eliminated under reduced pressure. The crude was purified by column chromatography (SiO₂, CHCl₃) to obtain **2-1** as a deep purple solid (50 mg, 67 % yield).

¹H NMR (500 MHz, Chloroform-*d*): δ 8.85 (s, 8H, Pyr-*H*), 8.23-8.21 (m, 8H, Ar-*H*), 7.77-7.75 (m, 11H, Ar-*H*), 6.93-6.81 (m, 7H, Ar-*H*), 5.49 (s, 2H, ArCH₂-O-), 5.10 (s, 2H, -O-CH₂-Ar), 4.18-4.06

(m, 8H, -O-CH₂CH₂-O-), 3.86-3.81 (m, 8H, -O-CH₂CH₂-O-), 3.75 (s, 8H, -O-CH₂CH₂-O-), 2.89-2.81 (m, 4H, -OOC-CH₂CH₂-COO-), -2.77 (s, 2H, Pyr-*H*). ¹³C NMR (126 MHz Chloroform-*d*): δ 172.52, 172.39, 149.25, 149.12, 142.36, 142.34, 135.51, 134.92, 134.77, 129.02, 127.95, 126.91, 126.62, 121.94, 121.61, 120.48, 120.42, 119.65, 114.61, 114.29, 113.87, 71.44, 71.41, 70.08, 70.02, 69.97, 69.70, 69.64, 69.59, 69.55, 66.85, 66.74, 29.58, 29.56. IR (KBr): cm⁻¹ 2918, 2889, 1730, 1630, 1597, 1408, 1380, 1347, 1258, 1219, 1147, 1125, 1058, 997, 969, 808, 741, 713. MS (ES⁺): found 1203.4 (M - H⁺), C₇₄H₆₈N₄O₁₂ requires = 1204.48.

2-2 5,15-Bis{[(3-carboxypropanoyl)oxy]methyl}dibenzo[24]crown-8-15,20-diphenylporphyrin

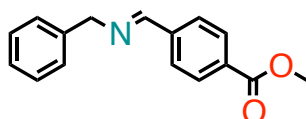


To a solution of **2-10** (90 mg, 0.156 mmol), **2-14** (25 mg, 0.037 mmol) and 4-DMAP (19 mg, 0.156 mmol) in CH₂Cl₂ (6 mL) was added EDC·HCl (30 mg, 0.156 mmol) at 0 °C, under Ar. The reaction was left to warm up to r.t. and was left stirring overnight, under Ar. The solvent was removed under reduced pressure and the residue was dissolved in CH₂Cl₂. The organic layer was washed with with 0.1 M aq. HCl, sat. aq. K₂CO₃ solution and H₂O, dried (Na₂SO₄) and eliminated under reduced pressure. The mixture was purified by column chromatography (SiO₂, CHCl₃ → CHCl₃/MeOH 99:1) to obtain **2-2** as a deep purple solid (36 mg, 54 % yield).

¹H NMR (500 MHz, Chloroform-*d*): δ 8.85 (s, 8H, Pyr-*H*), 8.23-8.19 (m, 8H, Ph-*H*), 7.78-7.71 (m, 10H, Ph-*H*), 6.95-6.81 (m, 14H, Ar-*H*), 5.49 (s, 4H, ArCH₂-O-), 5.11 (s, 4H, ArCH₂-O-), 4.17-4.06 (m, 16H, -O-CH₂CH₂-O-), 3.88-3.81 (m, 16H, -O-CH₂CH₂-O-), 3.76 (s, 16H, -O-CH₂CH₂-O-), 2.90-2.81 (m, 8H, -OOC-CH₂CH₂-COO-), -2.78 (s, 2H, Pyr-NH). ¹³C NMR (126 MHz Chloroform-*d*): δ 172.53, 172.40, 149.26, 149.14, 142.32, 142.30, 135.54, 134.92, 134.77, 129.02, 127.99, 126.93, 126.63, 121.94, 121.61, 120.48, 119.78, 114.60, 114.29, 113.87, 71.47, 71.44, 70.11, 70.04, 69.99, 69.72, 69.67, 69.60, 69.57, 66.86, 66.73, 29.58, 29.56. IR (KBr): cm⁻¹ 2917, 2889, 1732, 1599, 1505,

1452, 1385, 1352, 1256, 1127, 1044, 955, 802, 740. **MS** (**ES**⁺): found 1794.7 ($M - H^+$), $C_{104}H_{106}N_4O_{24}$ requires = 1795.7.

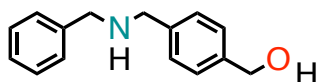
2-15 Methyl 4-[(benzylimino)methyl]benzoate



A solution of methyl 4-formylbenzoate (2.84 g, 17.30 mmol) and benzylamine (1.92 mL, 17.55 mmol) in MeOH (50 mL) was heated to reflux for 4 hrs, in the presence of 4 Å molecular sieves. The solvent was evaporated under reduced pressure and the residue treated with CH_2Cl_2 . The suspension was filtered through a celite pad, which then washed with more CH_2Cl_2 . The filtrates were evaporated under vacuum to yield a white solid as product (4.40 g, quantitative yield).

¹H NMR (200 MHz, Chloroform-*d*): δ 8.44 (s, 1H, -N=CH-Ar), 8.09 (d, $J = 8.3$ Hz, 2H, Ar-*H*), 7.85 (d, $J = 8.3$ Hz, 2H, Ar-*H*), 7.42 – 7.28 (m, 5H, Ph-*H*), 4.86 (s, 2H, Ar- CH_2 -N-), 3.94 (s, 3H, ArCOOCH₃). **MS** (**ES**⁺): found 254.1 ($M + H^+$), $C_{16}H_{15}NO_2$ requires = 253.11. Characterization in accordance with literature.⁶⁵⁹

2-16 Benzyl-4-hydroxymethylbenzylamine

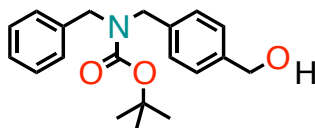


A solution of **2-15** (4.30 g, 16.98 mmol) in dry THF (50 mL) was added dropwise (over 20 min) to a suspension of $LiAlH_4$ (1.87 g, 49.24 mmol) in THF (15 mL) at 0 °C, under Ar. The reaction mixture was stirred at r.t. for 8 h, before being cooled down to 0 °C. The reaction was quenched with H_2O

(100 mL) slowly and carefully, then the mixture was extracted with CH_2Cl_2 . The organic layer was filtered through a celite pad and the filtrate was washed with brine, dried (Na_2SO_4), to provide product as a yellowish oil (3.40 g, 88 % yield).

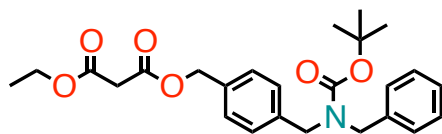
$^1\text{H NMR}$ (200 MHz, Chloroform- d): δ 7.44 – 7.27 (m, 9H, Ar- H), 4.68 (s, 2H, Ar- CH_2 -OH), 3.81 (s, 4H, Ar- CH_2 -NH- CH_2 -Ar). **MS** (**ES+**): found 228.1 ($M + \text{H}^+$), $\text{C}_{15}\text{H}_{17}\text{NO}$ requires = 227.13. Characterization in accordance with literature.⁶⁵⁹

2-17 *N*-BOC-benzyl-4-hydroxymethylbenzylamine



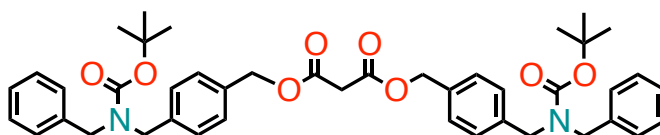
To a solution of **2-16** (1.50 g, 6.60 mmol) in MeOH (50 mL) was added BOC_2O (1.87 g, 8.25 mmol), with a catalytic amount of DMAP. The mixture was left stirring at r.t. overnight. The solvent was removed under reduced pressure, the residue was dissolved in CH_2Cl_2 and washed with 0.1 M aq. HCl, H_2O , the organic phase dried (Na_2SO_4) and removed under reduce pressure. The crude was purified by column chromatography (SiO_2 , Petroleum ether \rightarrow Petroleum ether/AcOEt 6:4) to obtain a colorless oil as pure product (2.10 g, 97 % yield).

$^1\text{H NMR}$ (200 MHz, Methylene Chloride- d_2): δ 7.40 – 7.13 (m, 9H, Ar- H), 4.65 (s, 2H, Ar- CH_2 -OH), 4.36 (bs, 4H, Ar- CH_2 -N), 1.47 (s, 9H, N-COO- CH_3). **MS** (**ES+**): found 350.2 ($M + \text{Na}^+$), $\text{C}_{20}\text{H}_{25}\text{NO}_3$ requires = 327.18. Characterization in accordance with literature.⁶⁶⁰

2-18 4-(*N*-benzyl-*N*-BOC-aminomethyl)-benzyl] ethyl malonate

To a solution of *N*-BOC-benzyl-4-hydroxymethylbenzylamine **2-17** (1.64 g, 5.0 mmol) and pyridine (0.81 mL, 10.0 mmol) in dry CH₂Cl₂ (100 mL) was added ethyl malonyl chloride (1.3 mL, 10.0 mmol) at 0 °C and the mixture was stirred 2 hrs, under Ar for. The solution was washed with sat. aq. NH₄Cl solution and H₂O, the organic phase was dried (Na₂SO₄) and removed under reduced pressure. The crude was purified by column chromatography (SiO₂, CHX/EtOAc 2:1) to provide the product as colorless oil (1.01 g, 46 % yield).

¹H NMR (500 MHz, Chloroform-*d*): δ 7.36 – 7.29 (m, 5H, Ph-*H*), 7.22 (apparent d, *J* = 17.7 Hz, 4H, Ar-*H*), 5.18 (s, 2H, Ar-CH₂-OOC-), 4.38 (apparent d, *J* = 43.4 Hz, 4H, Ar-CH₂-N), 4.21 (q, *J* = 7.1 Hz, 2H, -COOCH₂CH₃), 3.43 (s, 2H, -OCCH₂CO-), 1.50 (s, 9H, -COO(CH₃)₃), 1.26 (t, *J* = 7.2 Hz, 3H, -COOCH₂CH₃). MS (ES⁺): found 464.3 (M + Na⁺), C₂₅H₃₁NO₆ requires = 441.22. Characterization in accordance with literature.¹¹⁴

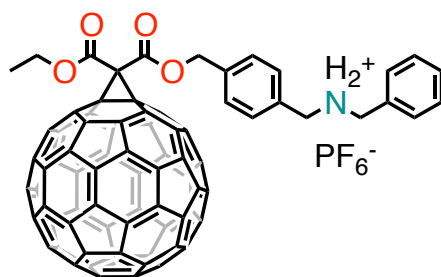
2-19 Bis[4-(*N*-benzyl-*N*-BOC-aminomethyl)-benzyl] malonate

To a solution of *N*-BOC-benzyl-4-hydroxymethylbenzylamine **2-17** (2.29 g, 7.0 mmol) and pyridine (0.56 mL, 7.0 mmol) in dry CH₂Cl₂ (65 mL), malonyl chloride (0.29 mL, 3.0 mmol) was added and the mixture was stirred overnight at r.t., under Ar. The solution was washed with sat. aq. NH₄Cl solution and H₂O, the organic phase was dried (Na₂SO₄) and removed under reduced

pressure. The crude was purified by column chromatography (SiO₂, CHX/EtOAc 2:1) to provide the product as colorless oil (1.42 g, 28 % yield).

¹H NMR (500 MHz, Chloroform-*d*): δ 7.36 – 7.27 (m, 10H, Ph-*H*), 7.21 (d, *J* = 18.3 Hz, 8H, Ar-*H*), 5.17 (s, 4H, Ar-CH₂-OOC-), 4.37 (apparent d, *J* = 43.1 Hz, 8H, Ar-CH₂-N), 3.48 (s, 2H, OCCCH₂CO), 1.49 (s, 18H, -COO(CH₃)₃). MS (ES⁺): found 745.5 (M + Na⁺), C₄₃H₅₀N₂O₈ requires = 722.36. Characterization was in accordance with literature.⁶⁶¹

2-3H₂·PF₆ [4-(*N*-benzylammoniomethyl)benzyl]-3-ethyl-1,2-methano[60]fullerene-61,61-dicarboxylatemetano[60]fullerene hexafluorophosphate



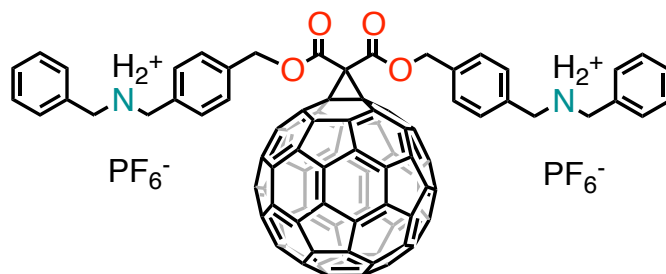
To a solution of malonate **2-18** (0.10 g, 0.23 mmol), C₆₀ (0.17 g, 0.24 mmol) and I₂ (0.08 g, 0.23 mmol) in PhCH₃ (0.20 L) was added DBU (0.35 mL, 2.30 mmol) and the mixture was stirred for 10 h at r.t., under Ar. The mixture was concentrated and loaded onto a silica column (SiO₂, PhCH₃ to elute unreacted fullerene and PhCH₃/AcOEt 95:5 for the product), followed by precipitation from CH₂Cl₂ with CH₃OH yielded the product as brown-red glassy solid (0.11 g, 41 % yield). ¹H NMR (500 MHz, Chloroform-*d*): δ 7.49 – 7.16 (m, 9H, Ar-*H*), 5.52 (s, 2H, Ar-CH₂-O), 4.51 (q, *J* = 7.1 Hz, 2H, -OCH₂CH₃), 4.45 – 4.30 (m, 4H, Ar-CH₂-N), 1.50 (s, 9H, -NCOO(CH₃)₃), 1.39 (t, *J* = 7.1 Hz, 3H, -OCH₂CH₃).

A solution of the above BOC-intermediate (0.10 g, 0.09 mmol) and TFA (0.13 mL, 1.72 mmol) in PhCH₃ (10 mL) was stirred at r.t. overnight, under Ar. After removal of the solvents under reduced pressure, the residue was taken up into CH₂Cl₂ and washed with 6 M aq. NaOH. The aq. phase was washed with CH₂Cl₂ and the combined organic layers were dried (Na₂SO₄) and evaporated under

reduced pressure to yield the corresponding amine which was re-dissolved in CHCl_3 . 4 M aq. HCl solution was added, the solvent was removed under reduced pressure and the resultant solid suspended in acetone (125 mL). Sat. aq. NH_4PF_6 solution was added to the suspension until a clear solution formed. Evaporation of the solvent under reduced pressure, filtration of the resulting suspension, and washing with copious amounts of H_2O yielded the product as a brown solid (81 mg, 77 % yield).

m.p. > 250 °C. $^1\text{H NMR}$ (500 MHz, Chloroform- d /Acetonitrile- d_3): δ 7.61 – 7.32 (m, 9H, Ar- H), 5.48 (s, 2H, Ar- CH_2 -O), 4.46 (q, $J = 7.1$ Hz, 2H, $-\text{OCH}_2\text{CH}_3$), 4.16 (d, $J = 10.4$ Hz, 4H, Ar- CH_2 - N^+), 1.34 (t, $J = 7.1$ Hz, 3H, $-\text{OCH}_2\text{CH}_3$). **MS** (MALDI): found 1060.0, $\text{C}_{80}\text{H}_{22}\text{NO}_4^+$ requires 1060.15. Characterization in accordance with literature.¹¹⁴

2-4H₄·2PF₆ Bis[4-(*N*-benzylammoniomethyl)benzyloxycarbonyl]methano[60]fullerene bis(hexafluorophosphate)



To a solution of malonate **2-19** (0.17 g, 0.23 mmol), C_{60} (0.17 g, 0.24 mmol) and I_2 (0.08 g, 0.23 mmol) in PhCH_3 (0.20 L) was added DBU (0.35 mL, 2.30 mmol) and the mixture was stirred for 10 h at r.t. under Ar. The mixture was concentrated and loaded onto a silica column (SiO_2 , PhCH_3 to elute unreacted fullerene and $\text{PhCH}_3/\text{AcOEt}$ 95:5 for the product), followed by precipitation from CH_2Cl_2 with CH_3OH yielded the product as brown-red glassy solid (0.13 g, 39 % yield). $^1\text{H NMR}$ (500 MHz, Chloroform- d): δ 7.44 – 7.14 (m, 18H, Ar- H), 5.48 (s, 4H, Ar- CH_2 -O), 4.45 – 4.27 (m, 8H, Ar- CH_2 -N), 1.48 (d, $J = 3.0$ Hz, 18H, $-\text{NCOO}(\text{CH}_3)_3$).

A solution of the above BOC-intermediate (0.10 g, 0.07 mmol) and TFA (0.13 mL, 1.72 mmol) in PhCH_3 (10 mL) was stirred at r.t. overnight, under Ar. After removal of the solvents under reduced

pressure, the residue was taken up into CH_2Cl_2 and washed with 6 M aq. NaOH. The aq. phase was washed with CH_2Cl_2 and the combined organic layers were dried (Na_2SO_4) and evaporated under reduced pressure to yield the corresponding amine which was re-dissolved in CHCl_3 . 4 M aq. HCl solution was added, the solvent was removed under reduced pressure and the resultant solid suspended in acetone (125 mL). Sat. aq. NH_4PF_6 solution was added to the suspension until a clear solution formed. Evaporation of the solvent under reduced pressure, filtration of the resulting suspension, and washing with copious amounts of H_2O yielded the product as a brown solid (70 mg, 72 % yield).

m.p. > 250 °C. $^1\text{H NMR}$ (500 MHz, Acetonitrile- d_3): δ 7.66 – 7.41 (m, 18H, Ar-*H*), 5.55 (bs, 4H, Ar- CH_2O -), 4.23 (bs, 8H, -Ar CH_2N^+ -). MS (MALDI): found 1243.2, $\text{C}_{93}\text{H}_{34}\text{N}_2\text{O}_4^{2+}$ requires 1242.25. Characterization in accordance with literature.⁶⁶¹

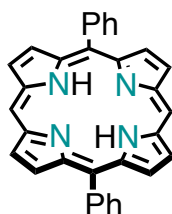
3-2 Dipyrromethane



A suspension of $(\text{HCHO})_n$ (1.9 g, 62.0 mmol) in freshly distilled pyrrole (100.0 mL, 1.4 mol) was degassed for 10 minutes at room temperature. The mixture was heated at 70 °C until a clear solution was obtained. TFA (1.2 mL, 16.2 mmol) was then added, and the mixture was stirred at 70 °C for 2 hours. The heat source was removed and the reaction was quenched with 0.5 M aq. NaOH. CH_2Cl_2 was added and the organic phase was washed with H_2O , dried (Na_2SO_4) and removed under reduced pressure. The excess of pyrrole was recovered by distillation and the dark crude solid was purified by column chromatography (SiO_2 , Pet. Et./EtOAc 85:15) to obtain the product as crystalline white solid (4.6 g, 51 % yield).

m.p. 69-70 °C. $^1\text{H-NMR}$ (500 MHz, Chloroform-*d*): δ 7.82 (bs, 2H, Pyr-NH), 6.72 – 6.57 (m, 2H, Pyr-*H*), 6.19 – 6.12 (m, 2H, Pyr-*H*), 6.04 (s, 2H, Pyr-*H*), 3.97 (s, 2H, Pyr- CH_2 -Pyr). $^{13}\text{C-NMR}$ (126 MHz, Chloroform-*d*): δ 129.19, 117.41, 108.51, 106.53, 26.52. IR (KBr): cm^{-1} 3336, 3086, 2960, 2897, 1715, 1656, 1583, 1561, 1471, 1439, 1421, 1397, 1328, 1267, 1245, 1227, 1182, 1120, 1109, 1096, 1026, 962, 886, 857, 798, 749, 734, 724, 684, 665, 587. MS (ES +): found 146.08 (M^+), $\text{C}_9\text{H}_{10}\text{N}_2$ requires 146.08. Characterization in accordance with literature.^{662,663}

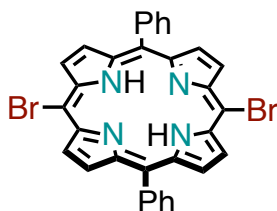
3-3 5,15-Diphenylporphyrin



A solution of dipyrromethane **3-2** (1.10 g, 7.52 mmol) and benzaldehyde (0.80 mL, 7.90 mmol) in dry CH₂Cl₂ (1.50 L) was deoxygenated by bubbling Ar for 60 minutes. TFA (0.13 mL, 1.67 mmol) was added dropwise and the mixture was stirred overnight at room temperature, under dark. DDQ (5.18 g, 22.83 mmol) was added and the mixture was refluxed for 2 hours. Et₃N (0.5 mL) was added and the mixture was concentrated under reduced pressure. The solution was passed through a silica plug (CH₂Cl₂) and the crude was purified by column chromatography (SiO₂, Pet. Et./CH₂Cl₂ 4:1) to obtain product as purple crystals (0.85 g, 49 % yield).

m.p. > 250 °C. ¹H-NMR (500 MHz, Chloroform-*d*): δ 10.32 (s, 2H, meso-*H*), 9.40 (d, *J* = 4.5 Hz, 4H, Pyr-*H*), 9.09 (d, *J* = 4.5 Hz, 4H, Pyr-*H*), 8.34 – 8.24 (m, 4H, Ph-*H*), 7.84 – 7.80 (m, 6H, Ph-*H*). ¹³C-NMR (126 MHz, Chloroform-*d*): δ 147.33, 145.36, 141.54, 135.00, 131.76, 131.20, 127.87, 127.12, 119.25, 105.41. IR (KBr): cm⁻¹ 1594, 1580, 1532, 1483, 1438, 1416, 1238, 1197, 1178, 1147, 1066, 1052, 1002, 987, 973, 957, 860, 850, 796, 787, 749, 719, 690. MS (ES +): found 463.15 (M + H⁺), C₃₂H₂₂N₄ requires 462.18. Characterization in accordance with literature.⁶⁶³

3-4 5,15-Dibromo-10,20-diphenylporphyrin

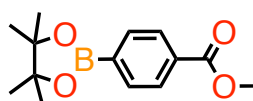


To a solution of 5,15-diphenylporphyrin **3-3** (200 mg, 0.43 mmol) in CHCl₃ (100 mL) at 0 °C was added pyridine (1.0 mL) and N-bromosuccinimide (154 mg, 0.85 mmol). The reaction was followed by TLC (Pet. Et./CH₂Cl₂ 1:1) and was quenched with acetone (10 mL) after 15 minutes. The solvent was removed under reduced pressure, the crude was passed through a silica plug (Pet. Et./CH₂Cl₂ 1:1) and finally washed with MeOH to obtain product as reddish purple crystals (223 mg, 84 % yield).

m.p. > 250 °C. ¹H-NMR (500 MHz, Chloroform-*d*): δ 9.86 (d, *J* = 4.8 Hz, 4, Pyr-*H*), 9.08 (d, *J* = 4.8 Hz, 4, Pyr-*H*), 8.42–8.37 (m, 4H, Ph-*H*), 8.11–7.94 (m, 6H, Ph-*H*). ¹³C-NMR (126 MHz, Chloroform-*d*): δ 141.61, 134.73, 128.28, 127.05, 121.64, 103.9; 4 signals missing due to low

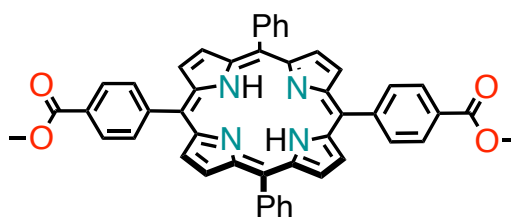
solubility. **IR** (KBr): cm^{-1} 1597, 1558, 1464, 1440, 1350, 1334, 1269, 1243, 1192, 1174, 1072, 1056, 997, 979, 961, 844, 794, 784, 737, 730, 706, 695. **MS** (ES +): found 619.01 ($M + H^+$), $C_{32}H_{20}Br_2N_4$ requires 618.01. Characterization in accordance with literature.³⁵⁴

3-5 Methyl 4-(4,4,5,5-tetramethyl-1,3,2-dioxaborolan-2-yl)benzoate



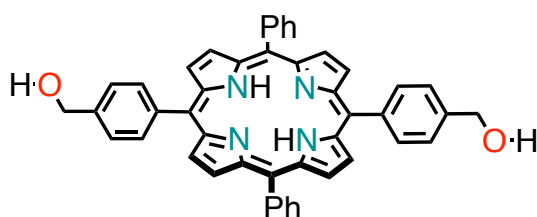
A mixture of methyl 4-bromobenzoate (2.0 g, 9.30 mmol), B_2pin_2 (2.8 g, 11.16 mmol) and KOAc (2.7 g, 27.9 mmol) in $PhCH_3$ (30 mL) was degassed for about 20 minutes under Ar. $Pd(dppf)Cl_2$ (0.034 g, 0.46 mmol, 5 % mmol) was added, the flask was sealed and the mixture was heated at 90 °C for 2 hours. The mixture was quenched with 1 M aq. NH_4Cl , extracted with CH_2Cl_2 , the organic phase washed with H_2O , dried (Na_2SO_4) and removed under reduced pressure. The crude was purified by column chromatography (SiO_2 , Pet. Et./EtOAc 95:5) to obtain the product as white solid (1.8 g, 91 % yield).

m.p. 78-79 °C. **1H -NMR** (500 MHz, Chloroform-*d*): δ 8.02 (d, $J = 8.2$ Hz, 2H, Ar-*H*), 7.87 (d, $J = 8.1$ Hz, 2H, Ar-*H*), 3.92 (s, 3H, Ar-COOCH₃), 1.35 (s, 12H, -BC₂(CH₃)₄). **^{13}C -NMR** (126 MHz, Chloroform-*d*): δ 167.28, 134.80, 132.45, 128.74, 84.33, 52.29, 25.03. **IR** (KBr): cm^{-1} 2986, 1724, 1509, 1435, 1398, 1372, 1361, 1327, 1278, 1141, 1110, 1018, 962, 857, 773, 710, 652. **MS** (ES +): found 263.12 ($M + H^+$), $C_{14}H_{19}BO_4$ requires 262.14. Characterization in accordance with literature.⁶⁶⁴

3-6 5,15-Bis(4-methoxycarbonylphenyl)-10,20-diphenylporphyrin

To a solution of porphyrin **3-4** (0.10 g, 0.16 mmol) in dry THF (35 mL) was added boronate ester **3-5** (0.85 g, 3.22 mmol) and K_3PO_4 (1.36 g, 6.40 mmol). The mixture was degassed with a 'freeze-pump-thaw' cycle. $Pd(PPh_3)_4$ (36 mg, 0.03 mmol, 20 % mmol) was added and the mixture was degassed once again. The mixture was refluxed at 85 °C overnight, under dark. The reaction mixture was cooled down and filtered over celite (with aid of CH_2Cl_2). The solvents were removed under reduced pressure and the crude was purified by column chromatography (SiO_2 , Pet. Et./EtOAc 95:5) to obtain the pure product as purple solid (80 mg, 91 % yield).

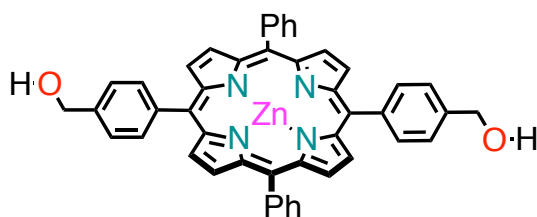
m.p. > 250 °C. ^1H-NMR (500 MHz, Chloroform-*d*): δ 8.87 (d, $J = 4.8$ Hz, 4H, Pyr-*H*), 8.80 (d, $J = 4.8$ Hz, 4H, Pyr-*H*), 8.45 (d, $J = 8.2$ Hz, 4H, Ar-*H*), 8.31 (d, $J = 8.2$ Hz, 4H, Ar-*H*), 8.24 – 8.20 (m, 4H, Ph-*H*), 7.82 – 7.69 (m, 6H, Ph-*H*), 4.12 (s, 6H, Ar- $COOCH_3$). $^{13}C-NMR$ (126 MHz, Chloroform-*d*): δ 167.53, 147.15, 142.12, 134.88, 134.77, 134.74, 129.85, 128.81, 128.14, 128.08, 126.97, 120.82, 119.16, 52.66. IR (KBr): cm^{-1} 1720, 1606, 1558, 1474, 1435, 1400, 1350, 1311, 1276, 1213, 1178, 1110, 1099, 1019, 1001, 981, 964, 878, 866, 800, 754, 731, 702. MS (ES +): found 731.22 ($M + H^+$) and 753.20 ($M + Na^+$), $C_{48}H_{34}N_4O_4$ requires 730.26. Characterization in accordance with literature.³⁵⁵

3-1 5,15-Bis(4-hydroxymethylphenyl)-10,20-diphenylporphyrin

To a solution of porphyrin **3-6** (70.0 mg, 0.10 mmol) in dry THF (10.0 mL) was added dropwise a suspension of LiAlH_4 (4.6 mg, 0.12 mmol) in dry THF (5.0 mL) at 0 °C. The mixture was left to warm up to room temperature and was left stirring for 60 minutes. The mixture was cooled back to 0 °C and the reaction was quenched with MeOH. The mixture was concentrated under reduced pressure, diluted with CHCl_3 , the organic phase was washed with H_2O , dried (Na_2SO_4) and eliminated under reduced pressure. The crude was purified by column chromatography (SiO_2 , $\text{CH}_2\text{Cl}_2/\text{MeOH}$ 98:2) to obtain pure product as purple solid (59 mg, 88 % yield).

m.p. > 250 °C. $^1\text{H-NMR}$ (500 MHz, Tetrahydrofuran- d_8): δ 8.88 – 8.79 (m, 8H, Pyr-*H*), 8.21 (dd, J = 7.3, 2.0 Hz, 4H, Ph-*H*), 8.16 (d, J = 8.0 Hz, 4H, Ar-*H*), 7.84 – 7.65 (m, 10H, Ar-*H*, Ph-*H*), 4.94 (d, J = 5.6 Hz, 4H, Ar- $\text{CH}_2\text{-OH}$), 4.51 (t, J = 5.8 Hz, 2H, Ar- $\text{CH}_2\text{-OH}$), -2.68 (bs, 2H). $^{13}\text{C-NMR}$ (126 MHz, Tetrahydrofuran- d_8): δ 143.68, 143.36, 141.59, 135.33, 135.18, 128.62, 127.60, 125.64, 121.11, 120.93, 64.89. **IR** (KBr): cm^{-1} 3435, 3308, 1597, 1474, 1442, 1401, 1349, 1215, 1185, 1014, 1002, 981, 966, 878, 853, 797, 755, 733, 700. **MS** (ES +): found 675.27 ($\text{M} + \text{H}^+$) and 697.26 ($\text{M} + \text{Na}^+$), $\text{C}_{46}\text{H}_{34}\text{N}_4\text{O}_2$ requires 674.27.

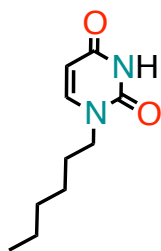
3-1-Zn Zinc (II) 5,15-bis(4-hydroxymethylphenyl)-10,20-diphenylporphyrin



To a vigorously stirred solution of free base porphyrin **3-1** (50.0 mg, 0.07 mmol) in CHCl_3 (10.0 mL) was added dropwise a solution of $\text{Zn}(\text{OAc})_2 \cdot \text{H}_2\text{O}$ (162.7 mg, 0.74 mmol) in MeOH (3.0 mL) and the mixture was stirred at room temperature, under dark. After 2 hours, the organic phase was diluted with CHCl_3 and was washed with H_2O , dried (Na_2SO_4) and removed under reduced pressure. Finally, the porphyrin was crystallized from THF/hexane to obtain the desired product as purple crystals (53 mg, quant.).

m.p. > 250 °C. **¹H-NMR** (500 MHz, Tetrahydrofuran-*d*₈): δ 8.86 (d, *J* = 4.6 Hz, 4H, Pyr-*H*), 8.83 (d, *J* = 4.6 Hz, 4H, Pyr-*H*), 8.20 (dd, *J* = 7.3, 2.0 Hz, 4H, Ph-*H*), 8.15 (d, *J* = 7.9 Hz, 4H, Ar-*H*), 7.79 – 7.69 (m, 10H, Ar-*H*, Ph-*H*), 4.94 (d, *J* = 5.7 Hz, 4H, Ar-CH₂-OH), 4.48 (t, *J* = 5.9 Hz, 2H, Ar-CH₂-OH). **¹³C-NMR** (126 MHz, Tetrahydrofuran-*d*₈): δ 151.15, 150.99, 144.66, 143.11, 142.94, 135.37, 135.18, 132.24, 132.14, 128.11, 127.20, 125.30, 121.58, 121.43, 65.00. **IR** (KBr): cm⁻¹ 3435, 1595, 1522, 1485, 1440, 1204, 1120, 1067, 995, 904, 797, 719, 703. **MS** (ES +): found 736.18 (M⁺), C₄₆H₃₂N₄O₂Zn requires 736.18.

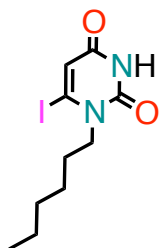
3.3-6 1-Hexyluracil



To a suspension of uracil (5.0 g, 44.6 mmol) in DMSO (50 mL), dry K_2CO_3 (6.8 g, 49.0 mmol) was added and the suspension stirred 30 minutes. 1-Bromohexane (6.2 mL, 44.6 mmol) was then added and the reaction mixture stirred overnight at 40 °C. The suspension was diluted with $CHCl_3$, washed with a 0.1 M aq. HCl solution, H_2O and brine. The organic layer was dried (Na_2SO_4) and concentrated under reduced pressure. The residue was poured in cold hexane under vigorous stirring. The resulting precipitate was filtered and washed with cold hexane to afford compound as a white solid **3.3-6** (3.8 g, 44 % yield).

m.p. 92-95 °C. 1H NMR (400 MHz, Chloroform-*d*): δ 8.83 (bs, 1H, -CONHCO-), 7.13 (dd, J = 7.7, 1.5 Hz, 1H, -COCH-), 5.69 (dd, J = 7.9, 1.9 Hz, 1H, -NCH-), 3.71 (t, J = 7.4 Hz, 2H, $NCH_2(CH_2)_4CH_3$), 1.73 – 1.54 (m, 2H, $-NCH_2CH_2(CH_2)_3CH_3$), 1.30 (d, J = 4.1 Hz, 6H, $-N(CH_2)_2(CH_2)_3CH_3$), 0.87 (t, J = 6.8 Hz, 3H, $-N(CH_2)_5CH_3$). ^{13}C -NMR (50 MHz, Chloroform-*d*): δ 164.14, 150.93, 144.37, 101.92, 48.78, 31.24, 28.92, 25.98, 22.39, 13.91. MS (ES): found 196 (M^+), $C_{10}H_{16}N_2O_2$ requires 196.09. Characterization in accordance with literature.³⁷⁴

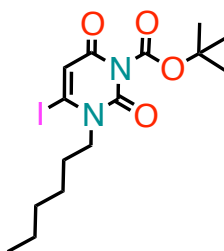
3.3-7 1-Hexyl-6-iodouracil



To a solution of 1-hexyluracil **3.3-6** (1.7 g, 8.7 mmol) in dry THF (55 mL), LDA (24.0 mL of a 1.8 M solution, 43.5 mmol) was added dropwise. The resulting solution was stirred under Ar at -78 °C for 1.5 h. I₂ (11.0 g, 43.5 mmol) was added and the reaction mixture stirred for 2 h, keeping the temperature at -78 °C. The solution was then treated with AcOH (1.2 mL), and allowed to warm to r.t. The mixture was diluted with CHCl₃, washed with sat. aq. NaHCO₃ solution, sat. aq. Na₂S₂O₅ solution and brine. The organic phase was dried (Na₂SO₄) and removed under reduced pressure. The crude was purified by column chromatography (SiO₂, AcOEt/CHX 1:1) yielded compound **3.3-7** as a white solid (1.7 g, 60 % yield).

m.p. 121-124 °C. ¹H NMR (400 MHz, Chloroform-*d*): δ 8.52 (bs, 1H, -CONHCO-), 6.40 (d, *J* = 1.7 Hz, 1H, -COCH-), 4.04 (t, *J* = 8.1 Hz, 2H, NCH₂(CH₂)₄CH₃), 1.66 (p, *J* = 7.5 Hz, 2H, -NCH₂CH₂(CH₂)₃CH₃), 1.39 – 1.30 (m, 6H, -N(CH₂)₂(CH₂)₃CH₃), 0.89 (t, *J* = 6.8 Hz, 3H, -N(CH₂)₅CH₃). ¹³C-NMR (50 MHz, Chloroform-*d*): δ 161.04, 148.02, 115.73, 113.92, 53.84, 31.46, 28.85, 25.14, 22.69, 14.17. MS (ES +): found 322 (M⁺), C₁₀H₁₅IN₂O₂ requires 322.02. Characterization in accordance with literature.³⁷⁴

3.3-8 1-Hexyl-3-(*tert*-butyloxycarbonyl)-6-iodouracil

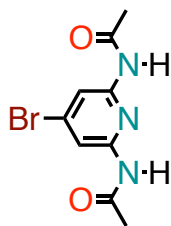


To a solution of **3.3-7** (1.60 g, 4.9 mmol) in dry CH₃CN (10.0 mL), 1.3 mL of pyridine was added and the resulting solution was stirred at 55 °C for 15 minutes. BOC₂O (2.03 g, 14.3 mmol) was added and the whole solution stirred overnight, at 55 °C. The mixture was diluted with CHCl₃ and the organic phase washed with H₂O, dried (Na₂SO₄) and removed under reduced pressure. The crude was purified by column chromatography (SiO₂, CHX/AcOEt 9:1) to yield product **3.3-8** as yellowish oil

(0.83 g, 40 % yield).

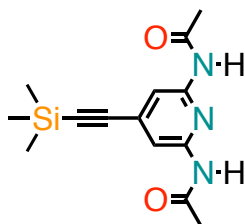
$^1\text{H NMR}$ (200 MHz, Chloroform-*d*): δ 6.43 (s, 1H, COCH), 4.03 (t, $J = 8.1$ Hz, 2H, $\text{NCH}_2(\text{CH}_2)_3\text{CH}_3$), 1.77-1.62 (m, 2H, $\text{NCH}_2\text{CH}_2(\text{CH}_2)_3\text{CH}_3$), 1.58 (s, 9H, $-\text{COC}(\text{CH}_3)_3$), 1.40 – 1.25 (m, 6H, $-\text{N}(\text{CH}_2)_2(\text{CH}_2)_3\text{CH}_3$), 0.88 (s, $J = 6.8$ Hz, 3H, $-\text{N}(\text{CH}_2)_5\text{CH}_3$). $^{13}\text{C NMR}$ (50 MHz, Chloroform-*d*): δ 158.4, 147.2, 146.2, 115.1, 113.3, 86.9, 54.2, 31.3, 28.6, 27.4, 25.9, 22.5, 13.9. **MS** (ES): found 444.9 ($\text{M} + \text{Na}^+$), $\text{C}_{15}\text{H}_{23}\text{IN}_2\text{O}_4\text{Na}$ requires = 422.07. Characterization in accordance with literature.³⁷³

3.3-9 2,6-Di(acetylamino)-4-bromo-pyridine



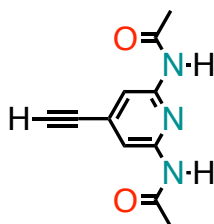
To a solution of 2,6-diamino-4-bromopyridine (1.00 g, 5.35 mmol) in pyridine (3.1 mL) was added Ac_2O (5.6 mL, 43.87) and the reaction mixture stirred overnight, at r.t. The grey precipitate was extensively washed with Et_2O to yield product **3.3-9** as a light grey solid (1.23 g, 84 % yield).

m.p. 210-215 °C. $^1\text{H NMR}$ (500 MHz, Chloroform-*d* + Methanol-*d*₃): δ 8.01 (s, 2H, Py-*H*), 2.14 (s, 6H, Py- NHCOCH_3). $^{13}\text{C NMR}$ (126 MHz, Chloroform-*d* + Methanol-*d*₃): δ 169.27, 150.19, 136.12, 112.54, 24.57. **IR** (KBr): cm^{-1} 3312, 3125, 1686, 1578, 1538, 1415, 1367, 1281, 1238, 1200, 1035, 997, 861, 777, 747, 693, 603, 561, 549. **MS** (ES): found 293.9 ($\text{M} + \text{Na}^+$), $\text{C}_9\text{H}_{10}\text{BrN}_3\text{O}_2$ requires = 271.00. Characterization in accordance with literature.³⁷⁴

3.3-10 2,6-Di(acetylamino)-4-[(trimethylsilyl)ethynyl]pyridine

To a degassed solution of 2,6-diamido-4-bromopyridine **3.3-9** (0.40 g, 1.47 mmol) in THF/Et₃N/DMF (20:10:2 mL), were added [(Pd(PPh₃)₄)] (0.09 g, 0.07 mmol) and CuI (0.03 g, 0.15 mmol) and the solution degassed a second time. TMSA (0.78 mL, 5.51 mmol) was then added and the reaction mixture was degassed one last time, and stirred overnight at 85 °C under Ar. The resulting dark mixture was filtered over celite and washed with CHCl₃/MeOH (1:1). Removal of the solvents under reduced pressure and purification of the crude by column chromatography (SiO₂, CHX/AcOEt 1:1) yielded product **3.3-10** as an off-white solid (0.40 g, 94 % yield).

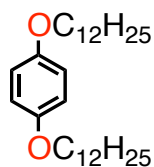
m.p. 85-89 °C. ¹H NMR (500 MHz, Chloroform-*d* + Methanol-*d*₃): δ 7.91 (bs, 2H, Py-*H*), 2.16 (s, 6H, Py-NHCOCH₃), 0.22 (s, 9H, Si(CH₃)₃). ¹³C NMR (126 MHz, Chloroform-*d* + Methanol-*d*₃): δ 168.80, 149.56, 134.61, 111.90, 81.52, 81.33, 24.34, 5.98. IR (KBr): cm⁻¹ 3423, 3276, 2960, 2162, 1681, 1612, 1558, 1416, 1370, 1276, 1250, 1206.9, 1145, 1033, 997, 983, 954, 848, 760, 705, 641, 626, 570, 539. MS (ES): found 290.0 (M + H⁺), C₁₄H₁₉N₃O₂Si requires = 289.12. Characterization in accordance with literature.³⁷⁴

3.3-11 2,6-Di(acetylamino)-4-ethynylpyridine

To a solution of TMS-protected ethynylpyridine **3.3-10** (0.40 g, 1.38 mmol) in THF/MeOH (20 mL, 1:1), K_2CO_3 (0.02 g, 0.14 mmol) was added and the mixture stirred at r.t. for 2 hrs. The mixture was diluted with $CHCl_3$ and the organic phase washed with H_2O , dried (Na_2SO_4) and removed under reduced pressure to yield product as ochre solid (0.28 g, 89 % yield)

m.p. 208-211 °C. 1H NMR (500 MHz, Chloroform-*d* + Methanol-*d*₃): δ 7.87 (bs, 2H, Py-*H*), 3.24 (s, 1H, Py-C \equiv CH), 2.15 (s, 6H, Py-NHCOCH₃). ^{13}C NMR (126 MHz, Chloroform-*d* + Methanol-*d*₃): δ 162.17, 149.90, 134.68, 112.04, 81.61, 81.53, 24.53. IR (KBr): cm^{-1} 3319, 3253, 312, 2115, 1716, 1670, 1612, 1561, 1518, 1416, 1366, 1278, 1236, 1203, 1037, 999, 950, 876, 854, 725, 703, 674, 637, 562, MS (ES): Found 218.0 ($M + H^+$), $C_{11}H_{11}N_3O_2$ requires = 217.09. Characterization in accordance with literature.³⁷⁴

3.3-12 1,4-Bis(dodecyloxy)benzene



To a solution of hydroquinone (4.0 g, 36.3 mmol) in acetone (60 mL), K_2CO_3 (50.1 g, 36.3 mmol) was added and the reaction mixture was allowed to stir at r.t. for 30 minutes. Following this, 1-bromododecane (26.0 mL, 109.0 mmol) was added to the mixture and the whole was refluxed overnight. The suspension was concentrated under reduced pressure, redissolved in $CHCl_3$, washed with sat. aq. K_2CO_3 , H_2O and brine. The organic phase was dried (Na_2SO_4) and concentrated under reduced pressure. The crude was purified by column chromatography (SiO_2 , CHX) to yield the product **3.3-12** as a pale yellow crystalline solid (12.1 g, 75 % yield).

m.p. 72-73 °C. 1H NMR (500 MHz, Chloroform-*d*): δ 6.82 (s, 4H, Ar-*H*), 3.89 (t, $J = 6.6$ Hz, 4H, Ar-OCH₂(CH₂)₁₀CH₃), 1.80 – 1.70 (m, 4H, Ar-OCH₂CH₂(CH₂)₉CH₃), 1.48 – 1.23 (m, 36H, Ar-O(CH₂)₂(CH₂)₉CH₃), 0.88 (t, $J = 6.9$ Hz, 6H, Ar-O(CH₂)₁₁CH₃). ^{13}C NMR (50 MHz, Chloroform-

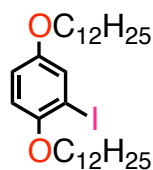
d): δ 153.35, 115.58, 68.91, 32.19, 29.94, 29.91, 29.86, 29.69, 29.58, 29.63, 26.34, 22.97, 14.40. **IR** (KBr): cm^{-1} 2918, 2850, 1515, 1474, 1397, 1293, 1285, 1243, 1112, 1037, 826, 773, 729, 720, 538. **MS** (ES +): found 446 (M^+), $C_{30}H_{54}O_2$ requires = 446.41. Characterization in accordance with literature.⁵⁰⁴

3.3-13 1,4-Bis(dodecyloxy)-2,5-diiodobenzene



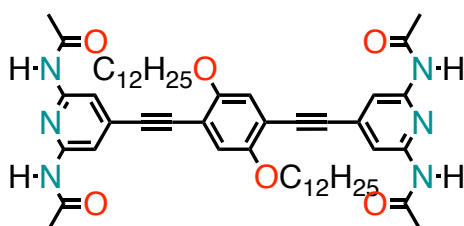
To a solution of H_5IO_6 (1.5 g, 6.4 mmol) in CH_3OH/CH_2Cl_2 (20 mL, 1:1) was added I_2 (3.2 g, 12.5 mmol) and the mixture was stirred for 15 minutes. Subsequently 1,4-bis(dodecyloxy)benzene **3.3-12** (4.5 g, 10 mmol) was added and the mixture refluxed for 5 hrs. The mixture was concentrated under reduced pressure, dissolved in CH_2Cl_2 and washed with sat. aq. Na_2SO_3 solution, H_2O , dried (Na_2SO_4) and concentrated under reduced pressure. Finally, crystallization from boiling EtOH yielded product **3.3-13** as white crystalline solid (6.1 g, 88 % yield).

m.p. 64-67 °C. **1H NMR** (200 MHz, Chloroform-*d*): δ 7.2 (s, 2H, Ar-*H*), 3.9 (t, 4H, Ar- $OCH_2(CH_2)_{10}CH_3$), 1.8 (*m*, 4H, Ar- $OC_2HCH_2(CH_2)_9CH_3$), 1.3 (br, 36H, Ar- $O(CH_2)_2(CH_2)_9CH_3$), 0.9 (t, 6H, Ar- $O(CH_2)_{11}CH_3$). **^{13}C NMR** (50 MHz, Chloroform-*d*): δ 152.92, 122.88, 86.43, 70.51, 32.10, 29.83, 29.76, 29.54, 29.73, 29.46, 29.32, 26.21, 22.89, 14.33. **IR** (KBr): cm^{-1} 2919, 2848, 1488, 1460, 1389, 1353, 1263, 1216, 1071, 1053, 995, 847, 722. **MS** (ES): found 698 (M^+), $C_{30}H_{52}I_2O_2$ requires = 698.21. Characterization in accordance with literature.⁵⁰⁴

3.3-14 1,4-Bis(dodecyloxy)-2-iodobenzene

To a solution of CH_3COOH (10.0 mL), H_2SO_4 (0.1 mL) and H_2O (1.0 mL) was added 1,4-bis(dodecyloxy)benzene **3.3-12** (380 mg, 0.85 mmol), KIO_3 (36 mg, 0.17 mmol) and I_2 (119 mg, 0.47 mmol). The mixture was slowly brought to reflux and continued refluxing for 6 hrs. After cooling the mixture, the iodine was quenched by addition of 0.2 M aq. Na_2SO_3 solution. The precipitate was collected and washed with water. The crude was purified by column chromatography (SiO_2 , CHX) to obtain the product as white solid **3.3-14** (136 mg, 28 % yield).

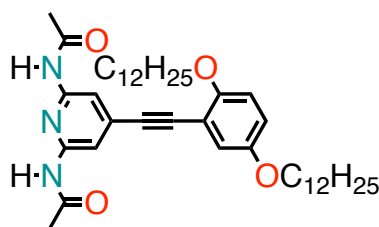
$^1\text{H NMR}$ (500 MHz, Chloroform-*d*): δ 7.04 (d, $J = 3.0$ Hz, 1H, Ar-*H*), 6.88 (dd, $J = 9.0, 3.0$ Hz, 1H, Ar-*H*), 6.83 (d, $J = 9.1$ Hz, 1H, Ar-*H*), 4.02 (t, $J = 6.6$ Hz, 2H, Ar- $\text{OCH}_2(\text{CH}_2)_{10}\text{CH}_3$), 3.94 (t, $J = 6.6$ Hz, 2H, Ar- $\text{OCH}_2(\text{CH}_2)_{10}\text{CH}_3$), 1.80 – 1.70 (m, 4H, Ar- $\text{OCH}_2\text{CH}_2(\text{CH}_2)_9\text{CH}_3$), 1.48 – 1.23 (m, 36H, Ar- $\text{O}(\text{CH}_2)_2(\text{CH}_2)_9\text{CH}_3$), 0.88 (t, $J = 6.9$ Hz, 6H, Ar- $\text{O}(\text{CH}_2)_{11}\text{CH}_3$). $^{13}\text{C NMR}$ (126 MHz, Chloroform-*d*) δ 153.76, 152.14, 125.32, 115.43, 113.11, 86.98, 70.19, 68.85, 31.91, 29.66, 29.65, 29.62, 29.59, 29.57, 29.56, 29.36, 29.35, 29.33, 29.27, 26.09, 25.99, 22.69, 14.11. **MS** (ES): found 572 (M^+), $\text{C}_{30}\text{H}_{53}\text{IO}_2$ requires = 572.31. Characterization in accordance with literature.⁶⁶⁵

3.3-2 1,4-Bis(dodecyloxy)-2,5-bis[(2,6-di(acetylamino)pyridin-4-yl)ethynyl]benzene

In a 20-mL microwave-reactor tube containing a stirring bar, 1,4-bis(dodecyloxy)-2,5-diiodobenzene **3.3-13** (0.20 g, 0.29 mmol), Pd(PPh₃)₄ (0.014 g, 0.012 mmol) and CuI (4 mg, 0.023 mmol) were dissolved in DMF/Et₃N/THF (4:2:2 mL) and was purged with Ar. 2,6-Diamido-4-ethynylpyridine **3.3-11** (0.16 g, 0.73 mmol) was added and the reaction vessel was sealed and placed into the microwave reactor. The temperature heating profile for the reaction mixture was as follows: r.t. → 120 °C over a 2-min period (200-W maximum power), the reaction mixture was held at 120 °C (dynamic, 200-W maximum power) for 30 min. The crude mixture was then filtered over celite (CHCl₃), concentrated under reduced pressure and purified by column chromatography (SiO₂, CHX/AcOEt, 1:1 → AcOEt) yielding product as a bright yellow solid (0.171 g, 68 % yield).

m.p. > 250 °C. ¹H NMR (500 MHz, Chloroform-*d*): δ 8.02 (s, 4H, Py-*H*), 7.52 (s, 4H, CH₃CONH-Py), 7.03 (s, 2H, Ar-*H*), 4.05 (t, *J* = 6.7 Hz, 4H, Ar- OCH₂(CH₂)₁₀CH₃), 2.21 (s, 12H, CH₃CONH-Py), 1.87 (m, 4H, Ar-OCH₂CH₂(CH₂)₉CH₃), 1.23 (m, 36H, Ar-O(CH₂)₂(CH₂)₉CH₃), 0.87 (t, *J* = 6.9 Hz, 6, Ar-O(CH₂)₁₁CH₃). ¹³C NMR (50 MHz, Chloroform-*d*): δ 168.28, 153.66, 149.45, 136.13, 117.33, 113.62, 111.49, 92.95, 90.57, 69.83, 32.11, 29.83, 29.56, 29.51, 29.29, 26.14, 24.97, 22.88, 14.32. IR (KBr): cm⁻¹ 3285, 2959, 2926, 2220, 2162, 1708, 1685, 1612, 1555, 1419, 1249.8, 869, 843, 759, 642. MS (ES): Found 876.7 (M⁺), C₅₂H₇₂N₆O₆ requires = 876.55. Characterization in accordance with literature.⁵⁰⁴

3.3-5 *N,N'*-(4-((2,5-bis(dodecyloxy)phenyl)ethynyl)pyridine-2,6-diyl)diacetamide

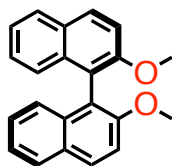


In a 10-mL microwave-reactor tube containing a stirring bar, 1,4-bis(dodecyloxy)-2-iodobenzene **3.3-14** (50.0 mg, 87.3 μmol), Pd(PPh₃)₄ (5.0 mg, 4.3 μmol), CuI (1.6 mg, 8.4 μmol) were dissolved in DMF/Et₃N/THF (2:1:1 mL) and was purged with Ar. 2,6-Diacetylamino-4-ethynylpyridine **3.3-11**

(20.0 mg, 92.1 μmol) was added and the reaction vessel was sealed and placed into the microwave reactor. The temperature heating profile for the reaction mixture was as follows: r.t. \rightarrow 120 $^{\circ}\text{C}$ over a 2-min period (200-W maximum power), the reaction mixture was held at 120 $^{\circ}\text{C}$ (dynamic, 200-W maximum power) for 30 min. The crude reaction mixture was diluted with CHCl_3 and washed with H_2O , the organic phase dried (Na_2SO_4) and removed under reduced pressure. The crude was purified by preparative TLC (Pet. Et./AcOEt 1:1) to obtain the product as a waxy white solid (16.8 mg, 29 % yield).

m.p. 61-62 $^{\circ}\text{C}$. $^1\text{H NMR}$ (500 MHz, Chloroform-*d*): δ 8.01 (s, 2H, Py-*H*), 7.6 (s, 2H, $\text{CH}_3\text{CONH-Py}$), 7.03 (d, $J = 3.0$ Hz, 1H; Ar-*H*), 6.87 (dd, $J = 3.0$ Hz, 9.0 Hz, 1H, Ar-*H*), 6.81 (d, $J = 9.0$ Hz, 1H, Ar-*H*), 4.01 (t, $J = 7.5$, 2H, Ar- $\text{OCH}_2(\text{CH}_2)_{10}\text{CH}_3$), 3.92 (t, $J = 7.5$ Hz, 2H, Ar- $\text{OCH}_2(\text{CH}_2)_{10}\text{CH}_3$), 2.19 (s, 6H, $\text{CH}_3\text{CONH-Py}$), 1.83 (m, 2H, Ar- $\text{OCH}_2\text{CH}_2(\text{CH}_2)_9\text{CH}_3$), 1.76 (m, 2H, Ar- $\text{OCH}_2\text{CH}_2(\text{CH}_2)_9\text{CH}_3$), 1.45 (m, 4H, $\text{O}(\text{CH}_2)_2\text{CH}_2(\text{CH}_2)_8\text{CH}_3$), 1.36-1.22 (m, 32H, Ar- $\text{O}(\text{CH}_2)_3(\text{CH}_2)_8\text{CH}_3$), 0.89-0.85 (m, 6H, Ar- $\text{O}(\text{CH}_2)_{11}\text{CH}_3$). $^{13}\text{C NMR}$ (125 MHz, Chloroform-*d*): δ 168.44, 154.70, 152.98, 149.61, 136.59, 118.60, 118.22, 114.44, 112.66, 111.65, 91.29, 91.07, 70.12, 69.00, 32.15, 29.91, 29.89, 29.88, 29.86, 29.84, 29.83, 29.81, 29.63, 29.59, 29.57, 29.56, 29.54, 29.47, 26.24, 26.22, 24.96, 22.91, 14.34. **IR** (KBr): $\text{cm}^{-1} = 3437, 3309, 2920, 2851, 2360, 2211, 1697, 1671, 1614, 1159, 1504, 1471, 1419, 1374, 1340, 1325, 1308, 1274, 1233, 1207, 1148, 1037, 8634, 795, 720, 695, 630, 596, 542$. **HRMS**: found 662.4886 $[\text{M} + \text{H}]^+$, $\text{C}_{41}\text{H}_{63}\text{N}_3\text{O}_4$ requires 661.4891.

3.3-15 (*R*)-2,2'-Dimethoxy-1,1'-binaphthalene

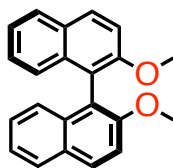


To a stirred mixture of (*R*)-BINOL (3.00 g, 10.5 mmol) and K_2CO_3 (3.18 g, 23.0 mmol) in acetone (60 mL) at 50 $^{\circ}\text{C}$ under Ar, CH_3I (3.27 g, 23.0 mmol) was slowly added, and the mixture was stirred for 48 h at reflux. The mixture was allowed to cool to r.t. and concentrated under reduced pressure (to approximately 20 mL) and poured into a flask containing H_2O (200 mL) and the mixture was left to

stir for 8 hrs. The solid was recovered by filtration, washed with H₂O and dried to obtain product as white solid (3.27 g, quant.).

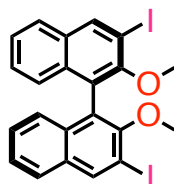
m.p. 222-225 °C. $[\alpha]_{\text{D}}^{25} = +54^{\circ}$ ($c = 1.0$, CHCl₃). ¹H NMR (200 MHz, Chloroform-*d*): δ 7.95 (d, $J = 9.0$ Hz, 2H, Ar-*H*₄), 7.85 (d, $J = 8.1$, 2H, Ar-*H*₈), 7.44 (d, $J = 9.0$ Hz, 2H, Ar-*H*₃), 7.30-7.10 (m, 6H, Ar-*H*_{6,7,8}), 3.74 (s, 6H, Ar-OCH₃). ¹³C NMR (50 MHz, Chloroform-*d*): δ 154.92, 133.98, 129.36, 129.19, 127.89, 126.26, 125.22, 123.48, 119.56, 114.21, 56.86. IR (KBr): cm⁻¹ 3044, 2933, 2836, 1618, 1590, 1506, 1461, 1354, 1264, 1250, 1091, 1064, 811. MS (ES +): found 314.2 (M⁺), C₂₂H₁₈O₂ requires 314.13.

3.3-15 (*S*)-2,2'-Dimethoxy-1,1'-binaphthalene



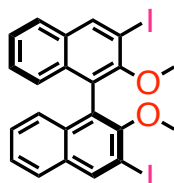
To a stirred mixture of (*S*)-BINOL (3.00 g, 10.5 mmol) and K₂CO₃ (3.18 g, 23.0 mmol) in acetone (60 mL) at 50 °C under Ar, CH₃I (3.27 g, 23.0 mmol) was slowly added, and the mixture was stirred for 48 h at reflux. The mixture was allowed to cool to r.t. and concentrated under reduced pressure (to approximately 20 mL) and poured into a flask containing H₂O (200 mL) and the mixture was left to stir for 8 hrs. The solid was recovered by filtration, washed with H₂O and dried to obtain product as white solid (3.23 g, quantitative).

m.p. 223-224 °C. $[\alpha]_{\text{D}}^{25} = -55^{\circ}$ ($c = 1.0$, CHCl₃). ¹H NMR (200 MHz, Chloroform-*d*): δ 7.95 (d, $J = 9.0$ Hz, 2H, Ar-*H*₄), 7.85 (d, $J = 8.1$, 2H, Ar-*H*₈), 7.44 (d, $J = 9.0$ Hz, 2H, Ar-*H*₃), 7.30-7.10 (m, 6H, Ar-*H*_{6,7,8}), 3.74 (s, 6H, Ar-OCH₃). ¹³C NMR (50 MHz, Chloroform-*d*): δ 154.92, 133.98, 129.36, 129.19, 127.89, 126.26, 125.22, 123.48, 119.56, 114.21, 56.86. IR (KBr): cm⁻¹ 3044, 2933, 2836, 1618, 1590, 1506, 1461, 1354, 1264, 1250, 1091, 1064, 811. MS (ES +): found 314.2 (M⁺), C₂₂H₁₈O₂ requires 314.13.

3.3-16 (*R*)-3,3'-Diodo-2,2'-Dimethoxy-1,1'-binaphthalene

A solution of (*R*)-2,2'-dimethoxy-1,1'-binaphthalene **3.3-15** (2.7 g, 8.6 mmol) in dry THF (150 mL) was cooled to $-78\text{ }^{\circ}\text{C}$ under Ar, and $n\text{BuLi}$ (20.0 mL, 1.6 M solution in hexanes, 31.8 mmol) was added dropwise. The mixture was stirred at $-78\text{ }^{\circ}\text{C}$ for 1 h before adding I_2 (8.7 g, 34.3 mmol) in THF (50 mL). After stirring for 1 h, sat. aq. NH_4Cl solution was added, and the mixture was allowed to warm to r.t., and the organic layer was washed with H_2O and brine, dried over Na_2SO_4 and removed under reduced pressure. The crude was purified by column chromatography (SiO_2 , CHX/AcOEt 10 : 1) that gave product as an off-white solid (2.2 g, 45 % yield).

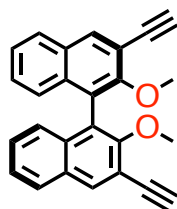
m.p. $197\text{ }^{\circ}\text{C}$. $[\alpha]_{\text{D}}^{25} = +41^{\circ}$ ($c = 0.5$, CHCl_3). $^1\text{H NMR}$ (200 MHz, Chloroform-*d*): δ 8.70 (s, 2H, Ar- H_4), 7.96 (d, $J = 8.0$ Hz, 2H, Ar- H_5), 7.58 (t, $J = 7.5$ Hz, 2H, Ar- H_6), 7.43 (t, $J = 7.6$ Hz, 2H, Ar- H_7), 7.46 (d, $J = 8.4$ Hz, 2H, Ar- H_8), 3.58 (s, 6H, Ar- OCH_3). $^{13}\text{C NMR}$ (50 MHz, Chloroform-*d*): δ 180.42, 154.65, 140.09, 134.03, 132.37, 127.30, 125.98, 125.58, 97.33, 92.62, 61.41. IR (KBr): cm^{-1} 2931, 2823, 1619, 1593, 1508, 1464, 1390, 1352, 1262, 1248, 1146, 1089, 1054, 1018, 896, 812, 752. MS (ES): found: 566.3 (M^+), $\text{C}_{22}\text{H}_{16}\text{I}_2\text{O}_2$ requires 565.92.

3.3-16 (*S*)-3,3'-Diodo-2,2'-Dimethoxy-1,1'-binaphthalene

A solution of (*R*)-2,2'-dimethoxy-1,1'-binaphthalene **3.3-15** (2.7 g, 8.6 mmol) in dry THF (150 mL) was cooled to $-78\text{ }^{\circ}\text{C}$ under Ar, and $n\text{-BuLi}$ (20.0 mL, 1.6 M solution in hexanes, 31.8 mmol) was added dropwise. The mixture was stirred at $-78\text{ }^{\circ}\text{C}$ for 1 h before adding I_2 (8.7 g, 34.3 mmol) in THF (50 mL). After stirring for 1 h, sat. aq. NH_4Cl solution was added, and the mixture was allowed to warm to r.t., and the organic layer was washed with H_2O and brine, dried over Na_2SO_4 and removed under reduced pressure. The crude was purified by column chromatography (SiO_2 , CHX/AcOEt 10 :1) that gave product as an off-white solid (1.7 g, 35 % yield).

m.p. $197\text{ }^{\circ}\text{C}$. $[\alpha]_D^{25} = -42^{\circ}$ ($c = 0.5$, CHCl_3). $^1\text{H NMR}$ (200 MHz, Chloroform-*d*): δ 8.70 (s, 2H, Ar- H_4), 7.96 (d, $J = 8.0$ Hz, 2H, Ar- H_5), 7.58 (t, $J = 7.5$ Hz, 2H, Ar- H_6), 7.43 (t, $J = 7.6$ Hz, 2H, Ar- H_7), 7.46 (d, $J = 8.4$ Hz, 2H, Ar- H_8), 3.58 (s, 6H, Ar- OCH_3). $^{13}\text{C NMR}$ (50 MHz, Chloroform-*d*): δ 180.42, 154.65, 140.09, 134.03, 132.37, 127.30, 125.98, 125.58, 97.33, 92.62, 61.41. IR (KBr): cm^{-1} 2931, 2823, 1619, 1593, 1508, 1464, 1390, 1352, 1262, 1248, 1146, 1089, 1054, 1018, 896, 812, 752. MS (ES): found: 566.0(M^+), $\text{C}_{22}\text{H}_{16}\text{I}_2\text{O}_2$ requires 565.92.

3.3-17 (*R*)-3,3'-Diethynyl-2,2'-dimethoxy-1,1'-binaphthalene

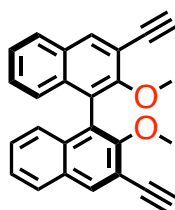


To a degassed solution of (*R*)-3,3'-diiodo-2,2'-dimethoxy-1,1'-binaphthalene **3.3-16** (1.13 g, 2.0 mmol) and $\text{Pd}(\text{PPh}_3)_2\text{Cl}_2$ (144 mg, 0.2 mmol) in PhCH_3 (10 mL) and Et_3N (12 mL) was added TMSA (4 mL, 328.3 mmol) and CuI (76 mg, 0.4 mmol). After the mixture was heated to reflux overnight, the reaction mixture was cooled to r.t. The solid was filtered off and the filtrate was evaporated to dryness. The residue was dissolved in THF (30 mL) and MeOH (30 mL) and to this solution was added K_2CO_3 . After stirring for 1 h at r.t., the crude was extracted with CH_2Cl_2 and washed with H_2O . The organic layer was dried (Na_2SO_4) and removed under reduced pressure. The crude was purified by column chromatography (SiO_2 , CHX/AcOEt 5:1) to yield product as light

yellow solid (0.47 g, 65 % yield).

$[\alpha]_D^{25} = +7.5^\circ$ ($c = 0.5$, CHCl_3). $^1\text{H NMR}$ (200 MHz, Chloroform- d): δ 8.20 (s, 2H, Ar- H_4), 7.85 (d, $J = 8.0$, 2H, Ar- H_5), 7.40 (t, $J = 7.46$, 2H, Ar- H_6), 7.27 (t, $J = 7.40$, 2H, Ar- H_7), 7.09 (d, $J = 8.43$, 2H, Ar- H_8), 3.66 (s, 6H, Ar- OCH_3), 3.37 (s, 2H, Ar- $\text{C}\equiv\text{C}-\text{H}$). $^{13}\text{C NMR}$ (50 MHz, Chloroform- d): δ 155.94, 135.29, 134.02, 130.02, 127.78, 127.43, 125.62, 125.35, 124.82, 116.15, 81.55, 80.53, 61.13. **IR** (KBr): cm^{-1} 3436, 3292, 3057, 2956, 2917, 2850, 1730, 1588, 1458, 1247, 1099, 842. **MS** (ES): found: 362.1 (M^+), $\text{C}_{26}\text{H}_{18}\text{O}_2$ requires 362.13.

3.3-17 (*S*)-3,3'-Diethynyl-2,2'-dimethoxy-1,1'-binaphthalene

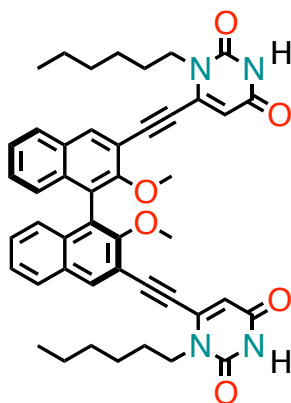


To a degassed solution of (*S*)-3,3'-diiodo-2,2'-dimethoxy-1,1'-binaphthalene **3.3-16** (1.13 g, 2.0 mmol) and $\text{Pd}(\text{PPh}_3)_2\text{Cl}_2$ (144 mg, 0.2 mmol) in PhCH_3 (10 mL) and Et_3N (12 mL) was added TMSA (4 mL, 328.3 mmol) and CuI (76 mg, 0.4 mmol). After the mixture was heated to reflux overnight, the reaction mixture was cooled to r.t. The solid was filtered off and the filtrate was evaporated to dryness. The residue was dissolved in THF (30 mL) and MeOH (30 mL) and to this solution was added K_2CO_3 . After stirring for 1 h at r.t., the crude was extracted with CH_2Cl_2 and washed with H_2O . The organic layer was dried (Na_2SO_4) and removed under reduced pressure. The crude was purified by column chromatography (SiO_2 , CHX/AcOEt 5:1) to yield product as light yellow solid (0.59 g, 75 % yield).

$[\alpha]_D^{25} = -7.0^\circ$ ($c = 0.5$, CHCl_3). $^1\text{H NMR}$ (200 MHz, Chloroform- d): δ 8.20 (s, 2H, Ar- H_4), 7.85 (d, $J = 8.0$, 2H, Ar- H_5), 7.40 (t, $J = 7.46$, 2H, Ar- H_6), 7.27 (t, $J = 7.40$, 2H, Ar- H_7), 7.09 (d, $J = 8.43$, 2H, Ar- H_8), 3.66 (s, 6H, Ar- OCH_3), 3.37 (s, 2H, Ar- $\text{C}\equiv\text{C}-\text{H}$). $^{13}\text{C NMR}$ (50 MHz, Chloroform- d): δ 155.94, 135.29, 134.02, 130.02, 127.78, 127.43, 125.62, 125.35, 124.82, 116.15, 81.55, 80.53, 61.13. **IR** (KBr):

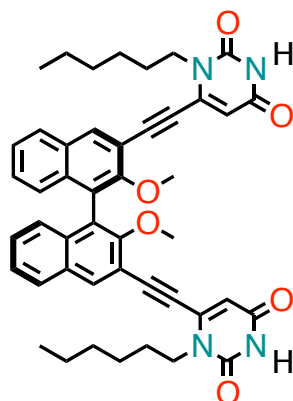
cm⁻¹ 3436, 3292, 3057, 2956, 2917, 2850, 1730, 1588, 1458, 1247, 1099, 842. **MS** (ES): found: 362.1 (M⁺), C₂₆H₁₈O₂ requires 362.13.

3.3-1 (*R*)-6,6'-(2,2'-Dimethoxy-1,1'-binaphthyl-3,3'-diyl)bis[ethyne-2,1-diyl-(1-hexyluracil)]



To a degassed solution of dry Et₃N (2.0 mL) and THF (2.0 mL), 1-hexyl-6-iodouracil **3.3-7** (40.0 mg, 124.2 μmol), Pd(PPh₃)₄ (10.0 mg, 8.7 μmol) and CuI (3.3 mg, 17.3 μmol) were added and the mixture degassed a second time. Compound (*R*)-3,3'-diethynyl-2,2'-dimethoxy-1,1'-binaphthalene **3.3-17** (18.0 mg, 49.7 μmol) was then added, the reaction mixture degassed one last time, and stirred overnight at r.t., under Ar. The crude mixture was filtered over celite, concentrated under reduced pressure and purified by column chromatography (SiO₂, CHX/AcOEt 7:3) yielding product as a white powder (22.4 mg, 60 % yield).

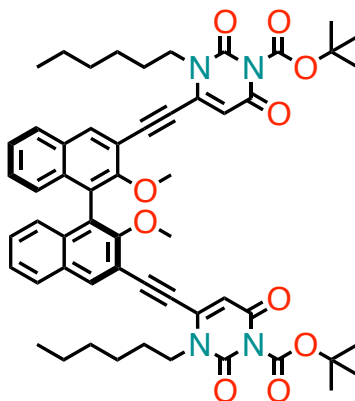
m.p. 193 °C. [α]_D²⁵ = -182.3 (*c* = 1.0, CHCl₃). ¹H NMR (500 MHz, Chloroform-*d*): δ 9.22 (s, 2H, NH), 8.25 (s, 2H, Ar-*H*), 7.92 (d, *J* = 8.5 Hz, 2H, Ar-*H*), 7.50 (t, *J* = 7.5 Hz, 2H, Ar-*H*), 7.37 (t, *J* = 7.5, 2H, Ar-*H*), 7.13 (d, *J* = 8.5, 2H, Ar-*H*), 6.06 (s, 2H, CH), 4.13 (t, *J* = 7.5, 4H, NCH₂(CH₂)₄CH₃), 3.61 (s, 6H, Ar-OCH₃), 1.83-1.80 (m, 4H, NCH₂CH₂(CH₂)₃CH₃), 1.43-1.29 (m, 12H, N(CH₂)₂(CH₂)₃CH₃), 0.84 (t, *J* = 7.5, 6H, N(CH₂)₅CH₃). ¹³C NMR (125 MHz, Chloroform-*d*): δ 162.68, 155.59, 150.90, 138.93, 136.14, 135.00, 130.19, 128.98, 128.58, 126.36, 125.79, 124.95, 114.77, 107.13, 97.70, 84.41, 61.73, 46.99, 31.68, 29.11, 26.52, 22.74, 14.20. **IR** (KBr): cm⁻¹ 3424, 2956, 2917, 2850, 1731, 1620, 1592, 1463, 1380, 1265, 1250, 1180, 1092, 1066, 1020, 897, 811, 747, 542. **HRMS**: found 751.3489 [M + H]⁺, C₄₆H₄₆N₄O₆ requires 750.3490.

3.3-1 (*S*)-6,6'-(2,2'-Dimethoxy-1,1'-binaphthyl-3,3'-diyl)bis[ethyne-2,1-diyl-(1-hexyluracil)]

To a degassed solution of dry Et₃N (2.0 mL) and THF (2.0 mL), 1-hexyl-6-iodouracil **3.3-7** (40.0 mg, 124.2 μmol), Pd(PPh₃)₄ (10.0 mg, 8.7 μmol) and CuI (3.3 mg, 17.3 μmol) were added and the mixture degassed a second time. Compound (*S*)-3,3'-diethynyl-2,2'-dimethoxy-1,1'-binaphthalene **3.3-17** (18.0 mg, 49.7 μmol) was then added; the reaction mixture degassed one last time, and stirred overnight at r.t., under Ar. The crude mixture was filtered over celite, concentrated under vacuum and purified by column chromatography (SiO₂, CHX/AcOEt 7:3) yielding product as a white powder (20.5 mg, 55 % yield).

m.p. 193 °C. $[\alpha]_D^{25} = +180.4^\circ$ ($c = 1.0$, CHCl₃). **¹H-NMR** (500 MHz, Chloroform-*d*): δ 9.22 (s, 2H, NH), 8.25 (s, 2H, Ar-*H*), 7.92 (d, $J = 8.0$ Hz, 2H, Ar-*H*), 7.49 (t, $J = 7.5$ Hz, 2H, Ar-*H*), 7.36 (t, $J = 7.5$ Hz, 2H, Ar-*H*), 7.14 (d, $J = 8.5$ Hz, 2H, Ar-*H*), 6.06 (s, 2H, CH), 4.13 (t, $J = 7.5$ Hz, 4H, NCH₂(CH₂)₄CH₃), 3.61 (s, 6H, OCH₃), 1.82 (m, 4H, NCH₂CH₂(CH₂)₃CH₃), 1.44-1.25 (m, 12H, N(CH₂)₂(CH₂)₃CH₃), 0.85 (t, $J = 7.5$ Hz, 6H, N(CH₂)₅CH₃). **¹³C NMR** (125 MHz, Chloroform-*d*): δ 162.65, 155.59, 150.88, 138.93, 136.14, 135.00, 130.19, 128.99, 128.59, 126.36, 125.79, 124.96, 114.77, 107.13, 97.71, 84.41, 61.73, 47.00, 31.68, 29.11, 26.52, 22.74, 14.20. **IR** (KBr): cm⁻¹ 3424, 2956, 2917, 2850, 1731, 1619, 1591, 1462, 1379, 1264, 1250, 1180, 1091, 1065, 1020, 896, 811, 747, 542. **HRMS**: found 751.3485 [M + H]⁺, C₄₆H₄₆N₄O₆ requires 750.3490.

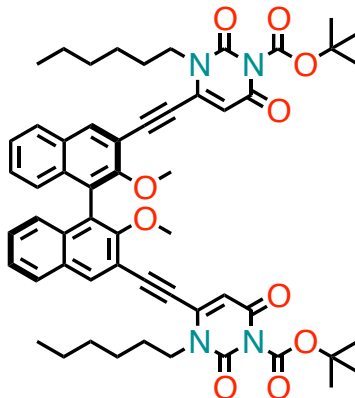
3.3-3 (*R*)-6,6'-(2,2'-Dimethoxy-1,1'-binaphthyl-3,3'-diyl)bis[ethyne-2,1-diyl-(1-hexyl-3-*tert*-Butyloxycarbonyluracil)]



To a degassed solution of dry Et₃N (2.0 mL) and THF (2.0 mL), 1-hexyl-3-BOC-6-iodouracil **3.3-8** (140.0 mg, 331.5 μmol), Pd(PPh₃)₄ (4.9 mg, 4.3 μmol) and CuI (1.6 mg, 8.6 μmol) were added and the reaction mixture was degassed a second time. Compound (*R*)-3,3'-diethynyl-2,2'-dimethoxy-1,1'-binaphthalene **3.3-17** (20.0 mg, 55.2 μmol) was then added, the reaction mixture degassed one last time, and stirred overnight at r.t., under Ar. The crude mixture was filtered over celite and the solvent was evaporated. Repeated precipitation cycles from CHCl₃ with pentane yielded product as a white powder (21.0 mg, 40 % yield).

m.p. 140 – 142 °C. [α]_D²⁵ = -142.6° (*c* = 1.0 CHCl₃). ¹H NMR (500 MHz, Chloroform-*d*): δ 8.25 (s, 2H, Ar-*H*), 7.92 (d, *J* = 8.0 Hz, 2H, Ar-*H*), 7.49 (t, *J* = 7.5 Hz, 2H, Ar-*H*), 7.36 (t, *J* = 7.5 Hz, 2H, Ar-*H*), 7.12 (d, *J* = 8.5 Hz, 2H, Ar-*H*), 6.07 (s, 2H, CH), 4.12 (t, *J* = 7.5 Hz, 4H, NCH₂(CH₂)₄CH₃), 3.60 (s, 6H, OCH₃), 1.85-1.79 (m, 4H, NCH₂CH₂(CH₂)₃CH₃), 1.61 (s, 18H, OCO(CH₃)₃), 1.43-1.29 (m, 12H, N(CH₂)₂(CH₂)₃CH₃), 0.83 (t, *J* = 7.5 Hz, 6H, N(CH₂)₅CH₃). ¹³C NMR (125 MHz, Chloroform-*d*): δ 159.82, 155.59, 149.11, 147.91, 138.17, 136.22, 135.05, 130.20, 129.06, 128.62, 126.41, 125.80, 124.97, 114.70, 106.74, 98.14, 87.13, 84.21, 61.74, 47.51, 31.64, 29.03, 27.69, 26.58, 22.76, 14.20. IR (KBr): cm⁻¹ 3442, 3092, 3055, 2955, 2933, 2857, 2764, 2679, 2479, 2336.24, 2214, 1786, 1712, 1673, 1619, 1599, 1581, 1491, 1456, 1428, 1390, 1369, 1330, 1252, 1226, 1189, 1147, 1106, 1038, 1018, 1000, 890, 843, 822, 785, 770, 752, 693, 661, 648, 621, 608, 542, 510, 468, 427. HRMS: found 951.4530 [M + H]⁺, C₅₆H₆₂N₄O₁₀ requires 950.4538.

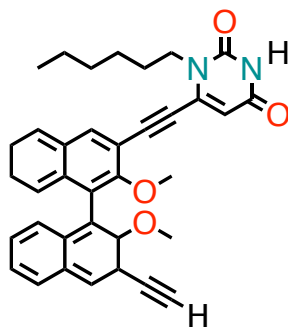
3.3-3 (*S*)-6,6'-(2,2'-Dimethoxy-1,1'-binaphthyl-3,3'-diyl)bis[ethyne-2,1-diyl-(1-hexyl-3-*tert*-Butyloxycarbonyluracil)]



To a degassed solution of dry Et₃N (2.0 mL) and THF (2.0 mL), 1-hexyl-3-BOC-6-iodouracil **3.3-8** (74.0 mg, 175.2 μmol), Pd(PPh₃)₄ (4.9 mg, 4.3 μmol) and CuI (1.6 mg, 8.6 μmol) were added and the reaction mixture was degassed a second time. Compound (*S*)-3,3'-diethynyl-2,2'-dimethoxy-1,1'-binaphthalene **3.3-17** (16.0 mg, 44.1 μmol) was then added, the reaction mixture degassed one last time, and stirred overnight at r.t., under Ar. The crude mixture was filtered over celite and the solvent was evaporated. Repeated precipitation cycles from CHCl₃ with pentane yielded product as a white powder (22.6 mg, 54 % yield).

m.p. 140-142°C. $[\alpha]_D^{25} = +140.85^\circ$ ($c = 1.0$, CHCl₃). ¹H NMR (500 MHz, Chloroform-*d*): δ 8.25 (s, 2H, Ar-*H*), 7.92 (d, $J = 8.5$ Hz, 2H, Ar-*H*), 7.49 (d, $J = 8.0$ Hz, 2H, Ar-*H*), 7.36 (d, $J = 8.0$ Hz, 2H, Ar-*H*), 7.12 (d, $J = 8.5$ Hz, 2H, Ar-*H*_s), 6.07 (s, 2H, CH), 4.12 (t, $J = 7.5$ Hz, 4H, NCH₂(CH₂)₄CH₃), 3.59 (s, 6H, OCH₃), 1.82 (m, 4H, NCH₂CH₂(CH₂)₃CH₃), 1.62 (s, 18H, OCO(CH₃)₃), 1.31 (m, 12H, N(CH₂)₂(CH₂)₃CH₃), 0.84 (t, $J = 7.5$ Hz, 6H, N(CH₂)₅CH₃). ¹³C NMR (125 MHz, Chloroform-*d*): δ 159.57, 155.33, 148.85, 147.66, 137.90, 135.98, 134.79, 129.95, 128.82, 128.37, 126.17, 125.56, 124.72, 114.44, 106.54, 97.88, 86.85, 83.96, 61.49, 47.26, 31.40, 28.82, 27.37, 26.31, 22.48, 13.90. IR (KBr): cm⁻¹ 3435, 2930, 2856, 2679, 2345, 2214, 1786, 1712, 1672, 1600, 1581, 1456, 1428, 1385, 1370, 1252, 1226, 1147, 1106, 1036, 1018, 889, 843, 822, 752, 693, 608, 542. HRMS: found 951.4533 [M + H]⁺, C₅₆H₆₂N₄O₁₀ requires 950.4538.

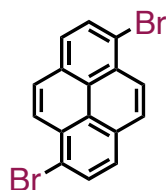
3.3-4 6-((3'-Ethynyl-2,2'-dimethoxy-[1,1'-binaphthalen]-3-yl)ethynyl)-1-hexyluracil



To a degassed solution of dry Et_3N (2.0 mL) and THF (3.5 mL), 1-hexyl-6-iodouracil (29.6 mg, 91.9 μmol), $\text{Pd}(\text{PPh}_3)_4$ (5.3 mg, 4.6 μmol), and CuI (1.7 mg, 9.2 μmol) were added and the mixture degassed a second time. Compound (*S*)-3,3'-diethynyl-2,2'-dimethoxy-1,1'-binaphthalene (200.0 mg, 551.8 μmol) was then added, and the reaction mixture was degassed one last time and stirred for 60 min at r.t., under Ar. The reaction mixture was filtered over celite (CHCl_3) and concentrated under reduced pressure. The crude was purified by column chromatography (SiO_2 , CHX/AcOEt 7:3) and finally precipitated from THF with Pet. Et. to obtain product as a white solid (22.3 mg, 44 % yield).

m.p. 124-125 °C. $[\alpha]_D^{25} = +13.5$ ($c = 1.0$, CHCl_3). $^1\text{H NMR}$ (500 MHz, Chloroform-*d*): δ 8.23-8.21 (m, 3H, $\text{NH} + \text{Ar-H}$), 7.90 (d, $J = 8.0$ Hz, 1H, Ar-H), 7.87 (d, $J = 8.0$ Hz, 1H, Ar-H), 7.48 – 7.41 (m, 2H, Ar-H), 7.36-7.27 (m, 2H, Ar-H), 7.14 (d, $J = 8.5$ Hz, 1H, Ar-H), 7.08 (d, $J = 8.5$ Hz, 1H, Ar-H), 6.06 (d, $J = 2.0$ Hz, 1H, CH), 4.12 (t, $J = 7.5$ Hz, 2H, $\text{NCH}_2(\text{CH}_2)_4\text{CH}_3$), 3.67 (s, 3H, OCH_3), 3.59 (s, 3H, OCH_3), 3.39 (s, 1H, CH) 1.81 (m, 2H, $\text{NCH}_2\text{CH}_2(\text{CH}_2)_3\text{CH}_3$), 1.46-1.25 (m, 6H, $\text{N}(\text{CH}_2)_2(\text{CH}_2)_3\text{CH}_3$), 0.84 (t, $J = 7.5$ Hz, 3H, $\text{N}(\text{CH}_2)_5\text{CH}_3$). $^{13}\text{C NMR}$ (125 MHz, Chloroform-*d*): δ 168.44, 154.70, 152.98, 149.61, 136.59, 118.60, 118.22, 114.44, 112.66, 111.65, 91.29, 91.07, 70.12, 69.00, 32.15, 29.91, 29.89, 29.88, 29.86, 29.84, 29.83, 29.81, 29.63, 29.59, 29.57, 29.56, 29.54, 29.47, 26.24, 26.22, 24.96, 22.91, 14.34. **IR** (KBr): cm^{-1} 3434, 3051, 2931, 2856, 2212, 1686, 1579, 1491, 1459, 1356, 1247, 1209, 1150, 195, 1008, 892, 820, 783, 753, 472. **HRMS**: found 557.2435 $[\text{M} + \text{H}]^+$, $\text{C}_{36}\text{H}_{32}\text{N}_2\text{O}_4$ requires 556.2362.

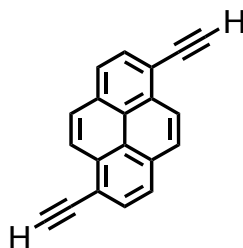
4-3 1,6-Dibromopyrene



Pyrene (1.00 g, 4.94 mmol) was dissolved in CCl_4 (15.0 mL) and stirred at room temperature until completely dissolved. Then, Br_2 (0.54 mL of pure Br_2 diluted in 20.0 mL of CCl_4) was added dropwise. The mixture was stirred at r.t. overnight. The reaction mixture was filtered to afford a pink precipitate that was crystallized several times from PhCH_3 to obtain the product as an off-white solid (0.57 g, 32 % yield).

m.p. 219-222 °C. $^1\text{H NMR}$ (500 MHz, Chloroform-*d*): δ 8.46 (d, $J=9.3$ Hz, 2H, Pyr- $H_{5,10}$), 8.27 (d, $J=8.2$ Hz, 2H, Pyr- $H_{2,7}$), 8.12 (d, $J=9.2$ Hz, 2H, Pyr- $H_{4,9}$), 8.05 (d, $J=8.2$ Hz, 2H, Pyr- $H_{3,8}$). $^{13}\text{C NMR}$ (126 MHz, Chloroform-*d*): δ 130.96, 130.66, 129.92, 128.91, 126.55, 126.21, 125.47, 121.02. IR (KBr): cm^{-1} 1598, 1579, 1479, 1451, 1426, 1368, 1284, 1233, 1199, 1161, 1025, 971, 851, 836, 818, 703, 676, 619. MS (ES +) found 360.1 (M^+), $\text{C}_{16}\text{H}_8\text{Br}_2$ requires 360.14. Characterization in accordance with literature.⁶⁶⁶

4-5 1,6-Diethynylpyrene

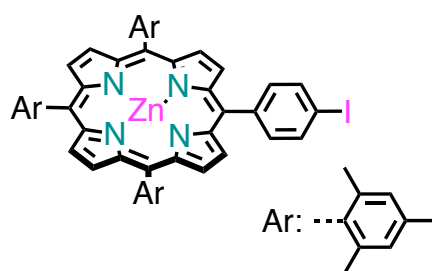


A mixture of 1,6-dibromopyrene **4-3** (200 mg, 0.56 mmol), TMSA (0.40 mL, 2.80 mmol), Pd(PPh₃)₄ (32 mg, 0.03 mmol) and CuI (5 mg, 0.03 mmol) was sealed in a microwave tube with THF (1.0 mL), PhCH₃ (1.0 mL) and Et₃N (1.0 mL). The temperature heating profile for the reaction mixture was as follows: r.t. → 120 °C over a 2-min period (200-W maximum power), the reaction mixture was held at 120 °C (dynamic, 200-W maximum power) for 60 min. The mixture was filtered over celite (CHCl₃) and the solvents removed under reduced pressure. The crude was purified over column chromatography (SiO₂, CHX) to yield the TMS protected intermediate **4-4**. ¹H NMR (500 MHz, Chloroform-*d*): δ 8.58 (d, *J* = 9.0 Hz, 2H), 8.17 – 8.11 (m, 6H), 0.39 (s, 18H).

The intermediate was dissolved in mixture of THF and MeOH mixture (2.0 mL, 1:1). Then a 1 M aq. solution of KOH (1.0 mL) was added dropwise. A yellow precipitate immediately appeared and the solution was stirred for 2 hrs. The product was purified by means of precipitation with MeOH to afford the product as a yellow solid (102 mg, 73 % over two steps).

m.p. 147 °C decomp. ¹H NMR (500 MHz, Chloroform-*d*): δ 8.62 (d, *J* = 9.1 Hz, 2H, Pyr-*H*_{5,10}), 8.19 (d, *J* = 7.9 Hz, 2H, Pyr-*H*_{2,7}), 8.17 – 8.13 (m, 4H, Pyr-*H*_{3,4,8,9}), 3.64 (s, Pyr-C≡CH). ¹³C NMR (50 MHz, Chloroform-*d*): 132.7, 131.6, 130.7, 128.5, 126.5, 125.3, 117.5, 83.3, 82.7. MS (ES +) found 250.1 (M⁺), C₂₀H₁₀ requires 250.08. Characterization in accordance with literature.⁶⁶⁷

4-6 Zinc(II) 5,10,15-Trimesityl-20-(4-iodophenyl)porphyrin

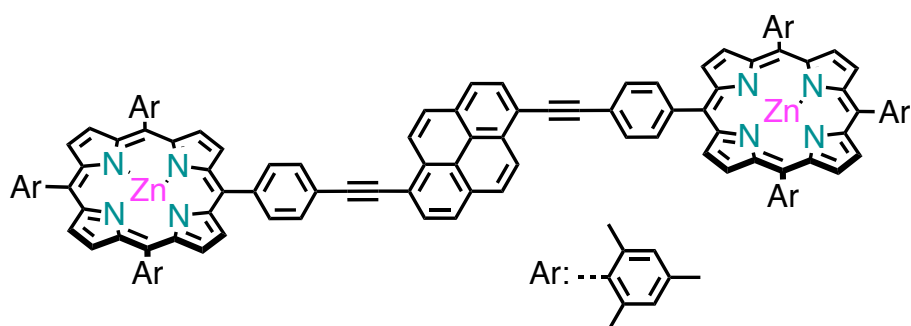


A solution of 4-iodobenzaldehyde (0.50 g, 2.72 mmol), pyrrole (0.76 mL, 10.88 mmol) and mesitaldehyde (1.21 mL, 8.16 mmol) in CHCl₃ (1.0 L, containing 0.75 % EtOH) was degassed by bubbling Ar for 30 minutes. BF₃·Et₂O (0.9 mL) was added and the solution was stirred for 1 h, under dark. DDQ (1.85 g, 8.16 mmol) was added and all was stirred for 1 h. Finally, Et₃N (0.7 mL) was

added, the reaction mixture was concentrated to about 200 mL and passed through a silica plug (CHX/CH₂Cl₂ 1:1) to recover a mixture of porphyrins. The overall mixture was then dissolved in CHCl₃ (20 mL) and 5 mL of sat. MeOH solution of Zn(AcO)₂·2H₂O was added in the dark and all was stirred at r.t. for 2 hrs. The reaction mixture was diluted with CHCl₃ and the organic phase washed with H₂O, brine, dried (Na₂SO₄) and removed under reduced pressure. The crude was purified by repetitive column chromatography (SiO₂, CHX/CH₂Cl₂ 85:15) to obtain product **4-6** as bright pink solid (201 mg, 7 % yield).

m.p > 250 °C. ¹H NMR (500 MHz, Chloroform-*d*): δ 8.84 (d, *J* = 4.6 Hz, 2H, Pyr-*H*), 8.77 (d, *J* = 4.5 Hz, 2H, Pyr-*H*), 8.70 (d, *J* = 12.0 Hz, 4H, Pyr-*H*), 8.07 (d, *J* = 7.8 Hz, 2H, Ar-*H*), 7.96 (d, *J* = 7.8 Hz, 2H, Ar-*H*), 7.31 – 7.25 (m, 6H, Ar-*H*), 2.65 – 2.61 (m, 9H, Ar-CH₃), 1.89 – 1.81 (m, 18H, Ar-CH₃). ¹³C NMR (126 MHz, Chloroform-*d*): δ 150.19, 150.16, 149.98, 149.93, 149.71, 142.77, 139.52, 139.49, 139.48, 139.19, 139.11, 137.66, 137.65, 137.53, 136.28, 135.83, 131.97, 131.45, 131.38, 131.12, 131.01, 127.87, 127.82, 119.21, 119.04, 118.66, 93.90, 21.98, 21.92, 21.90, 21.70. IR (KBr): cm⁻¹ 3049.8, 2917.1, 2849.1, 1653.6, 1457.9, 1264.1 744.4. MS (HRMS +): found 929.2056 (M+), C₅₃H₄₅IN₄Zn requires 929.2053. Characterization in accordance with literature.⁶⁶⁸

4-1 1,6-Bis-[(Zn(II)5-(1-phen-4-yl)-10,15,20-trimesitylporphyril)ethynyl]pyrene

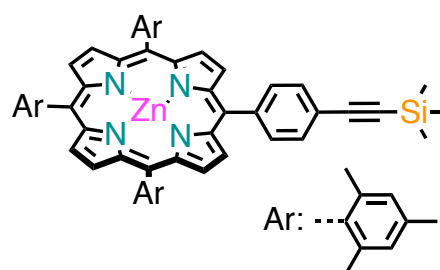


To a Schlenk tube, a solution of zinc(II) 5,10,15-trimesityl-20-(4-iodophenyl)porphyrin **4-6** (50.0 mg, 53.7 μmol) in PhCH₃/Et₃N (5:1, 15.0 mL) was added and the whole solution was degassed with a 'freeze-pump-thaw' cycle. After this Pd₂(dba)₃ (12.3 mg, 13.4 μmol) and AsPh₃ (16.4 mg, 53.6 μmol) were added and the suspension was subjected to another degassing cycle. Finally, 1,6-diethynylpyrene

(5.0 mg, 24.4 μmol) was added and all was degassed for the last time. All was stirred at r.t. overnight, under Ar atmosphere. The reaction mixture was filtered over celite (with the aid of CH_2Cl_2), evaporated and purified by column chromatography (SiO_2 , $\text{CHX}/\text{CH}_2\text{Cl}_2$ 85:15) to afford a dark red solid which was further purified by precipitation from CH_2Cl_2 with cold Pet. Et. to obtain the pure product as dark red solid (28.0 mg, 62 % yield). Crystals suitable for X-ray were obtained from from $\text{CHCl}_3/\text{MeOH}$.

m.p. > 250 $^\circ\text{C}$. $^1\text{H NMR}$ (500 MHz, Chloroform-*d*): δ 8.97-8.93 (m, 6 H, Ar-*H* + β -pyrrole), 8.82 (d, $J = 4.6$, 4 H, β -pyrrole), 8.74 (s, 8 H, β -pyrrole), 8.43 (d, $J = 7.7$ Hz, 2H, Pyr-*H*), 8.35-8.30 (m, 8 H, Ar-*H* + β -pyrrole), 8.14 (AA'BB', d, $J = 7.4$, 4 H, Ar-*H*), 7.30 (s, 12 H, Ar-*H*), 2.65 (s, 18 H, Ar- CH_3), 1.88 (s, 36 H, Ar- CH_3). $^{13}\text{C NMR}$ (126 MHz, Chloroform-*d*): δ 150.23, 150.20, 150.04, 149.90, 143.69, 139.54, 139.29, 139.20, 137.69, 137.67, 134.87, 132.52, 132.15, 131.65, 131.48, 131.41, 131.08, 130.46, 130.18, 128.63, 127.91, 126.80, 125.63, 124.70, 122.74, 119.43, 119.26, 119.06, 118.92, 96.08, 89.78, 22.03, 21.96, 21.74. IR (KBr): cm^{-1} 3446, 2921, 2851, 2337, 2030, 1952, 1639, 1432, 1384, 1112, 1061, 876, 616. MS (HR-MALDI, DCTAB) found 1850.6505 (M^+), $\text{C}_{126}\text{H}_{98}\text{N}_8\text{Zn}_2$ requires 1850.6497.

4-2 Zinc(II) 5,10,15-Trimesityl-20-{4-[2-(trimethylsilyl)ethynyl]phenyl}porphyrin

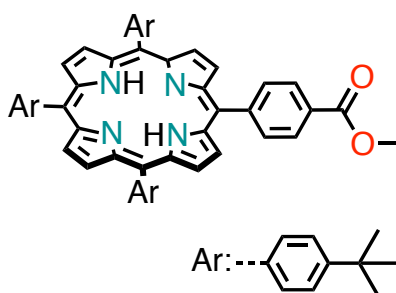


To a Schlenk tube, a solution of zinc(II) 5,10,15-trimesityl-20-(4-iodophenyl)porphyrin **4-6** (50.0 mg, 53.7 μmol) in $\text{PhCH}_3/\text{Et}_3\text{N}$ (5:1, 15.0 mL) was added and the whole solution was degassed with a 'freeze-pump-thaw' cycle. After this $\text{Pd}_2(\text{dba})_3$ (6.2 mg, 6.7 μmol) and AsPh_3 (8.2 mg, 26.7 μmol) were added and the suspension was subjected to another degassing cycle. Finally, TMSA (7.3 μL , 107.4 μmol) was added and all was degassed for the last time. All was stirred at r.t. overnight, under Ar

atmosphere. The reaction mixture was filtered over celite (with the aid of CH_2Cl_2), evaporated and purified by column chromatography (SiO_2 , $\text{CHX}/\text{CH}_2\text{Cl}_2$, 85:15) to afford a dark purple solid which was further purified by precipitation from CH_2Cl_2 with cold Pet. Et. to obtain the pure product as dark purple solid (45.0 mg, 93 % yield). Crystals suitable for X-ray were obtained by slow evaporation of a CHCl_3 /pyridine solution.

m.p. > 250 °C. $^1\text{H NMR}$ (500 MHz, Dichloromethane- d_2): δ 8.86 (d, $J = 4.6$ Hz, 2H, β -pyrrole), 8.76 (d, $J = 4.6$ Hz, 2H, β -pyrrole), 8.72 (s, 4 H, β -pyrrole), 8.20 (AA'BB', d, $J = 7.6$ Hz, 2H, Ar- H), 7.86 (AA'BB', d, $J = 7.6$ Hz, 2H, Ar- H), 7.31 (s, 6 H, Ar- H), 2.64 (s, 9 H, Ar- CH_3), 1.85 (s, 6 H, Ar- CH_3), 0.39 (s, 9 H, Si- CH_3). $^{13}\text{C NMR}$ (126 MHz, Dichloromethane- d_2): δ 151.83, 151.78, 151.64, 151.51, 145.26, 141.06, 141.02, 140.84, 140.79, 139.44, 136.27, 133.69, 132.97, 132.87, 132.49, 131.91, 129.57, 129.49, 124.09, 121.04, 120.80, 120.72, 106.98, 97.01, 23.31, 23.24, 23.05, 1.62. **MS** (HRMS) found 899.3469 (M^+), $\text{C}_{58}\text{H}_{54}\text{N}_4\text{SiZn}$ requires 898.3409. Characterizations were in accordance with literature.⁶⁶⁹

4-7 5,10,15-Tri(4-*tert*-butylphenyl)-20-(4-carboxymethylphenyl)porphyrin

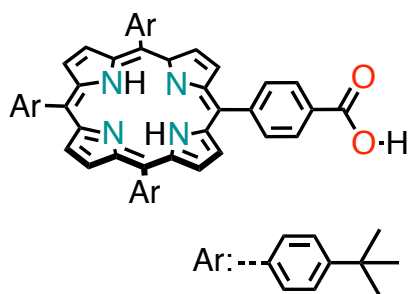


To a solution of 4-*tert*-butylbenzaldehyde (0.37 mL, 2.19 mmol), methyl 4-formylbenzoate (330 mg, 2.19 mmol) and freshly distilled pyrrole (0.30 mL, 4.38 mmol) in CHCl_3 (1.0 L with 0.75 % EtOH) was added $\text{BF}_3 \cdot \text{OEt}_2$ (0.36 mL), at r.t. and under Ar. The solution was stirred for 1 h before adding *p*-chloranil (400 mg, 1.63 mmol) and was left stirring for another hour. Finally, Et_3N (0.28 mL) was added and all was stirred for 15 min. The reaction mixture was concentrated under reduced pressure and passed over a silica plug ($\text{CHX}/\text{CH}_2\text{Cl}_2$ 1:1) to obtain a dark purple solid as a mixture of TPP and

porphyrin esters. The crude was purified by column chromatography with product eluting as the second band (SiO_2 , $\text{CHX} \rightarrow \text{CHX}/\text{AcOEt}$ 95:5) and finally crystallized from CH_2Cl_2 with pentane to obtain the purple product (294 mg, 15 % yield).

m.p. > 250 °C. $^1\text{H NMR}$ (500 MHz, Chloroform-*d*): δ 8.91 (d, $J = 4.9$ Hz, 2H), 8.89 (s, 4H), 8.77 (d, $J = 4.6$ Hz, 2H), 8.44 (d, $J = 8.1$ Hz, 2H), 8.32 (d, $J = 8.1$ Hz, 2H), 8.20 – 8.09 (m, 6H), 7.79 – 7.74 (m, 6H), 4.12 (s, 3H), 1.62 (s, 27H), -2.74 (s, 2H). $^{13}\text{C NMR}$ (126 MHz, Chloroform-*d*): δ 167.65, 150.82, 147.50, 139.37, 139.31, 134.89, 134.76, 134.71, 129.71, 128.12, 123.88, 123.85, 121.01, 120.72, 118.40, 52.65, 35.17, 31.96. **MS** (ES +): found 841.5 ($\text{M} + \text{H}^+$), $\text{C}_{58}\text{H}_{56}\text{N}_4\text{O}_2$ requires = 840.44. Characterization was in accordance with literature.⁶⁷⁰

4-8 5,10,15-Tri(4-*tert*-butylphenyl)-20-(4-carboxyphenyl)porphyrin

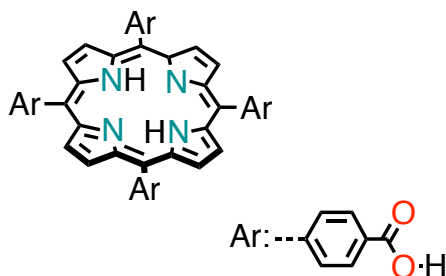


To a suspension of 5,10,15-tri(4-*tert*-butylphenyl)-20-(4-carboxymethylphenyl)porphyrin **4-7** (100 mg, 0.12 mmol) in EtOH (50 mL) was added an excess of aq. KOH and the mixture was refluxed overnight. The reaction mixture was acidified with 2 M aq. HCl and was concentrated under reduced pressure. The crude was extracted with CHCl_3 and the organic phase was washed with 1 M aq. NaHCO_3 and brine, dried (Na_2SO_4) and removed under reduced pressure. The crude was purified by column chromatography (SiO_2 , $\text{CH}_2\text{Cl}_2 \rightarrow \text{CH}_2\text{Cl}_2/\text{MeOH}$ 9:1) to obtain pure product as purple solid (86 mg, 89 % yield).

m.p. > 250 °C. $^1\text{H NMR}$ (500 MHz, Chloroform-*d*/dimethylsulfoxide-*d*₆ 9:1 v/v): δ 12.60 (s, 1H, Ar-COOH), 8.90 (d, $J = 4.9$ Hz, 2H, Pyr-*H*), 8.88 (s, 4H, Pyr-*H*), 8.80 (d, $J = 4.7$ Hz, 2H, Pyr-*H*), 8.44 (d, $J = 7.9$ Hz, 2H, Ar-*H*), 8.29 (d, $J = 7.9$ Hz, 2H, Ar-*H*), 8.15 – 8.10 (m, 6H, Ar-*H*), 7.78 (d, $J = 7.8$

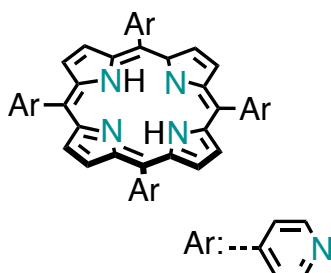
Hz, 6H, Ar-*H*), 1.61 (s, 27H, Ar-(CH₃)₃), -2.82 (s, 2H, Pyr-NH). ¹³C NMR (126 MHz, Chloroform-*d*/dimethylsulfoxide-*d*₆ 9:1 v/v): δ 169.52, 151.68, 147.53, 139.87, 139.82, 135.55, 135.49, 135.46, 131.61, 129.13, 124.81, 124.79, 121.73, 121.49, 119.53, 35.96, 32.77. IR (KBr): cm⁻¹ 3437, 2957, 1694, 1607, 1474, 1431, 1398, 1362, 1313, 1267, 1231, 1195, 1156, 1108, 1023, 982, 967, 800, 767, 734. MS (ES +): found 827.5 (M + H⁺), C₅₈H₅₆N₄O₂ requires = 862.42. Characterization was in accordance with literature.⁶⁷¹

4-9 5,10,15,20-Tetrakis(4-carboxyphenyl)porphyrin



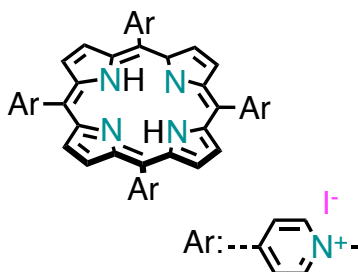
A solution of 4-formylbenzoic acid (0.50 g, 3.33 mmol) in propionic acid (20.0 mL) was heated to 80 °C until the aldehyde was fully dissolved. At this point, pyrrole (0.23 mL, 3.33 mmol) was added and the temperature was brought to reflux for 2 hrs. The reaction mixture was allowed to cool down to r.t. and left at - 20 °C overnight. The crystals were collected, washed with CH₂Cl₂ and dried to obtain product as dark purple solid (0.68 g, 26 % yield).

m.p. > 250 °C. ¹H NMR (500 MHz, Dimethylsulfoxide-*d*₆): δ 13.19 (s, 4H, Ar-COOH), 8.85 (s, 8H, Pyr-*H*), 8.38 (d, *J* = 8.0 Hz, 8H, Ar-*H*), 8.33 (d, *J* = 8.1 Hz, 8H, Ar-*H*), -2.91 (bs, 2H, Pyr-NH). IR (KBr): cm⁻¹ 3433, 1697, 1605, 1401, 1263, 1177, 1102, 1019, 965, 866, 797, 714. ES (MS -): 789.2 (M - H⁺), C₄₈H₃₀N₄O₈ requires 790.21. Characterization in accordance with literature.⁶⁷²

4-10 5,10,15,20-Tetrakis(4-pyridyl)porphyrin

A solution of pyrrole (1.25 mL, 18.00 mmol) and 4-pyridinecarboxaldehyde (1.70 mL, 18.00 mmol) in propionic acid (50.0 mL) was heated at reflux for 1 h. The mixture was cooled, concentrated under reduced pressure, diluted with MeOH and left at $-20\text{ }^{\circ}\text{C}$ over weekend to crystallize. Purple crystals were filtered and washed with cold MeOH to obtain product as purple crystals (0.86 g, 8 % yield).

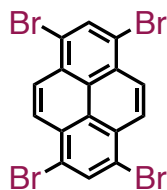
m.p. $> 250\text{ }^{\circ}\text{C}$. $^1\text{H NMR}$ (500 MHz, Chloroform-*d*): δ 9.07 (d, $J = 5.8$ Hz, 8H, Pyridine-*H*), 8.87 (s, 8H, Pyrrole-*H*), 8.17 (d, $J = 5.9$ Hz, 8H, Pyridine-*H*), -2.91 (s, 2H, Pyrrole-NH). IR (KBr): cm^{-1} 3435, 1593, 1542, 1467, 1401, 1351, 1210, 1157, 1069, 1004, 980, 971, 882, 843, 797, 785, 724, 659. ES (MS +): 619.3 ($M + \text{H}^+$), $\text{C}_{40}\text{H}_{26}\text{N}_8$ requires 618.23. Characterization in accordance with literature.⁶⁷³

4-11 5,10,15,20-Tetrakis(N-methyl-4-pyridinio)porphyrin tetraiodide

To a suspension of 5,10,15,20-tetrakis(4-pyridyl)porphyrin **4-10** (50 mg, 0.081 mmol) in dry DMF (5.0 mL) was added an excess of CH_3I (100 μL , 1.617 mmol) and the mixture was heated at $150\text{ }^{\circ}\text{C}$

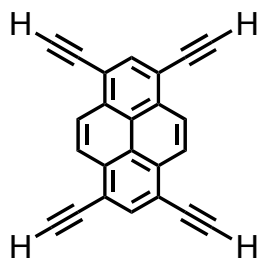
for 2 hrs. The mixture was cooled down to r.t. and diluted with acetone. The precipitate was filtered and washed with acetone and Et₂O to yield product as dark purple solid (74 mg, 77 % yield).

m.p. > 250 °C. ¹H NMR (500 MHz, Deuterium Oxide) δ 9.21 (d, *J* = 6.5 Hz, 8H, Pyridinium-*H*), 9.08 (s, 8H, Pyrrole-*H*), 8.88 (d, *J* = 6.7 Hz, 8H, Pyridinium-*H*), 4.68 (s, 12H, Pyridinium-*CH*₃). IR (KBr): cm⁻¹ 3429, 1639, 1561, 1509, 1459, 1401, 1279, 1215, 1185, 1003, 970, 888, 858, 800, 711. ES (MS +): 678.4 (M⁺), C₄₄H₃₈N₈⁴⁺ requires 678.32. Characterization in accordance with literature.⁶⁷⁴

5-4 1,3,6,8-Tetrabromopyrene

A solution of pyrene (2.0 g, 9.9 mmol) in PhNO₂ (40 mL) was stirred at 120 °C for 30 min. Following this Br₂ (2.3 mL, 44.9 mmol) was added dropwise. The mixture was vigorously stirred for 4 hrs and then EtOH (50 mL) was slowly added and the mixture stirred 1 h at r.t. The precipitate formed was filtered off, washed with EtOH and dried under reduced pressure yielding product as a pale-green solid (4.96 g, 96 % yield), insoluble in all common organic solvents.

m.p. > 250 °C. **IR** (KBr): cm⁻¹ 3436, 11741, 1630, 1592, 1466, 1453, 1358, 1279, 1227, 1160, 1055, 988, 874. **MS** (ES, TFA): found 518 (M⁺), C₁₆H₈Br₄ requires 517.72. Characterization in accordance with literature.⁶⁷⁵

5-5 1,3,6,8-Tetrakis[(trimethylsilyl)ethynyl]pyrene

To a degassed solution of dry *i*Pr₂NH (20 mL) and dry THF (20 mL), 1,3,6,8-tetrabromopyrene **5-4** (1 g, 1.93 mmol), Pd(PPh₃)₂Cl₂ (0.067 g, 0.096 mmol) and CuI (0.018 g, 0.096 mmol) were added and the resulting solution degassed a second time. Finally, TMSA (1.6 mL, 11.5 mmol) was added, the reaction mixture degassed one last time and stirred overnight at 80 °C under Ar. Notably, after a

few minutes the reaction color changed from green to intense orange. The resulting mixture was filtered over celite (CH_2Cl_2 and MeOH). Removal of the solvents under reduced pressure and purification of the crude by column chromatography (SiO_2 , CHX) yielded product as a bright orange solid (0.96 g, 85 % yield). m.p. > 250 °C. $^1\text{H NMR}$ (400 MHz, Chloroform-*d*): δ 8.60 (s, 4H, Pyr- $H_{4,5,9,10}$), 8.31 (s, 2H, Pyr- $H_{2,7}$), 0.39 (s, 36H, Pyr- $\text{C}\equiv\text{CSi}(\text{CH}_3)_3$).

To a solution of trimethylsilylethynylpyrene intermediate (0.17 g, 0.59 mmol) in $\text{CH}_2\text{Cl}_2/\text{MeOH}$ (20 mL, 1:1) was added 1 M aq. KOH solution (4 mL). The mixture was stirred overnight at r.t. As the reaction proceeded a yellow precipitate appeared. H_2O (10 mL) was then added to the mixture and the organic phase extracted multiple times with CHCl_3 , the organic phases combined and dried (Na_2SO_4). Evaporation of the solvent under reduced pressure yielded product as a yellow solid in a quantitative yield, which resulted insoluble in common organic solvents.

m.p. 182 °C decomp. $^1\text{H NMR}$ (200 MHz, Chloroform-*d* + Methanol-*d*₄): δ 8.7 (s, 4H, $H_{4,5,9,10}$), 8.4 (s, 2H, $H_{2,7}$), 3.7 (s, 4H, Pyr- $\text{C}\equiv\text{CH}$). IR (KBr): cm^{-1} 3435, 3280, 2100, 1600, 1468, 1115, 905, 832, 670, 608, 473. MS (ES): found 298 (M^+), $\text{C}_{24}\text{H}_{10}$ requires = 298.08. Characterization in accordance with literature.⁶⁷⁵

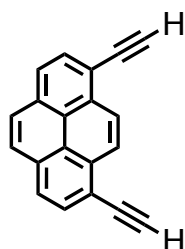
5-6 1,8-Diiodopyrene



Pyrene (5.0 g, 24.7 mmol) was dispersed in AcOH (150.0 mL) and the mixture heated up at 90 °C. Then, H_2O (16.0 mL), I_2 (6.27 g, 24.7 mmol), KIO_4 (2.11 g, 9.80 mmol) and H_2SO_4 (1.67 mL) were added carefully. The solution became red. Filtration of the reaction mixture afforded a brown precipitate that was then purified by crystallization with hot PhCH_3 to afford pure product (2.8 g, 25 %).

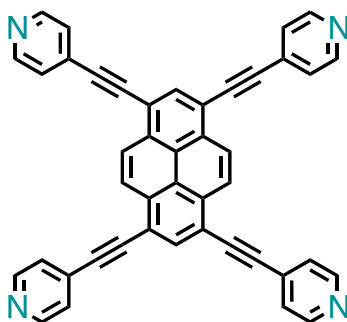
m.p. 132 °C. $^1\text{H NMR}$ (500 MHz, Chloroform-*d*): δ 8.54 (d, $J = 8.1$ Hz, 2H, Pyr- $H_{2,7}$), 8.39 (s, 2H, Pyr- $H_{9,10}$), 8.06 (s, 2H, Pyr- $H_{4,5}$), 7.90 (d, $J = 8.1$ Hz, 2H, Pyr, $H_{3,6}$). $^{13}\text{C NMR}$ (126 MHz, Chloroform-*d*): δ 137.64, 133.26, 132.78, 131.53, 127.94, 126.91, 125.11, 97.19. **IR** (KBr): cm^{-1} 2916, 2849, 1730, 1637, 1594, 1470, 1264, 1179, 1104, 1048, 990. **MS** (ES): found 453.9 (M^+), $\text{C}_{16}\text{H}_8\text{I}_2$ requires 453.87.

5-7 1,8-Diethynylpyrene



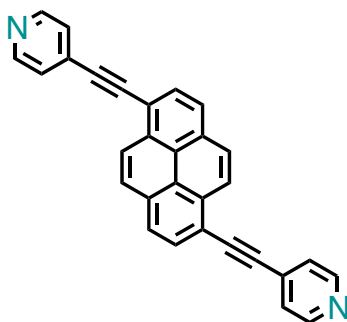
In a 10 mL microwave-reactor tube containing a stirring bar, 1,8-diiodopyrene **5-6** (0.20 g, 0.44 mmol), $\text{Pd}(\text{PPh}_3)_4$ (0.04 g, 0.03 mmol), CuI (0.02 g, 0.1 mmol) were dissolved in Tol/THF/ Et_3N (2:2:2 mL) and was purged with argon. TMSA (0.20 mL, 1.41 mmol) was added and the reaction vessel was sealed and placed into the microwave reactor. The temperature heating profile for the reaction mixture was as follows: r.t. \rightarrow 120 °C over a 2-min period (200-W maximum power), the reaction mixture was held at 120 °C (dynamic, 200-W maximum power) for 60 min. The reaction mixture was filtered over celite (CHCl_3) and the filtrates were removed under reduced pressure. The intermediate was purified by column chromatography (SiO_2 , $\text{CHX}/\text{CH}_2\text{Cl}_2$). The TMS intermediate fractions were dissolved in THF/MeOH (2.0 mL, 1:1) and 1 M aq. KOH solution (1.0 mL) was added dropwise and the mixture stirred for 2 hrs. The reaction mixture was purified by means of precipitation with MeOH to afford the final compound as a brown solid (0.09 g, 84 % yield).

m.p. 131 °C. $^1\text{H NMR}$ (400 MHz, Chloroform-*d*): δ 8.68 (s, 2H, Pyr- $H_{9,10}$), 8.19 (d, $J = 7.9$ Hz, 2H, Pyr- $H_{2,7}$), 8.12 (d, $J = 8.0$ Hz, 2H, Pyr, $H_{3,6}$), 8.07 (s, 2H, Pyr- $H_{4,5}$), 3.65 (s, 2H). $^{13}\text{C NMR}$ (50 MHz, Chloroform-*d*): 132.28, 131.55, 130.50, 128.11, 126.39, 125.02, 123.89, 117.33, 83.12, 82.47. **MS** (ES): found 250.1 (M^+), requires $\text{C}_{20}\text{H}_{10}$ 250.08.

5-1 1,3,6,8-Tetrakis(4-pyridylethynyl)pyrene

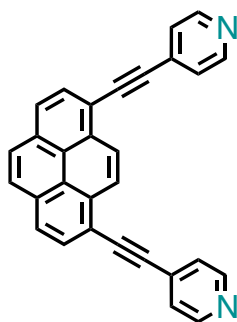
In a 10 mL microwave-reactor tube containing a stirring bar, 4-iodopyridine (0.121 g, 0.560 mmol), Pd(PPh₃)₄ (0.004 g, 0.004 mmol), CuI (0.001 g, 0.007 mmol) were dissolved in DMF/Et₃N (2:2 mL) and was purged with argon. Tetraethynylpyrene **5-5** (0.022 g, 0.074 mmol) was added and the reaction vessel was sealed and placed into the microwave reactor. The temperature heating profile for the reaction mixture was as follows: r.t. → 120 °C over a 2-min period (200-W maximum power), the reaction mixture was held at 120 °C (dynamic, 200-W maximum power) for 60 min. The crude reaction mixture was diluted with MeOH and the dark red solid was filtered and washed extensively with H₂O, acetone and MeOH. The solid was dissolved in boiling C₂H₂Cl₄ and filtered over celite to obtain pure product **5-1** as dark red solid (0.036 g, 80 % yield).

m.p. > 250 °C. ¹H NMR (500 MHz, 1,1,2,2-Tetrachloroethane-*d*₂, 353 K): δ = 8.84 (s, 4H, Pyrene-*H*_{4,5,9,10}), 8.75 (d, *J* = 4.9 Hz, 8H, Pyridine-*H*_{2,6}), 8.58 (s, 2H, Pyrene-*H*_{2,7}), 7.62 (d, *J* = 4.9 Hz, 8H, Pyridine-*H*_{3,5}). ¹³C NMR (126 MHz, 1,1,2,2-Tetrachloroethane-*d*₂, 353 K): δ = 149.85, 134.43, 132.20, 130.68, 127.24, 125.35, 120.20, 118.30, 93.75, 91.31. IR (KBr): cm⁻¹ 2205, 1627, 1601, 1591, 1538, 1471, 1399, 817 cm⁻¹. HRMS-MALDI (dctb matrix): found 606.1847 (M)⁺, 607.1905 (MH)⁺, 857.3168 (M+1dctb)⁺, 1107.4622 (M+2dctb)⁺, C₄₄H₂₂N₄ requires 606.1844.

5-2 1,6-Bis(4-pyridylethynyl)pyrene

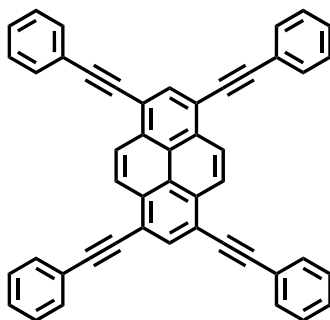
In a 10 mL microwave-reactor tube containing a stirring bar, 4-iodopyridine (0.328 g, 1.600 mmol), Pd(PPh₃)₄ (0.009 g, 0.008 mmol), CuI (0.004 g, 0.020 mmol) were dissolved in DMF/Et₃N (2:2 mL) and was purged with argon. 1,6-Diethynylpyrene **4-5** (0.100 g, 0.400 mmol) was added and the reaction vessel was sealed and placed into the microwave reactor. The temperature heating profile for the reaction mixture was as follows: r.t. → 120 °C over a 2-min period (200-W maximum power), the reaction mixture was held at 120 °C (dynamic, 200-W maximum power) for 30 min. The crude reaction mixture was diluted with MeOH and the yellow solid was filtered and washed extensively with H₂O, acetone and MeOH. The solid was dissolved in boiling C₂H₂Cl₄ and filtered over celite to obtain pure product **5-2** (0.142 g, 88 % yield) as bright yellow solid.

m.p. > 250 °C. ¹H NMR (500 MHz, 1,1,2,2-Tetrachloroethane-*d*₂): δ = 8.69 (d, *J* = 5.5 Hz, 4H, Pyridine-*H*_{2,6}), 8.65 (d, *J* = 9.0 Hz, 2H, Pyrene-*H*_{5,10}), 8.29 (d, *J* = 8.0 Hz, 2H, Pyrene-*H*_{2,7}), 8.23-8.21 (m, 4H, Pyrene-*H*_{3,4,8,9}), 7.60 (d, *J* = 6.0 Hz, 4H, Pyridine-*H*_{3,5}). ¹³C NMR (126 MHz, 1,1,2,2-Tetrachloroethane-*d*₂): δ = 149.63, 132.02, 131.50, 131.30, 130.43, 128.50, 126.27, 125.55, 125.50, 123.75, 117.17, 92.90, 92.75. IR (KBr): cm⁻¹ 2203, 1604, 1569, 1483, 1435, 1420, 1215, 1098, 1059, 845, 830, 694 cm⁻¹. HRMS-MALDI (dctb matrix): found 404.1308 (M)⁺, 405.1369 (M+H)⁺, 654.3 (M+1dctb)⁺, 905.5 (M+2dctb)⁺, C₃₀H₁₆N₂ requires 404.1313.

5-3 1,8-Bis(4-pyridylethynyl)pyrene

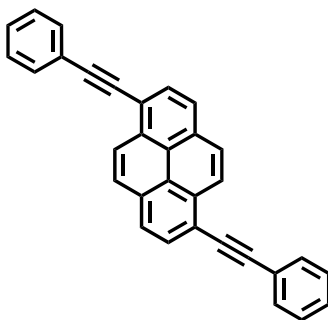
To a degassed solution of dry Et_3N (2.5 mL) and THF (2.5 mL), 4-iodopyridine (0.072 g, 0.35 mmol), $\text{Pd}(\text{PPh}_3)_4$ (0.010 g, 0.008 mmol) and CuI (0.006 g, 0.032 mmol) were added and the mixture degassed a second time. 1,8-Diethynylpyrene **5-7** (0.040 g, 0.16 mmol) was then added, the reaction mixture degassed one last time, and stirred overnight at room temperature under Ar. After 1 h an orange precipitate was formed. The precipitate was then separated by centrifugation and washed with copious amount of MeOH, AcCN and PhCH_3 and submitted to column chromatography (SiO_2 , PhCH_3/Py 85:15) affording the final compound **5-3** as a light orange powder (0.025 g, 45 % yield).

m.p. > 250°C. $^1\text{H NMR}$ (500 MHz, Pyridine- d_5): δ = 9.02 (s, 2H, Pyrene- $H_{9,10}$), 8.87 (d, J = 4.5 Hz, 4H, Pyridine- $H_{2,6}$), 8.39 (d, J = 8.0 Hz, 2H, Pyrene- $H_{2,7}$), 8.28 (d, J = 8.0 Hz, 2H, Pyrene- $H_{3,6}$), 8.19 (s, 2H, Pyrene- $H_{4,5}$), 7.68 (d, J = 4.5 Hz, 4H, Pyridine- $H_{4,5}$). $^{13}\text{C NMR}$ (126 MHz, Pyridine- d_5): δ = 151.11, 132.92, 131.74, 131.38, 129.48, 127.47, 126.69, 126.36, 124.82, 123.53, 118.26, 94.21, 93.56. **IR** (KBr): cm^{-1} 2202, 1600, 1492, 1443, 1162, 1027, 845, 755, 693, 523 cm^{-1} . **HRMS-MALDI** (dctb matrix): found 404.1308 (M) $^+$, 405.1369 ($\text{M}+\text{H}$) $^+$, 654.3 ($\text{M}+1\text{dctb}$) $^+$, 905.5 ($\text{M}+2\text{dctb}$) $^+$, $\text{C}_{30}\text{H}_{16}\text{N}_2$ requires 404.1313.

5-1a 1,3,6,8-Tetrakis(phenylethynyl)pyrene

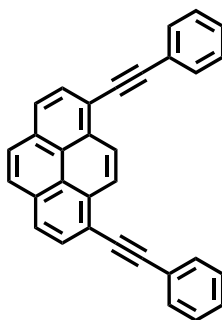
In a 10 mL microwave-reactor tube containing a stirring bar, 1,3,6,8-tetrabromopyrene **5-4** (0.250 g, 0.481 mmol), Pd(PPh₃)₂Cl₂ (0.017 g, 0.024 mmol), CuI (0.005 g, 0.026 mmol) were dissolved in DMF/Et₃N (2:2 mL) and was purged with argon. Phenylacetylene (0.317 g, 2.884 mmol) was added and the reaction vessel was sealed and placed into the microwave reactor. The temperature heating profile for the reaction mixture was as follows: r.t. → 120 °C over a 2-min period (200-W maximum power), the reaction mixture was held at 120 °C (dynamic, 200-W maximum power) for 60 min. The crude reaction mixture was diluted with MeOH and the solid was filtered and washed extensively with H₂O, acetone and MeOH to obtain pure product **5-1a** as bright orange solid (0.246 g, 85 % yield).

m.p. > 250 °C. ¹H NMR (500 MHz, 1,1,2,2-Tetrachloroethane-*d*₂, 353 K): δ 8.83 (s, 4H, Pyrene-*H*_{4,5,9,10}), 8.51 (2H, Pyrene-*H*_{2,7}), 7.81-7.78 (m, 8H, Ph-*H*_{2,6}), 7.52-7.46 (m, 12H, Ph-*H*_{3,4,5}). ¹³C NMR (126 MHz, 1,1,2,2-Tetrachloroethane-*d*₂, 353 K): δ 133.63, 131.70, 131.68, 128.60, 128.38, 126.79, 123.99, 123.05, 118.98, 96.34, 87.62. IR (KBr): cm⁻¹ 2200, 1599, 1499, 1442, 1069, 885, 830, 754, 687 cm⁻¹. MS (ESI): 603 (M)⁺, 301 (M)²⁺, C₄₈H₂₆ requires 602.2.

5-2a 1,6-Bis(phenylethynyl)pyrene

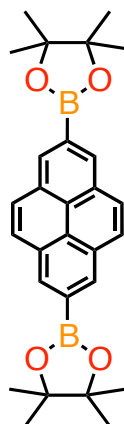
To a degassed solution of dry Et_3N (2.5 mL) and THF (2.5 mL), 4-iodobenzene (0.071 g, 0.350 mmol), $\text{Pd}(\text{PPh}_3)_4$ (0.010 g, 0.008 mmol) and CuI (0.006 g, 0.032 mmol) were added and the mixture degassed a second time. 1,6-Diethynylpyrene **4-5** (0.040 g, 0.160 mmol) was then added, the reaction mixture degassed one last time, and stirred overnight at room temperature under Ar. The precipitate was then filtered over celite (CHCl_3), the solvent was removed under reduced pressure. The crude was purified with column chromatography (SiO_2 , CHX/DCM 85:15) affording the final compound **5-2a** (0.046 g, 78 % yield) as a yellow powder.

m.p. > 250 °C. $^1\text{H NMR}$ (500 MHz, Chloroform-*d*): δ 8.70 (d, $J = 9.0$ Hz, 2H, Pyrene- $H_{5,10}$), 8.23 (d, $J = 8.0$ Hz, 2H, Pyrene- $H_{2,7}$), 8.19-8.16 (m, 4H, Pyrene- $H_{3,4,8,9}$), 7.74 (m, 4H, Ph- $H_{2,6}$), 7.46-7.71 (m, 6H, Ph- $H_{3,4,5}$). $^{13}\text{C NMR}$ (126 MHz, Chloroform-*d*): 132.27, 131.95, 131.40, 130.19, 128.76, 128.73, 128.38, 126.53, 125.39, 124.48, 123.65, 118.71, 95.75, 88.72. **IR** (KBr): cm^{-1} 2201, 1600, 1492, 1442, 1161, 1071, 1027, 845, 755, 693 cm^{-1} . **MS** (ESI): found 402.1 (M) $^+$, requires $\text{C}_{32}\text{H}_{18}$ 402.1.

5-3a 1,8-Bis(phenylethynyl)pyrene

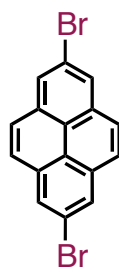
To a degassed solution of dry Et₃N (2.5 mL) and THF (2.5 mL), 4-iodobenzene (0.071 g, 0.350 mmol), Pd(PPh₃)₄ (0.010 g, 0.008 mmol) and CuI (0.006 g, 0.032 mmol) were added and the mixture degassed a second time. 1,8-Diethynylpyrene **5-7** (0.040 g, 0.160 mmol) was then added, the reaction mixture degassed one last time, and stirred overnight at r.t. under Ar. The precipitate was then filtered over celite (CHCl₃), the solvent was removed under reduced pressure. The crude was purified with column chromatography (SiO₂, CHX/DCM 85:15) affording the final compound **5-3a** as a yellow powder (0.046 g, 72 % yield).

m.p. > 250 °C. ¹H NMR (500 MHz, Chloroform-*d*): δ 8.78 (s, 2H, Pyrene-*H*_{9,10}), 8.22 (d, *J* = 8.0 Hz, 2H, Pyrene-*H*_{2,7}), 8.13 (d, *J* = 8.0 Hz, 2H, Pyrene-*H*_{3,6}), 8.06 (s, 2H, Pyrene-*H*_{4,5}), 7.75-7.73 (m, 4H, Ph-*H*_{2,6}), 7.46-7.41 (m, 6H, Ph-*H*_{3,4,5}). ¹³C NMR (126 MHz, Chloroform-*d*): 132.08, 131.95, 131.56, 130.11, 128.73, 128.71, 128.17, 126.67, 125.32, 124.44, 123.68, 118.74, 95.85, 88.74. IR (KBr): cm⁻¹ 2200, 1601, 1495, 1442, 1176, 1159, 1069, 1026, 845, 749, 686 cm⁻¹. MS (ESI): found 402.1 (M)⁺, requires C₃₂H₁₈ 402.1.

5-8 Pyrene-2,7-bis(4,4,5,5-tetramethyl-[1,3,2]dioxaborolane)

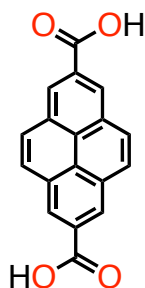
A Schlenk flask, under Ar, was charged with pyrene (1.00 g, 4.94 mmol) and B₂pin₂ (2.70 g, 10.62 mmol) in dry THF (5.0 mL) and the solution was degassed with a 'freeze-pump-thaw' cycle. To this mixture was added a degassed solution of [Ir(μ-OMe)cod]₂ (33 mg, 0.05 mmol), 4,4'-di-*tert*-butyl-2,2'-bipyridine (29 mg, 0.10 mmol) and B₂pin₂ (55 mg, 0.21 mmol) in dry THF (2.5 mL). The tube was sealed, degassed one last time with 'freeze-pump-thaw' cycle and the reaction mixture was stirred at 80 °C for 16 h. The reaction mixture was left to cool to r.t. and then passed through a silica plug (CH₂Cl₂) and the solvent was removed under reduced pressure. The crude was purified by column chromatography (SiO₂, hexane/CH₂Cl₂ 7:3) to obtain product as white solid (1.81 g, 81 % yield).

m.p. > 250 °C. ¹H NMR (400 MHz, Chloroform-*d*): δ 8.62 (s, 4H, Pyr-*H*_{1,3,6,8}), 8.08 (s, 4H, Pyr-*H*_{4,5,9,10}), 1.46 (s, 24H, -BO₂C₂(CH₃)₂). MS (ES +): found 454 (M⁺), C₂₈H₃₂B₂O₄ requires 454.25. Characterization in accordance with literature.⁶¹⁴

5-9 2,7-Dibromopyrene

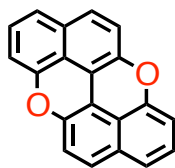
To a solution of 2,7-bis(pinacolborano)pyrene **5-8** (0.35 g, 0.75 mmol) in THF/MeOH (10 mL, 1:3) was added a solution of CuBr₂ (1.04 g, 4.64 mmol) in H₂O (7.5 mL). The mixture was heated at 90 °C overnight and concentrated under reduced pressure. H₂O was added and the white precipitate collected by filtration and washed with H₂O, Et₂O and hexane. The product was extracted in hot PhCH₃ and the solvent was removed under reduced pressure. Finally, the product was obtained as an off-white solid by crystallization from boiling acetone (0.17 g, 64 % yield).

m.p. > 250 °C. ¹H NMR (400 MHz, Chloroform-*d*) δ 8.31 (s, 4H, Pyr-*H*_{1,3,6,8}), 8.01 (s, 4H, Pyr-*H*_{4,5,9,10}). MS (ES +): found 360 (M⁺), C₁₆H₈Br₂ requires 357.90. Characterization in accordance with literature.⁶¹⁴

5-10 Pyrene-2,7-dicarboxylic acid

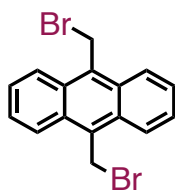
To a solution of 2,7-dibromopyrene **5-9** (0.10 g, 0.28 mmol) in dry THF (25 mL) under Ar and at -78 °C an excess of ⁿBuLi (1.4 mL of a 1.6 M hexane solution, 2.26 mmol) was added dropwise. The mixture was stirred at -78 °C for 30 minutes under Ar. At this point, excess CO₂ gas was added (dry ice in a 1 L round-bottom flask was bubbled into the solution by cannula). The mixture was left to warm up to room temperature and left stirring overnight. H₂O was added and the mixture was concentrated under reduced pressure. The residual aqueous phase was treated with 1 M aq. HCl solution to yield a precipitate that was collected by filtration and washed with H₂O, hexane, EtOAc and finally Et₂O. The solid was dried to obtain product as bright yellow solid (74 mg, 91 % yield).

m.p. > 250 °C. ¹H NMR (400 MHz, Dimethylsulfoxide-*d*₆): δ 13.39 (s, 2H, Pyr-COOH), 8.91 (s, 4H, Pyr-*H*_{1,3,6,8}), 8.40 (s, 4H, Pyr-*H*_{4,5,9,10}). MS (ES +): found 290 (M⁺), C₁₈H₁₀O₄ requires 290.06. Characterization in accordance with literature.⁶¹⁵

PXX Peri-xanthenoxanthene

To a Schlenk flask was added 1,1'-bi-2-naphthol (0.50 g, 1.75 mmol), CuI (1.00 g, 5.25 mmol), PivOH (0.36 g, 3.52 mmol) and DMSO (20 mL). The resulting mixture was stirred open to air at 140 °C for 2 hrs. The mixture was cooled down, diluted with EtOAc and the organic phase washed with a sat. aq. solution of NH₄OH and brine. The aqueous phases were extracted with EtOAc. The combined organic layers were dried (Na₂SO₄) and evaporated under reduced pressure. The residue was purified by column chromatography (SiO₂, CHX/CH₂Cl₂, 8:2) affording product as a bright yellow powder (0.38 g, 77 % yield).

¹H NMR (500 MHz, Benzene-*d*₆): δ 6.88 (d, *J* = 9.0 Hz, 2H), 6.81 (d, *J* = 2.1 Hz, 2H), 6.80 (s, 2H), 6.68 (d, *J* = 9.0 Hz, 2H), 6.56 (dd, *J* = 5.2, 3.3 Hz, 2H). ¹³C NMR (126 MHz, Benzene-*d*₆): δ 153.18, 144.70, 131.76, 127.35, 126.55, 122.12, 120.36, 117.49, 112.00, 108.95. HRMS (EI⁺): found C₂₀H₁₀O₂ requires 282.0681, found 282.0682.

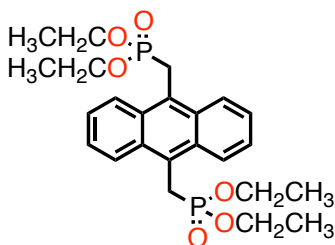
5-11 9,10-Bis(bromomethyl)anthracene

To a mixture of anthracene (1.9 g, 10.5 mmol), (HCHO)_{*n*} (1.2 g, 40.0 mmol) and AlCl₃ (catalytic amount) was added a solution of HBr (15 mL, 33 % HBr in CH₃COOH). The reaction mixture was heated to 50 °C for 5 hrs. The mixture was cooled down to r.t., the solid collected by filtration and

washed with H₂O. The product was obtained from crystallization from hot PhCH₃ as a bright yellow solid (2.3 g, 59 % yield).

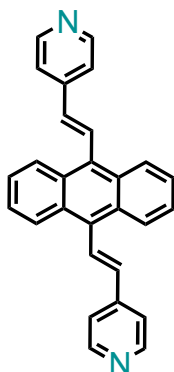
m.p. > 250 °C. ¹H NMR (500 MHz, Chloroform-*d*): δ 8.38 (dd, *J* = 7.1, 3.3 Hz, 4H, Ant-*H*_{1,4,5,8}), 7.68 (dd, *J* = 7.1, 3.3 Hz, 4H, Ant-*H*_{2,3,6,7}), 5.52 (s, 4H, Ant-*CH*₂Br). **MS** (ES +): found 364 (M⁺), C₁₆H₁₂Br₂ requires 361.93. Characterization in accordance with literature.⁶⁷⁶

5-12 9,10-Bis(diethylphosphorylmethyl)anthracene



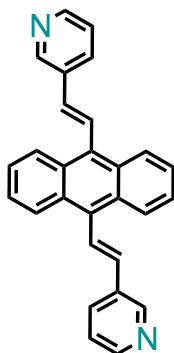
9,10-Bis(bromomethyl)anthracene **5-11** (1.2 g, 3.3 mmol) was added to triethyl phosphite (10 mL) and the resulting suspension was carefully heated up to 150 °C and heated overnight. The solution was left to cool down and the yellow solid was filtered and washed with water to afford an off-white solid in (1.2 g, 76 % yield)

¹H NMR (500 MHz, Chloroform-*d*): δ 8.38 (dd, *J* = 6.8, 3.3 Hz, 4H, Ant-*H*_{1,4,5,8}), 7.57 (dd, *J* = 6.8, 3.3 Hz, 4H, Ant-*H*_{2,3,6,7}), 4.24 (d, *J* = 20.3 Hz, 4H, Ant-*CH*₂-P), 3.94–3.76 (m, 8H, -POCH₂CH₃), 1.06 (t, *J* = 7.1 Hz, 12H, -POCH₂CH₃). **MS** (ES +): found 501.1 (M + Na⁺), requires 478.5. Characterization in accordance with literature.⁶⁷⁶

5-13a 9,10-Bis(*E*)-2-(pyridin-4-yl)vinyl)anthracene

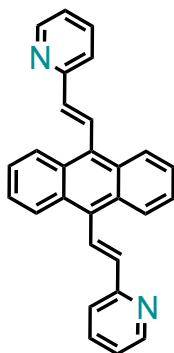
To a solution of 9,10-bis(diethylphosphorylmethyl)anthracene **5-12** (91 mg, 0.19 mmol) and 4-pyridinecarboxyaldehyde (60 mg, 0.56 mmol) in dry THF (15.0 mL) was added ^tBuONa (137 mg, 1.43 mmol) at r.t. under Ar. The color of the solution changed from yellow to orange and the reaction mixture was left stirring overnight. The solvent was removed under reduced pressure and the crude purified by column chromatography (SiO₂, CHX/AcOEt 1:1) to obtain the pure product as a bright yellow solid (47 mg, 64 % yield).

m.p. > 250 °C. ¹H NMR (500 MHz, Chloroform-*d*): δ 8.70 (d, *J* = 6.1 Hz, 4H, Pyr-*H*₂), 8.33 (dd, *J* = 6.7, 3.3 Hz, 4H, Ant-*H*_{1,4,5,8}), 8.17 (d, *J* = 16.5 Hz, 2H, Pyr-*CH=CH*-Ant), 7.55 (d, *J* = 6.2 Hz, 4H, Pyr-*H*₃), 7.52 (dd, *J* = 6.9, 3.2 Hz, 4H, Ant-*H*_{2,3,6,7}), 6.91 (d, *J* = 16.5 Hz, 2H, Pyr-*CH=CH*-Ant). ¹³C NMR (126 MHz, Chloroform-*d*): δ 150.72, 144.42, 135.50, 132.29, 130.11, 129.59, 126.36, 126.01, 121.18. MS (ES +): found 385.0 (M⁺), C₂₈H₂₀N₂ requires 384.5.

5-13b 9,10-Bis((*E*)-2-(pyridin-3-yl)vinyl)anthracene

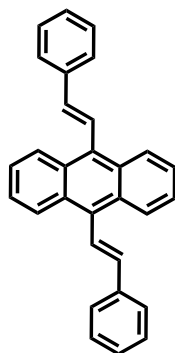
To a solution of 9,10-bis(diethylphosphorylmethyl)anthracene **5-12** (91 mg, 0.19 mmol) and 3-pyridinecarboxaldehyde (60 mg, 0.56 mmol) in dry THF (15.0 mL) was added ^tBuONa (137 mg, 1.43 mmol) at r.t. under Ar. The color of the solution changed from yellow to orange and the reaction mixture was left stirring overnight. The solvent was removed under reduced pressure and the crude purified by column chromatography (SiO₂, CHX/AcOEt 1:1) to obtain the pure product as a bright yellow solid (42 mg, 57 % yield).

m.p. > 250 °C. ¹H NMR (500 MHz, Chloroform-*d*): δ 8.89 (d, *J* = 1.9 Hz, 2H, Pyr-*H*₂), 8.61 (dd, *J* = 4.8, 1.6 Hz, 2H, Pyr-*H*₆), 8.37 (dd, *J* = 6.7, 3.3 Hz, 4H, Ant-*H*_{1,4,5,8}), 8.06 – 7.99 (m, 4H, Pyr-*H*₄ + Pyr-CH=CH-Ant), 7.52 (dd, *J* = 6.9, 3.2 Hz, 4H, Ant-*H*_{2,3,6,7}), 7.41 (dd, *J* = 7.8, 4.9 Hz, 2H, Pyr-*H*₅), 6.95 (d, *J* = 16.6 Hz, 2H, Pyr-CH=CH-Ant). ¹³C NMR (126 MHz, Chloroform-*d*): δ 149.36, 148.82, 134.25, 133.11, 133.01, 132.54, 129.70, 127.63, 126.46, 125.82, 123.91. MS (ES +): found 385.0 (M⁺), C₂₈H₂₀N₂ requires 384.5.

5-13c 9,10-Bis((*E*)-2-(pyridin-2-yl)vinyl)anthracene

To a solution of 9,10-bis(diethylphosphorylmethyl)anthracene **5-12** (91 mg, 0.19 mmol) and 2-pyridinecarboxaldehyde (60 mg, 0.56 mmol) in dry THF (15.0 mL) was added ^tBuONa (137 mg, 1.43 mmol) at r.t. under Ar. The color of the solution changed from yellow to orange and the reaction mixture was left stirring overnight. The solvent was removed under reduced pressure and the crude purified by column chromatography (SiO₂, CHX/AcOEt 1:1) to obtain the pure product as a bright yellow solid (51 mg, 70 % yield).

m.p. > 250 °C. ¹H NMR (500 MHz, Chloroform-*d*): δ 8.77 – 8.72 (m, 2H, Pyr-*H*₆), 8.56 (d, *J* = 16.1 Hz, 2H, Pyr-CH=CH-Ant), 8.44 (dd, *J* = 6.8, 3.3 Hz, 4H, Ant-*H*_{1,4,5,8}), 7.75 (td, *J* = 7.8, 1.6 Hz, 2H Pyr-*H*₄), 7.52 – 7.45 (m, 6H, Pyr-*H*₅ + Ant-*H*_{2,3,6,7}), 7.04 (d, *J* = 16.2 Hz, 2H, Pyr-CH=CH-Ant); two protons missing due to overlap with chloroform. ¹³C NMR (126 MHz, Chloroform-*d*): δ 155.50, 150.13, 136.95, 132.74, 129.97, 129.68, 126.67, 125.62, 122.73, 122.72. MS (ES +): found 385.0 (M⁺), C₂₈H₂₀N₂ requires 384.5.

5-13d 9,10-Bis((E)-styryl)anthracene

To a solution of 9,10-bis(diethylphosphorylmethyl)anthracene **5-12** (50 mg, 104 μmol) in dry THF (5.0 mL) under Ar was added $t\text{BuONa}$ (22 mg, 230 μmol) and the yellow solution turned brown. Finally, benzaldehyde (28 μL , 260 μmol) was added and the solution became bright yellow. The reaction mixture was stirred under Ar at r.t. overnight. The solvent was removed under reduced pressure and the crude was purified by column chromatography (SiO_2 , CHX) to obtain the pure product as a bright yellow solid (22 mg, 55 % yield).

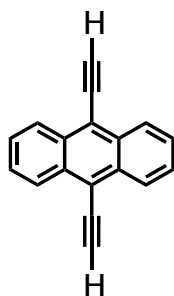
m.p. > 250 $^{\circ}\text{C}$. $^1\text{H NMR}$ (500 MHz, Chloroform- d): δ 8.41 (dd, $J = 6.8, 3.3$ Hz, 4H, Ant- $H_{1,4,5,8}$), 7.94 (d, $J = 16.5$ Hz, 2H), 7.72 – 7.68 (m, 4H, Ph- H_2), 7.51 – 7.45 (m, 8H, Ph- H_3 + Ant- $H_{2,3,6,7}$), 7.43 – 7.33 (m, 2H, Ph- H_4), 6.95 (d, $J = 16.5$ Hz, 2H, Pyr- $\text{CH}=\text{CH}$ -Ant). $^{13}\text{C NMR}$ (126 MHz, Chloroform- d): δ 137.70, 137.53, 132.92, 129.80, 129.07, 128.26, 126.83, 126.69, 125.47, 125.40. **MS** (ES +): found 382.2 (M^+), $\text{C}_{30}\text{H}_{22}$ requires 382.17.

5-14 9,10-Dibromoanthracene

To a solution of anthracene (2.50 g, 14.03 mmol) in CHCl_3 (50 mL) was added dropwise a solution of Br_2 (1.40 mL, 28.10 mmol) in CHCl_3 (25 mL). The mixture was stirred for 4 hrs. The solvent was removed under reduced pressure and the crude solid was purified by re-crystallization from CH_2Cl_2 yielding the product as yellow needles (4.43 g, 94 % yield).

m.p. 217-219 °C. $^1\text{H NMR}$ (500 MHz, Chloroform-*d*): δ 8.59 (dd, $J = 6.8, 3.2$ Hz, 4H, Ant- $H_{1,4,5,8}$), 7.64 (dd, $J = 6.8, 3.2$ Hz, 4H, Ant- $H_{2,3,6,7}$). $^{13}\text{C-NMR}$ (125 MHz, Chloroform-*d*): δ 131.05, 128.27, 127.45, 123.52. **MS** (ES +): found 336.0 (M^+), $\text{C}_{14}\text{H}_8\text{Br}_2$ requires 333.90. Characterization in accordance with literature.⁶⁷⁷

5-15 9,10-Diethynylantracene

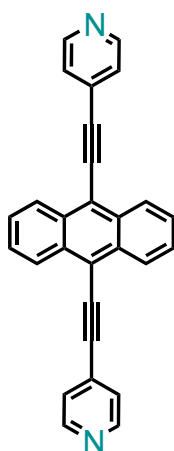


To a degassed solution of 9,10-dibromoanthracene **5-14** (0.50 g, 1.49 mmol) in THF/*i*Pr₂NH (10 mL, 1:1) was added Pd(PPh₃)₂Cl₂ (53 mg, 0.08 mmol) and CuI (29 mg, 0.15 mmol) and finally TMSA (0.86 mL, 6.00 mmol). The mixture was heated to 80 °C and stirred overnight. The mixture was filtered over celite (CH_2Cl_2), the solvent removed under reduced pressure and the crude product was further purified by column chromatography (SiO₂, CHX) to obtain the TMS protected intermediate as dark red solid.

To a degassed solution of the TMS-protected intermediate (0.34 g, 0.92 mmol) in THF (15 mL) was added a solution of KOH (0.11 g, 1.932). After 1 h, the mixture was diluted (CH_2Cl_2) and the organic phase was washed with H₂O and dried (Na₂SO₄). The solvents were removed under reduced pressure to obtain product as yellow-brownish solid (0.22 g, 56 % yield over two steps).

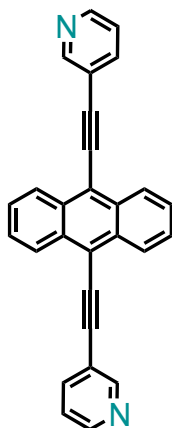
$^1\text{H NMR}$ (500 MHz, Chloroform-*d*): δ 8.62 (dd, $J = 6.6, 3.3$ Hz, 4H, Ant- $H_{1,4,5,8}$), 7.63 (dd, $J = 6.7, 3.2$ Hz, 4H, Ant- $H_{2,3,6,7}$), 4.08 (s, 2H, Ant- CCH). $^{13}\text{C NMR}$ (126 MHz, Chloroform-*d*): δ 132.45, 127.02, 127.00, 117.78, 89.85, 80.17. **MS** (ES +): found 226.1 (M^+), $\text{C}_{18}\text{H}_{10}$ requires 226.08. Characterization in accordance with literature.⁶⁷⁸

5-16a 9,10-Bis(pyridin-4-ylethynyl)anthracene



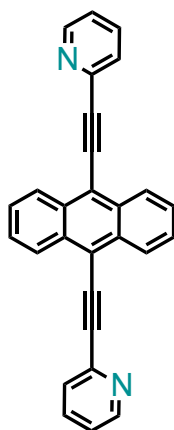
To a degassed solution of dry Et_3N (2.0 mL) and THF (2.0 mL), 9,10-diethynylanthracene **5-15** (100 mg, 442 μmol), $\text{Pd}(\text{PPh}_3)_4$ (13 mg, 11 μmol) and CuI (4 mg, 22 μmol) were added and the mixture degassed a second time. 4-Iodopyridine (271 mg, 1326 μmol) was then added, the reaction mixture degassed one last time and stirred overnight, at r.t. under Ar. The crude mixture was filtered over celite (CHCl_3), concentrated under reduced pressure and purified by column chromatography (SiO_2 , $\text{CH}_2\text{Cl}_2/\text{MeOH}$ 99:1) yielding product as a dark red solid (80 mg, 48 % yield).

m.p. > 250 $^\circ\text{C}$. $^1\text{H NMR}$ (500 MHz, Chloroform-*d*): δ 8.73 (d, $J = 5.5$ Hz, 4H, Pyr- H_2), 8.65 (dd, $J = 6.5, 3.1$ Hz, 4H, Ant- $H_{1,4,5,8}$), 7.70 (dd, $J = 6.7, 3.2$ Hz, 4H, Ant- $H_{2,3,6,7}$), 7.63 (d, $J = 5.7$ Hz, 4H, Pyr- H_3). $^{13}\text{C NMR}$ (126 MHz, Chloroform-*d*): δ 150.27, 132.47, 131.43, 127.66, 127.24, 125.69, 118.42, 99.92, 90.82. **MS** (ES +): found 191.1 (M^{2+}), 381.1 (M^+), $\text{C}_{28}\text{H}_{16}\text{N}_2$ requires 380.1.

5-16b 9,10-Bis(pyridin-3-ylethynyl)anthracene

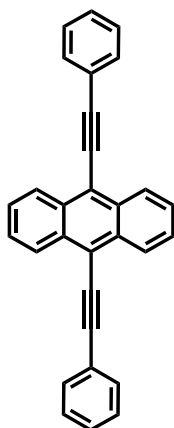
To a degassed solution of dry Et₃N (2.0 mL) and THF (2.0 mL), 9,10-diethynylanthracene **5-15** (100 mg, 442 μmol), Pd(PPh₃)₄ (13 mg, 11 μmol) and CuI (4 mg, 22 μmol) were added and the mixture degassed a second time. 3-Iodopyridine (271 mg, 1326 μmol) was then added, the reaction mixture degassed one last time and stirred overnight, at r.t. under Ar. The crude mixture was filtered over celite (CHCl₃), concentrated under reduced pressure and purified by column chromatography (SiO₂, CH₂Cl₂/MeOH 95:5) yielding product as a dark red solid (55 mg, 33 % yield).

m.p. > 250 °C. ¹H NMR (500 MHz, Chloroform-*d*): δ 9.02 (s, 2H, Pyr-*H*₂), 8.70 – 8.62 (m, 6H, Ant-*H*_{1,4,5,8} + Pyr-*H*₆), 8.05 (dt, *J* = 7.8, 1.8 Hz, 2H, Pyr-*H*₄), 7.68 (dd, *J* = 6.6, 3.2 Hz, 4H, Ant-*H*_{2,3,6,7}), 7.40 (dd, *J* = 7.4, 5.3 Hz, 2H, Pyr-*H*₅). ¹³C NMR (126 MHz, Chloroform-*d*): δ 152.46, 149.26, 138.68, 132.33, 127.43, 127.31, 123.48, 120.74, 118.44, 99.18, 89.79. MS (ES +): found 191.1 (M²⁺), 381.1 (M⁺), C₂₈H₁₆N₂ requires 380.1.

5-16c 9,10-Bis(pyridin-2-ylethynyl)anthracene

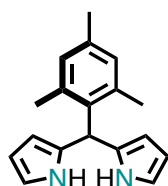
To a degassed solution of dry Et_3N (2.0 mL) and THF (2.0 mL), 9,10-diethynylanthracene **5-15** (100 mg, 442 μmol), $\text{Pd}(\text{PPh}_3)_4$ (13 mg, 11 μmol) and CuI (4 mg, 22 μmol) were added and the mixture degassed a second time. 2-Iodopyridine (271 mg, 1326 μmol) was then added, the reaction mixture degassed one last time and stirred overnight, at rt under Ar. The crude mixture was filtered over celite (CHCl_3), concentrated under reduced pressure and purified by column chromatography (SiO_2 , $\text{CH}_2\text{Cl}_2/\text{MeOH}$ 95:5) yielding product as a dark red solid (87 mg, 52 % yield).

m.p. > 250 °C. $^1\text{H NMR}$ (500 MHz, Chloroform-*d*): δ 8.78 – 8.74 (m, 6H, Pyr- H_6 + Ant- $H_{1,4,5,8}$), 7.82 – 7.77 (m, 4H, Pyr- $H_{3,4}$), 7.67 (dd, $J = 6.7, 3.2$ Hz, 4H, Ant- $H_{2,3,6,7}$), 7.36 – 7.31 (m, 2H, Pyr- H_2). $^{13}\text{C NMR}$ (126 MHz, Chloroform-*d*): δ 150.64, 143.81, 136.51, 132.64, 127.83, 127.48, 123.31, 118.44, 101.85, 86.33. **MS** (ES +): found 191.1 (M^{2+}), 381.1 (M^+), $\text{C}_{28}\text{H}_{16}\text{N}_2$ requires 380.1.

5-16d 9,10-bis(phenylethynyl)anthracene

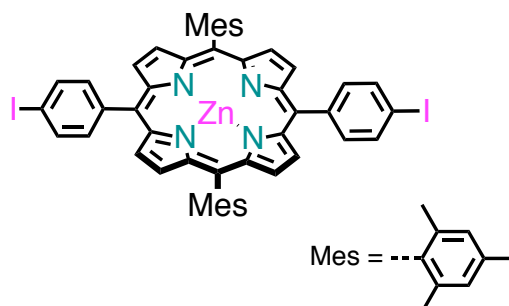
To a degassed solution of dry Et₃N (2 mL) and THF (2 mL), 9,10-diethynylanthracene **5-15** (100 mg, 442 μmol), Pd(PPh₃)₄ (13 mg, 11 μmol) and CuI (4 mg, 22 μmol) were added and the mixture degassed a second time. Iodobenzene (270 mg, 1326 μmol) was then added, the reaction mixture degassed one last time and stirred overnight, at rt under Ar. The crude mixture was filtered over celite (CHCl₃), concentrated under reduced pressure and the crude purified by column chromatography (SiO₂, CHX) yielding product as a yellow solid (106 mg, 64 % yield).

m.p. > 250 °C. ¹H NMR (500 MHz, Chloroform-*d*): δ 8.74 – 8.67 (dd, *J* = 6.5, 3.1 Hz, 4H, Ant-*H*_{1,4,5,8}), 7.79 (d, *J* = 7.3 Hz, 4H, Ph-*H*₂), 7.65 (dd, *J* = 6.7, 3.2 Hz, 4H, Ant-*H*_{2,3,6,7}), 7.50 – 7.40 (m, 6H, Ph-*H*_{3,4}). ¹³C NMR (126 MHz, Chloroform-*d*): δ 132.44, 131.95, 128.92, 128.81, 127.53, 127.04, 123.80, 118.80, 102.70, 86.82. MS (ES +): 378.2 (M⁺), C₃₀H₁₈ requires 378.14.

5-17 *Meso*-(mesityl)dipyrromethane

To a degassed solution of mesitaldehyde (1.47 mL, 9.97 mmol) and pyrrole (27.8 mL, 0.40 mol) $\text{BF}_3 \cdot \text{OEt}_2$ (0.369 mL, 3.0 mmol) was added. The light brown mixture was stirred for 30 min at r.t., then diluted with CH_2Cl_2 , washed with 0.1 M aq. NaOH solution. The organic phase was washed with H_2O and dried (Na_2SO_4). Evaporation of the solvent under reduced pressure resulted in a brown oil. Unreacted pyrrole was removed by further evaporation to yield a light brown solid. The crude was purified by column chromatography (SiO_2 , CHX/AcOEt 4:1) to yield the product as a light yellow solid (1.04 g, 39 % yield).

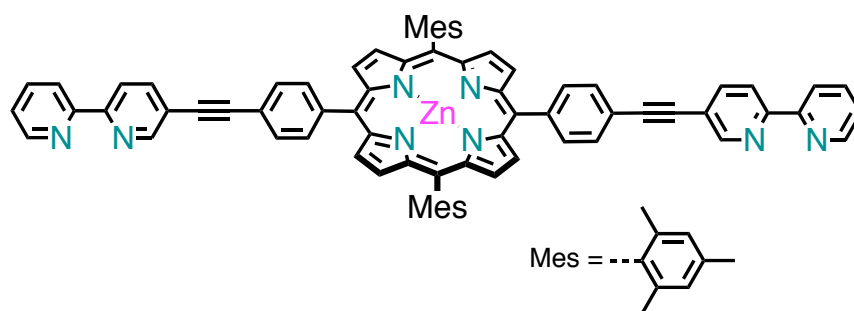
m.p. 165-167 °C. $^1\text{H NMR}$ (200 MHz, Chloroform-*d*): δ 7.95 (bs, 2H, Py-NH), 6.88 (s, 4H, Ar-H), 6.67 (t, 2H, Py-H), 6.19 (q, 2H, Py-H), 6.03 (t, 2H, Py-H), 5.92 (s, 1, meso-H). **MS** (ES): found 264.3 (M^+), $\text{C}_{18}\text{H}_{20}\text{N}_2$ requires 264.16. Characterization in accordance with literature.⁶⁷⁹

5-18 Zn(II) 5,15-Dimesityl-10,20-bis(4-iodophenyl)porphyrin

A solution of 4-iodobenzaldehyde (232 mg, 1.0 mmol) and *meso*-(mesityl)dipyrromethane **5-17** (264 mg, 0.1 mmol) in CHCl_3 (100 mL) was purged with Ar for 10 min, then $\text{BF}_3 \cdot \text{OEt}_2$ (42 μL , 0.33 mmol) was added. The solution was stirred for 1 h at r.t. and then DDQ (172 mg, 0.76 mmol) was added. The mixture was stirred at r.t. for an additional 1 h and then the mixture was concentrated under reduced pressure and then filtered through a silica plug. The purple solid was redissolved in CHCl_3 (10 mL) and sat. methanolic solution of $\text{Zn}(\text{OAc})_2 \cdot 2\text{H}_2\text{O}$ and left stirring under dark for 4 hrs. The organic phase was washed with 0.1 M aq. NaHCO_3 solution, H_2O , dried (Na_2SO_4) and eliminated under reduced pressure. Purification by column chromatography (SiO_2 , $\text{CHX}/\text{CH}_2\text{Cl}_2$ 85:15) afforded the porphyrin as the first moving band (323 mg, 32% yield).

m.p. > 250 °C. $^1\text{H NMR}$ (200 MHz, Chloroform-*d*): δ 8.83 (dd, 8H, $J = 4.6$ Hz), 8.10 (dd, 8H, $J = 8.2$ Hz), 7.29 (s, 4H, partial overlap with solvent), 2.64 (s, 6H), 1.82 (s, 12H). **MS** (ES⁺): found 1012.1, $\text{C}_{50}\text{H}_{38}\text{I}_2\text{N}_4\text{Zn}$ requires 1012.05. Characterization in accordance with literature.⁶⁷⁹

5-19 Zn(II) 5,15-Dimesityl-10,20-bis(4-[[2,2'-bipyridin]-5-ylethynyl]phenyl)porphyrin

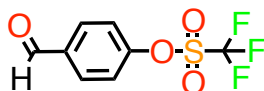


A 10 mL microwave-reactor tube containing a stirring bar was charged with Zn(II) 5,15-dimesityl-10,20-bis(4-iodophenyl)porphyrin **5-18** (85 mg, 0.084 mmol) and $\text{Pd}(\text{PPh}_3)_4$ (17 mg, 0.015 mmol) and was purged with argon. DMF/ Et_3N (2:1 ml) were added by syringe, 5-ethynyl-2,2'-bipyridine **5-23** (32 mg, 0.176 mmol) was added and the reaction vessel was sealed and placed into the microwave reactor. The temperature heating profile for the reaction mixture was as follows: r.t. \rightarrow 120 °C over a 2-min period (200-W maximum power), the temperature was held at 120 °C (dynamic, 200-W maximum power) for a set amount of time (60 min). The crude reaction mixture was diluted with

CHCl₃ and washed with H₂O, dried (Na₂SO₄) and concentrated. The crude was purified by column chromatography (SiO₂, CHX/AcOEt 7:3) to afford the product as a purple solid (67 mg, 71% yield).

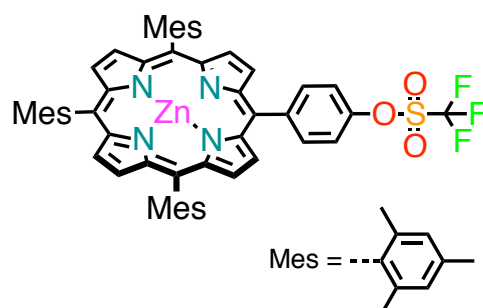
m.p. > 250 °C. ¹H NMR (500 MHz, Dimethylsulfoxide-*d*₆): δ 9.02 (d, 2H, *J* = 1.0 Hz), 8.76 (m, 6H), 8.61 (d, 4H, *J* = 5 Hz), 8.53 (d, 2H, *J* = 8.0 Hz), 8.28-8.25 (m, 6H), 8.02-7.99 (m, 6H), 7.53-7.50 (m, 4H), 7.32 (s, 4H), 2.58 (s, 6H), 1.79 (s, 12H). ¹³C NMR was not performed due to low solubility of the compound. MS (ES): found 1118.9 (M+2H⁺), 1141.9 (M+Na⁺), C₇₄H₅₂N₈Zn requires 1116.36.

5-20 4-Formylphenyl trifluoromethanesulfonate



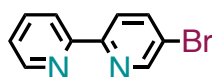
To a solution of 4-hydroxybenzaldehyde (1.21 g, 10 mmol) in pyridine (10 mL) at 0 °C and was added triflic anhydride (1.85 mL, 11 mmol) was added dropwise at 0 °C and stirred for 10 minutes at 0 °C. The reaction was then allowed to stir at r.t. for 12 hrs. The solution was diluted with Et₂O and extracted with a 1 M aq. K₂CO₃ solution. The organic layer was then washed with H₂O, dried (Na₂SO₄), and concentrated under reduced pressure. The crude product was purified via column chromatography (SiO₂, 4:1 CHX/EtOAc) and the desired product was obtained as a colorless liquid (2.16 g, 85 % yield).

¹H NMR (500 MHz, Chloroform-*d*): δ 10.05 (s, 1H), 8.00 (d, *J* = 8.7 Hz, 2H), 7.46 (d, *J* = 8.7 Hz, 2H). ¹³C NMR (126 MHz, Chloroform-*d*): δ 190.05, 153.18, 135.89, 131.71, 118.66, 109.99. MS (ES): found 254.0 (M⁺), C₈H₅F₃O₄S requires 253.99. Characterization in accordance with literature.⁶⁸⁰

5-21 5,10,15-Trimesityl-20-(4-triflylphenyl)porphyrin

A solution of 4-formylphenyl trifluoromethanesulfonate **5-20** (0.68 g, 2.66 mmol), mesitaldehyde (1.18 mL, 7.98 mmol) and pyrrole (0.74 mL, 10.64 mmol) was purged with Ar for 15 minutes before $\text{BF}_3 \cdot \text{OEt}_2$ (0.50 mL, 3.54 mmol) was added. After 1 h at r.t., *p*-chloranil (2.04 g, 8.13 mmol) was added in and the reaction mixture was left stirring. After 1 h, Et_3N (490 μL , 3.54 mmol) was added, and the solution was evaporated to dryness. The crude product was scraped from the flask, placed on a filter, and washed with methanol until the filtrate was clear. The porphyrin mixture was dissolved in CHCl_3 (50 mL) and metalated with a methanolic solution of $\text{Zn}(\text{OAc})_2 \cdot \text{H}_2\text{O}$ (438, 2.00 mmol) and left stirring overnight under dark. The reaction mixture was washed with 0.1 M aq. NaHCO_3 solution, dried (Na_2SO_4), and concentrated under reduced pressure, affording the zinc chelate as a purple solid. A fraction of the porphyrin mixture was purified by column chromatography (SiO_2 , CHX/AcOEt 9:1) to obtain the product as a purple solid (80 mg, 8 % yield).

m.p. > 250 °C. $^1\text{H NMR}$ (200 MHz, Chloroform-*d*): δ 8.77 (m, 8H), 8.08 (AA'BB', 2 H), 7.94 (AA'BB', 2H), 7.29 (s, 6H), 2.64 (s, 8H), 1.82 (s, 18H). **MS** (ES): calculated for $\text{C}_{54}\text{H}_{45}\text{F}_3\text{N}_4\text{O}_3\text{SZn}$ 950.25, found 950.4 (M^+).

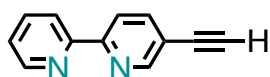
5-22 5-Bromo-2,2'-bipyridine

To a solution of 2-bromopyridine (2.0 g, 12.6 mmol) in dry THF (10.0 mL) was added dropwise ⁿBuLi (10.0 mL, 1.6 M in hexane, 15.8 mmol) at -78 °C and the mixture was stirred for 1 h. Bu₃SnCl (4.3 mL, 15.9 mmol) was added to the solution at -78 °C, and stirring continued for 3 hrs at -78 °C, and 30 mins at room temperature. The reaction was quenched with sat. aq. NH₄Cl solution (10 mL) and extracted with EtOAc. The organic phase was washed with H₂O, brine, dried (Na₂SO₄) and removed under reduced to give 2-(tributylstannyl) pyridine as a dark brown liquid. The resulting intermediate was used in the following reaction without any further treatment.

To a degassed solution of 2,6-dibromopyridine (2.6 g, 11.0 mmol) and 2-(tributylstannyl)pyridine (3.8 g, 10.3 mmol) in PhCH₃ (5.0 mL) was added Pd(PPh₃)₄ (608 mg, 0.53 mmol). The reaction was refluxed overnight. The reaction mixture was cooled to r.t., 2 M aq. NaOH was added, the mixture extracted with PhCH₃ and dried (Na₂SO₄). The solvent was removed under reduced pressure and the crude solid product was purified via column chromatography (SiO₂, CHX/EtOAc 5:1) to yield product as white crystalline powder (2.1 g, 87 % yield).

m.p. 70-72 °C. ¹H NMR (500 MHz, Chloroform-*d*): δ 8.72 (dd, *J* = 2.4, 0.7 Hz, 1H), 8.67 (ddd, *J* = 4.8, 1.8, 0.9 Hz, 1H), 8.37 (dt, *J* = 8.0, 1.1 Hz, 1H), 8.32 (dd, *J* = 8.5, 0.8 Hz, 1H), 7.94 (dd, *J* = 8.5, 2.4 Hz, 1H), 7.82 (td, *J* = 7.8, 1.8 Hz, 1H), 7.33 (ddd, *J* = 7.5, 4.8, 1.2 Hz, 1H). ¹³C NMR (126 MHz, Chloroform-*d*): δ 155.38, 150.42, 149.44, 139.72, 137.26, 124.22, 122.57, 121.37, 121.21. MS (ES +): found 234.9 (M + H⁺), C₁₀H₇BrN₂ requires 233.98. Characterization in accordance with literature.⁶⁸¹

5-23 5-Ethynyl-2,2'-bipyridine



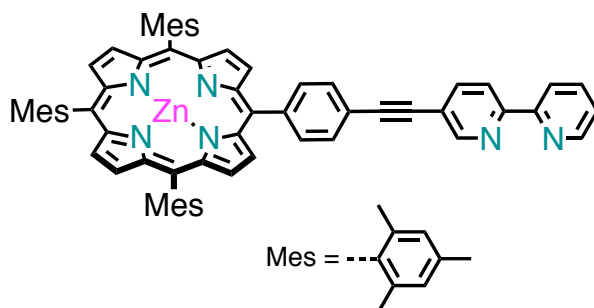
To a degassed solution of 5-bromo-2,2'-bipyridine (600 mg, 2.55 mmol), TMSA (0.73 mL, 5.10 mmol) and PPh₃ (15 mg, 0.06 mmol) in Et₃N (30 mL) was added Pd(PPh₃)₂Cl₂ (20 mg, 0.028 mmol) and the solution was further degassed, finally CuI (11 mg, 0.06 mmol) was added. After stirring, was added via syringe. The mixture was then heated to 80 °C overnight. The solvent was removed under

reduced pressure, the crude dissolved in CH_2Cl_2 , the organic phase was washed with H_2O and dried (Na_2SO_4). After removal of the solvent, the crude product was purified with column chromatography (SiO_2 , CHX/EtOAc 5:1) to obtain a colorless oil. $^1\text{H NMR}$ (500 MHz, Chloroform- d): δ 8.74 (dd, $J = 2.1, 0.9$ Hz, 1H), 8.69 (ddd, $J = 4.8, 1.8, 0.9$ Hz, 1H), 8.41 (dt, $J = 8.0, 1.0$ Hz, 1H), 8.37 (dd, $J = 8.3, 0.9$ Hz, 1H), 7.88 (dd, $J = 8.2, 2.1$ Hz, 1H), 7.86 – 7.79 (m, 1H), 7.32 (ddd, $J = 7.4, 4.8, 1.2$ Hz, 1H), 0.30 (s, 9H).

To a solution of the above TMS-protected intermediate (480 mg, 1.90 mmol) in MeOH (25 mL) was added K_2CO_3 (26 mg, 0.19 mmol) and the solution was stirred at room temperature for 3 hrs. CH_2Cl_2 and H_2O were added, the organic layer was separated, and the aqueous layer was extracted with CH_2Cl_2 . The combined organic layers were washed with brine, dried (Na_2SO_4) and the solvent was removed under reduced pressure to yield the product as white solid (340 mg, 74% yield over two steps).

$^1\text{H NMR}$ (500 MHz, Chloroform- d): δ 8.77 (dd, $J = 2.2, 0.9$ Hz, 1H), 8.69 (ddd, $J = 4.8, 1.8, 0.9$ Hz, 1H), 8.42 – 8.38 (m, 2H), 7.90 (dd, $J = 8.2, 2.1$ Hz, 1H), 7.83 (ddd, $J = 8.0, 7.5, 1.8$ Hz, 1H), 7.32 (ddd, $J = 7.5, 4.8, 1.2$ Hz, 1H), 3.29 (s, 1H). $^{13}\text{C NMR}$ (126 MHz, Chloroform- d): δ 155.65, 155.55, 152.42, 149.51, 140.23, 137.21, 124.26, 121.63, 120.49, 119.32, 81.52, 80.91. **MS** (ES $^+$): found 202.9 ($M + \text{H}^+$), $\text{C}_{12}\text{H}_8\text{N}_2$ requires 180.07. Characterization in accordance with literature.⁶⁸²

5-24 Zn(II) 5,10,15-Trimesityl-20-(4-[[2,2'-bipyridin]-5-ylethynyl]phenyl)porphyrin

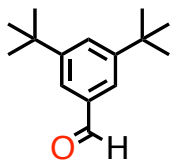


In a 10 mL microwave-reactor tube containing a stirring bar, 5,10,15-trimesityl-20-(4-triflylphenyl)porphyrin **5-21** (30.0 mg, 0.031 mmol), $\text{Pd}(\text{PPh}_3)_4$ (5.1 mg, 4.41 μmol) and LiCl (10.5

mg, 0.248 mmol) were dissolved in DMF/Et₃N (2:1 ml) and was purged with argon. 5-Ethynyl-2,2'-bipyridine **5-23** (7.0 mg, 0.038 mmol) was added and the reaction vessel was sealed and placed into the microwave reactor. The temperature heating profile for the reaction mixture was as follows: r.t. → 120 °C over a 2-min period (200-W maximum power), the reaction mixture was held at 120 °C (dynamic, 200-W maximum power) for a set amount of time (60 min). The crude reaction mixture was diluted with CHCl₃ and washed with H₂O, dried (Na₂SO₄) and concentrated. The crude was purified by column chromatography (SiO₂, CHX/AcOEt 9:1) to afford the product as a purple solid (21 mg, 68 % yield).

m.p. > 250 °C. ¹H NMR (500 MHz, Dimethylsulfoxide-*d*₆): δ 9.02 (s, 1H), 8.76 (m, 1H), 8.72 (dd, 2H, *J* = 4.5 Hz), 8.57 (dd, 2H, *J* = 72.7, 8.0 Hz), 8.53 (m, 3H), 8.47 (d, 1H, *J* = 8.47), 8.31 (s, 6H), 8.28-8.23 (m, 2H), 8.02-8.00 (m, 2H), 7.54-7.51 (m, 1H), 7.31 (s, 6H), 2.58 (s, 9H), 1.79 (m, 18H).

3,5-Di-*tert*-butylbenzaldehyde

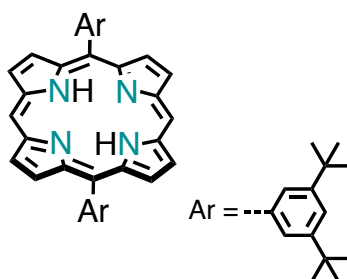


A mixture of 3,5-di-*tert*-butyltoluene (10.0 g, 48.8 mmol), *N*-bromosuccinimide (17.4 g, 97.6 mmol) and benzoyl peroxide (0.1 g, 0.5 mmol) in CCl₄ (90 mL) was refluxed for 4 hrs. The solution was cooled, filtered and concentrated under reduced pressure to afford a yellow oil that was used directly in the next step. The crude material (17.7 g, 48.8 mmol) and hexamethylenetetraamine (28.5 g, 203.0 mmol) in MeOH/H₂O (80 mL, 1:1) was refluxed for 5 hrs. At this point, conc. HCl (25 mL of 37 % aq. soln.) was added dropwise and the mixture refluxed for 30 min. The mixture was cooled down and extracted with CH₂Cl₂, the organic phase dried (Na₂SO₄) and concentrated under reduced pressure. Crystallization from hot MeOH/H₂O (1:1) gave white crystals as product (9.3 g, 87 % yield).

m.p. 85-88 °C. ¹H NMR (500 MHz, Chloroform-*d*): δ 10.01 (s, 1H), 7.75 – 7.68 (m, 3H), 1.37 (s, 18H). ¹³C NMR (126 MHz, Chloroform-*d*): δ 193.40, 152.05, 136.42, 129.09, 124.36, 35.19, 31.54.

MS (ES +): found 241.0 ($M + Na^+$), $C_{15}H_{22}O$ requires 218.17. Characterization in accordance with literature.⁶⁸³

5-24 5,15-Bis[3,5-di(*tert*-butyl)phenyl]porphyrin



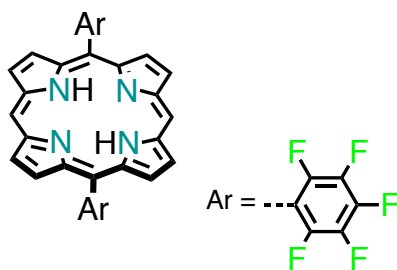
Method A⁶⁸⁴: A solution of dipyrromethane **3-2** (1.2 g, 8.3 mmol) and 3,5-di-*tert*-butylbenzaldehyde (1.9 g, 8.5 mmol) in CH_2Cl_2 (2.0 L) was degassed by bubbling Ar through for 1 h. TFA (145 μ L, 1.8 mmol) was added dropwise, and the mixture was vigorously stirred in the dark at r.t. for 16 hrs. *p*-Chloranil (6.2 g, 25.1 mmol) was added, and the mixture was heated to reflux for 2 hrs. The mixture was then concentrated, and stirred with 0.1 M aq. $Na_2S_2O_3$ soln. and MeOH (100 mL) until all *p*-chloranil was consumed. The org. phase was separated and washed with H_2O , dried (Na_2SO_4), and the solvent was removed under reduced pressure. The crude was purified by column chromatography (SiO_2 , CHX/ CH_2Cl_2 1:1) and precipitation from CH_2Cl_2 /MeOH yielded product (1.1 g, 38 % yield).

Method B⁶⁸⁵: A solution of 3,5-di-*tert*-butylbenzaldehyde (1.79 g, 8.21 mmol) and dipyrromethane **3-2** (1.20 g, 8.21 mmol) in CH_2Cl_2 (1.6 L) was degassed three times by evacuation and purging with Ar. TFA (0.37 mL, 4.9 mmol) was added and the reaction mixture stirred in the dark for 3 hrs. DDQ (2.42 g, 10.7 mmol) was added and stirring continued for 30 min. After quenching of the acid by addition of Et_3N (8 mL) the mixture was passed over a short silica plug (CH_2Cl_2). The crude was purified by column chromatography (SiO_2 , CHX/ CH_2Cl_2 1:1) and finally crystallized from CH_2Cl_2 /MeOH to yield product (1.52 g, 54 % yield).

m.p. > 250 °C. **1H NMR** (500 MHz, Chloroform-*d*): δ 10.32 (s, 2H, meso-*H*), 9.41 (d, $J = 4.5$ Hz, 4H, Pyr-*H*), 9.15 (d, $J = 4.5$ Hz, 4H, Pyr-*H*), 8.16 (d, $J = 1.8$ Hz, 4H, Ar-*H*), 7.85 (t, $J = 1.9$ Hz, 2H, Ar-*H*),

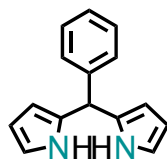
1.59 (s, 36H, Ar-C(CH₃)₃), -2.99 (s, 2H, Pyr-NH). **MS** (ES +): found 686.4 (M⁺), C₄₈H₅₄N₄ requires 686.43. Characterization in accordance with literature.^{684,685}

5-29 5,15-Bis(pentafluorophenyl)porphyrin



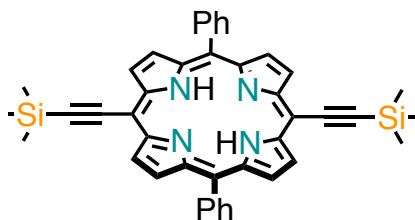
A solution of dipyrromethane **3-2** (0.44 g, 3.00 mmol) and pentafluorobenzaldehyde (0.59 g, 3.00 mmol) in CHCl₃ (0.30 L) was degassed with Ar for 15 min before being treated with BF₃·OEt₂ (0.12 mL, 0.97 mmol). The reaction vessel was shielded from ambient light and stirred under Ar for 3 hrs. DDQ (2.04 g, 8.99 mmol) was added to the reaction mixture and was stirred for 1 h. After concentration of the mixture, silica gel was added and the resulting slurry was concentrated to dryness and dry-loaded on a column chromatography (SiO₂, CHX/CH₂Cl₂ 4:1) to afford a purple solid (0.11 g, 6 % yield).

m.p. > 250 °C. ¹H NMR (500 MHz, Tetrahydrofuran-*d*₈): δ 10.54 (s, 2H, meso-*H*), 9.59 (d, *J* = 4.6 Hz, 4H, Pyr-*H*), 9.18 (d, *J* = 4.6 Hz, 4H, Pyr-*H*), -3.22 (s, 2H, Pyr-NH). **MS** (ES +): found 642.2 (M⁺), C₃₂H₁₂F₁₀N₄ requires 642.09. Characterization in accordance with literature.⁶⁸⁶

5-30 5-Phenyldipyrromethane

A solution of benzaldehyde (0.44 mL, 4.32 mmol) and pyrrole (30 mL, 412.22 mmol) was degassed with Ar for 15 min. MgBr₂ (0.40 g, 2.16 mmol) was added and the mixture stirred at r.t. for 1.5 hrs. The reaction mixture was treated with powdered NaOH (0.86 g, 21.6 mmol), stirred for 1 h and filtered. The filtrate was concentrated to dryness and the crude purified by column chromatography (SiO₂, CHX/AcOEt 9:1) to yield product as white powder (0.65 g, 66 % yield).

m.p. 98-100 °C. **¹H NMR** (500 MHz, Chloroform-*d*): δ 7.92 (bs, 2H), 7.35 – 7.29 (m, 2H), 7.25 – 7.20 (m, 2H), 6.72 – 6.68 (m, 2H), 6.16 (q, *J* = 2.9 Hz, 2H), 5.95 – 5.89 (m, 1H), 5.49 (s, 1H). **¹³C NMR** (126 MHz, Chloroform-*d*): δ 132.67, 132.30, 128.87, 128.62, 127.21, 117.40, 108.67, 107.43, 44.23. **MS** (ES +): found 223. 2 (M + H⁺), C₁₅H₁₄N₂ requires 222.12. Characterization in accordance with literature.⁶⁶²

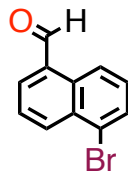
5-31 5,15-Bis(trimethylsilylethynyl)-10,20-diphenylporphyrin

A solution of dipyrromethane **5-30** (0.40 g, 1.80 mmol) and TMS-propynal (0.26 mL, 1.80 mmol) in CH₂Cl₂ (150 mL) was degassed with a stream of Ar, at 0 °C. BF₃·OEt₂ (0.04 mL, 0.32 mmol) was added and the reaction allowed to stir for 5 min. DDQ (0.42 g, 1.86 mmol) was added and the reaction

was stirred at r.t. for 30 min. Upon addition of Et₃N (1 mL), the mixture was filtered through a silica plug (CH₂Cl₂) and concentrated under reduced pressure. The crude was purified by column chromatography (SiO₂, CHX/ CH₂Cl₂ 4:1) and finally precipitated from CH₂Cl₂/MeOH to yield the final product (0.31 g, 26 % yield)

m.p. > 250 °C. ¹H NMR (500 MHz, Chloroform-*d*): δ 9.60 (d, *J* = 4.7 Hz, 4H), 8.82 (d, *J* = 4.7 Hz, 4H), 8.18 (dd, *J* = 7.7, 1.6 Hz, 4H), 7.83 – 7.71 (m, 6H), 0.60 (s, 18H). ¹³C NMR (126 MHz, Chloroform-*d*): δ 141.50, 134.71, 128.17, 127.09, 121.96, 107.02, 102.90, 101.03, 0.50. MS (ES +): found 654.3 (M⁺), C₄₂H₃₈N₄Si₂ requires 654.26. Characterization in accordance with literature.⁶⁸⁷

5-32 5-Bromo-1-naphthaldehyde



To a flask containing 1-naphthaldehyde (4.3 mL, 32.0 mmol) was added a solution of Br₂ (1.7 mL, 32.0 mmol) in CHCl₃ (7.5 mL) and the reaction mixture was refluxed for 4 hrs. The mixture was cooled down and filtered. The filtrate was washed with H₂O, brine and dried (Na₂SO₄). The pale yellow solid was crystallized from hot ethanol to give product as white solid (3.1 g, 41 % yield).

m.p. 97-99 °C. ¹H NMR (500 MHz, Chloroform-*d*): δ 10.41 (s, 1H), 9.28 (dd, *J* = 8.6, 1.0 Hz, 1H), 8.59 (dd, *J* = 8.5, 1.1 Hz, 1H), 8.05 (dd, *J* = 7.0, 1.2 Hz, 1H), 7.90 (dd, *J* = 7.5, 1.0 Hz, 1H), 7.75 (dd, *J* = 8.5, 7.1 Hz, 1H), 7.53 (dd, *J* = 8.6, 7.5 Hz, 1H). ¹³C NMR (126 MHz, Chloroform-*d*): δ 193.15, 137.42, 134.45, 132.50, 132.17, 131.80, 131.47, 129.56, 126.47, 124.93, 123.61. MS (ES +): found 234.1 (M⁺), C₁₁H₇BrO requires 233.97. Characterization in accordance with literature.⁶⁸⁸

5-33 Zn(II) 5,15-Bis(5-bromo-1-naphthyl)porphyrin

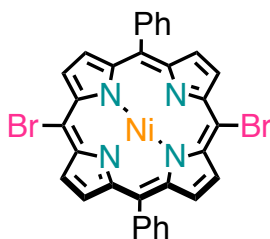
To a solution of dipyrromethane **3-2** (0.57 g, 3.87 mmol) and 5-bromo-1-naphthaldehyde **5-32** (1.00 g, 4.25 mmol) in dry CH_2Cl_2 (0.57 L) was degassed for 10 min and shielded from light. TFA (68 μL , 0.89 mmol) was added and the reaction mixture was stirred at r.t. overnight. DDQ (2.63 g, 11.61 mmol) was added and the mixture was stirred for 1 h. Et_3N (1.0 mL) was added to terminate the reaction, the mixture was then concentrated under reduced pressure and passed over a silica plug (CH_2Cl_2). The crude was re-dissolved in CHCl_3 (20 mL) and sat. methanolic $\text{Zn}(\text{OAc})_2 \cdot 2\text{H}_2\text{O}$ was added and the mixture refluxed, shielded from light, for 3 hrs. The mixture was diluted with CHCl_3 and washed with H_2O , the organic phase dried (Na_2SO_4) and eliminated under reduced pressure. The crude was purified by column chromatography (SiO_2 , $\text{CHX}/\text{CH}_2\text{Cl}_2$ 7:3) to yield the product as bright violet solid (0.21 g, 7 % yield).

m.p. > 250 °C. $^1\text{H NMR}$ (400 MHz, Tetrahydrofuran- d_8): δ 10.26 (s, 2H), 9.32 (d, $J = 4.4$ Hz, 4H), 8.76 (d, $J = 8.7$ Hz, 2H), 8.69 (d, $J = 4.5$ Hz, 4H), 8.42 (dd, $J = 6.9, 1.1$ Hz, 2H), 8.07 (dd, $J = 8.7, 6.9$ Hz, 2H), 7.83 (d, $J = 7.2$ Hz, 2H), 7.18 – 7.04 (m, 2H), 6.96 – 6.81 (m, 2H). $^{13}\text{C NMR}$ (126 MHz, Tetrahydrofuran- d_8): δ 151.46, 150.75, 142.28, 139.39, 134.38, 132.71, 132.54, 132.54, 132.47, 130.54, 129.98, 128.16, 126.87, 126.37, 123.88, 117.04. **MS** (HRMS): found 779.9504, $\text{C}_{40}\text{H}_{22}\text{Br}_2\text{N}_4\text{Zn}$ requires 779.9503.

5-34 Nickel(II) 5,15-diphenylporphyrin

A solution of 5,15-diphenylporphyrin **3-3** (200 mg, 0.43 mmol) and Ni(acac)₂ (122 mg, 0.48 mmol) in PhCH₃ (30 mL) was refluxed for 3 hrs. The mixture was concentrated under reduced pressure and the crude purified by column chromatography (SiO₂, CHX/CH₂Cl₂ 3:2) to yield product as dark red solid (207 mg, 93 % yield).

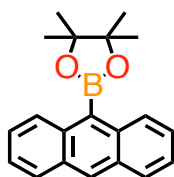
m.p. > 250 °C. ¹H NMR (400 MHz, Chloroform-*d*): δ 9.94 (s, 2H), 9.19 (d, *J* = 4.8 Hz, 3H), 8.94 (d, *J* = 4.8 Hz, 3H), 8.07 (dd, *J* = 7.7, 1.8 Hz, 3H), 7.77 – 7.72 (m, 4H). MS (ES +): found 518.2 (M⁺), C₃₂H₂₀N₄Ni requires 518.10. Characterization in accordance with literature.⁶⁸⁹

5-35 Nickel(II) 5,15-dibromo-10,20-diphenylporphyrin

To a solution of Ni (II) 5,15-diphenylporphyrin **5-34** (150 mg, 0.29 mmol) in CH₂Cl₂/MeOH (15 mL, 5:1 v/v) was added *N*-bromosuccinimide (115 mg, 0.65 mmol) and the reaction mixture was stirred at r.t. for 20 minutes before being quenched with acetone (1 mL). The mixture was brought to dryness under reduced pressure. The crude was purified by column chromatography (SiO₂, CHX/CH₂Cl₂ 2:1) to yield the final product (135 mg, 90 % yield).

m.p. > 250 °C. $^1\text{H NMR}$ (400 MHz, Chloroform-*d*): δ 9.42 (d, $J = 5.0$ Hz, 4H), 8.70 (d, $J = 5.0$ Hz, 5H), 8.04 – 7.87 (m, 4H), 7.79 – 7.61 (m, 6H). **MS** (ES +): found 518.2 (M^+), $\text{C}_{32}\text{H}_{20}\text{N}_4\text{Ni}$ requires 518.10. Characterization in accordance with literature.⁶⁹⁰

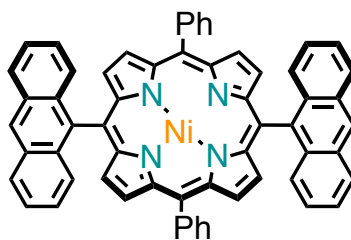
5-36 9-(4,4,5,5-Tetramethyl-1,3,2-dioxaborolan-2-yl)anthracene



To a degassed solution of 9-bromoanthracene (500 mg, 2.33 mmol), B_2pin_2 (685 mg, 2.85 mmol), KOAc (467 mg, 4.75 mmol) in toluene (8.0 mL) was added $\text{PdCl}_2(\text{PPh}_3)_2$ (165 mg, 0.20 mmol) and the mixture was degassed. The reaction mixture was heated to 90 °C overnight. H_2O was added to the mixture and was extracted with EtOAc, the organic phases collected, dried (Na_2SO_4) and removed under reduced pressure. The crude was purified by column chromatography (SiO_2 , CHX/ CH_2Cl_2 + 0.1 % Et_3N) to yield the product as an off-white solid (367 mg, 52 % yield).

m.p. 133-136 °C. $^1\text{H NMR}$ (500 MHz, Methylene Chloride-*d*₂): δ 8.50 (s, 1H), 8.47 – 8.39 (m, 2H), 8.04 – 7.99 (m, 2H), 7.53 – 7.41 (m, 4H), 1.57 (s, 12H). **MS** (ES +): found 305.2 ($M + \text{H}^+$), $\text{C}_{20}\text{H}_{21}\text{BO}_2$ requires 304.16. Characterization in accordance with literature.⁶⁹¹

5-37 Ni(II) 5,15-Dianthracenyl-10,20-diphenylporphyrin



To a stirred slurry of Cs_2CO_3 (176 mg, 0.5 mmol) in dry THF (10 mL), Ni(II) 5,15-dibromo-10,20-diphenylporphyrin **5-35** (67.7 mg, 0.1 mmol), borylanthracene **5-36** (304 mg, 1.0 mmol), $\text{PdCl}_2(\text{PPh}_3)_2$ (14 mg, 0.02 mmol) and AsPh_3 (12 mg, 0.04 mmol) were added and the mixture was degassed by two 'freeze-pump-thaw' cycles. The reaction mixture was shielded from light and heated to reflux overnight under Ar. The mixture was diluted with CHCl_3 and washed with sat. aq. NaHCO_3 solution, H_2O , dried (Na_2SO_4) and eliminated under reduced pressure. Purification by preparative TLCs ($\text{CHX}/\text{CH}_2\text{Cl}_2$ 4:1) and crystallization from $\text{CH}_2\text{Cl}_2/\text{MeOH}$ yielded product as dark red crystals (56 mg, 64 % yield).

m.p. > 250 °C. $^1\text{H NMR}$ (500 MHz, Chloroform-*d*) δ 8.87 (s, 2H), 8.61 (d, $J = 5.0$, 4H), 8.25 (d, $J = 8.7$ Hz, 4H), 8.22 (d, $J = 5.0$ Hz, 4H), 8.02 – 7.97 (m, 4H), 7.66 – 7.53 (m, 8H), 7.50 – 7.41 (m, 4H), 7.13 – 7.03 (m, 6H). **MS** (ES +): found 871.3 ($\text{M} + \text{H}^+$), $\text{C}_{60}\text{H}_{36}\text{N}_4\text{Ni}$ requires 870.23. Characterization in accordance with literature.⁶⁹²

6.4. Appendix

6.4.1. Crystal Structures

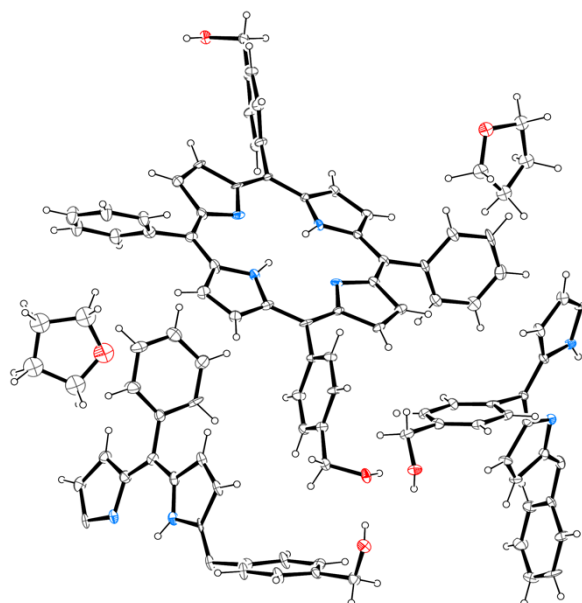


Figure S6.2. Asymmetric unit content for **3-1** ($2C_{46}H_{34}N_4O_2 \cdot C_4H_8O$; 50% probability ellipsoids). THF molecules have been modelled with alternative conformations (hidden for clarity).

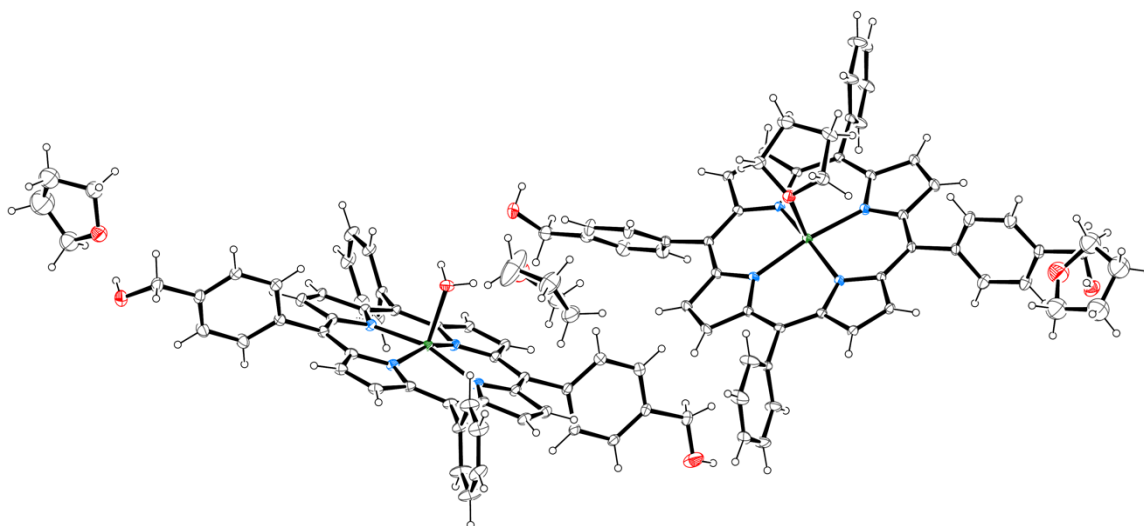


Figure S6.3. Ellipsoid representation of **3-1-Zn** ASU content ($2C_{46}H_{34}N_4O_2Zn \cdot 4C_4H_8O \cdot H_2O$; 50% probability). Two different zinc coordination environments have been found for the two crystallographically independent porphyrins.

Data collections were performed at the X-ray diffraction beamline (XRD1) of the Elettra Synchrotron, Trieste (Italy), with a Pilatus 2M image plate detector. Complete datasets were collected at 100 K (nitrogen stream supplied through an Oxford Cryostream 700) with a monochromatic wavelength of 0.700 Å through the rotating crystal method. The crystals of **3-1** and **3-1·Zn** were dipped in N-paratone and mounted on the goniometer head with a nylon loop. The diffraction data were indexed, integrated and scaled using XDS.⁶⁹³ For each sample, complete datasets have been obtained merging two data collections obtained from different orientations of the same crystal. The structures were solved by direct methods using SIR2014,⁶⁹⁴ Fourier analyzed and refined by the full-matrix least-squares based on F^2 implemented in SHELXL-2014.⁶⁹⁵ The Coot program was used for modeling.⁶⁹⁶ Anisotropic thermal motion was then applied to all atoms excluding disordered THF solvent molecules, in **3-1** model. Hydrogen atoms were included at calculated positions with isotropic $U_{\text{factors}} = 1.2 U_{\text{eq}}$ or $U_{\text{factors}} = 1.5 U_{\text{eq}}$ for methyl and hydroxyl groups. Restrain on bond lengths, angles and thermal motion (DFIX, DANG, SIMU and/or DELU) have been applied for poorly defined THF solvent molecules.

Both **3-1** and **1·3·Zn** crystal forms obtained showed twinning: 2-component inversion twin for **3-1** and 4-component inversion twin for **3-1·Zn**. Enantiomorphic domains in **1** model show a 'not perfect' 70%:30% population.

Pseudo-merohedral twin law has been identified in **3-1·Zn** data, using COSET program,⁶⁹⁷ as a 90° roto-inversion about (010) direct lattice direction. This relation is consistent with a monoclinic unit cell with tetragonal supergroup's symmetry metrically available ($a \approx c$ and $\beta \approx 90^\circ$). Population of the four domains has been refined, using Shelxl BASF command, and appear to be evenly distributed (~20-30%).

One full and two half porphyrin molecules have been found in crystal **3-1** asymmetric unit (ASU) (Figure 1S): crystallographic inversion centres lying in the middle of the partial moieties generate the complete molecules. A chiral helicoidal arrangement of hydrogen bonds connects 32 neighbour porphyrins ($d_{o-o} = 2.749(8)$ Å). Two THF molecules with partial occupancies (50%) lies on 2-fold crystallographic axis, occupying crystal channels parallel to unit cell *a* axis.

3-1·Zn model shows two crystallographically independent porphyrin molecules with different coordinated ligand: one bound to a THF, while the other is bound to a water molecule (Figure 2S). As previously seen for molecule **1** packing, neighbour porphyrins show intermolecular

hydrogen bonds connections (average $d_{O-O} = 3.126(7)$ Å). Interstitial voids are filled by three additional THF molecules tightly connected to exposed hydroxyl groups (from porphyrins and water). Essential crystal and refinement data (**Table S6.2**) are reported below.

Table S6.2. Crystallographic data and refinement details for compound **3-1** and **3-1·Zn**

	3-1	3-1·Zn
CCDC Number	1442721	1442722
Moiety Formula	$C_{46}H_{34}N_4O_2 \cdot 0.5C_4H_8O$	$2C_{46}H_{34}N_4O_2Zn \cdot 4C_4H_8O \cdot H_2O$
Sum Formula	$C_{48}H_{38}N_4O_{2.5}$	$C_{108}H_{98}N_8O_9Zn_2$
Formula weight (Da)	710.82	1782.68
Temperature (K)	100(2)	100(2)
Wavelength (Å)	0.700	0.700
Crystal system	Monoclinic	Triclinic
Space Group	$P2/c$	$P1$
<i>a</i> (Å)	32.628(7)	11.311(2)
<i>b</i> (Å)	6.9070(14)	14.100(3)
<i>c</i> (Å)	32.568(7)	14.556(3)
α (°)	90	102.09(3)
β (°)	90.64(3)	98.80(3)
γ (°)	90	99.49(3)
<i>V</i> (Å ³)	7339(3)	2196.2(8)
<i>Z</i>	8	1
ρ (g·cm ⁻³)	1.287	1.348
<i>F</i> (000)	2992	934
μ (mm ⁻¹)	0.077	0.588
θ min,max (°)	0.6, 24.6	1.4, 29.1
Resolution (Å)	0.84	0.72
Total refl. collectd	25205	74269
Independent refl.	13431 [R(int) = 0.0275]	23000 [R(int) = 0.0158]
Obs. Refl. [Fo>4σ(Fo)]	12616	22806
<i>I</i> /σ (<i>I</i>) (all data)	31.57	75.57
<i>I</i> /σ (<i>I</i>) (max resltn)	13.42	38.39
Completeness (all data)	0.99	0.98
Completeness (max resltn)	0.99	0.96
Rmerge (all data)	0.0200	0.0267
Rmerge (max resltn)	0.0421	0.0528
Multiplicity (all data)	1.8	6.0
Multiplicity (max resltn)	1.8	5.1
Data/restraint/parameters	13431/245/1155	23000/26/1128
Goof	1.063	1.017
R_1^a [<i>I</i> >2.0σ(<i>I</i>)], wR_2^a [<i>I</i> >2.0σ(<i>I</i>)]	0.1274, 0.3324	0.0486, 0.1319
R_1^a (all data), wR_2^a (all data)	0.1374, 0.3453	0.0489, 0.1323

$$^a R_1 = \sum |F_o| - |F_c| / \sum |F_o|, wR_2 = [\sum w(F_o^2 - F_c^2)^2 / \sum w(F_o^2)^2]^{1/2}.$$

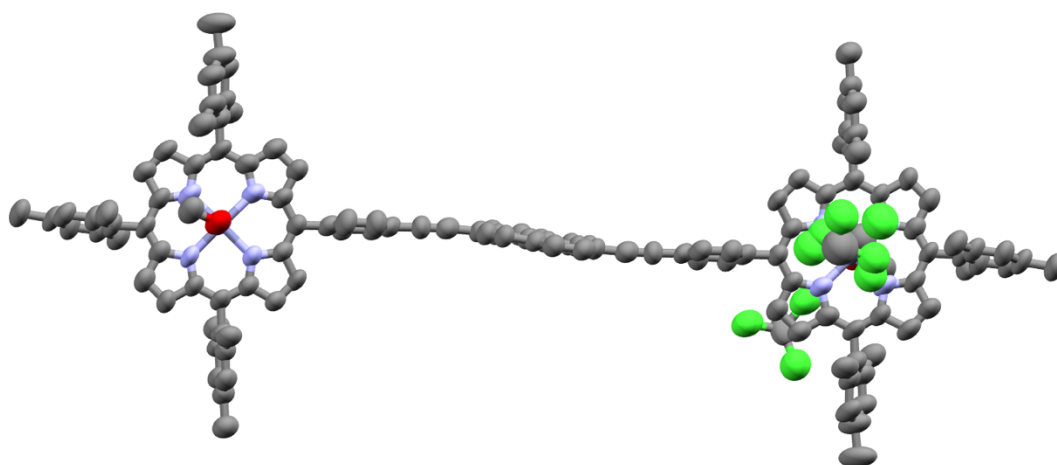


Figure S6.4. X-Ray structure of compound **4-1**. Ellipsoid at 50 % probability.

Table S6.3. Crystallographic data for **4-1**.

CCDC Number	1432475
Formula	$[(C_{126}H_{98}NaO_{24}S_4).(CH_4O)_2], 2CHCl_2$
Crystal system	Monoclinic
Space group	$P2_1/n$
Z	2
Unit cell dimensions (\AA , $^\circ$)	$a = 10.969(1)$; $b = 22.632(1)$; $c = 23.491(1)$; $\beta = 101.771(5)$
$V(\text{\AA}^3)$	5709.0
ρ_{calcd} (g/cm^{-3})	1.254
μ (mm^{-1})	0.993
Resolution (\AA)	50.00-0.94
Reflecs. coll./unique	12205/6459
Goof	1.699
R_1 ($I > 2\sigma(I)$)	0.1384
wR_2 ($I > 2\sigma(I)$)	0.395

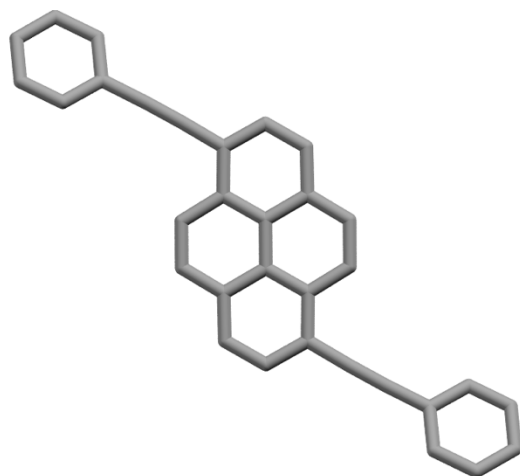


Figure S6.5. X-Ray structure of compound 5-2a.

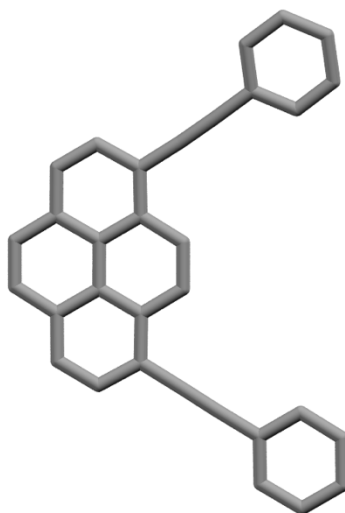
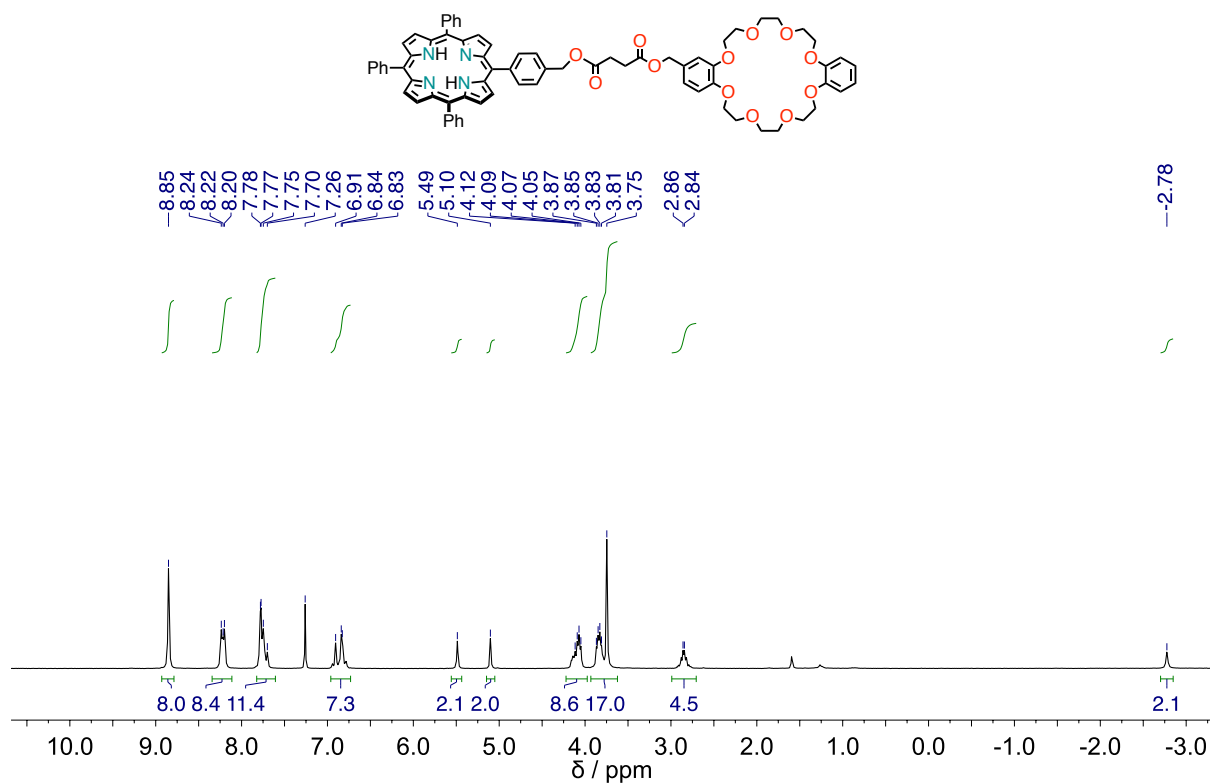
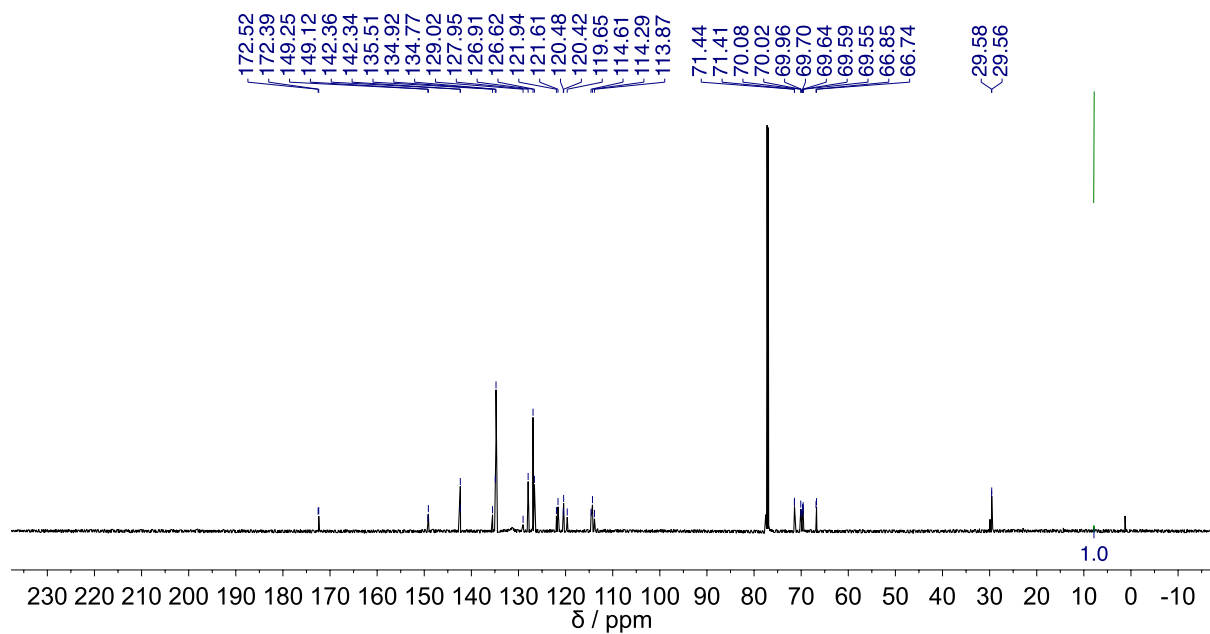


Figure S6.6. X-Ray structure of compound 5-3a.



Figure S6.7. Emission properties of prepared anthracene derivatives **5-13** and **5-16**: a) solid state fluorescence (under 365 nm irradiation) and aggregation induced emission in a of pyridylethenylantracene derivative in THF solution (left) THF/1M aq. HCl solution (1:9 v/v) and THF/H₂O (1:9 v/v). In solid-state they show bright emission in a range of colors. In solution, especially the ethenyl series showed low emission properties. However, by inducing aggregation (with H₂O for example) the emission is enhanced, as expended in aggregation-induced emission (AIE) enhancement phenomenon. The aryl-ethenyl groups dissipate the excited-state energy via intramolecular rotations when the molecules are molecularly dissolved. However, the aryl-ethenyl groups also are able to prevent π - π stacking interactions and therefore block the non-radiative decay channels resulting in the AIE effect. Additionally, the pyridyl groups can be involved in acid-base equilibria and there is no surprise that by changing the pH of the water, we can induce aggregation of the pyridium anthracene derivatives (figure on the right).

6.4.2. Selected Characterizations

Figure S6.8. ¹H NMR (500 MHz, 298 K, CDCl₃) of compound 2-1.Figure S6.9. ¹³C NMR (126 MHz, 298 K, CDCl₃) of compound 2-1.

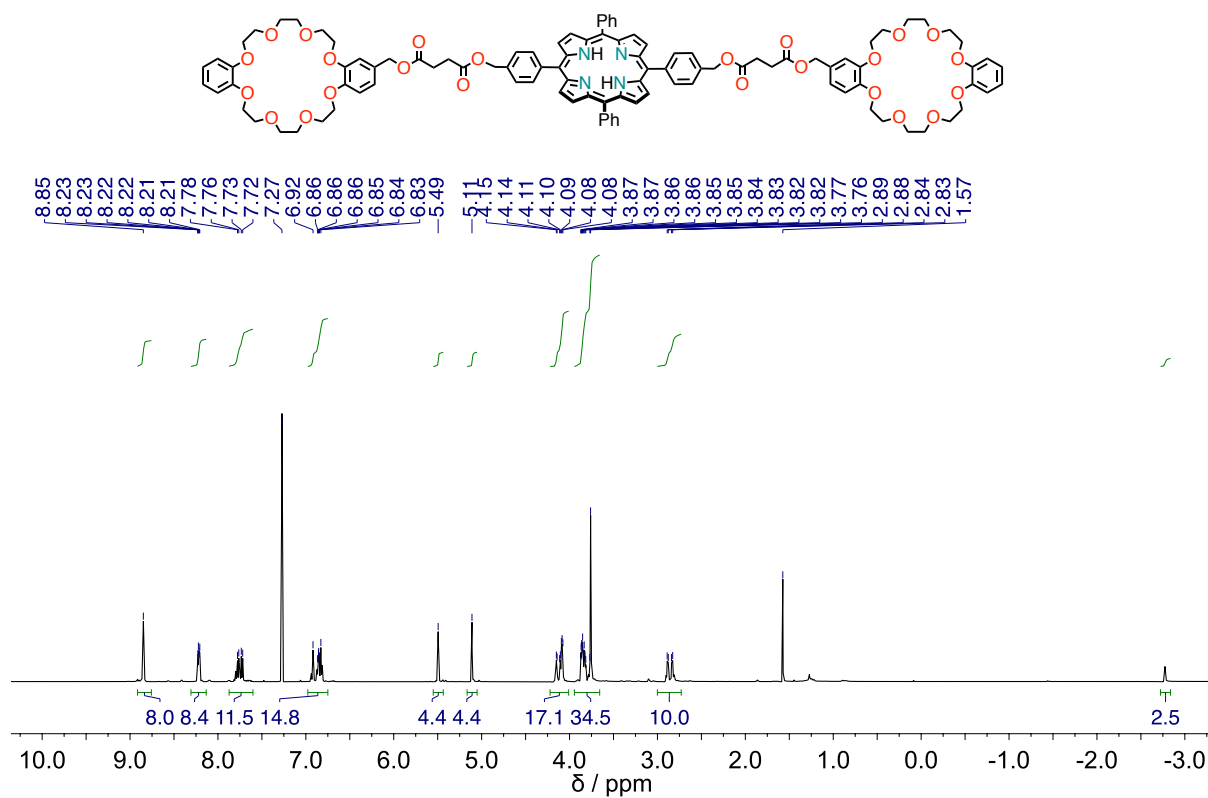


Figure S6.10. ^1H NMR (500 MHz, 298 K, CDCl_3) of compound 2-2.

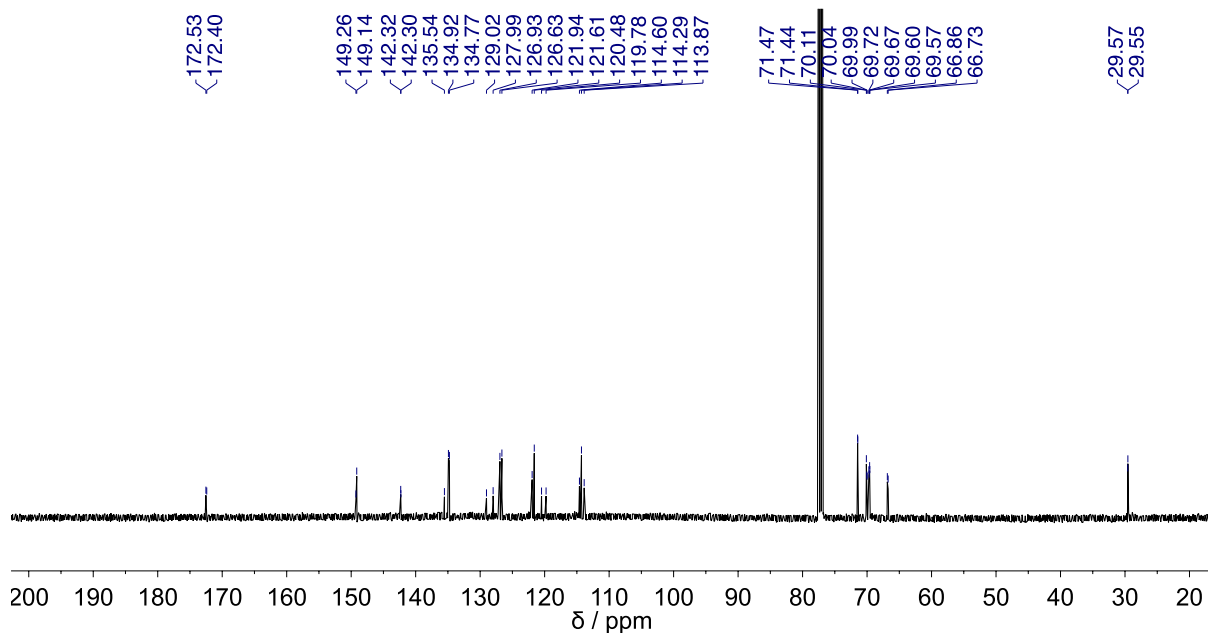


Figure S6.11. ^{13}C NMR (126 MHz, 298 K, CDCl_3) of compound 2-2.

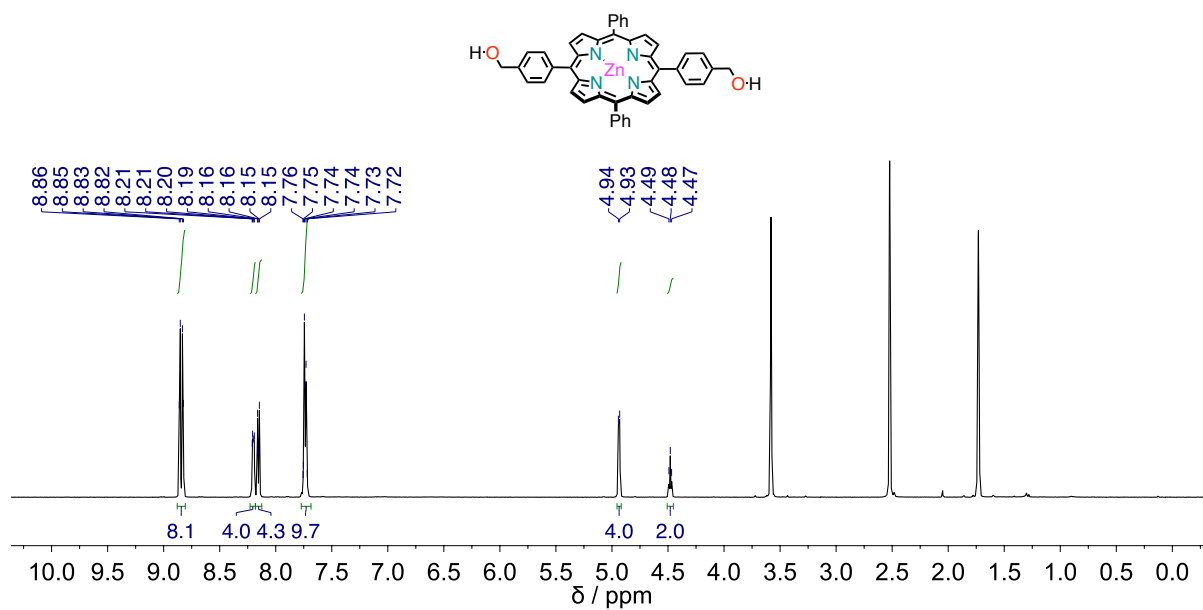
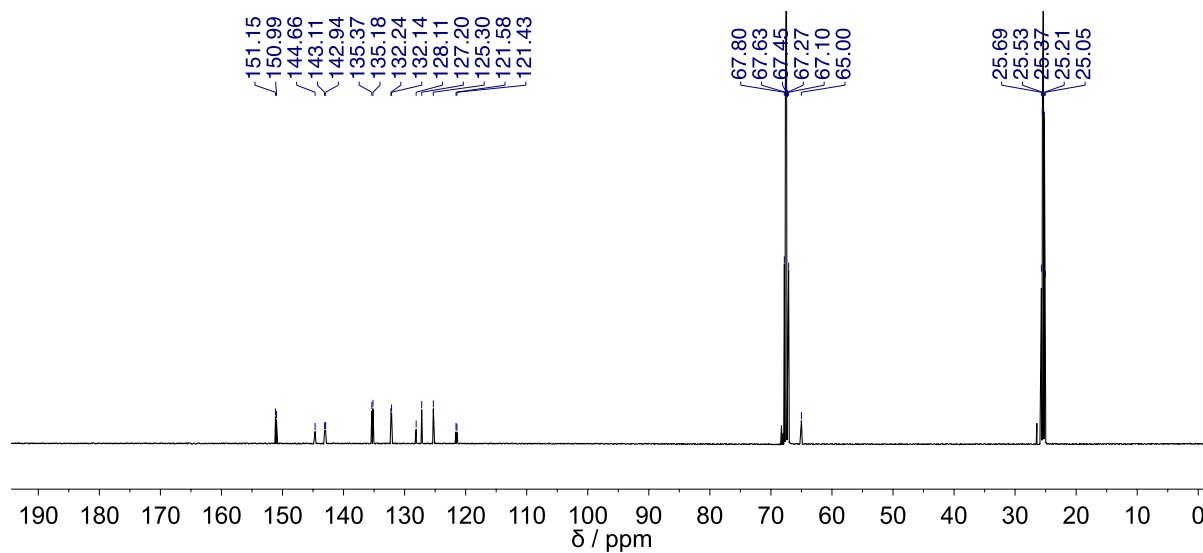
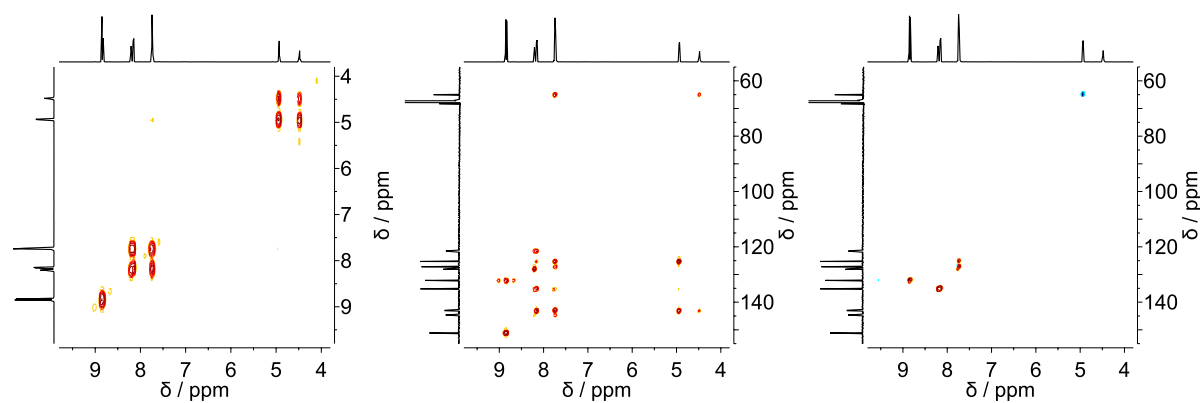
Figure S6.12. $^1\text{H NMR}$ (500 MHz, 298 K, $\text{THF-}d_8$) of compound 3-1-Zn.Figure S6.13. $^{13}\text{C NMR}$ (126 MHz, 298 K, $\text{THF-}d_8$) of compound 3-1-Zn.

Figure S6.14. 2-D NMR characterization for compound 3-1-Zn: gCOSY, HSQC and gHMBCAD.

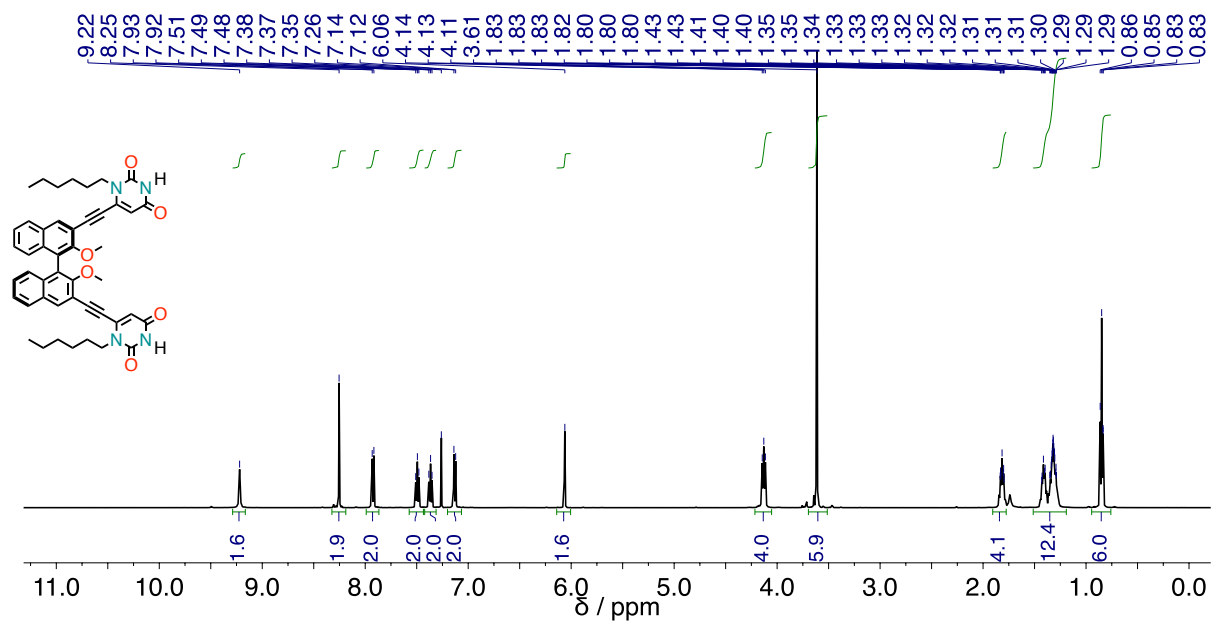


Figure S6.15. ^1H NMR (500 MHz, 298 K, CDCl_3) of compound 3.3-(R)-1.

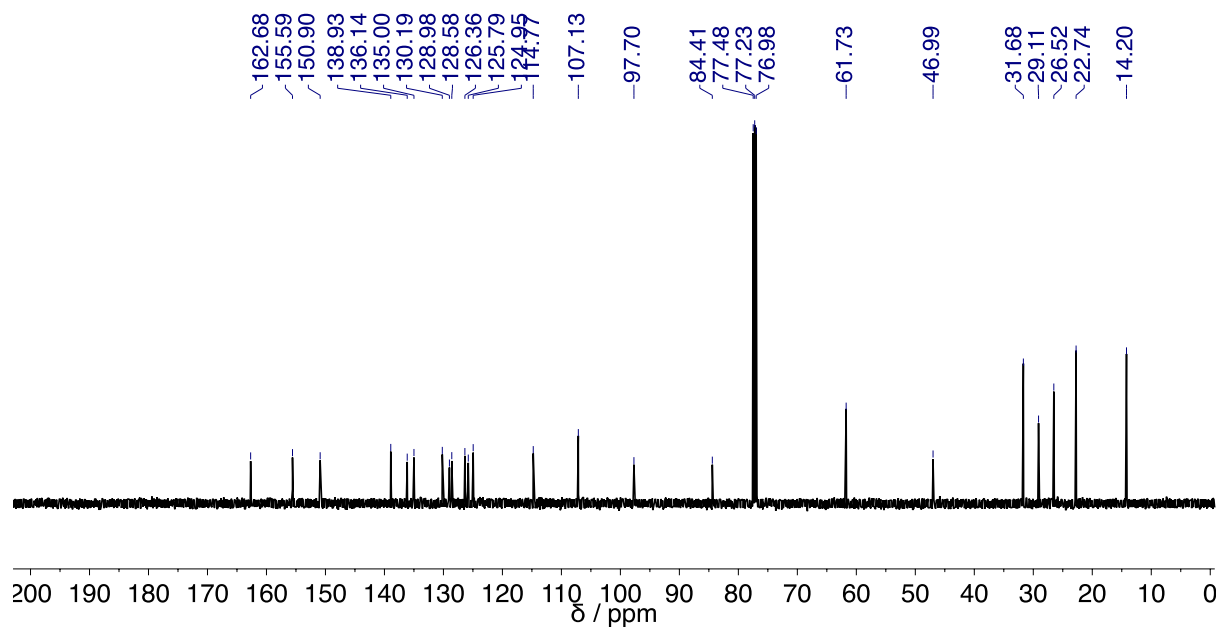
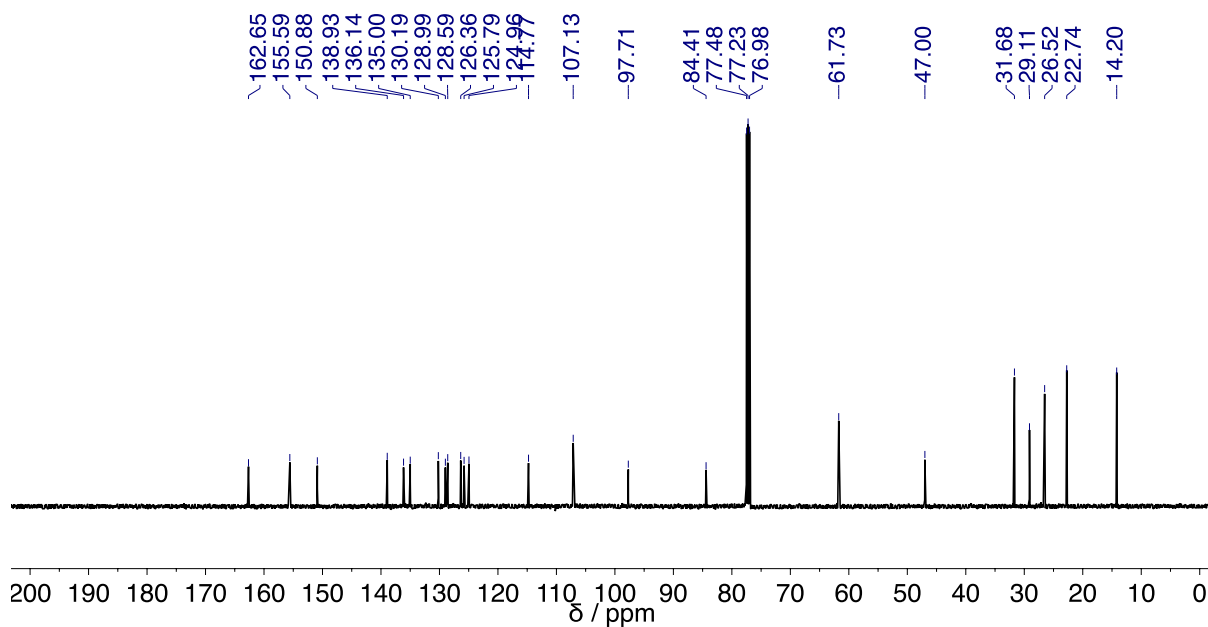
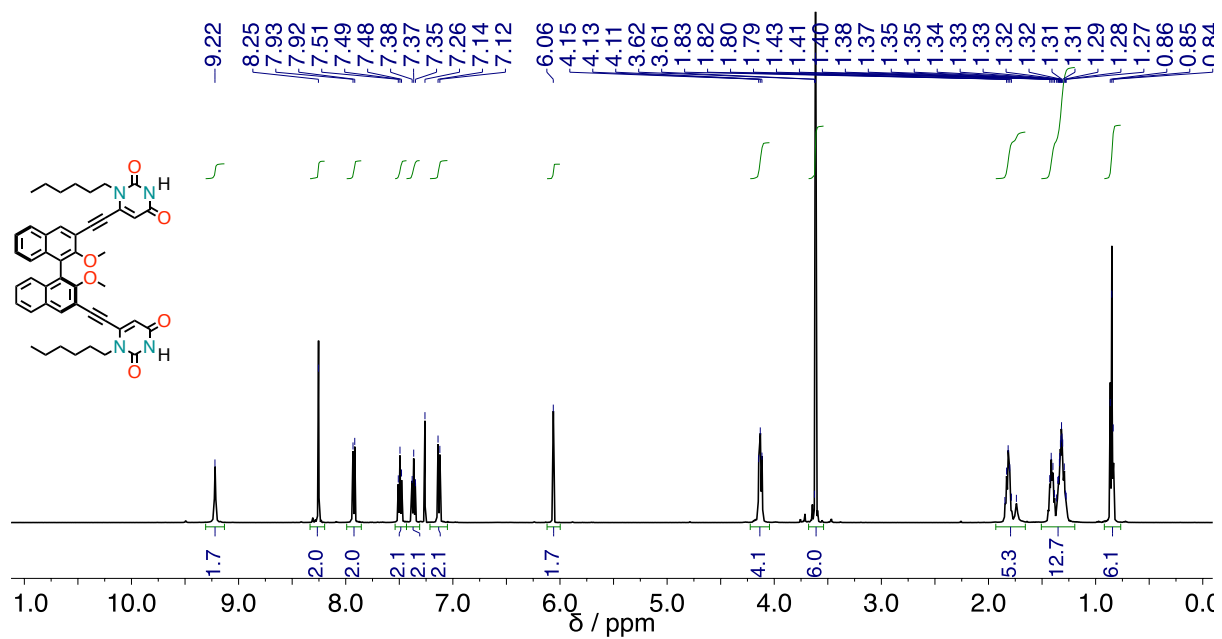


Figure S6.16. ^{13}C NMR (126 MHz, 298 K, CDCl_3) of compound 3.3-(R)-1.



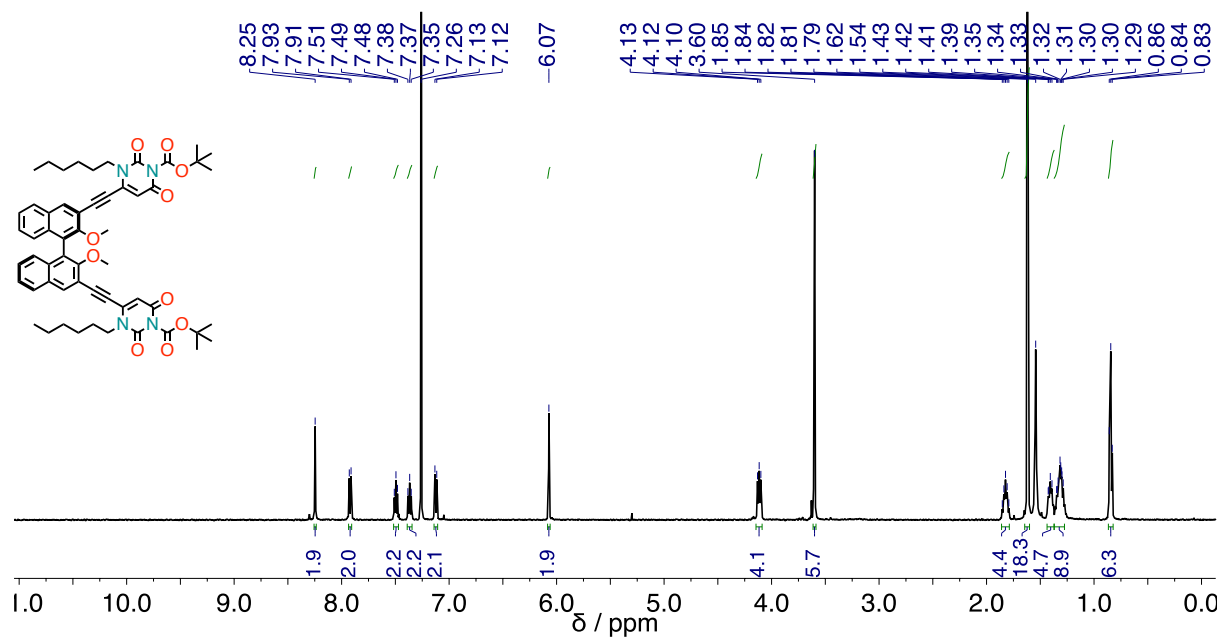


Figure S6.19. ¹H NMR (500 MHz, 298 K, CDCl₃) of compound 3.3-(*R*)-3.

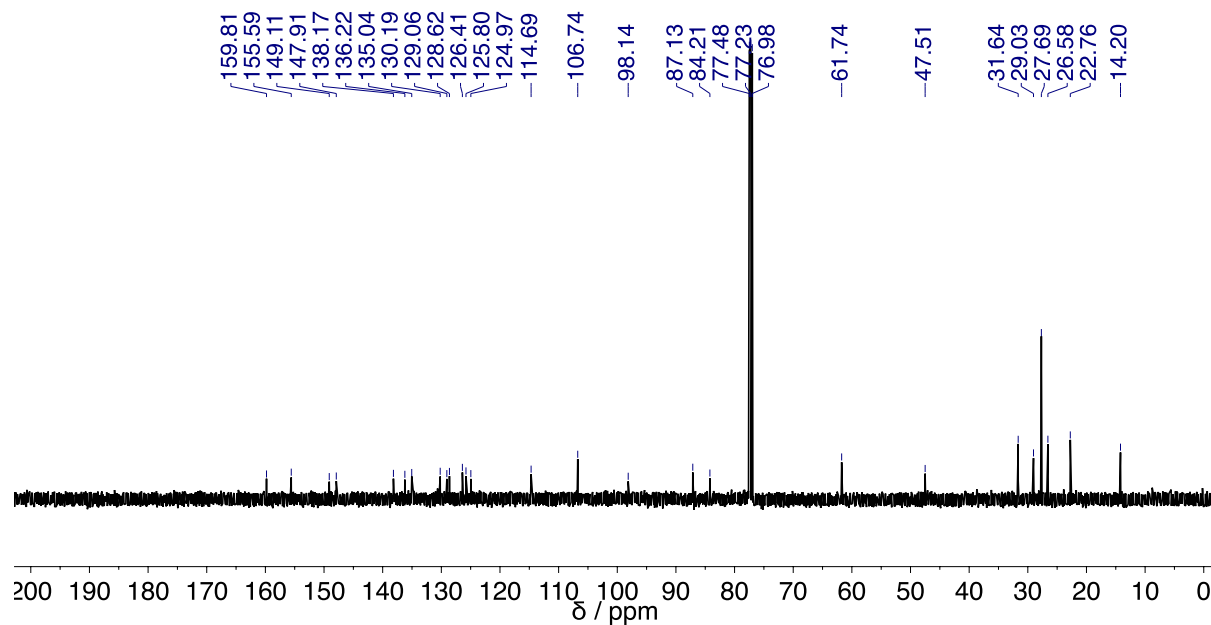


Figure S6.20. ¹³C NMR (126 MHz, 298 K, CDCl₃) of compound 3.3-(*R*)-3.

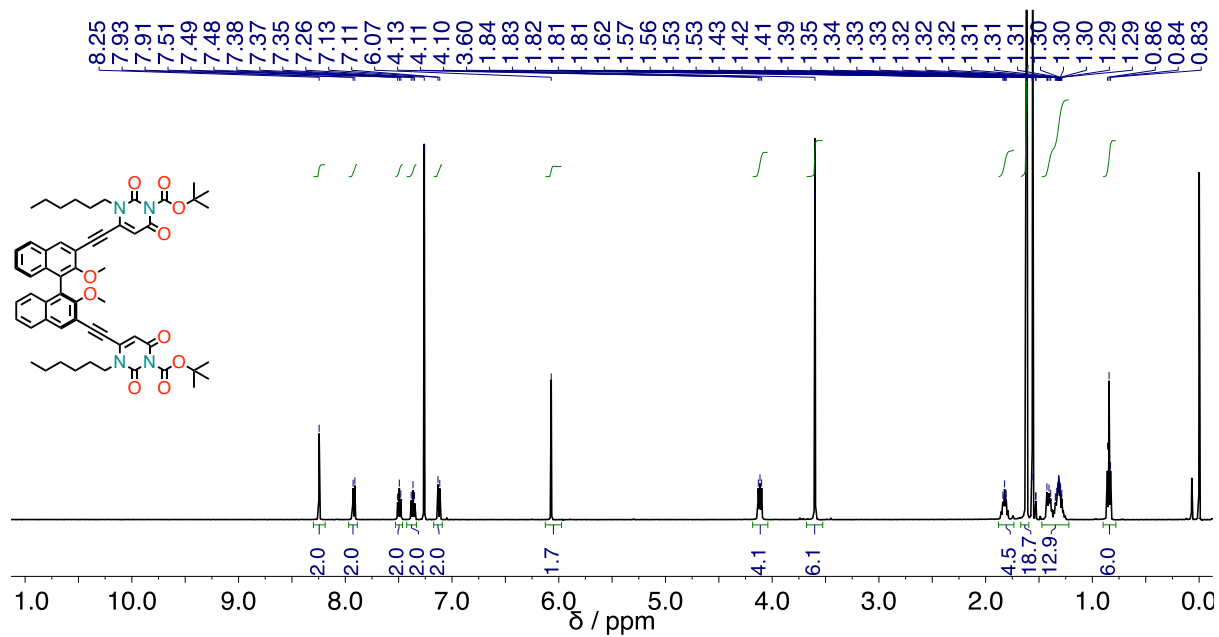


Figure S6.21. ^1H NMR (500 MHz, 298 K, CDCl_3) of compound 3.3-(S)-3.

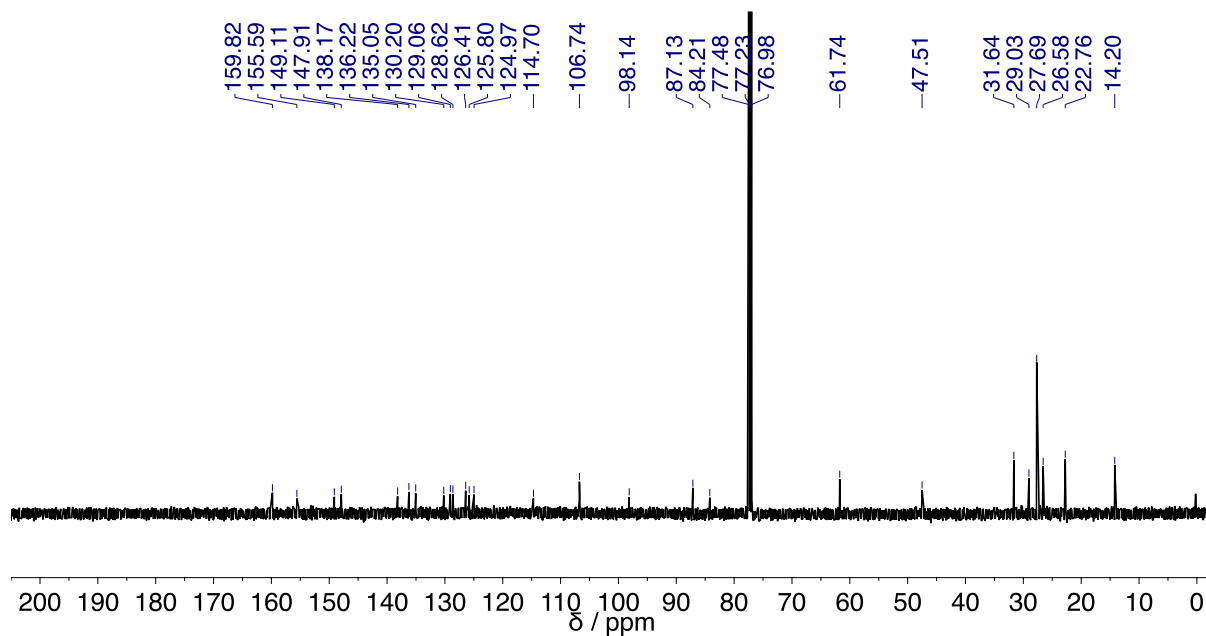


Figure S6.22. ^{13}C NMR (126 MHz, 298 K, CDCl_3) of compound 3.3-(S)-3.

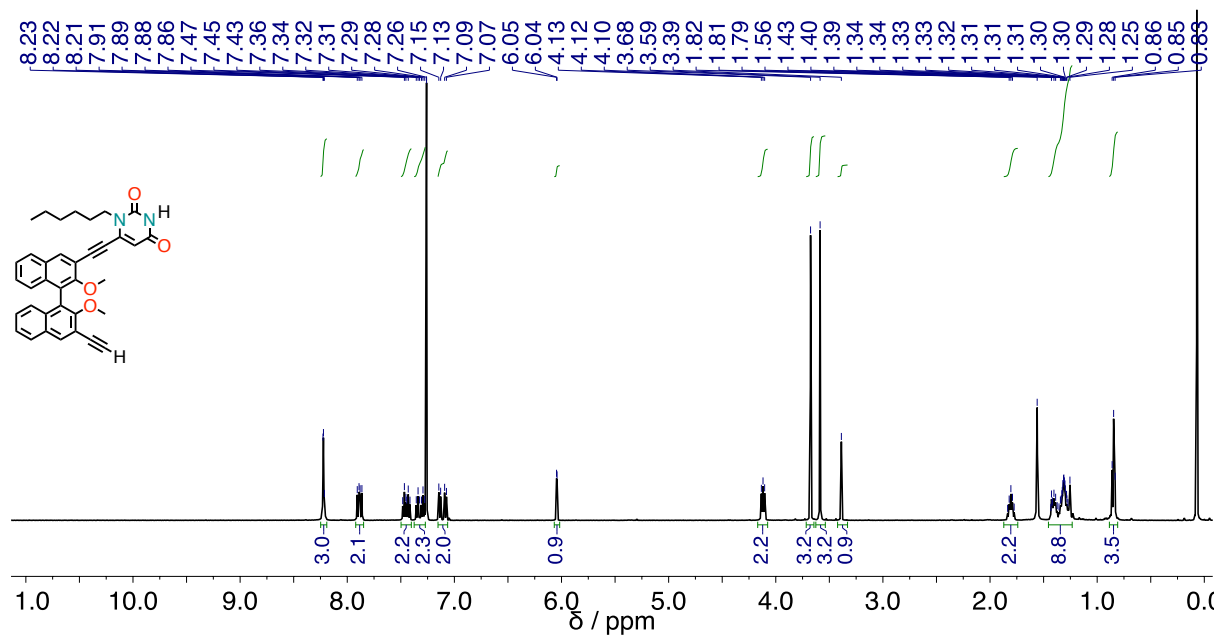


Figure S6.23. ^1H NMR (500 MHz, 298 K, CDCl_3) of compound 3.3-4.

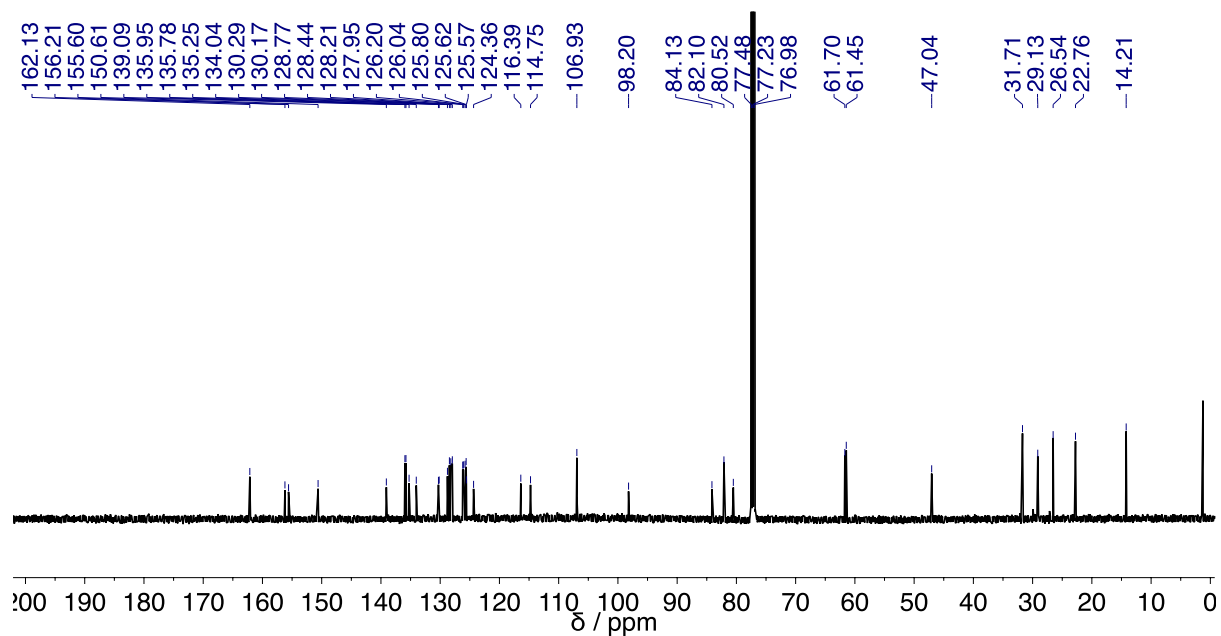
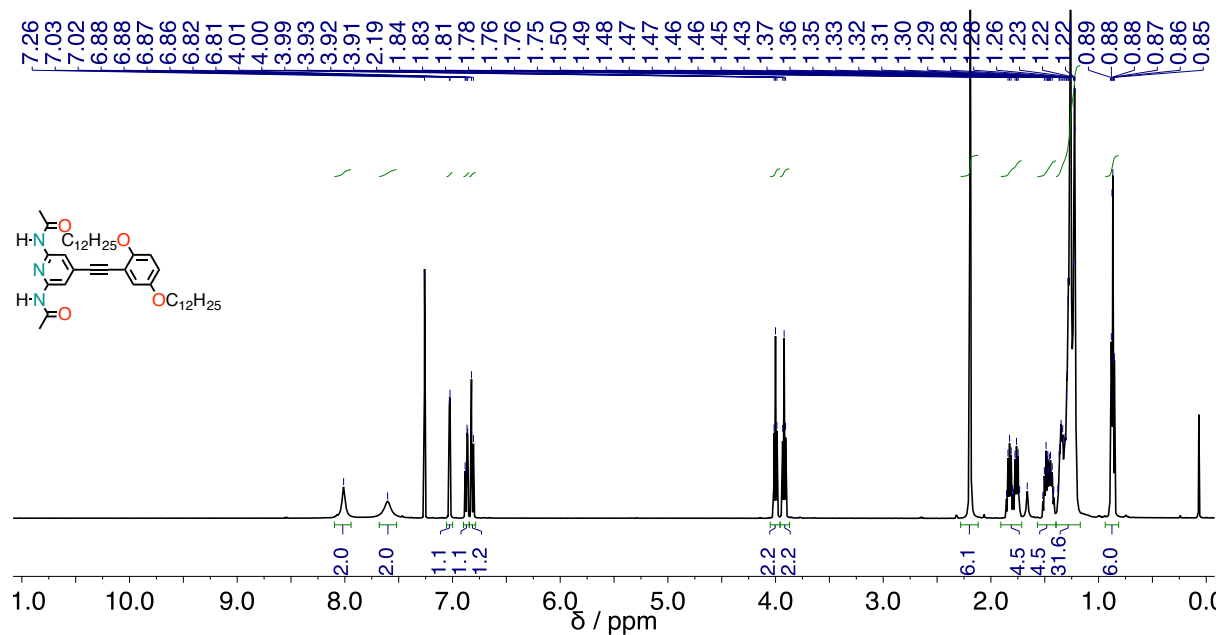
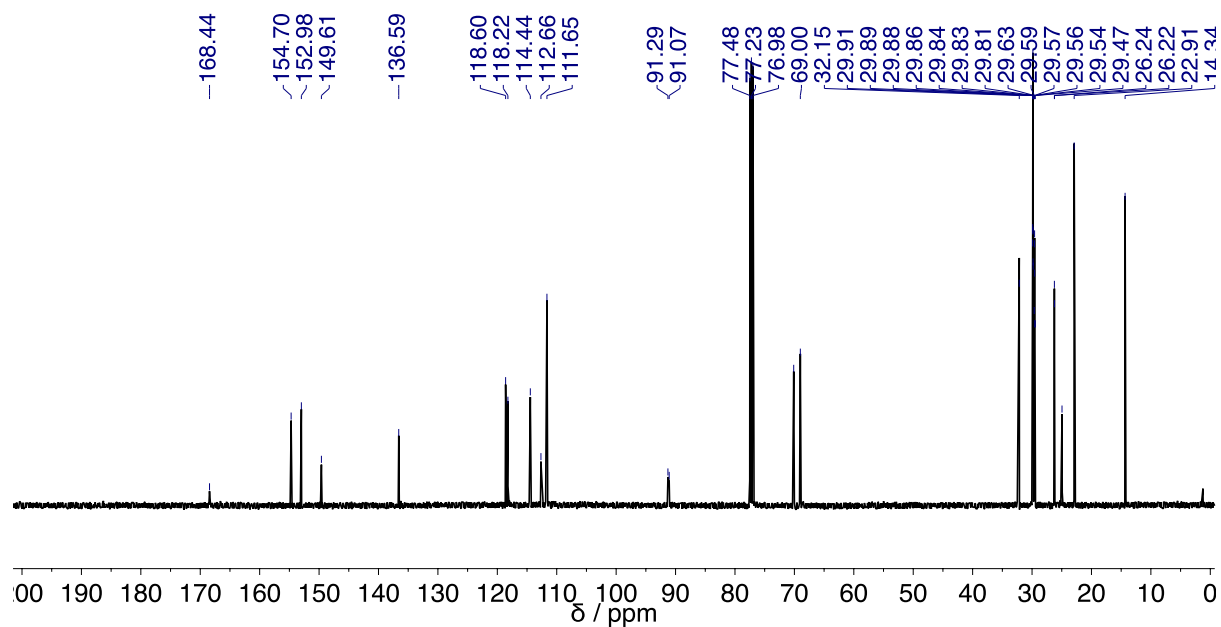


Figure S6.24. ^{13}C NMR (126 MHz, 298 K, CDCl_3) of compound 3.3-4.

Figure S6.25. $^1\text{H NMR}$ (500 MHz, 298 K, CDCl_3) of compound 3.3-5.Figure S6.26. $^{13}\text{C NMR}$ (126 MHz, 298 K, CDCl_3) of compound 3.3-5.

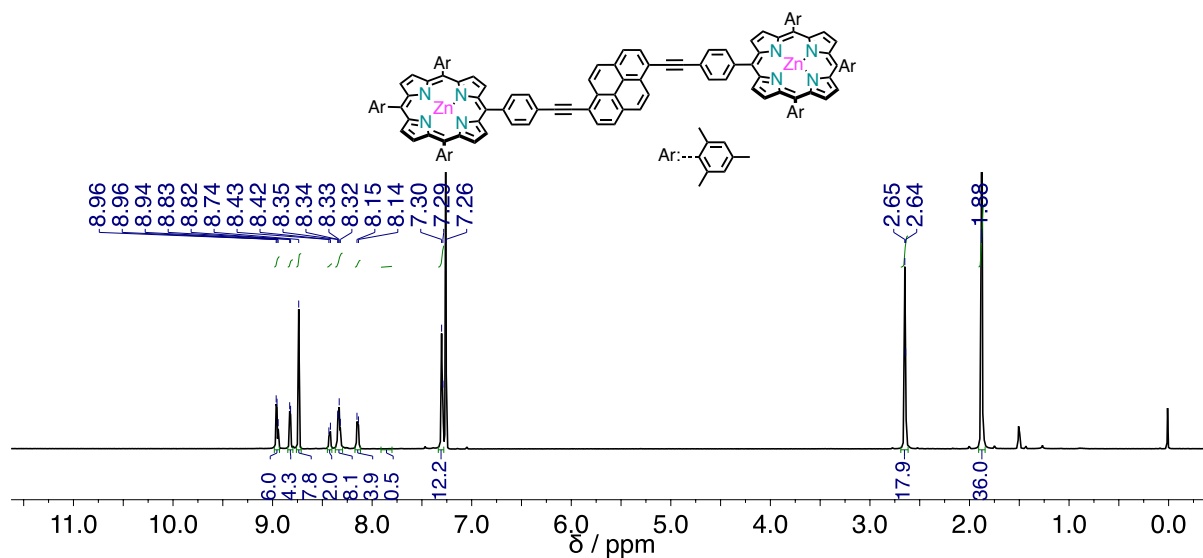


Figure S6.27. ^1H NMR (500 MHz, 298 K, CDCl_3) of compound 4-1.

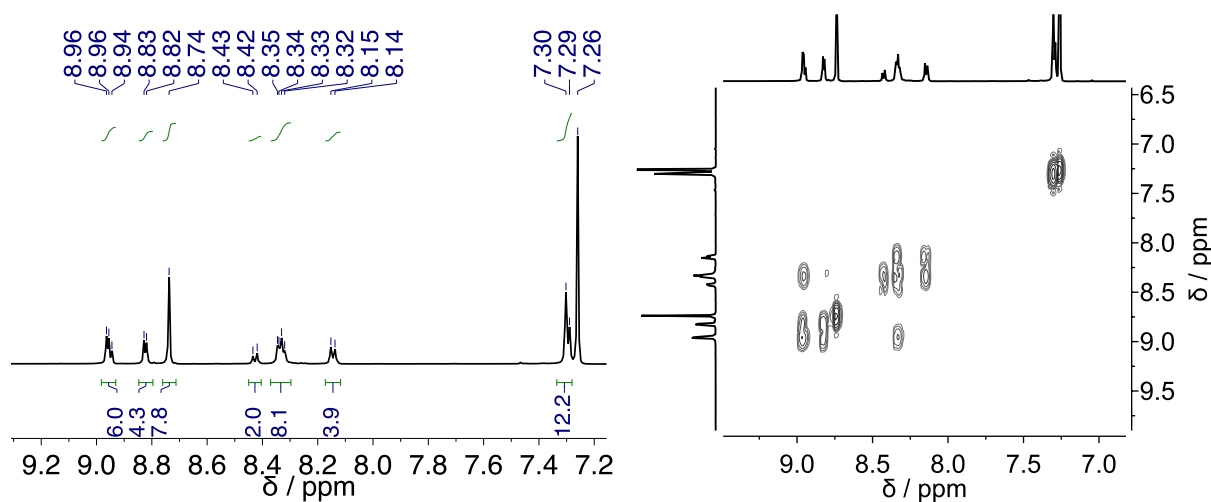


Figure S6.28. Enlarged aromatic region along with gCOSY spectrum for compound 4-1.

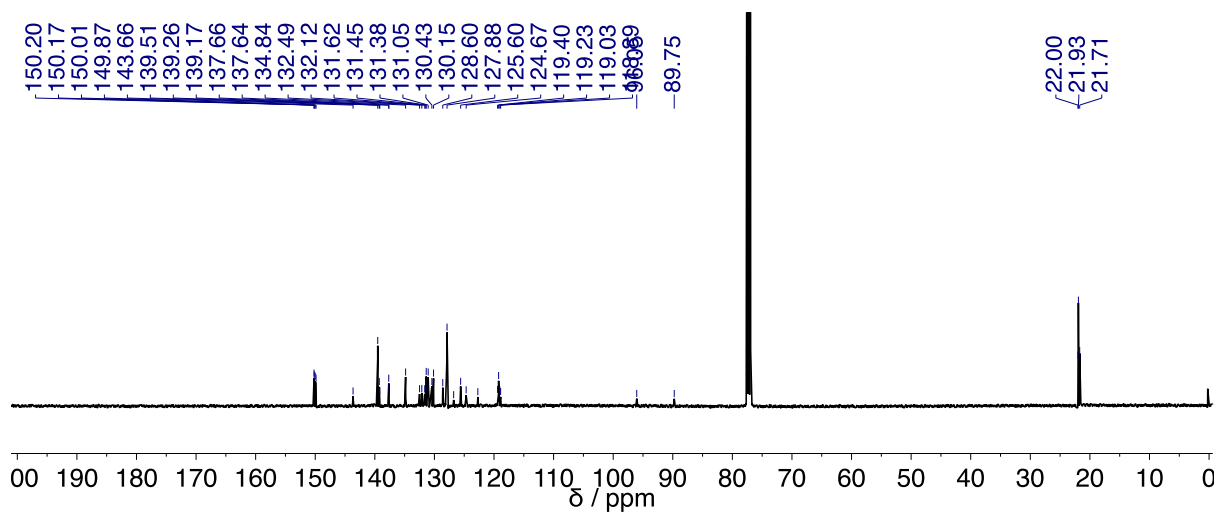


Figure S6.29. ^{13}C NMR (126 MHz, 298 K, CDCl_3) of compound 4-1.

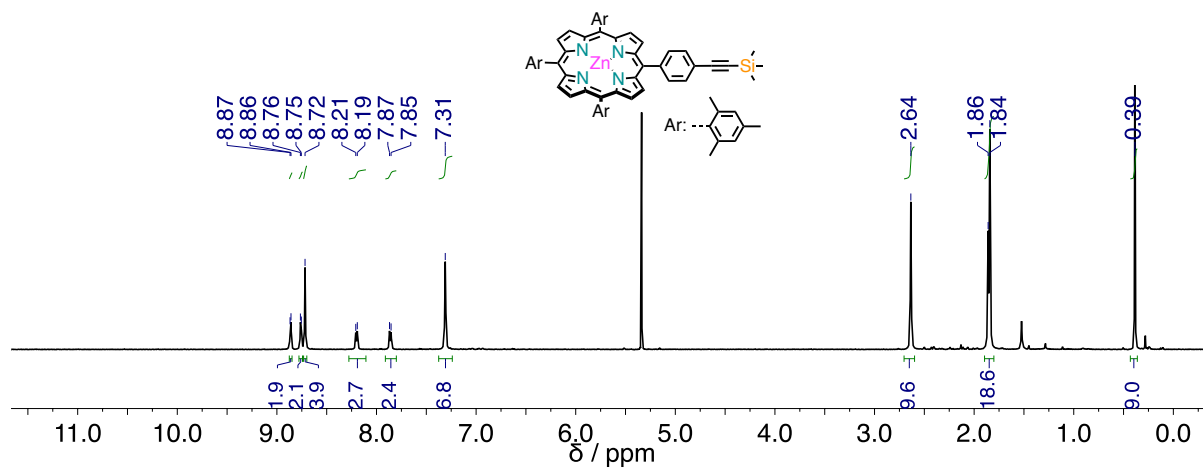


Figure S6.30. ^1H NMR (500 MHz, 298 K, CD_2Cl_2) of compound 4-2.

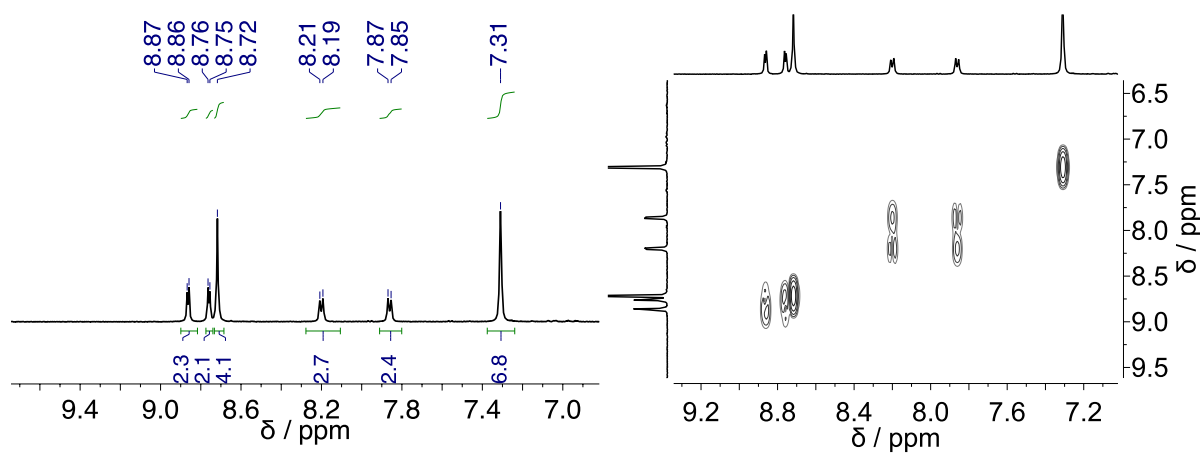


Figure S6.31. Enlarged aromatic region along with gCOSY spectrum for compound 4-2.

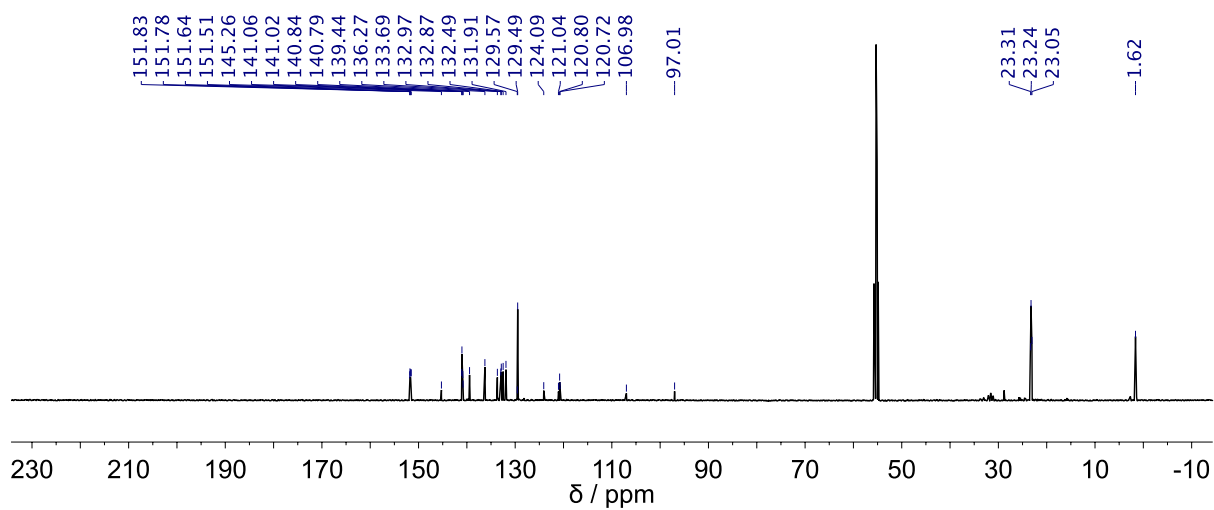


Figure S6.32. ^{13}C NMR (126 MHz, 298 K, CD_2Cl_2) of compound 4-2.

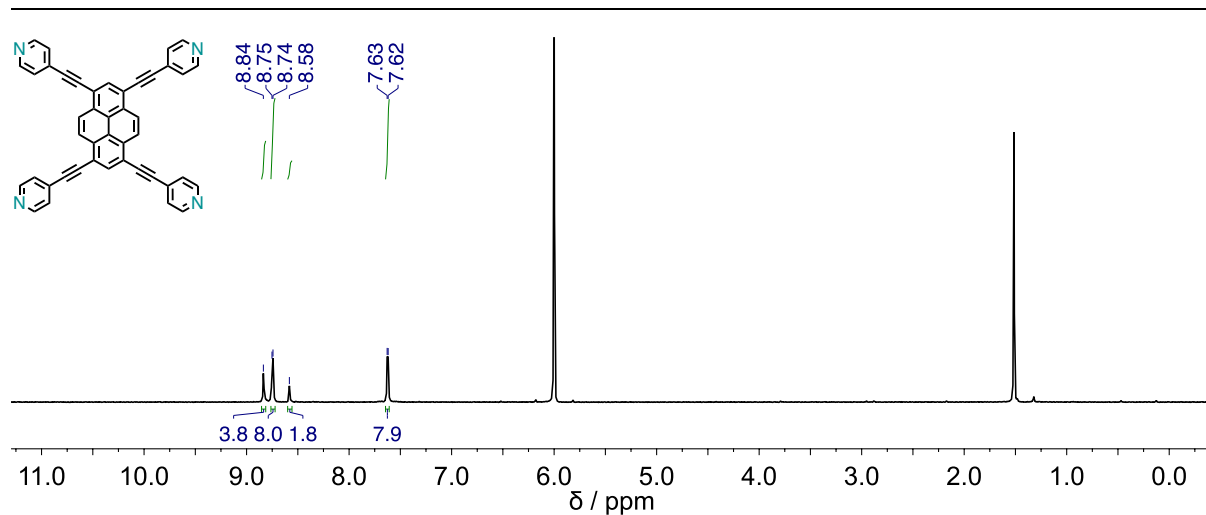


Figure S6.33. ¹H NMR (500 MHz, 353 K, TCE-*d*₂) of compound 5-1.

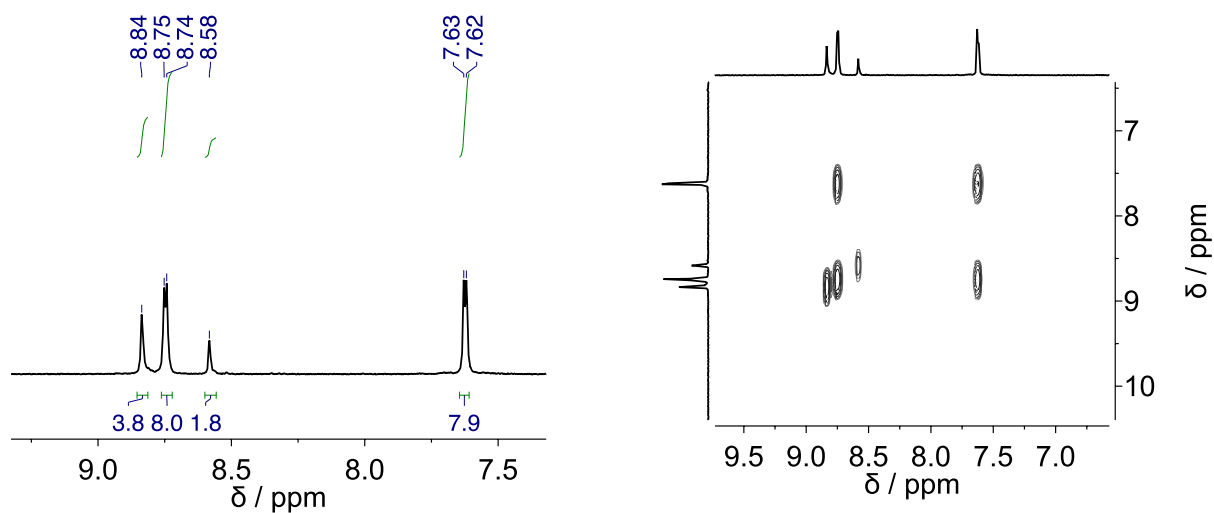


Figure S6.34. Enlarged aromatic region along with gCOSY spectrum for compound 5-1.

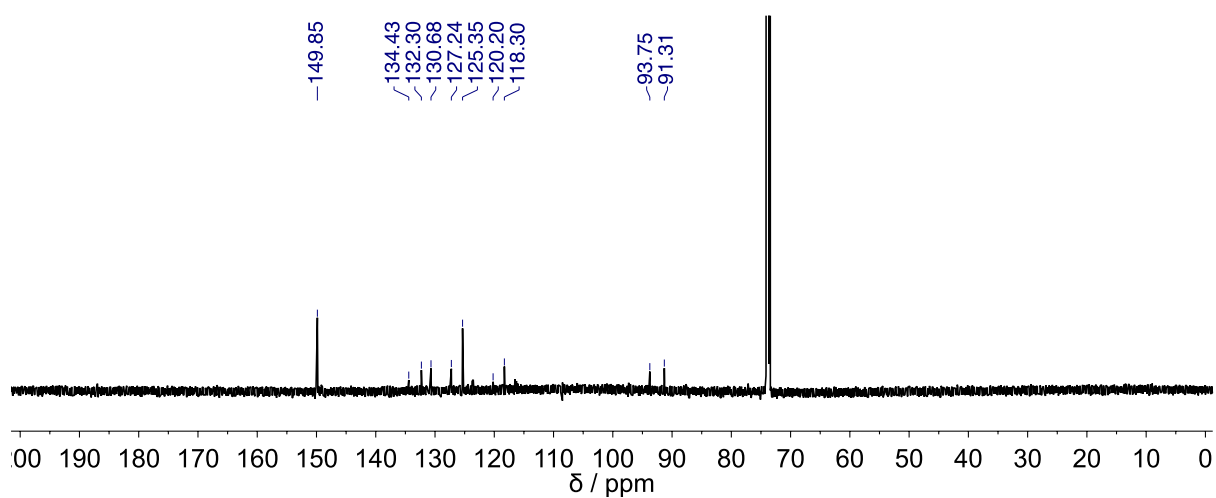


Figure S6.35. ¹³C NMR (126 MHz, 353 K, TCE-*d*₂) of compound 5-1.

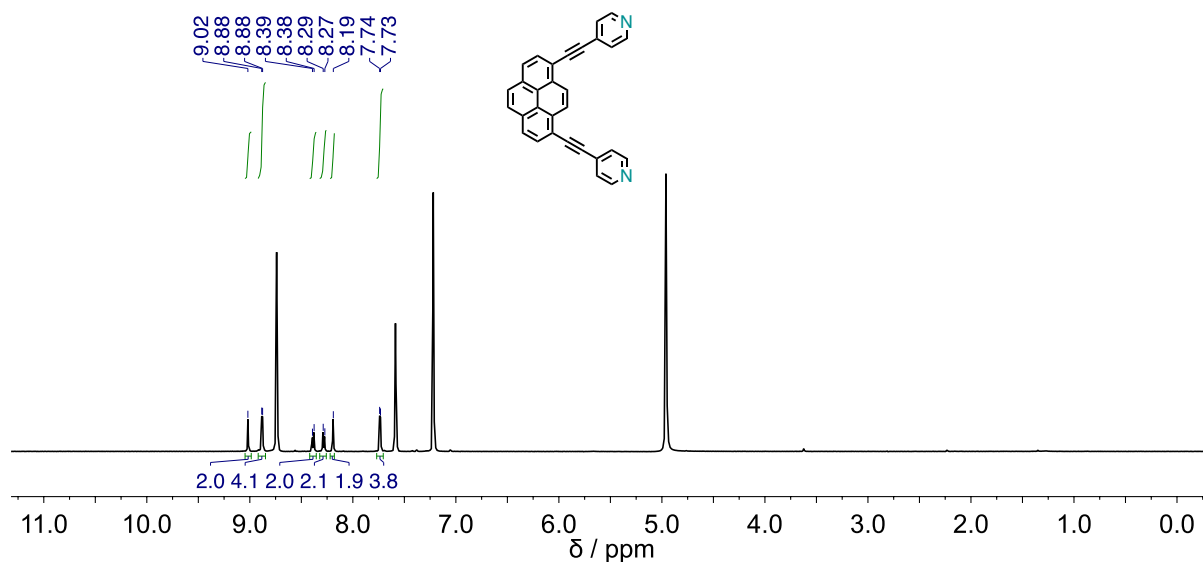


Figure S6.39. ¹H NMR (500 MHz, 298 K, Py-*d*₅) of compound 5-3.

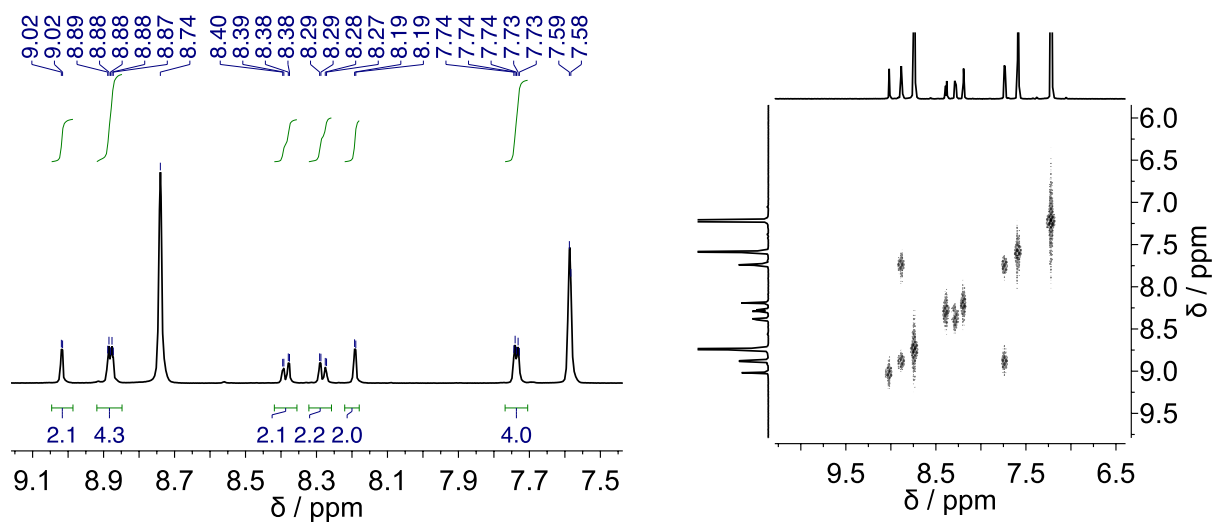


Figure S6.40. Enlarged aromatic region along with gCOSY spectrum for compound 5-3.

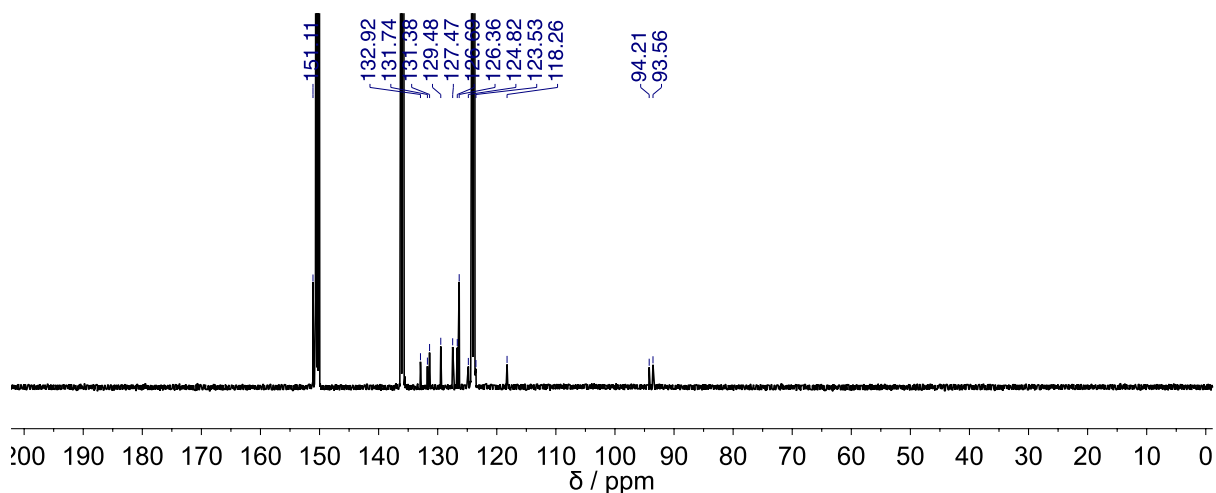


Figure S6.41. ¹³C NMR (126 MHz, 353 K, Py-*d*₅) of compound 5-3.

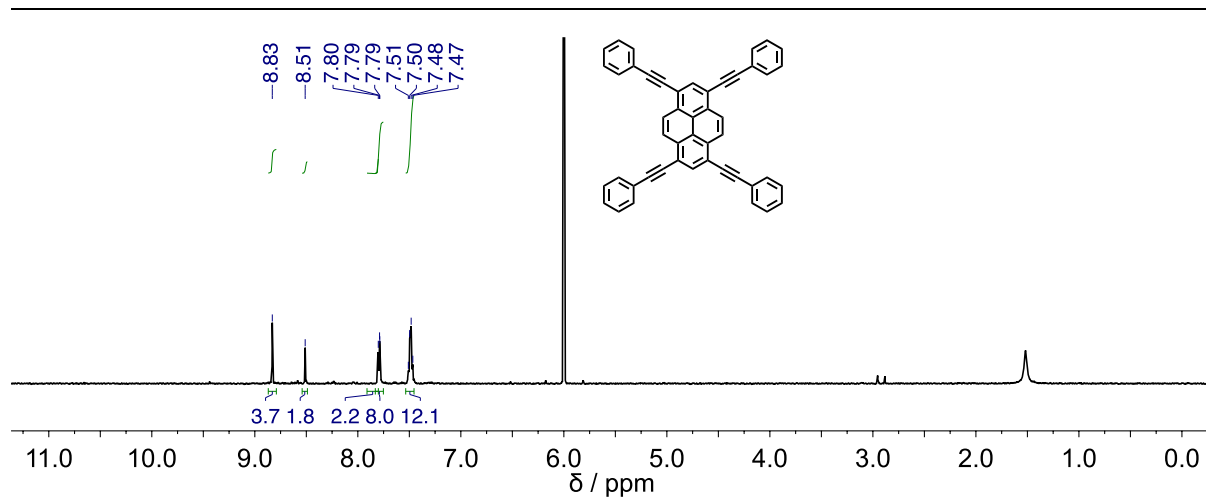
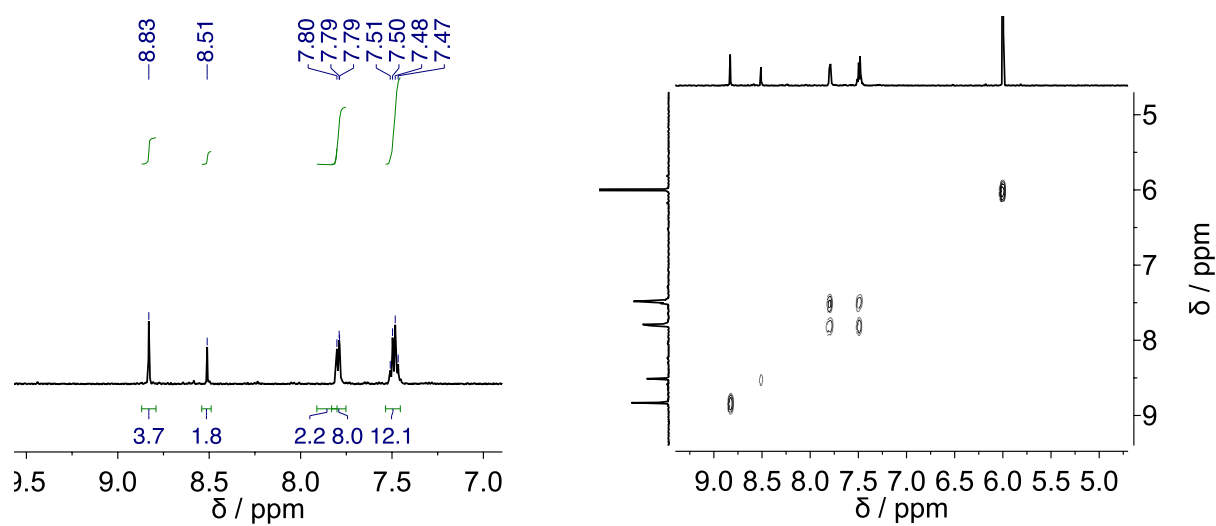
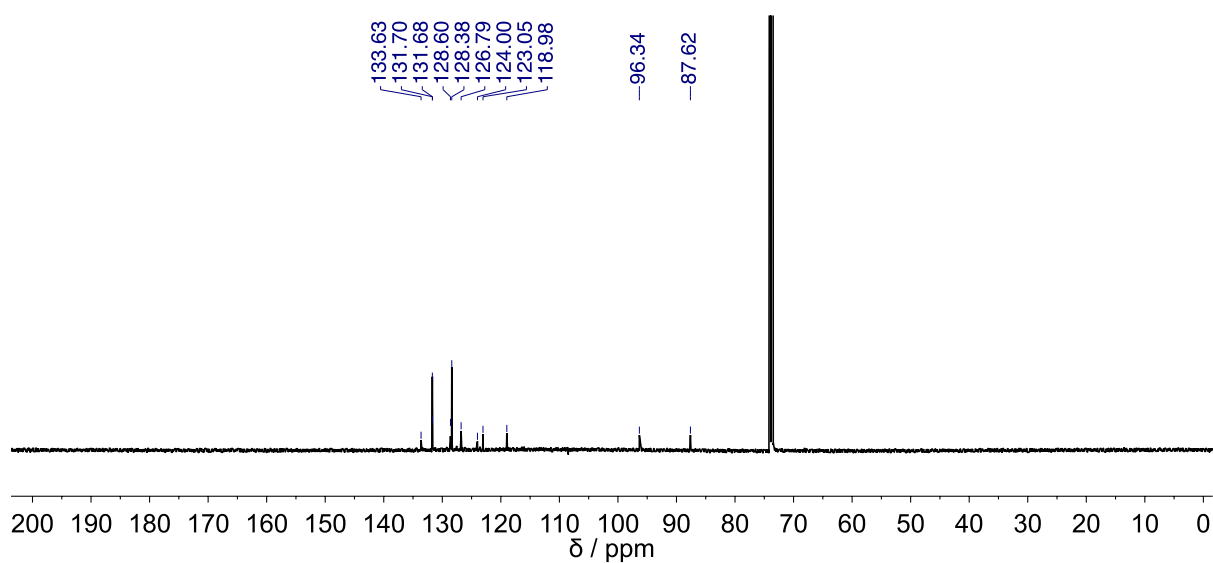
Figure S6.42. $^1\text{H NMR}$ (500 MHz, 353 K, $\text{TCE-}d_2$) of compound 5-1a.

Figure S6.43. Enlarged aromatic region along with gCOSY spectrum for compound 5-1a.

Figure S6.44. $^{13}\text{C NMR}$ (126 MHz, 353 K, $\text{TCE-}d_2$) of compound 5-1a.

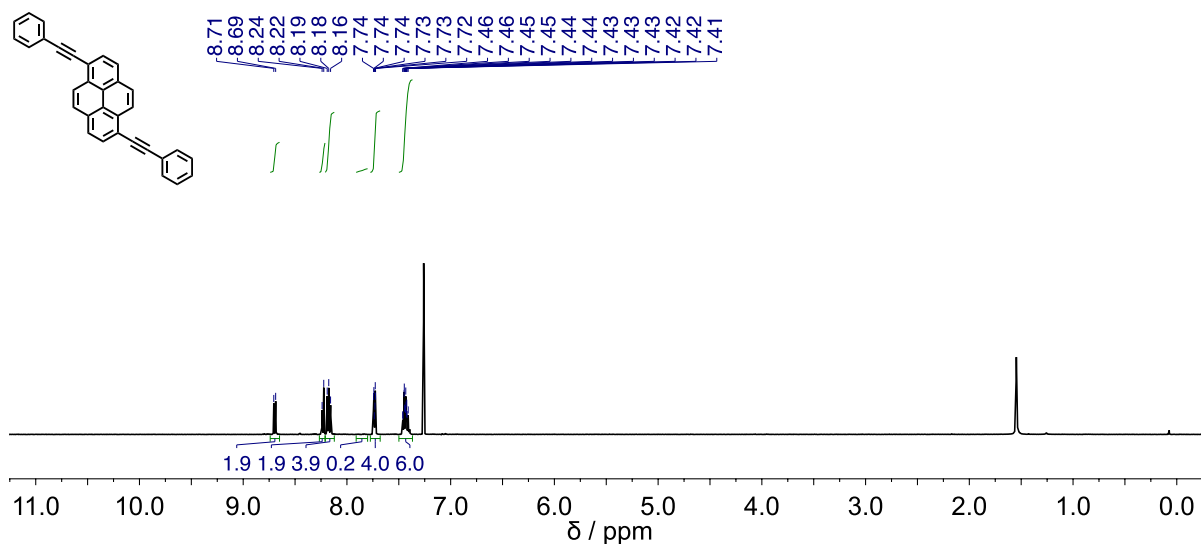


Figure S6.45. ¹H NMR (500 MHz, 298 K, CDCl₃) of compound 5-2a.

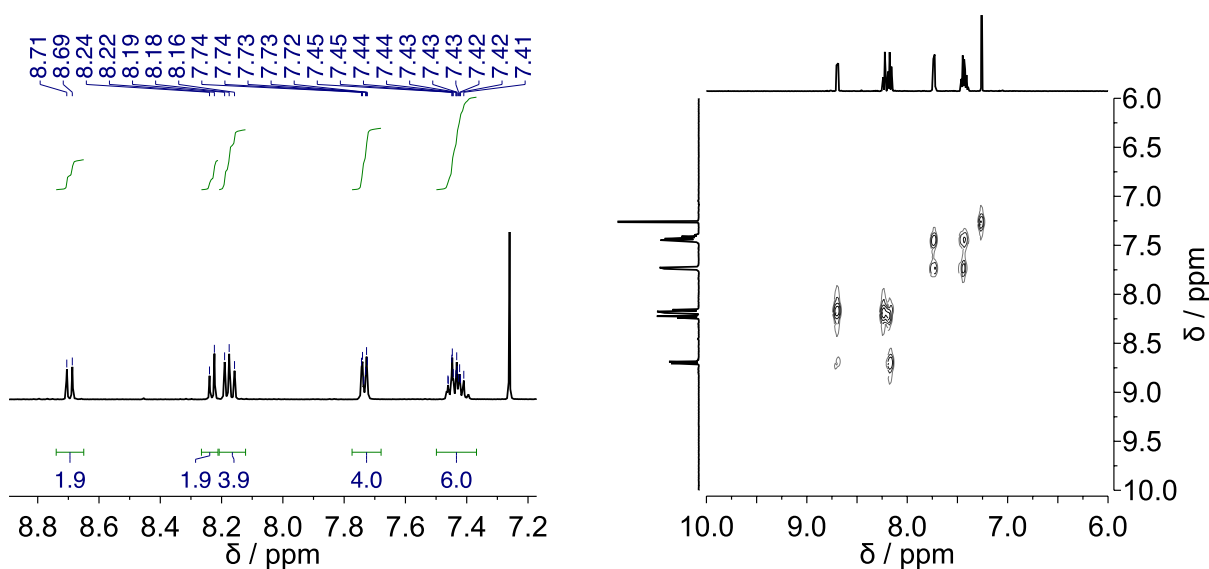


Figure S6.46. Enlarged aromatic region along with gCOSY spectrum for compound 5-2a.

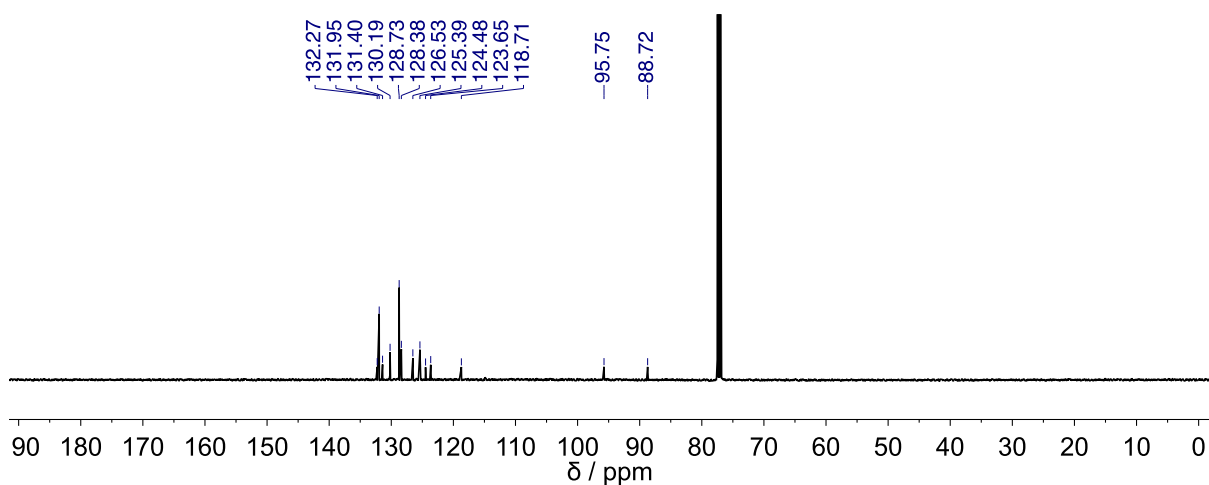


Figure S6.47. ¹³C NMR (500 MHz, 298 K, CDCl₃) of compound 5-2a.

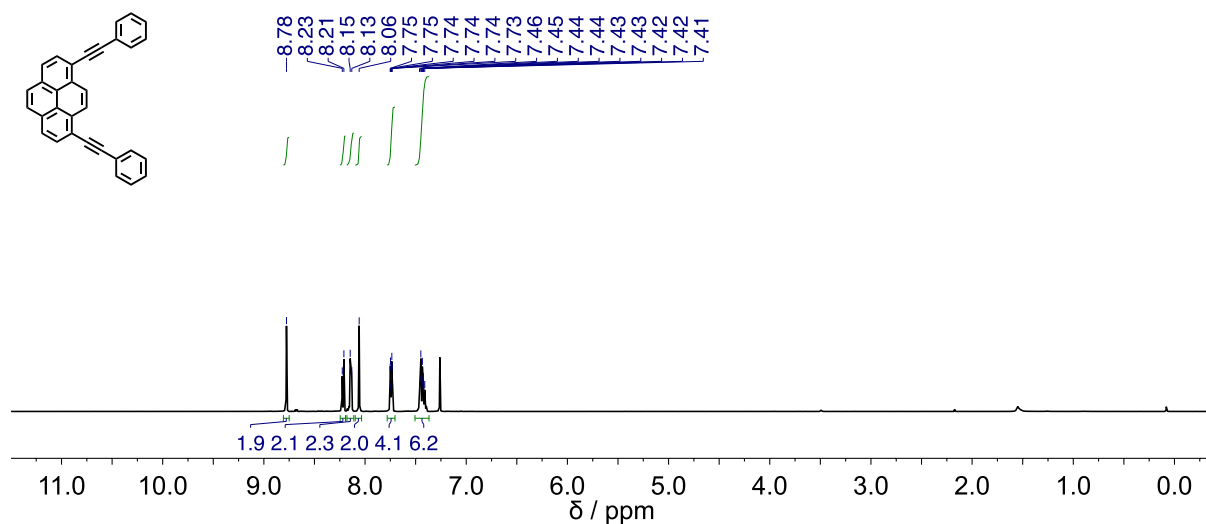


Figure S6.48. $^1\text{H NMR}$ (500 MHz, 298 K, CDCl_3) of compound 5-3a.

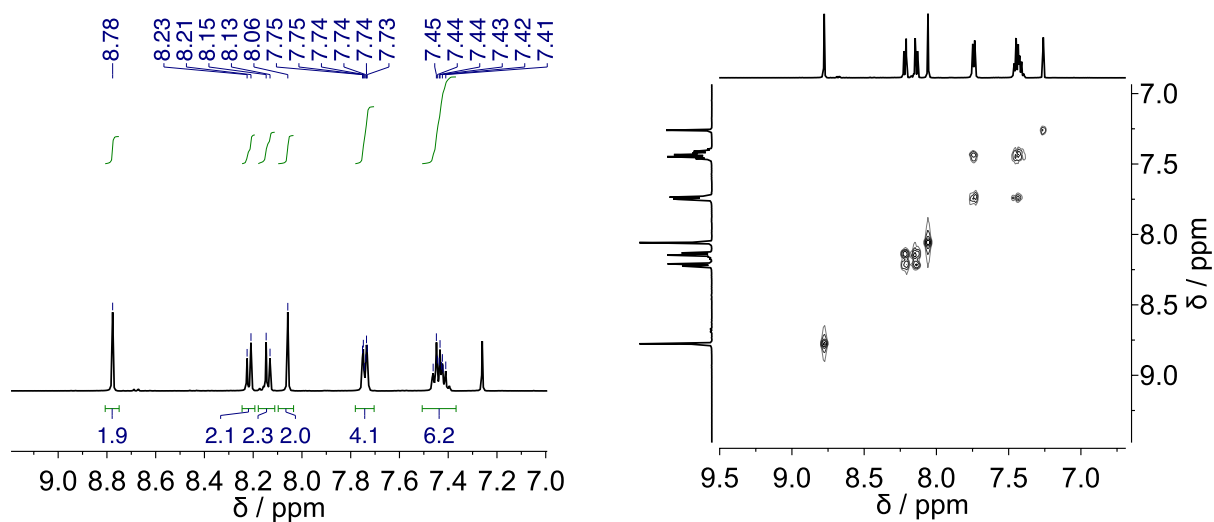


Figure S6.49. Enlarged aromatic region along with gCOSY spectrum for compound 5-3a.

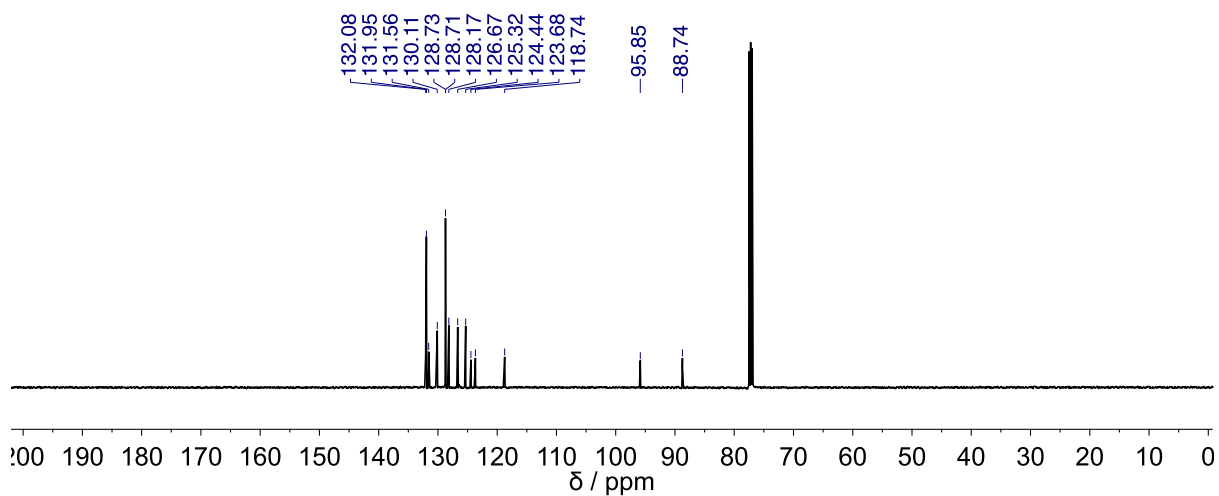


Figure S6.50. $^{13}\text{C NMR}$ (500 MHz, 298 K, CDCl_3) of compound 5-3a.

Bibliography

- (1) Lehn, J.-M. *Supramolecular Chemistry: Concepts and Perspectives*; Wiley-VCH Verlag GmbH & Co. KGaA: Weinheim, FRG, 1995.
 - (2) Lehn, J.-M. Perspectives in Supramolecular Chemistry—From Molecular Recognition towards Molecular Information Processing and Self-Organization. *Angew. Chem. Int. Ed.* **1990**, *29*, 1304–1319.
 - (3) Lehn, J.-M. Toward Self-Organization and Complex Matter. *Science* **2002**, *295*, 2400–2403.
 - (4) Lehn, J.-M. From Supramolecular Chemistry towards Constitutional Dynamic Chemistry and Adaptive Chemistry. *Chem. Soc. Rev.* **2007**, *36*, 151–160.
 - (5) *Supramolecular Chemistry: From Molecules to Nanomaterials*; Gale, P. A.; Steed, J. W., Eds.; John Wiley & Sons, Ltd: Chichester, UK, 2012.
 - (6) Pedersen, C. J. Cyclic Polyethers and Their Complexes with Metal Salts. *J. Am. Chem. Soc.* **1967**, *89*, 7017–7036.
 - (7) Dietrich, B.; Lehn, J.-M.; Sauvage, J. P. Diaza-Polyoxa-Macrocycles et Macrobicycles. *Tetrahedron Lett.* **1969**, *10*, 2885–2888.
 - (8) Cram, D. J.; Kaneda, T.; Helgeson, R. C.; Lein, G. M. Spherands - Ligands Whose Binding of Cations Relieves Enforced Electron-Electron Repulsions. *J. Am. Chem. Soc.* **1979**, *101*, 6752–6754.
 - (9) Desiraju, G. R. A Bond by Any Other Name. *Angew. Chem. Int. Ed.* **2011**, *50*, 52–59.
 - (10) Gilday, L. C.; Robinson, S. W.; Barendt, T. A.; Langton, M. J.; Mullaney, B. R.; Beer, P. D. Halogen Bonding in Supramolecular Chemistry. *Chem. Rev.* **2015**, *115*, 7118–7195.
 - (11) Metrangolo, P.; Meyer, F.; Pilati, T.; Resnati, G.; Terraneo, G. Halogen Bonding in Supramolecular Chemistry. *Angew. Chem. Int. Ed.* **2008**, *47*, 6114–6127.
 - (12) Elemans, J. A. A. W.; van Hameren, R.; Nolte, R. J. M.; Rowan, A. E. Molecular Materials by Self-Assembly of Porphyrins, Phthalocyanines, and Perylenes. *Adv. Mater.* **2006**, *18*, 1251–1266.
 - (13) Becker, M.; Nagarajan, V.; Parson, W. W. Properties of the Excited Singlet States of Bacteriochlorophyll a and Bacteriopheophytin a in Polar Solvents. *J. Am. Chem. Soc.* **1991**, *113*, 6840–6848.
 - (14) *Light-Harvesting Antennas in Photosynthesis*; Green, B. R.; Parson, W. W., Eds.; Advances in Photosynthesis and Respiration; Springer Netherlands: Dordrecht, 2003.
 - (15) McDermott, G.; Prince, S. M.; Freer, A. A.; Hawthornthwaite-Lawless, A. M.; Papiz, M. Z.; Cogdell, R. J.; Isaacs, N. W. Crystal Structure of an Integral Membrane Light-Harvesting Complex from Photosynthetic Bacteria. *Nature*, 1995, *374*, 517–521.
 - (16) Cleary, L.; Chen, H.; Chuang, C.; Silbey, R. J.; Cao, J. Optimal Fold Symmetry of LH2 Rings on a Photosynthetic Membrane. *Proc. Natl. Acad. Sci. U. S. A.* **2013**, *110*, 8537–8542.
 - (17) Pullerits, T.; Sundström, V. Photosynthetic Light-Harvesting Pigment–Protein Complexes: Toward Understanding How and Why. *Acc. Chem. Res.* **1996**, *29*, 381–389.
 - (18) Sundström, V.; Pullerits, T.; van Grondelle, R. Photosynthetic Light-Harvesting: Reconciling
-

- Dynamics and Structure of Purple Bacterial LH2 Reveals Function of Photosynthetic Unit. *J. Phys. Chem. B* **1999**, *103*, 2327–2346.
- (19) Bahatyrova, S.; Frese, R. N.; Siebert, C. A.; Olsen, J. D.; Van Der Werf, K. O.; Van Grondelle, R.; Niederman, R. A.; Bullough, P. A.; Otto, C.; Hunter, C. N. The Native Architecture of a Photosynthetic Membrane. *Nature* **2004**, *430*, 1058–1062.
- (20) *Handbook of Porphyrin Science*; Kadish, K. M.; Smith, K. M.; Guillard, R., Eds.; World Scientific: Singapore, 2010.
- (21) Drain, C. M.; Varotto, A.; Radivojevic, I. Self-Organized Porphyrinic Materials. *Chem. Rev.* **2009**, *109*, 1630–1658.
- (22) Li, L.-L.; Diao, E. W.-G. Porphyrin-Sensitized Solar Cells. *Chem. Soc. Rev.* **2013**, *42*, 291–304.
- (23) Hasobe, T.; Sakai, H. Supramolecular Porphyrin Nanorods for Light Energy Conversion. In *Chemical Science of π -Electron Systems*; Akasaka, T.; Osuka, A.; Fukuzumi, S.; Kandori, H.; Aso, Y., Eds.; Springer Japan: Tokyo, 2015; pp. 475–491.
- (24) Auwärter, W.; Écija, D.; Klappenberger, F.; Barth, J. V. Porphyrins at Interfaces. *Nat. Chem.* **2014**, *7*, 105–120.
- (25) Sengupta, S.; Würthner, F. Chlorophyll J-Aggregates: From Bioinspired Dye Stacks to Nanotubes, Liquid Crystals, and Biosupramolecular Electronics. *Acc. Chem. Res.* **2013**, *46*, 2498–2512.
- (26) Holten, D.; Bocian, D. F.; Lindsey, J. S. Probing Electronic Communication in Covalently Linked Multiporphyrin Arrays. A Guide to the Rational Design of Molecular Photonic Devices. *Acc. Chem. Res.* **2002**, *35*, 57–69.
- (27) Bonifazi, D.; Kiebele, A.; Stöhr, M.; Cheng, F.; Jung, T. A.; Diederich, F.; Spillmann, H. Supramolecular Nanostructuring of Silver Surfaces via Self-Assembly of [60]Fullerene and Porphyrin Modules. *Adv. Funct. Mater.* **2007**, *17*, 1051–1062.
- (28) Mohnani, S.; Bonifazi, D. Supramolecular Architectures of Porphyrins on Surfaces: The Structural Evolution from 1D to 2D to 3D to Devices. *Coord. Chem. Rev.* **2010**, *254*, 2342–2362.
- (29) O’Sullivan, M. C.; Sprafke, J. K.; Kondratuk, D. V.; Rinfrey, C.; Claridge, T. D. W.; Saywell, A.; Blunt, M. O.; O’Shea, J. N.; Beton, P. H.; Malfois, M.; *et al.* Vernier Templating and Synthesis of a 12-Porphyrin Nano-Ring. *Nature* **2011**, *469*, 72–75.
- (30) Hasobe, T. Porphyrin-Based Supramolecular Nanoarchitectures for Solar Energy Conversion. *J. Phys. Chem. Lett.* **2013**, *4*, 1771–1780.
- (31) Babu, S. S.; Bonifazi, D. Self-Organization of Polar Porphyrinoids. *ChemPlusChem* **2014**, *79*, 895–906.
- (32) Miyatake, T.; Tamiaki, H. Self-Aggregates of Natural Chlorophylls and Their Synthetic Analogues in Aqueous Media for Making Light-Harvesting Systems. *Coord. Chem. Rev.* **2010**, *254*, 2593–2602.
- (33) Neuhaus, P.; Cnossen, A.; Gong, J. Q.; Herz, L. M.; Anderson, H. L. A Molecular Nanotube with Three-Dimensional π -Conjugation. *Angew. Chem. Int. Ed.* **2015**, *54*, 7344–7348.
- (34) Kondratuk, D. V.; Perdigão, L. M. A.; Esmail, A. M. S.; O’Shea, J. N.; Beton, P. H.; Anderson, H. L. Supramolecular Nesting of Cyclic Polymers. *Nat. Chem.* **2015**, *7*, 317–322.

-
- (35) The colors of life <http://departments.colgate.edu/chemistry/images/geier-fig1.gif> (accessed Mar 8, 2016).
- (36) Senge, M. O.; Ryan, A.; Letchford, K.; MacGowan, S.; Mielke, T. Chlorophylls, Symmetry, Chirality, and Photosynthesis. *Symmetry* **2014**, *6*, 781–843.
- (37) Gouterman, M. Spectra of Porphyrins. *J. Mol. Spectrosc.* **1961**, *6*, 138 – &.
- (38) Gouterman, M.; Wagnière, G. H.; Snyder, L. C. Spectra of Porphyrins. *J. Mol. Spectrosc.* **1963**, *11*, 108–127.
- (39) Rothemund, P. A New Porphyrin Synthesis. The Synthesis of Porphin. *J. Am. Chem. Soc.* **1936**, *58*, 625–627.
- (40) Rothemund, P. Porphyrin Studies. IV. The Synthesis of $\text{A},\beta,\gamma,\delta$ -Tetraphenylporphine. *J. Am. Chem. Soc.* **1941**, *63*, 267–270.
- (41) Adler, A. D.; Longo, F. R.; Shergalis, W. Mechanistic Investigations of Porphyrin Syntheses. I. Preliminary Studies on Ms -Tetraphenylporphin. *J. Am. Chem. Soc.* **1964**, *86*, 3145–3149.
- (42) Das, A.; Ghosh, S. Supramolecular Assemblies by Charge-Transfer Interactions between Donor and Acceptor Chromophores. *Angew. Chem. Int. Ed.* **2014**, *53*, 2038–2054.
- (43) Cubberley, M. S.; Iverson, B. L. ^1H NMR Investigation of Solvent Effects in Aromatic Stacking Interactions. *J. Am. Chem. Soc.* **2001**, *123*, 7560–7563.
- (44) Das, A.; Molla, M. R.; Banerjee, A.; Paul, A.; Ghosh, S. Hydrogen-Bonding Directed Assembly and Gelation of Donor-Acceptor Chromophores: Supramolecular Reorganization from a Charge-Transfer State to a Self-Sorted State. *Chem. Eur. J.* **2011**, *17*, 6061–6066.
- (45) Das, A.; Molla, M. R.; Maity, B.; Koley, D.; Ghosh, S. Hydrogen-Bonding Induced Alternate Stacking of Donor (D) and Acceptor (A) Chromophores and Their Supramolecular Switching to Segregated States. *Chem. Eur. J.* **2012**, *18*, 9849–9859.
- (46) Ghosh, S.; Ramakrishnan, S. Aromatic Donor-Acceptor Charge-Transfer and Metal-Ion-Complexation-Assisted Folding of a Synthetic Polymer. *Angew. Chem. Int. Ed.* **2004**, *43*, 3264–3268.
- (47) Ghosh, S.; Ramakrishnan, S. Small-Molecule-Induced Folding of a Synthetic Polymer. *Angew. Chem. Int. Ed.* **2005**, *44*, 5441–5447.
- (48) Scott Lokey, R.; Iverson, B. L. Synthetic Molecules That Fold into a Pleated Secondary Structure in Solution. *Nature* **1995**, *375*, 303–305.
- (49) Zych, A. J.; Iverson, B. L. Synthesis and Conformational Characterization of Tethered, Self-Complexing 1,5-Dialkoxynaphthalene/1,4,5,8-Naphthalenetetracarboxylic Diimide Systems. *J. Am. Chem. Soc.* **2000**, *122*, 8898–8909.
- (50) Gabriel, G. J.; Iverson, B. L. Aromatic Oligomers That Form Hetero Duplexes in Aqueous Solution. *J. Am. Chem. Soc.* **2002**, *124*, 15174–15175.
- (51) Kumar, N. S. S.; Gujrati, M. D.; Wilson, J. N. Evidence of Preferential π -Stacking: A Study of Intermolecular and Intramolecular Charge Transfer Complexes. *Chem. Commun.* **2010**, *46*, 5464–5466.
- (52) Colquhoun, H. M.; Zhu, Z.; Cardin, C. J.; Gan, Y.; Drew, M. G. B. Sterically Controlled Recognition of Macromolecular Sequence Information by Molecular Tweezers. *J. Am. Chem. Soc.* **2007**, *129*, 16163–16174.
-

-
- (53) Bryce, M. R.; Cooke, G.; Duclairoir, F. M. A.; Rotello, V. M. An Investigation of the Complexation Behaviour of Structurally Modified Tetrathiafulvalene Derivatives with the Electron Deficient Cyclophane Cyclobis(paraquat-P-Phenylene). *Tetrahedron Lett.* **2001**, *42*, 1143–1145.
- (54) Nielsen, M. B.; Jeppesen, J. O.; Lau, J.; Lomholt, C.; Damgaard, D.; Jacobsen, J. P.; Becher, J.; Stoddart, J. F. Binding Studies between Tetrathiafulvalene Derivatives and Cyclobis(paraquat-P-Phenylene). *J. Org. Chem.* **2001**, *66*, 3559–3563.
- (55) Barnes, J. C.; Juriček, M.; Strutt, N. L.; Frasconi, M.; Sampath, S.; Giesener, M. A.; McGrier, P. L.; Bruns, C. J.; Stern, C. L.; Sarjeant, A. A.; *et al.* ExBox: A Polycyclic Aromatic Hydrocarbon Scavenger. *J. Am. Chem. Soc.* **2013**, *135*, 183–192.
- (56) Juriček, M.; Barnes, J. C.; Dale, E. J.; Liu, W.-G.; Strutt, N. L.; Bruns, C. J.; Vermeulen, N. A.; Ghooray, K. C.; Sarjeant, A. A.; Stern, C. L.; *et al.* Ex2Box: Interdependent Modes of Binding in a Two-Nanometer-Long Synthetic Receptor. *J. Am. Chem. Soc.* **2013**, *135*, 12736–12746.
- (57) Dale, E. J.; Vermeulen, N. A.; Juriček, M.; Barnes, J. C.; Young, R. M.; Wasielewski, M. R.; Stoddart, J. F. Supramolecular Explorations: Exhibiting the Extent of Extended Cationic Cyclophanes. *Acc. Chem. Res.* **2016**, *49*, 262–273.
- (58) Spenst, P.; Würthner, F. A Perylene Bisimide Cyclophane as a “Turn-On” and “Turn-Off” Fluorescence Probe. *Angew. Chem. Int. Ed.* **2015**, *54*, 10165–10168.
- (59) Haino, T.; Watanabe, A.; Hirao, T.; Ikeda, T. Supramolecular Polymerization Triggered by Molecular Recognition between Bisporphyrin and Trinitrofluorenone. *Angew. Chem. Int. Ed.* **2012**, *51*, 1473–1476.
- (60) Nielsen, K. A.; Cho, W. S.; Jeppesen, J. O.; Lynch, V. M.; Becher, J.; Sessler, J. L. Tetra-TTF calix[4]pyrrole: A Rationally Designed Receptor for Electron-Deficient Neutral Guests. *J. Am. Chem. Soc.* **2004**, *126*, 16296–16297.
- (61) Kim, D. S.; Chang, J.; Leem, S.; Park, J. S.; Thordarson, P.; Sessler, J. L. Redox- and pH-Responsive Orthogonal Supramolecular Self-Assembly: An Ensemble Displaying Molecular Switching Characteristics. *J. Am. Chem. Soc.* **2015**, *137*, 16038–16042.
- (62) Bähring, S.; Martín-Gomis, L.; Olsen, G.; Nielsen, K. A.; Kim, D. S.; Duedal, T.; Sastre-Santos, Á.; Jeppesen, J. O.; Sessler, J. L. Design and Sensing Properties of a Self-Assembled Supramolecular Oligomer. *Chem. Eur. J.* **2016**, *22*, 1958–1967.
- (63) Rudolf, M.; Kirner, S. V.; Guldi, D. M. A Multicomponent Molecular Approach to Artificial Photosynthesis – the Role of Fullerenes and Endohedral Metallofullerenes. *Chem. Soc. Rev.* **2016**, *45*, 612–630.
- (64) Schubert, C.; Margraf, J. T.; Clark, T.; Guldi, D. M. Molecular Wires – Impact of π -Conjugation and Implementation of Molecular Bottlenecks. *Chem. Soc. Rev.* **2015**, *44*, 988–998.
- (65) Urbani, M.; Grätzel, M.; Nazeeruddin, M. K.; Torres, T. Meso-Substituted Porphyrins for Dye-Sensitized Solar Cells. *Chem. Rev.* **2014**, *114*, 12330–12396.
- (66) Kroto, H. W.; Heath, J. R.; O’Brien, S. C.; Curl, R. F.; Smalley, R. E. C₆₀: Buckminsterfullerene. *Nature* **1985**, *318*, 162–163.
- (67) Hirsch, A.; Brettreich, M. *Fullerenes: Chemistry and Reactions*; Wiley-VCH Verlag GmbH & Co. KGaA: Weinheim, FRG, 2004.
-

-
- (68) Leonardo da Vinci's Polyhedra <http://www.georgehart.com/virtual-polyhedra/leonardo.html> (accessed Mar 8, 2016).
- (69) Kroto, H. W. The Stability of the Fullerenes C_n , with $N = 24, 28, 32, 36, 50, 60$ and 70 . *Nature* **1987**, *329*, 529–531.
- (70) Schmalz, T. G.; Klein, D. J. Buckminsterfullerenes. In *Buckminsterfullerenes*; Billups, W. E.; Ciufolini, M. A., Eds.; VCH Publishers, Inc.: New York, USA, 1993; pp. 83–102.
- (71) Lu, X.; Chen, Z. Curved Pi-Conjugation, Aromaticity, and the Related Chemistry of Small Fullerenes ($<C_{60}$) and Single-Walled Carbon Nanotubes. *Chem. Rev.* **2005**, *105*, 3643–3696.
- (72) Kordatos, K.; Bosi, S.; Da Ros, T.; Zambon, A.; Lucchini, V.; Prato, M. Isolation and Characterization of All Eight Bisadducts of Fulleropyrrolidine Derivatives. *J. Org. Chem.* **2001**, *66*, 2802–2808.
- (73) Kordatos, K.; Da Ros, T.; Prato, M.; Bensasson, R.; Leach, S. Absorption Spectra of the Mono-Adduct and Eight Bis-Adduct Regioisomers of Pyrrolidine Derivatives of C_{60} . *Chem. Phys.* **2003**, *293*, 263–280.
- (74) Ruoff, R. S.; Tse, D. S.; Malhotra, R.; Lorents, D. C. Solubility of Fullerene (C_{60}) in a Variety of Solvents. *J. Phys. Chem.* **1993**, *97*, 3379–3383.
- (75) Prato, M. [60]Fullerene Chemistry for Materials Science Applications. *J. Mater. Chem.* **1997**, *7*, 1097–1109.
- (76) Nierengarten, J.-F.; Gramlich, V.; Cardullo, F.; Diederich, F. Regio- and Diastereoselective Bisfunctionalization of C_{60} and Enantioselective Synthesis of a C_{60} Derivative with a Chiral Addition Pattern. *Angew. Chem. Int. Ed.* **1996**, *35*, 2101–2103.
- (77) Boyd, P. D. W.; Reed, C. A. Fullerene–Porphyrin Constructs. *Acc. Chem. Res.* **2005**, *38*, 235–242.
- (78) Sun, Y.; Drovetskaya, T.; Bolskar, R. D.; Bau, R.; Boyd, P. D. W.; Reed, C. A. Fullerides of Pyrrolidine-Functionalized C_{60} . *J. Org. Chem.* **1997**, *62*, 3642–3649.
- (79) Sun, D.; Tham, F. S.; Reed, C. A.; Chaker, L.; Burgess, M.; Boyd, P. D. W. Porphyrin–Fullerene Host–Guest Chemistry. *J. Am. Chem. Soc.* **2000**, *122*, 10704–10705.
- (80) Hosseini, A.; Taylor, S.; Accorsi, G.; Armaroli, N.; Reed, C. A.; Boyd, P. D. W. Calix[4]arene-Linked Bisporphyrin Hosts for Fullerenes: Binding Strength, Solvation Effects, and Porphyrin–Fullerene Charge Transfer Bands. *J. Am. Chem. Soc.* **2006**, *128*, 15903–15913.
- (81) Tashiro, K.; Aida, T.; Zheng, J.-Y.; Kinbara, K.; Saigo, K.; Sakamoto, S.; Yamaguchi, K. A Cyclic Dimer of Metalloporphyrin Forms a Highly Stable Inclusion Complex with C_{60} . *J. Am. Chem. Soc.* **1999**, *121*, 9477–9478.
- (82) Zheng, J.-Y.; Tashiro, K.; Hirabayashi, Y.; Kinbara, K.; Saigo, K.; Aida, T.; Sakamoto, S.; Yamaguchi, K. Cyclic Dimers of Metalloporphyrins as Tunable Hosts for Fullerenes: A Remarkable Effect of Rhodium(III). *Angew. Chem. Int. Ed.* **2001**, *40*, 1857–1861.
- (83) Gil-Ramírez, G.; Karlen, S. D.; Shundo, A.; Porfyakis, K.; Ito, Y.; Briggs, G. A. D.; Morton, J. J. L.; Anderson, H. L. A Cyclic Porphyrin Trimer as a Receptor for Fullerenes. *Org. Lett.* **2010**, *12*, 3544–3547.
- (84) Song, J.; Aratani, N.; Shinokubo, H.; Osuka, A. A Porphyrin Nanobarrel That Encapsulates C_{60} . *J. Am. Chem. Soc.* **2010**, *132*, 16356–16357.
-

-
- (85) Meng, W.; Breiner, B.; Rissanen, K.; Thoburn, J. D.; Clegg, J. K.; Nitschke, J. R. A Self-Assembled M8L6 Cubic Cage That Selectively Encapsulates Large Aromatic Guests. *Angew. Chem. Int. Ed.* **2011**, *50*, 3479–3483.
- (86) Wood, D. M.; Meng, W.; Ronson, T. K.; Stefankiewicz, A. R.; Sanders, J. K. M.; Nitschke, J. R. Guest-Induced Transformation of a Porphyrin-Edged FeII4L6 Capsule into a CuIFeII2L4 Fullerene Receptor. *Angew. Chem. Int. Ed.* **2015**, *54*, 3988–3992.
- (87) García-Simón, C.; Garcia-Borràs, M.; Gómez, L.; Parella, T.; Osuna, S.; Juanhuix, J.; Imaz, I.; Maspoch, D.; Costas, M.; Ribas, X. Sponge-like Molecular Cage for Purification of Fullerenes. *Nat. Commun.* **2014**, *5*, 5557.
- (88) Satake, A.; Kobuke, Y. Dynamic Supramolecular Porphyrin Systems. *Tetrahedron* **2005**, *61*, 13–41.
- (89) Armaroli, N.; Diederich, F.; Echegoyen, L.; Habicher, T.; Flamigni, L.; Marconi, G.; Nierengarten, J.-F. A New Pyridyl-Substituted Methanofullerene Derivative. Photophysics, Electrochemistry and Self-Assembly with zinc(II) Meso-Tetraphenylporphyrin (ZnTPP). *New J. Chem.* **1999**, *23*, 77–83.
- (90) D'Souza, F.; Deviprasad, G. R.; Rahman, M. S.; Choi, J. Self-Assembled Porphyrin–C60 and Porphycene–C60 Complexes via Metal Axial Coordination. *Inorg. Chem.* **1999**, *38*, 2157–2160.
- (91) Trabolsi, A.; Elhabiri, M.; Urbani, M.; Delgado de la Cruz, J. L.; Ajamaa, F.; Solladié, N.; Albrecht-Gary, A.-M.; Nierengarten, J.-F. Supramolecular Click Chemistry for the Self-Assembly of a Stable Zn(II)–porphyrin–C60 Conjugate. *Chem. Commun.* **2005**, 5736–5738.
- (92) D'Souza, F.; Smith, P. M.; Zandler, M. E.; McCarty, A. L.; Itou, M.; Araki, Y.; Ito, O. Energy Transfer Followed by Electron Transfer in a Supramolecular Triad Composed of Boron Dipyrin, Zinc Porphyrin, and Fullerene: A Model for the Photosynthetic Antenna-Reaction Center Complex. *J. Am. Chem. Soc.* **2004**, *126*, 7898–7907.
- (93) Sánchez, L.; Sierra, M.; Martín, N.; Myles, A. J.; Dale, T. J.; Rebek, J.; Seitz, W.; Guldi, D. M. Exceptionally Strong Electronic Communication through Hydrogen Bonds in Porphyrin–C60 Pairs. *Angew. Chem. Int. Ed.* **2006**, *45*, 4637–4641.
- (94) Chang, S. K.; Hamilton, A. D. Molecular Recognition of Biologically Interesting Substrates: Synthesis of an Artificial Receptor for Barbiturates Employing Six Hydrogen Bonds. *J. Am. Chem. Soc.* **1988**, *110*, 1318–1319.
- (95) Wessendorf, F.; Grimm, B.; Guldi, D. M.; Hirsch, A. Pairing Fullerenes and Porphyrins: Supramolecular Wires That Exhibit Charge Transfer Activity. *J. Am. Chem. Soc.* **2010**, *132*, 10786–10795.
- (96) Schuster, D. I.; Li, K.; Guldi, D. M.; Ramey, J. Novel Porphyrin-Fullerene Assemblies: From Rotaxanes to Catenanes. *Org. Lett.* **2004**, *6*, 1919–1922.
- (97) Li, K.; Schuster, D. I.; Guldi, D. M.; Herranz, M. Á.; Echegoyen, L. Convergent Synthesis and Photophysics of [60]Fullerene/Porphyrin-Based Rotaxanes. *J. Am. Chem. Soc.* **2004**, *126*, 3388–3389.
- (98) Faiz, J. A.; Heitz, V.; Sauvage, J.-P. Design and Synthesis of Porphyrin-Containing Catenanes and Rotaxanes. *Chem. Soc. Rev.* **2009**, *38*, 422–442.
- (99) Wu, Z.; Shao, X.; Li, C.; Hou, J.; Wang, K.; Jiang, X.; Li, Z. Hydrogen-Bonding-Driven
-

- Preorganized Zinc Porphyrin Receptors for Efficient Complexation of C60 , C70 , and C60 Derivatives. *J. Am. Chem. Soc.* **2005**, *127*, 17460–17468.
- (100) D'Souza, F.; Smith, P. M.; Gadde, S.; McCarty, A. L.; Kullman, M. J.; Zandler, M. E.; Itou, M.; Araki, Y.; Ito, O. Supramolecular Triads Formed by Axial Coordination of Fullerene to Covalently Linked Zinc Porphyrin–Ferrocene(s): Design, Syntheses, Electrochemistry, and Photochemistry. *J. Phys. Chem. B* **2004**, *108*, 11333–11343.
- (101) Solladié, N.; Walther, M. E.; Gross, M.; Figueira Duarte, T. M.; Bourgoigne, C.; Nierengarten, J.-F. A Supramolecular Cup-and-Ball C60–porphyrin Conjugate System. *Chem. Commun.* **2003**, 2412–2413.
- (102) Moreira, L.; Calbo, J.; Illescas, B. M.; Aragón, J.; Nierengarten, I.; Delavaux-Nicot, B.; Ortí, E.; Martín, N.; Nierengarten, J.-F. Metal-Atom Impact on the Self-Assembly of Cup-and-Ball Metalloporphyrin–Fullerene Conjugates. *Angew. Chem. Int. Ed.* **2015**, *54*, 1255–1260.
- (103) Calderon, R. M. K.; Valero, J.; Grimm, B.; de Mendoza, J.; Guldi, D. M. Enhancing Molecular Recognition in Electron Donor–Acceptor Hybrids via Cooperativity. *J. Am. Chem. Soc.* **2014**, *136*, 11436–11443.
- (104) Xue, M.; Yang, Y.; Chi, X.; Yan, X.; Huang, F. Development of Pseudorotaxanes and Rotaxanes: From Synthesis to Stimuli-Responsive Motions to Applications. *Chem. Rev.* **2015**, *115*, 7398–7501.
- (105) Ashton, P. R.; Chrystal, E. J. T.; Glink, P. T.; Menzer, S.; Schiavo, C.; Spencer, N.; Stoddart, J. F.; Tasker, P. A.; White, A. J. P.; Williams, D. J. Pseudorotaxanes Formed Between Secondary Dialkylammonium Salts and Crown Ethers. *Chem. Eur. J.* **1996**, *2*, 709–728.
- (106) Asakawa, M.; Iqbal, S.; Stoddart, J. F.; Tinker, N. D. Prototype of an Optically Responsive Molecular Switch Based on Pseudorotaxane. *Angew. Chem. Int. Ed.* **1996**, *35*, 976–978.
- (107) Balzani, V.; Credi, A.; Marchioni, F.; Stoddart, J. F. Artificial Molecular-Level Machines. Dethreading-Rethreading of a Pseudorotaxane Powered Exclusively by Light Energy. *Chem. Commun.* **2001**, 1860–1861.
- (108) Ballardini, R.; Balzani, V.; Credi, A.; Gandolfi, M. T.; Venturi, M. Artificial Molecular-Level Machines: Which Energy to Make Them Work? *Acc. Chem. Res.* **2001**, *34*, 445–455.
- (109) Liu, Y.; Flood, A. H.; Stoddart, J. F. Thermally and Electrochemically Controllable Self-Complexing Molecular Switches. *J. Am. Chem. Soc.* **2004**, *126*, 9150–9151.
- (110) Zhang, H.; Wang, Q.; Liu, M.; Ma, X.; Tian, H. Switchable V-Type [2]Pseudorotaxanes. *Org. Lett.* **2009**, *11*, 3234–3237.
- (111) McNitt, K. A.; Parimal, K.; Share, A. I.; Fahrenbach, A. C.; Witlicki, E. H.; Pink, M.; Bediako, D. K.; Plaisier, C. L.; Le, N.; Heeringa, L. P.; *et al.* Reduction of a Redox-Active Ligand Drives Switching in a Cu(I) Pseudorotaxane by a Bimolecular Mechanism. *J. Am. Chem. Soc.* **2009**, *131*, 1305–1313.
- (112) Glink, P. T.; Schiavo, C.; Stoddart, J. F.; Williams, D. J. The Genesis of a New Range of Interlocked Molecules. *Chem. Commun.* **1996**, 1483–1490.
- (113) Ashton, P. R.; Glink, P. T.; Martínez-Díaz, M.-V.; Stoddart, J. F.; White, A. J. P.; Williams, D. J. Thermodynamically Controlled Self-Assembly of Pseudorotaxanes and Pseudopolyrotaxanes with Different Recognition Motifs Operating Self-Selectively. *Angew. Chem. Int. Ed.* **1996**, *35*, 1930–1933.

-
- (114) Diederich, F.; Echegoyen, L.; Gómez-López, M.; Kessinger, R.; Stoddart, J. F. The Self-Assembly of Fullerene-Containing [2]pseudorotaxanes: Formation of a Supramolecular C60 Dimer. *J. Chem. Soc. Perkin Trans. 2* **1999**, *Diederich*, 1577–1586.
- (115) Guldi, D. M.; Ramey, J.; Martínez-Díaz, M.-V.; Escosura, A. de la; Torres, T.; Da Ros, T.; Prato, M. Reversible Zinc Phthalocyanine Fullerene Ensembles. *Chem. Commun.* **2002**, 2774–2775.
- (116) Martínez-Díaz, M.-V.; Fender, N. S.; Rodríguez-Morgade, M. S.; Gómez-López, M.; Diederich, F.; Echegoyen, L.; Stoddart, J. F.; Torres, T. A Supramolecular Approach for the Formation of Fullerene–phthalocyanine Dyads. *J. Mater. Chem.* **2002**, *12*, 2095–2099.
- (117) Díaz, M. C.; Illescas, B. M.; Martín, N.; Stoddart, J. F.; Canales, M. A.; Jiménez-Barbero, J.; Sarova, G.; Guldi, D. M. Supramolecular Pseudo-Rotaxane Type Complexes from π -Extended TTF Dimer Crown Ether and C60. *Tetrahedron* **2006**, *62*, 1998–2002.
- (118) Illescas, B. M.; Santos, J.; Díaz, M. C.; Martín, N.; Atienza, C. M.; Guldi, D. M. Supramolecular Threaded Complexes from Fullerene–Crown Ether and π -Extended TTF Derivatives. *Eur. J. Org. Chem.* **2007**, *2007*, 5027–5037.
- (119) Nie, W. Optical Nonlinearity: Phenomena, Applications, and Materials. *Adv. Mater.* **1993**, *5*, 520–545.
- (120) Kaino, T.; Tomaru, S. Organic Materials for Nonlinear Optics. *Adv. Mater.* **1993**, *5*, 172–178.
- (121) Nalwa, H. S. Organic Materials for Third-Order Nonlinear Optics. *Adv. Mater.* **1993**, *5*, 341–358.
- (122) Kanis, D. R.; Ratner, M. A.; Marks, T. J. Design and Construction of Molecular Assemblies with Large Second-Order Optical Nonlinearities. Quantum Chemical Aspects. *Chem. Rev.* **1994**, *94*, 195–242.
- (123) Marder, S. R. Organic Nonlinear Optical Materials: Where We Have Been and Where We Are Going. *Chem. Commun.* **2006**, 131–134.
- (124) Long, N. J. Organometallic Compounds for Nonlinear Optics—The Search for Enlightenment! *Angew. Chem. Int. Ed.* **1995**, *34*, 21–38.
- (125) Innocenzi, P.; Brusatin, G. Fullerene-Based Organic–Inorganic Nanocomposites and Their Applications. *Chem. Mater.* **2001**, *13*, 3126–3139.
- (126) Innocenzi, P.; Lebeau, B. Organic–inorganic Hybrid Materials for Non-Linear Optics. *J. Mater. Chem.* **2005**, *15*, 3821–3831.
- (127) Guldi, D. M.; Illescas, B. M.; Atienza, C. M.; Wielopolski, M.; Martín, N. Fullerene for Organic Electronics. *Chem. Soc. Rev.* **2009**, *38*, 1587–1597.
- (128) Accorsi, G.; Armaroli, N. Taking Advantage of the Electronic Excited States of [60]-Fullerenes. *J. Phys. Chem. C* **2010**, *114*, 1385–1403.
- (129) Senge, M. O.; Fazekas, M.; Notaras, E. G. A.; Blau, W. J.; Zawadzka, M.; Locos, O. B.; Ni Mhuircheartaigh, E. M. Nonlinear Optical Properties of Porphyrins. *Adv. Mater.* **2007**, *19*, 2737–2774.
- (130) Aratani, N.; Kim, D.; Osuka, A. π -Conjugation Enlargement Toward the Creation of Multi-Porphyrinic Systems with Large Two-Photon Absorption Properties. *Chem. Asian J.* **2009**, *4*, 1172–1182.
- (131) Pawlicki, M.; Collins, H. A.; Denning, R. G.; Anderson, H. L. Two-Photon Absorption and the
-

- Design of Two-Photon Dyes. *Angew. Chem. Int. Ed.* **2009**, *48*, 3244–3266.
- (132) Imahori, H.; Sakata, Y. Fullerenes as Novel Acceptors in Photosynthetic Electron Transfer. *Eur. J. Org. Chem.* **1999**, 2445–2457.
- (133) Imahori, H. Porphyrin–fullerene Linked Systems as Artificial Photosynthetic Mimics. *Org. Biomol. Chem.* **2004**, *2*, 1425–1433.
- (134) Imahori, H.; Fukuzumi, S. Porphyrin-and Fullerene-Based Molecular Photovoltaic Devices. *Adv. Funct. Mater.* **2004**, *14*, 525–536.
- (135) Pérez, E. M.; Martín, N. Curves Ahead: Molecular Receptors for Fullerenes Based on Concave–convex Complementarity. *Chem. Soc. Rev.* **2008**, *37*, 1512.
- (136) Fukuzumi, S. Development of Bioinspired Artificial Photosynthetic Systems. *Phys. Chem. Chem. Phys.* **2008**, *10*, 2283.
- (137) D'Souza, F.; Ito, O. Supramolecular Donor–acceptor Hybrids of Porphyrins/phthalocyanines with Fullerenes/carbon Nanotubes: Electron Transfer, Sensing, Switching, and Catalytic Applications. *Chem. Commun.* **2009**, 4913–4928.
- (138) D'Souza, F.; Ito, O. Photosensitized Electron Transfer Processes of Nanocarbons Applicable to Solar Cells. *Chem. Soc. Rev.* **2012**, *41*, 86–96.
- (139) Pérez, E. M.; Martín, N. Π – π Interactions in Carbon Nanostructures. *Chem. Soc. Rev.* **2015**, *44*, 6425–6433.
- (140) Xenogiannopoulou, E.; Medved, M.; Iliopoulos, K.; Couris, S.; Papadopoulos, M. G.; Bonifazi, D.; Sooambar, C.; Mateo-Alonso, A.; Prato, M. Nonlinear Optical Properties of Ferrocene- and Porphyrin–[60]Fullerene Dyads. *ChemPhysChem* **2007**, *8*, 1056–1064.
- (141) Aloukos, P.; Iliopoulos, K.; Couris, S.; Guldi, D. M.; Sooambar, C.; Mateo-Alonso, A.; Nagaswaran, P. G.; Bonifazi, D.; Prato, M. Photophysics and Transient Nonlinear Optical Response of donor–[60]fullerene Hybrids. *J. Mater. Chem.* **2011**, *21*, 2524–2534.
- (142) Sun, Y.-P.; Lawson, G. E.; Riggs, J. E.; Ma, B.; Wang, N.; Moton, D. K. Photophysical and Nonlinear Optical Properties of [60]Fullerene Derivatives. *J. Phys. Chem. A* **1998**, *102*, 5520–5528.
- (143) Koudoumas, E.; Konstantaki, M.; Mavromanolakis, A.; Couris, S.; Fanti, M.; Zerbetto, F.; Kordatos, K.; Prato, M. Large Enhancement of the Nonlinear Optical Response of Reduced Fullerene Derivatives. *Chem. Eur. J.* **2003**, *9*, 1529–1534.
- (144) Mateo-Alonso, A.; Iliopoulos, K.; Couris, S.; Prato, M. Efficient Modulation of the Third Order Nonlinear Optical Properties of Fullerene Derivatives. *J. Am. Chem. Soc.* **2008**, *130*, 1534–1535.
- (145) Loboda, O.; Zalesny, R.; Avramopoulos, A.; Luis, J.-M.; Kirtman, B.; Tagmatarchis, N.; Reis, H.; Papadopoulos, M. G. Linear and Nonlinear Optical Properties of [60]Fullerene Derivatives. *J. Phys. Chem. A* **2009**, *113*, 1159–1170.
- (146) Zalesny, R.; Loboda, O.; Iliopoulos, K.; Chatzikyriakos, G.; Couris, S.; Rotas, G.; Tagmatarchis, N.; Avramopoulos, A.; Papadopoulos, M. G. Linear and Nonlinear Optical Properties of Triphenylamine-Functionalized C60: Insights from Theory and Experiment. *Phys. Chem. Chem. Phys.* **2010**, *12*, 373–381.
- (147) Bottari, G.; Trukhina, O.; Ince, M.; Torres, T. Towards Artificial Photosynthesis:

-
- Supramolecular, Donor-Acceptor, Porphyrin- and Phthalocyanine/carbon Nanostructure Ensembles. *Coord. Chem. Rev.* **2012**, *256*, 2453–2477.
- (148) Konarev, D. V.; Khasanov, S. S.; Lyubovskaya, R. N. Fullerene Complexes with Coordination Assemblies of Metalloporphyrins and Metal Phthalocyanines. *Coord. Chem. Rev.* **2014**, *262*, 16–36.
- (149) Nierengarten, J.; Solladié, N. Self-Assembly of a C₆₀ Derivative Bearing an Ammonium Unit with Porphyrin-Crown Ether Conjugates. *J. Porphyr. Phthalocyanines* **2005**, *09*, 760–768.
- (150) Armaroli, N.; Marconi, G.; Echegoyen, L.; Bourgeois, J.; Diederich, F. Charge-Transfer Interactions in Face-to-Face Porphyrin-Fullerene Systems: Solvent-Dependent Luminescence in the Infrared Spectral Region. *Chem. Eur. J.* **2000**, *6*, 1629–1645.
- (151) Jiang, W.; Nowosinski, K.; Löw, N. L.; Dzyuba, E. V.; Klautzsch, F.; Schäfer, A.; Huuskonen, J.; Rissanen, K.; Schalley, C. A. Chelate Cooperativity and Spacer Length Effects on the Assembly Thermodynamics and Kinetics of Divalent Pseudorotaxanes. *J. Am. Chem. Soc.* **2012**, *134*, 1860–1868.
- (152) Frisch, M. J.; Trucks, G. W.; Schlegel, H. B.; Scuseria, G. E.; Robb, M. A.; Cheeseman, J. R.; Scalmani, G.; Barone, V.; Mennucci, B.; Petersson, G. A.; *et al.* Gaussian 09, Revision A.1, 2009.
- (153) Armaroli, N.; Accorsi, G.; Song, F.; Palkar, A.; Echegoyen, L.; Bonifazi, D.; Diederich, F. Photophysical and Electrochemical Properties Of meso,meso-Linked Oligoporphyrin Rods with Appended Fullerene Terminals. *ChemPhysChem* **2005**, *6*, 732–743.
- (154) D'Souza, F.; Chitta, R.; Gadde, S.; Zandler, M. E.; McCarty, A. L.; Sandanayaka, A. S. D.; Araki, Y.; Ito, O. Effect of Axial Ligation or π - π -Type Interactions on Photochemical Charge Stabilization in “Two-Point” Bound Supramolecular Porphyrin-Fullerene Conjugates. *Chem. Eur. J.* **2005**, *11*, 4416–4428.
- (155) D'Souza, F.; Chitta, R.; Gadde, S.; Rogers, L. M.; Karr, P. A.; Zandler, M. E.; Sandanayaka, A. S. D.; Araki, Y.; Ito, O. Photosynthetic Reaction Center Mimicry of a “Special Pair” Dimer Linked to Electron Acceptors by a Supramolecular Approach: Self-Assembled Cofacial Zinc Porphyrin Dimer Complexed with Fullerene(s). *Chem. Eur. J.* **2007**, *13*, 916–922.
- (156) Sheik-Bahae, M.; Said, A. A.; Wei, T.-H.; Hagan, D. J.; Van Stryland, E. W. Sensitive Measurement of Optical Nonlinearities Using a Single Beam. *IEEE J. Quantum Electron.* **1990**, *26*, 760–769.
- (157) Aloukos, P.; Chatzikyriakos, G.; Papagiannouli, I.; Liaros, N.; Couris, S. Transient Nonlinear Optical Response of Some Symmetrical Nickel Dithiolene Complexes. *Chem. Phys. Lett.* **2010**, *495*, 245–250.
- (158) Zhang, W.-S.; Wang, D.; Cao, H.; Yang, H. Energy Level Tunable Pre-Click Functionalization of [60]fullerene for Nonlinear Optics. *Tetrahedron* **2014**, *70*, 573–577.
- (159) Wang, W.-Y.; Wang, L.; Ma, N.-N.; Zhu, C.-L.; Qiu, Y.-Q. Ferrocene/fullerene Hybrids Showing Large Second-Order Nonlinear Optical Activities: Impact of the Cage Unit Size. *Dalt. Trans.* **2015**, *44*, 10078–10088.
- (160) Imahori, H. Porphyrin – Fullerene Linked Systems as Artificial Photosynthetic Mimics. *Org. Biomol. Chem.* **2004**, *2*, 1425–1433.
- (161) Kirner, S. V.; Arteaga, D.; Henkel, C.; Margraf, J. T.; Alegret, N.; Ohkubo, K.; Insuasty, B.; Ortiz, A.; Martín, N.; Echegoyen, L.; *et al.* On-off Switch of Charge-Separated States of
-

- Pyridine-Vinylene-Linked porphyrin–C60 Conjugates Detected by EPR. *Chem. Sci.* **2015**, *6*, 5994–6007.
- (162) Imahori, H.; Sekiguchi, Y.; Kashiwagi, Y.; Sato, T.; Araki, Y.; Ito, O.; Yamada, H.; Fukuzumi, S. Long-Lived Charge-Separated State Generated in a Ferrocene–meso,meso-Linked Porphyrin Trimer–Fullerene Pentad with a High Quantum Yield. *Chem. Eur. J.* **2004**, *10*, 3184–3196.
- (163) D’Souza, F.; Maligaspe, E.; Karr, P. A.; Schumacher, A. L.; El Ojaimi, M.; Gros, C. P.; Barbe, J.-M.; Ohkubo, K.; Fukuzumi, S. Face-to-Face Pacman-Type Porphyrin–Fullerene Dyads: Design, Synthesis, Charge-Transfer Interactions, and Photophysical Studies. *Chem. Eur. J.* **2008**, *14*, 674–681.
- (164) Sahraoui, B.; Kityk, I. V.; Bieleninik, J.; Hudhomme, P.; Gorgues, A. Optical Limiting Processes in C60-2-Thioxo-1,3-Dithiole Cycloadduct. *Opt. Mater.* **1999**, *13*, 349–353.
- (165) Sahraoui, B.; Fuks-Janczarek, I.; Bartkiewicz, S.; Matczyszyn, K.; Mysliwiec, J.; Kityk, I. V.; Berdowski, J.; Allard, E.; Cousseau, J. Enhancement of Third-Order Optical Susceptibility of C60-TTF Compounds Using Nematic Liquid Crystal. *Chem. Phys. Lett.* **2002**, *365*, 327–332.
- (166) Alam, M. M.; Chattopadhyaya, M.; Chakrabarti, S.; Ruud, K. High-Polarity Solvents Decreasing the Two-Photon Transition Probability of Through-Space Charge-Transfer Systems — A Surprising In Silico Observation. *J. Phys. Chem. Lett.* **2012**, *3*, 961–966.
- (167) Zyss, J.; Ledoux, I.; Volkov, S.; Chernyak, V.; Mukamel, S.; Bartholomew, G. P.; Bazan, G. C. Through-Space Charge Transfer and Nonlinear Optical Properties of Substituted Paracyclophane. *J. Am. Chem. Soc.* **2000**, *122*, 11956–11962.
- (168) Ball, P. Water as an Active Constituent in Cell Biology. *Chem. Rev.* **2008**, *108*, 74–108.
- (169) Krieg, E.; Bastings, M. M. C.; Besenius, P.; Rybtchinski, B. Supramolecular Polymers in Aqueous Media. *Chem. Rev.* **2016**, *116*, 2414–2477.
- (170) Oshovsky, G. V.; Reinhoudt, D. N.; Verboom, W. Supramolecular Chemistry in Water. *Angew. Chem. Int. Ed.* **2007**, *46*, 2366–2393.
- (171) Görl, D.; Zhang, X.; Würthner, F. Molecular Assemblies of Perylene Bisimide Dyes in Water. *Angew. Chem. Int. Ed.* **2012**, *51*, 6328–6348.
- (172) Philp, D.; Stoddart, J. F. Self-Assembly in Natural and Unnatural Systems. *Angew. Chem. Int. Ed.* **1996**, *35*, 1154–1196.
- (173) Reichardt, C.; Welton, T. *Solvents and Solvent Effects in Organic Chemistry*; Wiley-VCH Verlag GmbH & Co. KGaA: Weinheim, Germany, 2010.
- (174) Laidler, K. J. *The World of Physical Chemistry*; Oxford University Press: Oxford, U.K., 1995.
- (175) Smallwood, I. M. *Handbook of Organic Solvent Properties*; 1st ed.; John Wiley & Sons Inc.: New York, 1996.
- (176) Ohtaki, H. Development of Modern Solution Chemistry: A Search of New Fields. *Coord. Chem. Rev.* **1999**, *185-6*, 735–759.
- (177) *Solvent Effects and Chemical Reactivity*; Tapia, O.; Bertrán, J., Eds.; Understanding Chemical Reactivity; Kluwer Academic Publishers: Dordrecht, 2002.
- (178) Stupp, S. I.; Palmer, L. C. Supramolecular Chemistry and Self-Assembly in Organic Materials Design. *Chem. Mater.* **2013**, *26*, 507–518.

-
- (179) Würthner, F.; Saha-Möller, C. R.; Fimmel, B.; Ogi, S.; Leowanawat, P.; Schmidt, D. Perylene Bisimide Dye Assemblies as Archetype Functional Supramolecular Materials. *Chem. Rev.* **2016**, *116*, 962–1052.
- (180) Würthner, F.; Meerholz, K. Systems Chemistry Approach in Organic Photovoltaics. *Chem. Eur. J.* **2010**, *16*, 9366–9373.
- (181) Li, S.-L.; Xiao, T.; Lin, C.; Wang, L. Advanced Supramolecular Polymers Constructed by Orthogonal Self-Assembly. *Chem. Soc. Rev.* **2012**, *41*, 5950–5968.
- (182) *Supramolecular Dye Chemistry*; Würthner, F., Ed.; Topics in Current Chemistry; Springer Berlin Heidelberg: Berlin, Heidelberg, 2005.
- (183) *Organic Nanostructures for Next Generation Devices*; Al-Shamery, K.; Rubahn, H.-G.; Sitter, H., Eds.; Springer Series in Materials Science; Springer Berlin Heidelberg: Berlin, Heidelberg, 2008.
- (184) *Supramolecular Materials for Opto-Electronics*; Koch, N., Ed.; RSC Smart Materials; Royal Society of Chemistry: Cambridge, 2014.
- (185) Moulin, E.; Cid, J.-J. J.; Giuseppone, N. Advances in Supramolecular Electronics - From Randomly Self-Assembled Nanostructures to Addressable Self-Organized Interconnects. *Adv. Mater.* **2013**, *25*, 477–487.
- (186) Giuseppone, N. Towards Self Constructing Materials: A Systems Chemistry Approach. *Acc. Chem. Res.* **2012**, *45*, 2178–2188.
- (187) Yagai, S.; Kitamura, A. Recent Advances in Photoresponsive Supramolecular Self-Assemblies. *Chem. Soc. Rev.* **2008**, *37*, 1520–1529.
- (188) Zheng, B.; Wang, F.; Dong, S.; Huang, F. Supramolecular Polymers Constructed by Crown Ether-Based Molecular Recognition. *Chem. Soc. Rev.* **2012**, *41*, 1621–1636.
- (189) Brunsveld, L.; Folmer, B. J. B.; Meijer, E. W.; Sijbesma, R. P. Supramolecular Polymers. *Chem. Rev.* **2001**, *101*, 4071–4098.
- (190) Grimsdale, A. C.; Müllen, K. The Chemistry of Organic Nanomaterials. *Angew. Chem. Int. Ed.* **2005**, *44*, 5592–5629.
- (191) Hunter, C. A. Quantifying Intermolecular Interactions: Guidelines for the Molecular Recognition Toolbox. *Angew. Chem. Int. Ed.* **2004**, *43*, 5310–5324.
- (192) Cabot, R.; Hunter, C. A. Molecular Probes of Solvation Phenomena. *Chem. Soc. Rev.* **2012**, *41*, 3485–3492.
- (193) Rekharsky, M.; Inoue, Y. Solvation Effects in Supramolecular Recognition. In *Supramolecular Chemistry*; Steed, J. W.; Gale, P. A., Eds.; John Wiley & Sons, Ltd: Chichester, UK, 2012; pp. 117–133.
- (194) Muthukumar, M.; Ober, C. K.; Thomas, E. L. Competing Interactions and Levels of Ordering in Self-Organizing Polymeric Materials. *Science* **1997**, *277*, 1225–1232.
- (195) Nelson, J. C.; Saven, J. G.; Moore, J. S.; Peter G. Wolynes; Wolynes, P. G. Solvophobicity Driven Folding of Nonbiological Oligomers. *Science* **1997**, *277*, 1793–1796.
- (196) Zhang, Z.; Che, Y.; Smaldone, R. A.; Xu, M.; Bunes, B. R.; Moore, J. S.; Zang, L. Reversible Dispersion and Release of Carbon Nanotubes Using Foldable Oligomers. *J. Am. Chem. Soc.* **2010**, *132*, 14113–14117.
-

-
- (197) Prince, R. B.; Barnes, S. A.; Moore, J. S. Foldamer-Based Molecular Recognition. *J. Am. Chem. Soc.* **2000**, *122*, 2758–2762.
- (198) Tanatani, A.; Mio, M. J.; Moore, J. S. Chain Length-Dependent Affinity of Helical Foldamers for a Rodlike Guest. *J. Am. Chem. Soc.* **2001**, *123*, 1792–1793.
- (199) Prince, R. B.; Okada, T.; Moore, J. S. Controlling the Secondary Structure of Nonbiological Oligomers with Solvophobic and Coordination Interactions. *Angew. Chem. Int. Ed.* **1999**, *38*, 233–236.
- (200) Gin, M. S.; Yokozawa, T.; Prince, R. B.; Moore, J. S. Helical Bias in Solvophobicity of Folded Oligo(Phenylene Ethynylene)s. *J. Am. Chem. Soc.* **1999**, *121*, 2643–2644.
- (201) Hill, D. J.; Moore, J. S. Helicogenicity of Solvents in the Conformational Equilibrium of Oligo(m-Phenylene Ethynylene)s: Implications for Foldamer Research. *Proc. Natl. Acad. Sci. U. S. A.* **2002**, *99*, 5053–5057.
- (202) Stone, M. T.; Fox, J. M.; Moore, J. S. A Helicene-Containing Foldamer Displaying Highly Solvent-Dependent CD Spectra. *Org. Lett.* **2004**, *6*, 3317–3320.
- (203) Prince, R. B.; Brunsveld, L.; Meijer, E. W.; Moore, J. S. Twist Sense Bias Induced by Chiral Side Chains in Helically Folded Oligomers. *Angew. Chem. Int. Ed.* **2000**, *39*, 228–230.
- (204) Brunsveld, L.; Prince, R. B.; Meijer, E. W.; Moore, J. S. Conformational Ordering of Apolar, Chiral M-Phenylene Ethynylene Oligomers. *Org. Lett.* **2000**, *2*, 1525–1528.
- (205) Brunsveld, L.; Meijer, E. W.; Prince, R. B.; Moore, J. S. Self-Assembly of Folded M-Phenylene Ethynylene Oligomers into Helical Columns. *J. Am. Chem. Soc.* **2001**, *123*, 7978–7984.
- (206) Oh, K.; Jeong, K. S.; Moore, J. S. Folding-Driven Synthesis of Oligomers. *Nature* **2001**, *414*, 889–893.
- (207) Lahiri, S.; Thompson, J. L.; Moore, J. S. Solvophobically Driven π -Stacking of Phenylene Ethynylene Macrocycles and Oligomers. *J. Am. Chem. Soc.* **2000**, *122*, 11315–11319.
- (208) Chen, Z.; Lohr, A.; Saha-Möllner, C. R.; Würthner, F. Self-Assembled π -Stacks of Functional Dyes in Solution: Structural and Thermodynamic Features. *Chem. Soc. Rev.* **2009**, *38*, 564–584.
- (209) Hunter, C. A.; Sanders, J. K. M. The Nature of π - π Interactions. *J. Am. Chem. Soc.* **1990**, *112*, 5525–5534.
- (210) Hunter, C. A. Meldola Lecture. The Role of Aromatic Interactions in Molecular Recognition. *Chem. Soc. Rev.* **1994**, *23*, 101–109.
- (211) Grimme, S.; Antony, J.; Schwabe, T.; Mück-Lichtenfeld, C. Density Functional Theory with Dispersion Corrections for Supramolecular Structures, Aggregates, and Complexes of (Bio)organic Molecules. *Org. Biomol. Chem.* **2007**, *5*, 741–758.
- (212) Grimme, S. Do Special Noncovalent π - π Stacking Interactions Really Exist? *Angew. Chem. Int. Ed.* **2008**, *47*, 3430–3434.
- (213) Diederich, F. Complexation of Neutral Molecules by Cyclophane Hosts. *Angew. Chem. Int. Ed.* **1988**, *27*, 362–386.
- (214) Schneider, H. J.; Kramer, R.; Simova, S.; Schneider, U. Host-Guest Chemistry. 14. Solvent and Salt Effects on Binding Constants of Organic Substrates in Macrocyclic Host Compounds. A General Equation Measuring Hydrophobic Binding Contributions. *J. Am. Chem. Soc.* **1988**,
-

- 110, 6442–6448.
- (215) Smithrud, D. B.; Diederich, F. Strength of Molecular Complexation of Apolar Solutes in Water and in Organic Solvents Is Predictable by Linear Free Energy Relationships: A General Model for Solvation Effects on Apolar Binding. *J. Am. Chem. Soc.* **1990**, *112*, 339–343.
- (216) Smithrud, D. B.; Wyman, T. B.; Diederich, F. Enthalpically Driven Cyclophane Arene Inclusion Complexation - Solvent-Dependent Calorimetric Studies. *J. Am. Chem. Soc.* **1991**, *113*, 5420–5426.
- (217) Breault, G. A.; Hunter, C. A.; Mayers, P. C. Influence of Solvent on Aromatic Interactions in Metal Tris-Bipyridine Complexes. *J. Am. Chem. Soc.* **1998**, *120*, 3402–3410.
- (218) Würthner, F.; Yao, S. Dipolar Dye Aggregates: A Problem for Nonlinear Optics, but a Chance for Supramolecular Chemistry. *Angew. Chem. Int. Ed.* **2000**, *39*, 1978–1981.
- (219) Hill, D. J.; Mio, M. J.; Prince, R. B.; Hughes, T. S.; Moore, J. S. A Field Guide to Foldamers. *Chem. Rev.* **2001**, *101*, 3893–4011.
- (220) Würthner, F.; Yao, S.; Debaerdemaeker, T.; Wortmann, R. Dimerization of Merocyanine Dyes. Structural and Energetic Characterization of Dipolar Dye Aggregates and Implications for Nonlinear Optical Materials. *J. Am. Chem. Soc.* **2002**, *124*, 9431–9447.
- (221) Hoeben, F. J. M.; Jonkheijm, P.; Meijer, E. W.; Schenning, A. P. H. J. About Supramolecular Assemblies of π -Conjugated Systems. *Chem. Rev.* **2005**, *105*, 1491–1546.
- (222) Zang, L.; Che, Y.; Moore, J. S. One-Dimensional Self-Assembly of Planar π -Conjugated Molecules: Adaptable Building Blocks for Organic Nanodevices. *Acc. Chem. Res.* **2008**, *41*, 1596–1608.
- (223) Schmidt, J.; Schmidt, R.; Würthner, F. Synthesis, Optical Properties, and LFER Analysis of Solvent-Dependent Binding Constants of Hamilton-Receptor-Connected Merocyanine Chromophores. *J. Org. Chem.* **2008**, *73*, 6355–6362.
- (224) Mati, I. K.; Adam, C.; Cockroft, S. L. Seeing through Solvent Effects Using Molecular Balances. *Chem. Sci.* **2013**, *4*, 3965–3972.
- (225) Yang, L.; Brazier, J. B.; Hubbard, T. A.; Rogers, D. M.; Cockroft, S. L. Can Dispersion Forces Govern Aromatic Stacking in an Organic Solvent? *Angew. Chem. Int. Ed.* **2016**, *55*, 912–916.
- (226) Arjona-Esteban, A.; Stolte, M.; Würthner, F. Conformational Switching of π -Conjugated Junctions from Merocyanine to Cyanine States by Solvent Polarity. *Angew. Chem. Int. Ed.* **2016**, *55*, 2470–2473.
- (227) Cockroft, S. L.; Hunter, C. A. Desolvation Tips the Balance: Solvent Effects on Aromatic Interactions. *Chem. Commun.* **2006**, 3806–3808.
- (228) Mati, I. K.; Cockroft, S. L. Molecular Balances for Quantifying Non-Covalent Interactions. *Chem. Soc. Rev.* **2010**, *39*, 4195–4205.
- (229) Liu, T.; Schneider, H. J. Additivity and Quantification of Dispersive Interactions - From Cyclopropyl to Nitro Groups: Measurements on Porphyrin Derivatives. *Angew. Chem. Int. Ed.* **2002**, *41*, 1368–1370.
- (230) Schneider, H. J. Dispersive Interactions in Solution Complexes. *Acc. Chem. Res.* **2015**, *48*, 1815–1822.
- (231) Schneider, H. J.; Wang, M. Supramolecular Chemistry. 49. Ligand-Porphyrin Complexes:

- Quantitative Evaluation of Stacking and Ionic Contributions. *J. Org. Chem.* **1994**, *59*, 7464–7472.
- (232) Kim, E.; Paliwal, S.; Wilcox, C. S. Measurements of Molecular Electrostatic Field Effects in Edge-to-Face Aromatic Interactions and CH- π Interactions with Implications for Protein Folding and Molecular Recognition. *J. Am. Chem. Soc.* **1998**, *120*, 11192–11193.
- (233) Yang, L.; Adam, C.; Cockroft, S. L. Quantifying Solvophobic Effects in Nonpolar Cohesive Interactions. *J. Am. Chem. Soc.* **2015**, *137*, 10084–10087.
- (234) Yang, L.; Adam, C.; Nichol, G. S.; Cockroft, S. L. How Much Do van Der Waals Dispersion Forces Contribute to Molecular Recognition in Solution? *Nat. Chem.* **2013**, *5*, 1006–1010.
- (235) Chen, Z.; Fimmel, B.; Würthner, F. Solvent and Substituent Effects on Aggregation Constants of Perylene Bisimide π -Stacks – a Linear Free Energy Relationship Analysis. *Org. Biomol. Chem.* **2012**, *10*, 5845–5855.
- (236) Smulders, M. M. J.; Nieuwenhuizen, M. M. L.; De Greef, T. F. A.; Van Der Schoot, P.; Schenning, A. P. H. J.; Meijer, E. W. How to Distinguish Isodesmic from Cooperative Supramolecular Polymerisation. *Chem. Eur. J.* **2010**, *16*, 362–367.
- (237) Dehm, V.; Büchner, M.; Seibt, J.; Engel, V.; Würthner, F. Foldamer with a Spiral Perylene Bisimide Staircase Aggregate Structure. *Chem. Sci.* **2011**, *2*, 2094–2100.
- (238) Son, M.; Fimmel, B.; Dehm, V.; Würthner, F.; Kim, D. Folding-Induced Modulation of Excited-State Dynamics in an Oligophenylene-Ethynylene-Tethered Spiral Perylene Bisimide Aggregate. *ChemPhysChem* **2015**, *16*, 1757–1767.
- (239) Fimmel, B.; Son, M.; Sung, Y. M.; Grüne, M.; Engels, B.; Kim, D.; Würthner, F. Phenylene Ethynylene-Tethered Perylene Bisimide Folda-Dimer and Folda-Trimer: Investigations on Folding Features in Ground and Excited States. *Chem. Eur. J.* **2015**, *21*, 615–630.
- (240) Zitzler-Kunkel, A.; Kirchner, E.; Bialas, D.; Simon, C.; Würthner, F. Spacer-Modulated Differentiation between Self-Assembly and Folding Pathways for Bichromophoric Merocyanine Dyes. *Chem. Eur. J.* **2015**, *21*, 14851–14861.
- (241) Würthner, F.; Yao, S.; Beginn, U. Highly Ordered Merocyanine Dye Assemblies by Supramolecular Polymerization and Hierarchical Self-Organization. *Angew. Chem. Int. Ed.* **2003**, *42*, 3247–3250.
- (242) Glusker, J. P. Directional Aspects of Intermolecular Interactions. *Top. Curr. Chem.* **1998**, *198*, 1–56.
- (243) Rehm, T.; Schmuck, C. How to Achieve Self-Assembly in Polar Solvents Based on Specific Interactions? Some General Guidelines. *Chem. Commun.* **2008**, 801–813.
- (244) Spencer, J. N.; Sweigart, J. R.; Brown, M. E.; Bensing, R. L.; Hassinger, T. L.; Kelly, W.; Housel, D. L.; Reisinger, G. W.; Reifsnnyder, D. S. Solvation Effects on the Thermodynamics of Hydrogen Bonded Systems. 3. *J. Phys. Chem.* **1977**, *81*, 2237–2240.
- (245) Emsley, J. Very Strong Hydrogen Bonding. *Chem. Soc. Rev.* **1980**, *9*, 91–124.
- (246) Spencer, J. N.; Holmboe, E. S.; Firth, D. W.; Kirschenbaum, M. R. Solvent Effects on Hydrogen-Bond Formation. *J. Solut. Chem.* **1981**, *10*, 745–756.
- (247) Spencer, J. N.; Campanella, C. L.; Harris, E. M.; Wolbach, W. S. Solvent Effects on Hydrogen-Bond Formation. *J. Phys. Chem.* **1985**, *89*, 1888–1891.

-
- (248) Rospenk, M.; Zeegers-Huyskens, T. Solvent Effect on the Intramolecular Hydrogen Bond Strength in a Trisubstituted Mannich Base. *J. Phys. Chem.* **1987**, *91*, 3974–3977.
- (249) Schneider, H. J.; Juneja, R. K.; Simova, S. Host-Guest Chemistry. Part 21. Solvent and Structural Effect on Hydrogen Bonds in Some Amides and Barbiturates. An Additive Scheme for the Stability of Corresponding Host-Guest Complexes. *Chem. Ber.* **1989**, *122*, 1211–1213.
- (250) Wyler, R.; de Mendoza, J.; Rebek, J. A Synthetic Cavity Assembles Through Self-Complementary Hydrogen Bonds. *Angew. Chem. Int. Ed.* **1993**, *32*, 1699–1701.
- (251) Kelly, T. R.; Kim, M. H. Relative Binding Affinity of Carboxylate and Its Isosteres: Nitro, Phosphate, Phosphonate, Sulfonate, and Delta-Lactone. *J. Am. Chem. Soc.* **1994**, *116*, 7072–7080.
- (252) Cook, J. L.; Hunter, C. A.; Low, C. M. R.; Perez-Velasco, A.; Vinter, J. G. Solvent Effects on Hydrogen Bonding. *Angew. Chem. Int. Ed.* **2007**, *46*, 3706–3709.
- (253) Cook, J. L.; Hunter, C. A.; Low, C. M. R.; Perez-Velasco, A.; Vinter, J. G. Preferential Solvation and Hydrogen Bonding in Mixed Solvents. *Angew. Chem. Int. Ed.* **2008**, *47*, 6275–6277.
- (254) Abraham, M. H.; Platts, J. A. Hydrogen Bond Structural Group Constants. *J. Org. Chem.* **2001**, *66*, 3484–3491.
- (255) Marangoni, T.; Bonifazi, D. Nano- and Microstructuration of Supramolecular Materials Driven by H-Bonded uracil-2,6-Diamidopyridine Complexes. *Nanoscale* **2013**, *5*, 8837–8851.
- (256) Yang, L.; Tan, X.; Wang, Z.; Zhang, X. Supramolecular Polymers: Historical Development, Preparation, Characterization, and Functions. *Chem. Rev.* **2015**, *115*, 7196–7239.
- (257) Marangoni, T.; Bonifazi, D. H-Bond-Based Nanostructuration of Supramolecular Organic Materials. In *Organic Synthesis and Molecular Engineering*; John Wiley & Sons, Inc.: Hoboken, NJ, USA, 2013; pp. 128–178.
- (258) Lin, C.; Xiao, T.; Wang, L. Hydrogen-Bonded Supramolecular Polymers. In *Hydrogen Bonded Supramolecular Structures*; Li, Z.-T.; Wu, L.-Z., Eds.; Springer Berlin Heidelberg: Berlin, Heidelberg, 2015; pp. 321–350.
- (259) Schenning, A. P. H. J.; González-Rodríguez, D. On the Role of Hydrogen-Bonding in the Nanoscale Organization of π -Conjugated Materials. In *Organic Nanomaterials*; Torres, T.; Bottari, G., Eds.; John Wiley & Sons, Inc.: Hoboken, NJ, USA, 2013; pp. 33–57.
- (260) Brunsveld, L.; Zhang, H.; Glasbeek, M.; Vekemans, J. A. J. M.; Meijer, E. W. Hierarchical Growth of Chiral Self-Assembled Structures in Protic Media. *J. Am. Chem. Soc.* **2000**, *122*, 6175–6182.
- (261) van Herrikhuyzen, J.; Jonkheijm, P.; Schenning, A. P. H. J.; Meijer, E. W. The Influence of Hydrogen Bonding and Π - π Stacking Interactions on the Self-Assembly Properties of C3-Symmetrical Oligo(p-Phenylenevinylene) Discs. *Org. Biomol. Chem.* **2006**, *4*, 1539–1545.
- (262) Jonkheijm, P.; van der Schoot, P.; Schenning, A. P. H. J.; Meijer, E. W. Probing the Solvent-Assisted Nucleation Pathway in Chemical Self-Assembly. *Science* **2006**, *313*, 80–83.
- (263) Korevaar, P. A.; Schaefer, C.; De Greef, T. F. A.; Meijer, E. W. Controlling Chemical Self-Assembly by Solvent-Dependent Dynamics. *J. Am. Chem. Soc.* **2012**, *134*, 13482–13491.
- (264) Gillissen, M. A. J.; Koenigs, M. M. E.; Spiering, J. J. H.; Vekemans, J. A. J. M.; Palmans, A. R. A.; Voets, I. K.; Meijer, E. W. Triple Helix Formation in Amphiphilic Discotics: Demystifying
-

- Solvent Effects in Supramolecular Self-Assembly. *J. Am. Chem. Soc.* **2014**, *136*, 336–343.
- (265) Leenders, C. M. A.; Baker, M. B.; Pijpers, I. A. B.; Lafleur, R. P. M.; Albertazzi, L.; Palmans, A. R. A.; Meijer, E. W. Supramolecular Polymerisation in Water; Elucidating the Role of Hydrophobic and Hydrogen-Bond Interactions. *Soft Matter* **2016**, *12*, 2887–2893.
- (266) van Hameren, R.; Schon, P.; van Buul, A. M.; Hoogboom, J.; Lazarenko, S. V.; Gerritsen, J. W.; Engelkamp, H.; Christianen, P. C. M.; Heus, H. A.; Maan, J. C.; *et al.* Macroscopic Hierarchical Surface Patterning of Porphyrin Trimers via Self-Assembly and Dewetting. *Science* **2006**, *314*, 1433–1436.
- (267) van Hameren, R.; van Buul, A. M.; Castriciano, M. A.; Villari, V.; Micali, N.; Schön, P.; Speller, S.; Monsù Scolaro, L.; Rowan, A. E.; Elemans, J. A. A. W.; *et al.* Supramolecular Porphyrin Polymers in Solution and at the Solid–Liquid Interface. *Nano Lett.* **2008**, *8*, 253–259.
- (268) Veling, N.; van Hameren, R.; van Buul, A. M.; Rowan, A. E.; Nolte, R. J. M.; Elemans, J. A. A. W. Solvent-Dependent Amplification of Chirality in Assemblies of Porphyrin Trimers Based on Benzene Tricarboxamide. *Chem. Commun.* **2012**, *48*, 4371–4373.
- (269) Đorđević, L.; Marangoni, T.; Miletić, T.; Rubio-Magnieto, J.; Mohanraj, J.; Amenitsch, H.; Pasini, D.; Liaros, N.; Couris, S.; Armaroli, N.; *et al.* Solvent Molding of Organic Morphologies Made of Supramolecular Chiral Polymers. *J. Am. Chem. Soc.* **2015**, *137*, 8150–8160.
- (270) Beijer, F. H.; Sijbesma, R. P.; Kooijman, H.; Spek, A. L.; Meijer, E. W. Strong Dimerization of Ureidopyrimidones via Quadruple Hydrogen Bonding. *J. Am. Chem. Soc.* **1998**, *120*, 6761–6769.
- (271) Hirschberg, J. H. K. K.; Brunsveld, L.; Ramzi, A.; Vekemans, J. A. J. M.; Sijbesma, R. P.; Meijer, E. W. Helical Self-Assembled Polymers from Cooperative Stacking of Hydrogen-Bonded Pairs. *Nature* **2000**, *407*, 167–170.
- (272) Cantekin, S.; De Greef, T. F. A.; Palmans, A. R. A. Benzene-1,3,5-Tricarboxamide: A Versatile Ordering Moiety for Supramolecular Chemistry. *Chem. Soc. Rev.* **2012**, *41*, 6125–6137.
- (273) Smulders, M. M. J.; Schenning, A. P. H. J.; Meijer, E. W. Insight into the Mechanisms of Cooperative Self-Assembly: The “Sergeants-and-Soldiers” Principle of Chiral and Achiral C₃-Symmetrical Discotic Triamides. *J. Am. Chem. Soc.* **2008**, *130*, 606–611.
- (274) Nakano, Y.; Hirose, T.; Stals, P. J. M.; Meijer, E. W.; Palmans, A. R. A. Conformational Analysis of Supramolecular Polymerization Processes of Disc-like Molecules. *Chem. Sci.* **2012**, *3*, 148–155.
- (275) Bushey, M. L.; Hwang, A.; Stephens, P. W.; Nuckolls, C. Enforced Stacking in Crowded Arenes. *J. Am. Chem. Soc.* **2001**, *123*, 8157–8158.
- (276) Helicity, A. M.; Bushey, M. L.; Hwang, A.; Stephens, P. W.; Nuckolls, C. The Consequences of Chirality in Crowded Assembly. *Angew. Chem. Int. Ed.* **2002**, *41*, 2828–2831.
- (277) Nguyen, T. Q.; Martel, R.; Avouris, P.; Bushey, M. L.; Brus, L. E.; Nuckolls, C. Molecular Interactions in One-Dimensional Organic Nanostructures. *J. Am. Chem. Soc.* **2004**, *126*, 5234–5242.
- (278) Palmans, A. R. A.; Vekemans, J. A. J. M.; Havinga, E. E.; Meijer, E. W. Sergeants-and-Soldiers Principle in Chiral Columnar Stacks of Disc-Shaped Molecules with C₃ Symmetry. *Angew. Chem. Int. Ed.* **1997**, *36*, 2648–2651.
- (279) Schenning, A. P. H. J.; Jonkheijm, P.; Peeters, E.; Meijer, E. W. Hierarchical Order in

- Supramolecular Assemblies of Hydrogen-Bonded Oligo(p-Phenylene Vinylene)s. *J. Am. Chem. Soc.* **2001**, *123*, 409–416.
- (280) Metzroth, T.; Hoffmann, A.; Martín-Rapún, R.; Smulders, M. M. J.; Pieterse, K.; Palmans, A. R. A.; Vekemans, J. A. J. M.; Meijer, E. W.; Spiess, H. W.; Gauss, J. Unravelling the Fine Structure of Stacked Bipyridine Diamine-Derived C3-Discotics as Determined by X-Ray Diffraction, Quantum-Chemical Calculations, Fast-MAS NMR and CD Spectroscopy. *Chem. Sci.* **2011**, *2*, 69–76.
- (281) Kulkarni, C.; Balasubramanian, S.; George, S. J. What Molecular Features Govern the Mechanism of Supramolecular Polymerization? *ChemPhysChem* **2013**, *14*, 661–673.
- (282) De Greef, T. F. A.; Smulders, M. M. J.; Wolfs, M.; Schenning, A. P. H. J.; Sijbesma, R. P.; Meijer, E. W. Supramolecular Polymerization. *Chem. Rev.* **2009**, *109*, 5687–5754.
- (283) Kulkarni, C.; Bejagam, K. K.; Senanayak, S. P.; Narayan, K. S.; Balasubramanian, S.; George, S. J. Dipole-Moment-Driven Cooperative Supramolecular Polymerization. *J. Am. Chem. Soc.* **2015**, *137*, 3924–3932.
- (284) Würthner, F.; Thalacker, C.; Sautter, A. Hierarchical Organization of Functional Perylene Chromophores to Mesoscopic Superstructures by Hydrogen Bonding and π - π Interactions. *Adv. Mater.* **1999**, *11*, 754–758.
- (285) Würthner, F.; Thalacker, C.; Sautter, A.; Schärfl, W.; Ibach, W.; Hollricher, O. Hierarchical Self-Organization of Perylene Bisimide--Melamine Assemblies to Fluorescent Mesoscopic Superstructures. *Chem. Eur. J.* **2000**, *6*, 3871–3886.
- (286) Würthner, F. Perylene Bisimide Dyes as Versatile Building Blocks for Functional Supramolecular Architectures. *Chem. Commun.* **2004**, 1564–1579.
- (287) Ogi, S.; Stepanenko, V.; Sugiyasu, K.; Takeuchi, M.; Würthner, F. Mechanism of Self-Assembly Process and Seeded Supramolecular Polymerization of Perylene Bisimide Organogelator. *J. Am. Chem. Soc.* **2015**, *137*, 3300–3307.
- (288) Ogi, S.; Stepanenko, V.; Thein, J.; Würthner, F. Impact of Alkyl Spacer Length on Aggregation Pathways in Kinetically Controlled Supramolecular Polymerization. *J. Am. Chem. Soc.* **2016**, *138*, 670–678.
- (289) Kaiser, T. E.; Wang, H.; Stepanenko, V.; Würthner, F. Supramolecular Construction of Fluorescent J-Aggregates Based on Hydrogen-Bonded Perylene Dyes. *Angew. Chem. Int. Ed.* **2007**, *46*, 5541–5544.
- (290) Kaiser, T. E.; Stepanenko, V.; Würthner, F. Fluorescent J-Aggregates of Core-Substituted Perylene Bisimides: Studies on Structure-Property Relationship, Nucleation-Elongation Mechanism, and Sergeants-and-Soldiers Principle. *J. Am. Chem. Soc.* **2009**, *131*, 6719–6732.
- (291) Whitesides, G. M. Self-Assembly at All Scales. *Science* **2002**, *295*, 2418–2421.
- (292) Palermo, V.; Samorì, P. Molecular Self-Assembly across Multiple Length Scales. *Angew. Chem. Int. Ed.* **2007**, *46*, 4428–4432.
- (293) Palma, C.-A.; Samorì, P. Blueprinting Macromolecular Electronics. *Nat. Chem.* **2011**, *3*, 431–436.
- (294) Samorì, P. Exploring Supramolecular Interactions and Architectures by Scanning Force Microscopies. *Chem. Soc. Rev.* **2005**, *34*, 551–561.

-
- (295) Elemans, J. A. A. W.; Lei, S.; De Feyter, S. Molecular and Supramolecular Networks on Surfaces: From Two-Dimensional Crystal Engineering to Reactivity. *Angew. Chem. Int. Ed.* **2009**, *48*, 7298–7333.
- (296) Gomar-Nadal, E.; Puigmartí-Luis, J.; Amabilino, D. B. Assembly of Functional Molecular Nanostructures on Surfaces. *Chem. Soc. Rev.* **2008**, *37*, 490–504.
- (297) Deegan, R.; Bakajin, O.; Dupont, T. F.; Huber, G.; Nagel, S. R.; Witten, T. a. Capillary Flow as the Cause of Ring Stains from Dried Liquid Drops. *Nature* **1997**, *389*, 827–829.
- (298) Deegan, R. Pattern Formation in Drying Drops. *Phys. Rev. E* **2000**, *61*, 475–485.
- (299) Reiter, G. Dewetting of Thin Polymer Films. *Phys. Rev. Lett.* **1992**, *68*, 75–78.
- (300) Xie, R.; Karim, A.; Douglas, J.; Han, C.; Weiss, R. Spinodal Dewetting of Thin Polymer Films. *Phys. Rev. Lett.* **1998**, *81*, 1251–1254.
- (301) Thiele, U. Open Questions and Promising New Fields in Dewetting. *Eur. Phys. J. E* **2003**, *12*, 409–416.
- (302) Gentili, D.; Foschi, G.; Valle, F.; Cavallini, M.; Biscarini, F. Applications of Dewetting in Micro and Nanotechnology. *Chem. Soc. Rev.* **2012**, *41*, 4430–4443.
- (303) Samori, P.; Keil, M.; Friedlein, R.; Birgerson, J.; Watson, M.; Müllen, K.; Salaneck, W. R.; Rabe, J. P. Growth of Ordered Hexakis-Dodecyl-Hexabenzocoronene Layers from Solution: A SFM and ARUPS Study. *J. Phys. Chem. B* **2001**, *105*, 11114–11119.
- (304) Kastler, M.; Pisula, W.; Wasserfallen, D.; Pakula, T.; Müllen, K. Influence of Alkyl Substituents on the Solution- and Surface-Organization of Hexa-Peri-Hexabenzocoronenes. *J. Am. Chem. Soc.* **2005**, *127*, 4286–4296.
- (305) Pisula, W.; Menon, A.; Stepputat, M.; Lieberwirth, I.; Kolb, U.; Tracz, A.; Siringhaus, H.; Pakula, T.; Müllen, K. A Zone-Casting Technique for Device Fabrication of Field-Effect Transistors Based on Discotic Hexa-Peri-Hexabenzocoronene. *Adv. Mater.* **2005**, *17*, 684–689.
- (306) Tracz, A.; Jeszka, J. K.; Watson, M. D.; Pisula, W.; Müllen, K.; Pakula, T. Uniaxial Alignment of the Columnar Super-Structure of a Hexa (Alkyl) Hexa-Peri-Hexabenzocoronene on Untreated Glass by Simple Solution Processing. *J. Am. Chem. Soc.* **2003**, *125*, 1682–1683.
- (307) Wu, J.; Fechtenkötter, A.; Gauss, J.; Watson, M. D.; Kastler, M.; Fechtenkötter, C.; Wagner, M.; Müllen, K. Controlled Self-Assembly of Hexa-Peri-Hexabenzocoronenes in Solution. *J. Am. Chem. Soc.* **2004**, *126*, 11311–11321.
- (308) Treossi, E.; Liscio, A.; Feng, X.; Palermo, V.; Müllen, K.; Samori, P. Temperature-Enhanced Solvent Vapor Annealing of a C3 Symmetric Hexa-Peri-Hexabenzocoronene: Controlling the Self-Assembly from Nano- to Macroscale. *Small* **2009**, *5*, 112–119.
- (309) Wang, S.; Dössel, L.; Mavrinskiy, A.; Gao, P.; Feng, X.; Pisula, W.; Müllen, K. Self-Assembly and Microstructural Control of a Hexa-Peri-Hexabenzocoronene-Perylene Diimide Dyad by Solvent Vapor Diffusion. *Small* **2011**, *7*, 2841–2846.
- (310) Palermo, V.; Morelli, S.; Simpson, C.; Müllen, K.; Samori, P. Self-Organized Nanofibers from a Giant Nanographene: Effect of Solvent and Deposition Method. *J. Mater. Chem.* **2006**, *16*, 266–271.
- (311) Rabani, E.; Reichman, D. R.; Geissler, P. L.; Brus, L. E. Drying-Mediated Self-Assembly of
-

- Nanoparticles. *Nature* **2003**, *426*, 271–274.
- (312) Liu, D.; Zhang, H.; Grim, P. C. M.; De Feyter, S.; Wiesler, U. M.; Berresheim, A. J.; Müllen, K.; De Schryver, F. C. Self-Assembly of Polyphenylene Dendrimers into Micrometer Long Nanofibers: An Atomic Force Microscopy Study. *Langmuir* **2002**, *18*, 2385–2391.
- (313) Loi, S.; Butt, H. J.; Hampel, C.; Bauer, R.; Wiesler, U. M.; Müllen, K. Two-Dimensional Structure of Self-Assembled Alkyl-Substituted Polyphenylene Dendrimers on Graphite. *Langmuir* **2002**, *18*, 2398–2405.
- (314) Liu, D.; De Feyter, S.; Cotlet, M.; Wiesler, U. M.; Weil, T.; Herrmann, A.; Müllen, K.; De Schryver, F. C. Fluorescent Self-Assembled Polyphenylene Dendrimer Nanofibers. *Macromolecules* **2003**, *36*, 8489–8498.
- (315) Kim, J.; Park, C.; Park, J. E.; Chu, K.; Choi, H. C. Vertical Crystallization of C60 Nanowires by Solvent Vapor Annealing Process. *ACS Nano* **2013**, *7*, 9122–9128.
- (316) Park, C.; Song, H. J.; Choi, H. C. The Critical Effect of Solvent Geometry on the Determination of Fullerene (C60) Self-Assembly into Dot, Wire and Disk Structures. *Chem. Commun.* **2009**, 4803–4805.
- (317) Li, H.; Tee, B. C.-K.; Cha, J. J.; Cui, Y.; Chung, J. W.; Lee, S. Y.; Bao, Z. High-Mobility Field-Effect Transistors from Large-Area Solution-Grown Aligned C60 Single Crystals. *J. Am. Chem. Soc.* **2012**, *134*, 2760–2765.
- (318) Wu, J.; Fan, C.; Xue, G.; Ye, T.; Liu, S.; Lin, R.; Chen, H.; Xin, H. L.; Xiong, R.-G.; Li, H. Interfacing Solution-Grown C60 and (3-Pyrrolium)(CdCl₃) Single Crystals for High-Mobility Transistor-Based Memory Devices. *Adv. Mater.* **2015**, *27*, 4476–4480.
- (319) Schenning, A. P. H. J.; Benneker, F. B. G.; Geurts, H. P. M.; Liu, X. Y.; Nolte, R. J. M. Porphyrin Wheels. *J. Am. Chem. Soc.* **1996**, *118*, 8549–8552.
- (320) Hofkens, J.; Latterini, L.; Vanoppen, P.; Faes, H.; Jeuris, K.; De Feyter, S.; Kerimo, J.; Barbara, P. F.; De Schryver, F. C.; Rowan, A. E.; *et al.* Mesostructure of Evaporated Porphyrin Thin Films: Porphyrin Wheel Formation. *J. Phys. Chem. B* **1997**, *101*, 10588–10598.
- (321) Latterini, L.; Blosssey, R.; Hofkens, J.; Vanoppen, P.; De Schryver, F. C.; Rowan, A. E.; Nolte, R. J. M. Ring Formation in Evaporating Porphyrin Derivative Solutions. *Langmuir* **1999**, *15*, 3582–3588.
- (322) Foubert, P.; Vanoppen, P.; Martin, M.; Gensch, T.; Hofkens, J.; Helser, A.; Seeger, A.; Taylor, R. M.; Rowan, A. E.; Nolte, R. J. M.; *et al.* Mechanical and Optical Manipulation of Porphyrin Rings at the Submicrometre Scale. *Nanotechnology* **2000**, *11*, 16–23.
- (323) Lensen, M. C.; Takazawa, K.; Elemans, J. A. A. W.; Jeukens, C. R. L. P. N.; Christianen, P. C. M.; Maan, J. C.; Rowan, A. E.; Nolte, R. J. M. Aided Self-Assembly of Porphyrin Nanoaggregates into Ring-Shaped Architectures. *Chem. Eur. J.* **2004**, *10*, 831–839.
- (324) Jeukens, C. R. L. P. N.; Lensen, M. C.; Wijnen, F. J. P.; Elemans, J. A. A. W.; Christianen, P. C. M.; Rowan, A. E.; Gerritsen, J. W.; Nolte, R. J. M.; Maan, J. C. Polarized Absorption and Emission of Ordered Self-Assembled Porphyrin Rings. *Nano Lett.* **2004**, *4*, 1401–1406.
- (325) Yin, J.; Guo, Q.; Palmer, R. E.; Bampos, N.; Sanders, J. K. M. Supramolecular Monolayers of Zinc Porphyrin Trimers on Graphite. *J. Phys. Chem. B* **2003**, *107*, 209–216.
- (326) van Hameren, R.; van Buul, A. M.; Visser, D.; Heenan, R. K.; King, S. M.; Rowan, A. E.; Nolte, R. J. M.; Pyckhout-Hintzen, W.; Elemans, J. A. A. W.; Feiters, M. C. Solution Scattering Studies

- of the Hierarchical Assembly of Porphyrin Trimers Based on Benzene Triscarboxamide. *Soft Matter* **2014**, *10*, 9688–9694.
- (327) Xie, Y.; Akada, M.; Hill, J. P.; Ji, Q.; Charvet, R.; Ariga, K. Real Time Self-Assembly and Reassembly of Molecular Nanowires of Trigeminal Amphiphile Porphyrins. *Chem. Commun.* **2011**, *47*, 2285–2287.
- (328) Hizume, Y.; Tashiro, K.; Charvet, R.; Yamamoto, Y.; Saeki, A.; Seki, S.; Aida, T. Chiroselective Assembly of a Chiral Porphyrin-Fullerene Dyad: Photoconductive Nanofiber with a Top-Class Ambipolar Charge-Carrier Mobility. *J. Am. Chem. Soc.* **2010**, *132*, 6628–6629.
- (329) Sakakibara, K.; Hill, J. P.; Ariga, K. Thin-Film-Based Nanoarchitectures for Soft Matter: Controlled Assemblies into Two-Dimensional Worlds. *Small* **2011**, *7*, 1288–1308.
- (330) Rep, D. B. A.; Roelfsema, R.; Van Esch, J. H.; Schoonbeek, F. S.; Kellogg, R. M.; Feringa, B. L.; Palstra, T. T. M.; Klapwijk, T. M. Self-Assembly of Low-Dimensional Arrays of Thiophene Oligomers from Solution on Solid Substrates. *Adv. Mater.* **2000**, *12*, 563–566.
- (331) Wang, M.; Mohebbi, A. R.; Sun, Y.; Wudl, F. Ribbons, Vesicles, and Baskets: Supramolecular Assembly of a Coil-Plate-Coil Emeraldicene Derivative. *Angew. Chem. Int. Ed.* **2012**, *51*, 6920–6924.
- (332) Babu, S. S.; Mahesh, S.; Kartha, K. K.; Ajayaghosh, A. Solvent-Directed Self-Assembly of π Gelators to Hierarchical Macroporous Structures and Aligned Fiber Bundles. *Chem. Asian J.* **2009**, *4*, 824–829.
- (333) Widawski, G.; Rawiso, M.; François, B. Self-Organized Honeycomb Morphology of Star-Polymer Polystyrene Films. *Nature* **1994**, *369*, 387–389.
- (334) Srinivasarao, M. Three-Dimensionally Ordered Array of Air Bubbles in a Polymer Film. *Science* **2001**, *292*, 79–83.
- (335) Kim, J. H.; Seo, M.; Kim, S. Y. Lithographically Patterned Breath Figure of Photoresponsive Small Molecules: Dual-Patterned Honeycomb Lines from a Combination of Bottom-up and Top-down Lithography. *Adv. Mater.* **2009**, *21*, 4130–4133.
- (336) Zhang, A.; Bai, H.; Li, L. Breath Figure: A Nature-Inspired Preparation Method for Ordered Porous Films. *Chem. Rev.* **2015**, *115*, 9801–9868.
- (337) Zhang, X.; Jie, J.; Deng, W.; Shang, Q.; Wang, J.; Wang, H.; Chen, X.; Zhang, X. Alignment and Patterning of Ordered Small-Molecule Organic Semiconductor Micro-/Nanocrystals for Device Applications. *Adv. Mater.* **2016**, *28*, 2475–2503.
- (338) De Luca, G.; Liscio, A.; Maccagnani, P.; Nolde, F.; Palermo, V.; Müllen, K.; Samori, P. Nucleation-Governed Reversible Self-Assembly of an Organic Semiconductor at Surfaces: Long-Range Mass Transport Forming Giant Functional Fibers. *Adv. Funct. Mater.* **2007**, *17*, 3791–3798.
- (339) Liu, C.; Minari, T.; Li, Y.; Kumatani, A.; Lee, M. V.; Athena Pan, S. H.; Takimiya, K.; Tsukagoshi, K. Direct Formation of Organic Semiconducting Single Crystals by Solvent Vapor Annealing on a Polymer Base Film. *J. Mater. Chem.* **2012**, *22*, 8462–8469.
- (340) Hiszpanski, A. M.; Lee, S. S.; Wang, H.; Woll, A. R.; Nuckolls, C.; Loo, Y. L. Post-Deposition Processing Methods to Induce Preferential Orientation in Contorted Hexabenzocoronene Thin Films. *ACS Nano* **2013**, *7*, 294–300.
- (341) De Luca, G.; Treossi, E.; Liscio, A.; Mativetsky, J. M.; Scolaro, L. M.; Palermo, V.; Samori, P.

- Solvent Vapour Annealing of Organic Thin Films: Controlling the Self-Assembly of Functional Systems across Multiple Length Scales. *J. Mater. Chem.* **2010**, *20*, 2493–2498.
- (342) Wang, J.; Liu, K.; Yan, L.; Wang, A.; Bai, S.; Yan, X. Trace Solvent as a Predominant Factor To Tune Dipeptide Self-Assembly. *ACS Nano* **2016**, *10*, 2138–2143.
- (343) Balaban, T. S.; Linke-Schaetzl, M.; Bhise, A. D.; Vanthuyne, N.; Roussel, C.; Anson, C. E.; Buth, G.; Eichhöfer, A.; Foster, K.; Garab, G.; *et al.* Structural Characterization of Artificial Self-Assembling Porphyrins That Mimic the Natural Chlorosomal Bacteriochlorophylls C, D, and E. *Chem. Eur. J.* **2005**, *11*, 2267–2275.
- (344) Huber, V.; Sengupta, S.; Würthner, F. Structure-Property Relationships for Self-Assembled Zinc Chlorin Light-Harvesting Dye Aggregates. *Chem. Eur. J.* **2008**, *14*, 7791–7807.
- (345) Huber, V.; Katterle, M.; Lysetska, M.; Würthner, F. Reversible Self-Organization of Semisynthetic Zinc Chlorins into Well-Defined Rod Antennae. *Angew. Chem. Int. Ed.* **2005**, *44*, 3147–3151.
- (346) Chappaz-Gillot, C.; Marek, P. L.; Blaive, B. J.; Canard, G.; Bürck, J.; Garab, G.; Hahn, H.; Jávorfí, T.; Kelemen, L.; Krupke, R.; *et al.* Anisotropic Organization and Microscopic Manipulation of Self-Assembling Synthetic Porphyrin Microrods That Mimic Chlorosomes: Bacterial Light-Harvesting Systems. *J. Am. Chem. Soc.* **2012**, *134*, 944–954.
- (347) Helmich, F.; Lee, C. C.; Nieuwenhuizen, M. M. L.; Gielen, J. C.; Christianen, P. C. M.; Larsen, A.; Fytas, G.; Leclère, P. E. L. G.; Schenning, A. P. H. J.; Meijer, E. W. Dilution-Induced Self-Assembly of Porphyrin Aggregates: A Consequence of Coupled Equilibria. *Angew. Chem. Int. Ed.* **2010**, *49*, 3939–3942.
- (348) Lindsey, J. S.; Schreiman, I. C.; Hsu, H. C.; Kearney, P. C.; Marguerettaz, A. M. Rothmund and Adler-Longo Reactions Revisited: Synthesis of Tetraphenylporphyrins under Equilibrium Conditions. *J. Org. Chem.* **1987**, *52*, 827–836.
- (349) Đorđević, L.; Marangoni, T.; De Leo, F.; Papagiannouli, I.; Aloukos, P.; Couris, S.; Pavoni, E.; Monti, F.; Armaroli, N.; Prato, M.; *et al.* [60]Fullerene–porphyrin [N]pseudorotaxanes: Self-Assembly, Photophysics and Third-Order NLO Response. *Phys. Chem. Chem. Phys.* **2016**.
- (350) Balaban, T. S.; Eichhöfer, A.; Lehn, J. Self-Assembly by Hydrogen Bonding and Π – π Interactions in the Crystal of a Porphyrin – Attempts to Mimic Bacteriochlorophyll c. *Eur. J. Org. Chem.* **2000**, *2000*, 4047–4057.
- (351) Arsenault, G. P.; Bullock, E.; MacDonald, S. F. Pyrromethanes and Porphyrins Therefrom. *J. Am. Chem. Soc.* **1960**, *82*, 4384–4389.
- (352) Senge, M. O. Stirring the Porphyrin Alphabet Soup—functionalization Reactions for Porphyrins. *Chem. Commun.* **2011**, *47*, 1943–1960.
- (353) Brückner, C.; Posakony, J. J.; Johnson, C. K.; Boyle, R. W.; James, B. R.; Dolphin, D. Novel and Improved Syntheses of 5,15-Diphenylporphyrin and Its Dipyrrolic Precursors. *J. Porphyrins Phthalocyanines* **1998**, *2*, 455–465.
- (354) Dimagno, S. G.; Lin, V. S. Y.; Therien, M. J. Facile Elaboration of Porphyrins Via Metal-Mediated Cross-Coupling. *J. Org. Chem.* **1993**, *58*, 5983–5993.
- (355) Bakar, M. B.; Oelgemöller, M.; Senge, M. O. Lead Structures for Applications in Photodynamic Therapy. Part 2: Synthetic Studies for Photo-Triggered Release Systems of Bioconjugate Porphyrin Photosensitizers. *Tetrahedron* **2009**, *65*, 7064–7078.

-
- (356) Hatada, M. H.; Tulinsky, A.; Chang, C. K. Crystal and Molecular Structure of Cofacial Dicopper Hexyldiporphyrin-7. *J. Am. Chem. Soc.* **1980**, *102*, 7115–7116.
- (357) Hirasawa, K.; Yuge, H.; Miyamoto, T. K. Enantiomorphs of a carbene–ruthenium(II)–porphyrin Complex with Four ‘chiral Pillars’. *Acta Cryst. C* **2008**, *64*, m97–m100.
- (358) Weissbuch, I.; Lahav, M. Crystalline Architectures as Templates of Relevance to the Origins of Homochirality. *Chem. Rev.* **2011**, *111*, 3236–3267.
- (359) Hoeben, F. J. M.; Wolfs, M.; Zhang, J.; De Feyter, S.; Leclère, P.; Schenning, A. P. H. J.; Meijer, E. W. Influence of Supramolecular Organization on Energy Transfer Properties in Chiral Oligo(p-Phenylene Vinylene) Porphyrin Assemblies. *J. Am. Chem. Soc.* **2007**, *129*, 9819–9828.
- (360) Würthner, F.; Kaiser, T. E.; Saha-Möllner, C. R. J-Aggregates: From Serendipitous Discovery to Supramolecular Engineering of Functional Dye Materials. *Angew. Chem. Int. Ed.* **2011**, *50*, 3376–3410.
- (361) Ogi, S.; Sugiyasu, K.; Manna, S.; Samitsu, S.; Takeuchi, M. Living Supramolecular Polymerization Realized through a Biomimetic Approach. *Nat. Chem.* **2014**, *6*, 188–195.
- (362) Piot, L.; Palma, C.-A.; Llanes-Pallas, A.; Prato, M.; Szekrényes, Z.; Kamarás, K.; Bonifazi, D.; Samori, P. Selective Formation of Bi-Component Arrays Through H-Bonding of Multivalent Molecular Modules. *Adv. Funct. Mater.* **2009**, *19*, 1207–1214.
- (363) Beijer, F. H.; Sijbesma, R. P.; Vekemans, J. A. J. M.; Meijer, E. W.; Kooijman, H.; Spek, A. L. Hydrogen-Bonded Complexes of Diaminopyridines and Diaminotriazines: Opposite Effect of Acylation on Complex Stabilities. *J. Org. Chem.* **1996**, *61*, 6371–6380.
- (364) Cohen, Y.; Avram, L.; Frish, L. Diffusion NMR Spectroscopy in Supramolecular and Combinatorial Chemistry: An Old Parameter - New Insights. *Angew. Chem. Int. Ed.* **2005**, *44*, 520–554.
- (365) Macchioni, A.; Ciancaleoni, G.; Zuccaccia, C.; Zuccaccia, D. Determining Accurate Molecular Sizes in Solution through NMR Diffusion Spectroscopy. *Chem. Soc. Rev.* **2008**, *37*, 479–489.
- (366) Brinker, C. J.; Lu, Y.; Sellinger, A.; Fan, H. Evaporation-Induced Self-Assembly: Nanostructures Made Easy. *Adv. Mater.* **1999**, *11*, 579–585.
- (367) Grosso, D.; Cagnol, F.; Soler-Illia, G. J. de A. A.; Crepaldi, E. L.; Amenitsch, H.; Brunet-Bruneau, A.; Bourgeois, A.; Sanchez, C. Fundamentals of Mesostructuring Through Evaporation-Induced Self-Assembly. *Adv. Funct. Mater.* **2004**, *14*, 309–322.
- (368) Li, B.; Puigmartí-Luis, J.; Jonas, A. M.; Amabilino, D. B.; De Feyter, S. Hierarchical Growth of Curved Organic Nanowires upon Evaporation Induced Self-Assembly. *Chem. Commun.* **2014**, *50*, 13216–13219.
- (369) Sijbesma, R. P.; Beijer, F. H.; Brunsveld, L.; Folmer, B. J. B.; Hirschberg, J. H. K. K.; Lange, R. F.; Lowe, J. K.; Meijer, E. W. Reversible Polymers Formed from Self-Complementary Monomers Using Quadruple Hydrogen Bonding. *Science* **1997**, *278*, 1601–1604.
- (370) Marangoni, T.; Mezzasalma, S. A.; Llanes-Pallas, A.; Yoosaf, K.; Armaroli, N.; Bonifazi, D. Thermosolubal Self-Organization of Supramolecular Polymers into Nanocraters. *Langmuir* **2011**, *27*, 1513–1523.
- (371) Jonkheijm, P.; Hoeben, F. J. M.; Kleppinger, R.; van Herrikhuyzen, J.; Schenning, A. P. H. J.; Meijer, E. W. Transfer of π -Conjugated Columnar Stacks from Solution to Surfaces. *J. Am.*
-

-
- Chem. Soc.* **2003**, *125*, 15941–15949.
- (372) Surin, M.; Janssen, P. G. A.; Lazzaroni, R.; Leclère, P.; Meijer, E. W.; Schenning, A. P. H. J. Supramolecular Organization of ssDNA-Templated π -Conjugated Oligomers via Hydrogen Bonding. *Adv. Mater.* **2009**, *21*, 1126–1130.
- (373) Yoosaf, K.; Llanes-Pallas, A.; Marangoni, T.; Belbakra, A.; Marega, R.; Botek, E.; Champagne, B.; Bonifazi, D.; Armaroli, N. From Molecular to Macroscopic Engineering: Shaping Hydrogen-Bonded Organic Nanomaterials. *Chem. Eur. J.* **2011**, *17*, 3262–3273.
- (374) Llanes-Pallas, A.; Palma, C.-A.; Piot, L.; Belbakra, A.; Listorti, A.; Prato, M.; Samorì, P.; Armaroli, N.; Bonifazi, D. Engineering of Supramolecular H-Bonded Nanopolygons via Self-Assembly of Programmed Molecular Modules. *J. Am. Chem. Soc.* **2009**, *131*, 509–520.
- (375) Roe, R. J. *Methods of X-Ray and Neutron Scattering in Polymer Science*; Oxford University Press: New York, 2000.
- (376) Patterson, J. P.; Robin, M. P.; Chassenieux, C.; Colombani, O.; O'Reilly, R. K. The Analysis of Solution Self-Assembled Polymeric Nanomaterials. *Chem. Soc. Rev.* **2014**, *43*, 2412–2425.
- (377) Teixeira, C. V.; Amenitsch, H.; Fukushima, T.; Hill, J. P.; Jin, W.; Aida, T.; Hotokka, M.; Lindén, M. Form Factor of an N -Layered Helical Tape and Its Application to Nanotube Formation of Hexa- Peri -Hexabenzocoronene-Based Molecules. *J. Appl. Crystallogr.* **2010**, *43*, 850–857.
- (378) Becerril, H. A.; Woolley, A. T. DNA-Templated Nanofabrication. *Chem. Soc. Rev.* **2009**, *38*, 329–337.
- (379) Krueger, A. T.; Lu, H.; Lee, A. H. F.; Kool, E. T. Synthesis and Properties of Size-Expanded DNAs: Toward Designed, Functional Genetic Systems. *Acc. Chem. Res.* **2007**, *40*, 141–150.
- (380) Ruiz-Carretero, A.; Janssen, P. G. A.; Kaeser, A.; Schenning, A. P. H. J. DNA-Templated Assembly of Dyes and Extended π -Conjugated Systems. *Chem. Commun.* **2011**, *47*, 4340–4347.
- (381) Bandy, T. J.; Brewer, A.; Burns, J. R.; Marth, G.; Nguyen, T.; Stulz, E. DNA as Supramolecular Scaffold for Functional Molecules: Progress in DNA Nanotechnology. *Chem. Soc. Rev.* **2011**, *40*, 138–148.
- (382) Wang, Z. G.; Ding, B. DNA-Based Self-Assembly for Functional Nanomaterials. *Adv. Mater.* **2013**, *25*, 3905–3914.
- (383) Rothmund, P. W. K. Folding DNA to Create Nanoscale Shapes and Patterns. *Nature* **2006**, *440*, 297–302.
- (384) Nguyen, T.; Brewer, A.; Stulz, E. Duplex Stabilization and Energy Transfer in Zipper Porphyrin-DNA. *Angew. Chem. Int. Ed.* **2009**, *48*, 1974–1977.
- (385) Mayer-Enthart, E.; Wagner, C.; Barbaric, J.; Wagenknecht, H.-A. Helical Self-Assembled Chromophore Clusters Based on DNA-like Architecture. *Tetrahedron* **2007**, *63*, 3434–3439.
- (386) Nakamura, M.; Ohtoshi, Y.; Yamana, K. Helical Pyrene-Array along the outside of Duplex RNA. *Chem. Commun.* **2005**, 5163–5165.
- (387) Sezi, S.; Wagenknecht, H.-A. DNA-Templated Formation of Fluorescent Self-Assembly of Ethynyl Pyrenes. *Chem. Commun.* **2013**, *49*, 9257–9259.
- (388) Khorev, O.; Bösch, C. D.; Probst, M.; Häner, R. Observation of the Rare Chrysene Excimer.
-

-
- Chem. Sci.* **2014**, *5*, 1506–1512.
- (389) Gao, J.; Strässler, C.; Tahmassebi, D.; Kool, E. T. Libraries of Composite Polyfluors Built from Fluorescent Deoxyribosides. *J. Am. Chem. Soc.* **2002**, *124*, 11590–11591.
- (390) Baumstark, D.; Wagenknecht, H.-A. Perylene Bisimide Dimers as Fluorescent “Glue” for DNA and for Base-Mismatch Detection. *Angew. Chem. Int. Ed.* **2008**, *47*, 2612–2614.
- (391) Baumstark, D.; Wagenknecht, H.-A. Fluorescent Hydrophobic Zippers inside Duplex DNA: Interstrand Stacking of Perylene-3,4:9,10-Tetracarboxylic Acid Bisimides as Artificial DNA Base Dyes. *Chem. Eur. J.* **2008**, *14*, 6640–6645.
- (392) Benveniste, A. L.; Creeger, Y.; Fisher, G. W.; Ballou, B.; Waggoner, A. S.; Armitage, B. A. Fluorescent DNA Nanotags: Supramolecular Fluorescent Labels Based on Intercalating Dye Arrays Assembled on Nanostructured DNA Templates. *J. Am. Chem. Soc.* **2007**, *129*, 2025–2034.
- (393) Özalıcı-Ünal, H.; Armitage, B. A. Fluorescent DNA Nanotags Based on a Self-Assembled DNA Tetrahedron. *ACS Nano* **2009**, *3*, 425–433.
- (394) Liu, B.; Bazan, G. C. Interpolyelectrolyte Complexes of Conjugated Copolymers and DNA: Platforms for Multicolor Biosensors. *J. Am. Chem. Soc.* **2004**, *126*, 1942–1943.
- (395) Liu, B.; Bazan, G. C. Homogeneous Fluorescence-Based DNA Detection with Water-Soluble Conjugated Polymers. *Chem. Mater.* **2004**, *16*, 4467–4476.
- (396) Wang, S.; Gaylord, B. S.; Bazan, G. C. Fluorescein Provides a Resonance Gate for FRET from Conjugated Polymers to DNA Intercalated Dyes. *J. Am. Chem. Soc.* **2004**, *126*, 5446–5451.
- (397) Li, H.; Bazan, G. C. Conjugated oligoelectrolyte/ssDNA Aggregates: Self-Assembled Multicomponent Chromophores for Protein Discrimination. *Adv. Mater.* **2009**, *21*, 964–967.
- (398) D’Urso, A.; Mammanna, A.; Balaz, M.; Holmes, A. E.; Berova, N.; Lauceri, R.; Purrello, R. Interactions of a Tetraanionic Porphyrin with DNA: From a Z-DNA Sensor to a Versatile Supramolecular Device. *J. Am. Chem. Soc.* **2009**, *131*, 2046–2047.
- (399) Iwaura, R.; Yoshida, K.; Masuda, M.; Ohnishi-Kameyama, M.; Yoshida, M.; Shimizu, T. Oligonucleotide-Templated Self-Assembly of Nucleotide Bolaamphiphiles: DNA-Like Nanofibers Edged by a Double-Helical Arrangement of A–T Base Pairs. *Angew. Chem. Int. Ed.* **2003**, *42*, 1009–1012.
- (400) Iwaura, R.; Shimizu, T. Reversible Photochemical Conversion of Helicity in Self-Assembled Nanofibers from a 1, ω -Thymidylic Acid Appended Bolaamphiphile. *Angew. Chem. Int. Ed.* **2006**, *45*, 4601–4604.
- (401) Iwaura, R.; Hoeben, F. J. M.; Masuda, M.; Schenning, A. P. H. J.; Meijer, E. W.; Shimizu, T. Molecular-Level Helical Stack of a Nucleotide-Appended Oligo(p-Phenylenevinylene) Directed by Supramolecular Self-Assembly with a Complementary Oligonucleotide as a Template. *J. Am. Chem. Soc.* **2006**, *128*, 13298–13304.
- (402) Iwaura, R.; Ohnishi-Kameyama, M.; Shimizu, T. Nanofiber Formation from Sequence-Selective DNA-Templated Self-Assembly of a Thymidylic Acid-Appended Bolaamphiphile. *Chem. Commun.* **2008**, 5770–5772.
- (403) Iwaura, R.; Ohnishi-Kameyama, M.; Iizawa, T. Construction of Helical J-Aggregates Self-Assembled from a Thymidylic Acid Appended Anthracene Dye and DNA as a Template. *Chem. Eur. J.* **2009**, *15*, 3729–3735.
-

-
- (404) Janssen, P. G. A.; Vandenberg, J.; van Dongen, J. L. J.; Meijer, E. W.; Schenning, A. P. H. J. ssDNA Templated Self-Assembly of Chromophores. *J. Am. Chem. Soc.* **2007**, *129*, 6078–6079.
- (405) Janssen, P. G. A.; Jabbari-Farouji, S.; Surin, M.; Vila, X.; Gielen, J. C.; De Greef, T. F. A.; Vos, M. R. J.; Bomans, P. H. H.; Sommerdijk, N. A. J. M.; Christianen, P. C. M. Insights into Templated Supramolecular Polymerization: Binding of Naphthalene Derivatives to ssDNA Templates of Different Lengths. *J. Am. Chem. Soc.* **2008**, *131*, 1222–1231.
- (406) Janssen, P. G. A.; Ruiz-Carretero, A.; González-Rodríguez, D.; Meijer, E. W.; Schenning, A. P. H. J. PH-Switchable Helicity of DNA-Templated Assemblies. *Angew. Chem. Int. Ed.* **2009**, *48*, 8103–8106.
- (407) Janssen, P. G. A.; van Dongen, J. L. J.; Meijer, E. W.; Schenning, A. P. H. J. Electrospray-Ionization Mass Spectrometry for Screening the Specificity and Stability of Single-Stranded-DNA Templated Self-Assemblies. *Chem. Eur. J.* **2009**, *15*, 352–360.
- (408) de la Escosura, A.; Janssen, P. G. A.; Schenning, A. P. H. J.; Nolte, R. J. M.; Cornelissen, J. J. L. M. Encapsulation of DNA-Templated Chromophore Assemblies within Virus Protein Nanotubes. *Angew. Chem. Int. Ed.* **2010**, *49*, 5335–5338.
- (409) Janssen, P. G. A.; Brankaert, N. J. M.; Vila, X.; Schenning, A. P. H. J. ssDNA Templated Assembly of Oligonucleotides and Bivalent Naphthalene Guests. *Soft Matter* **2010**, *6*, 1494–1502.
- (410) Calzaferri, G.; Huber, S.; Maas, H.; Minkowski, C. Host-Guest Antenna Materials. *Angew. Chem. Int. Ed.* **2003**, *42*, 3732–3758.
- (411) Popović, Z.; Otter, M.; Calzaferri, G.; De Cola, L. Self-Assembling Living Systems with Functional Nanomaterials. *Angew. Chem. Int. Ed.* **2007**, *46*, 6188–6191.
- (412) Huber, S.; Calzaferri, G. Sequential Functionalization of the Channel Entrances of Zeolite L Crystals. *Angew. Chem. Int. Ed.* **2004**, *43*, 6738–6742.
- (413) Busby, M.; Kerschbaumer, H.; Calzaferri, G.; De Cola, L. Orthogonally Bifunctional Fluorescent Zeolite-L Microcrystals. *Adv. Mater.* **2008**, *20*, 1614–1618.
- (414) Strassert, C. A.; Otter, M.; Albuquerque, R. Q.; Hone, A.; Vida, Y.; Maier, B.; De Cola, L. Photoactive Hybrid Nanomaterial for Targeting, Labeling, and Killing Antibiotic-Resistant Bacteria. *Angew. Chem. Int. Ed.* **2009**, *48*, 7928–7931.
- (415) Tans, S. J.; Verschueren, A. R. M.; Dekker, C. Room-Temperature Transistor Based on a Single Carbon Nanotube. *Nature* **1998**, *393*, 49–52.
- (416) Postma, H. W. C. Carbon Nanotube Single-Electron Transistors at Room Temperature. *Science* **2001**, *293*, 76–79.
- (417) Berber, S.; Kwon, Y.-K.; Tománek, D. Unusually High Thermal Conductivity of Carbon Nanotubes. *Phys. Rev. Lett.* **2000**, *84*, 4613–4616.
- (418) Pop, E.; Mann, D.; Wang, Q.; Goodson, K.; Dai, H. Thermal Conductance of an Individual Single-Wall Carbon Nanotube above Room Temperature. *Nano Lett.* **2006**, *6*, 96–100.
- (419) Ajayan, P. M. Nanotubes from Carbon. *Chem. Rev.* **1999**, *99*, 1787–1800.
- (420) Coleman, J. N.; Khan, U.; Gun'ko, Y. K. Mechanical Reinforcement of Polymers Using Carbon Nanotubes. *Adv. Mater.* **2006**, *18*, 689–706.
-

-
- (421) Joussetme, B.; Filoramo, A.; Campidelli, S. Supramolecular Chemistry of Carbon Nanotubes. In *Supramolecular Chemistry of Fullerenes and Carbon Nanotubes*; Wiley-VCH Verlag GmbH & Co. KGaA: Weinheim, Germany, 2012; pp. 263–300.
- (422) Liu, J.; Rinzler, A. G.; Dai, H.; Hafner, J. H.; Bradley, R. K.; Boul, P. J.; Lu, A.; Iverson, T.; Shelimov, K.; Huffman, C. B.; *et al.* Fullerene Pipes. *Science* **1998**, *280*, 1253–1256.
- (423) Moore, V. C.; Strano, M. S.; Haroz, E. H.; Hauge, R. H.; Smalley, R. E.; Schmidt, J.; Talmon, Y. Individually Suspended Single-Walled Carbon Nanotubes in Various Surfactants. *Nano Lett.* **2003**, *3*, 1379–1382.
- (424) Wenseleers, W.; Vlasov, I. I.; Goovaerts, E.; Obraztsova, E. D.; Lobach, A. S.; Bouwen, A. Efficient Isolation and Solubilization of Pristine Single-Walled Nanotubes in Bile Salt Micelles. *Adv. Funct. Mater.* **2004**, *14*, 1105–1112.
- (425) Calvaresi, M.; Dallavalle, M.; Zerbetto, F. Wrapping Nanotubes with Micelles, Hemimicelles, and Cylindrical Micelles. *Small* **2009**, *5*, 2191–2198.
- (426) O’Connell, M. J.; Bachilo, S. M.; Huffman, C. B.; Moore, V. C.; Strano, M. S.; Haroz, E. H.; Rialon, K. L.; Boul, P. J.; Noon, W. H.; Kittrell, C.; *et al.* Band Gap Fluorescence from Individual Single-Walled Carbon Nanotubes. *Science* **2002**, *297*, 593–596.
- (427) Arnold, M. S.; Suntivich, J.; Stupp, S. I.; Hersam, M. C. Hydrodynamic Characterization of Surfactant Encapsulated Carbon Nanotubes Using an Analytical Ultracentrifuge. *ACS Nano* **2008**, *2*, 2291–2300.
- (428) Zheng, M.; Jagota, A.; Semke, E. D.; Diner, B. A.; Mclean, R. S.; Lustig, S. R.; Richardson, R. E.; Tassi, N. G. DNA-Assisted Dispersion and Separation of Carbon Nanotubes. *Nat. Mater.* **2003**, *2*, 338–342.
- (429) Duesberg, G. S.; Muster, J.; Krstic, V.; Burghard, M.; Roth, S. Chromatographic Size Separation of Single-Wall Carbon Nanotubes. *Appl. Phys. A Mater. Sci. Process.* **1998**, *67*, 117–119.
- (430) Strano, M. S.; Zheng, M.; Jagota, A.; Onoa, G. B.; Heller, D. A.; Barone, P. W.; Usrey, M. L. Understanding the Nature of the DNA-Assisted Separation of Single-Walled Carbon Nanotubes Using Fluorescence and Raman Spectroscopy. *Nano Lett.* **2004**, *4*, 543–550.
- (431) Heller, D. A.; Mayrhofer, R. M.; Baik, S.; Grinkova, Y. V.; Usrey, M. L.; Strano, M. S. Concomitant Length and Diameter Separation of Single-Walled Carbon Nanotubes. *J. Am. Chem. Soc.* **2004**, *126*, 14567–14573.
- (432) Zheng, M.; Jagota, A.; Strano, M. S.; Santos, A. P.; Barone, P. W.; Chou, S. G.; Diner, B. A.; Dresselhaus, M. S.; Mclean, R. S.; Onoa, G. B.; *et al.* Structure-Based Carbon Nanotube Sorting by Sequence-Dependent DNA Assembly. *Science* **2003**, *302*, 1545–1548.
- (433) Deria, P.; Olivier, J.-H.; Park, J.; Therien, M. J. Potentiometric, Electronic, and Transient Absorptive Spectroscopic Properties of Oxidized Single-Walled Carbon Nanotubes Helically Wrapped by Ionic, Semiconducting Polymers in Aqueous and Organic Media. *J. Am. Chem. Soc.* **2014**, *136*, 14193–14199.
- (434) Arnold, M. S.; Stupp, S. I.; Hersam, M. C. Enrichment of Single-Walled Carbon Nanotubes by Diameter in Density Gradients. *Nano Lett.* **2005**, *5*, 713–718.
- (435) Zheng, M.; Semke, E. D. Enrichment of Single Chirality Carbon Nanotubes. *J. Am. Chem. Soc.* **2007**, *129*, 6084–6085.
-

-
- (436) Ju, S.-Y.; Doll, J.; Sharma, I.; Papadimitrakopoulos, F. Selection of Carbon Nanotubes with Specific Chiralities Using Helical Assemblies of Flavin Mononucleotide. *Nat. Nanotechnol.* **2008**, *3*, 356–362.
- (437) Tu, X.; Manohar, S.; Jagota, A.; Zheng, M. DNA Sequence Motifs for Structure-Specific Recognition and Separation of Carbon Nanotubes. *Nature* **2009**, *460*, 250–253.
- (438) Krupke, R.; Linden, S.; Rapp, M.; Hennrich, F. Thin Films of Metallic Carbon Nanotubes Prepared by Dielectrophoresis. *Adv. Mater.* **2006**, *18*, 1468–1470.
- (439) Krupke, R. Separation of Metallic from Semiconducting Single-Walled Carbon Nanotubes. *Science* **2003**, *301*, 344–347.
- (440) Peng, X.; Komatsu, N.; Bhattacharya, S.; Shimawaki, T.; Aonuma, S.; Kimura, T.; Osuka, A. Optically Active Single-Walled Carbon Nanotubes. *Nat. Nanotechnol.* **2007**, *2*, 361–365.
- (441) Ghosh, S.; Bachilo, S. M.; Weisman, R. B. Advanced Sorting of Single-Walled Carbon Nanotubes by Nonlinear Density-Gradient Ultracentrifugation. *Nat. Nanotechnol.* **2010**, *5*, 443–450.
- (442) D'Souza, F.; Das, S. K.; Zandler, M. E.; Sandanayaka, A. S. D.; Ito, O. Bionano Donor–Acceptor Hybrids of Porphyrin, ssDNA, and Semiconductive Single-Wall Carbon Nanotubes for Electron Transfer via Porphyrin Excitation. *J. Am. Chem. Soc.* **2011**, *133*, 19922–19930.
- (443) Zhang, H.; Baker, B. A.; Cha, T.-G.; Sauffer, M. D.; Wu, Y.; Hinkson, N.; Bork, M. A.; McShane, C. M.; Choi, K.-S.; McMillin, D. R.; *et al.* DNA Oligonucleotide Templated Nanohybrids Using Electronic Type Sorted Carbon Nanotubes for Light Harvesting. *Adv. Mater.* **2012**, *24*, 5447–5451.
- (444) Nakashima, N.; Tomonari, Y.; Murakami, H. Water-Soluble Single-Walled Carbon Nanotubes via Noncovalent Sidewall-Functionalization with a Pyrene-Carrying Ammonium Ion. *Chem. Lett.* **2002**, 638–639.
- (445) Tomonari, Y.; Murakami, H.; Nakashima, N. Solubilization of Single-Walled Carbon Nanotubes by Using Polycyclic Aromatic Ammonium Amphiphiles in Water - Strategy for the Design of High-Performance Solubilizers. *Chem. Eur. J.* **2006**, *12*, 4027–4034.
- (446) Guldi, D. M.; Rahman, G. M. A.; Jux, N.; Tagmatarchis, N.; Prato, M. Integrating Single-Wall Carbon Nanotubes into Donor-Acceptor Nanohybrids. *Angew. Chem. Int. Ed.* **2004**, *43*, 5526–5530.
- (447) Rahman, G. M. A.; Guldi, D. M.; Cagnoli, R.; Mucci, A.; Schenetti, L.; Vaccari, L.; Prato, M. Combining Single Wall Carbon Nanotubes and Photoactive Polymers for Photoconversion. *J. Am. Chem. Soc.* **2005**, *127*, 10051–10057.
- (448) Sgobba, V.; Rahman, G. M. A.; Guldi, D. M.; Jux, N.; Campidelli, S.; Prato, M. Supramolecular Assemblies of Different Carbon Nanotubes for Photoconversion Processes. *Adv. Mater.* **2006**, *18*, 2264–2269.
- (449) Ehli, C.; Rahman, G. M. A.; Jux, N.; Balbinot, D.; Guldi, D. M.; Paolucci, F.; Marcaccio, M.; Paolucci, D.; Melle-Franco, M.; Zerbetto, F.; *et al.* Interactions in Single Wall Carbon Nanotubes/pyrene/porphyrin Nanohybrids. *J. Am. Chem. Soc.* **2006**, *128*, 11222–11231.
- (450) Guldi, D. M.; Rahman, G. M. A.; Jux, N.; Balbinot, D.; Hartnagel, U.; Tagmatarchis, N.; Prato, M. Functional Single-Wall Carbon Nanotube Nanohybrids--Associating SWNTs with Water-Soluble Enzyme Model Systems. *J. Am. Chem. Soc.* **2005**, *127*, 9830–9838.
-

-
- (451) Sandanayaka, A. S. D.; Chitta, R.; Subbaiyan, N. K.; D'Souza, L.; Ito, O.; D'Souza, F. Photoinduced Charge Separation in Ion-Paired Porphyrin–Single-Wall Carbon Nanotube Donor–Acceptor Hybrids. *J. Phys. Chem. C* **2009**, *113*, 13425–13432.
- (452) Chitta, R.; Sandanayaka, A. S. D.; Schumacher, A. L.; D'Souza, L.; Araki, Y.; Ito, O.; D'Souza, F. Donor - Acceptor Nanohybrids of Zinc Naphthalocyanine or Zinc Porphyrin Noncovalently Linked to Single-Wall Carbon Nanotubes for Photoinduced Electron Transfer. *J. Phys. Chem. C* **2007**, *111*, 6947–6955.
- (453) D'Souza, F.; Chitta, R.; Sandanayaka, A. S. D.; Subbaiyan, N. K.; D'Souza, L.; Araki, Y.; Ito, O. Self-Assembled Single-Walled Carbon Nanotube: Zinc-Porphyrin Hybrids through Ammonium Ion-Crown Ether Interaction: Construction and Electron Transfer. *Chem. Eur. J.* **2007**, *13*, 8277–8284.
- (454) Satake, A.; Miyajima, Y.; Kobuke, Y. Porphyrin-Carbon Nanotube Composites Formed by Noncovalent Polymer Wrapping. *Chem. Mater.* **2005**, *17*, 716–724.
- (455) Kavakka, J. S.; Heikkinen, S.; Kilpeläinen, I.; Mattila, M.; Lipsanen, H.; Helaja, J. Noncovalent Attachment of Pyro-Pheophorbidea to a Carbon Nanotube. *Chem. Commun.* **2007**, 519–521.
- (456) Maligaspe, E.; Sandanayaka, A. S. D.; Hasobe, T.; Ito, O.; Dsouza, F. Sensitive Efficiency of Photoinduced Electron Transfer to Band Gaps of Semiconductive Single-Walled Carbon Nanotubes with Supramolecularly Attached Zinc Porphyrin Bearing Pyrene Glues. *J. Am. Chem. Soc.* **2010**, *132*, 8158–8164.
- (457) Bartelmess, J.; Ballesteros, B.; de la Torre, G.; Kiessling, D.; Campidelli, S.; Prato, M.; Torres, T.; Guldi, D. M. Phthalocyanine–Pyrene Conjugates: A Powerful Approach toward Carbon Nanotube Solar Cells. *J. Am. Chem. Soc.* **2010**, *132*, 16202–16211.
- (458) Klare, J. E.; Murray, I. P.; Goldberger, J.; Stupp, S. I. Assembling P-Type Molecules on Single Wall Carbon Nanotubes for Photovoltaic Devices. *Chem. Commun.* **2009**, 3705–3707.
- (459) Guldi, D. M.; Menna, E.; Maggini, M.; Marcaccio, M.; Paolucci, D.; Paolucci, F.; Campidelli, S.; Prato, M.; Rahman, G. M. A.; Schergna, S. Supramolecular Hybrids of [60]Fullerene and Single-Wall Carbon Nanotubes. *Chem. Eur. J.* **2006**, *12*, 3975–3983.
- (460) Zhang, J.; Lee, J. K.; Wu, Y.; Murray, R. W. Photoluminescence and Electronic Interaction of Anthracene Derivatives Adsorbed on Sidewalls of Single-Walled Carbon Nanotubes. *Nano Lett.* **2003**, *3*, 403–407.
- (461) Voggu, R.; Rao, K. V.; George, S. J.; Rao, C. N. R. A Simple Method of Separating Metallic and Semiconducting Single-Walled Carbon Nanotubes Based on Molecular Charge Transfer. *J. Am. Chem. Soc.* **2010**, *132*, 5560–5561.
- (462) Murakami, H.; Nomura, T.; Nakashima, N. Noncovalent Porphyrin-Functionalized Single-Walled Carbon Nanotubes in Solution and the Formation of Porphyrin–nanotube Nanocomposites. *Chem. Phys. Lett.* **2003**, *378*, 481–485.
- (463) Chen, J.; Collier, C. P. Noncovalent Functionalization of Single-Walled Carbon Nanotubes with Water-Soluble Porphyrins. *J. Phys. Chem. B* **2005**, *109*, 7605–7609.
- (464) Rahman, G. M. A.; Guldi, D. M.; Campidelli, S.; Prato, M. Electronically Interacting Single Wall Carbon Nanotube-Porphyrin Nanohybrids. *J. Mater. Chem.* **2006**, *16*, 62–65.
- (465) Tanaka, H.; Yajima, T.; Matsumoto, T.; Otsuka, Y.; Ogawa, T. Porphyrin Molecular Nanodevices Wired Using Single-Walled Carbon Nanotubes. *Adv. Mater.* **2006**, *18*, 1411–
-

- 1415.
- (466) Roquelet, C.; Lauret, J.-S.; Alain-Rizzo, V.; Voisin, C.; Fleurier, R.; Delarue, M.; Garrot, D.; Loiseau, A.; Roussignol, P.; Delaire, J. A.; *et al.* II-Stacking Functionalization of Carbon Nanotubes through Micelle Swelling. *ChemPhysChem* **2010**, *11*, 1667–1672.
- (467) Roquelet, C.; Violla, F.; Diederichs, C.; Roussignol, P.; Delalande, C.; Deleporte, E.; Lauret, J.-S.; Voisin, C. Local Field Effects in the Energy Transfer between a Chromophore and a Carbon Nanotube: A Single-Nanocompound Investigation. *ACS Nano* **2012**, *6*, 8796–8802.
- (468) Zhong, Q.; Diev, V. V.; Roberts, S. T.; Antunez, P. D.; Brutchey, R. L.; Bradforth, S. E.; Thompson, M. E. Fused Porphyrin–Single-Walled Carbon Nanotube Hybrids: Efficient Formation and Photophysical Characterization. *ACS Nano* **2013**, *7*, 3466–3475.
- (469) Cheng, F.; Zhang, S.; Adronov, A.; Echegoyen, L.; Diederich, F. Triply Fused ZnII-Porphyrin Oligomers: Synthesis, Properties, and Supramolecular Interactions with Single-Walled Carbon Nanotubes (SWNTs). *Chem. Eur. J.* **2006**, *12*, 6062–6070.
- (470) Sprafke, J. K.; Stranks, S. D.; Warner, J. H.; Nicholas, R. J.; Anderson, H. L. Noncovalent Binding of Carbon Nanotubes by Porphyrin Oligomers. *Angew. Chem. Int. Ed.* **2011**, *50*, 2313–2316.
- (471) Backes, C.; Schmidt, C. D.; Hauke, F.; Böttcher, C.; Hirsch, A. High Population of Individualized SWCNTs through the Adsorption of Water-Soluble Perylenes. *J. Am. Chem. Soc.* **2009**, *131*, 2172–2184.
- (472) Backes, C.; Schmidt, C. D.; Rosenlehner, K.; Hauke, F.; Coleman, J. N.; Hirsch, A. Nanotube Surfactant Design: The Versatility of Water-Soluble Perylene Bisimides. *Adv. Mater.* **2010**, *22*, 788–802.
- (473) Romero-Nieto, C.; García, R.; Herranz, M. Á.; Ehli, C.; Ruppert, M.; Hirsch, A.; Guldi, D. M.; Martín, N. Tetrathiafulvalene-Based Nanotweezers—Noncovalent Binding of Carbon Nanotubes in Aqueous Media with Charge Transfer Implications. *J. Am. Chem. Soc.* **2012**, *134*, 9183–9192.
- (474) Brunetti, F. G.; Romero-Nieto, C.; López-Andarias, J.; Atienza, C. M.; López, J. L.; Guldi, D. M.; Martín, N. Self-Ordering Electron Donor-Acceptor Nanohybrids Based on Single-Walled Carbon Nanotubes Across Different Scales. *Angew. Chem. Int. Ed.* **2013**, *52*, 2180–2184.
- (475) Srinivasan, S.; Babu, S. S.; Praveen, V. K.; Ajayaghosh, A. Carbon Nanotube Triggered Self-Assembly of Oligo(p-phenylene Vinylene)s to Stable Hybrid π -Gels. *Angew. Chem. Int. Ed.* **2008**, *47*, 5746–5749.
- (476) Srinivasan, S.; Praveen, V. K.; Philip, R.; Ajayaghosh, A. Bioinspired Superhydrophobic Coatings of Carbon Nanotubes and Linear π Systems Based on the “Bottom-Up” Self-Assembly Approach. *Angew. Chem. Int. Ed.* **2008**, *47*, 5750–5754.
- (477) Deria, P.; Von Bargen, C. D.; Olivier, J.-H.; Kumbhar, A. S.; Saven, J. G.; Therien, M. J. Single-Handed Helical Wrapping of Single-Walled Carbon Nanotubes by Chiral, Ionic, Semiconducting Polymers. *J. Am. Chem. Soc.* **2013**, *135*, 16220–16234.
- (478) Shen, Y.; Skirtach, A. G.; Seki, T.; Yagai, S.; Li, H.; Möhwald, H.; Nakanishi, T. Assembly of Fullerene-Carbon Nanotubes: Temperature Indicator for Photothermal Conversion. *J. Am. Chem. Soc.* **2010**, *132*, 8566–8568.
- (479) Shen, Y.; Reparaz, J. S.; Wagner, M. R.; Hoffmann, A.; Thomsen, C.; Lee, J.-O.; Heeg, S.;

-
- Hatting, B.; Reich, S.; Saeki, A.; *et al.* Assembly of Carbon Nanotubes and Alkylated Fullerenes: Nanocarbon Hybrid towards Photovoltaic Applications. *Chem. Sci.* **2011**, *2*, 2243–2250.
- (480) Sun, Y.-P.; Zhou, B.; Lin, Y.; Wang, W.; Fernando, K. A. S.; Pathak, P.; Meziani, M. J.; Harruff, B. A.; Wang, X.; Wang, H.; *et al.* Quantum-Sized Carbon Dots for Bright and Colorful Photoluminescence. *J. Am. Chem. Soc.* **2006**, *128*, 7756–7757.
- (481) Xu, X.; Ray, R.; Gu, Y.; Ploehn, H. J.; Gearheart, L.; Raker, K.; Scrivens, W. A. Electrophoretic Analysis and Purification of Fluorescent Single-Walled Carbon Nanotube Fragments. *J. Am. Chem. Soc.* **2004**, *126*, 12736–12737.
- (482) Baker, S. N.; Baker, G. A. Luminescent Carbon Nanodots: Emergent Nanolights. *Angew. Chem. Int. Ed.* **2010**, *49*, 6726–6744.
- (483) Strauss, V.; Margraf, J. T.; Dolle, C.; Butz, B.; Nacken, T. J.; Walter, J.; Bauer, W.; Peukert, W.; Spiecker, E.; Clark, T.; *et al.* Carbon Nanodots: Toward a Comprehensive Understanding of Their Photoluminescence. *J. Am. Chem. Soc.* **2014**, *136*, 17308–17316.
- (484) Lim, S. Y.; Shen, W.; Gao, Z. Carbon Quantum Dots and Their Applications. *Chem. Soc. Rev.* **2015**, *44*, 362–381.
- (485) Roy, P.; Chen, P.-C.; Periasamy, A. P.; Chen, Y.-N.; Chang, H.-T. Photoluminescent Carbon Nanodots: Synthesis, Physicochemical Properties and Analytical Applications. *Mater. Today* **2015**, *18*, 447–458.
- (486) Zheng, H.; Wang, Q.; Long, Y.; Zhang, H.; Huang, X.; Zhu, R. Enhancing the Luminescence of Carbon Dots with a Reduction Pathway. *Chem. Commun.* **2011**, *47*, 10650–10652.
- (487) Dong, Y.; Pang, H.; Yang, H. Bin; Guo, C.; Shao, J.; Chi, Y.; Li, C. M.; Yu, T. Carbon-Based Dots Co-Doped with Nitrogen and Sulfur for High Quantum Yield and Excitation-Independent Emission. *Angew. Chem. Int. Ed.* **2013**, *52*, 7800–7804.
- (488) Chen, X.; Jin, Q.; Wu, L.; Tung, C.; Tang, X. Synthesis and Unique Photoluminescence Properties of Nitrogen-Rich Quantum Dots and Their Applications. *Angew. Chem. Int. Ed.* **2014**, *53*, 12542–12547.
- (489) Moon, J.; An, J.; Sim, U.; Cho, S.-P.; Kang, J. H.; Chung, C.; Seo, J.-H.; Lee, J.; Nam, K. T.; Hong, B. H. One-Step Synthesis of N-Doped Graphene Quantum Sheets from Monolayer Graphene by Nitrogen Plasma. *Adv. Mater.* **2014**, *26*, 3501–3505.
- (490) Luo, P. G.; Sahu, S.; Yang, S.-T.; Sonkar, S. K.; Wang, J.; Wang, H.; LeCroy, G. E.; Cao, L.; Sun, Y.-P. Carbon “quantum” Dots for Optical Bioimaging. *J. Mater. Chem. B* **2013**, *1*, 2116–2127.
- (491) Zhao, A.; Chen, Z.; Zhao, C.; Gao, N.; Ren, J.; Qu, X. Recent Advances in Bioapplications of C-Dots. *Carbon* **2015**, *85*, 309–327.
- (492) Li, X.; Rui, M.; Song, J.; Shen, Z.; Zeng, H. Carbon and Graphene Quantum Dots for Optoelectronic and Energy Devices: A Review. *Adv. Funct. Mater.* **2015**, *25*, 4929–4947.
- (493) Wang, X.; Cao, L.; Lu, F.; Meziani, M. J.; Li, H.; Qi, G.; Zhou, B.; Harruff, B. A.; Kermarrec, F.; Sun, Y.-P. Photoinduced Electron Transfers with Carbon Dots. *Chem. Commun.* **2009**, 3774–3776.
- (494) Strauss, V.; Margraf, J. T.; Clark, T.; Guldi, D. M. A Carbon–carbon Hybrid – Immobilizing Carbon Nanodots onto Carbon Nanotubes. *Chem. Sci.* **2015**, *6*, 6878–6885.
-

-
- (495) Strauss, V.; Margraf, J. T.; Dirian, K.; Syrgiannis, Z.; Prato, M.; Wessendorf, C.; Hirsch, A.; Clark, T.; Guldi, D. M. Carbon Nanodots: Supramolecular Electron Donor-Acceptor Hybrids Featuring Perylenediimides. *Angew. Chem. Int. Ed.* **2015**, *54*, 8292–8297.
- (496) Yu, P.; Wen, X.; Toh, Y.-R.; Lee, Y.-C.; Huang, K.-Y.; Huang, S.; Shrestha, S.; Conibeer, G.; Tang, J. Efficient Electron Transfer in Carbon Nanodot–graphene Oxide Nanocomposites. *J. Mater. Chem. C* **2014**, *2*, 2894–2901.
- (497) Tumpane, J.; Karousis, N.; Tagmatarchis, N.; Nordén, B. Alignment of Carbon Nanotubes in Weak Magnetic Fields. *Angew. Chem. Int. Ed.* **2008**, *47*, 5148–5152.
- (498) *Non-Covalent Multi-Porphyrin Assemblies*; Alessio, E., Ed.; Structure and Bonding; Springer-Verlag: Berlin/Heidelberg, 2006.
- (499) Beletskaya, I.; Tyurin, V. S.; Tsivadze, A. Y.; Guillard, R.; Stern, C. Supramolecular Chemistry of Metalloporphyrins. *Chem. Rev.* **2009**, *109*, 1659–1713.
- (500) Camara-Campos, A.; Hunter, C. A.; Tomas, S. Cooperativity in the Self-Assembly of Porphyrin Ladders. *Proc. Natl. Acad. Sci. U. S. A.* **2006**, *103*, 3034–3038.
- (501) Mulholland, A. R.; Thordarson, P.; Mensforth, E. J.; Langford, S. J. Porphyrin Dyads Linked by a Rotatable 3,3'-Biphenyl Scaffold: A New Binding Motif for Small Ditopic Molecules. *Org. Biomol. Chem.* **2012**, *10*, 6045–6053.
- (502) Oliva, A. I.; Gómez, K.; González, G.; Ballester, P. Diffusion-Ordered Spectroscopy (1H-DOSY) of Zn-Porphyrin Assemblies Induced by Coordination with DABCO. *New J. Chem.* **2008**, *32*, 2159–2163.
- (503) Timmerman, P.; Weidmann, J.-L.; Jolliffe, K. A.; Prins, L. J.; Reinhoudt, D. N.; Shinkai, S.; Frish, L.; Cohen, Y. NMR Diffusion Spectroscopy for the Characterization of Multicomponent Hydrogen-Bonded Assemblies in Solution. *J. Chem. Soc. Perkin Trans. 2* **2000**, 2077–2089.
- (504) Llanes-Pallas, A.; Yoosaf, K.; Traboulsi, H.; Mohanraj, J.; Seldrum, T.; Dumont, J.; Minoia, A.; Lazzaroni, R.; Armaroli, N.; Bonifazi, D. Modular Engineering of H-Bonded Supramolecular Polymers for Reversible Functionalization of Carbon Nanotubes. *J. Am. Chem. Soc.* **2011**, *133*, 15412–15424.
- (505) Materials Studio Overview <http://accelrys.com/products/collaborative-science/biovia-materials-studio/> (accessed Mar 13, 2016).
- (506) Sun, H. COMPASS: An Ab Initio Force-Field Optimized for Condensed-Phase Applications Overview with Details on Alkane and Benzene Compounds. *J. Phys. Chem. B* **1998**, *102*, 7338–7364.
- (507) Minoia, A.; Guo, Z.; Xu, H.; George, S. J.; Schenning, A. P. H. J.; Feyter, S. De; Lazzaroni, R. Assessing the Role of Chirality in the Formation of Rosette-like Supramolecular Assemblies on Surfaces. *Chem. Commun.* **2011**, *47*, 10924–10926.
- (508) Stopin, A.; Pineux, F.; Marega, R.; Bonifazi, D. Magnetically Active Carbon Nanotubes at Work. *Chem. Eur. J.* **2015**, *21*, 9288–9301.
- (509) Lu, J. P. Novel Magnetic Properties of Carbon Nanotubes. *Phys. Rev. Lett.* **1995**, *74*, 1123–1126.
- (510) Lin, M. F.; Shung, K. W. K. Magnetization of Graphene Tubules. *Phys. Rev. B* **1995**, *52*, 8423–8438.
-

-
- (511) Haddon, R. C.; Pasquarello, A. Magnetism of Carbon Clusters. *Phys. Rev. B* **1994**, *50*, 16459–16463.
- (512) Shklyarevskiy, I. O.; Jonkheijm, P.; Christianen, P. C. M.; Schenning, A. P. H. J.; Del Guerzo, A.; Desvergne, J. P.; Meijer, E. W.; Maan, J. C. Magnetic Alignment of Self-Assembled Anthracene Organogel Fibers. *Langmuir* **2005**, *21*, 2108–2112.
- (513) Liebi, M.; Van Rhee, P. G.; Christianen, P. C. M.; Kohlbrecher, J.; Fischer, P.; Walde, P.; Windhab, E. J. Alignment of Bicelles Studied with High-Field Magnetic Birefringence and Small-Angle Neutron Scattering Measurements. *Langmuir* **2013**, *29*, 3467–3473.
- (514) Rikken, R. S. M.; Nolte, R. J. M.; Maan, J. C.; van Hest, J. C. M.; Wilson, D. A.; Christianen, P. C. M. Manipulation of Micro- and Nanostructure Motion with Magnetic Fields. *Soft Matter* **2014**, *10*, 1295–1308.
- (515) Guldi, D. M. Fullerene–porphyrin Architectures; Photosynthetic Antenna and Reaction Center Models. *Chem. Soc. Rev.* **2002**, *31*, 22–36.
- (516) Umeyama, T.; Imahori, H. Photofunctional Hybrid Nanocarbon Materials. *J. Phys. Chem. C* **2013**, *117*, 3195–3209.
- (517) Delgado, J. L.; Herranz, M.; Martín, N. The Nano-Forms of Carbon. *J. Mater. Chem.* **2008**, *18*, 1417–1426.
- (518) Pagona, G.; Sandanayaka, A. S. D.; Araki, Y.; Fan, J.; Tagmatarchis, N.; Charalambidis, G.; Coutsolelos, A. G.; Boitrel, B.; Yudasaka, M.; Iijima, S.; *et al.* Covalent Functionalization of Carbon Nanohorns with Porphyrins: Nanohybrid Formation and Photoinduced Electron and Energy Transfer. *Adv. Funct. Mater.* **2007**, *17*, 1705–1711.
- (519) Karousis, N.; Sandanayaka, A. S. D.; Hasobe, T.; Economopoulos, S. P.; Sarantopoulou, E.; Tagmatarchis, N. Graphene Oxide with Covalently Linked Porphyrin Antennae: Synthesis, Characterization and Photophysical Properties. *J. Mater. Chem.* **2011**, *21*, 109–117.
- (520) Aymonier, C.; Schlotterbeck, U.; Antonietti, L.; Zacharias, P.; Thomann, R.; Tiller, J. C.; Mecking, S. Hybrids of Silver Nanoparticles with Amphiphilic Hyperbranched Macromolecules Exhibiting Antimicrobial Properties. *Chem. Commun.* **2002**, 3018–3019.
- (521) Rao, C. N. R.; Kulkarni, G. U.; Thomas, P. J.; Edwards, P. P. Metal Nanoparticles and Their Assemblies. *Chem. Soc. Rev.* **2000**, *29*, 27–35.
- (522) Whitesides, G. M. Nanoscience, Nanotechnology, and Chemistry. *Small* **2005**, *1*, 172–179.
- (523) Barth, J. V.; Costantini, G.; Kern, K. Engineering Atomic and Molecular Nanostructures at Surfaces. *Nature* **2005**, *437*, 671–679.
- (524) Gates, B. D.; Xu, Q.; Stewart, M.; Ryan, D.; Willson, C. G.; Whitesides, G. M. New Approaches to Nanofabrication: Molding, Printing, and Other Techniques. *Chem. Rev.* **2005**, *105*, 1171–1196.
- (525) Ito, T.; Okazaki, S. Pushing the Limits of Lithography. *Nature* **2000**, *406*, 1027–1031.
- (526) Elemans, J. A. A. W.; Rowan, A. E.; Nolte, R. J. M. Mastering Molecular Matter. Supramolecular Architectures by Hierarchical Self-Assembly. *J. Mater. Chem.* **2003**, *13*, 2661–2670.
- (527) Bonifazi, D.; Mohnani, S.; Llanes-Pallas, A. Supramolecular Chemistry at Interfaces: Molecular Recognition on Nanopatterned Porous Surfaces. *Chem. Eur. J.* **2009**, *15*, 7004–7025.
-

-
- (528) De Feyter, S.; De Schryver, F. C. Two-Dimensional Supramolecular Self-Assembly Probed by Scanning Tunneling Microscopy. *Chem. Soc. Rev.* **2003**, *32*, 139–150.
- (529) Barth, J. V. Molecular Architectonic on Metal Surfaces. *Annu. Rev. Phys. Chem.* **2007**, *58*, 375–407.
- (530) Binnig, G.; Rohrer, H. Scanning Tunneling Microscopy. *Helv. Phys. Acta* **1982**, *55*, 726–735.
- (531) Voigtländer, B. *Scanning Probe Microscopy*; NanoScience and Technology; Springer Berlin Heidelberg: Berlin, Heidelberg, 2015.
- (532) Woedtke, S. Pd.D. Thesis, Christian-Albrechts-Universität zu Kiel, 2002.
- (533) De Feyter, S.; De Schryver, F. C. Self-Assembly at the Liquid/Solid Interface: STM Reveals. *J. Phys. Chem. B* **2005**, *109*, 4290–4302.
- (534) Gross, L. Recent Advances in Submolecular Resolution with Scanning Probe Microscopy. *Nat. Chem.* **2011**, *3*, 273–278.
- (535) Repp, J.; Meyer, G.; Stojković, S. M.; Gourdon, A.; Joachim, C. Molecules on Insulating Films: Scanning-Tunneling Microscopy Imaging of Individual Molecular Orbitals. *Phys. Rev. Lett.* **2005**, *94*, 026803.
- (536) Liljeroth, P.; Repp, J.; Meyer, G. Current-Induced Hydrogen Tautomerization and Conductance Switching of Naphthalocyanine Molecules. *Science* **2007**, *317*, 1203–1206.
- (537) Samori, P. Scanning Probe Microscopies beyond Imaging. *J. Mater. Chem.* **2004**, *14*, 1353–1366.
- (538) Kudernac, T.; Lei, S.; Elemans, J. A. A. W.; De Feyter, S. Two-Dimensional Supramolecular Self-Assembly: Nanoporous Networks on Surfaces. *Chem. Soc. Rev.* **2009**, *38*, 402–421.
- (539) Barth, J. V.; Weckesser, J.; Lin, N.; Dmitriev, A.; Kern, K. Supramolecular Architectures and Nanostructures at Metal Surfaces. *Appl. Phys. A Mater. Sci. Process.* **2003**, *76*, 645–652.
- (540) Dmitriev, A.; Lin, N.; Weckesser, J.; Barth, J. V.; Kern, K. Supramolecular Assemblies of Trimesic Acid on a Cu(100) Surface. *J. Phys. Chem. B* **2002**, *106*, 6907–6912.
- (541) Ruben, M.; Payer, D.; Landa, A.; Comisso, A.; Gattinoni, C.; Lin, N.; Collin, J.; Sauvage, J.; De Vita, A.; Kern, K. 2D Supramolecular Assemblies of Benzene-1,3,5-Triyl-Tribenzoic Acid: Temperature-Induced Phase Transformations and Hierarchical Organization with Macrocyclic Molecules. *J. Am. Chem. Soc.* **2006**, *128*, 15644–15651.
- (542) Lin, N.; Payer, D.; Dmitriev, A.; Strunskus, T.; Wöll, C.; Barth, J. V.; Kern, K. Two-Dimensional Adatom Gas Bestowing Dynamic Heterogeneity on Surfaces. *Angew. Chem. Int. Ed.* **2005**, *44*, 1488–1491.
- (543) Stöhr, M.; Wahl, M.; Galka, C. H.; Riehm, T.; Jung, T. A.; Gade, L. H. Controlling Molecular Assembly in Two Dimensions: The Concentration Dependence of Thermally Induced 2D Aggregation of Molecules on a Metal Surface. *Angew. Chem. Int. Ed.* **2005**, *44*, 7394–7398.
- (544) Stöhr, M.; Wahl, M.; Spillmann, H.; Gade, L. H.; Jung, T. A. Lateral Manipulation for the Positioning of Molecular Guests within the Confinements of a Highly Stable Self-Assembled Organic Surface Network. *Small* **2007**, *3*, 1336–1340.
- (545) Pawin, G.; Wong, K. L.; Kwon, K.-Y.; Bartels, L. A Homomolecular Porous Network at a Cu(111) Surface. *Science* **2006**, *313*, 961–962.
-

-
- (546) Theobald, J. A.; Oxtoby, N. S.; Phillips, M. A.; Champness, N. R.; Beton, P. H. Controlling Molecular Deposition and Layer Structure with Supramolecular Surface Assemblies. *Nature* **2003**, *424*, 1029–1031.
- (547) Madueno, R.; Räsänen, M. T.; Silien, C.; Buck, M. Functionalizing Hydrogen-Bonded Surface Networks with Self-Assembled Monolayers. *Nature* **2008**, *454*, 618–621.
- (548) Silien, C.; Räsänen, M. T.; Buck, M. A Supramolecular Hydrogen-Bonded Network as a Diffusion Barrier for Metal Adatoms. *Angew. Chem. Int. Ed.* **2009**, *48*, 3349–3352.
- (549) Perdigão, L. M. A.; Perkins, E. W.; Ma, J.; Staniec, P. A.; Rogers, B. L.; Champness, N. R.; Beton, P. H. Bimolecular Networks and Supramolecular Traps on Au(111). *J. Phys. Chem. B* **2006**, *110*, 12539–12542.
- (550) Silly, F.; Shaw, A. Q.; Porfyraakis, K.; Warner, J. H.; Watt, A. A. R.; Castell, M. R.; Umamoto, H.; Akachi, T.; Shinohara, H.; Briggs, G. A. D. Grating of Single Lu@C82 Molecules Using Supramolecular Network. *Chem. Commun.* **2008**, 4616–4618.
- (551) Palma, C.-A.; Bonini, M.; Llanes-Pallas, A.; Breiner, T.; Prato, M.; Bonifazi, D.; Samori, P. Pre-Programmed Bicomponent Porous Networks at the Solid–liquid Interface: The Low Concentration Regime. *Chem. Commun.* **2008**, 5289–5291.
- (552) Yu, M.; Kalashnyk, N.; Xu, W.; Barattin, R.; Benjalal, Y.; Lægsgaard, E.; Stensgaard, I.; Hliwa, M.; Bouju, X.; Gourdon, A.; *et al.* Supramolecular Architectures on Surfaces Formed through Hydrogen Bonding Optimized in Three Dimensions. *ACS Nano* **2010**, *4*, 4097–4109.
- (553) Yu, M.; Kalashnyk, N.; Barattin, R.; Benjalal, Y.; Hliwa, M.; Bouju, X.; Gourdon, A.; Joachim, C.; Lægsgaard, E.; Besenbacher, F.; *et al.* Self-Assembly of Hydrogen-Bonded Chains of Molecular Landers. *Chem. Commun.* **2010**, *46*, 5545–5547.
- (554) Kalashnyk, N.; Yu, M.; Barattin, R.; Benjalal, Y.; Hliwa, M.; Joachim, C.; Lægsgaard, E.; Besenbacher, F.; Gourdon, A.; Bouju, X.; *et al.* Bicomponent Hydrogen-Bonded Nanostructures Formed by Two Complementary Molecular Landers on Au(111). *Chem. Commun.* **2014**, *50*, 10619–10621.
- (555) Fendt, L. A.; Stöhr, M.; Wintjes, N.; Enache, M.; Jung, T. A.; Diederich, F. Modification of Supramolecular Binding Motifs Induced by Substrate Registry: Formation of Self-Assembled Macrocycles and Chain-like Patterns. *Chem. Eur. J.* **2009**, *15*, 11139–11150.
- (556) Yokoyama, T.; Yokoyama, S.; Kamikado, T.; Okuno, Y.; Mashiko, S. Selective Assembly on a Surface of Supramolecular Aggregates with Controlled Size and Shape. *Nature* **2001**, *413*, 619–621.
- (557) Spillmann, H.; Kiebele, A.; Stöhr, M.; Jung, T. A.; Bonifazi, D.; Cheng, F.; Diederich, F. A Two-Dimensional Porphyrin-Based Porous Network Featuring Communicating Cavities for the Templated Complexation of Fullerenes. *Adv. Mater.* **2006**, *18*, 275–279.
- (558) Wintjes, N.; Hornung, J.; Lobo-Checa, J.; Voigt, T.; Samuely, T.; Thilgen, C.; Stöhr, M.; Diederich, F.; Jung, T. A. Supramolecular Synthons on Surfaces: Controlling Dimensionality and Periodicity of Tetraarylporphyrin Assemblies by the Interplay of Cyano and Alkoxy Substituents. *Chem. Eur. J.* **2008**, *14*, 5794–5802.
- (559) Urgel, J. I.; Écija, D.; Auwärter, W.; Stassen, D.; Bonifazi, D.; Barth, J. V. Orthogonal Insertion of Lanthanide and Transition-Metal Atoms in Metal-Organic Networks on Surfaces. *Angew. Chem. Int. Ed.* **2015**, *54*, 6163–6167.
-

-
- (560) Urgel, J. I.; Schwarz, M.; Garnica, M.; Stassen, D.; Bonifazi, D.; Écija, D.; Barth, J. V.; Auwärter, W. Controlling Coordination Reactions and Assembly on a Cu(111) Supported Boron Nitride Monolayer. *J. Am. Chem. Soc.* **2015**, *137*, 2420–2423.
- (561) Schlickum, U.; Decker, R.; Klappenberger, F.; Zoppellaro, G.; Klyatskaya, S.; Ruben, M.; Silanes, I.; Arnau, A.; Kern, K.; Brune, H.; *et al.* Metal–Organic Honeycomb Nanomeshes with Tunable Cavity Size. *Nano Lett.* **2007**, *7*, 3813–3817.
- (562) Klyatskaya, S.; Klappenberger, F.; Schlickum, U.; Kühne, D.; Marschall, M.; Reichert, J.; Decker, R.; Krenner, W.; Zoppellaro, G.; Brune, H.; *et al.* Surface-Confined Self-Assembly of Di-Carbonitrile Polyphenyls. *Adv. Funct. Mater.* **2011**, *21*, 1230–1240.
- (563) Palma, C.-A.; Björk, J.; Rao, F.; Kühne, D.; Klappenberger, F.; Barth, J. V. Topological Dynamics in Supramolecular Rotors. *Nano Lett.* **2014**, *14*, 4461–4468.
- (564) Palma, C.-A.; Björk, J.; Klappenberger, F.; Arras, E.; Kühne, D.; Stafström, S.; Barth, J. V. Visualization and Thermodynamic Encoding of Single-Molecule Partition Function Projections. *Nat. Commun.* **2015**, *6*, 6210.
- (565) Marschall, M.; Reichert, J.; Weber-Bargioni, A.; Seufert, K.; Auwärter, W.; Klyatskaya, S.; Zoppellaro, G.; Ruben, M.; Barth, J. V. Random Two-Dimensional String Networks Based on Divergent Coordination Assembly. *Nat. Chem.* **2010**, *2*, 131–137.
- (566) Écija, D.; Urgel, J. I.; Papageorgiou, A. C.; Joshi, S.; Auwärter, W.; Seitsonen, A. P.; Klyatskaya, S.; Ruben, M.; Fischer, S.; Vijayaraghavan, S.; *et al.* Five-Vertex Archimedean Surface Tessellation by Lanthanide-Directed Molecular Self-Assembly. *Proc. Natl. Acad. Sci.* **2013**, *110*, 6678–6681.
- (567) Urgel, J. I.; Écija, D.; Auwärter, W.; Papageorgiou, A. C.; Seitsonen, A. P.; Vijayaraghavan, S.; Joshi, S.; Fischer, S.; Reichert, J.; Barth, J. V. Five-Vertex Lanthanide Coordination on Surfaces: A Route to Sophisticated Nanoarchitectures and Tessellations. *J. Phys. Chem. C* **2014**, *118*, 12908–12915.
- (568) Li, S.; Northrop, B. H.; Yuan, Q.; Wan, L.; Stang, P. J. Surface Confined Metallosupramolecular Architectures: Formation and Scanning Tunneling Microscopy Characterization. *Acc. Chem. Res.* **2009**, *42*, 249–259.
- (569) Lin, N.; Stepanow, S.; Ruben, M.; Barth, J. V. Surface-Confined Supramolecular Coordination Chemistry. *Top. Curr. Chem.* **2009**, *287*, 1–44.
- (570) Spillmann, H.; Dmitriev, A.; Lin, N.; Messina, P.; Barth, J. V.; Kern, K. Hierarchical Assembly of Two-Dimensional Homochiral Nanocavity Arrays. *J. Am. Chem. Soc.* **2003**, *125*, 10725–10728.
- (571) Dmitriev, A.; Spillmann, H.; Lin, N.; Barth, J. V.; Kern, K. Modular Assembly of Two-Dimensional Metal-Organic Coordination Networks at a Metal Surface. *Angew. Chem. Int. Ed.* **2003**, *42*, 2670–2673.
- (572) Stepanow, S.; Lingenfelder, M.; Dmitriev, A.; Spillmann, H.; Delvigne, E.; Lin, N.; Deng, X.; Cai, C.; Barth, J. V.; Kern, K. Steering Molecular Organization and Host-Guest Interactions Using Two-Dimensional Nanoporous Coordination Systems. *Nat. Mater.* **2004**, *3*, 229–233.
- (573) Stepanow, S.; Lin, N.; Barth, J. V.; Kern, K. Surface-Template Assembly of Two-Dimensional Metal-Organic Coordination Networks. *J. Phys. Chem. B* **2006**, *110*, 23472–23477.
- (574) Langner, A.; Tait, S. L.; Lin, N.; Rajadurai, C.; Ruben, M.; Kern, K. Self-Recognition and Self-
-

- Selection in Multicomponent Supramolecular Coordination Networks on Surfaces. *Proc. Natl. Acad. Sci. U. S. A.* **2007**, *104*, 17927–17930.
- (575) Heim, D.; Seufert, K.; Auwärter, W.; Aurisicchio, C.; Fabbro, C.; Bonifazi, D.; Barth, J. V. Surface-Assisted Assembly of Discrete Porphyrin-Based Cyclic Supramolecules. *Nano Lett.* **2010**, *10*, 122–128.
- (576) Écija, D.; Seufert, K.; Heim, D.; Auwärter, W.; Aurisicchio, C.; Fabbro, C.; Bonifazi, D.; Barth, J. V. Hierarchic Self-Assembly of Nanoporous Chiral Networks with Conformationally Flexible Porphyrins. *ACS Nano* **2010**, *4*, 4936–4942.
- (577) Heim, D.; Écija, D.; Seufert, K.; Auwärter, W.; Aurisicchio, C.; Fabbro, C.; Bonifazi, D.; Barth, J. V. Self-Assembly of Flexible One-Dimensional Coordination Polymers on Metal Surfaces. *J. Am. Chem. Soc.* **2010**, *132*, 6783–6790.
- (578) Zheng, Q.-N.; Liu, X.-H.; Chen, T.; Yan, H.-J.; Cook, T. R.; Wang, D.; Stang, P. J.; Wan, L.-J. Formation of Halogen Bond-Based 2D Supramolecular Assemblies by Electric Manipulation. *J. Am. Chem. Soc.* **2015**, *137*, 6128–6131.
- (579) Kawai, S.; Sadeghi, A.; Xu, F.; Peng, L.; Orita, A.; Otera, J.; Goedecker, S.; Meyer, E. Extended Halogen Bonding between Fully Fluorinated Aromatic Molecules. *ACS Nano* **2015**, *9*, 2574–2583.
- (580) Pham, T. A.; Song, F.; Nguyen, M.-T.; Stöhr, M. Self-Assembly of Pyrene Derivatives on Au(111): Substituent Effects on Intermolecular Interactions. *Chem. Commun.* **2014**, *50*, 14089–14092.
- (581) Anh Pham, T.; Song, F.; Nguyen, M.-T.; Li, Z.; Studener, F.; Stöhr, M. Comparing Ullmann Coupling on Noble Metal Surfaces: On-Surface Polymerization of 1,3,6,8-Tetrabromopyrene on Cu(111) and Au(111). *Chem. Eur. J.* **2016**.
- (582) Pivetta, M.; Blüm, M.-C.; Patthey, F.; Schneider, W.-D. Coverage-Dependent Self-Assembly of Rubrene Molecules on Noble Metal Surfaces Observed by Scanning Tunneling Microscopy. *ChemPhysChem* **2010**, *11*, 1558–1569.
- (583) Tomba, G.; Stengel, M.; Schneider, W.-D.; Baldereschi, A.; De Vita, A. Supramolecular Self-Assembly Driven by Electrostatic Repulsion: The 1D Aggregation of Rubrene Pentagons on Au(111). *ACS Nano* **2010**, *4*, 7545–7551.
- (584) Della Pia, A.; Riello, M.; Floris, A.; Stassen, D.; Jones, T. S.; Bonifazi, D.; De Vita, A.; Costantini, G. Anomalous Coarsening Driven by Reversible Charge Transfer at Metal-Organic Interfaces. *ACS Nano* **2014**, *8*, 12356–12364.
- (585) Wegner, D.; Yamachika, R.; Wang, Y.; Brar, V. W.; Bartlett, B. M.; Long, J. R.; Crommie, M. F. Single-Molecule Charge Transfer and Bonding at an Organic/Inorganic Interface: Tetracyanoethylene on Noble Metals. *Nano Lett.* **2008**, *8*, 131–135.
- (586) Bedwani, S.; Wegner, D.; Crommie, M. F.; Rochefort, A. Strongly Reshaped Organic-Metal Interfaces: Tetracyanoethylene on Cu(100). *Phys. Rev. Lett.* **2008**, *101*, 216105.
- (587) Tseng, T.-C.; Urban, C.; Wang, Y.; Otero, R.; Tait, S. L.; Alcamí, M.; Écija, D.; Trelka, M.; Gallego, J. M.; Lin, N.; *et al.* Charge-Transfer-Induced Structural Rearrangements at Both Sides of Organic/metal Interfaces. *Nat. Chem.* **2010**, *2*, 374–379.
- (588) Fan, Q.; Gottfried, J. M.; Zhu, J. Surface-Catalyzed C-C Covalent Coupling Strategies toward the Synthesis of Low-Dimensional Carbon-Based Nanostructures. *Acc. Chem. Res.* **2015**, *48*,

- 2484–2494.
- (589) Novoselov, K. S.; Geim, A. K.; Morozov, S. V.; Jiang, D.; Katsnelson, M. I.; Grigorieva, I. V.; Dubonos, S. V.; Firsov, A. A. Two-Dimensional Gas of Massless Dirac Fermions in Graphene. *Nature* **2005**, *438*, 197–200.
- (590) Lafferentz, L.; Ample, F.; Yu, H. B.; Hecht, S.; Joachim, C.; Grill, L. Conductance of a Single Conjugated Polymer as a Continuous Function of Its Length. *Science* **2009**, *323*, 1193–1197.
- (591) Bombis, C.; Ample, F.; Lafferentz, L.; Yu, H.; Hecht, S.; Joachim, C.; Grill, L. Single Molecular Wires Connecting Metallic and Insulating Surface Areas. *Angew. Chem. Int. Ed.* **2009**, *48*, 9966–9970.
- (592) Nacci, C.; Ample, F.; Bleger, D.; Hecht, S.; Joachim, C.; Grill, L. Conductance of a Single Flexible Molecular Wire Composed of Alternating Donor and Acceptor Units. *Nat. Commun.* **2015**, *6*, 7397.
- (593) Grill, L.; Dyer, M.; Lafferentz, L.; Persson, M.; Peters, M. V.; Hecht, S. Nano-Architectures by Covalent Assembly of Molecular Building Blocks. *Nat. Nanotechnol.* **2007**, *2*, 687–691.
- (594) Lafferentz, L.; Eberhardt, V.; Dri, C.; Africh, C.; Comelli, G.; Esch, F.; Hecht, S.; Grill, L. Controlling on-Surface Polymerization by Hierarchical and Substrate-Directed Growth. *Nat. Chem.* **2012**, *4*, 215–220.
- (595) Talirz, L.; Ruffieux, P.; Fasel, R. On-Surface Synthesis of Atomically Precise Graphene Nanoribbons. *Adv. Mater.* **2016**.
- (596) Gunlycke, D.; Areshkin, D. A.; White, C. T. Semiconducting Graphene Nanostrips with Edge Disorder. *Appl. Phys. Lett.* **2007**, *90*, 7–10.
- (597) Stampfer, C.; Güttinger, J.; Hellmüller, S.; Molitor, F.; Ensslin, K.; Ihn, T. Energy Gaps in Etched Graphene Nanoribbons. *Phys. Rev. Lett.* **2009**, *102*, 1–4.
- (598) Ma, L.; Wang, J.; Ding, F. Recent Progress and Challenges in Graphene Nanoribbon Synthesis. *ChemPhysChem* **2013**, *14*, 47–54.
- (599) Ullmann, F.; Bielecki, J. Ueber Synthesen in Der Biphenylreihe. *Ber. Dtsch. Chem. Ges.* **1901**, *34*, 2174–2185.
- (600) Ullmann, F. Ueber Symmetrische Biphenyl-derivate. *Justus Liebigs Ann. Chem.* **1904**, *332*, 38–81.
- (601) Dössel, L.; Gherghel, L.; Feng, X.; Müllen, K. Graphene Nanoribbons by Chemists: Nanometer-Sized, Soluble, and Defect-Free. *Angew. Chem. Int. Ed.* **2011**, *50*, 2540–2543.
- (602) Lipton-Duffin, J. A.; Ivasenko, O.; Perepichka, D. F.; Rosei, F. Synthesis of Polyphenylene Molecular Wires by Surface-Confined Polymerization. *Small* **2009**, *5*, 592–597.
- (603) Cai, J.; Ruffieux, P.; Jaafar, R.; Bieri, M.; Braun, T.; Blankenburg, S.; Muoth, M.; Seitsonen, A. P.; Saleh, M.; Feng, X.; *et al.* Atomically Precise Bottom-up Fabrication of Graphene Nanoribbons. *Nature* **2010**, *466*, 470–473.
- (604) Zhang, H.; Lin, H.; Sun, K.; Chen, L.; Zagranyarski, Y.; Aghdassi, N.; Duhm, S.; Li, Q.; Zhong, D.; Li, Y.; *et al.* On-Surface Synthesis of Rylene-Type Graphene Nanoribbons. *J. Am. Chem. Soc.* **2015**, *137*, 4022–4025.
- (605) Chen, Y.-C.; De Oteyza, D. G.; Pedramrazi, Z.; Chen, C.; Fischer, F. R.; Crommie, M. F. Tuning the Band Gap of Graphene Nanoribbons Synthesized from Molecular Precursors. *ACS*

-
- Nano* **2013**, *7*, 6123–6128.
- (606) Liu, J.; Li, B.-W.; Tan, Y.; Giannakopoulos, A.; Sanchez-Sanchez, C.; Beljonne, D.; Ruffieux, P.; Fasel, R.; Feng, X.; Müllen, K. Toward Cove-Edged Low Band Gap Graphene Nanoribbons. *J. Am. Chem. Soc.* **2015**, *137*, 6097–6103.
- (607) Ruffieux, P.; Wang, S.; Yang, B.; Sánchez-Sánchez, C.; Liu, J.; Dienel, T.; Talirz, L.; Shinde, P.; Pignedoli, C. A.; Passerone, D.; *et al.* On-Surface Synthesis of Graphene Nanoribbons with Zigzag Edge Topology. *Nature* **2016**, *531*, 489–492.
- (608) Cai, J.; Pignedoli, C. A.; Talirz, L.; Ruffieux, P.; Söde, H.; Liang, L.; Meunier, V.; Berger, R.; Li, R.; Feng, X.; *et al.* Graphene Nanoribbon Heterojunctions. *Nat. Nanotechnol.* **2014**, *9*, 896–900.
- (609) Cloke, R. R.; Marangoni, T.; Nguyen, G. D.; Joshi, T.; Rizzo, D. J.; Bronner, C.; Cao, T.; Louie, S. G.; Crommie, M. F.; Fischer, F. R. Site-Specific Substitutional Boron Doping of Semiconducting Armchair Graphene Nanoribbons. *J. Am. Chem. Soc.* **2015**, *137*, 8872–8875.
- (610) Kawai, S.; Saito, S.; Osumi, S.; Yamaguchi, S.; Foster, A. S.; Spijker, P.; Meyer, E. Atomically Controlled Substitutional Boron-Doping of Graphene Nanoribbons. *Nat. Commun.* **2015**, *6*, 8098.
- (611) Nguyen, G. D.; Toma, F. M.; Cao, T.; Pedramrazi, Z.; Chen, C.; Rizzo, D. J.; Joshi, T.; Bronner, C.; Chen, Y.-C.; Favaro, M.; *et al.* Bottom-Up Synthesis of N = 13 Sulfur-Doped Graphene Nanoribbons. *J. Phys. Chem. C* **2016**, *120*, 2684–2687.
- (612) Figueira-Duarte, T. M.; Müllen, K. Pyrene-Based Materials for Organic Electronics. *Chem. Rev.* **2011**, *111*, 7260–7314.
- (613) Coventry, D. N.; Batsanov, A. S.; Goeta, A. E.; Howard, J. A. K.; Marder, T. B.; Perutz, R. N. Selective Ir-Catalysed Borylation of Polycyclic Aromatic Hydrocarbons: Structures of Naphthalene-2,6-Bis(boronate), Pyrene-2,7-Bis(boronate) and Perylene-2,5,8,11-Tetra(boronate) Esters. *Chem. Commun.* **2005**, 2172–2174.
- (614) Crawford, A. G.; Liu, Z.; Mkhallid, I. A. I.; Thibault, M.-H.; Schwarz, N.; Alcaraz, G.; Steffen, A.; Collings, J. C.; Batsanov, A. S.; Howard, J. A. K.; *et al.* Synthesis of 2- and 2,7-Functionalized Pyrene Derivatives: An Application of Selective C-H Borylation. *Chem. Eur. J.* **2012**, *18*, 5022–5035.
- (615) Dang, H.; Marisa, T.; Yi, J. H.; Rosei, F.; Nanci, A.; Wuest, J. D. Ensuring Homology between 2D and 3D Molecular Crystals. *Langmuir* **2007**, *23*, 11980–11985.
- (616) Held, G. Low-Energy Electron Diffraction Crystallography of Surfaces and Interfaces. *Bunsen-Magazin* **2010**, *12*, 124–131.
- (617) Bischoff, F.; Seufert, K.; Auwärter, W.; Joshi, S.; Vijayaraghavan, S.; Écija, D.; Diller, K.; Papageorgiou, A. C.; Fischer, S.; Allegretti, F.; *et al.* How Surface Bonding and Repulsive Interactions Cause Phase Transformations: Ordering of a Prototype Macrocyclic Compound on Ag(111). *ACS Nano* **2013**, *7*, 3139–3149.
- (618) Gross, L.; Moresco, F.; Ruffieux, P.; Gourdon, A.; Joachim, C.; Rieder, K.-H. Tailoring Molecular Self-Organization by Chemical Synthesis: Hexaphenylbenzene, Hexa-Peri-Hexabenzocoronene, and Derivatives on Cu (111). *Phys. Rev. B* **2005**, *71*, 165428.
- (619) Yoshida, Y.; Yang, H.-H.; Huang, H.-S.; Guan, S.-Y.; Yanagisawa, S.; Yokosuka, T.; Lin, M.-T.; Su, W.-B.; Chang, C.-S.; Hoffmann, G.; *et al.* Scanning Tunneling Microscopy/spectroscopy
-

- of Picene Thin Films Formed on Ag(111). *J. Chem. Phys.* **2014**, *141*, 114701.
- (620) Park, J.; Kim, K. Y.; Chung, K.-H.; Yoon, J. K.; Kim, H.; Han, S.; Kahng, S.-J. Interchain Interactions Mediated by Br Adsorbates in Arrays of Metal–Organic Hybrid Chains on Ag(111). *J. Phys. Chem. C* **2011**, *115*, 14834–14838.
- (621) Fan, Q.; Wang, C.; Liu, L.; Han, Y.; Zhao, J.; Zhu, J.; Kuttner, J.; Hilt, G.; Gottfried, J. M. Covalent, Organometallic, and Halogen-Bonded Nanomeshes from Tetrabromo-Terphenyl by Surface-Assisted Synthesis on Cu(111). *J. Phys. Chem. C* **2014**, *118*, 13018–13025.
- (622) Sherwood, P. M. A. X-Ray Photoelectron Spectroscopic Studies of Some Iodine Compounds. *J. Chem. Soc. Faraday Trans. 2* **1976**, *72*, 1805–1820.
- (623) Gaarenstroom, S. W.; Winograd, N. Initial and Final State Effects in the ESCA Spectra of Cadmium and Silver Oxides. *J. Chem. Phys.* **1977**, *67*, 3500.
- (624) Wertheim, G. K.; DiCenzo, S. B.; Buchanan, D. N. E. Core-Electron Spectroscopy of Adsorbate Ions: Iodine on Ag(111). *Phys. Rev. B* **1982**, *25*, 3020–3025.
- (625) Castro, M. E.; Pressley, L. A.; Kiss, J.; Pylant, E. D.; Jo, S. K.; Zhou, X. L.; White, J. M. Adsorption and Decomposition of Trifluoroiodomethane on Clean and Iodine-Precovered silver(111). *J. Phys. Chem.* **1993**, *97*, 8476–8484.
- (626) Rais, D.; Mingos, D. M. P.; Vilar, R.; White, A. J. P.; Williams, D. J. π -Coordination of Silver and Copper to Mercury Bis-Alkynyls: Synthesis and Structural Characterization. *Organometallics* **2000**, *19*, 5209–5217.
- (627) Forstmann, F.; Berndt, W.; Büttner, P. Determination of the Adsorption Site by Low-Energy Electron Diffraction for Iodine on Silver (111). *Phys. Rev. Lett.* **1973**, *30*, 17–19.
- (628) Bardi, U.; Rovida, G. Leed, Aes and Thermal Desorption Study of Iodine Chemisorption on the Silver (100), (111) and (110) Faces. *Surf. Sci.* **1983**, *128*, 145–168.
- (629) Eliseeva, S. V.; Bünzli, J.-C. G. Rare Earths: Jewels for Functional Materials of the Future. *New J. Chem.* **2011**, *35*, 1165–1176.
- (630) Bünzli, J.-C. G. Lanthanide Coordination Chemistry: From Old Concepts to Coordination Polymers. *J. Coord. Chem.* **2014**, *67*, 3706–3733.
- (631) Urgel, J. I.; Écija, D.; Auwärter, W.; Barth, J. V. Controlled Manipulation of Gadolinium-Coordinated Supramolecules by Low-Temperature Scanning Tunneling Microscopy. *Nano Lett.* **2014**, *14*, 1369–1373.
- (632) Kobayashi, N.; Sasaki, M.; Nomoto, K. Stable Peri-Xanthenoxanthene Thin-Film Transistors with Efficient Carrier Injection. *Chem. Mater.* **2009**, *21*, 552–556.
- (633) Sony develops a “rollable” OLED display <http://www.sonyinsider.com/2010/05/26/sony-develops-a-rollable-oled-display/> (accessed Mar 16, 2016).
- (634) Stoessel, P.; Buesing, A.; Heil, H. Novel Materials for Organic Electroluminescent Devices. US 20100322867A1, 2010.
- (635) Asari, T.; Kobayashi, N.; Naito, T.; Inabe, T. Charge-Transfer Complexes of PXX (PXX = 6, 12-Dioxaanthanthrene). The Formal Charge and Molecular Geometry. *Bull. Chem. Soc. Jpn.* **2001**, *74*, 53–58.
- (636) Hjorth, M.; Thorup, N.; Frederiksen, P.; Bechgaard, K.; Undén, A.; Paulsen, G. B.; Nielsen, R. I.; Olsen, C. E.; Pedersen, C.; Stidsen, C. E. Crystal Structure of a Complex of Peri-

- Xanthenoxanthenone (PXX) with Tetracyanoquinodimethane (TCNQ). *Acta Chem. Scand.* **1994**, *48*, 139–143.
- (637) Bünzly, H.; Decker, H. Zur Oxydation Des B, β -Dinaphtols. *Ber. Dtsch. Chem. Ges.* **1905**, *38*, 3268–3273.
- (638) Pummerer, R.; Frankfurter, F. Über Ein Neues Organisches Radikal. I. Mitteilung Über Die Oxydation Der Phenole. *Ber. Dtsch. Chem. Ges.* **1914**, *47*, 1472–1493.
- (639) Pummerer, R.; Rieche, A. Über Aromatische Peroxyde Und Einwertigen Sauerstoff. (IX. Mitteilung) Über Die Oxydation Der Phenole). *Ber. Dtsch. Chem. Ges. A/B* **1926**, *59*, 2161–2175.
- (640) Pummerer, R.; Prell, E.; Rieche, A. Darstellung von Binaphthylendioxyd. *Ber. Dtsch. Chem. Ges. A/B* **1926**, *59*, 2159–2161.
- (641) Zhao, J.; Wang, Y.; He, Y.; Liu, L.; Zhu, Q. Cu-Catalyzed Oxidative C(sp²)-H Cycloetherification of O-Arylphenols for the Preparation of Dibenzofurans. *Org. Lett.* **2012**, *14*, 1078–1081.
- (642) Zhao, J.; Zhang, Q.; Liu, L.; He, Y.; Li, J.; Li, J.; Zhu, Q. CuI-Mediated Sequential Iodination/Cycloetherification of O-Arylphenols: Synthesis of 2- or 4-Iododibenzofurans and Mechanistic Studies. *Org. Lett.* **2012**, *14*, 5362–5365.
- (643) Fernández-Torrente, I.; Franke, K. J.; Pascual, J. I. Vibrational Kondo Effect in Pure Organic Charge-Transfer Assemblies. *Phys. Rev. Lett.* **2008**, *101*, 217203.
- (644) Gonzalez-Lakunza, N.; Fernández-Torrente, I.; Franke, K. J.; Lorente, N.; Arnau, A.; Pascual, J. I. Formation of Dispersive Hybrid Bands at an Organic-Metal Interface. *Phys. Rev. Lett.* **2008**, *100*, 156805.
- (645) Fernández-Torrente, I.; Kreikemeyer-Lorenzo, D.; Stróżecka, A.; Franke, K. J.; Pascual, J. I. Gating the Charge State of Single Molecules by Local Electric Fields. *Phys. Rev. Lett.* **2012**, *108*, 036801.
- (646) Pope, M.; Kallmann, H. P.; Magnante, P. Electroluminescence in Organic Crystals. *J. Chem. Phys.* **1963**, *38*, 2042–2043.
- (647) Anthony, J. E. Functionalized Acenes and Heteroacenes for Organic Electronics. *Chem. Rev.* **2006**, *106*, 5028–5048.
- (648) Wang, C.; Dong, H.; Hu, W.; Liu, Y.; Zhu, D. Semiconducting π -Conjugated Systems in Field-Effect Transistors: A Material Odyssey of Organic Electronics. *Chem. Rev.* **2012**, *112*, 2208–2267.
- (649) Babu, S. S.; Praveen, V. K.; Ajayaghosh, A. Functional π -Gelators and Their Applications. *Chem. Rev.* **2014**, *114*, 1973–2129.
- (650) Chakrabarty, R.; Mukherjee, P. S.; Stang, P. J. Supramolecular Coordination: Self-Assembly of Finite Two- and Three-Dimensional Ensembles. *Chem. Rev.* **2011**, *111*, 6810–6918.
- (651) Tanaka, T.; Osuka, A. Conjugated Porphyrin Arrays: Synthesis, Properties and Applications for Functional Materials. *Chem. Soc. Rev.* **2015**, *44*, 943–969.
- (652) Tsuda, A.; Osuka, A. Fully Conjugated Porphyrin Tapes with Electronic Absorption Bands That Reach into Infrared. *Science* **2001**, *293*, 79–82.
- (653) Anderson, H. L.; Martin, S. J.; Bradley, D. D. C. Synthesis and Third-Order Nonlinear Optical

- Properties of a Conjugated Porphyrin Polymer. *Angew. Chem. Int. Ed.* **1994**, *33*, 655–657.
- (654) Wiengarten, A.; Lloyd, J. A.; Seufert, K.; Reichert, J.; Auwärter, W.; Han, R.; Duncan, D. A.; Allegretti, F.; Fischer, S.; Oh, S. C.; *et al.* Surface-Assisted Cyclodehydrogenation; Break the Symmetry, Enhance the Selectivity. *Chem. Eur. J.* **2015**, *21*, 12285–12290.
- (655) Stewart, J. J. P. Optimization of Parameters for Semiempirical Methods V: Modification of NDDO Approximations and Application to 70 Elements. *J. Mol. Model.* **2007**, *13*, 1173–1213.
- (656) Wang, X.; Ervithayasuporn, V.; Zhang, Y.; Kawakami, Y. Reversible Self-Assembly of Dendrimer Based on Polyhedral Oligomeric Silsesquioxanes (POSS). *Chem. Commun.* **2011**, *47*, 1282–1284.
- (657) Cantrill, S. J.; Youn, G. J.; Stoddart, J. F.; Williams, D. J. Supramolecular Daisy Chains. *J. Org. Chem.* **2001**, *66*, 6857–6872.
- (658) Wang, F.; Han, C.; He, C.; Zhou, Q.; Jinqiang Zhang; Wang, C.; Li, N.; Huang, F. Self-Sorting Organization of Two Heteroditopic Monomers to Supramolecular Alternating Copolymers. *J. Am. Chem. Soc.* **2008**, *130*, 11254–11255.
- (659) Ashton, P. R.; Ballardini, R.; Balzani, V.; Fyfe, M. C. T.; Gandolfi, M. T.; Martínez-Díaz, M.-V.; Morosini, M.; Schiavo, C.; Shibata, K.; Stoddart, J. F.; *et al.* Selective Self-Assembly and Acid-Base Controlled De-/Rethreading of Pseudorotaxanes Constructed Using Multiple Recognition Motifs. *Chem. Eur. J.* **1998**, *4*, 2332–2341.
- (660) Sasabe, H.; Kihara, N.; Furusho, Y.; Mizuno, K.; Ogawa, A.; Takata, T. End-Capping of a Pseudorotaxane via Diels-Alder Reaction for the Construction of C60-Terminated [2]Rotaxanes. *Org. Lett.* **2004**, *6*, 3957–3960.
- (661) Gibson, H. W.; Ge, Z.; Jones, J. W.; Harich, K.; Pederson, A.; Dorn, H. C. Supramacromolecular Chemistry: Self-Assembly of Polystyrene-Based Multi-Armed Pseudorotaxane Star Polymers from Multi-Topic C60 Derivatives. *J. Polym. Sci. Part A Polym. Chem.* **2009**, *47*, 6472–6495.
- (662) Laha, J. K.; Dhanalekshmi, S.; Taniguchi, M.; Ambroise, A.; Lindsey, J. S. A Scalable Synthesis of Meso-Substituted Dipyrrromethanes. *Org. Process Res. Dev.* **2003**, *7*, 799–812.
- (663) Gou, F.; Jiang, X.; Fang, R.; Jing, H.; Zhu, Z. Strategy to Improve Photovoltaic Performance of DSSC Sensitized by Zinc Porphyrin Using Salicylic Acid as a Tridentate Anchoring Group. *ACS Appl. Mater. Interfaces* **2014**, *6*, 6697–6703.
- (664) Ye, Q.; Chen, S.; Zhu, D.; Lu, X.; Lu, Q. Preparation of Aggregation-Induced Emission Dots for Long-Term Two-Photon Cell Imaging. *J. Mater. Chem. B* **2015**, *3*, 3091–3097.
- (665) Gupta, J.; Vadukumpully, S.; Valiyaveetil, S. Synthesis and Property Studies of Linear and Kinked Poly(pyreneethynylene)s. *Polymer* **2010**, *51*, 5078–5086.
- (666) Suenaga, H.; Nakashima, K.; Mizuno, T.; Takeuchi, M.; Hamachi, I.; Shinkai, S. Pyrenylboronic Acids as a Novel Entry for Photochemical DNA Cleavage: Diradical-Forming Pyrene-1,6-Diylidiboronic Acid Mimics the Cleavage Mechanism of Eneidyne Antitumor Antibiotics. *J. Chem. Soc., Perkin Trans. 1* **1998**, *20*, 1263–1267.
- (667) Xiao, J.; Xu, J.; Cui, S.; Liu, H.; Wang, S.; Li, Y. Supramolecular Helix of an Amphiphilic Pyrene Derivative Induced by Chiral Tryptophan through Electrostatic Interactions. *Org. Lett.* **2008**, *10*, 645–648.
- (668) Wagner, R. W.; Ciringh, Y.; Clausen, C.; Lindsey, J. S. Investigation and Refinement of

- Palladium-Coupling Conditions for the Synthesis of Diarylethyne-Linked Multiporphyrin Arrays. *Chem. Mater.* **1999**, *11*, 2974–2983.
- (669) Wagner, R. W.; Johnson, T. E.; Li, F.; Lindsey, J. S. Synthesis of Ethyne-Linked or Butadiyne-Linked Porphyrin Arrays Using Mild, Copper-Free, Pd-Mediated Coupling Reactions. *J. Org. Chem.* **1995**, *60*, 5266–5273.
- (670) Wessendorf, F.; Gnichwitz, J. F.; Sarova, G. H.; Hager, K.; Hartnagel, U.; Guldi, D. M.; Hirsch, A. Implementation of a Hamilton-Receptor-Based Hydrogen-Bonding Motif toward a New Electron Donor-Acceptor Prototype: Electron versus Energy Transfer. *J. Am. Chem. Soc.* **2007**, *129*, 16057–16071.
- (671) Yan, X.; Goodson, T.; Imaoka, T.; Yamamoto, K. Up-Converted Emission in a Series of Phenylazomethine Dendrimers with a Porphyrin Core. *J. Phys. Chem. B* **2005**, *109*, 9321–9329.
- (672) Daly, D.; Al-Sabi, A.; Kinsella, G. K.; Nolan, K.; Dolly, J. O. Porphyrin Derivatives as Potent and Selective Blockers of Neuronal Kv1 Channels. *Chem. Commun.* **2015**, *51*, 1066–1069.
- (673) Naik, A.; Rubbiani, R.; Gasser, G.; Spingler, B. Visible-Light-Induced Annihilation of Tumor Cells with Platinum-Porphyrin Conjugates. *Angew. Chem. Int. Ed.* **2014**, *53*, 6938–6941.
- (674) Ren, Q.-Z.; Yao, Y.; Ding, X.-J.; Hou, Z.-S.; Yan, D.-Y. Phase-Transfer of Porphyrins by Polypeptide-Containing Hyperbranched Polymers and a Novel iron(III) Porphyrin Biomimetic Catalys. *Chem. Commun.* **2009**, 4732–4734.
- (675) Bernhardt, S.; Kastler, M.; Enkelmann, V.; Baumgarten, M.; Müllen, K. Pyrene as Chromophore and Electrophore: Encapsulation in a Rigid Polyphenylene Shell. *Chem. Eur. J.* **2006**, *12*, 6117–6128.
- (676) Zhang, H. C.; Guo, E. Q.; Zhang, Y. L.; Ren, P. H.; Yang, W. J. Donor-Acceptor-Substituted Anthracene-Centered Cruciforms: Synthesis, Enhanced Two-Photon Absorptions, and Spatially Separated Frontier Molecular Orbitals. *Chem. Mater.* **2009**, *21*, 5125–5135.
- (677) Stern, D.; Finkelmeier, N.; Meindl, K.; Henn, J.; Stalke, D. Consecutive Donor-Base Exchange in Anthracenyllithium Compounds. *Angew. Chem. Int. Ed.* **2010**, *49*, 6869–6872.
- (678) Lamm, J.-H.; Glatthor, J.; Weddelling, J.-H.; Mix, A.; Chmiel, J.; Neumann, B.; Stammler, H.-G.; Mitzel, N. W. Polyalkynylanthracenes – Syntheses, Structures and Their Behaviour towards UV Irradiation. *Org. Biomol. Chem.* **2014**, *12*, 7355.
- (679) Lee, C. H.; S. Lindsey, J. One-Flask Synthesis of Meso-Substituted Dipyromethanes and Their Application in the Synthesis of Trans-Substituted Porphyrin Building Blocks. *Tetrahedron* **1994**, *50*, 11427–11440.
- (680) Hu, J.; Lu, Y.; Li, Y.; Zhou, J. S. Highly Active Catalysts of Bisphosphine Oxides for Asymmetric Heck Reaction. *Chem. Commun.* **2013**, *49*, 9425–9427.
- (681) Hoang, T. N. Y.; Humbert-Droz, M.; Dutronc, T.; Gué'nee, L.; Besnard, C.; Pigu'et, C. A Polyaromatic Terdentate Binding Unit with Fused 5,6-Membered Chelates for Complexing S-, P-, D-, and F-Block Cations. *Inorg. Chem.* **2013**, *52*, 5570–5580.
- (682) Wu, W.; Sun, J.; Cui, X.; Zhao, J. Observation of the Room Temperature Phosphorescence of Bodipy in Visible Light-Harvesting Ru(II) Polyimine Complexes and Application as Triplet Photosensitizers for Triplet–triplet-Annihilation Upconversion and Photocatalytic Oxidation. *J. Mater. Chem. C* **2013**, *1*, 4577–4589.

-
- (683) Plater, M. J.; Aiken, S.; Bourhill, G. A New Synthetic Route to Donor-Acceptor Porphyrins. *Tetrahedron* **2002**, *58*, 2405–2413.
- (684) Bonifazi, D.; Accorsi, G.; Armaroli, N.; Song, F.; Palkar, A.; Echegoyen, L.; Scholl, M.; Seiler, P.; Jaun, B.; Diederich, F. Oligoporphyrin Arrays Conjugated to [60]Fullerene: Preparation, NMR Analysis, and Photophysical and Electrochemical Properties. *Helv. Chim. Acta* **2005**, *88*, 1839–1884.
- (685) Sprafke, J. K.; Kondratuk, D. V.; Wykes, M.; Thompson, A. L.; Hoffmann, M.; Drevinskas, R.; Chen, W.-H.; Yong, C. K.; Kärnbratt, J.; Bullock, J. E.; *et al.* Belt-Shaped π -Systems: Relating Geometry to Electronic Structure in a Six-Porphyrin Nanoring. *J. Am. Chem. Soc.* **2011**, *133*, 17262–17273.
- (686) Lahaye, D.; Muthukumaran, K.; Hung, C. H.; Gryko, D.; Reboucas, J. S.; Spasojevic, I.; Batinic-Haberle, I.; Lindsey, J. S. Design and Synthesis of Manganese Porphyrins with Tailored Lipophilicity: Investigation of Redox Properties and Superoxide Dismutase Activity. *Bioorganic Med. Chem.* **2007**, *15*, 7066–7086.
- (687) Goldberg, P. K.; Pundsack, T. J.; Splan, K. E. Photophysical Investigation of Neutral and Diprotonated Free-Base Bis(Arylethynyl)porphyrins. *J. Phys. Chem. A* **2011**, *115*, 10452–10460.
- (688) Coutts, I. G. C.; Allcock, R. W. Preparation of Aminoalkyl Aryl Ether Pharmaceutical Fungicides. WO 2002024619, 2002.
- (689) Lu, X.-Q.; Guo, Y.; Chen, Q.-Y. Efficient Synthesis of Meso-Meso-Linked Diporphyrins by Nickel(0)-Mediated Ullmann Homocoupling. *Synlett* **2011**, *2011*, 77–80.
- (690) Locos, O. B.; Arnold, D. P. The Heck Reaction for Porphyrin Functionalisation: Synthesis of Meso-Alkenyl Monoporphyrins and Palladium-Catalysed Formation of Unprecedented Meso-Beta Ethene-Linked Diporphyrins. *Org. Biomol. Chem.* **2006**, *4*, 902–916.
- (691) Sooambar, C.; Troiani, V.; Bruno, C.; Marcaccio, M.; Paolucci, F.; Listorti, A.; Belbakra, A.; Armaroli, N.; Magistrato, A.; De Zorzi, R.; *et al.* Synthesis, Photophysical, Electrochemical, and Electrochemiluminescent Properties of 5,15-bis(9-Anthracenyl)porphyrin Derivatives. *Org. Biomol. Chem.* **2009**, *7*, 2402–2413.
- (692) Davis, M.; Senge, M. O.; Locos, O. B. Anthracenylporphyrins. *Z. Naturforsch. B* **2010**, *65*, 1472–1484.
- (693) Kabsch, W. XDS. *Acta Cryst. D* **2010**, *66*, 125–132.
- (694) Burla, M. C.; Caliandro, R.; Carrozzini, B.; Cascarano, G. L.; Cuocci, C.; Giacovazzo, C.; Mallamo, M.; Mazzone, A.; Polidori, G. Crystal Structure Determination and Refinement via SIR2014. *J. Appl. Cryst.* **2015**, *48*, 306–309.
- (695) Sheldrick, G. M. A Short History of SHELX. *Acta Crystallogr. Sect. A Found. Crystallogr.* **2008**, *64*, 112–122.
- (696) Emsley, P.; Cowtan, K. Coot: Model-Building Tools for Molecular Graphics. *Acta Cryst. D* **2004**, *60*, 2126–2132.
- (697) Boyle, P. D. COSET: A Program for Deriving and Testing Merohedral and Pseudo-Merohedral Twin Laws. *J. Appl. Crystallogr.* **2014**, *47*, 467–470.
-

Curriculum Vitae

- 1988** Born on February 23rd, in Rijeka (Croatia)
- 2004-2006** International Baccalaureate, Adriatic United World College
- 2006-2011** Università degli Studi di Trieste, Diploma Studies in Chemical and Pharmaceutical Technology
- 2011** Diploma work under the supervision of Prof. *Maurizio Prato* and Prof. *Tatiana Da Ros*
- 2012-2016** Università degli Studi di Trieste
Ph.D. in Chemical Sciences under the direction of Prof. *Maurizio Prato* and Prof. *Davide Bonifazi* "Tailoring Organic Matter: From Molecular Design To Functional Supramolecular Species"
- 2014-2015** The Broad Institute of MIT and Harvard University
Visiting Scholar, Design and synthesis of bias ligands for the D2R
- 2014-2015** Harvard University
Courses in Organic Chemistry, Organic Chemistry and Synthesis of Small Molecules
- 2012 and 2015** Università degli Studi di Trieste, 'Cultore della Materia' in Organic Chemistry, Teaching assistant in 'Fondamenti di Chimica Organica' e 'Chimica Organica Avanzata'

Publications

- (1) Đorđević, L.; Marangoni, T.; Miletić, T.; Rubio-Magnieto, J.; Mohanraj, J.; Amenitsch, H.; Pasini, D.; Liaros, N.; Couris, S.; Armaroli, N.; Surin, M., Bonifazi D. Solvent Molding of Organic Morphologies Made of Supramolecular Chiral Polymers. *J. Am. Chem. Soc.* **2015**, *137*, 8150–8160.
- (2) Pacor, S.; Grillo, A.; Đorđević, L.; Zorzet, S.; Lucafò, M.; Da Ros, T.; Prato, M.; Sava, G. Effects of Two Fullerene Derivatives on Monocytes and Macrophages. *Biomed Res. Int.* **2015**, article ID 915130, doi:10.1155/2015/915130.
- (3) Arcudi, F.; Đorđević, L.; Prato, M. Synthesis, Separation, and Characterization of Small and Highly Fluorescent Nitrogen-Doped Carbon NanoDots. *Angew. Chem. Int. Ed.* **2016**, *55*, 2107–2112.
- (4) Đorđević, L.; Marangoni, T.; De Leo, F.; Papagiannouli, I.; Aloukos, P.; Couris, S.; Pavoni, E.; Monti, F.; Armaroli, N.; Prato, M.; Bonifazi D. [60]Fullerene-Porphyrin [n]Pseudorotaxanes: Self-Assembly, Photophysics and Third-Order NLO Responses. *Phys. Chem. Chem. Phys.* **2016**, doi: 10.1039/C5CP06055A.
- (5) Đorđević, L.; Demitri, N.; Bonifazi, D. Solvent-Dependent Moulding of Porphyrin-Based Nanostructures: Solid State, Solution and on Surface Self-Assembly. *Supramol. Chem.* **2016**, doi: 10.1080/10610278.2016.1158407.
- (6) Kaposi T., Joshi S., Hoh T., Wiengarten A., Seufert K. Paszkiewicz M., Klappenberger F., Ecija D., Auwärter W., Đorđević L., Marangoni T., Davide Bonifazi D., Barth J. V. Supramolecular spangling, crocheting and knitting of functionalized pyrene molecules on a silver surface, *submitted*.
- (7) Milano D., Đorđević L., Zangrando E., Iengo E., Tecilla P. Synthesis and characterization of a hydrophilic conjugated 4+4 Re(I)-porphyrin metallacycle, *manuscript in preparation*.
- (8) Cirera B., Đorđević L., Otero R., Gallego J. M., Bonifazi D., Miranda R., Ecija D. Lanthanide-carboxylate nanomeshes with tunable cavity size and coordination node, *manuscript in preparation*.
- (9) Đorđević L., Marangoni T., Liu M., De Zorzi R., Geremia S., Minoia A., Lazzaroni, R., Ishida Y., Bonifazi D. Templating porphyrin anisotropy via magnetically-aligned carbon nanotubes, *manuscript in preparation*.
- (10) Arcudi F., Strauss V., Đorđević L., Prato M., Guldi D. M. Carbon nanodots with porphyrin antennae: synthesis, characterization and photophysical properties, *manuscript in preparation*.
- (11) Đorđević L., Bonifazi D. Breaking molecular symmetries at interfaces: new stereoisomerisms, *manuscript in preparation*.
- (12) Bonifazi D., Đorđević L., Miletić T., Stassen D. Oxygen-doping of polycyclic aromatic hydrocarbons, *manuscript in preparation*.
- (13) Milano D., Đorđević L., Demitri, N.; Bonifazi, D. π -extension of pyrene via O annulation reaction, *manuscript in preparation*.